Politecnico di Milano

Department of Aerospace Science and Technology
Doctoral Programme in Aerospace Engineering

Skin-friction drag reduction in turbulent flows: physical understanding and practical applications

Doctoral dissertation of:
Federica Gattere

Supervisor:
Prof. Maurizio Quadrio

Academic year 2023-2024 - Cycle XXXVII

The research activities underlying this thesis were made possible thanks to the financial support received under the European project PON FSE REACT-EU, and the resources allocated by Ministerial Decree No. 1061 of August 10, 2021, for active and accredited doctoral programs in the framework of the XXXVII cycle.

Preface

This Thesis deals with turbulent flows, mostly wall-bounded flows, with a special focus on skin-friction drag reduction. It takes a global stance at the topic, by making new attempts to understand the elusive physics behind drag reduction with novel methods, and by addressing some of the many practical obstacles that still prevent drag reduction techniques to be deployed in applications.

The document is structured in two parts. Part I is an original summary of the work, where its main ideas and results are presented. It is organized in four Chapters. Chapter 1 presents the main research questions and provides a broad overview of the entire thesis. Chapter 2 introduces novel tools to give new insights on the physical mechanisms driving wall-bounded turbulent flows and their changes by skin-friction drag reduction. Chapter 3 addresses a number of practical aspects that need to be considered before drag reduction techniques become a viable strategy in applications. Lastly, Chapter 4 provides a concluding discussion and delineates possible future developments of the present work. The subsequent Part II details each part of the work through articles, which are presently at various stages of the editorial process. The list of papers included in the Thesis is reported below, along with the respective publication status and the description of my own contribution to each work.

Paper 1 Gattere, F., Codrignani A., Gatti, D. & Quadrio, M. Mean Impulse Response in a Turbulent Channel Flow. *Journal of Fluid Mechanics* (in preparation).
Contribution: The idea of the work started back with the Master thesis of A. Codrignani. I wrote missing codes, run the corresponding simulations, and furthered the simulations already performed. I improved the post-processing analysis, and investigated the physical implications of the results. I developed the codes for the final verification against DNS results. I wrote the current manuscript together with the co-authors.

Paper 2 Gattere, F., Chiarini, A., Gallorini, E. & Quadrio, M. 2023 Structure function tensor equations with triple decomposition. *Journal of Fluid Mechanics* **960**, A7.

Contribution: I started this work with my Master thesis, by extending the code for the anisotropic generalised Kolmogorov equations to compute its phase-aware variance, and by running part of the simulations. I investigated the results, wrote the first draft and the rebuttal letters to the reviewers, together with the co-authors.

Paper 3 Quadrio, M., Castelletti, M., Chiarini, A. & Gattere, F. On the optimal period of spanwise forcing for turbulent drag reduction. *Journal of Fluid Mechanics* (in preparation).
Contribution: I conceptualized this work together with A. Chiarini and M. Quadrio. I performed the simulations and handled the post-processing of the results. I investigated the results and wrote the manuscript together with the co-authors.

Paper 4 Gatti, D., Quadrio, M., Chiarini A., Gattere, F. & Pirozzoli, S. Turbulent skin-friction drag reduction via spanwise forcing at high Reynolds number. *Journal of Fluid Mechanics* (under review).
Contribution: I performed the preliminary analysis of the data and decided what simulations to perform together with A. Chiarini. I reviewed and edited the manuscript together with the co-authors.

Paper 5 Gattere, F., Zanolini, M., Gatti, D., Bernardini, M. & Quadrio, M. 2024 Turbulent drag reduction with streamwise-travelling waves in the compressible regime. *Journal of Fluid Mechanics* **987**, A30.
Contribution: This work started with the Master thesis of M. Zanolini. I run most of the simulations and performed part of the validation of the code. I developed the post-processing of the data and analyzed the results together with M. Zanolini. I wrote the first draft of the manuscript. I investigated the implications of the different comparison and replied to the reviewers together with D. Gatti, M. Bernardini e M. Quadrio.

Paper 6 Luchini, P., Gatti, D., Chiarini, A., Gattere, F., Atzori, M. & Quadrio, M. A simple and efficient immersed-boundary method for the incompressible Navier–Stokes equations. *Journal of Computational Physics* (under review).
Contribution: I prepared the literature review on the topic and wrote the Introduction together with A. Chiarini. Together with A. Chiarini and D. Gatti, I wrote the Methods section starting from an informal report written by P. Luchini. I reviewed and edited the manuscript together with the co-authors.

Paper 7 Gattere, F., Chiarini, A. & Quadrio, M. 2022 Dimples for Skin-Friction Drag Reduction: Status and Perspectives. *Fluids* **7** (7), 240.

Contribution: I conceptualized the work together with the co-authors. I prepared the literature review, and wrote the first draft of the manuscript. I replied to the reviewers together with the co-authors.

Paper 8 Cacciatori, L., Brignoli, C., Mele, B., Gattere, F., Monti, C.M. & Quadrio, M. 2022 Drag Reduction by Riblets on a Commercial UAV. *Applied Science* **12** (10), 5070.
Contribution: I co-supervised L. Cacciatori and C. Brignoli during their Master thesis. I reviewed and edited the first draft and I replied to the reviewers together with M. Quadrio.

Conferences

Part of this Thesis has been already presented at international conferences. Part of the conference work is only briefly mentioned in this Thesis. My name is underlined whenever I was the presenting author.

- Gattere, F., Chiarini, A., Cavallazzi, G. M., Rossi, A., Gatti, D., Luchini, P. & Quadrio, M. Towards Reliable and Cost-Effective DNS over Riblets. *European Drag Reduction and Flow Control Meeting (EDRFCM 2022)*, Paris, France 6-9 Sept 2022.

- Gattere, F., Chiarini, A., Zanolini M., Gatti, D., Bernardini M. & Quadrio, M. Turbulent drag reduction using spanwise forcing in compressible regime. *European Drag Reduction and Flow Control Meeting (EDRFCM 2022)*, Paris, France 6-9 Sept 2022.

- Gattere, F., Chiarini, A., Gallorini, E. & Quadrio, M. Scale-space budget equations for inhomogeneous (quasi-)periodic turbulent flows. *14th European Fluid Mechanics Conference (EFMC14)*, Athens, Greece 13-16 Sept 2022.

- Gattere, F., Chiarini, A., Zanolini, M., Gatti, D., Bernardini M. & Quadrio, M. Turbulent Drag Reduction with Streamwise Travelling Waves in Compressible Regime. *18th European Turbulence Conference (ETC18)*, Valencia, Spain 4-6 Sept 2023.

- Quadrio, M., Chiarini A., Conforti, A. & Gattere, F. Spanwise forcing for turbulent drag reduction: the meaning of the optimal oscillation period. *18th European Turbulence Conference (ETC18)*, Valencia, Spain 4-6 Sept 2023.

- Gatti, D., Cipelli S., Gattere F., Chiarini, A., Luchini P. & Quadrio, M. Accurate and Efficient Direct Numerical Simulation of Turbulent Drag Reduction via Riblets. *18th European Turbulence Conference (ETC18)*, Valencia, Spain 4-6 Sept 2023.

- Gattere, F., Codrignani, A., Gatti, D. & Quadrio, M. Mean Impulse Response in a Turbulent Channel Flow. *26th International Congress of Theoretical and Applied Mechanics (ICTAM 2024)*, Daegu, Republic of Korea 25-30 Aug 2024.

- Gattere, F., Chiarini, A., Castelletti, M. & Quadrio, M. On the Optimal Period of Spanwise Forcing for Turbulent Drag Reduction. *European Drag*

Reduction and Flow Control Meeting (EDRFCM 2024), Torino, Italy 10-13 Sept 2024.

- Cipelli S., Quadrio, M., Gattere, F., Chiarini, A., Luchini, P. & Gatti, D. Sinusoidal Riblets for Turbulent Drag Reduction. *European Drag Reduction and Flow Control Meeting (EDRFCM 2024)*, Torino, Italy 10-13 Sept 2024.

- Gatti, D., Quadrio, M., Chiarini, A., Gattere, F. & Pirozzoli, S. Numerical Study of Turbulent Skin-friction Drag Reduction via Spawise Forcing at Large Values of Reynolds Number. *European Drag Reduction and Flow Control Meeting (EDRFCM 2024)*, Torino, Italy 10-13 Sept 2024.

- Gattere, F., Codrignani, A., Gatti, D. & Quadrio, M. Mean Impulse Response in a Turbulent Channel Flow. *1st European Fluid Dynamics Conference (EFDC1)*, Aachen, Germany 16-20 Sept 2024.

Contents

Part I

Skin-friction drag reduction: physics and applications

1 Introduction

Turbulence is *ubiquitous* in natural and artificial flows; fathoming the physics behind turbulent flows and learning how to tame it is a long-standing effort in fluid mechanics. Turbulent flows are complex, especially those with practical interest that are usually confined by solid boundaries; they are strongly anisotropic and inhomogeneous, and have a finite (yet often large) Reynolds number that leads to an incomplete separation of scales. The nature of turbulent flows is *chaotic*; one can only hope to describe them statistically. However, for wall-bounded flows, a quasi-deterministic description of turbulence is also possible; some structures can be recognized through a random background, and their evolution is essentially deterministic. Turbulent flows are *multiscale*; fluctuations of different scales interact, and transfer energy (on average) from the large energy-containing scales embedding the geometrical information towards small dissipative local isotropic scales via a cascade mechanism. The presence of a solid wall also introduces the physical position as an additional independent variable; energy, beyond being transferred among scales, is transferred in space along the inhomogeneous directions, e.g. from the wall towards the bulk of the flow and vice versa. Turbulent flows possess a strong *non-linear* nature; non-linearity drives the energy cascade. However, linear mechanisms play a central role in the near-wall turbulence regeneration cycle. Turbulent flows are *diffusive*; through viscous mechanisms, small-scale fluctuations are spread and the transfer of momentum and energy is enhanced. In the presence of a wall, the diffusive nature of the turbulent flow results in more intense wall-shear stresses and a larger skin-friction drag than the laminar counterpart.

Owing to their complexity, anisotropy and inhomogeneity, wall-bounded turbulent flows can be studied with many approaches (see e.g. Pope, 2000; Davidson, 2004). Although Navier–Stokes equations are strongly non-linear, they are often studied after linearisation about a base flow. Linear mechanisms are key in the near-wall turbulent cycle; the streaks of streamwise velocity are due to quasi-streamwise vortices interacting with the mean velocity shear via a linear process. However, the self-sustainment of the cycle which regenerates the vortices from the streaks needs non-linearity (Reynolds & Tiedermann, 1967). Therefore, even if the linear behaviour of non-linear turbulent flows can be instructive, a complete

characterization needs the full non-linear description. Statistics are probably the best way to represent turbulence: despite turbulent flows are not deterministic, their statistics are. The simplest is the mean, i.e. the average over time (and usually homogeneous directions), useful to decompose the complete flow field into a mean field and turbulent fluctuations. Higher-order moments further enrich the description of the statistical distribution (e.g., the velocity here). For instance, the variance measures how data are spread around the mean, the skewness measures the asymmetry around the mean, and the kurtosis measures the importance of extreme events in the tails of the distribution. One-point statistics measure the intensity of the fluctuations, and they are usually associated to physical space where quantities are characterized in their evolution along a certain inhomogeneous direction. Two-point statistics, such as spectra (in homogeneous directions only) and correlations, indicate their spatial scales.

An alternative approach to statistics involves the identification of structures which share a sort of coherency compared to the background random turbulence and show a deterministic evolution (Robinson, 1991). The near-wall region is dominated by two classes of structures: streaks and quasi-streamwise vortices (QSV). The former are elongated and meandering regions of alternating streamwise low and high speed superimposed on the mean velocity, whereas the latter are vortical structures roughly aligned with the streamwise direction. Streaks and QSV are the two main actors of the self-sustaining cycle of the near-wall turbulence; through their mutual regeneration, turbulence is sustained. Vortices generate the low-speed and high-speed streaks by the interaction with the mean velocity profile, advecting low-streamwise velocity upwards and high-streamwise velocity downwards. In turn, QSV are generated by a transient growth of perturbations, driven either by the streaks instability or by the mean shear (Jiménez, 2018).

The complexity of turbulent flows and the practical consequence of their properties in applications drive researchers towards the comprehension of the physical mechanism of turbulence and the discovery of ways to control it for specific purposes, such as reducing its harmful interaction with the wall, i.e. reducing the skin-friction drag. The current incomplete knowledge of the turbulence physics reflects into currently unsatisfactory drag reduction strategies.

Regardless of their significant room for improvement, both numerical and experimental studies have amply documented the effectiveness of some flow control techniques in decreasing skin-friction drag. Most of the studies (particularly numerical ones) seeking to understand the physics of turbulent flows and how they are modified by control are carried out in simple configurations such as internal flows, i.e. plane channel flows or circular pipe flows, in the incompressible regime and at low values of the Reynolds number. These features make it feasible to carry out computations using Direct Numerical Simulations (DNS), which resolve every scale of the flow and produce high-fidelity data without modelling errors.

However, practical applications for skin-friction drag reduction techniques include complex external flows, such as for example wind turbines and aircraft. Aeronautical applications are of particular interest. About 50% of a civil aircraft's drag comes from viscous effects caused by the turbulent boundary layer near the solid surface. So, an efficient drag reduction technology which develops even a tiny reduction would have huge economic and environmental benefits.

A highly promising approach to reduce skin-friction drag is spanwise forcing (Ricco *et al.*, 2021), which involves generating an unsteady spanwise cross flow that interacts with the near-wall turbulence, attenuating the turbulent activity and decreasing skin-friction drag. This spanwise motion can be achieved through various methods, including transverse oscillations of the wall (Quadrio, 2011), incorporation of rotating discs on the surface (Ricco & Hahn, 2013), or the use of plasma actuators (Choi *et al.*, 2011). Among spanwise forcing strategies, in-plane oscillation of the wall is an interesting category. The two simplest techniques are the oscillating wall (Jung *et al.*, 1992) which induces the wall to move in the spanwise direction with a harmonic time law and the steady waves (Viotti *et al.*, 2009) which impose a steady spanwise wall velocity that varies periodically in the streamwise direction. The most significant reduction in drag is attained when the two techniques are combined in the streamwise travelling waves of spanwise velocity (Quadrio *et al.*, 2009) involving periodic oscillation both in time and space. Besides achieving large drag reduction rates, travelling waves also yields considerable net benefit, meaning they are still convenient after the energy cost of the actuation is considered.

Before declaring a drag reduction technique as a viable option for implementation in practical applications, such as on commercial aircraft, some aspects must be investigated. Typical flight Reynolds number (Re) is on the order of $Re \approx 10^7$; thus, an important aspect to consider is the dependence of the drag reduction rate on the Reynolds number. Gatti & Quadrio (2016) measured the drag reduction achieved by streamwise-travelling waves of spanwise velocity (Quadrio *et al.*, 2009). They found out that drag reduction presents a mild logarithmic decrease with increasing Reynolds number and proposed a model to extrapolate the drag reduction at high Reynolds number from its value at low-Re. Even though the performance deteriorates, they measured that a significant level of drag reduction can still be attained at values of Re commonly encountered in aviation. Recently, Marusic *et al.* (2021) offered a new view for the exploitation of spanwise forcing at high Re, measuring an increasing drag reduction rate with Re thanks to the interaction of the near-wall forcing with the large-scale outer motions, whose importance grows with Re.

Also, typical commercial airplanes fly in transonic regime; a quantification of the compressibility effects on the drag reduction performance is needed through the study of the dependence of the drag reduction on the Mach number. Yao &

Hussain (2019) and Ruby & Foysi (2022) investigated the oscillating wall and the spanwise steady waves, respectively and found a large positive effect of the compressibility on drag reduction, hinting at a possible beneficial application of spanwise forcing in aeronautics.

Finally, practical applications feature complex surfaces with non-planar walls, where pressure drag comes into play and provides extra drag. Quadrio *et al.* (2022) studied travelling waves applied on a portion of a wing in transonic flight, finding that localized actuation has the potential to boost the aerodynamic efficiency of the whole aircraft via indirect effects on the pressure drag. These results are highly encouraging, suggesting the potential for the successful implementation of drag reduction strategies in real scenarios, particularly within the field of aviation.

This Thesis concerns itself with turbulent drag reduction and its practical applications. On one hand, novel tools are introduced to improve our understanding of the interaction between near-wall turbulence and an external forcing. On the other hand, skin-friction control is applied to flows of practical interest, to clarify a number of open issues related to a future industrial exploitation.

2 Understanding wall-bounded turbulence towards its control

The first goal of the present Thesis is to provide a comprehensive description of turbulent flows and of how they are modified by the skin-friction drag reduction control. We aim at disentangling the different mechanisms that drive turbulent flows with and without control, by analyzing their contributions separately.

Due to the key role of linear mechanisms in the creation of the structures of the near-wall turbulent cycle (Kim & Lim, 2000), an obvious starting point is separating the linear and non-linear dynamics of turbulence. To this aim, we exploit the linear impulse response function, a fundamental tool of signal theory. Within the limit of linearity, the response function informs us of positions and scales of forcing that are required to achieve a desired effect. Instead of following the classic approach where the equations of motion are linearized about either the laminar (Jovanović & Bamieh, 2005) or the mean turbulent (Högberg *et al.*, 2003) velocity profile, here we measure (numerically) the mean linear response function of a fully non-linear turbulent flow, to also account for the mean effect of turbulent diffusion (Luchini *et al.*, 2006). Even though turbulent flows are strongly non-linear, as long as they are forced by a sufficiently small perturbation, non-linearity does not kick in, and the linear response of the system can be isolated.

The linear response could be exploited in linear control algorithms as the best model of the plant. However, a complete description of turbulence and the quantitative assessment of drag reduction techniques require non-linear processes to be fully accounted for. For this, we resort to the anisotropic generalised Kolmogorov equations (AGKE) (Gatti *et al.*, 2020), which describe the production, redistribution, transfer and dissipation of turbulent fluctuations across both scales and positions, simultaneously. This is the most informative description of a turbulent flow from the standpoint of velocity second moments. To enable such a complete description when flow control comes into play, we start from the observation that most of the skin-friction drag reduction strategies possess a coherent, deterministic component. For instance, active techniques (which need extra energy to work) such travelling waves both in-plane (Quadrio *et al.*, 2009; Zhao *et al.*, 2004) and

of wall-deformation (Nakanishi *et al.*, 2012; Tomiyama & Fukagata, 2013) are coherent in time and/or space. Among passive techniques (which do not need extra energy) riblets (Walsh & Weinstein, 1979), dimples (Lienhart *et al.*, 2008), permeable substrates (Abderrahaman-Elena & García-Mayoral, 2017) and superhydrophobic surfaces (Daniello *et al.*, 2009) are organized roughness featuring a spatial periodic pattern. To understand how the coherent deterministic forcing interacts with the non-deterministic small-scale turbulence, the two contributions to the fluctuating field can be separated. Building upon a triple decomposition of the variables into mean, deterministic and stochastic components, we derive a phase-aware version of the AGKE which describes the dynamics of both the coherent and stochastic fields, as well as their interplay at each phase of the coherent pattern. This tool enables connecting scales and positions of the forcing to scales and positions at which turbulence is modified.

Lastly, in the context of active flow control, the need for an actuator involves substantial limitations to the control strategy. For example, given a mechanical system to create a spanwise motion of the wall, the penetration depth of the induced motion cannot be chosen at will. Here, we propose to free the control law from the limitations inherited by the actuator, an endeavor that is only possible in numerical simulations. A thought numerical experiment is therefore carried out to appreciate under a new angle the role of various control parameters in spanwise forcing: limitations derived from a specific actuator are lifted, thus revealing the true dependence of drag reduction upon the various quantities.

In this Chapter we exploit these new developed tools to describe the characteristics of a simple, turbulent, wall-bounded flow: a fully developed, incompressible, low-Reynolds-number, turbulent channel flow. The turbulent channel flow is the simplest configuration of a wall-bounded turbulent flow; it possesses two statistically homogeneous directions (streamwise x and spanwise z) parallel to the flat, smooth, indefinite walls, and only one non-homogeneous direction (y) perpendicular to the walls. Also, the incompressibility constraint removes the thermodynamics from the Navier–Stokes equations and the low-Reynolds number limits the size of the smallest flow structures, that scale with $Re^{-3/4}$. This simple configuration therefore allows employing Direct Numerical Simulations (DNS), although they are in general very computationally demanding. DNS resolve all spatial and temporal scales of the flow and produce high fidelity data, which are necessary to understand the physics of the flow.

We leverage DNS in this simple configuration also to perform parametric studies to investigate how the change of the control parameters affects the drag reduction performance. With the aim to describe the interaction between drag

reduction and turbulence, we focus on one of the simplest active drag reduction techniques: the spanwise-oscillating wall. First, active techniques reduce drag more than passive ones. So, their effects on the flow are larger and easier to detect and study. Second, unlike most passive techniques, the oscillating wall is flat, so that only skin-friction drag matters, leaving out pressure drag. Third, the oscillating wall is described by few parameters, so it is easier to track their single effects on the flow field.

The oscillating wall, introduced by Jung *et al.* (1992), forces the wall to move in the spanwise direction with a harmonic oscillation in time, i.e.

$$w(y = 0, t) = A \sin\left(\frac{2\pi}{T}t\right), \tag{2.1}$$

where A is the amplitude and T the period of the oscillation. The wall's harmonic oscillation generates a cross-flow that is periodic after space- and phase-averaging, and that superimposes to and interacts with the turbulent flow. The phase-averaged spanwise flow matches the analytical laminar solution of the second Stokes problem (Quadrio & Sibilla, 2000), hereafter referred to as the Stokes layer (SL), with small deviations for large T:

$$w_{SL}(y, t) = A \exp\left(-\sqrt{\frac{\pi}{\nu T}}y\right) \sin\left(\frac{2\pi}{T}t - \sqrt{\frac{\pi}{\nu T}}y\right). \tag{2.2}$$

where ν is the kinematic viscosity.

The drag reduction performance of the oscillating wall have been extensively studied in the past 30 years from the seminal work of Jung *et al.* (1992). Quadrio & Ricco (2004) found the drag reduction rate increasing monotonically with the amplitude of the forcing A; at fixed A the maximum drag reduction is always attained for the optimum period $T^+ \approx 100$. Hereinafter the superscript + identifies quantities made dimensionless with the friction velocity $u_\tau = \sqrt{\tau_w/\rho}$ of the uncontrolled case where τ_w is the average wall shear stress.

In an channel flow configuration run at constant mass flow rate, the drag reduction ($\mathcal{R}$) is defined as the difference between the skin-friction drag coefficient (C_f) of the controlled and uncontrolled flow, i.e.

$$\mathcal{R} = 100 \times \frac{C_{f,0} - C_f}{C_{f,0}}, \tag{2.3}$$

where the subscript 0 refers to the uncontrolled flow. The skin-friction coefficient is defined as $C_f = 2\tau_w/(\rho \mathcal{U}^2)$, with τ_w the average wall shear stress, ρ a reference density and $\mathcal{U}$ a reference velocity, usually defined as bulk quantities (ρ_b, U_b) for internal flow, such as the channel flow; in the particular case of incompressible flow, the density is constant, i.e. $\rho_b = \rho$.

2.1 A linear description of turbulence

First, we introduce a new tool to investigate the linear behavior of a turbulent flow. Although a turbulent flow is a highly non-linear system, the study of its linear dynamics is of capital interest. The suggestion (see for example Kim & Lim, 2000) that linear mechanisms are central to the near-wall turbulence regeneration cycle means that linear models of turbulence may suffice for flow control purposes. Linear model-based controls, either iterative (adjoint-based) and direct (Riccati-based) approaches, applied to turbulent flows need the mean state equations; unfortunately, in the turbulent regime they are not available and must be replaced by a linearized laminar model. The applicability of linear control approaches to turbulent flows lies upon the assumption that appropriately linearized models faithfully represent at least some of the important dynamic processes of turbulent flow systems. However a model obtained by linearizing the non-linear governing equations of a turbulent flow fails to capture some of its distinctive features such as the turbulent diffusion. Capturing such behaviour may be of non-negligible importance when trying to optimize a control algorithm and understand the mechanism by which the control disrupts turbulence. We propose exploting the linear impulse response function (LIRF), a classic tool for the description of linear time-invariant dynamical systems that we aim at applying to a non-linear system such as a turbulent flow. In the simplest single-input single-output (SISO) case of scalar variables and dependency on the time only, the LIRF $\mathcal{H}$ links the input f and the output q of a system in the time domain through a convolution, i.e.:

$$q(t) = \int_{-\infty}^{+\infty} \mathcal{H}(t-\tau) f(\tau)\, \mathrm{d}\tau. \tag{2.4}$$

By setting the input to a Dirac delta function $\delta(\tau)$, then $q(t) = \mathcal{H}(t)$, hence the name LIRF. It is the most complete description of the linear dynamics of a system and provides information about where and how apply a forcing to achieve the desired mean effect elsewhere and after a certain time delay. Although the response is linear, our approach fully accounts for the mean effects of turbulent mixing, otherwise lost via linearization.

In a non-linear setting such as a turbulent flow, the linearity of the response is only guaranteed by the small amplitude of the forcing. Indeed, although the system is non-linear, if it is forced by a sufficiently small perturbation, then it responds linearly. Although inconsequential in the noiseless laminar case, this limitation makes the approach highly unpractical in the turbulent case. Turbulent fluctuations are akin to noise, which can be averaged out by employing ensemble averaging, or at least an average over periodic repetitions of the same impulsive forcing over a long enough simulation time. Unfortunately, the forcing amplitudes

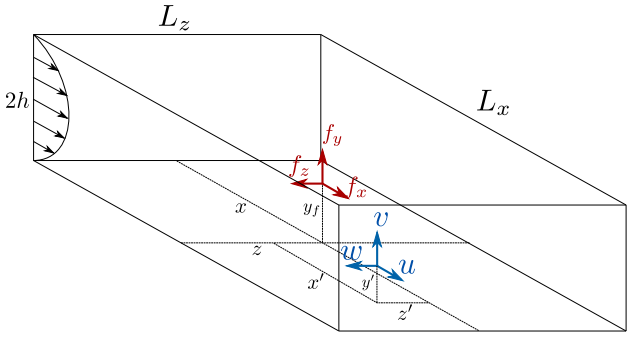

Figure 2.1: Sketch of the plane channel with reference system and definition of quantities related to the linear impulse response function.

required for linearity are much smaller than the natural turbulent noise, so that the simulation time required to bring down the statistical noise at a level at which the deterministic part of the response appears is simply not affordable. A viable alternative consists in the measure of the response of the system in the frequency domain, as employed by Hussain & Reynolds (1972). In the frequency domain, the constraint on the intensity of the forcing for linearity is less strict and a phase-locked average enables separating the deterministic part of the response from the random part. The obvious drawback of this approach is that a single experiment only yields the LIRF for a single frequency. To overcome this problem we rely on a property of the signal theory that avoids the direct measure of the response to an impulse either in physical or frequency domain and brings together the best of the two approaches, i.e. it has a decent signal to noise ratio and it provides a complete measurement in one shot. The approach, originally introduced by Luchini *et al.* (2006) relies on the property that when the system is forced by a white noise, the LIRF can be computed as the correlation between the output and the input.

We test the LIRF for the multiple-input multiple-output (MIMO) case of a turbulent channel flow, where the inputs are body forces and the outputs are the velocity components, both defined for each point of the channel and in time. The body force vector components are f_x, f_y and f_z and the velocity components u, v, w in the streamwise x, wall-normal y and spanwise z directions, respectively. The channel and the reference system are sketched in figure 2.1. The LIRF, written as the correlation between the input and the output of the system and in frequency domain (owing to the symmetries of the channel flow), reads:

$$\hat{\mathcal{H}}_{i\to j}(\alpha, y, \beta, \mathcal{T}; y_f) = \frac{\langle \hat{u}_j(\alpha, y, \beta, t)\hat{\mathrm{f}}_i^*(\alpha, y_f, \beta, t-\mathcal{T})\rangle_t}{\epsilon_i^2}, \tag{2.5}$$

after converting the convolutions into products in the homogeneous directions. Here the hat indicates Fourier transform, α and β are the wavenumbers in the

streamwise x and spanwise z directions; y_f is the wall-normal location of the impulsive forcing, where y_f spans from the first inner point up to the centerline (h); $\mathcal{T}$ is the elapsed time after the application of the impulse and $\langle\cdot\rangle_t$ is the average over the simulation time; $(\cdot)^*$ is the conjugate transpose and ϵ_i is the vector of the amplitudes of the forcing. The measured LIRF $\mathcal{H}_{i\to j}$ describes the linear response of the velocity of the system in every direction of the channel, at each point of the space and in time, after the application of a forcing directed in a specific direction and placed at a certain point of the space and at a previous time.

The LIRF is computed on the fly while running a DNS at $Re_b = U_b h/\nu = 2280$, where U_b is the bulk velocity, h the channel half-height and ν is the kinematic viscosity of the fluid, corresponding to a friction Reynolds number of $Re_\tau = u_\tau h/\nu = 150$ with $u_\tau = \sqrt{\tau_w/\rho}$ being τ_w the shear stress at the wall and ρ the density. The deterministic response emerges progressively averaging out the noise from the turbulent fluctuations while the simulation proceeds. Hence, the simulation needs to be run as long as possible and in the present case it is advanced for $20000h/U_b$ (or, equivalently, 2×10^5 viscous time units).

The LIRF is a powerful tool since it provides altogether a large amount of information. The computed impulse response function $\mathcal{H}_{i\to j}(\alpha, y, \beta, \mathcal{T}; y_f)$ of a turbulent channel flow depends on five variables: the wavenumbers α and β in the two homogeneous (streamwise and spanwise, respectively) directions of the channel, the position y in the wall-normal direction, the time $\mathcal{T}$ elapsed after the impulsive forcing is applied and the parameter y_f describing the distance from the wall where the forcing is applied.

Figure 2.2 shows the LIRF tensor $\mathcal{H}_{i\to j}$ in the physical space at a fixed bulk time $\mathcal{T} = 0.48$ after being forced at $y_f^+ = 15$. This picture brings to light the high anisotropic character of the response.

First of all the shape of the impulse response can be associated to different flow structures which respond to the external forcing. The components $\mathcal{H}_{f_y\to j}$ and $\mathcal{H}_{f_z\to j}$ with $j = u, v, w$ show that the forcing acts on the structures of the near wall-cycle (Jeong *et al.*, 1997). The streamwise component of the response ($j = u$) yields to structures elongated in the streamwise direction, with alternating positive and negative sign in the spanwise direction. Such structures are compatible with the amplification of the near-wall high- and low-speed streaks. The wall-normal ($j = v$) and spanwise ($j = w$) components of the response identify alternated vertical and spanwise fluctuations typical of the turbulent quasi-streamwise vortices (QSV). The relative position of the isosurfaces in figure 2.2 indicate the simultaneous presence of streaks and QSV, which mutually interact in the cycle for the self-sustainment of turbulence. This picture is compatible with what found by Jovanović & Bamieh (2005) and confirmed by the present work in the wavenumbers plane investigating the same problem for a laminar channel flow. In the laminar regime, the most amplified disturbances to a wall-normal

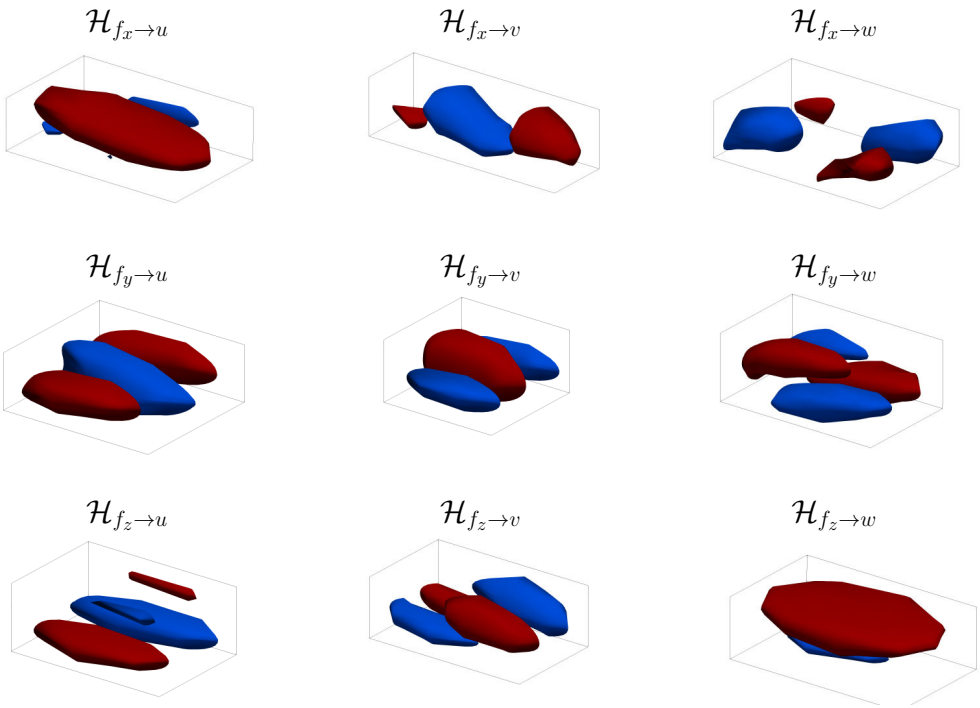

Figure 2.2: Isosurfaces of the response tensor $\mathcal{H}_{i \to j}$ at the non dimensional time $\mathcal{T} = 0.48$ of a turbulent channel flow forced at the wall-normal distance $y_f = 0.1h$ or $y_f^+ = 15$. All the isosurfaces are at the value ± 0.5 except for the diagonal components, $\mathcal{H}_{f_y \to u}$ and $\mathcal{H}_{f_z \to u}$ which are at the value ± 1. Red is for positive values, blue for negative ones.

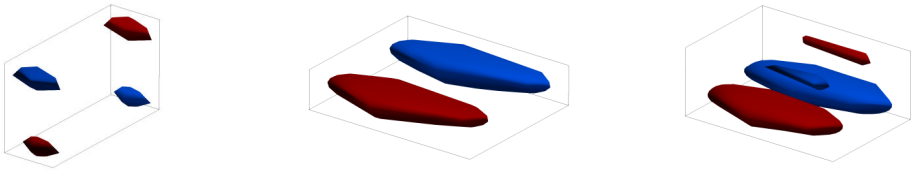

Figure 2.3: Isosurfaces of the response tensor $\mathcal{H}_{f_z \to u}$ at bulk time $\mathcal{T} = 0.48$ for the laminar (left), pseudo-turbulent (center) and turbulent (right) case. The forcing is at the wall-normal distance $y_f = 0.1h$. All the isosurfaces are at the value ± 1.

and a spanwise forcing $\mathcal{H}_{f_y \to j}$ and $\mathcal{H}_{f_z \to j}$ are found to be either oblique waves or streamwise perturbations which yield after transition to turbulence to streamwise streaks and quasi-streamwise vortices. Similarly, the relative position of the isosurfaces of $\mathcal{H}_{f_x \to j}$ suggests that the streamwise forcing acts on the hairpin vortices (Theodorsen, 1952) near the wall, as highlighted by Vadarevu *et al.* (2019) by Linearized Navier–Stokes Equations (LNSE) augmented with eddy-viscosity (eLNSE). This agrees with the idea that the Tollmien–Schlichting waves detected in the laminar regime for this forcing (Jovanović & Bamieh, 2005) evolves into 3D hairpin vortices in the late stage of transition to turbulence.

Although we find compatible information from the response of the linear and turbulent channel flow, it does not mean they provide the same exact information. The inadequacy of a linearized channel flow to provide the complete response of a turbulent channel flow has been recently emphasized by the results obtained by Russo & Luchini (2016). They measured the LIRF of a linearized and of a fully turbulent channel flow to a steady volume force finding that they are significantly different, which implies that the "background" turbulence has a non-negligible impact on the linear response. Moreover, they demonstrated that it is impossible to conceive a (positive and finite) eddy viscosity that makes the results obtained with eLNSE compatible with the true measurement. To investigate this discrepancy, we additionally compute the response to external volume forces of a laminar channel flow and of a pseudo-turbulent channel flow, i.e. where turbulence is absent but the base flow is the mean flow of the turbulent case, at the same Re_b of the turbulent case. Owing to the small intensity of the forcing, the response is again linear and coincides with the one obtained by the LNSE. Figure 2.3 plots as an example $\mathcal{H}_{f_z \to u}$ for the laminar, pseudo-turbulent and turbulent cases. Although the same response shape is shared by all the investigated regimes, the shape and intensity of the response show non-negligible differences. We conclude that the dynamics of the impulse response in the turbulent regime has a linear component, yet this is not sufficient for its complete description.

A second aspect of the anisotropic nature of the response of the channel flow is the different intensity of each term of the tensor. As expected, the largest response

corresponds to the diagonal components of the LIRF tensor, meaning that the forcing mostly amplifies the velocity component in its same direction. Among the off-diagonal terms, $\mathcal{H}_{f_y \to u}$ and $\mathcal{H}_{f_z \to u}$ show the largest magnitude of the response. (See the caption of figure 2.2 for the details about the different contour levels used for each term of the tensor).

Third, the components of the LIRF tensor also show different behaviour depending on the time and on the distance from the wall of the forcing. Again $\mathcal{H}_{f_y \to u}$ and $\mathcal{H}_{f_z \to u}$ show particular characteristics, different from the ones of the other terms. Whereas the other components decay monotonically to zero, their response in time exhibits a transient growth (Schmid, 2007) in the first instants after the application of the forcing, before decaying. Moreover, whereas the other terms of the LIRF tensor show an almost monotonic increase of the response with the increased distance from the wall at which the impulsive body force is applied, the two off-diagonal terms involving the response in the streamwise direction exhibit a local peak in the buffer layer. This is a second hint of the link of the maximum $\mathcal{H}_{f_y \to u}$ and $\mathcal{H}_{f_z \to u}$ to the amplification of the near-wall structures. This results comply with the idea that an external forcing in the buffer layer directed either in wall-normal direction (e.g. blowing and suction (Mickley *et al.*, 1954), opposition control (Choi *et al.*, 1994)) or in the spanwise direction (e.g. spanwise forcing Ricco *et al.*, 2021) are the most effective techniques to perturb the streamwise velocity field, e.g. with the aim to reduce the drag in the turbulent regime.

Figure 2.4 shows as an example the response $\mathcal{H}_{f_z \to u}$ in time (left) and depending on the position y_f (right), comparing laminar, pseudo-turbulent and turbulent cases. The turbulent diffusion, lacking in the laminar and pseudo-turbulent cases, damps the turbulent response faster so that the turbulent case possesses a considerably smaller transient growth compared to the other two cases. Moreover, for larger $\mathcal{T}$, the turbulent response does not decay to zero but shows a lower bound representing the background noise of the turbulence overwhelming the deterministic part of the response. This noise floor is due to the finite horizon of the response computation. Looking at the dependence of the LIRF on y_f,the response of the laminar channel flow completely fails to capture the local peak in the buffer layer, whereas the pseudo-turbulent channel captures it, although with a different intensity and position compared to the fully turbulent case. This confirms that the complete characterization of the turbulence needs to be accounted for a complete linear description of a turbulent channel flow.

Once the response function $\mathcal{H}_{i \to j}$ is computed, it can be used to predict the linear response of the system through direct convolution between the LIRF itself and the given (not necessarily small) input forcing, exploiting Eq. (2.4) after tailoring it for the channel flow. This approach can be leveraged to predict the linear behaviour of the channel flow to whatever external forcing shape at a fraction of the cost of a DNS.

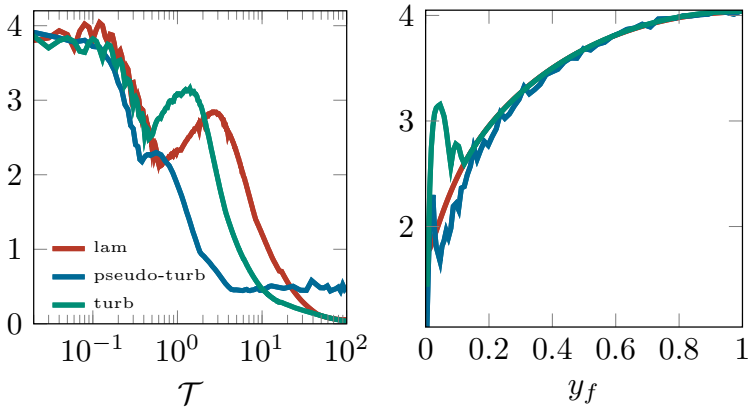

Figure 2.4: Linear impulse response function as a function of time, i.e. $\mathcal{H}_{f_z \to u}(\mathcal{T})$ (left) and as a function of the forcing position y_f, i.e. $\mathcal{H}_{f_z \to u}(y_f)$ (right) for the laminar, pseudo-turbulent and turbulent cases, after taking the absolute maximum value of the other variables.

2.2 A complete description of turbulence

A linear representation of the flow may be sufficient to design a linear controller for skin-friction drag reduction. However, for a complete characterization of the dynamics of a turbulent flow and to investigate the effects of the control on the turbulent activity, a full non-linear description of the (controlled) flow is needed. The anisotropic generalised Kolmogorov equations (AGKE) provide information about the mechanisms occurring at different scales and at different positions, simultaneously. They bring together the scale information of the spectral analysis and the position information of the analysis in physical space, thus providing a natural definition of scales in the inhomogeneous directions, and describing fluxes across scales. The AGKE are the budget equations for the second order structure function $\langle \delta u_i \delta u_j \rangle$, where δu_i is the increment of the i-th velocity between two points x_1 and x_2, identified by their midpoint $X = (x_1 + x_2)/2$ and their separation vector $r = (x_2 - x_1)$, i.e. $\delta u_i = u_i(X + r/2) - u_i(X - r/2)$; $\langle \cdot \rangle$ represents the average in time and homogeneous directions.

When the structure function is written for the fluctuating velocity $\boldsymbol{u'}$, after a Reynolds decomposition divides the velocity field $\boldsymbol{u}$ into mean $\boldsymbol{U}$ and fluctuating $\boldsymbol{u'}$ fields, the structure function $\left\langle \delta u'_i \delta u'_j \right\rangle$ is related to the sum of the single-point Reynolds stresses evaluated at the two points $\boldsymbol{X} \pm \boldsymbol{r}/2$, i.e. V_{ij} and the two-points correlation tensor R_{ij} (Davidson *et al.*, 2006) as

$$\left\langle \delta u'_i \delta u'_j \right\rangle (\boldsymbol{X}, \boldsymbol{r}, t) = V_{ij}(\boldsymbol{X}, \boldsymbol{r}, t) - R_{ij}(\boldsymbol{X}, \boldsymbol{r}, t) - R_{ij}(\boldsymbol{X}, -\boldsymbol{r}, t) \tag{2.6}$$

where

$$V_{ij}(\boldsymbol{X},\boldsymbol{r},t) = \left\langle u_i' u_j' \right\rangle \left(\boldsymbol{X}+\frac{\boldsymbol{r}}{2},t\right) + \left\langle u_i' u_j' \right\rangle \left(\boldsymbol{X}-\frac{\boldsymbol{r}}{2},t\right) \tag{2.7}$$

and

$$R_{ij}(\boldsymbol{X},\boldsymbol{r},t) = \left\langle u_i' \left(\boldsymbol{X}+\frac{\boldsymbol{r}}{2},t\right) u_j' \left(\boldsymbol{X}-\frac{\boldsymbol{r}}{2},t\right) \right\rangle. \tag{2.8}$$

The AGKE is an extension of the generalised Kolmogorov equation (GKE) by Hill (2001), also referred to as Kármán-Howarth-Monin-Hill equation (Alves Portela *et al.*, 2017). GKE is the exact budget equation for half the trace of the second-order structure function tensor, i.e. the scale energy, whereas the AGKE consider each component of the tensor separately. The AGKE have already been successfully employed to describe the key features of a channel flow (Gatti *et al.*, 2020) at low and moderate Re, to investigate the ascending/descending and direct/inverse cascades of the Reynolds stresses in a turbulent plane Couette flow (Chiarini *et al.*, 2022*b*), to describe the structure of turbulence of the flow past a rectangular cylinder (Chiarini *et al.*, 2022*a*) and to characterize the effects of the curvature on the structure of near-wall turbulence (Selvatici *et al.*, 2023). It has also been employed in the context of drag reduction to investigate the differences between an uncontrolled channel flow and one subjected to the wall-oscillation control (Chiarini *et al.*, 2019).

In all the above cited cases, AGKE are derived for the fluctuating velocity field, after a Reynolds decomposition is employed to separate the mean flow and the turbulent fluctuations. However, in the wall oscillation case the fluctuating field sums together the contributions of the purely stochastic turbulent field with the coherent one of the periodic oscillation of the wall. To separate the contribution of the turbulence and the one of the control, and to investigate how they interact and exchange energy, we define the mean field with a simple temporal average $\boldsymbol{U}(\boldsymbol{x}) \equiv \lim_{\tau\to+\infty} \frac{1}{\tau}\int_0^\tau \boldsymbol{u}(\boldsymbol{x},t)dt$, the coherent field $\tilde{\boldsymbol{u}}(\boldsymbol{x},\varphi) = \overline{\boldsymbol{u}}(\boldsymbol{x},\varphi) - \boldsymbol{U}(\boldsymbol{x})$ with a phase average $\overline{\boldsymbol{u}}(\boldsymbol{x},\varphi) \equiv \lim_{N\to+\infty} \frac{1}{N}\sum_{n=0}^{N-1} \boldsymbol{u}\left(\boldsymbol{x},\left(\frac{\varphi}{2\pi}+n\right)T\right)$ and the stochastic field as what is left, i.e. $\boldsymbol{u''} = \boldsymbol{u} - \boldsymbol{U} - \tilde{\boldsymbol{u}}$. After decomposing the velocity and pressure fields with such definitions, three tensorial budget equations, called φAGKE, can be written for $\delta U_i \delta U_j$, $\delta\tilde{u}_i\delta\tilde{u}_j$ and $\overline{\delta u_i'' \delta u_j''}$, which add to the standard AGKE the interplay among the mean, coherent and stochastic fields at each phase φ.

The φAGKE, i.e. the budget equation for the mean $\delta U_i \delta U_j$, the coherent $\delta\tilde{u}_i\delta\tilde{u}_j$ and the stochastic $\overline{\delta u_i'' \delta u_j''}$ second-order structure functions, in their compact form

read

$$\frac{\partial \Phi^m_{k,ij}}{\partial r_k} + \frac{\partial \Psi^m_{k,ij}}{\partial X_k} = \Xi^m_{ij} \tag{2.9}$$

$$\frac{2\pi}{T}\frac{\partial \delta\tilde{u}_i\delta\tilde{u}_j}{\partial \varphi} + \frac{\partial \phi^c_{k,ij}}{\partial r_k} + \frac{\partial \psi^c_{k,ij}}{\partial X_k} = \xi^c_{ij} + \zeta^c_{ij} \tag{2.10}$$

$$\frac{2\pi}{T}\frac{\partial \overline{\delta u_i''\delta u_j''}}{\partial \varphi} + \frac{\partial \phi^s_{k,ij}}{\partial r_k} + \frac{\partial \psi^s_{k,ij}}{\partial X_k} = \xi^s_{ij}, \tag{2.11}$$

where repeated index k implies summation. They describe how a structure function evolves in time and in space (both scale and physical). The terms Φ^m, ϕ^c,ϕ^s and Ψ^m, ψ^c,ψ^s represent the fluxes across scales and in the physical space, respectively; Ξ^m, ξ^c,ξ^s represent the source terms, denoting the net production of $\delta U_i\delta U_j$, $\delta\tilde{u}_i\delta\tilde{u}_j$ and $\overline{\delta u_i''\delta u_j''}$, respectively. The source is the balance between the production, the redistribution due to velocity-pressure interaction and the dissipation of the second-order structure function. The coherent equations also feature the term ζ^c at the right hand side, representing the interaction among different phases driven by the coherent flow field.

Beyond dividing the coherent and stochastic field contributions, the φAGKE also add additional terms to the equations, that describe the interplay between the fields. Originally, the fluxes, either in the space of scales or positions, feature the mean transport, the viscous diffusion and the fluctuating transport; the latter is now broken down into coherent and stochastic transport to account for the transport processes either due to the coherent and the stochastic field, separately. The same happens for the source, which beyond the pressure strain, the dissipation and interaction between the velocity field and the external forcing, also breaks down the former production due to the interaction between the mean and fluctuating fields into the production between the mean and coherent fields p^{mc}_{ij} and the production between the coherent and the stochastic fields p^{cs}_{ij} in the equations of $\delta\tilde{u}_i\delta\tilde{u}_j$ and into the production between the mean and stochastic fields p^{ms}_{ij} and the production between the coherent and the stochastic fields p^{cs}_{ij} in the equations of $\overline{\delta u_i''\delta u_j''}$. The coherent-stochastic production p^{cs}_{ij} indicates the exchange of stresses between the coherent and the stochastic fields, and appear in both the equations but with opposite sign. It describes the position, the scales and the phase at which the exchange of energy between the two fields takes place.

In this study, we employ the phase-aware φAGKE as a framework to analyze the interplay between an external harmonic control and the turbulent fluctuations present in a fully developed turbulent channel flow subjected to the drag reduction technique of wall oscillation introduced in the preamble of the present Chapter. The channel flow configuration reduces the independent variables from seven to

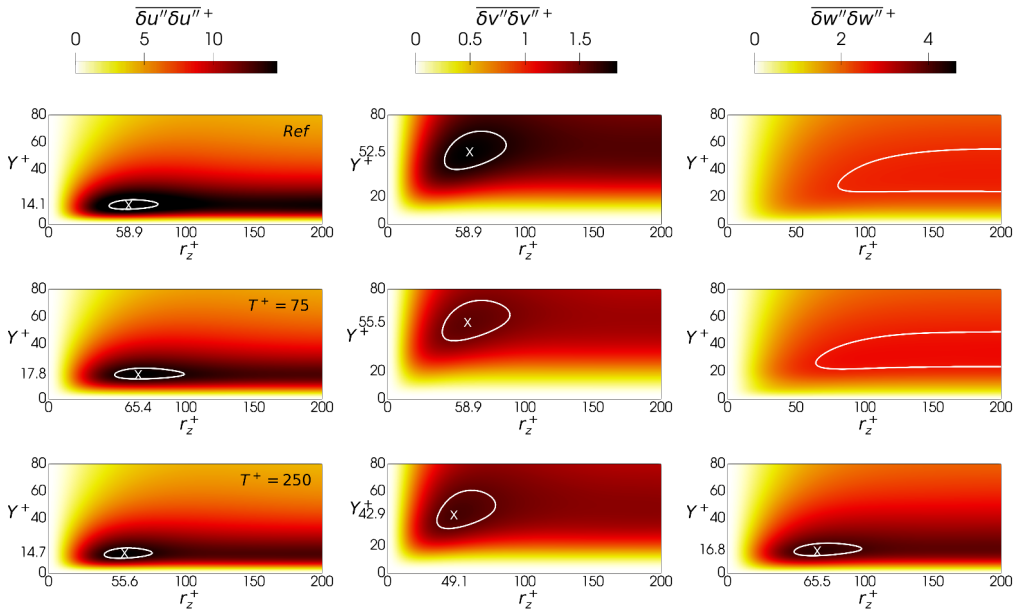

Figure 2.5: Diagonal components of the stochastic tensor $\overline{\delta u_i'' \delta u_j''}^+$ at $\varphi = \pi$ in the (r_z^+, Y^+) plane. From top to bottom: uncontrolled case with $A = 0$, $T^+ = 75$ and $T^+ = 250$. The contour is set at 95% of each maximum. The coordinates of the maximum, marked with a cross, can be read on the axes. Taken from Gattere *et al.* (2023).

five: three separations r_x, r_y and r_z in the streamwise, wall-normal and spanwise directions, the position in wall-normal direction Y and the phase φ; in the channel flow, φ-AGKE do not depend on X and Z, being homogeneous directions. The spanwise-wall-oscillation control (see Eq. 2.1) generates above the wall a spanwise velocity profile called Stokes layer of Eq. 2.2, where $\varphi = 2\pi/T\ t$ is the phase of the oscillation. The external oscillation has amplitude $A^+ = 12$ and two periods are investigated, namely $T^+ = 75$, close to the optimum value for maximum drag reduction and $T^+ = 250$, a suboptimal case. The simulation is run at $Re_\tau = 200$. The objectives of this study are threefold: first, examining the impact of coherent motion on the dimensions and spatial configuration of near-wall structures throughout the control period; second, characterizing the interaction between mean, coherent, and stochastic fields within both scale and physical spaces; and third, analyzing the phase dependency of the interaction between the coherent and stochastic fields. For this problem the mean velocity is $(U, V, W) = (U(y), 0, 0)$, the coherent velocity is $(\tilde{u}, \tilde{v}, \tilde{w}) = (\tilde{u}(y, \varphi), 0, w_{SL}(y, \varphi))$ and the stochastic field is $(u'', v'', w'') = (u''(x, y, z, \varphi), v''(x, y, z, \varphi), w''(x, y, z, \varphi))$.

The scales and wall-normal position at which the diagonal terms of the structure

function tensor peak are associated to the statistic trace of the turbulent structures (Gatti *et al.*, 2020). In the uncontrolled case (see "Ref" in figure 2.5), $\overline{\delta u'' \delta u''}_m$ (where the subscript m stays for the maximum) is in the buffer layer and for $r_z \neq 0$ and $r_x = r_y = 0$ meaning that the streamwise structure function is associated to structures aligned in the streamwise direction ($r_x = 0$) and negatively correlated ($\overline{\delta u'' \delta u''} > 0$ means $R_{ij} < 0$) in spanwise direction ($r_z \neq 0$); it represents the positive and negative streaks of the near-wall cycle. Instead, both $\overline{\delta v'' \delta v''}$ and $\overline{\delta w'' \delta w''}$ peak in the buffer layer and for $r_x = 0$; the former for $r_z \neq 0$, the latter for $r_y \neq 0$ (result not shown) so that they are associated to the statistical trace of the QSV which induce vertical velocity at the sides and spanwise velocity at the top and the bottom of a vortex. The oscillating wall leaves $\overline{\delta u'' \delta u''}_m$ and $\overline{\delta v'' \delta v''}_m$ almost unchanged (see figure 2.5), indicating that the dimension and intensity of the near-wall structures only marginally depend on the drag reduction rate. However, the streaks are slightly pushed away from the wall: $\overline{\delta u'' \delta u''}_m$ shifts upwards, highlighting a thickening of the viscous sublayer with the control (Choi *et al.*, 1997). Interestingly, in the controlled case with $T^+ = 250$, a local peak of $\overline{\delta w'' \delta w''}$ appears in the $r_y = r_z = 0$ plane (not shown) and in the $r_x = r_y = 0$ plane at a wall-normal distance resembling the one of $\overline{\delta u'' \delta u''}$. We associate it to the statistical trace of the streaks tilted in wall-parallel planes under the spanwise velocity of the control, that deviates their direction from the streamwise alignment. This effect is visible only for the suboptimal case $T^+ = 250$, for which the near-wall structures have time to tilt and align with the instantaneous shear vector ($\mathrm{d}U/\mathrm{dy}$, $\partial \tilde{w}/\partial \mathrm{y}$). The same effect is visible investigating the phase evolution of the maximum of the diagonal terms of the structure function tensor $\overline{\delta u_i'' \delta u_j''}$. In figure 2.6, $\overline{\delta u'' \delta u''}_m$ and $\overline{\delta w'' \delta w''}_m$ share the same trend and show a phase-shift compared to $\overline{\delta v'' \delta v''}_m$. This is consistent with the different wall normal distance of streaks and QSV which implies a different shear to which they are subjected because of the Stokes layer profile (Baron & Quadrio, 1996). Similar information about the turbulent structures are usually extracted from phase-locked conditional averages (Yakeno *et al.*, 2014), which are unavoidably subjected to some degree of arbitrary, e.g. one need to determine *a priori* a specific wall distance for the eduction procedure. With φAGKE we obtain equivalent information via statistical analysis that is free from assumption and hypothesis.

A part of the wall-parallel modulation of $\overline{\delta w'' \delta w''}_m$ is also induced by the interaction between the QSV and the coherent spanwise shear $\partial \tilde{w}/\partial \mathrm{y}$ introduced by the wall oscillation. At the phase and distances from the wall for which $\partial \tilde{w}/\partial y > 0$, the quasi-streamwise vortices move low-spanwise-velocity fluid ($w'' < 0$) upwards, and high-spanwise-velocity fluid ($w'' > 0$) downwards. The opposite happens when the coherent shear is negative. This leads to the change in the statistical scale-wise trace of the spanwise stresses $\overline{\delta w'' \delta w''}$, which have their largest peak

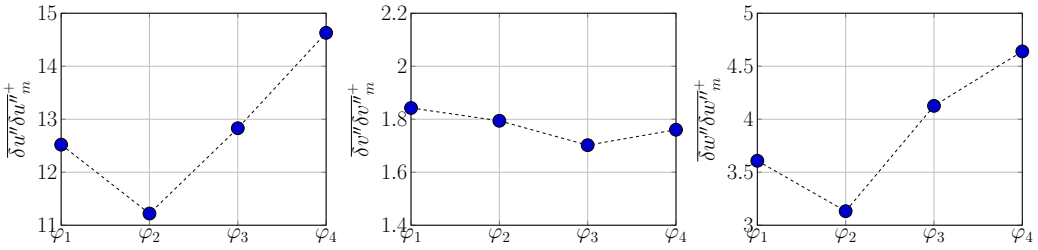

Figure 2.6: Phase variation of the maxima $\overline{\delta u_i'' \delta u_i''}^{+}_{m}$ in the (r_z^+, Y^+) plane for the case at $T^+ = 250$. $\varphi_i = i\pi/4$. Taken from Gattere *et al.* (2023).

in $r_z \neq 0$.

This interaction mechanism between the coherent Stokes layer and the stochastic turbulent fluctuations is captured by the coherent-stochastic production of the spanwise fluctuations, that in the $r_y = 0$ space reduces to $p^{cs}_{ww} = -2\overline{\delta v'' \delta w''}(\partial \tilde{w}/\partial \mathrm{y})$. The interaction mechanism between the Stokes layer and the QSV, which moves low (high)-spanwise-velocity fluid w'' upwards ($v'' > 0$) (downwards ($v'' < 0$)), and high (low)-spanwise-velocity fluid downwards (upwards) for positive (negative) spanwise shear, also leads to the creation of shear stresses $\overline{\delta v'' \delta w''}$, otherwise null in the uncontrolled channel. The sign of $\overline{\delta v'' \delta w''}$ changes, with the same mechanism which leads to the change of sign of the Reynolds shear stresses $\langle \delta u'' \delta v'' \rangle$ at the sides of QSV due to the sweep and ejections of streamwise velocity fluctuations u'' caused by the mean shear $\mathrm{d}U/\mathrm{d}y$. The wall normal position of such an interaction depends on both the shape of the Stokes layer directly and on its influence on $\overline{\delta v'' \delta w''}$, leading to the alternation of positive and negative stripes of energy exchange between coherent and stochastic field, differently at each phase of the oscillation. Stripes of $p^{cs}_{ij} > 0$ means energy going from the coherent motion to the turbulent field as expected, whereas $p^{cs}_{ij} < 0$ means that the turbulence has a feedback on the coherent field. The change of $\overline{\delta v'' \delta w''}$ also influences the scales at which the energy exchange between coherent and stochastic field takes place. Figure 2.7 shows for a specific phase, p^{cs}_{ww} in the $r_z - Y$ plane. Going from the optimal $T^+ = 75$ to the sub-optimal $T^+ = 250$ period, the stripes of energy exchange from the stochastic to the coherent field weaken, while those from the coherent to the stochastic field strengthen; overall, the contribution of the spanwise velocity to the energy drained from the coherent and given to the stochastic part becomes larger. A larger period of oscillation implies a larger Stokes layer thickness, proportional to $\sqrt{\nu T}$; as a result, the coherent spanwise shear and, as a consequence, the scale-space map of $\overline{\delta v'' \delta w''}$ are stretched outwards, yielding an overall increase of the positive transfer of energy towards the turbulent fluctuations. Anyway, when p^{cs}_{ww} is averaged over the phases, it turns out to be positive for both the periods investigated, meaning that overall

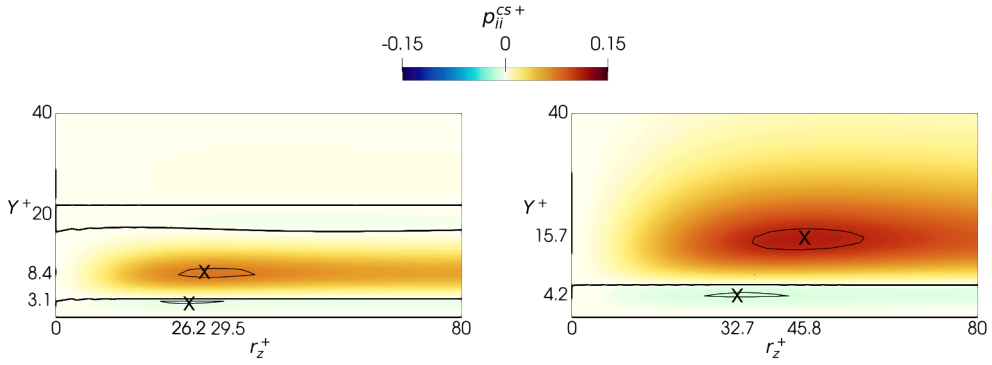

Figure 2.7: Coherent-stochastic production ${p_{ww}^{cs}}^+$ in the (r_z^+, Y^+) plane for $T^+ = 75$ (left) and $T^+ = 250$ (right) for $\varphi = \pi$. The thin contour line is set at 95% of the smallest (positive and negative) maximum over the phases; the thick black contour line is $p_{ww}^{cs} = 0$. The coordinates of the maximum, marked with a cross, can be read on the axes. Taken from Gattere *et al.* (2023).

turbulence drains energy from the external harmonic motion.

Thanks to φAGKE a description of the phase by phase modification of the flow field of a turbulent channel flow due to interaction between the near-wall turbulent structures and the coherent spanwise velocity generated by the wall oscillation control is made possible for the first time simultaneously in the space of scales and physical space. However, φAGKE is suitable to study many different flows where stochastic fluctuations coexist with some sort of coherent motion, very common in turbulent flows. For instance, turbulent flows controlled by an external periodic forcing, such as oscillating airfoils, rotors and turbines; the turbulent flow past bluff bodies, where large-scale motions of the Kármán-like vortices in the wake coexist with small-scale stochastic motion; the Couette flow where large rolls and small perturbations live together; the atmospheric boundary layer, featuring quasi-two-dimensional structures forced at smaller scales.

2.3 A conceptual description of controlled turbulence

Thanks to the φAGKE, one can fully characterize a wall-bounded turbulent flow and its modification by the oscillating wall. While we can identify the variations in the turbulent flow due to two distinct oscillation periods and link these to the dynamics of the near-wall cycle, the underlying physical mechanisms governing drag reduction control remain elusive. Understanding how a control inhibits the regeneration of turbulence concerns researchers since the pioneering work by Jung

et al. (1992). The available evidence points to the existence of an optimal value T_{opt} for the oscillation period to reduce the skin-friction drag, and there is broad consensus that this value is $T^+_{opt} \approx 100$. Despite the evidence, however, there is no consensus on the physical interpretation of the optimum period, and more than one meaning can be attached to these specific value. For example, T_{opt} can be associated to time scales of the flow, such as the characteristic life time of the near-wall coherent structures (Quadrio & Luchini, 2003). Owing to the convective nature of the flow, T_{opt} can be also converted into a longitudinal length scale in terms of a convection length scale, and be compared with typical lengths of the near-wall coherent structures (Touber & Leschziner, 2012). The optimum T might also identify the maximum lateral displacement of the moving wall $D_{max} = AT$, which is another (possibly) relevant length scale of the flow (Quadrio & Ricco, 2004). Finally the optimum period can also be associated to a wall-normal length scale δ; the more obvious definition (Baron & Quadrio, 1996) of a wall-normal length scale is through the relation:

$$\delta = \delta_{SL} \equiv \sqrt{\nu T/\pi}. \tag{2.12}$$

The length scale δ_{SL} represents the penetration of the effects of the wall oscillation far from the wall into the bulk of the flow and it is defined as the wall distance where the maximum spanwise velocity during the oscillation reduces to $\exp(-1)$ times the maximum wall velocity A.

As mentioned in the preamble of the present Chapter, the harmonic oscillation of the wall generates a spanwise periodic cross-flow that superimposes to and interacts with the turbulent flow and coincides with the analytical laminar solution $w_{SL}(y,t)$ of the Stokes second problem (Quadrio & Sibilla, 2000), with small deviations for large T. The generated time-varying velocity profile, called Stokes layer (SL), already described by Eq. (2.2) is rewritten exploiting Eq. (2.12) as:

$$w_{SL}(y,t) = A \exp\left(-\frac{y}{\delta_{SL}}\right) \sin\left(\frac{2\pi}{T}t - \frac{y}{\delta_{SL}}\right), \tag{2.13}$$

where δ_{SL} is also known as the SL thickness, representing the wall-normal diffusion length scale associated to the Stokes layer.

As discussed in §2.2, the coherent SL cross-flow is at the root of the drag reduction process, yet no consensus exists regarding the details of how it interacts with the incoming turbulent flow. Our inability to discriminate among the different possible interpretations of T_{opt} reflects our current limited understanding of the whole drag reduction mechanism of the oscillating wall set up. Aiming at understanding how the generated Stokes layer interacts with the underlying turbulence and what time and space scales are actually targeted by the oscillation of the wall to reduce drag, we decouple the effects of the period T and of the penetration

depth δ of the Stokes layer. Based on Direct Numerical Simulations, we go beyond the concept of the conventional oscillating wall and get rid of the $\delta = \delta_{SL}$ constraint: we explore the complete (T, δ) two-dimensional space of parameters and investigate separately the role of T and δ. Instead of imposing the harmonic spanwise oscillation of the wall to generate the SL, we enforce at each time step of the simulation a mean spanwise velocity profile of the form

$$w_{SL} = \langle w(y, t; \delta, T) \rangle_h = A \exp\left(-\frac{y}{\delta}\right) \sin\left(\frac{2\pi}{T} t - \frac{y}{\delta}\right), \tag{2.14}$$

which we dub extended Stokes layer (ESL), and vary δ and T independently. The operator $\langle \cdot \rangle_h$ indicates spatial averaging along the homogeneous directions. It should be remarked that our procedure is equivalent to solve the Navier–Stokes equations with the boundary condition of the wall oscillation and an additional volume forcing that is practically zero whenever the extended Stokes layer reduces to the standard Stokes layer.

We perform a set of DNS at $Re_\tau = 400$. We increase the value of Re compared to the previously used $Re_\tau = 200$ (see §2.2) since at this value of Re the forcing of Eq. (2.14) can be significantly more effective than the conventional oscillating wall, such that the turbulent flow is prone to relaminarization. For the control, the amplitude is set constant to $A^+ = 12$, whereas the space of parameters (T, δ) is investigated varying the period in the $10 \leq T^+ \leq 200$ range, while the SL thickness varies between $2 \leq \delta^+ \leq 20$.

Figure 2.8 shows the drag reduction on the $(T - \delta)$ plane. The black line represents the results pertaining the oscillating wall, when T and δ are constrained by Eq. (2.12) and clearly shows that the maximum $\mathcal{R}$ when being constrained to move on the line is achieved at $T^+ \approx 100$. Instead, once T and δ are made independent, then $T^+ \approx 100$ (thus $\delta^+ \approx 6$ following Eq. (2.12)) is not particularly meaningful and to reach larger $\mathcal{R}$ is convenient to move towards smaller periods of oscillation, i.e. $T^+_{opt} \approx 30$ and larger SL thickness, i.e. $\delta^+_{opt} \approx 14$. It is worth noting that, when moving along the SL line, it is impossible to change T and δ in opposite directions.

The peak of drag reduction $(T^+, \delta^+) \approx (30, 14)$ is quite broad and flat, and the value of δ_{opt} corresponds to the position in the buffer layer where the near-wall cycle takes place, suggesting that the maximum $\mathcal{R}$ is gained for the ESL effectively interacting with the near-wall coherent structures. Instead, for either $\delta^+ \lessapprox 4$ or for $T^+ \lessapprox 20$, the characteristic space and time lengths of the forcing are too small compared to the characteristic lengths of the turbulent structures of the near-wall cycle, thus they do not successfully target them. For both T and δ larger the optimum, the $\mathcal{R}$ performances degrade due to the enhanced turbulent activity. We conclude that the values of the parameters $(T^+, \delta^+) \approx (100, 6)$, well known in literature to provide the maximum $\mathcal{R}$ with the wall oscillation, do not possess

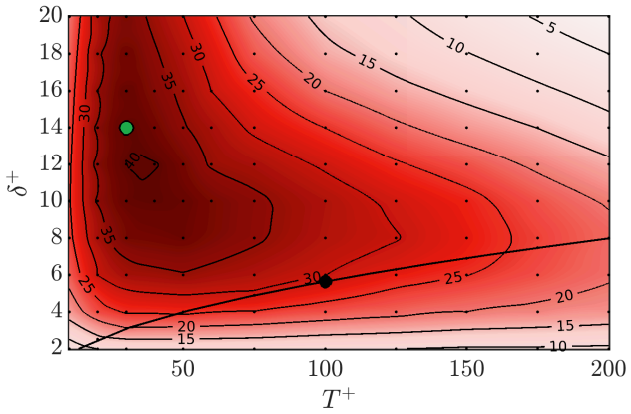

Figure 2.8: Drag reduction map in the (T, δ) two-dimensional space of parameters. The black thick line indicates the $\delta = \delta_{SL}$ constraint. The green dot identifies the point of maximum drag reduction, whereas the black dot indicates the maximum along the line $\delta = \delta_{SL}(T)$. Small back points indicates evey simulation's parameters.

a special meaning. Instead, the global maximum $(T^+, \delta^+) \approx (30, 14)$ might be associated to some characteristic scales of turbulence.

As highlighted above, the optimal oscillating period T_{opt} can be obviously compared to other time scales in the turbulent flow. Quadrio & Luchini (2003) computed the integral scale T_I of the space-time autocorrelation of velocity fluctuations along the path of maximum correlation in the space-time plane, and interpreted it as the integral lifetime of near-wall structures. We perform the same analysis at the present $Re_\tau = 400$ and at δ^+_{opt}, we measure $T_{I,u} = 75$ for the streamwise velocity fluctuations. These value is of the same order of $T^+ = 30$, yet quite far from it. Moreover our results of decreasing T for increasing δ are not compatible with this interpretation since the integral lifetime increases with the distance from the wall, being e.g. $T_{I,u} = 62$ at $y^+ = 5$ and $T_{I,u} = 75$ at $y^+ = 15$.

A possible alternative is to associate the optimal oscillating period T_{opt} to the characteristic timescale of the near-wall cycle. Jimenez (2013) measured its period to be $T^+ = 400$, with a bursting phase lasting $T^+ \approx 100$ followed by a longer phase of quiescence. Half of the bursting phase ($T^+ \approx 50$, comparable to our $T^+_{opt} = 30$) is taken for the eruption and growth of the burst and the remaining for its decay. The same time-scale $T^+ \approx 50$ has been measured by Blesbois *et al.* (2013) and Ricco (2004) as the regeneration time-scale of the streaks. Again, our results of decreasing T for increasing δ contradict also this interpretation, being the bursting period proportional to the distance from the wall of the structures.

Due to the convective nature of the near-wall flow, T_{opt} can be compared to the convective time scale T_c of the near-wall structures, which can be estimated

looking at the convection velocity U_c. The convection velocity U_c is known to substantially differ from the local mean velocity in the near-wall region (Kim & Hussain, 1993); it is nearly constant with a value $U_c^+ \approx 10$ in the viscous sublayer, whereas it increases from the buffer layer upwards approaching the mean flow (Quadrio & Luchini, 2003). The increase of U_c with y translates into a decrease of T_c, as these two quantities are inversely proportional $T_c = L/U_c$, with L being a length scale. This is consistent with our data that report a decrease of the local optimum T_{opt} as δ increases.

Finally, we consider the dominant interpretation of the optimal period for the SL in terms of the wall-normal diffusion length scale δ. This view is as simple as appealing, and has been put forward very early by Baron & Quadrio (1996), who noticed that the different wall-normal average positions of low-speed streaks ($y^+ \lessapprox 10$) and streamwise vortices ($10 \lessapprox y^+ \lessapprox 50$) enables an optimally configured Stokes layer to break their coherency and alter the relative spanwise position between them. The optimum value of $\delta_{opt}^+ \approx 14$ might be linked to this interpretation.

The information of the optimal (T, δ) is crucial when developing alternative strategies that produce near-wall spanwise motion, without the need of moving the wall, in a view of the possible simplest implementation in practical applications. Some examples may be plasma actuators Jukes & Choi (2012), the alternation of slip and no-slip stripes (Hasegawa *et al.*, 2011) or texture (García-Mayoral *et al.*, 2019), sinusoidal riblets (Sasamori *et al.*, 2014), dimples (Lashkov & Samoilova, 2002), elettroactive polymers combined with an electromagnetic actuator (Gouder *et al.*, 2013).

From this perspective, the search for a control law should not be necessarily dictated by the selection of an actuator, as done over the years for the wall oscillation. Instead, it may be more advantageous to seek first what is the most effective control action, and start thinking of an actuator afterwards. Furthermore, the strategy proposed in this study allows for a wider understanding of how spanwise motion influences near-wall turbulence.

3 Understanding controlled turbulence towards applications

Probing natural turbulence with drag reduction is useful to understand the nature of turbulence itself. However, despite our partial understanding of turbulence and drag reduction, it is undeniable that several flow control techniques are definitely effective at reducing turbulent skin friction. Hence, it is of no lesser importance to assess whether or not such techniques can be exploited in practical applications, e.g. for decreasing fuel consumption and pollutant emissions in the transportation field, or for increasing the energy production of wind turbines.

Several practical aspects need to be investigated before claiming that drag reduction strategies are a viable real-world solution. In the previous Chapter, the physics of wall-bounded turbulence has been studied in extremely simple and idealized flows, but we are particularly interested in aeronautics, one of the industries where drag reduction holds the highest potential. The most important parameters to account for are the Reynolds number and the Mach number. The former describes the relative importance of the inertial forces compared to the viscous forces and in typical aeronautical applications ranges from $Re \approx 10^3 - 10^5$ for Unmanned Aerial Vehicles (UAVs) up to $Re \approx 10^6 - 10^8$ for commercial and military airplanes. The latter is a measure of the velocity made dimensionless by the speed of sound, and quantifies how much the flow deviates from the incompressible regime; it ranges from $M \lessapprox 0.3$ for UAVs and gliders, to $M \approx 1$ for commercial flights, up to $M \approx 10$ for hypersonic vehicles such as reentry space capsules. Also, in practical applications the geometry is often more complex than a flat wall, both because the body has a non-planar shape, and because the locally planar wall may possess small-scale patterns. Applications such as wind turbines or airplanes clearly involve solid objects that are far away from a flat plate, possessing complex shapes featuring curved walls and multi-body configurations. When passive drag reduction techniques are considered, most often these involve a sort of smart roughness, i.e. small-scale modifications of the flat geometry which interact with the near-wall turbulence to reduce the skin-friction drag.

In the first part of the Chapter we still remain on the simple geometry of the plane channel flow, to study the effects of the Reynolds and Mach numbers on the drag reduction. We control the channel with one of the most promising active technique: the streamwise travelling waves of spanwise velocity (StTW) (Quadrio *et al.*, 2009). StTW not only attain large drag reduction rates, but are also capable of large net savings, i.e. they are still convenient after the energy cost of the actuation is accounted for. For this type of forcing, the spanwise velocity at the wall depends on both time and the streamwise coordinate as:

$$w(x, y = 0, t) = A \sin(\kappa x - \omega t), \tag{3.1}$$

where A is the forcing amplitude, x is the streamwise direction and t is the time, κ is the wavenumber (which defines the wavelength $\lambda = 2\pi/\kappa$) and ω is the frequency (which defines the oscillation period $T = 2\pi/\omega$). The oscillating wall of Eq. 2.1 (Jung *et al.*, 1992), obtained for $\kappa = 0$ and the stationary wave (Quadrio *et al.*, 2007), obtained for $\omega = 0$, are two limit cases of this general type of forcing.

To assess the efficacy of an active drag reduction technique, the benefit, i.e. the reduction of drag, needs to be compared to the cost of the actuation, i.e. the power spent to move the wall. To do so, we disregard the actuator losses, which are actually unavoidable in a practical implementation, and only consider the power transferred from an ideal actuator towards the viscous fluid. Following the definitions of the dimensionless indicators provided by Kasagi *et al.* (2009), the control power per unit wetted area is defined as a fraction of the pumping power per unit wetted area $P_0 = U_b \tau_{x,0}$, where $\tau_{x,0}$ is the streamwise component of the wall shear stress, as:

$$P_{in} = \frac{100}{P_0} \langle w(y = 0)\ \tau_z \rangle, \tag{3.2}$$

with $w(y = 0)$ the velocity imposed at the wall by the control and τ_z the spanwise component of the wall shear stress. Finally, to compare benefits and costs of the control, the net energy saving rate P_{net} is defined as:

$$P_{net} = \mathcal{R} - P_{in}. \tag{3.3}$$

Depending on the couple of parameters (κ, ω), drag increase or drag reduction can be achieved. Quadrio *et al.* (2009) considered a channel flow at $Re_\tau = 200$ and $A^+ = 12$, and found a largest drag reduction of 48% which translates into a positive net power saving of 17% for low frequency and small wavenumber. For smaller forcing intensities A, a net power saving of as high as 32% can be achieved at this value of Re.

3.1 Drag reduction and the Reynolds number

Despite the very large drag reduction and net power saving achieved, the results of Quadrio *et al.* (2009) have been obtained for a Reynolds number ($Re_b \approx 10^3 - 10^4$) that is quite far from the typical aeronautical values. Gatti & Quadrio (2016) examined the relationship between the drag reduction performance and the Reynolds number. Although they confirmed the decrease of drag reduction with Re, they found it to degrade at a much slower rate than with the previously suggested power law (Touber & Leschziner, 2012; Hurst *et al.*, 2014). They also demonstrated that the drag reduction rate by spanwise forcing becomes almost constant with Re, provided that it is expressed not via $\mathcal{R}$, that is *per se* Re-dependent, but through the Re-invariant parameter ΔB^*, i.e. the shift of the logarithmic portion of the mean velocity profile, which expresses the main effect of the StTW on the flow:

$$U^*(y^*) = \frac{1}{k} \ln y^* + B_0^* + \Delta B^* \,, \tag{3.4}$$

with k the von Kàrmàn constant, B_0^* the additive constant in the reference channel flow, and $B^* = B_0^* + \Delta B^*$ the additive constant of the controlled flow, where the superscript $*$ indicates quantities made dimensionless with the friction velocity of the controlled flow. Thus, from the knowledge of the drag reduction at low-Re, they were able to extrapolate drag reduction at higher Re, showing that a drag reduction of $\mathcal{R} = 50\%$ at $Re_\tau = 1000$ translates into $\mathcal{R} = 34\%$ at $Re_\tau = 10^5$, so that travelling waves are still of large interest for aeronautical purposes. Their model (hereinafter indicated as GQ model) hinges on the assumption that ΔB^* depends on the control parameters $(A^*, \kappa^*, \omega^*)$ but not on Re and reads:

$$\Delta B^* = \sqrt{\frac{2}{C_{f,0}}} \left[(1 - \mathcal{R})^{-1/2} - 1 \right] - \frac{1}{2k} \ln (1 - \mathcal{R}) \,, \tag{3.5}$$

where the Re-dependence is embedded in $C_{f,0}$. However, this study has two limitations. First, they used relatively small computational domains (Jiménez & Moin, 1991) to limit the otherwise prohibitive computational cost needed to explore a large portion of the parameter space. Second, their study varies the Reynolds number up to $Re_\tau = 1000$, which may not be sufficiently large for the log-law in Eq. 3.4 to be well developed, thus jeopardizing the correct extrapolation at higher Re. More recently, Marusic *et al.* (2021) observed for the first time $\mathcal{R}$ increasing with Re and justified it with the particularly slow timescale of forcing employed ($T^+ = |2\pi/\omega^+| > 350$), aiming at targeting the large outer-scaled turbulent structures whose importance increases with Re. They found that with a backward travelling wave ($\omega/\kappa < 0$) with $\omega^+ = -0.0105$ ($T^+ \approx -600$), $\kappa^+ = 0.0008$ and $A^+ \approx 5$,

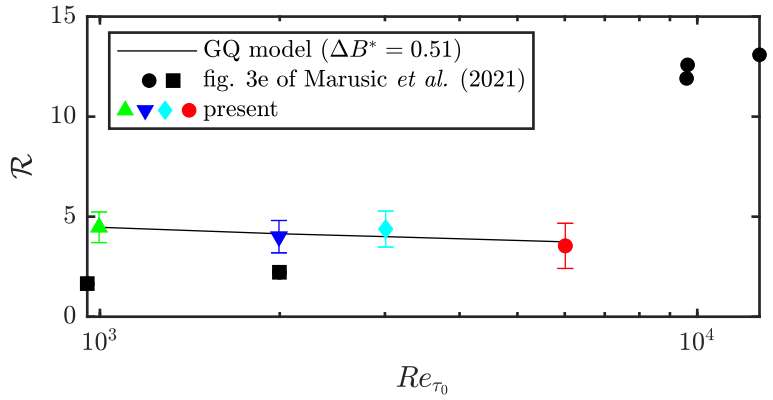

Figure 3.1: Drag reduction rate ($\mathcal{R}$) as function of the reference friction Reynolds number (Re_{τ_0}) for backward-travelling wave with parameters $A^+ = 5$, $\kappa^+ = 0.00078$ and $\omega^+ = -0.0105$; colored symbols are the present data; experimental data by Marusic *et al.* (2021) are black circles, while black squares denote their LES numerical data; the straight line is the prediction of the GQ model (3.5).

$\mathcal{R}$ increases from 1.6% at $Re_\tau = 1000$ (obtained by numerical simulations for an open-channel flow), up to 13.1% at $Re_\tau \approx 12800$ (obtained by experiments for a boundary layer). This result would open up new frontiers, suggesting that spanwise forcing is more efficient at Reynolds number typical of real problems. Despite the promising results, this study also have shortcomings; it relies on the joint observation of data for a low-Re open channel flow obtained by Large Eddy Simulations (LES) and data for a high-Re boundary layer flow (up to $Re_\tau \approx 12000$) obtained by experiments, bringing together different flow configurations and methods. Also, the experimental setup, whose dimensions are fixed in external units, does not allow to keep the control parameters constant in viscous units while varying Re_τ. The relevance of this result encourages us to provide a new accurate database produced by high fidelity data obtained by DNS in a single configuration, i.e. an open channel. The computational domain employed in the present simulations is sufficiently large to properly account for all relevant scales of turbulence, and the investigated Reynolds numbers, ranging $1000 \leq Re_\tau \leq 6000$, are large enough to avoid low-Re effects.

Figure 3.1 compares the numerical results of the present simulations with the same control parameters of Marusic *et al.* (2021) with their numerical and experimental results. Figure 3.1 confirms the validity of the predictive model for drag reduction by Gatti & Quadrio (2016) and its underlying hypothesis. This result implies that the drag reduction induced by streamwise travelling waves at a given combination of the parameters $(A^+, \omega^+, \kappa^+)$ monotonically decreases with the Reynolds number, suggesting that the large outer inertial structures do not

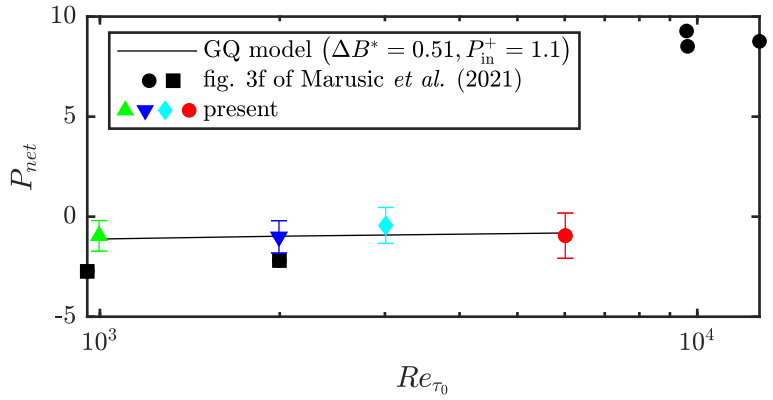

Figure 3.2: Net power saving (P_{net}) as function of reference friction Reynolds number ($Re_{\tau 0}$) for backward-travelling waves with the same parameters of figure 3.1. Colored symbols are the present data; experimental data by Marusic *et al.* (2021) are black circles, while black squares denote their LES numerical data; the straight line is the theoretical prediction obtained by combining the GQ model (3.5) with the expression of P_{in} provided by Gatti & Quadrio (2013).

significantly interfere with the working mechanism of wall-based strategies for drag reduction, confirming the predictive model based on ΔB^* proposed by Gatti & Quadrio (2016) and their results.

For a potential application of StTW to real world, not only the benefit but also the cost of the actuation needs to be considered. Figure 3.2 reports for the same parameters of figure 3.1 the net power saving P_{net}, i.e. the balace between the reduction of drag and the power spent to actuate the wall. Although we could not confirm the improvement of the drag reduction rate with Re measured by Marusic *et al.* (2021), the increase of the net saving P_{net} with Re is verified, and it gives to StTW a great potential to their exploitation for aviation. The control cost may decrease with Re at a faster rate than $\mathcal{R}$, so that P_{net} can actually increase with Re. However, P_{net} increasing with Re can happen only for StTW parameters far from the optimum (as for the present combination of parameters), where both $\mathcal{R}$ and P_{in} contribute. Unfortunately, the portion of the StTW parameter space where P_{net} is maximum is dominated by $\mathcal{R}$ and hence exhibits similar Re-dependence.

3.2 Drag reduction and the Mach number

The second parameter which is of paramount importance in aeronautics and has received limited attention so far for friction drag reduction studies is the Mach number. The first comprehensive study of the compressibility effects on drag reduction via spanwise forcing was carried out by Yao & Hussain (2019) who

performed a set of DNS of a channel flow controlled by spanwise wall oscillation at Mach number $M = 0.3, 0.8, 1.5$, at $Re_\tau = 200$ and $A^+ = 12$. They reported $\mathcal{R}$ increasing with M until reaching relaminarization for slow oscillations. More recently, Ruby & Foysi (2022) discussed the drag reduction for a channel flow at $Re_\tau = 200 - 1000$, at $M = 0.3, 1.5, 3$ forced by stationary waves at $A^+ = 12$ and they confirmed the beneficial effect of compressibility. We have extended their work to the more general and more effective travelling waves, to investigate the effect of compressibility both on drag reduction and net power saving to assess the applicability of this drag reduction techniques to real scenarios.

Following the approach of the previous studies, we perform DNS of a compressible channel flow for subsonic ($M = 0.3$), transonic ($M = 0.8$) and supersonic ($M = 1.5$) speed at the baseline friction Reynolds number of $Re_\tau = 400$ to avoid relaminarization occurring at lower Re due to the larger performance compared to the incompressible case. When compressibility is accounted for, the picture noticeably complicates and the problem of fairly compare results is not straightforward. When studying the drag reduction effect at different Re, the problem of comparison relates to choosing the proper figure of merit to measure the reduction of skin-friction drag that is Re-independent and to decide how to compare the uncontrolled and controlled cases as well as different controls. The former is the shift of the mean velocity profile ΔB. The latter can be either a scaling in nominal or actual viscous units, i.e. employing the friction velocity of the uncontrolled or controlled flow, respectively. When compressibility brings thermodynamics into the picture, the problem of comparison complicates since more quantities come into play implying more scalings available. Again it is fundamental to find the correct way to compare drag reduction at different Mach numbers, but also to compare the uncontrolled and controlled flows and the results at different control parameters.

A turbulent flow confined by walls in a compressible regime requires characterization through three distinct parameters: the Reynolds number, the Mach number, and an additional parameter that delineates the thermal state of the wall. In the context of channel flow, the relevant parameters are typically expressed as bulk quantities, specifically the bulk density ρ_b, the bulk velocity U_b, and the bulk temperature T_b. The bulk Reynolds number, i.e. $Re_b = \rho_b U_b h/\mu_w$, where μ_w is the dynamic viscosity at the wall, is kept constant during each simulation, which is run at a constant flow rate (CFR) (Quadrio *et al.*, 2016*a*) where the pressure gradient is adjusted at each time step to keep a constant U_b. Being the control wall-based and being the control parameters known to scale in viscous units (Gatti & Quadrio, 2016), Re_b is chosen so that the corresponding friction Reynolds number is fixed to the target value $Re_\tau = 400$ for the uncontrolled simulations. For the same reason, it is convenient to define the Mach number as $M = U_b/c_w$, in which the velocity scale is U_b and the speed of sound $c_w = \sqrt{\gamma R T_w}$ is evaluated at

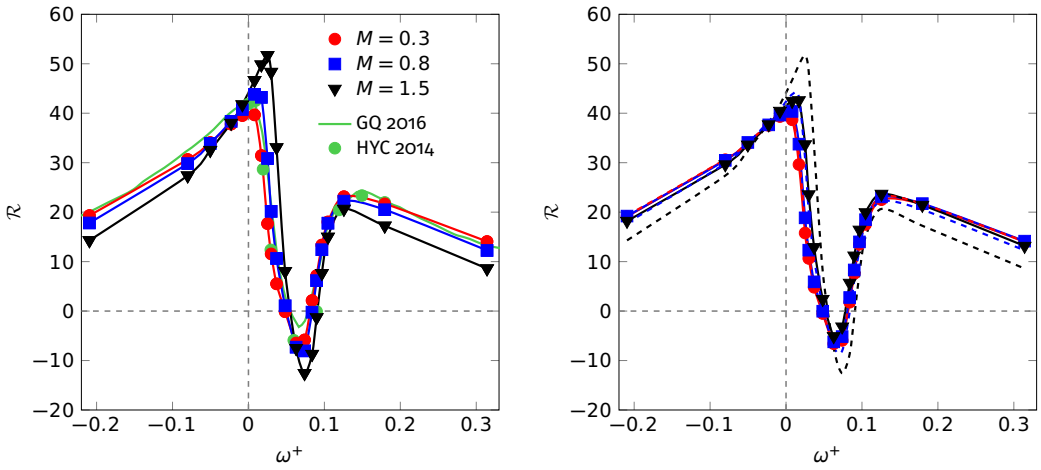

Figure 3.3: Drag reduction rate ($\mathcal{R}$) versus frequency ω^+ for the streamwise-travelling waves at $\kappa^+ = 0.005$, for ZBC (left) and CBC (right). Incompressible data are in green: solid line without symbols from Gatti & Quadrio (2016) and solid symbols from Hurst *et al.* (2014). The dashed lines data are for ZBC case. Taken from Gattere *et al.* (2024).

the wall temperature T_w. Following Yao & Hussain (2019), the Mach number is varied as $M = 0.3, 0.8, 1.5$.

In a confined flow scenario, such as that observed in channel flow, the bulk temperature is not fixed and can evolve freely until it attains an asymptotic state at which the heat produced within the flow is balanced by the heat flux through the isothermal walls. This methodology results in varying bulk temperatures across different simulations, complicating the physical interpretation of the outcomes. The discrepancies in heat transfer rates makes it difficult to discern the effects of compressibility and wall cooling. Furthermore, the elevated heat transfer rates at the wall do not accurately reflect the characteristics of typical external flows, which is the context in which we aim to implement active techniques like spanwise forcing. Exploiting this approach (the one followed by both Yao & Hussain (2019) and Ruby & Foysi (2022)) that we dub Zero Bulk Cooling (ZBC), we find compressibility having a favorable effect for most of the control parameters, especially for small wavenumbers and frequencies. We explore 42 points on the (κ, ω) parameter space located in the most interesting areas of the map (see Quadrio *et al.*, 2009). The left panel of figure 3.3 shows the drag reduction for some points of the parameter space of StTW at $M = 0.3, 0.8, 1.5$ for the ZBC case for a fixed value of the wavenumber $\kappa^+ = 0.005$. The peak of $\mathcal{R}$ increases from 40% to 52% going from the $M = 0.3$ to $M = 1.5$. However, to discern the direct effect of compressibility and the indirect effect of changed thermodynamics due to the specific geometry

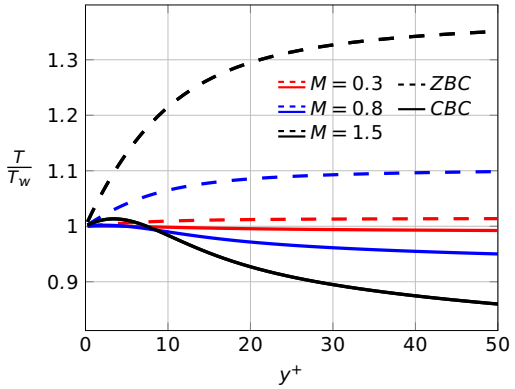

Figure 3.4: Temperature profiles in the wall region of an uncontrolled compressible channel flow at $M = 0.3$, 0.8 and 1.5, with ZBC (dashed lines) and CBC (continuous lines) approaches. Taken from Gattere *et al.* (2024).

employed, we propose a second approach to compare the results. Following Cogo *et al.* (2023) we suggest to keep the value of the so-called diabatic parameter, defined as $\theta = (T_w - T_b)/(T_r - T_b)$ where T_w is the wall temperature, T_b the bulk temperature and T_r the recovery temperature, fixed across the values of the Mach number, the uncontrolled and controlled cases and across the control parameters of the StTW. Keeping θ constant means that a fixed portion of bulk flow kinetic energy is converted into thermal energy for each simulation. To fix it constant during the simulation we add to the energy equation a cooling source term, that is computed and adjusted at each time step. It resembles the CFR technique to advance the momentum equation for which the pressure gradient evolves in time to keep a constant flow rate. This approach, we call Constrained Bulk Cooling (CBC) leads to two desirable effects at the same time. First, it is an artifact to obtain an internal flow (computationally cheaper) with a temperature profile that resembles that on an external flow, which is the configuration the active techniques are meant for. Second, the profiles of the thermodynamics quantities are such that their value do not change much between the wall and the buffer layer, so that the parameters of the control scaled in viscous units with the wall thermodynamics properties, still have the same value in the buffer layer, where the spanwise Stokes layer interacts with the near-wall structures to weaken them. Figure 3.4 shows for the uncontrolled case the different temperature profiles of $T(y)/T_w$ for both the ZBC and CBC cases. On the right panel of figure 3.3, the results for $\kappa^+ = 0.005$ with the CBC approach shows the maximum of $\mathcal{R}$ increasing only from 40% to 43% going from the subsonic to the supersonic case. Overall, spanwise forcing remains fully effective in transonic and supersonic regimes, yet the increased performance with M is substantial only with ZBC approach, whereas when $\mathcal{R}$ is compared at

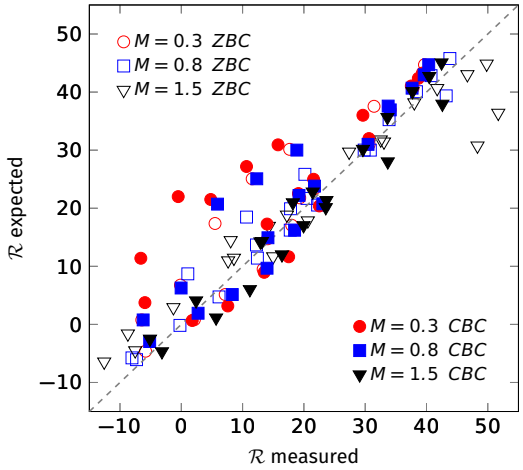

Figure 3.5: Drag reduction for the streamwise-travelling waves at $\kappa^+ = 0.005$ and $-0.2 \lessapprox \omega^+ \lessapprox 0.3$ measured in the compressible regime versus drag reduction of the incompressible regime when the control parameters are scaled with the thermodynamic properties of each different case at $y^+ = 10$. Open symbols are for the ZBC case and solid symbols for the CBC case. Taken from Gattere *et al.* (2024).

different M with CBC approach the increment in performance is very limited and only marginal improvements are detected.

In conclusion, we find that when the control parameters are made dimensionless with the actual (of each controlled case) thermodynamic properties in the buffer layer, the altered effect of the thermodynamics is removed and drag reduction becomes constant with the Mach number. Figure 3.5 shows for the same parameters of figure 3.3 the drag reduction measured by the present simulations plotted against the drag reduction expected from incompressible case for the same control parameters after being scaled with the actual (of each controlled case) thermodynamic properties in the buffer layer at $y^+ = 10$. The majority of the points lie on the diagonal line meaning that drag reduction becomes constant with the Mach number, after removing the spurious effects of the changed thermodynamics. The few outliers represent those points of the map where the drag reduction gradients are extremely large, and the incompressible data by Gatti & Quadrio (2016) are not sufficiently dense, thus they provide a poor interpolation. This result demonstrates that, once the spurious thermodynamic changes due to the internal flow configuration employed are factored out, compressibility has little to no effect on the drag reduction performance of the StTW.

In the end, to assess the overall efficacy of StTW at increasing Mach number, we also account for the cost of the actuation. Compared to the expression of

equation (3.2), the CBC case also features an extra cost due to the additional term added to the energy equation to cool the flow. However, this term serves the purpose of yielding an internal flow with a temperature profile that resembles an external flow; yet in true external flows cooling would occur naturally, so we discard this additional term in the computation of P_{in}. Under the CBC approach, P_{in} almost perfectly collapses for different values of M. This leads to P_{net} being practically constant with M, with a positive value for some parameters of the (κ, ω) space; this result declares StTW effective also at large Mach number, making the exploitation of this strategy interesting in aeronautics.

3.3 Drag reduction and the real world

When integrating drag reduction into real-world scenarios, two main issues come into play.

First, although active techniques provide large drag reduction and power saving, to date no actuators are available to enforce their control laws. On the other hand, passive techniques reach smaller drag reduction but they can be actually produced and installed. Classic passive drag reduction techniques involve small-scale organized roughness at the wall, which can be either arrays of small protrusions, e.g. riblets (Walsh & Weinstein, 1979) or small indentations, e.g. dimples (Alekseev *et al.*, 1998) or compliant surfaces (Gad-el-Hak, 1996), where the surface moves in response to the interaction with the flow above and adapts to reduce drag. Other examples include permeable substrates (Abderrahaman-Elena & García-Mayoral, 2017) made by coatings with anisotropic permeability, superhydrophobic surfaces (Daniello *et al.*, 2009) where air gaps form between the substrate and the liquid fluid, and polymeric additives, which make the fluid in fact non-Newtonian (Lumley, 1977). We are particularly interested in the classic passive techniques, involving single-phase flow and a simple modification of the wall geometry, but do not require slots, ducts or internal equipment of any kind. Riblets fall in this category. They are among the most promising techniques and have already been produced in the form of adhesive plastic films, laser machining and coatings. Riblets are small. This not only translates into production and maintenance issues, but becomes a burden whenever one is interested in an accurate numerical simulation to predict their performance in terms of drag reduction. The use of DNS is mandatory, but each riblet element needs to be properly resolved in the simulation for quantitatively accurate results. The sharp riblet corner is a further obstacle to their accurate numerical simulation.

Second, the plane channel flow employed so far is a simplified geometry which does not exist in practice, and drag reduction techniques must be applied on bodies that are way more complicated, e.g. transportation vehicles and wind turbines.

On one hand, relevant flow configurations for which drag reduction techniques are meant for, are external flows, more computationally demanding to simulate than internal flows. On the other hand, typical practical applications features non-planar wall and three-dimensional geometry i.e. large-scale modifications of the flat wall. Once again, riblets have already been extensively tested covering the surface of airplanes by seminal experiments by Boeing (McLean *et al.*, 1987), Airbus (Coustols & Savill, 1992; Szodruch, 1991) and NASA (Walsh *et al.*, 1989). In 2022 and 2023 Boeing installed riblets on the first passenger and first cargo planes on regular operations.

In this Section we deal with surfaces featuring either small-scale or large-scale modifications of the flat wall. Thus, the drag reduction definition needs to account not only for the skin-friction drag, but also for the pressure drag, i.e.:

$$\mathcal{R} = 100 \times \frac{C_D - C_{D,0}}{C_{D,0}} \tag{3.6}$$

where C_D is the sum of the skin-friction coefficient C_f and the pressure drag coefficient C_p. The former has been already defined in Chapter §2 as $C_f = 2\tau_w/(\rho\mathcal{U}^2)$ with τ_w the average wall shear stress and the latter is defined as $C_p = 2P/(\rho\mathcal{U}^2)$ with P the average pressure over the surface; the reference density ρ and velocity $\mathcal{U}$ are typically defined as bulk quantities (ρ_b, U_b) for internal flows (as used so far in this Thesis) or as free-stream quantities (ρ_∞, U_∞) for external flows.

3.3.1 A novel immersed-boundary method for non-planar walls

Passive techniques that introduce a micro-scale pattern on an otherwise flat wall in a sort of organized roughness can be studied numerically via DNS. This requires sophisticated tools to measure drag reduction with proper quantitative accuracy. To resolve the geometry of a non-planar surface, the mainstream solution is to resort to a body-fitted computational grid, where the mesh adapts to the surface's shape. This is less than optimal, and an alternative approach exists, where the discretization is operated on a Cartesian grid, with the solid body being "immersed" in it: the contour of the body does not generally coincide with the grid points. Cartesian grids offers significant benefits over body-conforming grids, including easier structured mesh generation, simpler and more efficient solution algorithms and parallel processing, as well as reductions in memory usage and computational time. Given these advantages, we opt for this second approach and introduce an

original immersed-boundary method (IBM) to simulate the turbulent flow above a non-planar wall via DNS.

Our novel IBM for the incompressible Navier–Stokes equations employs a discrete forcing formulation for a sharp discrimination of the solid-fluid interface, based upon and tightly integrated with a second-order finite difference method with a staggered grid.

To account for the presence of the solid boundary, the velocity value of the first point inside the body is linearly extrapolated from the first point in the fluid and the point on the real boundary (which has null velocity for a still body) only, both along an arm of the computational stencil. This value is not actually computed nor stored, but its contribution is accounted for implicitly by modifying the weight of the central point of the stencil, pictured in the left panel of figure 3.6. The method stands out for its simplicity and efficiency: only the weight of the center point of the Laplacian stencil in the momentum equation of the Navier–Stokes equations is modified, under the assumption that close to the boundary the viscous term is dominant compared to the temporal and advection terms, and no corrections for the continuity equation and the pressure are required. The method is implicit, meaning that the point in the solid which is nearest to the interface is accounted for implicitly; it is also implicit in time, when applied to time-dependent problems, benefitting its stability and convergence properties.

The IBM is second-order accurate in space and preserves the temporal accuracy of the underlying temporal discretization. We verify it by two examples with high geometrical complexity: the turbulent flow in a channel with a sinusoidal wall, and the flow in a human nasal cavity. The proof of the spatial second-order accuracy for the latter example is shown in the right panel of figure 3.6, where the time-averaged value of the flow rate Q at the trachea of nasal cavity for the fixed pressure drop of $5Pa$ is observed as the spatial resolution is changed.

3.3.2 Dimples

We exploit the IBM solver described above to study dimples. In their simplest geometry, dimples are small spherical caps imprinted on a surface with the recess and the flat surface being smoothly connected to avoid sharp edges. They have been extensively studied in the past for their ability to enhance the heat transfer of a surface (Kiknadze *et al.*, 1984), to influence the separation on bluff bodies (e.g. golf balls) (Bearman & Harvey, 1976) and more recently to investigate their possible drag reduction capabilities (Lashkov & Samoilova, 2002). Over the past 20 years, a few research groups have focused their efforts on the potential use of dimples to reduce drag, trying to determine the ideal size and shape. Unfortunately, there is still lack of agreement on the very possibility that dimples can lower skin-friction drag, and on their working mechanism. Several studies have reported drag

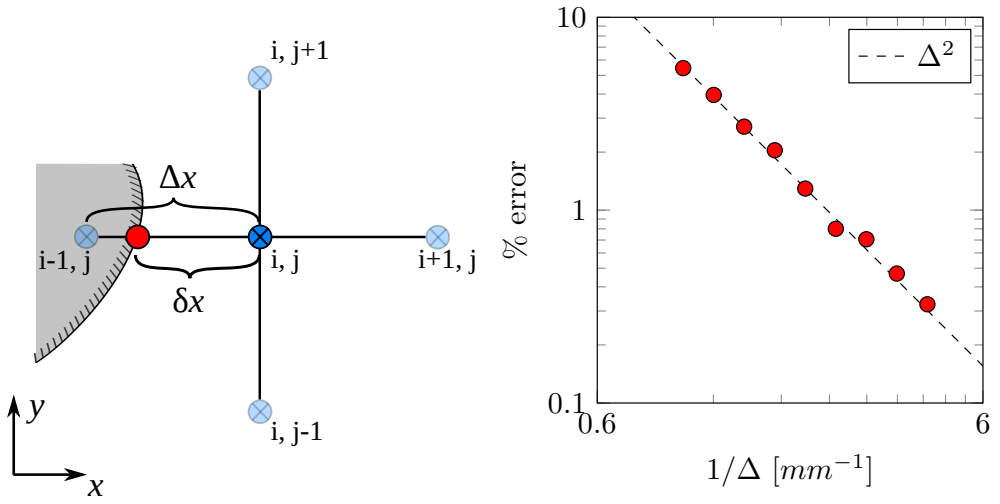

Figure 3.6: Left: a solid body (gray background) is immersed in a fluid (white background) with an overlaid computational stencil for the w velocity component in the $x - y$ plane. Dull colors denote the fully internal/external points, and vivid colors the points where the immersed-boundary correction is applied. A red dot denotes the actual boundary intersection. Right: Convergence of the flow rate for the nose test case. Percentage error $100(Q^{(e)} - Q)/Q^{(e)}$ of the mean flow rate versus spatial resolution. The dashed line shows the expected second-order decrease.

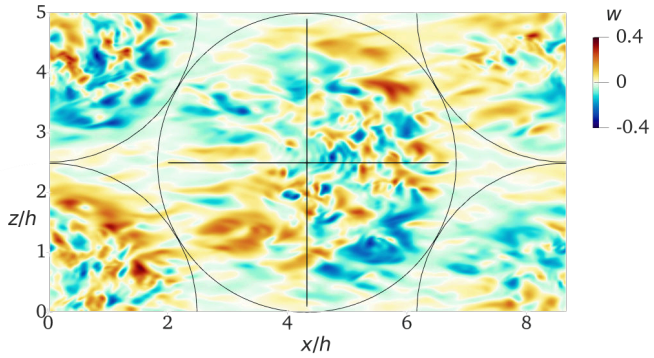

Figure 3.7: Instantaneous spanwise velocity component w on a wall-parallel plane at $y^+ = 1.3$ from the flat part of the wall. Lengths and velocities are made dimensionless with h and U_b. The velocity field is computed by DNS for a circular dimple, which actually yields drag increase. Taken from Gattere *et al.* (2022*b*).

reduction, while several others have not. We have revised the whole literature body on the topic, founding a great variety of results, ranging from 14% of drag reduction to 20% of drag increase. This ambiguity stems from the absence of a widely recognized standard for measuring drag and comparing various shapes with the reference flat wall. There are unavoidable discrepancies between simulations and experiments, as well as between internal (like plane channels) and external (like boundary layers) flows. The inconsistent results can also be attributed to our incomplete knowledge of how dimples impact the surrounding flow field.

Flow visualizations (see figure 3.7) show that, near the wall, streamlines coming from a flat surface bend towards the dimple centerline in the recess's upstream portion, then away from it in the downstream part. This creates a converging-diverging pattern, leading to an alternating spanwise velocity that resembles the spanwise-oscillating wall. A minimum spanwise velocity is required for the active technique to work. The amplitude of the spanwise velocity at the wall, A^+, must be of the same order of the natural spanwise velocity fluctuations in the near-wall region, so that a threshold value is $A^+ \approx 1$.

Figure 3.7 shows an instantaneous flow field over a circular dimple; the values of the spanwise velocity w are very large, up to 40% of the bulk velocity (or $w^+ \approx 6$). However, in the spanwise forcing case, the spanwise velocity is homogeneous in the spanwise direction, different from what happens for the flow over a dimple, for which patches of positive and negative w are detected. Moreover, even with spanwise forcing, one should only be concerned with friction drag when dealing with a flat wall. In contrast, the presence of dimples introduces both viscous and pressure drag, complicating the measurement of small variations in

aerodynamic drag, especially within turbulent flow conditions. When assessing the drag characteristics of a reference flat surface against those of a rough surface, it is crucial to be aware of the subtlety of the measurement. This includes the necessity of precisely defining and controlling the Reynolds number, differentiating between internal and external flows, and accurately establishing the equivalent "flat wall" flow to compare with.

After accounting for all these issues with precision, our computations at $2700 \lessapprox Re_b \lessapprox 10400$ using the most standardized circular dimples configuration (Chen *et al.*, 2012) cannot find any drag reduction for any of the tested geometry parameters. We are also interested in understanding the scaling of drag changes caused by circular dimples when their shape is maintained but only their dimensions are altered. Only the value of the depth (either in inner or outer units) has been varied independently, and all the other parameters did vary accordingly to maintain the geometry similar. The findings suggest an outer scaling; this outcome aligns with expectations, given that the examined dimples are relatively deep, resembling a form of large-scale d-type roughness (Jiménez, 2004). In this context, the large cavities effectively disrupt the near-wall layer, which is the only region where inner scaling would be applicable.

3.3.3 Riblets on a flat plate

Among passive techniques, riblets are most promising, and currently under design and test to be extensively applied on commercial airplanes. In their simplest configuration, riblets are small two-dimensional streamwise-aligned micro-grooves on the surface which have a periodic pattern in the spanwise direction. Riblets have been extensively studied over the last 45 years, starting from the seminal paper by Walsh & Weinstein (1979) and have been proven to achieve about 10% of drag reduction at low Reynolds number. Experiments by Bechert *et al.* (2000) and studies by Luchini *et al.* (1991) have clarified the essentials of the drag reduction mechanism.

When riblets are extremely small compared to the characteristic length scales of the near-wall turbulence, i.e. in the so-called viscous regime, the above flow does not perceive the local geometry of the rough surface, but only a homogenized effect of it. The homogenized effect experienced by the mean streamwise flow is a flat plane where the velocity vanishes, situated at a depth beneath the riblet tips. The distance between a reference plane (usually the riblet's tip) and this virtual wall is called parallel protrusion height $h_{\parallel}$. In contrast, the turbulence encounter a distinct virtual flat boundary; the distance between the reference plane and the turbulence virtual wall is known as the perpendicular protrusion height $h_{\perp}$. The latter is the virtual origin perceived by the quasi-streamwise vortices, and it is defined by the plane where the spanwise fluctuations vanish. This lies

on the assumption that QSV induce a transverse shear over their virtual origin, but no wall-normal velocity, due to the spanwise velocity varying linearly and the wall-normal velocity varying quadratically with the distance from the wall, just above it. Luchini *et al.* (1991) proved that the effectiveness of riblets in reducing drag depends on the difference of the two above mentioned protrusion heights $\Delta h = h_{\parallel} - h_{\perp}$ only. Whenever $\Delta h > 0$, the turbulence is impeded more than the mean flow inside the riblets' valleys, meaning that the quasi-streamwise vortices are displaced away from the wall, leading to the decrease of the near-wall turbulent mixing, thus to the reduction of skin-friction drag. The difference in the virtual origin of the mean flow and the turbulence causes the shift of the logarithmic portion of the mean velocity profile ΔB^+ of Eq.(3.4); due to the linearity of the viscous regime, $\Delta B^+ \propto \Delta h^+$ (Jimenez, 1994; Luchini, 1996).

More recently, Gómez-de-Segura *et al.* (2018) argued that the displacement of the QSV would ultimately reach a saturation point, unless the shift of the origin perceived by the spanwise fluctuations was accompanied by a corresponding shift for the wall-normal fluctuations. In general, when the virtual origins perceived by the two fluctuations differ, the QSV would experience an intermediate virtual origin, whose distance from the reference wall is referred to as the turbulence protrusion height h_T. If the definition of the protrusion height difference is corrected as $\Delta h^+ = h_{\parallel}^+ - h_T^+$, then $\Delta B^+ = \Delta h^+$ is proved (Ibrahim *et al.*, 2021).

In the viscous regime, the effectiveness of riblets increases linearly with their dimension, measured as their cross-sectional area A_g. However, for riblets larger than their optimum size ($\sqrt{A_g^+} \approx 11$) (García-Mayoral & Jiménez, 2011), the proportionality breaks down and riblets show a typical k-type roughness behavior (Jiménez, 2004), increasing drag.

The IBM code introduced in §3.3.1 has been successfully employed (Gattere *et al.*, 2022*a*; Gatti *et al.*, 2023; Cipelli *et al.*, 2024) for the reliable prediction of the drag reduction capabilities of two-dimensional riblets. Here the documented spatio-temporal accuracy near a non-trivial boundary made possible by our IBM implementation is crucial to obtain reliable measurements of the friction coefficients and of their differences (i.e. drag reduction). In fact, measuring (small, sometimes very small) differences in C_f is a challenging task, no less in numerical simulations than in laboratory experiments. In the past, very few experimental setups have managed to measure drag reduction reliably enough to give significance to figures as small as 0.1 percentage point. A notable example is the Berlin oil channel (Bechert *et al.*, 1992), where the entire setup was designed around the goal of measuring a drag difference directly instead than measuring two drag forces and then taking the difference. Another example is the air channel at KIT (Güttler, 2015; Gatti *et al.*, 2015), where a combination of unconventional layout, careful design and extremely controlled experimental procedures allow measuring

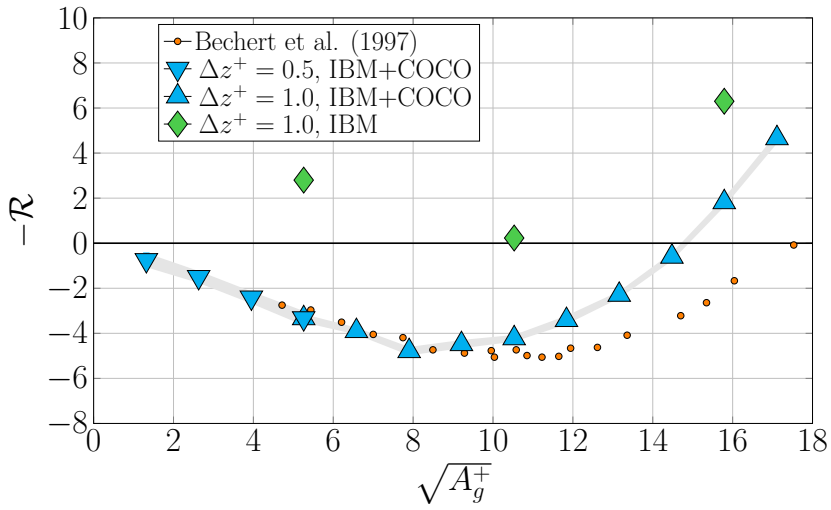

Figure 3.8: Drag reduction curve for riblets of equilateral triangle shape. Triangles are results from Cipelli *et al.* (2024) obtained for two different spanwise grid resolutions Δz^+. IBM refers to immersed boundary implementation of §3.3.1, COCO refers to the corner correction activated at geometrical singularity. The gray area represents the temporal uncertainty. Orange circles are experimental data from Bechert *et al.* (1997).

ΔC_f within an uncertainty of 0.4%. In DNS, several issues plaguing the experiments do not exist, but we have to deal with the geometric singularity at the sharp tip of each riblet. Tip sharpness is essential for drag reduction (García-Mayoral & Jiménez, 2011), but obviously poses overwhelming requirements in terms of space-time resolution. We have tackled the problem by following a method, originally proposed by Luchini (1991), that has been implemented on top of the IBM solver. In this method, the local solution close to the singularity is analytically determined and compensated for, so that a reasonable spatial resolution can be used. The analytical solution hinges upon the observation that near the tip the velocity gradients become infinitely large, leading to dominating viscous effects and to a local solution that is well described by the Stokes equations. The IBM augmented with the corner correction has made possible the results shown in figure 3.8, where drag reduction data for a given riblet geometry are obtained that not only compare very well with the high-quality experimental reference, but also are robust with respect to a large change in size of the computational grid.

3.3.4 Riblets on a three-dimensional body

The last considered topic is the outcome of friction drag reduction techniques applied on realistic, non-planar geometries. Applying e.g. a friction-reducing textured surface to a complex body, such as an aircraft or the blades of a wind turbine, could bring to light secondary effects compared to the application on a flat wall. Banchetti *et al.* (2020) demonstrated via DNS the beneficial effect of StTW not only on skin-friction drag but also on pressure drag when applied to a simple bump over an otherwise flat wall. Quadrio *et al.* (2022) studied by DNS the StTW applied to a portion of a wing in transonic flight, finding that a localized actuation has the potential to boost the aerodynamic efficiency of the whole aircraft. These are very promising results which open up the possibility to effectively install drag reduction techniques on airplanes not only to reduce skin-friction drag but also to exploit positive secondary effects.

The use of reliable numerical tools such as DNS is, once again, unavoidable. However, at the moment, DNS can only be used for simple cases. The simulations are too costly for complex, high-Reynolds-number aeronautical configurations, like for an entire aircraft.

Therefore, numerical simulations of complex shapes are usually based on the Reynolds-averaged Navier–Stokes equations (RANS) equipped with a turbulence model. Gadda *et al.* (2017) simulated the effect of travelling waves on the surface of a modern transport aircraft at $Re = 3\times10^6$ in transonic flight. The forcing could not be introduced directly, but it was accounted for via a modified wall function which provides the shift in the mean velocity profile ΔB. They found a decrease in the skin-friction drag as expected and also an additional positive effect in the pressure drag reduction for certain angles of attack. These results lead to two indirect positive effects, i.e. a delay in the onset of the shock, and a lift increase.

Having considered riblets on a flat wall with DNS in §3.3.3, we also test the effectiveness of riblets on aeronautical configurations with RANS. Aupoix *et al.* (2012) modified the Spalart–Allmaras turbulence model to account for riblets by using smooth-wall geometry, and Koepplin *et al.* (2017) extended this model to describe riblets which are locally misaligned with the mean flow and to account for mean pressure gradients. Similarly, Mele *et al.* (2016) introduced a modified boundary condition for the $k-\omega$ turbulence model; it correctly simulates standard riblets, but fails to account for devices inducing larger drag reduction, such as spanwise forcing.

More recently, Mele & Tognaccini (2018) developed a new model based on the slip-length concept, whose application can be extended to model all surfaces with passive/active treatments that have as a main effect a shift of the mean velocity profile ΔB in the turbulent boundary layer. The effect of the shift of the mean velocity profile can be equally seen as a shift of the wall, which is the place where

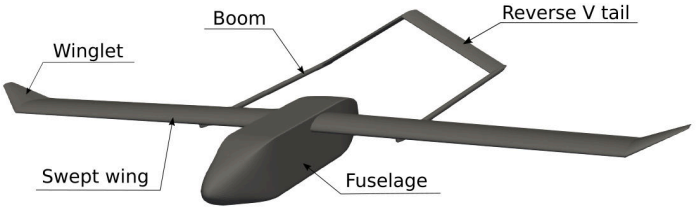

Figure 3.9: Geometry of the UAV. Taken from Cacciatori *et al.* (2022).

the velocity vanishes due to the no-slip constraint. A shift of the zero-velocity plane ($y_{no-slip}$) implies that the velocity at the geometric wall ($y = 0$) is different from zero; therefore, a slip condition should be applied there. The velocity at the geometric wall can be extrapolated as

$$u^+(y = 0) = u^+(y = y_{no-slip}) + \Delta B^+ \left.\frac{\partial U^+}{\partial y^+}\right|_{y=0},$$

where $u^+(y = y_{no-slip}) = 0$. In the viscous sublayer the velocity is linear with the distance from the wall, i.e. $u^+ = y^+$. This implies that $\Delta y^+ = \Delta B^+$, where ΔB^+ is the shift of the mean velocity profile (see §3.1). Knowing that in the viscous sublayer $\Delta y^+ = \Delta B^+$ equals the protrusion height difference Δh^+ (see §3.3.3), we get

$$u^+(y = 0) = \Delta h^+ \left.\frac{\partial U^+}{\partial y^+}\right|_{y=0},$$

which is the partial-slip boundary condition to apply at the geometric wall to account for the shift of the mean velocity profile due to the manipulation of the surface with drag reduction control.

We leverage the partial-slip boundary condition to study the effects of riblets on the surface of a simplified geometric model of an Unmanned Aerial Vehicle (UAV), depicted in figure 3.9, at flight Reynolds number $Re = U_\infty c \rho_\infty / \mu_\infty = 5 \times 10^5$, where c is the chord length, employing RANS simulations. We imagine covering the surface of the UAV with the best performing riblets which can attain roughly $\mathcal{R} \approx 10\%$ at low Re which translates through Eq.(3.5) into a shift of $\Delta B^+ \approx 1$. Fixing the shift in viscous units means assuming riblets are locally optimal everywhere, thus they change their physical size along the body depending on the local friction velocity of the flow. The discrete counterpart of the above boundary condition with derivatives approximated with finite differences reads:

$$u_0 = u_1 \frac{\Delta h^+}{\Delta h^+ + (y_1 - y_0)},$$

where the subscript 0 and 1 refer to the grid point at the wall and the first grid point in wall-normal direction, respectively.

The application of simulated riblets to the UAV has revealed indirect and beneficial effects that extend beyond merely decreasing friction drag. This makes the implementation of a friction-reduction mechanism particularly appealing in low-speed scenarios. Specifically, riblets alter the pressure distribution over the aircraft's wing, resulting in a notable decrease in form drag and an increase in lift. While this increase in lift naturally leads to a rise in lift-induced drag, the necessity for the aircraft to maintain a specific lift during cruise operations necessitates a lower angle of attack, which further aids in drag reduction. Ultimately, the use of riblets can achieve a total drag reduction of up to 3% for the aircraft during cruise conditions. This result derives from a combination of a friction drag (which contributes to 32% of the total drag) reduced by 6.1 % and a pressure drag (which contributes to 68% of the total drag) reduced by 1.5 %.

Cost-effective simulations can elucidate the potential drag reduction associated with specific extents and placements of riblets coverage on the aircraft's surface. To this aim, we have designed a set of simulations to explore partial coverage of the aircraft surface with riblets. The amount of coverage is quantified by the ratio β between the riblets-covered area and the total area, with $\beta = 1$ indicating total coverage. In these simulations, the full aircraft is considered, but riblets coverage varies. Figure 3.10 illustrates the pressure, friction and total drag reduction for the various coverage scenarios: (A) the exclusion of riblets from the trailing edge surface only, (B) from the boom surface only, (C) from the entire surface except for the wings, and (D) from the entire surface except the wings' suction side. Given the significant role of secondary effects in diminishing pressure drag due to riblets, almost 2/3 of the maximum drag reduction achieved with full coverage can be achieved with the coverage of the suction side of the wings only, accounting for 1/3 of the total area. Furthermore, the costs associated with the production, application, and maintenance of riblets are directly proportional to the surface area covered. This particular configuration not only yields a favorable cost-benefit ratio but also preserves the integrity of the UAV fuselage, where various systems such as sensors, cameras, and transmitters are intended to be installed.

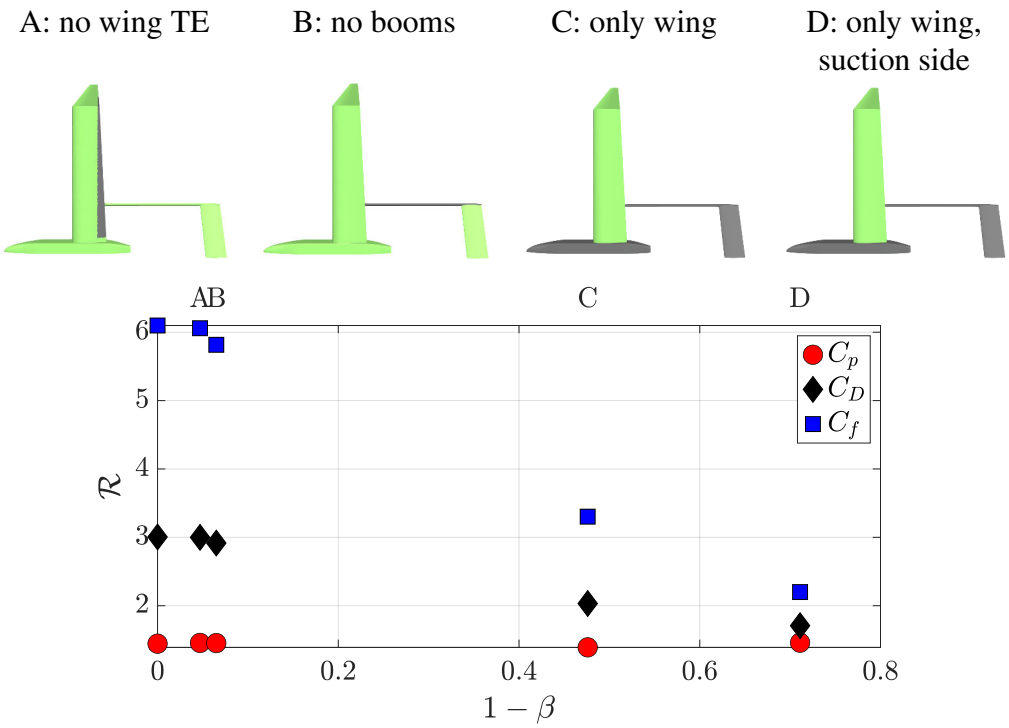

Figure 3.10: Pressure, friction and total drag reduction contributions for different configurations of riblets coverage. $\beta = 1$: full coverage; $\beta = 0.953$: riblets on the whole aircraft except the wings' trailing edge; $\beta = 0.935$: riblets on the whole aircraft except the booms (B); $\beta = 0.524$: riblets on the wings only (C); $\beta = 0.289$: riblets on the suction side of the wings only (D).

4 Conclusions and outlook

In this Thesis, we have considered some of the unresolved issues concerning wall-bounded turbulence and its control for drag reduction. Inhibiting the self-sustainment of near-wall turbulence, possibly up to a point where the flow becomes laminar again, requires a comprehensive understanding of the physics involved, and the ability to alter it effectively.

Some novel, dedicated tools can be profitably used towards this goal. A rigorous statistical description of the channel flow system via the linear response function, as well as a somewhat less rigorous spanwise forcing devised irrespective of its practical realization, have led us to understand a little more of the turbulent flow, and to put into focus additional interesting questions that motivate further research.

The linear impulse response function (LIRF), i.e. the linear relationship between the input and the output of a dynamical system, has been defined and measured for a turbulent channel flow, with the input being a body force placed at different distances from the wall. The LIRF contains a large amount of information, yet it answers simple questions, and for example identifies the optimal location and manner to apply volume forces to achieve a desired effects anywhere in the system. As such, it is of particular interest for the design of feedback control laws, where a linear model of the plant (the turbulent channel flow) is needed; within the linear approximation, the LIRF is the best possible plant model.

The conceptual experiments carried out with the extended Stokes layer (ESL) fully belong to the non-linear regime. It is important to note, once again, that while the time-dependent spanwise velocity profile was straightforwardly enforced in the DNS, in principle one could solve the Navier–Stokes equations with a non-homogeneous boundary condition (made by the conventional oscillating wall in our case) complemented with a suitable wall-normal distribution of spanwise body force. Using an ESL has been instrumental to discriminate the effects of its temporal (T) and spatial (δ) scales. Our findings suggest that the widely recognized optimal period for minimizing skin-friction drag, namely $T^+ = 100$, may lack physical significance as a time scale, and simply represents the parameter combination nearest to the global optimum, that is permissible under the constraints

of the oscillating wall. Both T and δ play a role in the reduction of drag, with larger performance achieved when their values are inversely related: while a large frequency is beneficial, the influence of the SL should extend further from the wall into the bulk flow. The key take-away of this experiment is the finding that we should think of the oscillating wall not as an actuation strategy, but simply as a (possibly far from optimal) means to modify the flow to achieve drag reduction. What is the crucial flow modification needed to achieve the goal is still unclear, and the search for a feasible actuator should be postponed until such a fundamental piece of information is obtained.

The two tools mentioned above could also be combined. The LIRF lends itself to testing flow control ideas in a quick and simple way, dispensing with the need of lengthy and costly simulations. By aggregating information obtained from these approaches, linear and non-linear effects can be discriminated, thereby highlighting the main pathway to drag reduction. This could be interesting also for near-wall turbulence in general; in fact, generation of the streaks from the vortices is a linear process, while the regeneration of the vortices from the streaks needs a non-linear mechanism.

To obtain a complete view of how flow control interacts with turbulence, the multiscale, inhomogeneous and anisotropic nature of the latter must be properly represented. To this purpose the anisotropic generalised Kolmogorov equations (AGKE) seem the perfect tool; they are budget equations for the second-order structure function tensor, and represent the Reynolds stresses in the compound space of scales and positions. Since most of active (e.g. oscillating wall) and passive (e.g. riblets) drag reduction techniques possess a coherent (in time and/or in space) deterministic component, the AGKE have been extended to their phase-aware version (φ-AGKE). The φ-AGKE include, thanks to a triple decomposition, the mean, coherent and stochastic parts of a flow field, and describe their interaction. In a sense, while tools like LIRF and ESL are made to understand and optimize the input of the drag reduction process (i.e. the forcing itself), the φ-AGKE are made to understand the output, i.e. the turbulent flow with drag reduction.

Although the physical mechanism underlying drag reduction through spanwise forcing remains partially understood, the effectiveness of spanwise forcing is empirically evident. Therefore, it makes sense to also consider the applied side of the problem. Current studies have been conducted mostly in simplified flow set-ups, such as incompressible channel flows at low Reynolds number, and further research is needed to determine the advantages of spanwise forcing in practical applications, especially in aviation, where even a tiny reduction of skin-friction drag could provide huge environmental and economic benefits, but the configuration is quite far away from the incompressible, low-Re plane channel flow. We have verified to what extent the drag reduction rate is still effective at high Reynolds

numbers (up to $Re_\tau = 6000$) and in the supersonic regime (up to $M = 1.5$). We have found that the reduction of drag remains comparable to that observed in incompressible and low-Re conditions, as long as the drag reduction figures are properly compared. This indicates that: i) the underlying physics of drag reduction via spanwise forcing is independent of both Reynolds and Mach numbers (under the tested flow conditions and geometries); ii) spanwise forcing retains its utility under realistic flow conditions, paving the way for its exploitation in aviation.

From a practical standpoint, the most relevant metric for evaluating the effectiveness of a drag reduction technique is the net power saving, which represents the trade-off between the advantages of actuation (i.e., drag reduction) and the associated costs (i.e., power required to implement the control law). Our analysis has revealed that net power saving remains almost constant as Reynolds and Mach numbers increase; under specific control parameters, significant net power savings can be realized, thereby enhancing the potential of spanwise forcing.

We have also explored the performance of drag reduction methods in specific applications. Active techniques, such as spanwise forcing, demonstrate significant drag reduction capabilities but, to date, suitable actuators are not available. Therefore, passive techniques, which do not require actuation while yielding comparatively modest reductions in drag, are worth considering. Presently, riblets stand out as the most promising passive method, having undergone extensive numerical and experimental testing. They can achieve drag reductions of approximately 7-10% at low Reynolds numbers and are already in use on aircraft surfaces during regular operations.

Using a boundary condition that indirectly accounts for the effects of riblets without the need of describing their geometry, the performance of riblets on an unmanned aerial vehicle (UAV) has been studied with RANS. This study has led to the expected local reduction in skin-friction drag, accompanied by additional, indirect benefits, including decreased pressure drag, increased lift, and an overall enhancement in aerodynamic efficiency. Although our measurements indicate that riblets continue to provide drag reduction in complex, realistic configurations, the most effective riblets can only reduce total drag by up to 3% for the tested UAV at a chord-based $Re_\infty = 5 \times 10^5$. This level of reduction rate may not justify the high costs associated with their production, application, and maintenance, particularly given the riblets' extremely small size (whose optimal dimension scales in viscous units) and the requirement for a sharp tip to function effectively. This calls for a further optimization process, that stems from understanding that the benefit of covering the unit surface area of the aircraft with riblets is not uniform. A model boundary conditions and the ability to use cheap RANS to simulate various configurations become essential tools to carry out such optimization.

Of course, the enhancement of the current passive techniques is another road to explore. To achieve this, insights gained from spanwise forcing techniques,

which are capable of delivering substantial drag reduction and energy saving also at high Reynolds and Mach numbers, could be taken advantage of. The obvious example is three-dimensional riblets, whose tip could vary its spanwise position along the streamwise direction to mimic spanwise forcing. Sinusoidal riblets has been already studied numerically with LES (Peet *et al.*, 2008) and experimentally (Cafiero & Iuso, 2022), arriving at conflicting conclusions. Current research efforts are focused on improving the drag reduction capabilities of sinusoidal riblets in turbulent flows. This involves modifying the riblet tips to accurately capture the effects of singularities without necessitating an excessively fine mesh Luchini (1991), while also maintaining precision in skin-friction measurements. Preliminary findings have been reported by Gattere *et al.* (2022*c*); Gatti *et al.* (2023); Cipelli *et al.* (2024) and found a relative improvement of about 30% with sinusoidal riblets with a streamwise wavelength of about $\lambda^+ = 1500$ and an amplitude $A^+ \approx 8$. However, only two combinations (λ, A) have been tested and a parametric study could bring up larger performance. While work in this field is just starting, it is important to stress how the numerical method that has been developed, with extreme control of its accuracy near the boundary and the ability of taking care of the geometrical singularity corresponding to the riblet tip, is an enabling step, without which future numerical experiments would just produce another data point in a confusing data set.

Different types of surface patterns, such as dimples, may offer a suitable framework for passive spanwise forcing. Dimples do not present sharp tips, and therefore are much easier to produce and maintain (and study). After reviewing the limited and often contradictory literature on this subject, we have concluded that there is no evidence that circular dimples, the most commonly studied shape, do yield drag reduction. However, we do not dismiss the possibility that alternative dimple shapes could produce favorable outcomes. A systematic investigation, however, is essential to discover an optimal design.

Drag reduction in practical turbulent flows is still quite a far fetched goal, yet the efforts of the research community are making this goal progressively less unfeasible. While is difficult to underestimate the tremendous challenge posed by the development of suitable technologies, the limited understanding of the physics of turbulence and of the drag-reduced turbulent flows constitutes an even more important and more fundamental obstacle. I hope that the research effort spent during this PhD represents a contribution, however minor, in the right direction.

Part II

Papers

Impulse Response in Turbulent Channel Flow

This manuscript has been written with
Codrignani A., Gatti, D. & Quadrio, M.

Impulse Response in Turbulent Channel Flow

Abstract

The mean linear response of a turbulent channel flow to a small enough, impulsive (in space and time) body force is defined and measured through direct numerical simulations, by considering the continuous range of wall distances from the wall to the centerline. A zero-mean, white-noise body force is used to probe the turbulent flow, and the response function is obtained efficiently by accumulating the space-time correlation between the white forcing input and the velocity field obtained as output. Three different responses are measured, at the same Reynolds number, for a laminar channel flow, a channel flow where the mean velocity profile has the turbulent shape but no turbulence is present, and a true turbulent channel flow. The impulse response analysis leads to confirming and extending some important results known in literature in the laminar case. However, the amplitude and shape of the responses to the laminar and turbulent flows are not identical. The mean effects of the turbulence, including turbulent diffusion, are needed to be consider to completely characterize the linear behavior of a turbulent flow.

1.1 Introduction

The linear impulse response function (LIRF) is a classic tool for the description of linear, time-invariant dynamical systems. Its use in relation to physical phenomena that involve moving fluids is not particularly widespread, as it is well known that the Navier–Stokes equations which govern the fluid motion are highly non-linear. However, instances in fluid mechanics exist where the LIRF concept has been used, including the study of turbulent flows.

The analysis of the LIRF of the flow to small perturbations is a natural approach in the (linear) hydrodynamic stability theory. A comprehensive review of the latest developments in the field has been given by Schmid (2007). In this context, the Navier–Stokes equations are linearized about an equilibrium solution, the base flow. The non-normal nature of the linearized Navier–Stokes (LNS) operator in wall-bounded shear flows implies the possibility for a transient growth of the perturbation energy, which explains how e.g. the Hagen–Poiseuille flow or the plane Couette flow undergo laminar-to-turbulent transition even though the linear modal stability theory predicts that the critical Reynolds number for transition is infinite.

The importance of transient growth in shear flows has been fully appreciated in recent years, starting with the seminal contribution by Butler & Farrell (1992); Farrell & Ioannou (1993); Trefethen *et al.* (1993). In this context, Jovanović & Bamieh (2005) examined the input-output properties of the LNS equations for a plane channel, and described the spatio-temporal response of the flow to an impulsive body force. They showed that the flow features typically observed during transition can be interpreted as input-output resonances of the LIRF. Under the limitation of a linearized setting, they were also able to rank the body force components in terms of their potential for transient energy amplification, finding that body forces acting along the spanwise and wall-normal directions entice the strongest response, with the streamwise velocity component being the most affected.

The importance of transient growth for the transition to turbulence prompted researchers to consider whether such linear mechanisms play an important role also in the dynamics of fully-fledged turbulent flows. Here, the obvious difficulty is that turbulence is highly non-linear, implying that the stochastic "background" turbulence can affect the amplified disturbances. In the context of LNS, the effect of turbulent fluctuations on the disturbances is usually neglected, and turbulence is simply taken into account (as done e.g. by Högberg *et al.*, 2003) by linearizing about the turbulent mean flow, although this is not a solution of the Navier–Stokes equations. The resolvent analysis for wall bounded turbulent flows introduced by McKeon & Sharma (2010) relies on this assumption. It interprets the turbulent velocity field as the output of the Navier–Stokes equations linearised about the mean turbulent flow profile, with their non-linear terms acting as an external forcing. The modal analysis of the linear transfer function (the so-called resolvent) of the system describes the linear amplification mechanisms for each structure within the turbulent flow. In some cases, the average effect of the Reynolds stresses is modelled by augmenting the linear governing equations with an eddy viscosity (Hussain & Reynolds, 1972) defined *a priori* (see, for instance, del Álamo & Jiménez, 2006). A recent review by McKeon (2017) summarizes the recent efforts in the analysis of the LNS, which confirms how transient amplification

plays an essential role in the self-sustainment of turbulence (Kim & Lim, 2000), and connects it to properties of some small- and large-scale coherent structures observed in turbulent flows (see, for instance, Schoppa & Hussain, 2002; del Álamo & Jiménez, 2006; McKeon & Sharma, 2010; Davis *et al.*, 2019). However, mean-flow-based linear analysis is non-unique since the characteristics of the linearised operator depend on the state variables considered (Karban *et al.*, 2020).

Recently, Vadarevu *et al.* (2019) considered the evolution of velocity fluctuations due to an isolated spatio-temporal impulse using the LNS equations augmented with eddy viscosity (eLNSE) in a channel flow at a friction Reynolds number of $Re_\tau = 10\,000$. They found that the impulse response evolves into self-similar coherent structures, which remain attached to the wall and are reminiscent of the so-called attached eddies discussed by Townsend (1976), which populate wall-bounded turbulent flows. Such structures could not be observed when the same experiments was repeated with the same base flow but without eddy viscosity. Madhusudanan *et al.* (2019) confirmed the previous results by showing that LNS are capable to predict the three-dimensional velocity field given two-dimensional information obtained from direct numerical simulation (DNS) of turbulent channels only when eddy viscosity was taken into account.

Provided the disturbances have a small enough amplitude, a linear response of the flow to an external disturbance can be defined, albeit in a time-averaged sense, even in a fully non-linear setting. If avoiding to resort to the LNS means that the influence of non-linear turbulence on the linear response can be fully accounted for. The importance of accounting for the turbulence effects has been recently emphasized by the results obtained by Russo & Luchini (2016). They measured the LIRF of a turbulent channel flow to a steady volume force, and compared their results to the prediction obtained on the basis of the LNS equations. They found that the two linear responses are significantly different, which implies that the "background" turbulence has a non-negligible impact on the linear response. Moreover, they demonstrated that it is impossible to conceive a (positive and finite) eddy viscosity that makes the results obtained with eLNSE compatible with the true measurement.

Prompted by the previous studies, the present works aims at measuring the time-mean response of a turbulent channel flow to a impulsive body force in space and time, while accounting for the full non-linearity of the system. Beside assessing the importance of non-linear turbulent transport, the mean impulse response is of greatest interest, thanks to the aforementioned relevance of linear mechanisms in turbulent flows and the potential for assisting in the design of control laws for turbulence. The measurement is carried out numerically, with a fully non-linear code for the direct numerical simulation (DNS) of the Navier–Stokes equations.

The importance of properly defining and measuring the channel flow LIRF goes beyond what discussed above. In fact, the response contains full information

of the linear, time-invariant system and as such could be exploited in flow control algorithms, where the LIRF is a complete model of the plant. With that, one would possess the information on *where* and *how* a control should be applied to achieve the desired mean effect. It was suggested (see for example Kim & Lim, 2000) that linear mechanisms are central to the near-wall turbulence regeneration cycle, and that linear models of turbulence may suffice for flow control purposes. Among the several attempts appeared in the literature along this direction (Kim & Bewley, 2007), some used the LIRF concept: Luchini *et al.* (2005) and later Martinelli (2009) established the basis for a Wiener–Hopf feedback controller, where the observer and the controller could be both designed thanks to the knowledge of the LIRF.

In a non-linear setting, the linearity of the response is only guaranteed by the small amplitude of the forcing. In doing so, at least in the turbulent case, the problem arises that the small forcing allowed by linearity is much smaller that the natural turbulent fluctuations, leading to an extremely low signal-to-noise ratio. To circumvent this problem, in this work we resort to the approach introduced by Quadrio & Luchini (2002) and Luchini *et al.* (2006) when measuring with DNS the mean linear impulse response of a turbulent channel flow to blowing/suction applied at the wall. Instead of applying an impulsive forcing, they used a zero-mean, white-noise signal as an input, and computed the space-time correlation between the input (blowing/suction at the wall) and the output (the whole flow): since the input signal is random and therefore uncorrelated to the turbulent fluctuations, the input-output correlation immediately provides the LIRF, with the advantage of a much higher signal-to-noise ratio. The same strategy was later applied by Carini & Quadrio (2010) to measure the LIRF in an homogeneous and isotropic turbulent flow to an impulsive body force, thus providing direct access to a quantity central in the Direct Interaction Approximation theory developed by Kraichnan (1959).

In the present work, the mean LIRF is properly defined and subsequently measured with DNS in a channel flow, to provide the complete description of the relationship between a generic body force input and the resulting velocity field. In doing so, we will consider: i) the impulse response in absence of turbulence, i.e. the laminar impulse reponse; ii) the impulse response when the equations are linearized about the turbulent mean velocity profile and turbulence is neglected, i.e. with an approach similar to that of the resolvent analysis; iii) the full impulse response, which includes the mean diffusive effects of turbulence, and whose linearity only derives from the small amplitude of the forcing. A detailed comparison of the three responses is instructive to understand the propagation mechanism of small perturbations in a turbulent flow, and has a foundational interest for applications regarding flow control and turbulence modelling.

The structure of the paper is as follows. After this Introduction, section §1.2 defines the LIRF and describes how to measure it. The computational details

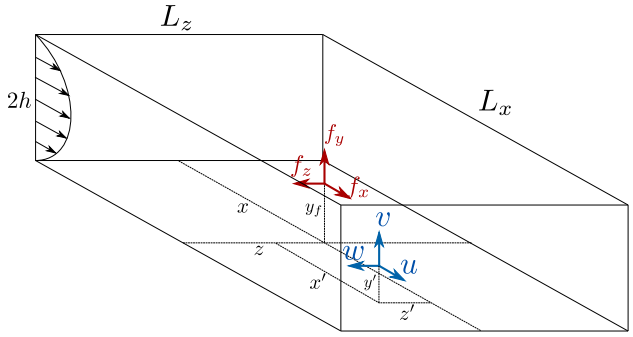

Figure 1.1: Sketch of the plane channel with reference system and definition of quantities related to the response function.

employed in the study are presented in §1.3 and the validation of the present approach against existing literature is reported in §1.4. Sections §1.5 describes the characteristics of the impulse response both in wavenumber and physical space and §1.6 apply it to a test case; finally, a brief concluding discussion is elaborated in §1.7.

1.2 The LIRF of the turbulent channel flow

1.2.1 Definition of LIRF

We begin with the definition of the LIRF for a turbulent channel flow, followed by the approach employed for measuring it via DNS, and by the description of the discretization choices.

The linear impulse response function $\mathcal{H}$ (in the frequency or the time domain) is defined for a non-linear system, under the condition that the input is small enough. In the simplest scalar and purely temporal case, $\mathcal{H}$ links the input f and the output q of a system in the time domain through a convolution, i.e.:

$$q(t) = \int_{-\infty}^{+\infty} \mathcal{H}(t-\tau) f(\tau)\, \mathrm{d}\tau, \tag{1.1}$$

or, equivalently, in the frequency domain as $\hat{q}(s) = \hat{\mathcal{H}}(s)\hat{f}(s)$, where the hat indicates Fourier transform in time. By setting the input to a Dirac delta function $\delta(\tau)$, equation (1.1) immediately shows that $q(t) = \mathcal{H}(t)$, hence the name LIRF.

The extension to the plane channel flow system is relatively straightforward. Instead of a generic linear system, we consider an incompressible (laminar or turbulent) flow in an indefinite channel, bounded by two plane parallel walls, located at $y = 0$ and $y = 2h$. The velocity components u in the streamwise x

directions, v in the wall-normal y direction and w in the spanwise z direction are also indicated throughout the paper as u_i, with $i = 1, 2, 3$. The channel and the reference system are sketched in figure 1.1.

The flow is governed by the incompressible Navier–Stokes equations, here written in dimensionless form:

$$\boldsymbol{\nabla} \cdot \mathbf{u} = 0 \tag{1.2}$$

$$\frac{\partial \mathbf{u}}{\partial t} + \mathbf{u} \cdot \boldsymbol{\nabla}\mathbf{u} = -\boldsymbol{\nabla} p + \frac{1}{Re}\nabla^2 \mathbf{u} + \mathbf{f} \tag{1.3}$$

and the LIRF now becomes a second-order tensor that links an impulsive body force input vector $\mathbf{f}$ to the output vector $\mathbf{u}$. Besides the increased dimensionality in comparison to the SISO linear system described by equation (1.1), two main differences need to be emphasised. One is that, being the governing equations non-linear, the linearity of the LIRF tensor is not guaranteed, but is conditional on the input being sufficiently small. The second is that, in the turbulent case, the LIRF needs a statistical description, i.e. we seek for the mean LIRF. By assuming that the external forcing is small enough for linearity to hold, one obtains:

$$\langle u_j(x, y, z, t) \rangle = \int_0^{L_x} \int_0^{2h} \int_0^{L_z} \int_{-\infty}^{+\infty} \langle \mathcal{H}_{i\to j}(x-\xi, y-\eta, z-\zeta, t-\tau) f_i(\xi, \eta, \zeta, \tau) \rangle \, \mathrm{d}\tau \, \mathrm{d}\zeta \, \mathrm{d}\eta \, \mathrm{d}\xi \tag{1.4}$$

where $\langle \cdot \rangle$ represents the average over time. We define the function $\mathcal{H}_{i\to j}$ as the mean impulse response so it already embed the time average and the forcing is known *a priori* so it does not need to be averaged, thus to ease the notation the symbol $\langle \cdot \rangle$ is dropped. Eq.(1.2.1) shows that the LIRF tensor $\mathcal{H}_{i\to j}$ linearly relates the impulsive input f_i to the velocity output $\langle u_j \rangle$ of the flow.

Further simplifications are possible owing to the symmetries of the plane channel flow, for which the x and z directions are homogeneous and the flow is stationary (in the statistical sense in the turbulent case). Hence the above definition can be simplified, converting the relevant convolutions into products, as:

$$\langle \hat{u}_j(\alpha, y, \beta, t) \rangle = \int_0^{2h} \int_{-\infty}^{+\infty} \hat{\mathcal{H}}_{i\to j}(\alpha, y-\eta, \beta, t-\tau) \hat{f}_i(\alpha, \eta, \beta, \tau) \, \mathrm{d}\tau \, \mathrm{d}\eta \tag{1.5}$$

where the hat now indicates quantities spatially Fourier-transformed along the wall-parallel directions.

The impulsive forcing is localised in the wall-normal direction, hence its expression can be further specialised as:

$$\hat{f}_i(\alpha, y, \beta, t) = \hat{\mathrm{f}}_i(\alpha, \beta, t) \delta(y - y_f) \tag{1.6}$$

where y_f is the wall-normal location of the impulsive forcing. If this functional form is substituted into Eq.(1.5), one obtains:

$$\langle \hat{u}_j(\alpha, y, \beta, t) \rangle = \int_{-\infty}^{+\infty} \hat{\mathcal{H}}_{i\to j}(\alpha, y - y_f, \beta, t - \tau) \hat{\mathrm{f}}_i(\alpha, \beta, \tau, y_f)\, \mathrm{d}\tau. \tag{1.7}$$

In the following, to indicate the mean LIRF we will employ the notation $\hat{\mathcal{H}}_{i\to j}(\alpha, y, \beta, t; y_f)$ to emphasise that, because of the non-homogeneous wall-normal direction, the dependence on the forcing position is an important independent variable, which we will consider as a parameter.

1.2.2 How to measure the LIRF

As explained by Quadrio & Luchini (2002), in the present context there are diverse and equivalent strategies to measure the LIRF. They are briefly described below.

1.2.2.1 Measuring the LIRF in the frequency domain

In this approach, used for example by Hussain & Reynolds (1972) in a laboratory experiment, one measures the frequency response of the system. For the simple SISO system of equation (1.1) it means employing the following form for the forcing:

$$\mathrm{f}(t) = \epsilon \sin(\omega_f t) \tag{1.8}$$

where ϵ is the amplitude of the forcing, and ω_f is assigned values of frequency. Its extension to the MIMO plane channel flow system of equation (1.2.1) implies the forcing to be:

$$\mathrm{f}_i(x, z, t; y_f) = \epsilon_i \sin(\alpha_f x) \sin(\beta_f z) \sin(\omega_f t) \tag{1.9}$$

where ϵ_i is not a scalar but a vector of small enough amplitudes, one for each direction of the forcing f_i, and α_f, β_f and ω_f are assigned values of wavenumbers and frequency. In a noiseless system like a laminar flow, this type of forcing leads to a straightforward and direct observation of the LIRF, and repeated observations for different values α_f, β_f and ω_f enable the complete characterisation of the tensor $\mathcal{H}_{i\to j}$. When statistical noise is present, as in the turbulent case where the natural turbulent fluctuations act as noise, a phase-locked average in principle enables separating the deterministic part of the response from the random part. The obvious drawback of this approach is that a single experiment only yields the LIRF in a single point of the three-dimensional (α, β, ω) space.

1.2.2.2 Measuring the LIRF in the physical domain

An alternative approach that yields the entire LIRF at once consists in using a Dirac delta function as input, which, for a SISO system, leads to the following form for the forcing in the physical domain:

$$\mathrm{f}(t) = \epsilon\delta(t - t_f).$$

For a noiseless (laminar) system, this provides the entire LIRF. In fact, substituting this in Eq.(1.1), the response reads:

$$q(t) = \int_{-\infty}^{+\infty} \mathcal{H}(t-\tau)\epsilon\delta(\tau - t_f)\,\mathrm{d}\tau = \epsilon\mathcal{H}(t - t_f).$$

so that:

$$\mathcal{H}(t - t_f) = \frac{q(t)}{\epsilon}.$$

The same reasoning holds for the present specific case of plane channel flow, for which the external forcing in physical domain reads:

$$\mathrm{f}_i(x, z, t; y_f) = \epsilon_i\delta(x - x_f)\delta(z - z_f)\delta(t - t_f);$$

in Fourier space the above forcing becomes $\hat{\mathrm{f}}_i(\alpha, \beta, t_f) = \epsilon_i\delta(t - t_f)$ which substituted into Eq.(1.7) provides

$$\begin{aligned}\langle\hat{u}_j(\alpha, y, \beta, t; y_f)\rangle &= \int_{-\infty}^{+\infty} \hat{\mathcal{H}}_{i\to j}(\alpha, y - y_f, \beta, t-\tau)\epsilon_i\delta(\tau - t_f),\,\mathrm{d}\tau \qquad (1.10)\\ &= \epsilon_i\hat{\mathcal{H}}_{i\to j}(\alpha, y, \beta, t - t_f; y_f),\end{aligned}$$

so that the LIRF is directly proportional to the response of the system:

$$\hat{\mathcal{H}}_{i\to j}(\alpha, y, \beta, t - t_f; y_f) = \frac{\langle\hat{u}_j(\alpha, y, \beta, t)\rangle}{\epsilon_i}. \qquad (1.11)$$

Unfortunately, the obvious advantage of getting the whole LIRF with a single measurement is overwhelmed by the need to obey linearity constraint, which mandates extremely small amplitudes ϵ_i. Although inconsequential in the noiseless laminar case, this limitation makes the approach highly unpractical in the turbulent case. Turbulent fluctuations are akin to noise, which can be averaged out by employing ensemble averaging, or at least an average over periodic repetitions of the same impulsive forcing over a long enough simulation time. Unfortunately, the forcing amplitudes required for linearity are much smaller than the natural turbulent noise, so that the simulation time required to bring down the statistical noise at a level at which the deterministic part of the response appears is simply not affordable.

1.2.2.3 Measuring the LIRF as an input-output correlation

The third approach combines a decent S/N ratio (as in the first approach) with the ability to carry out a complete measurement in one shot (as in second approach). The approach, originally introduced by Luchini *et al.* (2006), relies on a well-known result in signal theory: they forced the flow with a zero-mean white-noise signal as an input, and instead of the actual velocity output they measured the space-time correlation between input and output. This exploits the well-known result from signal theory that, when a white noise (i.e., a delta-correlated signal) is passed through a linear system, the correlation between input and output is proportional to the impulse response of the system.

The correlation between the input and the output, exploiting the definition of Eq. (1.1) reads:

$$\langle q(t) f(\tau - T) \rangle = \int_0^{+\infty} \langle \mathcal{H}(t-\tau) f(\tau) f(\tau - T) \rangle \, \mathrm{d}\tau \tag{1.12}$$

Being the system forced with a white-noise signal, i.e.:

$$f(t) = \epsilon \omega(t), \tag{1.13}$$

and recalling that $\langle \omega(t)\omega(t-\tau) \rangle = \delta(\tau)$, the correlation of Eq. (1.12) becomes:

$$\langle q(t) f(\tau - T) \rangle = \int_0^{+\infty} \mathcal{H}(t-\tau)\epsilon^2 \delta(T) \, \mathrm{d}\tau = \epsilon^2 \mathcal{H}(t - (\tau - T)) \tag{1.14}$$

As a result, after redefining $\mathcal{T} = t - (\tau - T)$, the impulse response function from time 0 to time $\mathcal{T}$ can be computed as the correlation between the output and the white-noise input, as:

$$\mathcal{H}(\mathcal{T}) = \frac{\langle q(t) f(t - \mathcal{T}) \rangle}{\epsilon^2}. \tag{1.15}$$

In the case of plane channel flow, the correlation between the input and the output, exploiting the definition of Eq. (1.7) reads:

$$\langle \hat{u}_j(\alpha, y, \beta, t) \hat{\mathrm{f}}_i^*(\alpha, \beta, \tau - T) \rangle = \int_0^{+\infty} \hat{\mathcal{H}}_{i\to j}(\alpha, y - y_f, \beta, t - \tau) \langle \hat{\mathrm{f}}_i(\alpha, \beta, \tau) \hat{\mathrm{f}}_i^*(\alpha, \beta, \tau - T) \rangle \, \mathrm{d}\tau \tag{1.16}$$

where $(\cdot)^*$ is the conjugate transpose. Forcing the system with a white noise $\omega_i(\alpha, \beta, t)$ leads to the correlation of Eq. (1.16) becoming:

$$\langle \hat{u}_j(\alpha, y, \beta, t) \hat{\mathrm{f}}_i^*(\alpha, \beta, \tau - T) \rangle = \int_0^{+\infty} \hat{\mathcal{H}}_{i\to j}(\alpha, y - y_f, \beta, t - \tau) \epsilon_i^2 \delta(T) \, \mathrm{d}\tau, \tag{1.17}$$

resulting, after defining $\mathcal{T} = t - (\tau - T)$, in the impulse response as a function of the correlation between the output and the white-noise input, as:

$$\hat{\mathcal{H}}_{i\to j}(\alpha, y, \beta, \mathcal{T}; y_f) = \frac{\langle \hat{u}_j(\alpha, y, \beta, t; y_f) \hat{\mathrm{f}}_i^*(\alpha, \beta, t - \mathcal{T}) \rangle}{\epsilon_i^2}. \tag{1.18}$$

1.3 Computational details

1.3.1 Discretization of the DNS

We employ the pseudo-spectral DNS solver introduced by Luchini & Quadrio (2006), which is based on a mixed discretization where variables in the homogeneous directions are represented with Fourier modes, whereas collocation points are used in the wall-normal direction, and derivatives are discretized with fourth-order accurate, compact explicit finite-difference schemes. Temporal integration is partially implicit with a low-storage Runge-Kutta explicit scheme for the convective terms and a Crank-Nicolson implicit scheme for the viscous terms.

Three sets of simulations are carried out: a laminar flow, a fully turbulent flow, and a pseudo-turbulent flow where turbulence is absent but the base flow is the mean flow of the turbulent case. In each set of simulations, independent cases are run where the impulsive forcing is placed at different distances y_f from the wall (see figure 1.1).

A first set of parameters concerns the baseline channel flow DNS simulation. The Reynolds number is set at $Re_b = U_b h/\nu = 2280$, where U_b is the bulk velocity, h the channel half-height and ν is the kinematic viscosity of the fluid. It corresponds to a friction Reynolds number of $Re_\tau = u_\tau h/\nu = 150$, with $u_\tau = \sqrt{\tau_w/\rho}$, being τ_w the shear stress at the wall and ρ the density; it is quite low in consideration of the demanding computational study.

The computational domain has dimensions of $L_x = 4\pi h$, $L_y = 2h$ and $L_z = 2\pi h$. The wall-normal direction is resolved with $N_y = 128$ points for all the cases. The homogeneous directions are discretized with $N_x = N_z = 64$ modes (further increased by a factor of 3/2 for dealiasing) for the laminar and pseudo-turbulent cases. The turbulent case is more demanding in terms of spatial discretization, and employs $N_x = N_z = 192$ modes plus de-aliasing; in terms of viscous units, the equivalent grid has a spacing of $\Delta x^+ = 9.8$ and $\Delta z^+ = 4.9$ (or $\Delta x^+ = 6.5$ and $\Delta z^+ = 3.3$ with dealiasing) and $0.6 < \Delta y^+ < 4$.

In the turbulent case, the deterministic response emerges progressively averaging out the noise from the turbulent fluctuations while the simulation runs. Hence, the simulation needs to be run as long as possible and in the present case is remarkably large at $20000h/U_b$ (or, equivalently, 2×10^5 viscous time units). The temporal discretization uses a fixed time step of $\Delta t = 0.02h/U_b$, which keeps the CFL number far from the stability limit of the Runge–Kutta scheme. The other simulations, where turbulent fluctuations are absent, do not require averaging, and are carried out for as long as the response function needs to be observed equal to $\mathcal{T} = 100h/U_b$ convective time units, with a fixed time step $\Delta t = 0.01h/U_b$.

The forcing amplitude of the forcing is set to $\epsilon_i = \epsilon = 0.0001$ for both the laminar and pseudo-turbulent case and $\epsilon_i = \epsilon = 0.001$ for the turbulent case. The

choice of the these values is delicate due to the linearity constraint to which this approach builds on; a brief discussion is presented in §1.4.2.

1.3.2 Computation of the response

For the laminar and pseudo-turbulent cases the mean impulse response function is directly computed in the physical domain as described in §1.2.2.2.

For the fully turbulent case the above approach is unfeasible and the LIRF is measured by the input-output correlation introduced in §1.2.2.3. The mean LIRF is computed as the correlation between the forcing white-noise input and the output velocity. The discrete counterpart of Eq.(1.18) reads:

$$\hat{\mathcal{H}}_{i\to j}(\alpha, y, \beta, k\Delta t; y_f) = \frac{1}{\epsilon_i^2}\frac{1}{N}\sum_{n=0}^{N-1} \hat{u}_i(\alpha, y, \beta, (n+k)\Delta t)\hat{f}_i^*(\alpha, \beta, n\Delta t; y_f) \quad (1.19)$$

with $n, k \in \mathbb{N}$, Δt is the time step on the n-th instant, and $\mathcal{T} = N\Delta t$ when constant Δt is employed, where N is the maximum number of time steps. A white-noise input is enforced in the system and reads:

$$\hat{f}_i(\alpha, \beta, n\Delta t; y_f) = \epsilon_i e^{I2\pi \mathrm{rand}(n\Delta t)} \quad (1.20)$$

where I at the superscript is the imaginary unit and $\mathrm{rand}(n\Delta t_n)$ is a random number between 0 and 1 at the time $n\Delta t$.

Most frequently used algorithm, required the knowledge of the whole time history of both the correlating elements. This traditional approach is unfeasible in a DNS simulation, because the memory storage of the whole history of the velocity field clearly overshoot the limits. Therefore, only the forcing history f_i is saved each updating time step Δt sample. It is computed as:

$$\begin{cases} \mathcal{F}^{it}(\alpha, \beta, 1) = \hat{f}_i^*(\alpha, \beta, n\Delta t) \\ \mathcal{F}^{it}(\alpha, \beta, l+1) = \mathcal{F}^{it-1}(\alpha, \beta, l) \quad \text{for} \quad l = 2..N\Delta t \end{cases} \quad (1.21)$$

Correlation computation simply becomes a sum, between the old term and the product of the velocity field and the forcing history f_i. At the update iteration it, the LIRF is updated as:

$$\hat{\mathcal{H}}_{i\to j}^{it}(\alpha, y, \beta, k\Delta t) = \hat{\mathcal{H}}_{i\to j}^{it-1}(\alpha, y, \beta, k\Delta t) + \frac{1}{\epsilon_i^2 N}\hat{u}_i^{it}(\alpha, y, \beta, 0)\mathcal{F}_i^{it}(\alpha, \beta, k\Delta t) \quad (1.22)$$

for $k = 0..N$ and for each α, β, y. Proceeding this way only the instantaneous velocity field is required, since the previous fields are implicitly considered in the LIRF of the previous time-step.

1.3.3 Discretisation of the response

Peculiar to the present study is the need to discretise the response function. Given the focus of the present work on the position y_f where the forcing is located, in the wall-normal direction $\mathcal{H}_{i\to j}$ is discretised with the same resolution and on the same collocation points used for the velocity, and the parameter y_f is varied from the first inner point to the centreline. However, the statistical symmetry of the plane channel allows the forcing locations y_f to vary only in one channel half, i.e. $0 < y_f \leq 1$. Hence, for ech of the three considered cases, 64 independent simulations have been carried out by varying the parameter y_f.

The response function, which is known to be significant at relatively large wavenumbers only, is also truncated spatially with respect to the modes used in the DNS. Based on previous experience, the response is stored for the highest 64 modes in both streamwise and spanwise direction.

Previous experience has also been useful to decide the temporal extent for which $\mathcal{H}$ is observed. All the measured response functions are truncated after a delay of $\mathcal{T} = 100$ convective time units h/U_b. However, the temporal changes of the response manifest themselves at a highly variable rate, with fast changes at short times followed by a slower evolution. Hence, a non-uniform temporal discretization is useful to minimise storage requirements, by using 100 time instants non-uniformly distributed to increase resolution where the changes take place at the highest rates.

Since the phenomenology of the impulse response is more meaningful in the first transient instants, a finer time discretization should be preferable at the beginning. In the laminar and pseudo-turbulent case, the time step at which the response is computed changes as follow:

$$\Delta t = \begin{cases} 0.01, & k \leq 100 \\ 0.05, & 100 < k \leq 200 \\ 0.1, & 200 < k \leq 300 \\ 1, & 300 < k \leq 384. \end{cases} \tag{1.23}$$

In the turbulent case, the response time step changes as follows

$$\Delta t = \begin{cases} 0.02, & k \leq 24 \\ 0.08, & 25 < k \leq 56 \\ 0.32, & 57 < k \leq 87 \\ 5.12, & 88 < k \leq 104. \end{cases} \tag{1.24}$$

1.3.4 Visualisation of the response

The impulse response function $\hat{\mathcal{H}}_{i\to j}(\alpha, y, \beta, \mathcal{T}; y_f)$ of a turbulent channel flow depends, for a given value of the parameter y_f, on the wavenumbers α, β in the homogeneous directions, on the position y in the wall-normal direction, and on the time $\mathcal{T}$ elapsed after the impulsive forcing.

A sort of aggregation of such a large amount of data is needed to visualise the response. Following Jovanović & Bamieh (2005), one can visualise the response in wavenumber space and quantify which modes are more amplified by a disturbance after averaging the response in time and wall-normal direction. The temporal and wall-normal dynamics are thus aggregated by taking the H_2 norm of $\mathcal{H}$ in the time domain and along y, as:

$$\|\hat{\mathcal{H}}_{i\to j}(\alpha, \beta; y_f)\|_2^2 = \frac{1}{2\pi}\int_0^\infty \frac{1}{2h}\int_0^{2h} \hat{\mathcal{H}}_{i\to j}(\alpha, y, \beta, t; y_f)\hat{\mathcal{H}}^*_{i\to j}(\alpha, y, \beta, t; y_f)\,\mathrm{d}t\,\mathrm{d}y \tag{1.25}$$

The linear response can be also aggregated further by averaging over all the forcing locations y_f.

The impulse response measure presented by Jovanović & Bamieh (2005) is based on a linearization of the Navier–Stokes equations solved within the state-space framework. One of the main benefits of the DNS-based measurement employed in this work, is the possibility to visualize the impulse response not only in the wavenumber space, but also in the physical space. It can be done either by taking the absolute maximum over the wavenumbers, the wall-normal positions and the position of the forcing and analyzing its variation over time:

$$\mathcal{H}_{i\to j,m}(t) = \max_{\alpha,y,\beta,y_f} |\hat{\mathcal{H}}_{i\to j}(\alpha, y, \beta, t; y_f)|, \tag{1.26}$$

or alternatively by taking the absolute maximum over the wavenumbers, time and wall-normal position to describe its dependence on the forcing position y_f:

$$\mathcal{H}_{i\to j,m}(y_f) = \max_{\alpha,y,\beta,t} |\hat{\mathcal{H}}_{i\to j}(\alpha, y, \beta, t; y_f)|. \tag{1.27}$$

Finally, a more complete comparison is performed by looking at the isosurfaces of the response in three dimensional space.

To fairly compare the laminar and pseudo-turbulent cases to the turbulent case, the LIRF of the latter is divided by 2, to account for the different time window for which the forcing is applied, namely $\Delta t = 0.01$ for the former regimes and $\Delta t = 0.02$ for the latter.

1.4 Validation

Despite the novelty of the LIRF concept in turbulent flows, and of the technique employed in the present work for its measurement, a validation is possible in the laminar case. Analogous results exist in the literature, and cross-validation can be achieved by comparing the outcome of alternative approaches.

In the following, the analogies between this work and the available literature information are first addressed; the response functions measured in the laminar flow via direct impulsive forcing and via the input-output correlation are then compared. Lastly, the linearity constraint is addressed, and the amplitude of the white-noise forcing is discussed.

1.4.1 Comparison with literature and alternative approaches

Previous works considered the effects of body force perturbations with different aims, such as: the transient energy growth and input-output analysis (Reddy *et al.*, 1998; Jovanović & Bamieh, 2005), the pseudo-spectral analysis (Trefethen *et al.*, 1993), and the amplification of stochastic excitations (Farrell & Ioannou, 1993; Bamieh & Dahleh, 2001).

In particular, as far as the laminar case is concerned, the present work is closely related to that by Jovanović & Bamieh (2005), who studied the spatio-temporal response of the linearised Navier–Stokes equations in a laminar channel flow to an impulsive body force. In their dynamical system formulation, the response is obtained from the algebraic Lyapunov equation, for an impulsive input which is white-noise distributed in wavenumber and frequency, while a discretised delta function centered at y_f is employed among the wall normal direction, so that the compound response function turns out to be $\tilde{\mathcal{H}}_{i\to j} = \mathcal{H}_{i\to j}(\alpha, \beta, y, t)$. Their temporal and wall-normal dynamics are further aggregated by taking the H_2 norm of $\tilde{\mathcal{H}}_{i\to j}$ in the time domain and along y, according to Eq.(1.25).

More information are provided by the present measurement technique, namely the description of the response both in the Fourier and in the physical space, the effect of the forcing wall-normal distance y_f on the LIRF and the behaviour of the LIRF in time.

To compare the results of the reference paper with the H_2 norm of the full response computed in the present work, we run two dedicated DNS laminar simulations to match their $Re_c = U_c h/\nu = 2000$ where U_c is the centerline velocity. Within the linearity constraint (see below §1.4.2 for the linearity check), the forcing location y_f is made to span all the available wall distances. The laminar cases are used to validate two alternative measurement techniques: the lack of noise (i.e. turbulence) allows both the impulsive forcing described in §1.2.2.2 and the

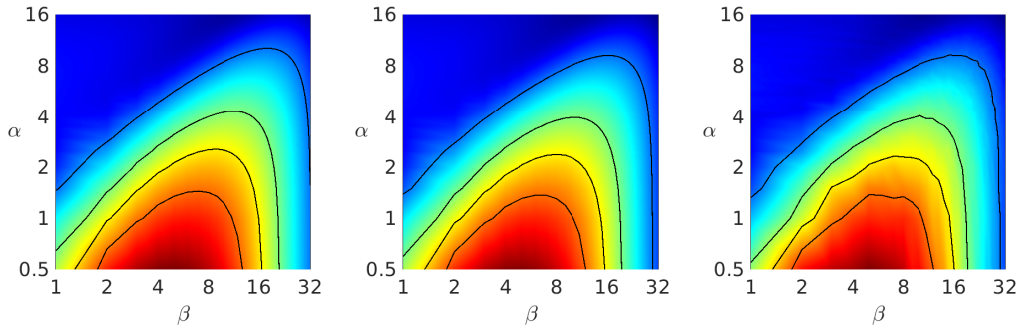

Figure 1.2: Plot of $\log_{10} \|\hat{\mathcal{H}}_{y\to u}\|_2$ as a function of the wavenumbers α and β. Comparison of three measurement techniques: a) the method by Jovanović & Bamieh (2005); b) DNS-based direct impulsive forcing, §1.2.2.2; c) DNS-based measurement of the input-output correlation with white-noise input, §1.2.2.3.

input-ouput correlation described in §1.2.2.3 to be used.

Figure 3.1 compares the three LIRF in terms of its $\hat{\mathcal{H}}_{y\to u}$ component. (Similar results are obtained by comparing the other components). The leftmost panel shows the results by Jovanović & Bamieh (2005), reproduced by following their methodology by running the Matlab script (kindly provided to us by M. Jovanović); the central and rightmost panels show the output of the present simulations, where equation (1.25) is used to compute the norm $\|\hat{\mathcal{H}}_{i\to j}\|_2$ for the impulsive forcing and the statistical white-noise measuring technique, respectively. To match the results of Jovanović & Bamieh (2005), the response is nomalised by the time step of the forcing and by $(\Delta y_c)^2$, where Δy_c is the size of the discretization in wall-normal direction at the centreline.

The comparison of the three panels demonstrates an excellent qualitative and quantitative agreement between such diverse measurement methods. In particular, figure 3.1 shows an extremely good agreement between the response obtained by impulsive forcing in panel (b) and the response obtained by the white-noise method in panel (c). The latter appears slightly more noisy than the others, which is to be expected given the statistical nature of the measurement. In the remainder of this paper, we use results from the direct impulse when referring to laminar and pseudo-turbulent case.

1.4.2 Linearity of the impulse response in a non-linear system

The cornerstone of the $\mathcal{H}_{i\to j}$ measurement is the linearity hypothesis, which mandates a careful choice of the forcing amplitude ϵ_i in equation (1.9). The forcing amplitude must be empirically determined as the largest forcing that guarantees linearity, to maximise the S/N ratio and/or minimise the averaging time.

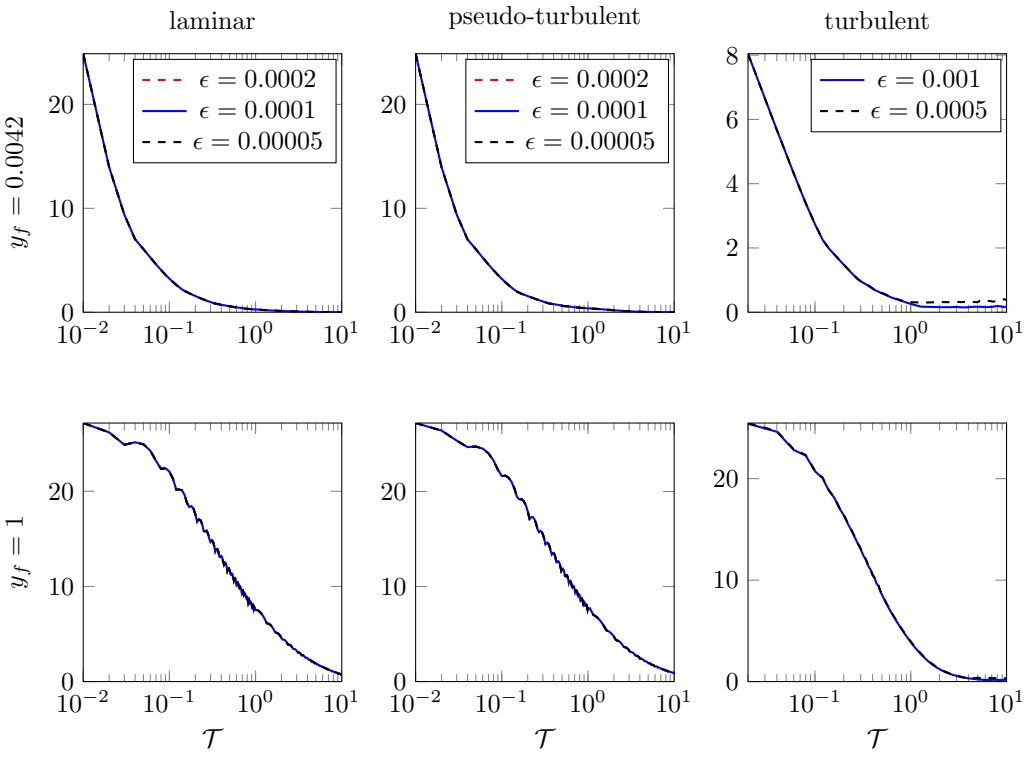

Figure 1.3: Temporal evolution of the spatial absolute maximum $\mathcal{H}_{z\to w,m}(t; y_f)$ of the laminar (left), pseudo-turbulent (center) (both computed with impulsive forcing, but same results holds for the input-output correlation strategy) and turbulent (right) response at various forcing amplitudes and forcing positions. Top row: first near-wall position at $y_f = 0.0042$; bottom row: centerline at $y_f = 1$.

A systematic campaign of tests has been carried out to identify the largest admissible ϵ_i, for each forcing direction i and for a subset of forcing locations y_f, for the laminar, pseudo-turbulent and turbulent cases. Indeed, the two former cases are less critical: the tests themselves are cheaper, and the S/N ratio is not important as the production simulations are noiseless.

Figure 1.3 reports an example result that we used to determine the forcing amplitudes for the rest of the study. Laminar, pseudo-turbulent and turbulent cases are considered, at six values of y_f, from the very-near-wall region to the centerline; however, figure 1.3 only reports two values of y_f, namely $y_f = 0.0042$ and $y_f = 1$. Moreover, although figure 1.3 only concerns the component $\mathcal{H}_{z\to w}$, every component of the response tensor was considered.

It can be seen that, for both distances, linearity is guaranteed by all the three forcing amplitude for the laminar and pseudo-turbulent cases (see the left and middle columns of figure 1.3). However, for the turbulent case, close to the wall the two amplitudes considered perfectly match until $\mathcal{T} \approx 1$. For larger $\mathcal{T}$ the smallest forcing amplitude shows a lower bound which represents the background noise overwhelming the deterministic part of the response. This noise floor is due to the finite horizon of the response computation and its magnitude changes for different components of the LIRF tensor.

1.5 Results

1.5.1 The shape and intensity of the LIRF

The impulse response is highly anisotropic, both among different components of the response tensor and depeding on the wavenumbers. We start with figure 1.4, where the H_2 norm of the nine components of $\hat{\mathcal{H}}_{i\to j}$ for the laminar case is plotted, after averaging over the forcing location. This figure emphasises the anisotropy of the LIRF, and shows that the components with the largest energetic content are always those related to the streamwise velocity component, and in particular the components $\hat{\mathcal{H}}_{y\to u}$ and $\hat{\mathcal{H}}_{z\to u}$, whose maxima are at least one order of magnitude larger than the maxima of the other components. They also share a similar shape in the (α, β) plane, with their maximum located at $\alpha = 0$. The same features was noted by Jovanović & Bamieh (2005), who interpret these responses as the amplification of the streamwise elongated structures. A similar tendency for a maximum at $\alpha = 0$ is shown by $\hat{\mathcal{H}}_{y\to w}$ and $\hat{\mathcal{H}}_{z\to v}$. Since they involve wall-normal and spanwise velocities, we connect them to the amplification of the perturbations that lead to the quasi-streamwise vortices. The components $\hat{\mathcal{H}}_{x\to v}$ and $\hat{\mathcal{H}}_{x\to w}$ have their maximum at $\beta = 0$, and thus their physical space representation recalls structures with spanwise elongated shape. Jovanović & Bamieh (2005) relate

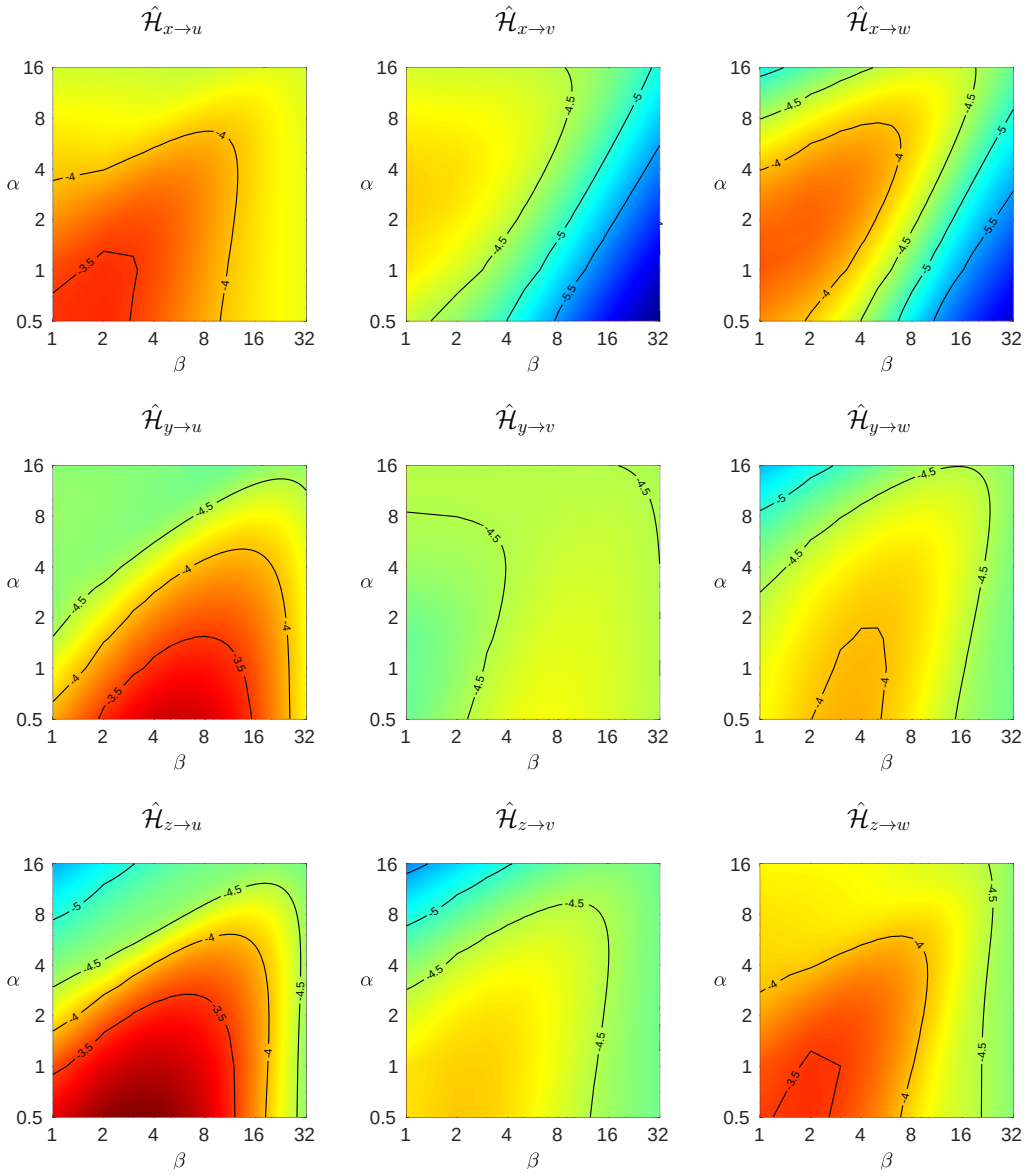

Figure 1.4: Plot of $\log_{10}\|\hat{\mathcal{H}}_{i\to j}\|_2$ for the laminar case averaged among forcing locations. The contour lines correspond to $\log_{10}\|\hat{\mathcal{H}}_{i\to j}\|_2 = -4, -3, -2.5, -2, -1$. Axes are in base-10 logarithmic scale. Colormap is between -4.55 and -0.81. Columns: forcing direction f_x, f_y, f_z, rows: response velocity component u, v, w.

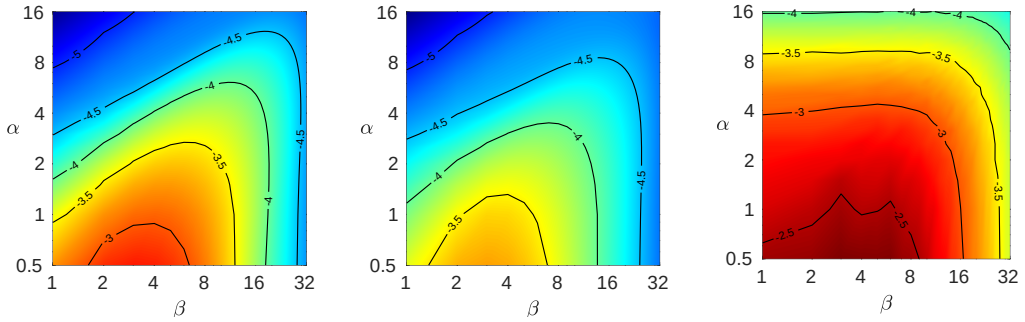

Figure 1.5: Plot of $\log_{10} \|\hat{\mathcal{H}}_{z\to u}\|_2$ for the laminar (left), pseudo-turbulent (centre) and turbulent (right) case averaged among forcing locations. The contour lines correspond to $\log_{10} \|\hat{\mathcal{H}}_{i\to j}\|_2 = -5, -4.5, -4, -3.5, -3, -2.5$. Axes are in base-10 logarithmic scale. Colormap is between -5.48 and -2.35.

these response components to the amplification of the Tollmien–Schlichting waves. Similarly $\hat{\mathcal{H}}_{y\to v}$ is slightly preferentially large along the spanwise wavenumbers, but it presents also non negligible amplification for large values of α. The remaining two components whose energy is equally distributed in α and β are related by those authors to the oblique waves. This picture is consistent with Jovanović & Bamieh (2005) showing that the energy in the oblique waves and streamwise streaks are larger than the TS-wave.

Figure 1.5 plots the H_2 norm of $\hat{\mathcal{H}}_{z\to u}$ for the laminar, pseudo-turbulent and turbulent case. To make a fair comparison the turbulent case response is halved to account for the different time for which the forcing is injected in the system ($\Delta t = 0.01$ for laminar and pseudo-turbulent cases and $\Delta t = 0.02$ for the turbulent case). First we notice that for all the three regimes $\hat{\mathcal{H}}_{z\to u}$ has a peak for $\alpha = 0$ and $\beta \approx 3$, although the turbulent case show a larger influence of the streamwise wavenumber up to one order of magnitude larger intensity compared to the other two regimes. Although more intense, the turbulent response is more spreaded in the wavenumber space and highlights a non-negligile contribution of the streamwise wavenumber.

The shape and intensity of the impulse response is also investigated in the three-dimensional physical space, without averaging over the wall-normal direction y. In figure 1.6), the isosurfaces of each component of the turbulent LIRF $\mathcal{H}_{i\to j}$ are plotted for a fixed value $y_f^+ = 15$ of the forcing position, at the fixed time $\mathcal{T} = 0.48$.

The components $\mathcal{H}_{y\to j}$ and $\mathcal{H}_{z\to j}$ show that the forcing acts on the structures of the near wall-cycle. The streamwise component of the response yields structures elongated in the streamwise direction, with alternating positive and negative sign in the spanwise direction. Such structures are compatible with the amplifica-

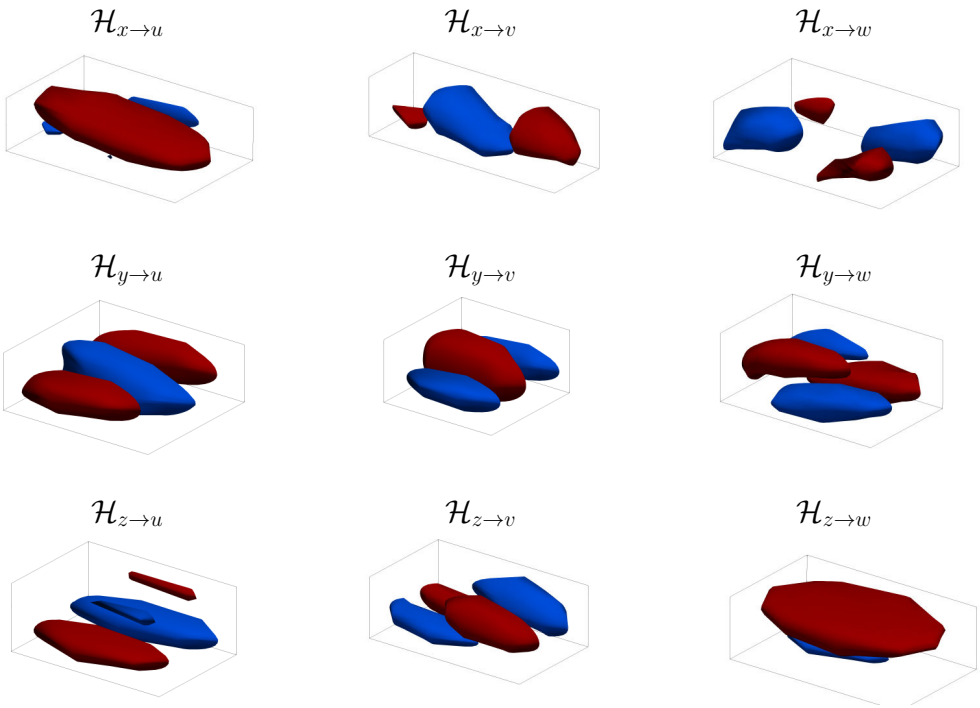

Figure 1.6: Isosurfaces of the response tensor $\mathcal{H}_{i\to j}$ at the non dimensional time $\mathcal{T} = 0.48$ for the turbulent case. The forcing is at the wall-normal distance $y_f = 0.1h$ or $y_f^+ = 15$. All the isosurfaces are at the value ± 0.5 except for the diagonal components, $\mathcal{H}_{y\to u}$ and $\mathcal{H}_{z\to u}$ which are at the value ± 1. Red is for positive values, blue for negative ones.

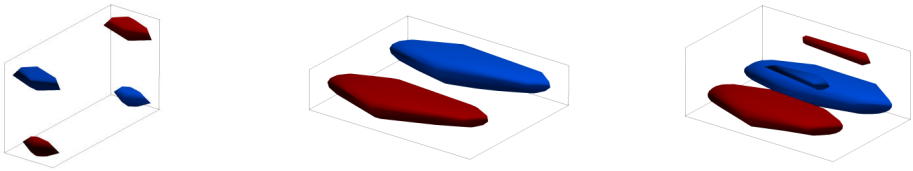

Figure 1.7: Isosurfaces of the response tensor $\mathcal{H}_{z\to u}$ at the non dimensional time $\mathcal{T} = 0.48$ for the laminar (left), pseudo-turbulent (centre) and turbulent (right) case. The forcing is at the wall-normal distance $y_f = 0.1h$ or $y_f^+ = 15$. All the isosurfaces are at the value ± 1.

tion of the near-wall high- and low-speed streaks. The wall-normal and spanwise components of the response identify alternated vertical and spanwise fluctuations typical of the turbulent quasi-streamwise vortices (QSV). The relative position of $\mathcal{H}_{y\to j}$ with $j = u, v, w$ indicate the simultaneous presence of streaks and QSV, which mutually interact in the cycle for the self-sustainment of turbulence. This picture is compatible with the peak in the wavenumbers plane. The most amplified disturbancies of $\mathcal{H}_{y\to j}$ and $\mathcal{H}_{z\to j}$ were found to be either oblique waves or streamwise perturbations which yields after transition to turbulence to stremwise streaks and quasi-streawise vortices. Similarly, the relative position of the isosurfaces of $\mathcal{H}_{x\to j}$ suggests that the streamwise forcing acts on the hairpin vortices (Theodorsen, 1952) near the wall, as highlighted by Vadarevu *et al.* (2019) by eLNSE. This agrees with the idea that the Tollmien–Schlichting waves (see $\mathcal{H}_{x\to v}$ and $\mathcal{H}_{x\to w}$ in figures 1.4) evolves into 3D hairpin vortices in the late stage of transition to turbulence.

Figure 1.7 plots the isosurfaces of $\mathcal{H}_{z\to u}$ for the laminar, pseudo-turbulent and turbulent case. Again, as mentioned before, the turbulent case response is halved to be compared to the other two responses obtained at a halved dt.

The shape of the turbulent LIRF reseambles the shape of the structures typical of the near-wall turbulent cycle such as streamwise streaks, quasi-streamwise vortices and hairpin vortices. However, even the same response shape is shared by all the investigated regimes, the shape and intensity of the response have non-negligible differences. We conclude that the dynamics of the impulse response in the turbulent regime has a laminar component, yet this is not sufficient for its complete description.

1.5.2 The LIRF as a function of the forcing location

The results by Jovanović & Bamieh (2005) are extended in this work to consider the effect of the forcing location, that so far has not been considered either averaging the response across every y_f (see figure 1.4) or fixing a constant value of y_f (see

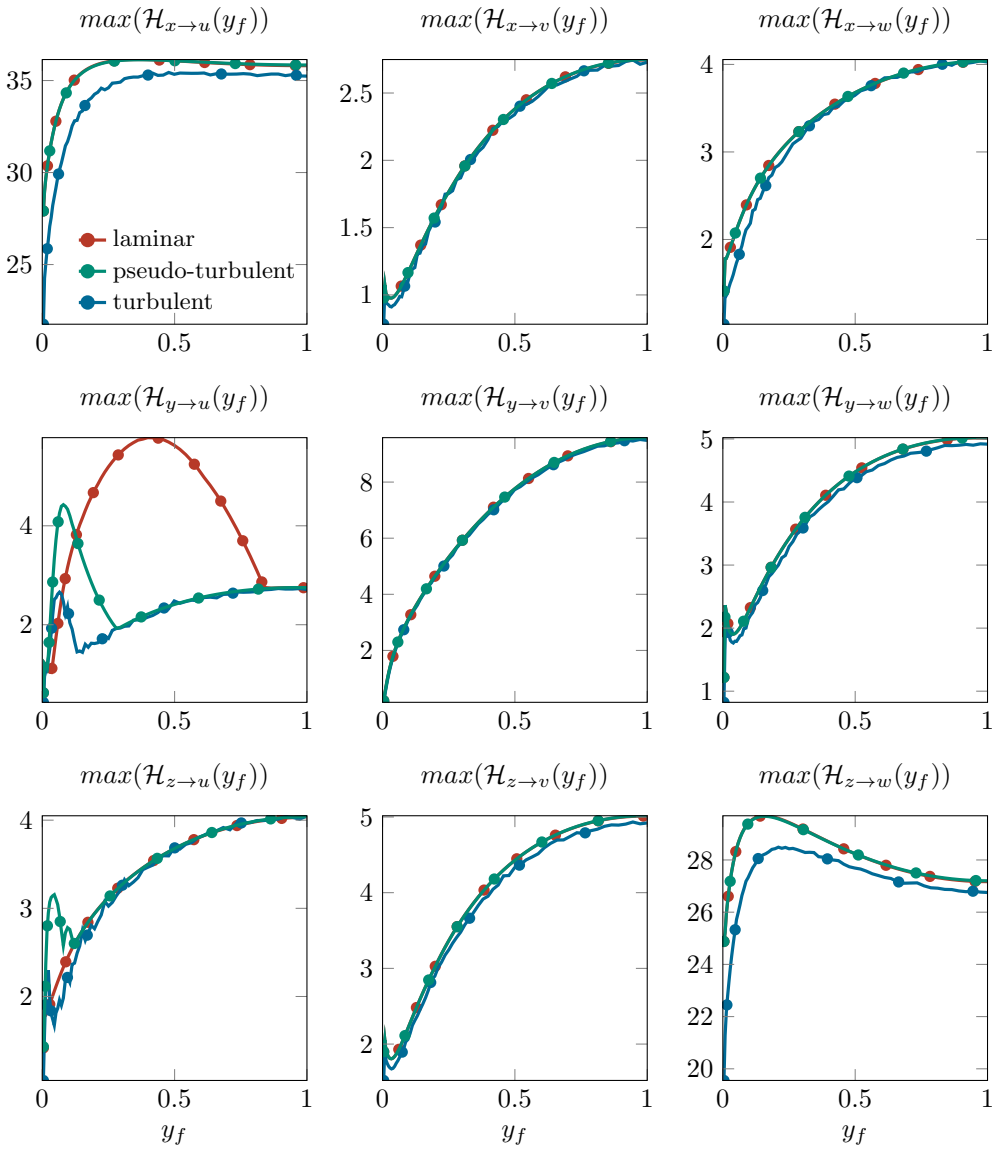

Figure 1.8: Absolute maxima $\mathcal{H}_{i\to j,m}(y_f)$ in the physical space as a function of the forcing position y_f for the laminar, pseudo-turbulent and turbulent cases.

figure 1.6).

How $\mathcal{H}_{i\to j}$ depends upon the forcing distance is shown in figure 1.8 for all the regimes. Here the maximum over time, wavenumbers and in wall-normal direction is considered for each component of the LIRF. Even though some components present a slightly non-monotonic trend, the general picture is that the position nearest to the wall yields the smallest response, and the centreline yields the largest.

The diagonal components are the largest. The component $\mathcal{H}_{y\to v}$ differs from the other two, and shows a gradual increase toward the centreline maximum (which is the lowest of the three); the three LIRF coincide in this representation. The other two diagonal components $\mathcal{H}_{x\to u}$ and $\mathcal{H}_{z\to w}$, instead, present a weak but noticeable non-monotonic trend; the latter, in particular, peaks at $y_f \approx 0.2$, with a tendency for the peak to move slightly off-wall in the turbulent case. For both the components the laminar and the pseudo-turbulent cases perfecly match, wheres the turbulent case shows a smaller response at every y_f.

The off-diagonal components $\mathcal{H}_{x\to v}$,$\mathcal{H}_{z\to v}$ and $\mathcal{H}_{y\to w}$ are quite similar, with a local minimum very close to the wall and then a monotonic increase up to the centreline. Instead, the component $\mathcal{H}_{x\to w}$ monotonic increases from the wall up to the centerline.

The component $\mathcal{H}_{z\to u}$ is similar to the previously described off-diagonal components with a small peak, but the spikes of the three cases are quite different. The laminar case shows an almost negligible local maximum very close to the wall, the pseudo-turbulent case has a wider and larger local maximum for $y_f \approx 0.04$ ($y_f^+ = 6$), and the turbulent case has an intermediate behaviour at a y_f between the other two. The three curves then tend to collapse for larger values of y_f.

The component with the most interesting behaviour is $\mathcal{H}_{y\to u}$. The three cases present an evident peak, each at different y_f. Except for the very first forcing position close to the wall, the laminar response monotonically increases until its maximum is reached at $y_f \approx 0.4$, then decreases until $y_f \approx 0.75$ and then stays constant up to the centreline. In the pseudo-turbulent case, the peak is sharper and observed at a lower wall-normal forcing position, namely $y_f = 0.08$ (or $y_f^+ = 12$). Lastly, the turbulent case is qualitatively similar to the pseudo-turbulent one, but presents a less intense peak closer to the wall at $y_f = 0.065$ (or $y_f^+ \approx 10$). Position-wise, the peaks of the pseudo-turbulent and turbulent cases are compatible with the amplification of the streaks of the near-wall cycle.

Hence, $\mathcal{H}_{y\to u}$ and $\mathcal{H}_{z\to u}$ being the largest response and peaking for a forcing placed close to the wall complies with the idea that an external forcing in the buffer layer directed either in wall-normal direction (e.g. blowing and suction (Mickley *et al.*, 1954), opposition control Choi *et al.* (1994)) or in the spanwise direction (e.g. spanwise forcing (Akhavan *et al.*, 1993), (Quadrio *et al.*, 2009)) are the most effective techniques to perturb the streamwise velocity field, e.g. with the aim to

reduce the drag in the turbulent regime.

1.5.3 The LIRF as a function of time

Observing the temporal evolution of the component-wise maxima of the LIRF in physical space is an effective means to appreciate its anisotropy. Figure 1.9 presents these quantities in comparative form among the laminar, the pseudo-turbulent and the turbulent LIRF: for each tensor component, the maximum (in absolute value) in the whole space and across all forcing position y_f is tracked, following the definition of Eq. (1.26).

The largest maxima are invariably those related to the diagonal terms of the LIRF tensor. At zero time, these components present peak values that are one order of magnitude larger than those of the other components. For the diagonal terms, laminar, pseudo-turbulent and turbulent maxima all decrease monotonically in time; laminar and pseudo-turbulent cases almost perfectly overlap, whereas the turbulent curves consistently lie below the others, at any time. This behaviour, which can actually be observed for every component of $\hat{\mathcal{H}}_{i\to j}$, is the direct manifestation of the (mean) diffusive action of turbulence, entirely neglected in the laminar and pseudo-turbulent cases. The maxima of both $\hat{\mathcal{H}}_{x\to u}$ and $\hat{\mathcal{H}}_{z\to w}$ for the three cases take place at $\mathcal{T} = 0$, and reduce by 50% quickly, within $\mathcal{T} = 0.5$; a 95% reduction requires an elapsed time of $\mathcal{T} \approx 6.5 - 7$. The peak value of $\hat{\mathcal{H}}_{y\to v}$ decreases more gently in time.

As far as the off-diagonal terms are concerned, only $\hat{\mathcal{H}}_{z\to v}$ decreases monotonically (in all cases). The off-diagonal components associated to the x forcing or to the w response are monotonically decreasing for the pseudo-turbulent and turbulent case, but a local maximum for the laminar case is registered at $\mathcal{T} \approx 2-3$. The off-diagonal components associated to the u response show a non-monotonic behaviour for all curves. The laminar LIRF shows a local maximum at $\mathcal{T} \approx 2.5$, the pseudo-turbulent LIRF presents it earlier at $\mathcal{T} \approx 1 - 2$, and turbulent one even earlier at $\mathcal{T} \approx 0.5 - 0.6$. For $\hat{\mathcal{H}}_{y\to u}$, the growth rate of the maximum over time is approximately constant across the three LIRF, so that the maxima occurring later are also the largest. This is clearly not the case for $\hat{\mathcal{H}}_{z\to u}$, for which the pseudo-turbulent peak is the largest, but the laminar one occurs last.

The largest non-monotonic behavior, i.e. that of $\hat{\mathcal{H}}_{y\to u}$, can be explained by recalling the non-normal property of the eigenvectors of the Orr–Sommerfeld's linearized system, as done by Orr (1907) and Schmid (2007). Here, however, we are constrained by linearity, and the relative growth maxes out at 2-3 times. The turbulent diffusion, which lacks in the laminar and pseudo-turbulent cases damps the turbulent response faster such that it shows a considerably smaller transient growth compared to the other two cases.

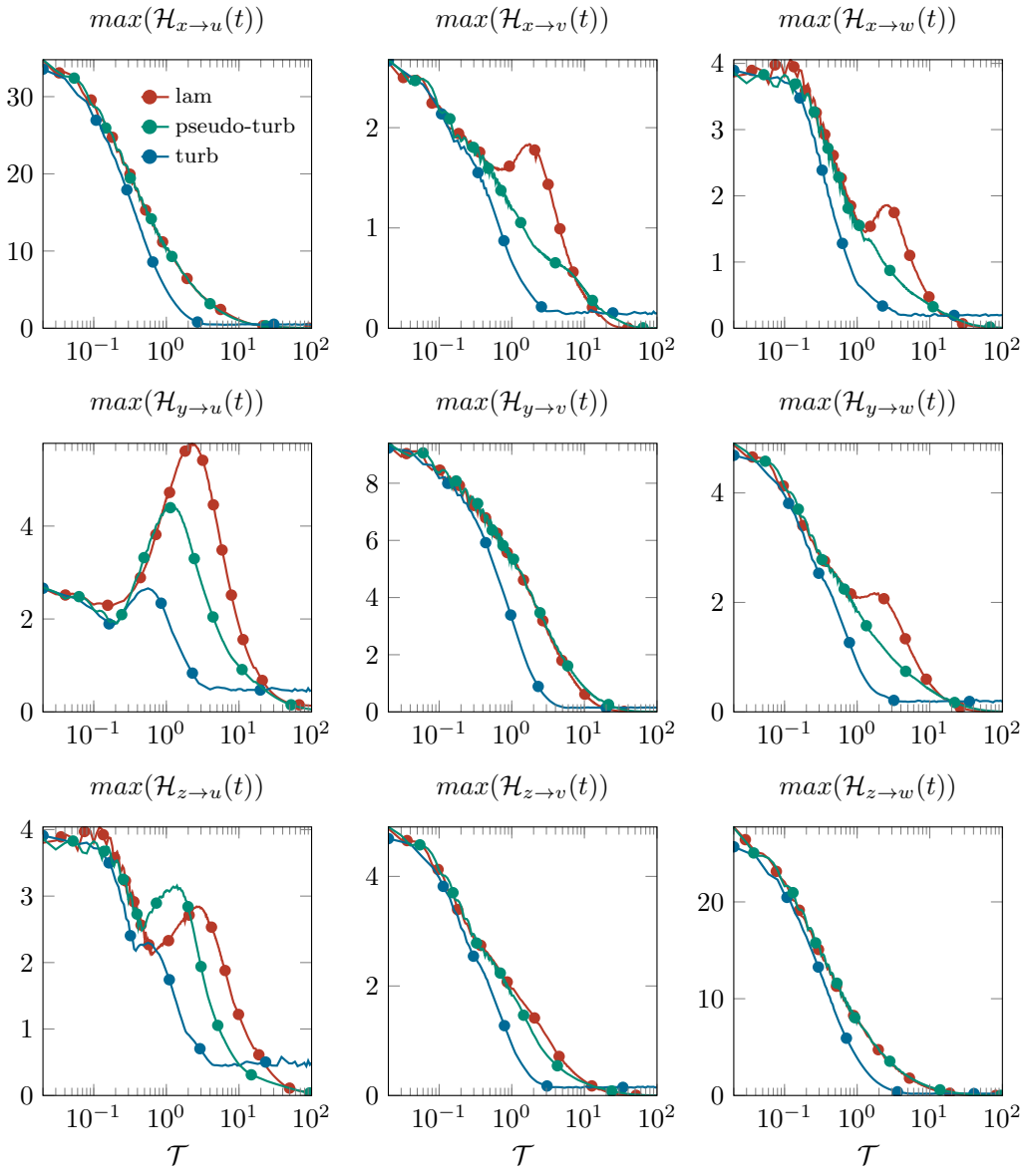

Figure 1.9: Absolute maxima $\mathcal{H}_{i\to j,m}(t)$ in the physical space as a function of the non-dimensional time $\mathcal{T}$ for the laminar, pseudo-turbulent and turbulent cases.

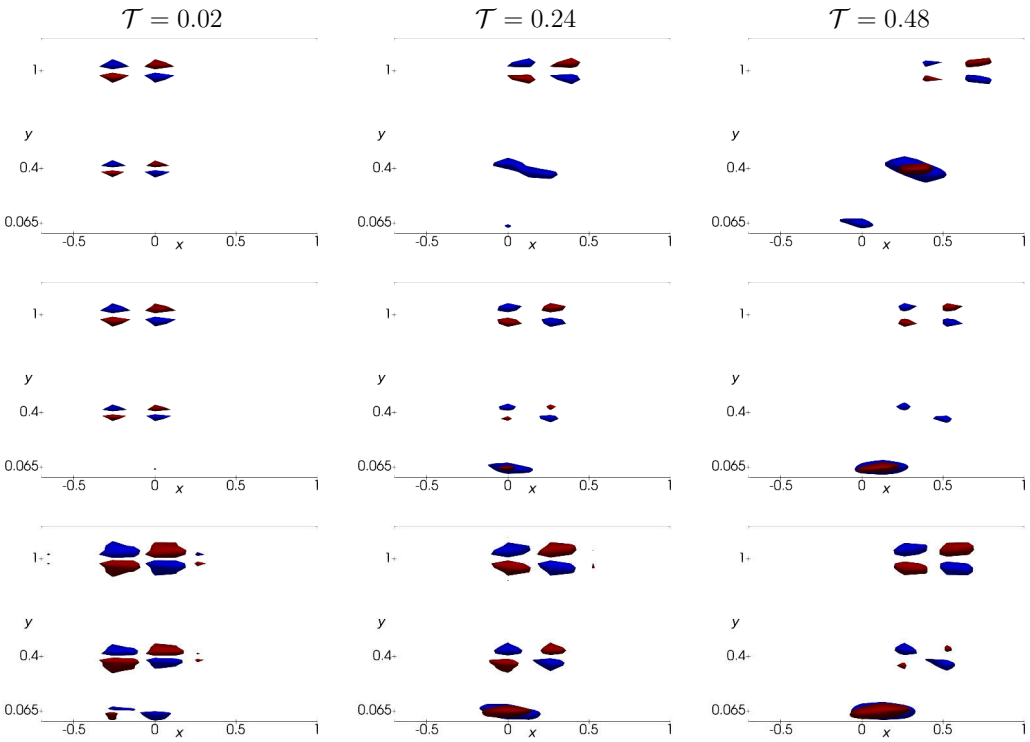

Figure 1.10: Isosurfaces of the response component $\mathcal{H}_{y\to u}$ at the non-dimensional time $\mathcal{T} = 0.02$ (left column), 0.24 (center column) and 0.48 (right column) for the forcing locations $y_f = 0.065h$, $0.4h$ and h for the laminar (top), pseudo-turbulent (middle) and turbulent (bottom) LIRFs. All the isosurfaces are at the value ± 1. Red is for positive values, blue for negative ones.

1.5.4 The LIRF in the whole space-time domain

The whole LIRF, plotted in the form of isosurfaces, already shown in figure 1.6 and 1.7 has also been investigated in their evolution in time and depending on the forcing location y_f. Figure 1.10 represents the $\mathcal{H}_{y\to u}$ component at different elapsed time (columns), for three values of y_f (namely $y_f = 0.065$, $y_f = 0.4$ and $y_f = 1.0$), in comparative form between the three LIRF (rows). A short time after the impulsive forcing, namely at $\mathcal{T} = 0.02$, the response is symmetric with respect to the spanwise direction and anti-symmetric with respect to the streamwise and wall-normal directions. The near-wall response is below the threshold and therefore not visible for the laminar and pseudo-turbulent cases, while it is small but visible for the turbulent case. The asymmetry of the response to the impulsive forcing at $y_f = 0.065$ is due the presence of the solid wall. At larger times, the response to the forcing at $y_f = 1$ remains almost symmetric and only slightly damped for all the regimes. The convection velocity matches the mean velocity,

thus the laminar response is convected faster than the turbulent one owing to the larger centerline velocity of the laminar profile compared to the turbulent one. It is worth recalling that pseudo-turbulent and turbulent cases share the same mean velocity profile, thus the same convection velocity of the response. Differently the response to the forcing at the intermediate position $y_f = 0.4$ changes depending on the regime: in the turbulent and pseudo-turbulent cases it gets progressively damped, with the positive part vanishing sooner; however, in the laminar case the two negative regions merge into one which is surrounded by two smaller positive regions at both sides at $\mathcal{T} = 0.48$. At $y_f = 0.4$ the structure are convected roughly at the same speed for all the cases, being the laminar and turbulent mean velocity profile almost matching. Close to the wall, the response is amplified in time and show a central negative region with a positive region at each side, resembling the structure of positive and negative streamwise streaks. The amplification is largest for the turbulent case and smallest for the laminar case. Turbulent and pseudo-turbulent cases are advected at larger velocity in this region, owing to the largest shear and therefore largest near-wall velocity.

1.6 A posteriori validation

The full time-space structure of (mean) linear response computed and measured in the present work by DNS is the best estimator of the linear dynamics of the laminar, pseudo-turbulent and turbulent channel flow when a body forcing is impulsively applied. Once the response function is computed it can be used to predict the response of the system through direct convolution of the LIRF itself and a given input forcing, i.e.:

$$\langle \hat{u}_j(\alpha, y, \beta, t; y_f) \rangle = \int_0^{+\infty} \hat{\mathcal{H}}_{i\to j}(\alpha, y, \beta, t-\tau; y_f) \hat{f}_i(\alpha, y - y_f, \beta, \tau)\, \mathrm{d}\tau. \quad (1.28)$$

This approach is also useful to assess whether the computed LIRF is a good linear estimator of the system by comparing the output of the direct convolution to the velocity field computed by a DNS with the same forcing. In the present case, the channel flow is forced by a periodic body force in the spanwise direction:

$$f_z(x, z, t; y_f) = \epsilon cos(2\pi x) cos(2\pi z) sin(2\pi t), \quad (1.29)$$

which, in the wavenumber space reduces to

$$\hat{f}_z(\alpha, \beta, t; y_f) = \epsilon sin(2\pi t). \quad (1.30)$$

We set the parameters as $\alpha = 1, \beta = 4, y_f = 0.1$ (corresponding to $y_f^+ = 15$ in the turbulent case) and a finite ampitude $\epsilon = 0.001$ for the laminar and pseudo-turbulent case, whereas $\epsilon = 0.1$ for the turbulent case. The same discretization

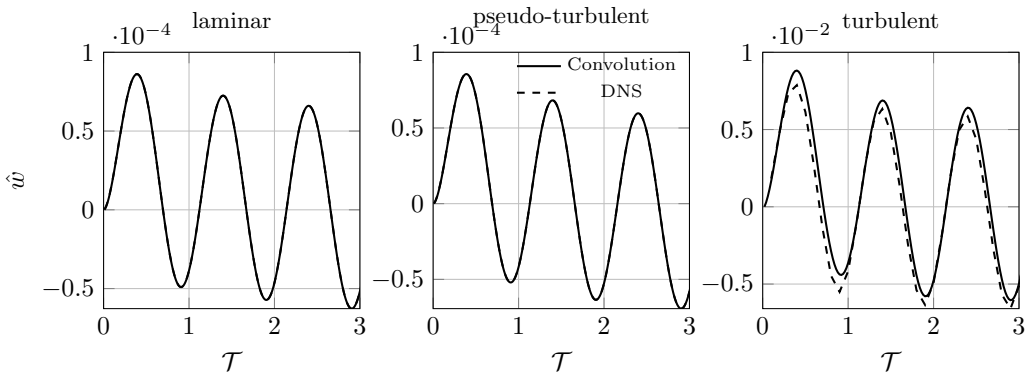

Figure 1.11: Fourier coefficient of the spanwise velocity $\hat{w}(\alpha = 1, \beta = 4, y = 0.1, t)$ as a response to a periodic forcing $\hat{f}_z(\alpha = 1, \beta = 4, y_f = 0.1, t)$ as a function of the non-dimensional time $\mathcal{T}$ for the laminar (left), pseudo-turbulent (middle) and turbulent (right) cases obtained by convolution with $\mathcal{H}_{z\to w}$ (solid line) and by DNS (dashed line).

used to compute $\mathcal{H}_{i\to j}$ (see §1.3.3) is used for the DNS. The time discretization is set to $\Delta t = 0.01$ for the laminar and pseudo-turbulent cases and to $\Delta t = 0.02$ for the fully turbulent case as in §1.3.1. To match the same time discretization of the DNS, the unequally time-spaced LIRF is linearly interpolated in time.

Figure 1.11 shows the Fourier coefficient of the spanwise velocity $\hat{w}(\alpha = 1, \beta = 4, y = 0.1, t)$ for the laminar (left), pseudo-turbulent (middle) and turbulent (right) channel flow as a response to the periodic forcing of Eq. 1.30 both by direct convolution with $\mathcal{H}_{z\to w}$ and by DNS up to a time of $\mathcal{T} = 3$.

Due to the linearity of $\mathcal{H}_{i\to j}$, we expect the output to be periodic with the same frequency of the forcing input. For laminar and pseudo-turbulent cases the response perfectly match the frequency of the input and the results obtained by convolution and DNS are identical meaning that the LIRF perfectly describes the behaviour of the channel flow.

The comparison between direct convolution and DNS, which is straighforward in the laminar and pseudo-turbulent cases becomes challenging when turbulence plays a role. For the turbulent case the measure are not deterministic but can only be computed in a statistical sense, with a time average that can be very long for the statistics to converge. To compute the response by DNS, 250 simulations of the forced channel are run starting from different uncorrelated initial turbulent fields; ten equally spaced flow fields are saved for each period of oscillation up to the desired simulation time and then an ensable average is computed. The very good match both in terms of frequency and amplitude between the response obtained through direct convolution and through DNS means that once the LIRF is computed, it can be leveraged to predict the response of the channel flow to

whatever forcing at a fraction of the cost of a DNS.

In the present work the diagonal component $\mathcal{H}_{z\to w}$ is chosen to be shown here for two reasons. First, diagonal components of the LIRF tensor are the ones showing a smaller noise floor so that we are capable to catch the signal for a longer response time (see 1.9). Second, diagonal components show a larger amplification of the input so that in the turbulent cases averaging over 250 simulations is enough for the response to emerge from the turbulent noise. This highlights the potential of having a response function which describes the mean linear behaviour of a turbulent channel flow and after being computed once, it allows to accurately predict the response to any forcing.

1.7 Conclusions

The present work has introduced the first DNS based measurement of the mean linear impulse response function (LIRF) for a channel flow, considering the response to an impulsive body force locate at various wall-normal positions, thus extending the work of Luchini *et al.* (2006), where an impulsive wall-normal velocity forcing at the wall was considered.

Our primary interest resides in the fully turbulent case, but for comparison purposes we have also measured the LIRF of the laminar Poiseuille flow, and what we call the pseudo-turbulent LIRF, where there is no turbulence but the base flow is the mean turbulent profile.

The equivalent laminar and pseudo-turbulent LIRF could be computed rather easily, as the system is noise-less and it is straightforward to literally apply the impulsive forcing and to examine the outcome via DNS. This approach, however, becomes unfeasible in the turbulent case, which contains significant turbulent fluctuations which act as a noise that overcomes the forcing, whose amplitude must be tiny because of the linearity constraint. Even though the problem can be solved in principle by resorting to phase averaging, the averaging time needed for the deterministic response to emerge out of the statistical noise is impractical. Therefore, we apply here the same workaround exploited by Luchini *et al.* (2006), who measured the LIRF of a turbulent channel flow by computing the input-output correlation between a zero-mean white-noise input signal and the output made by the DNS-computed flow field.

The measurement approach has been validated in the laminar case, where the lack of statistical noise allows comparing the impulsive forcing and the input-output correlation. Moreover, in that case the algebraic Lyapunov equation approach introduced by Jovanović & Bamieh (2005) provides an independent verification.

The LIRF is a four-dimensional tensor with four independent variables, plus one parameter made by the wall-normal position y_f where the forcing is applied. Its

description is therefore non-trivial. In the Fourier space, the response is visualised through its H_2 norm after averaging over time, the wall-normal direction and all the forcing locations. Examining the wavenumber content of the various LIRF brings to light their anisotropic character, as every component of the LIRF tensor differs in terms of both wavenumber distribution and intensity.

The components of the LIRF eventually decay, but some exhibit a transient amplification at finite times. The laminar and pseudo-turbulent LIRF are nearly identical in terms of those components which go to zero monotonically. However, the laminar LIRF shows a local maximum that is not present in the other cases. The turbulent LIRF is always smaller than the others, reflecting the presence of turbulent diffusion.

About the forcing location yielding the largest response, the majority of the cases suggest the best forcing location to be at channel centre. However, most of the components of the response show a local (or global for the solely $\hat{\mathcal{H}}_{y\to u}$) maximum for y_f closer to the wall; the precise position varies depending on the LIRF type.

The LIRF can be also observed in the three-dimensional space and in time. Perturbations leading to the formation of turbulent structures typical of the near-wall turbulence cycle, namely the low- and high-speed streaks, the quasi-streamwise vortices and the hairpin vortices are the most amplified. The three-dimensional structure of the response is similar across the laminar, pseudo-turbulent and turbulent cases, yet the amplitude is different. The time evolution of the LIRF depends on the LIRF type; the advection velocity of the structures reflects the different shape of the base flow profile.

The full time-space structure of mean linear response computed and measured in the present work by DNS is the best estimator of the linear dynamics of the turbulent channel flow when a body forcing is impulsively applied. This is of particular interest for the design of a feedback control for which the model of the plant (the channel flow in this case) is needed. This study highlights that relying on the impulse response of a laminar or a pseudo-turbulent (laminar with a superimposed base mean flow of the turbulent flow) case to model the dynamics of a turbulent channel flow can be useful to approximate the behaviour of the response, yet it fails to capture some of its distinctive behaviours. Thus, the approach presented here paves the way to more reliable estimation of the linear response of the turbulent flow and consequently a more effective control design.

Structure function tensor equations with triple decomposition

The content of this Paper has been published in
Gattere, F., Chiarini, A., Gallorini, E. & Quadrio, M. 2023
Structure function tensor equations with triple decomposition.
Journal of Fluid Mechanics **960**, A7.
Minor editing has been done for formatting purposes.

Structure function tensor equations with triple decomposition

Abstract

Exact budget equations are derived for the coherent and stochastic contributions to the second-order structure function tensor. They extend the anisotropic generalised Kolmogorov equations (AGKE) by considering the coherent and stochastic parts of the Reynolds stress tensor, and are useful for the statistical description of turbulent flows with periodic or quasi-periodic features, like e.g. the alternate shedding after a bluff body. While the original AGKE describe production, transport, inter-component redistribution and dissipation of the Reynolds stresses in the combined space of scales and positions, the new equations, called φAGKE, contain the phase φ as an additional independent variable, and describe the interplay among the mean, coherent and stochastic fields at the various phases. The newly derived φAGKE are then applied to a case where an exactly periodic external forcing drives the flow: a turbulent plane channel flow modified by harmonic spanwise oscillations of the wall to reduce drag. The phase-by-phase action of the oscillating transversal Stokes layer generated by the forcing on the near-wall turbulent structures is observed, and a detailed description of the scale-space interaction among mean, coherent and stochastic fields is provided thanks to the φAGKE.

2.1 Introduction

Understanding the multiscale nature of turbulence and the sustaining mechanisms of turbulent fluctuations is a long-standing effort in fluid mechanics, motivated by the ambition to determine and possibly to manipulate the mean flow. According to the classic arguments by Richardson and Kolmogorov, at large enough Reynolds

numbers a clear scale separation is expected between the large energy-containing scales and the small dissipative ones. Fluctuations of different scales interact non-linearly, and a cascade mechanism transfers energy (on average) towards the dissipating scales. The geometrical information embedded in the larger scales vanishes at smaller ones, so that turbulence becomes locally isotropic below a small enough scale. However, in turbulent flows with practical interest, the scale separation is often incomplete, owing to the finite value of the Reynolds number and to the presence of boundaries; studying such flows is particularly challenging, because of their strongly anisotropic and inhomogeneous nature, which implies that the very concept of scale comes to depend on the position in the physical space.

Among the approaches developed over the years to describe anisotropic and inhomogeneous flows, the anisotropic generalised Kolmogorov equations, or AGKE, are well suited to account for the multiscale nature of turbulence. The AGKE (Gatti *et al.*, 2020) are exact budget equations for each component of the second-order structure function tensor. They extend the generalised Kolmogorov equation or GKE (see e.g. Hill, 2001; Danaila *et al.*, 2001), sometimes referred to as Kármán–Howarth–Monin–Hill equation (Alves Portela *et al.*, 2017), which, in turn, is the exact budget equation for half the trace of the second-order structure function tensor, i.e. the scale energy. The AGKE, which consider each tensor component separately, describe the production, inter-component redistribution, transport, and dissipation of the Reynolds stresses simultaneously across the scales and in the physical space. Unlike the GKE, they fully account for anisotropy and inhomogeneity, and feature a pressure–strain term that plays a central role in redistribution. Moreover, the AGKE simplify the structural analysis of turbulence, owing to the direct link of each tensor component to the correlation function (Davidson *et al.*, 2006; Gatti *et al.*, 2020).

The GKE has been already applied to several flows to describe how inhomogeneity changes the Richardson–Kolmogorov scenario, possibly leading to inverse (from small to large scales) energy transfer: the plane channel flow at different Re (Cimarelli *et al.*, 2013, 2016), the flow over a bump (Mollicone *et al.*, 2018), the wake of a square cylinder (Alves Portela *et al.*, 2017) and the plane jet Cimarelli *et al.* (2021). Using GKE, Yao *et al.* (2022*a*) showed that an intense inverse cascade dominates a boundary layer undergoing bypass transition. Danaila *et al.* (2017) derived the variable-viscosity GKE and proved that, in flows with mixing of two or more fluids, all scales evolve in a similar fashion only for regions where viscosity is uniform. Lai *et al.* (2018) derived the variable-density GKE and studied the multi-material effects on the interscale energy transfers in a turbulent round jet, finding that the deformation of smaller turbulent eddies into larger ones accompanies energy transfers. Arun *et al.* (2021) derived the budget equation for the derivative of the two-point velocity correlation for compressible flows, and

identified the effects of variable density and dilatation on the energy cascades. The more recent AGKE, instead, have been first demonstrated in a plane channel flow (Gatti *et al.*, 2020), and then used to investigate the ascending/descending and direct/inverse cascades of the Reynolds stresses in a turbulent Couette flow (Chiarini *et al.*, 2022*b*) and to characterise the structure of turbulence in the flow past a rectangular cylinder (Chiarini *et al.*, 2022*a*).

It is not uncommon to encounter turbulent flows in which large scales are relatively organised in space, and follow a temporally repeating pattern. This happens in presence of an external periodic forcing, or when the flow is quasi-periodic because of instabilities, as in the turbulent wake of bluff bodies. An example of the former class, which is considered in the second half of this paper as a simpler test-bench, is the canonical turbulent channel flow modified by periodic spanwise wall oscillation to obtain skin-friction drag reduction (Jung *et al.*, 1992). The spanwise forcing creates a coherent periodic velocity field, known as the generalised Stokes layer (Quadrio & Ricco, 2011), which superimposes on the stochastic turbulent fluctuations. The latter class includes the quasi-periodic Kármán-like vortices in the turbulent wake of bluff bodies, forming after the roll-up of the separating shear layers. Such quasi-periodic structures, usually referred to as coherent motions, interact with the stochastic fluctuations and affect their organisation.

A complete, multiscale description of the interaction among the mean, the coherent (e.g. periodic) and the stochastic fields is highly desirable. Indeed, one can resort to a triple decomposition of the velocity and pressure fields into mean, coherent and stochastic motions, and use it, together with the single-point Reynolds stress budget equations, to describe how these large-scale motions interact with the turbulent fluctuations in the physical space. For the spanwise-oscillating wall, Agostini *et al.* (2014) found that the phase variation of the stochastic contribution to the Reynolds stresses is mainly driven by production, and that the dissipation plays only a marginal role; they concluded that the increase of the dissipation can not be the cause of drag reduction. For the alternate shedding behind a bluff body, Kiya & Matsumura (1988) experimentally investigated the various frequency components of the stochastic motions in the wake behind a flat plate perpendicular to the flow. They found that the frequency of the main contributions to the stochastic shear stresses is one half of the vortex-shedding frequency, explaining it with the different spanwise arrangement of consecutive coherent vortices. In both cases, however, the description was incomplete: a triple decomposition alone does not capture the interaction between coherent and stochastic motions in the space of scales.

Alves Portela *et al.* (2020) followed Thiesset *et al.* (2014) and used the GKE together with a triple decomposition to describe the interaction between the coherent and stochastic motions in the space of scales and positions. They arrived at two budget equations for the coherent and stochastic parts of the scale energy,

and applied them to the turbulent wake past a square cylinder. Interestingly, they found that the mean flow does not feed the stochastic field directly, but it produces kinetic energy that feeds the large-scale coherent structures shed in the wake. Part of this energy is then transferred towards the stochastic turbulent fluctuations, at all scales. Although promising, the approach by Alves Portela *et al.* (2020) is still affected by limitations, discussed by Thiesset & Danaila (2020), that prevent a complete understanding of the interaction among the three fields. This is because their budget equations are obtained by averaging over the phase of the coherent motions, and the phase dependence is lost in the process. Furthermore, being based on the GKE, their procedure considers only the scale energy, and does not describe the pressure–strain redistribution among the various components of the Reynolds stress tensor. Finally, Alves Portela *et al.* (2020) additionally discard directional information by taking orientation averages of every term of the budget equations.

The present work goes one step further to overcome these limitations. We use a triple decomposition to extend the AGKE, and arrive at two phase-by-phase budget equations for the coherent and stochastic parts of each component of the structure function tensor. These equations, named φAGKE, describe the phase-by-phase mean-coherent-stochastic interaction of each component of the Reynolds stresses in the combined space of scales and positions. There is no phase-average involved, so that the description is complete. The paper is structured as follows. After this introduction, in §2.2 we briefly recall the AGKE for the classic Reynolds decomposition and introduce the φAGKE for the triple decomposition, discussing the meaning of the various terms. In the second part of the contribution, in §2.3, we provide a relatively simple example, and apply the new budget equations to a turbulent channel flow subjected to an oscillatory spanwise wall motion, chosen because of the deterministic nature of the periodic component. In §2.4 we demonstrate how the φAGKE describe the mean-coherent-stochastic interaction, and shed light into the complex working mechanism of the oscillating wall. The paper closes with a brief discussion in §2.5. Appendix 2.A contains the detailed derivation of the φAGKE from the Navier–Stokes equations, followed in Appendix 2.B by their specialization to the plane channel flow with oscillating walls. In Appendix 2.C the velocity field induced by the ensemble-averaged quasi-streamwise vortex at different phases is computed and used to support the φAGKE-based analysis of the channel flow with oscillating walls.

2.2 Mathematical formulation

In this Section we introduce the triple decomposition and recall briefly the standard AGKE, before presenting the new φAGKE, whose detailed derivation is reported

in Appendix 2.A.

2.2.1 Triple decomposition of the velocity field

An incompressible turbulent flow, varying in space $\boldsymbol{x}$ and time t, is typically described via its mean and fluctuating velocity and pressure fields, defined after the classic Reynolds decomposition. Provided the flow exhibits well-defined non-stochastic (e.g. periodic) features, the fluctuating field can be further decomposed into a coherent and a stochastic part. Therefore, the velocity field reads:

$$\boldsymbol{u} = \boldsymbol{U} + \underbrace{\tilde{\boldsymbol{u}} + \boldsymbol{u}''}_{\boldsymbol{u}'}, \tag{2.1}$$

where $\boldsymbol{U}$, $\boldsymbol{u}'$, $\tilde{\boldsymbol{u}}$ and $\boldsymbol{u}''$ indicate the mean, fluctuating, coherent and stochastic parts of the velocity field $\boldsymbol{u}$. The mean velocity $\boldsymbol{U}$ is defined as $\boldsymbol{U} \equiv \langle \boldsymbol{u} \rangle$, with the operator $\langle \cdot \rangle$ indicating ensemble averaging, which under the ergodic hypothesis becomes equivalent to averaging over homogeneous directions and time (if the flow is statistically stationary). For a single realisation without homogeneous directions, the mean is simply a temporal average:

$$\boldsymbol{U}(\boldsymbol{x}) \equiv \lim_{\tau \to +\infty} \frac{1}{\tau} \int_0^{\tau} \boldsymbol{u}(\boldsymbol{x}, t) dt. \tag{2.2}$$

Considering a periodic motion with period T and phase $\varphi \in (0, 2\pi]$, the overbar $\overline{\cdot}$ denotes the phase average operator over an integer number N of periods. Like $\langle \cdot \rangle$, it includes averaging over the homogeneous directions. Considering again a single realisation without homogeneous directions, $\overline{\cdot}$ is defined as:

$$\overline{\boldsymbol{u}}(\boldsymbol{x}, \varphi) \equiv \lim_{N \to +\infty} \frac{1}{N} \sum_{n=0}^{N-1} \boldsymbol{u}\left(\boldsymbol{x}, \left(\frac{\varphi}{2\pi} + n\right) T\right). \tag{2.3}$$

The coherent field $\tilde{\boldsymbol{u}}$ is thus defined as

$$\tilde{\boldsymbol{u}}(\boldsymbol{x}, \varphi) = \overline{\boldsymbol{u}}(\boldsymbol{x}, \varphi) - \boldsymbol{U}(\boldsymbol{x}),$$

and the stochastic vector field $\boldsymbol{u}''$ is defined after the triple decomposition (2.1) as $\boldsymbol{u}'' = \boldsymbol{u} - \boldsymbol{U} - \tilde{\boldsymbol{u}}$. An analogous triple decomposition is used to decompose the pressure field $p = P + \tilde{p} + p''$, with $\tilde{p} + p'' = p'$.

2.2.2 The anisotropic generalised Kolmogorov equations (AGKE)

Before presenting the φAGKE, the standard AGKE based on the Reynolds' decomposition are recalled. Full details on their derivation from the incompressible Navier–Stokes equations are provided by Gatti *et al.* (2020).

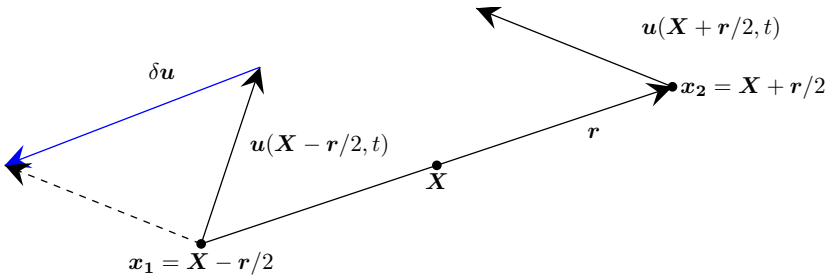

Figure 2.1: Sketch of two points $\boldsymbol{x}_1$ and $\boldsymbol{x}_2$ involved in the definition of the second-order structure function tensor. $\boldsymbol{X} = (\boldsymbol{x}_1 + \boldsymbol{x}_2)/2$ and $\boldsymbol{r} = \boldsymbol{x}_2 - \boldsymbol{x}_1$ indicate their mid-point and separation vector, respectively. $\delta\boldsymbol{u} = \boldsymbol{u}_2 - \boldsymbol{u}_1$ is the velocity increment between the two points.

Exact budget equations can be written for the components of the second-order structure function tensor $\langle \delta u_i \delta u_j \rangle$, where $\delta u_i = u_i(\boldsymbol{X}+\boldsymbol{r}/2,t) - u_i(\boldsymbol{X}-\boldsymbol{r}/2,t)$ is the $i-$th component of the velocity difference between two points $\boldsymbol{x}_1$ and $\boldsymbol{x}_2$, identified by their midpoint $\boldsymbol{X} = (\boldsymbol{x}_1 + \boldsymbol{x}_2)/2$ and their separation vector $\boldsymbol{r} = (\boldsymbol{x}_2 - \boldsymbol{x}_1)$, as shown by the sketch in figure 2.1. The Reynolds' decomposition leads to budget equations for $\delta U_i \delta U_j$ and $\left\langle \delta u_i' \delta u_j' \right\rangle$. In general, the time-independent tensor $\delta U_i \delta U_j$ depends upon six independent variables, i.e. the six coordinates of $\boldsymbol{X}$ and $\boldsymbol{r}$. The tensor $\left\langle \delta u_i' \delta u_j' \right\rangle$ additionally features time t as an independent variable if the process is not statistically stationary (e.g. periodic), and is related to the Reynolds stresses $\left\langle u_i' u_j' \right\rangle$ and to the spatial correlation tensor R_{ij} (Davidson *et al.*, 2006; Agostini & Leschziner, 2017) as

$$\left\langle \delta u_i' \delta u_j' \right\rangle (\boldsymbol{X}, \boldsymbol{r}, t) = V_{ij}(\boldsymbol{X}, \boldsymbol{r}, t) - R_{ij}(\boldsymbol{X}, \boldsymbol{r}, t) - R_{ij}(\boldsymbol{X}, -\boldsymbol{r}, t) \tag{2.4}$$

where

$$V_{ij}(\boldsymbol{X}, \boldsymbol{r}, t) = \left\langle u_i' u_j' \right\rangle \left(\boldsymbol{X} + \frac{\boldsymbol{r}}{2}, t \right) + \left\langle u_i' u_j' \right\rangle \left(\boldsymbol{X} - \frac{\boldsymbol{r}}{2}, t \right) \tag{2.5}$$

is the sum of the single-point Reynolds stresses evaluated at the two points $\boldsymbol{X} \pm \boldsymbol{r}/2$, and

$$R_{ij}(\boldsymbol{X}, \boldsymbol{r}, t) = \left\langle u_i' \left(\boldsymbol{X} + \frac{\boldsymbol{r}}{2}, t \right) u_j' \left(\boldsymbol{X} - \frac{\boldsymbol{r}}{2}, t \right) \right\rangle \tag{2.6}$$

is the two-points spatial correlation function.

The budget equations for the components of the mean second-order structure function tensor $\delta U_i \delta U_j$ are presented here for the first time; they were not reported by Gatti *et al.* (2020), and the tensor has received little attention so far, owing to its irrelevance in homogeneous isotropic turbulence, where there is no mean flow.

The mean AGKE are written compactly as

$$\frac{\partial \Phi^m_{k,ij}}{\partial r_k} + \frac{\partial \Psi^m_{k,ij}}{\partial X_k} = \Xi^m_{ij}, \tag{2.7}$$

where the repeated index k implies summation. The following notation is adopted. Uppercase letters (e.g. Φ, Ψ and Ξ) will be used to denote time-averaged quantities, and lowercase letters (e.g. ϕ, ψ and ξ) for phase-dependent quantities. Furthermore, superscripts m, f, c and s are used to label terms in the budget equations for the mean structure function tensor $\delta U_i \delta U_j$, the fluctuating structure function tensor $\left\langle \delta u'_i \delta u'_j \right\rangle$, the coherent structure function tensor $\overline{\delta \tilde{u}_i \delta \tilde{u}_j} = \delta \tilde{u}_i \delta \tilde{u}_j$, and the stochastic structure function tensor $\overline{\delta u''_i \delta u''_j}$.

The fluxes $\Phi^m_{k,ij}$ and $\Psi^m_{k,ij}$ are the mean scale- and physical-space fluxes, i.e.

$$\Phi^m_{k,ij} = \underbrace{\delta U_k \delta U_i \delta U_j}_{\text{Mean transport}} + \underbrace{\delta U_j \left\langle \delta u'_k \delta u'_i \right\rangle + \delta U_i \left\langle \delta u'_k \delta u'_j \right\rangle}_{\text{Fluctuating transport}} \underbrace{-2\nu \frac{\partial \delta U_i \delta U_j}{\partial r_k}}_{\text{Viscous diffusion}} \quad k = 1, 2, 3 \tag{2.8}$$

and

$$\Psi^m_{k,ij} = \underbrace{U^*_k \delta U_i \delta U_j}_{\text{Mean transport}} + \underbrace{\delta U_j \left\langle u'^*_k \delta u'_i \right\rangle + \delta U_i \left\langle u'^*_k \delta u'_j \right\rangle}_{\text{Fluctuating transport}} \underbrace{+ \frac{1}{\rho} \delta P \delta U_j \delta_{ki} + \frac{1}{\rho} \delta P \delta U_i \delta_{kj}}_{\text{Pressure transport}} +$$
$$\underbrace{-\frac{\nu}{2} \frac{\partial \delta U_i \delta U_j}{\partial X_k}}_{\text{Viscous diffusion}} \quad k = 1, 2, 3. \tag{2.9}$$

where δ_{ij} is the Kronecker delta, ν is the kinematic viscosity, and the asterisk superscript $(\cdot)^*$ indicates the arithmetic average of a quantity between the two points $\boldsymbol{X} \pm \boldsymbol{r}/2$. The term Ξ^m_{ij}, instead, is the mean source and reads

$$\Xi^m_{ij} = \underbrace{-\left[-\left\langle u'^*_k \delta u'_j \right\rangle \delta \left(\frac{\partial U_i}{\partial x_k} \right) - \left\langle u'^*_k \delta u'_i \right\rangle \delta \left(\frac{\partial U_j}{\partial x_k} \right) - \left\langle \delta u'_k \delta u'_j \right\rangle \left(\frac{\partial U_i}{\partial x_k} \right)^* - \left\langle \delta u'_k \delta u'_i \right\rangle \left(\frac{\partial U_j}{\partial x_k} \right)^* \right]}_{\text{Mean-fluctuating production } (P^{mf}_{ij})} +$$
$$\underbrace{+ \frac{1}{\rho} \delta P \frac{\partial \delta U_i}{\partial X_j} + \frac{1}{\rho} \delta P \frac{\partial \delta U_j}{\partial X_i}}_{\text{Pressure strain } (\Pi^m_{ij})} \underbrace{-4\epsilon^{m*}_{ij}}_{\text{Dissipation } (D^m_{ij})} \underbrace{+ \delta U_j \delta F_i + \delta U_i \delta F_j}_{\text{Forcing interaction } (\mathrm{F}^m_{ij})}. \tag{2.10}$$

The standard AGKE, presented by Gatti *et al.* (2020), pertain to increments of the fluctuating velocity field, and describe the production, transport, redistribution

and dissipation of each component, in the physical space $\boldsymbol{X}$ and in the space of scales $\boldsymbol{r}$. They can be written compactly as:

$$\frac{\partial\left\langle \delta u_i' \delta u_j' \right\rangle}{\partial t} + \frac{\partial \Phi_{k,ij}^f}{\partial r_k} + \frac{\partial \Psi_{k,ij}^f}{\partial X_k} = \Xi_{ij}^f. \tag{2.11}$$

The scale-space fluxes $\Phi_{k,ij}^f$ and physical-space fluxes $\Psi_{k,ij}^f$ are defined as:

$$\Phi_{k,ij}^f = \underbrace{\left\langle \delta U_k \delta u_i' \delta u_j' \right\rangle}_{\text{Mean transport}} + \underbrace{\left\langle \delta u_k' \delta u_i' \delta u_j' \right\rangle}_{\text{Fluctuating transport}} \underbrace{-2\nu \frac{\partial}{\partial r_k}\left\langle \delta u_i' \delta u_j' \right\rangle}_{\text{Viscous diffusion}} \quad k = 1,2,3 \tag{2.12}$$

and

$$\Psi_{k,ij}^f = \underbrace{\left\langle U_k^* \delta u_i' \delta u_j' \right\rangle}_{\text{Mean transport}} + \underbrace{\left\langle u_k'^* \delta u_i' \delta u_j' \right\rangle}_{\text{Fluctuating transport}} + \underbrace{\frac{1}{\rho}\left\langle \delta p' \delta u_i' \right\rangle \delta_{kj} + \frac{1}{\rho}\left\langle \delta p' \delta u_j' \right\rangle \delta_{ki}}_{\text{Pressure transport}} +$$
$$\underbrace{-\frac{\nu}{2}\frac{\partial}{\partial X_k}\left\langle \delta u_i' \delta u_j' \right\rangle}_{\text{Viscous diffusion}} \quad k = 1,2,3. \tag{2.13}$$

The term Ξ_{ij}^f in (2.11) is the source for $\left\langle \delta u_i' \delta u_j' \right\rangle$ and reads:

$$\Xi_{ij}^f = \underbrace{-\left\langle u_k'^* \delta u_j' \right\rangle \delta\left(\frac{\partial U_i}{\partial x_k}\right) - \left\langle u_k'^* \delta u_i' \right\rangle \delta\left(\frac{\partial U_j}{\partial x_k}\right) - \left\langle \delta u_k' \delta u_j' \right\rangle \left(\frac{\partial U_i}{\partial x_k}\right)^* - \left\langle \delta u_k' \delta u_i' \right\rangle \left(\frac{\partial U_j}{\partial x_k}\right)^*}_{\text{Mean-fluctuating production}(P_{ij}^{mf})} +$$
$$\underbrace{\frac{1}{\rho}\left\langle \delta p' \frac{\partial \delta u_i'}{\partial X_j} \right\rangle + \frac{1}{\rho}\left\langle \delta p' \frac{\partial \delta u_j'}{\partial X_i} \right\rangle}_{\text{Pressure strain } (\Pi_{ij}^f)} \underbrace{-4\epsilon_{ij}^{f*}}_{\text{Dissipation } (D_{ij}^f)} + \underbrace{\left\langle \delta u_j' \delta f_i' \right\rangle + \left\langle \delta u_i' \delta f_j' \right\rangle}_{\text{Forcing interaction}(\mathrm{F}_{ij}^f)}. \tag{2.14}$$

in which ϵ_{ij}^f is the pseudo-dissipation tensor $\left\langle \partial u_i'/\partial x_k \partial u_j'/\partial x_k \right\rangle$. The source term Ξ_{ij}^f identifies scales and positions with a net sink ($\Xi_{ij}^f < 0$) or a net source ($\Xi_{ij}^f > 0$) for each component of the Reynolds stresses. The separation of Ξ_{ij}^f in its constituent terms provides insight on mean-fluctuating production P_{ij}^{mf} (which also appears in (2.10) with opposite sign), redistribution Π_{ij}^f, dissipation D_{ij}^f and interaction with external fluctuating volume forces F_{ij}^f of turbulent stresses among

scales and positions (note that the forcing interaction term was missing in the original AGKE formulated by Gatti *et al.* (2020)). The flux vectors describe the various transfer processes, and their field lines visualise how fluctuations are transferred among scales and positions, via direct and inverse cascades. It should be recalled that, as stressed by Gatti *et al.* (2020), when interpreting AGKE results to extract structural turbulence information, local peaks of the structure functions always need to be connected to local maxima/minima of the correlation functions whenever a separation along an inhomogeneous direction is involved.

2.2.3 The phase-aware AGKE, or φAGKE

By using the triple decomposition (2.1), the phase-averaged fluctuating structure function tensor $\overline{\delta u_i' \delta u_j'}(\boldsymbol{X}, \boldsymbol{r}, \varphi)$ can be separated into its coherent and stochastic parts, i.e.

$$\overline{\delta u_i' \delta u_j'}(\boldsymbol{X}, \boldsymbol{r}, \varphi) = \overline{\delta \tilde{u}_i \delta \tilde{u}_j}(\boldsymbol{X}, \boldsymbol{r}, \varphi) + \overline{\delta u_i'' \delta u_j''}(\boldsymbol{X}, \boldsymbol{r}, \varphi); \tag{2.15}$$

note that $\overline{\delta \tilde{u}_i \delta \tilde{u}_j} \equiv \delta \tilde{u}_i \delta \tilde{u}_j$ owing to the definition of the phase-average operator. Two budget equations, called φAGKE, can be written for $\delta \tilde{u}_i \delta \tilde{u}_j$ and $\overline{\delta u_i'' \delta u_j''}$, which include, unlike the standard AGKE, the interplay among the mean, coherent and stochastic fields at each phase φ. These new equations extend in a significant way the work made by Thiesset *et al.* (2014) and Alves Portela *et al.* (2020), that considered the budget equations for $\langle \delta \tilde{u}_i \delta \tilde{u}_i \rangle(\boldsymbol{X}, \boldsymbol{r})$ and $\left\langle \delta u_i'' \delta u_i'' \right\rangle(\boldsymbol{X}, \boldsymbol{r})$. They applied the triple decomposition to the trace $\left\langle \delta u_i' \delta u_i' \right\rangle$ of the second-order structure function tensor, instead of considering the whole tensor. The major difference, though, is that the dependence on the phase φ of the coherent motion (or external forcing) was lost, because of the use of the $\langle \cdot \rangle$ operator. On the contrary, the φAGKE retain full phase information.

The step-by-step derivation of the φAGKE from the incompressible Navier–Stokes equations is described in Appendix 2.A. At each phase φ, they link the phase variation of each component of the coherent and stochastic structure function tensors, at a given scale $\boldsymbol{r}$ and position $\boldsymbol{X}$, to the unbalance among inter-component redistribution, scale-space transport, dissipation and mean-coherent-stochastic interaction. The last term is obviously absent in the classic AGKE.

The equations for the coherent and stochastic parts can be compactly written as:

$$\frac{2\pi}{T} \frac{\partial \delta \tilde{u}_i \delta \tilde{u}_j}{\partial \varphi} + \frac{\partial \phi^c_{k,ij}}{\partial r_k} + \frac{\partial \psi^c_{k,ij}}{\partial X_k} = \xi^c_{ij} + \zeta^c_{ij} \tag{2.16}$$

and

$$\frac{2\pi}{T} \frac{\partial \overline{\delta u_i'' \delta u_j''}}{\partial \varphi} + \frac{\partial \phi^s_{k,ij}}{\partial r_k} + \frac{\partial \psi^s_{k,ij}}{\partial X_k} = \xi^s_{ij}, \tag{2.17}$$

where, as above, the repeated index k implies summation.

The first term in equations (2.16) and (2.17) represents the phase variation of the coherent and stochastic components of the structure function tensor. The coherent and stochastic scale fluxes $\phi^c_{k,ij}$ and $\phi^s_{k,ij}$, i.e. the fluxes of $\delta\tilde{u}_i\delta\tilde{u}_j$ and $\overline{\delta u''_i \delta u''_j}$ in the space of scales, are defined as:

$$\phi^c_{k,ij} = \underbrace{\delta U_k \delta\tilde{u}_i\delta\tilde{u}_j}_{\text{Mean transport}} + \underbrace{\delta\tilde{u}_k\delta\tilde{u}_i\delta\tilde{u}_j}_{\text{Coherent transport}} + \underbrace{\overline{\delta u''_k\delta u''_i}\delta\tilde{u}_j + \overline{\delta u''_k\delta u''_j}\delta\tilde{u}_i}_{\text{Stochastic transport}} \underbrace{-2\nu\frac{\partial\delta\tilde{u}_i\delta\tilde{u}_j}{\partial r_k}}_{\text{Viscous diffusion}} \quad k = 1,2,3 \tag{2.18}$$

and

$$\phi^s_{k,ij} = \underbrace{\delta U_k\overline{\delta u''_i\delta u''_j}}_{\text{Mean transport}} + \underbrace{\delta\tilde{u}_k\overline{\delta u''_i\delta u''_j}}_{\text{Coherent transport}} + \underbrace{\overline{\delta u''_k\delta u''_i\delta u''_j}}_{\text{Stochastic transport}} \underbrace{-2\nu\frac{\partial\overline{\delta u''_i\delta u''_j}}{\partial r_k}}_{\text{Viscous diffusion}} \quad k = 1,2,3. \tag{2.19}$$

The coherent and stochastic spatial flux terms $\psi^c_{k,ij}$ and $\psi^s_{k,ij}$, i.e. the fluxes of $\delta\tilde{u}_i\delta\tilde{u}_j$ and $\overline{\delta u''_i\delta u''_j}$ in the physical space, are defined as:

$$\psi^c_{k,ij} = \underbrace{U^*_k\delta\tilde{u}_i\delta\tilde{u}_j}_{\text{Mean transport}} + \underbrace{\tilde{u}^*_k\delta\tilde{u}_i\delta\tilde{u}_j}_{\text{Coherent transport}} + \underbrace{\overline{u''^*_k\delta u''_i}\delta\tilde{u}_j + \overline{u''^*_k\delta u''_j}\delta\tilde{u}_i}_{\text{Stochastic transport}} + \underbrace{\frac{1}{\rho}\delta\tilde{p}\delta\tilde{u}_i\delta_{kj}}_{\text{Pressure transport}} +$$
$$\underbrace{+\frac{1}{\rho}\delta\tilde{p}\delta\tilde{u}_j\delta_{ki}}_{\text{Pressure transport}} \underbrace{-\frac{\nu}{2}\frac{\partial\delta\tilde{u}_i\delta\tilde{u}_j}{\partial X_k}}_{\text{Viscous diffusion}} \quad k = 1,2,3 \tag{2.20}$$

$$\psi^s_{k,ij} = \underbrace{U^*_k\overline{\delta u''_i\delta u''_j}}_{\text{Mean transport}} + \underbrace{\tilde{u}^*_k\overline{\delta u''_i\delta u''_j}}_{\text{Coherent transport}} + \underbrace{\overline{u''^*_k\delta u''_i\delta u''_j}}_{\text{Stochastic transport}} + \underbrace{\frac{1}{\rho}\overline{\delta p''\delta u''_i}\delta_{kj} + \frac{1}{\rho}\overline{\delta p''\delta u''_j}\delta_{ki}}_{\text{Pressure transport}} +$$
$$\underbrace{-\frac{\nu}{2}\frac{\partial\overline{\delta u''_i\delta u''_j}}{\partial X_k}}_{\text{Viscous diffusion}} \quad k = 1,2,3. \tag{2.21}$$

The differences with the fluxes (2.12) and (2.13) appearing in the standard AGKE are worth noticing. Two new terms appear here to account for the effect of the coherent field upon transport in the stochastic field, labelled as coherent transport in equations (2.19) and (2.21). Vice versa, how the stochastic field affects transport in the coherent field is reflected by the stochastic transport term in equations (2.18) and (2.20)).

The coherent and stochastic source terms ξ^c_{ij} and ξ^s_{ij} denote the scale-space net production of $\delta\tilde{u}_i\delta\tilde{u}_j$ and $\overline{\delta u''_i \delta u''_j}$. They can be either positive or negative, and read:

$$\xi^c_{ij} = \underbrace{-\delta\tilde{u}_j\delta\tilde{u}_k\left(\frac{\partial U_i}{\partial x_k}\right)^* - \delta\tilde{u}_i\delta\tilde{u}_k\left(\frac{\partial U_j}{\partial x_k}\right)^* - \delta\tilde{u}_j\tilde{u}^*_k\delta\left(\frac{\partial U_i}{\partial x_k}\right) - \delta\tilde{u}_i\tilde{u}^*_k\delta\left(\frac{\partial U_j}{\partial x_k}\right)}_{\text{Mean-coherent production } (p^{mc}_{ij})} +$$
$$\underbrace{-\left[-\overline{\delta u''_j\delta u''_k}\left(\frac{\partial\tilde{u}_i}{\partial x_k}\right)^* - \overline{\delta u''_i\delta u''_k}\left(\frac{\partial\tilde{u}_j}{\partial x_k}\right)^* - \overline{\delta u''_j u''^*_k}\delta\left(\frac{\partial\tilde{u}_i}{\partial x_k}\right) - \overline{\delta u''_i u''^*_k}\delta\left(\frac{\partial\tilde{u}_j}{\partial x_k}\right)\right]}_{\text{Coherent-stochastic production } (p^{cs}_{ij})} +$$
$$\underbrace{+\frac{1}{\rho}\delta\tilde{p}\frac{\partial\delta\tilde{u}_i}{\partial X_j} + \frac{1}{\rho}\delta\tilde{p}\frac{\partial\delta\tilde{u}_j}{\partial X_i}}_{\text{Pressure strain } (\pi^c_{ij})} \quad \underbrace{-4\epsilon^{c*}_{ij}}_{\text{Dissipation } (d^c_{ij})} \quad + \underbrace{\delta\tilde{u}_j\delta\tilde{f}_i + \delta\tilde{u}_i\delta\tilde{f}_j}_{\text{Forcing interaction}(\mathrm{f}^c_{ij})} \tag{2.22}$$

$$\xi^s_{ij} = \underbrace{-\overline{\delta u''_j\delta u''_k}\left(\frac{\partial U_i}{\partial x_k}\right)^* - \overline{\delta u''_i\delta u''_k}\left(\frac{\partial U_j}{\partial x_k}\right)^* - \overline{\delta u''_j u''^*_k}\delta\left(\frac{\partial U_i}{\partial x_k}\right) - \overline{\delta u''_i u''^*_k}\delta\left(\frac{\partial U_j}{\partial x_k}\right)}_{\text{Mean-stochastic production } (p^{ms}_{ij})} +$$
$$\underbrace{+\left[-\overline{\delta u''_j\delta u''_k}\left(\frac{\partial\tilde{u}_i}{\partial x_k}\right)^* - \overline{\delta u''_i\delta u''_k}\left(\frac{\partial\tilde{u}_j}{\partial x_k}\right)^* - \overline{\delta u''_j u''^*_k}\delta\left(\frac{\partial\tilde{u}_i}{\partial x_k}\right) - \overline{\delta u''_i u''^*_k}\delta\left(\frac{\partial\tilde{u}_j}{\partial x_k}\right)\right]}_{\text{Coherent-stochastic production } (p^{cs}_{ij})} +$$
$$\underbrace{+\frac{1}{\rho}\overline{\delta p''\frac{\partial\delta u''_i}{\partial X_j}} + \frac{1}{\rho}\overline{\delta p''\frac{\partial\delta u''_j}{\partial X_i}}}_{\text{Pressure strain } (\pi^s_{ij})} \quad \underbrace{-4\epsilon^{s*}_{ij}}_{\text{Dissipation } (d^s_{ij})} \quad \underbrace{+\overline{\delta u''_j\delta f''_i} + \overline{\delta u''_i\delta f''_j}}_{\text{Forcing interaction}(\mathrm{f}^s_{ij})}. \tag{2.23}$$

Among the terms appearing in the source, the mean-coherent and mean-stochastic productions p^{mc}_{ij} and p^{ms}_{ij} indicate the scales and positions where the mean flow feeds, or drains energy from, the coherent and stochastic fields: they are not positive definite, and therefore can be either sources or sinks. They both contribute to the mean-fluctuating production P^{mf}_{ij} in equation (2.10), as $P^{mf}_{ij} = \left\langle p^{mc}_{ij}\right\rangle + \left\langle p^{ms}_{ij}\right\rangle$. The coherent-stochastic production p^{cs}_{ij} indicates the exchange of stresses between the coherent and stochastic fields, and appears in the budgets for $\delta\tilde{u}_i\delta\tilde{u}_j$ and $\overline{\delta u''_i\delta u''_j}$ with opposite sign. d^c_{ij} and d^s_{ij} denote viscous dissipation, and the pressure-strain terms π^c_{ij} and π^s_{ij} describe the interplay between pressure and velocity fields. Pressure–strain terms involve neither production nor

dissipation of energy, and no cross-talk between coherent and fluctuating fields. Overall, among the source terms, the productions p_{ij}^{mc}, p_{ij}^{ms} and p_{ij}^{cs} are the only ones that connect the mean, coherent and fluctuating budgets, and are essential to ascertain how the mean, stochastic and coherent fields force each other. The forcing interactions f_{ij}^{c} and f_{ij}^{s} represent the power injected into the system by the interaction of a coherent and stochastic external volume forcing with the coherent and stochastic flow fields, respectively.

Finally, in equation (2.16) for $\delta\tilde{u}_i\delta\tilde{u}_j$ a new term ζ_{ij}^{c} appears on the right-hand side. It describes the inter-phase interaction driven by the coherent flow field, and is defined as:

$$\begin{aligned}
\zeta_{ij}^{c} = {} & \frac{\partial}{\partial r_k}\left[\langle\delta\tilde{u}_i\delta\tilde{u}_k\rangle\delta\tilde{u}_j + \langle\delta\tilde{u}_j\delta\tilde{u}_k\rangle\delta\tilde{u}_i\right] + \frac{\partial}{\partial X_k}\left[\langle\tilde{u}_k^{*}\delta\tilde{u}_i\rangle\delta\tilde{u}_j + \langle\tilde{u}_k^{*}\delta\tilde{u}_j\rangle\delta\tilde{u}_i\right] + \\
& + \frac{\partial}{\partial r_k}\left[\left\langle\delta u_i''\delta u_k''\right\rangle\delta\tilde{u}_j + \left\langle\delta u_j''\delta u_k''\right\rangle\delta\tilde{u}_i\right] + \frac{\partial}{\partial X_k}\left[\left\langle u_k''^{*}\delta u_i''\right\rangle\delta\tilde{u}_j + \left\langle u_k''^{*}\delta u_j''\right\rangle\delta\tilde{u}_i\right] + \\
& - \langle\delta\tilde{u}_i\delta\tilde{u}_k\rangle\left(\frac{\partial\tilde{u}_j}{\partial x_k}\right)^{*} - \langle\delta\tilde{u}_j\delta\tilde{u}_k\rangle\left(\frac{\partial\tilde{u}_i}{\partial x_k}\right)^{*} - \langle\delta\tilde{u}_i\tilde{u}_k^{*}\rangle\delta\left(\frac{\partial\tilde{u}_j}{\partial x_k}\right) - \langle\delta\tilde{u}_j\tilde{u}_k^{*}\rangle\delta\left(\frac{\partial\tilde{u}_i}{\partial x_k}\right) + \\
& - \left\langle\delta u_i''\delta u_k''\right\rangle\left(\frac{\partial\tilde{u}_j}{\partial x_k}\right)^{*} - \left\langle\delta u_j''\delta u_k''\right\rangle\left(\frac{\partial\tilde{u}_i}{\partial x_k}\right)^{*} - \left\langle\delta u_i''u_k''^{*}\right\rangle\delta\left(\frac{\partial\tilde{u}_j}{\partial x_k}\right) - \left\langle\delta u_j''u_k''^{*}\right\rangle\delta\left(\frac{\partial\tilde{u}_i}{\partial x_k}\right).
\end{aligned} \tag{2.24}$$

The terms in the last two rows above resemble a production term, and indicate the production of $\delta\tilde{u}_i\delta\tilde{u}_j$ due to the correlation of each phase with all the others.

By averaging equations (2.16) and (2.17) over the phases, the budget equations for $\langle\delta\tilde{u}_i\delta\tilde{u}_j\rangle(\boldsymbol{X},\boldsymbol{r})$ and $\left\langle\delta u_i''\delta u_j''\right\rangle(\boldsymbol{X},\boldsymbol{r})$ are obtained. In doing this, the inter-phase contributions vanish, since by definition they have zero average. The sum of the equations for the three diagonal components of $\langle\delta\tilde{u}_i\delta\tilde{u}_j\rangle$ and $\left\langle\delta u_i''\delta u_j''\right\rangle$ yields the GKE equations used by Alves Portela *et al.* (2020). If the equations for $\langle\delta\tilde{u}_i\delta\tilde{u}_j\rangle$ and $\left\langle\delta u_i''\delta u_j''\right\rangle$ are added together, the standard AGKE for the fluctuating field $\left\langle\delta u_i'\delta u_j'\right\rangle$ are recovered.

2.3 Turbulent drag reduction by the spanwise-oscillating wall

The φAGKE are now applied to a fully developed turbulent channel flow subjected to a spanwise harmonic oscillation of the walls. This flow is a convenient example where the deterministic external periodic forcing provides an unambiguous definition of the phase, yet the physics behind drag reduction is interesting and not fully understood yet.

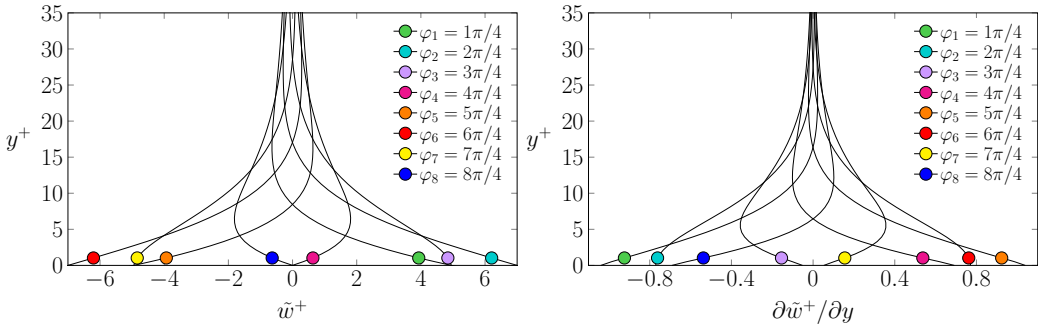

Figure 2.2: Wall-normal profile of the spanwise coherent velocity $\tilde{w}^+$ (left) and shear $\partial\tilde{w}^+/\partial y$ (right), plotted at 8 equally spaced phases $\varphi_1, \ldots \varphi_8$ along the period $T^+ = 250$.

The spanwise oscillating wall is a well-known skin-friction drag reduction technique, intensely studied over the last thirty years (see Ricco *et al.*, 2021, and references therein). The channel walls periodically move along the spanwise direction, according to:

$$w_w(t) = A \sin\left(\frac{2\pi}{T}t\right), \tag{2.25}$$

where A and T are the prescribed amplitude and period of the sinusoidal oscillation, and w_w is the spanwise velocity of the wall. x, y and z (u, v and w) denote the streamwise, wall-normal and spanwise directions (velocity components); the alternative notation $x_1 = x$ ($u_1 = u$), $x_2 = y$ ($u_2 = v$) and $x_3 = z$ ($u_3 = w$) is also used. The harmonic oscillation generates a periodic (coherent) spanwise cross-flow, that even for a turbulent streamwise flow is well described (Quadrio & Sibilla, 2000) by the analytical laminar solution of the second Stokes problem, usually referred to as the Stokes layer:

$$w(y, \varphi) = A \exp\left(-\sqrt{\frac{\omega}{2\nu}}y\right) \sin\left(\varphi - \sqrt{\frac{\omega}{2\nu}}y\right), \tag{2.26}$$

where φ is the phase of the oscillation, and $\omega = 2\pi/T$. Figure 2.2 shows the coherent spanwise velocity field (the Stokes layer) generated by the harmonic oscillations, and its derivative in wall-normal direction (the Stokes shear): the oscillating period is subdivided into eight equally spaced phases $\varphi_1, \varphi_2, \ldots \varphi_8$, where $\varphi_i = i\pi/4$. From here on, the + superscript is used to indicate quantities made dimensionless with the friction velocity $u_\tau = \sqrt{\tau_w/\rho}$ (ρ is the fluid density, and τ_w is the time-averaged streamwise wall shear stress; the spanwise component is zero) and the kinematic viscosity ν.

The interaction between the coherent Stokes layer and the stochastic near-wall turbulence influences the main structures of the near-wall cycle, i.e. the low-

speed streaks and the quasi-streamwise vortices, eventually yielding a reduction of turbulent friction. When the Reynolds number based on the friction velocity is $Re_\tau = 200$, the largest drag reduction rate for a given oscillation amplitude $A^+ = 12$ is about 45%, obtained for the optimal actuation period $T^+ \approx 100$ (Quadrio & Ricco, 2004). Larger or smaller periods result in smaller drag reduction. Several authors, for example Yakeno *et al.* (2014), observed that the orientation of near-wall structures in wall-parallel planes is cyclically altered by the coherent spanwise shear. Touber & Leschziner (2012) have shown that, provided the timescale of the spanwise shear oscillation is short enough, the low-speed streaks do not have the time to fully re-orient during the oscillation, and are thus weakened. Hence, at the root of drag reduction lies the interaction between the oscillating shear (a coherent component) and the natural streak regeneration mechanism (seen in the stochastic component).

Touber & Leschziner (2012) and later Agostini *et al.* (2014) applied a triple decomposition of the velocity field to the budgets of the single-point Reynolds stresses; the turbulent (stochastic) fluctuations were isolated and their interaction with the (coherent) Stokes layer was studied. It was found that the interaction between coherent and stochastic fields is mediated by the interplay between the coherent spanwise shear $\partial\tilde{w}/\partial y$ and the $\overline{v''w''}$ component of the Reynolds stress tensor, induced by the rotation of the vortical structures. For nearly optimal periods, the interaction between the coherent and stochastic fields is one-way, with the former altering the latter. This weakens the wall-normal velocity fluctuations and reduces the turbulent shear, reducing eventually the friction drag. For larger periods, instead, the interaction becomes two-ways, with coherent and stochastic fields mutually exchanging energy. In this case, however, the drag reduction effect is less important. By looking at different phases along the period, they found that, when large, the Stokes shear $\partial\tilde{w}/\partial y$ changes relatively slowly in time and allows the structures to become more vigorous and well-established (a process they referred to as lingering). Conversely, when $\partial\tilde{w}/\partial y$ is small, the structures appear weak and less tilted.

In this example, we intend to add scale information to the picture. We thus apply the φAGKE: (i) to describe the influence of the coherent motion on the spatial arrangement of the near-wall structures during the control period, (ii) to inspect the mean-coherent-stochastic interaction in the scale space and in the physical space, and (iii) to characterise the phase dependence of the interaction between the coherent and stochastic fields.

2.3.1 Database and computational details

The φAGKE terms are computed from two datasets obtained by direct numerical simulations (DNS). They are described by Gallorini *et al.* (2022), where the

interested reader can find full details.

The simulations are run under a constant pressure gradient (CPG) (Quadrio *et al.*, 2016*a*), with a friction Reynolds number of $Re_\tau = u_\tau h/\nu = 200$, where h is the channel half-height. CPG provides a unique value of u_τ with/without drag reduction, thus avoiding ambiguities in viscous scaling. The size of the computational domain is $(L_x, L_y, L_z) = (4\pi h, 2h, 2\pi h)$ in the streamwise, wall-normal and spanwise directions. The number of Fourier modes is $N_x = N_z = 256$ in the two homogeneous (streamwise and spanwise) directions, further increased by a factor of $3/2$ to remove aliasing error. In the wall-normal direction, a hyperbolic tangent distribution of $N_y = 192$ points provides a finer grid near the wall. The spatial resolution is $\Delta x^+ = 6.6$ and $\Delta z^+ = 3.3$ by considering the extra modes, while Δy^+ varies from $\Delta y^+ \approx 0.5$ close to the wall to $\Delta y^+ \approx 3.7$ at the centreline.

A first simulation of a plane channel with fixed walls is run as a reference, followed by two others in which wall oscillation according to (2.25) is enforced. The oscillation amplitude is fixed at $A^+ = 7$: a rather small value, which keeps the energy cost of the actuation limited, and might even provide a small net energy saving at optimal periods. As in Agostini & Leschziner (2014), we consider two control periods, namely $T^+ = 75$ and $T^+ = 250$. The value $T^+ = 75$ is nearly optimal, and yields drag reduction (defined here as a percentage decrease of the friction coefficient, determined by the increase in bulk velocity) of 25.2%. The value $T^+ = 250$ is suboptimal, and yields only 13.2% drag reduction. These figures are in agreement with existing information (see for example Gatti & Quadrio, 2016).

Simulations are started from an uncontrolled turbulent flow field. During the initial, transient phase, the solution is advanced by setting the Courant–Friedrichs–Lewy number at $CFL = 1$. After the transient, however, the time step is set to a fixed value, in order to synchronize data saving with predetermined control phases. The value of the time step is thus chosen as an integer submultiple of the forcing period that keeps the maximum CFL below the unit: it is $\Delta t^+ = 0.0938$ for the smaller period, and $\Delta t^+ = 0.0781$ for the longer period. After the transient, 376 complete velocity fields are saved, so that 47 control periods are stored for later analysis, each of them divided in 8 equally spaced phases.

The φAGKE terms are computed from the database with a post-processing code derived with modifications from that described by Gatti *et al.* (2020). It employs the same important numerical optimizations described in Gatti *et al.* (2019), which include the computation of correlations pseudo-spectrally whenever possible. The code, written in the CPL computer programming language (Luchini, 2020, 2021) has been validated by checking that the sum of each term of the budget of coherent and stochastic fields equals the corresponding term of $\left\langle \delta u_i' \delta u_j' \right\rangle$ within roundoff. Statistical convergence of the results is verified by ensuring that the residuals of the

budgets are negligible compared to the values of the production, pressure–strain and dissipation.

2.3.2 φAGKE tailored to the channel flow with oscillating walls

The general form (2.16) and (2.17) of the φAGKE can be simplified for the problem at hand. Since x and z are homogeneous, in an indefinite plane channel the φAGKE depend on five independent variables: the three components of the separation vector (r_x, r_y, r_z), the wall-normal component of the midpoint Y and the phase φ. Note that the finite distance between the two walls implies the constraint $r_y < 2Y$.

In an indefinite channel flow, the x direction aligns with the mean flow, hence $\boldsymbol{U}(y) = (U(y), 0, 0)$, and the wall-parallel derivatives of the mean velocity are zero. Moreover, in the specific case of the oscillating wall, the coherent velocity field is independent on x and z, as the wall control law (2.25) is a function of time only, so that $\partial\tilde{u}_i/\partial x = \partial\tilde{u}_i/\partial z = 0$. Therefore, incompressibility and no-penetration at the wall dictate that the wall-normal component of the coherent field is null everywhere, i.e. $\tilde{v}(y,t) = 0$. The streamwise coherent velocity $\tilde{u}$, instead, does not vanish, albeit it is known to be extremely small: (Yakeno *et al.*, 2014) report it to be two orders of magnitude smaller than the spanwise coherent velocity $\tilde{w}$. The non-zero components of the $\delta\tilde{u}_i\delta\tilde{u}_j$ tensor are $\delta\tilde{u}\delta\tilde{u}$, $\delta\tilde{w}\delta\tilde{w}$ and $\delta\tilde{u}\delta\tilde{w}$.

The specialised form of the φAGKE for the channel flow with oscillating walls is reported in Appendix 2.B. It can be observed that the mean-coherent production p_{ij}^{mc} is zero: in this particular case, there is no exchange of stresses between the mean and coherent fields, as the coherent field interacts directly with the external forcing and with the stochastic field only. However, this term does appear in other flows, and for example is important for the flow past a bluff body (Alves Portela *et al.*, 2020), where the mean flow supports the coherent vortex shedding, which in turn supports the stochastic fluctuations. In the budget for the stochastic part, the productions p_{ij}^{ms} and p_{ij}^{cs} represent the two avenues for the stochastic field to interact with the mean and coherent fields, involving distinct components of $\overline{\delta u_i'' \delta u_j''}$. The mean-stochastic production p_{ij}^{ms} is non-zero only for $\overline{\delta u'' \delta u''}$ and for the off-diagonal components $\overline{\delta u'' \delta v''}$ and $\overline{\delta u'' \delta w''}$. In contrast, the coherent-stochastic production contributes to all the elements of $\overline{\delta u_i'' \delta u_j''}$ except for $\overline{\delta v'' \delta v''}$, being $p_{22}^{cs} = 0$.

The flow symmetries and the type of forcing make only certain paths available for energy exchanges. This is represented graphically in figure 2.3, which shows an "energy circle" (Quadrio, 2011) to describe energy exchanges among the mean, coherent and stochastic fields after spatial and temporal integration. In the following, thanks to the φAGKE, these global energy exchanges and redistributions

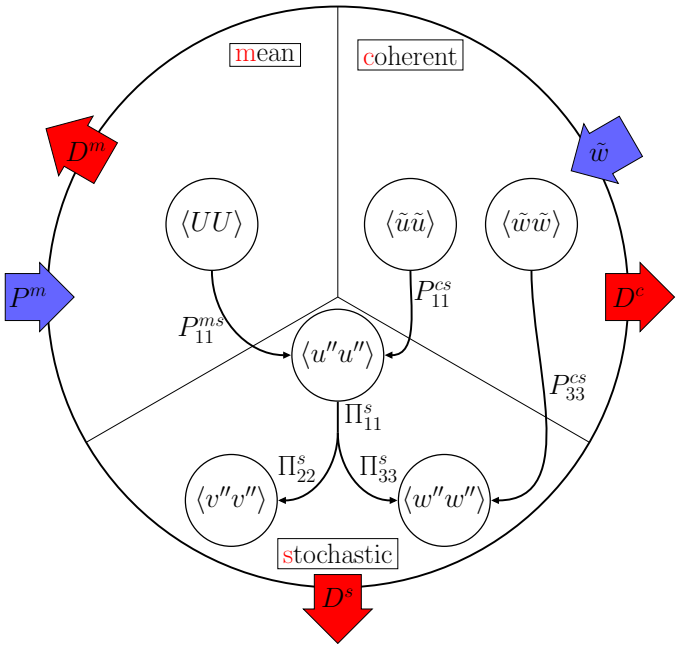

Figure 2.3: Sketch of the energy exchanges between mean, coherent and stochastic fields for the turbulent channel flow modified by spanwise-oscillating walls. Blue/red arrows indicate energy entering/leaving the system. The blue arrows P_m and $\tilde{w}$ represent the pumping energy required to move the flow, and the energy introduced by the moving walls.

are expanded and described in space and among scales, with a phase-by-phase analysis.

2.4 Effect of the spanwise forcing on the near-wall cycle

The influence of the oscillating wall on the structural organisation of the stochastic part of the velocity fluctuations in the near-wall region is considered first, at a single phase and then in terms of its phase evolution. The energy exchanges among mean, coherent and stochastic fields are then addressed, followed by the analysis of the pressure–strain redistribution. Eventually, the influence of the Stokes layer and the stochastic pressure–strain term π^s_{33} on the transfer of the spanwise stochastic stresses is described.

2.4.1 Near-wall structures

2.4.1.1 Description at a fixed phase

Figure 2.4 shows the diagonal components of $\overline{\delta u_i'' \delta u_j''}$ in the $r_y = r_x = 0$ plane for the uncontrolled channel (first row), $T^+ = 75$ (second row) and $T^+ = 250$ (third row). For the two controlled cases, only phase φ_4 is shown, but the discussion that follows is qualitatively valid for all phases.

The local maxima of $\overline{\delta u'' \delta u''}$ and $\overline{\delta v'' \delta v''}$, hereafter denoted with the $\cdot_m$ subscript, are the statistical trace of the structures of the near-wall cycle. In the $r_x = r_y = 0$ space, indeed, they indicate a negative peak of the streamwise and vertical stochastic correlation functions R_{11} and R_{22}; see equation (2.6). The coordinates $Y^+ \approx 14 - 18$ and $r_z^+ \approx 55 - 65$ of $\overline{\delta u'' \delta u''}_m$ in the (r_z^+, Y^+) plane indicate the characteristic wall distance and spanwise spacing of low- and high-speed streaks. The coordinates $Y^+ \approx 43 - 55$ and $r_z^+ \approx 49 - 59$ of $\overline{\delta v'' \delta v''}_m$ indicate the characteristic wall distance and spanwise size of the quasi-streamwise vortices, which induce at their spanwise sides regions of vertical velocity with negative correlation.

Figure 2.4 shows that the oscillating wall leaves $\overline{\delta u'' \delta u''}$ and $\overline{\delta v'' \delta v''}$ almost unchanged, indicating that the size and strength of the near-wall structures only marginally depend on the amount of drag reduction.

This is consistent with the CPG driving strategy, which forces the same level of wall friction; the large changes observed by various authors under different driving strategies simply derive trivially from the different friction, as discussed by Frohnapfel *et al.* (2012). However, the velocity streaks are slightly moved away from the wall: an upward shift of $\overline{\delta u'' \delta u''}_m$ can be seen in figure 2.4. The

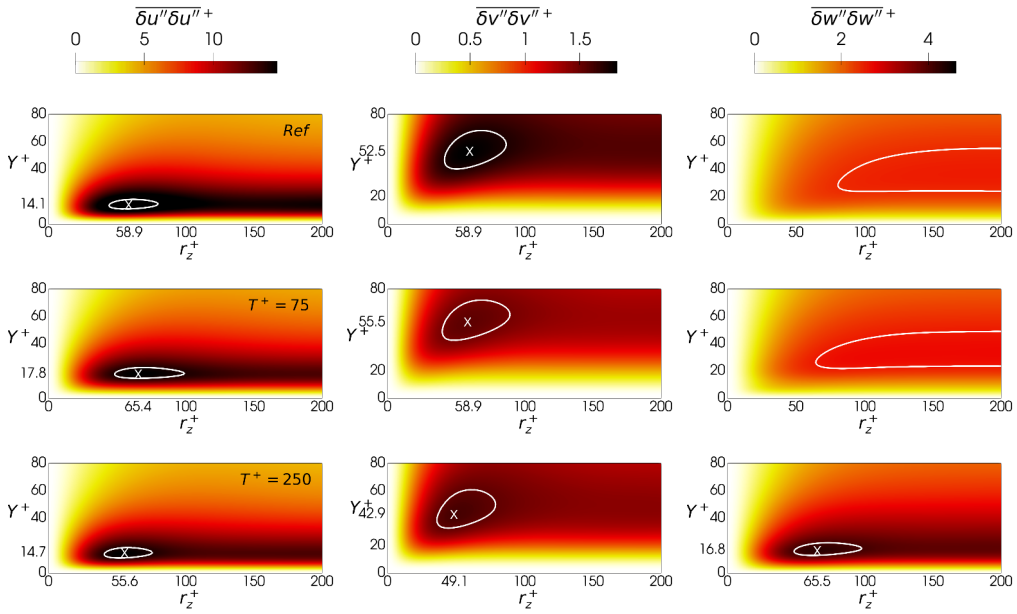

Figure 2.4: Diagonal components of the stochastic tensor $\overline{\delta u_i'' \delta u_j''}^+$ at φ_4 in the (r_z^+, Y^+) plane. From top to bottom: uncontrolled case with $A = 0$, $T^+ = 75$ and $T^+ = 250$. The contour is set at 95% of each maximum. The coordinates of the maximum, marked with a cross, can be read on the axes.

previous observation is confirmed by numerical data: the maximum moves from $Y^+ = 14.1$ in the reference case to $Y^+ = 17.8$ for $T^+ = 75$ and to $Y^+ = 14.7$ for $T^+ = 250$ (at phase φ_4). Both shifts are upwards, and the $T^+ = 75$ case with larger drag reduction has a larger shift. The quasi-streamwise vortices react differently to control: $\overline{\delta v'' \delta v''}_m$ moves from $Y^+ = 53$ in the reference case to $Y^+ = 55$ for $T^+ = 75$ and to $Y^+ = 43$ for $T^+ = 250$. These contrasting trends are consistent with the wall-normal displacement found by Gallorini *et al.* (2022) for conditionally-averaged quasi-streamwise vortices, but are extracted from the present analysis without the need for an (inevitably subjective) procedure for conditional structure extraction.

In the canonical channel flow, the map of $\overline{\delta w'' \delta w''}$ embeds information of the quasi-streamwise vortices only when the $r_y \neq 0$ space is considered, which contains the peak $\langle \delta w' \delta w' \rangle_m$ (Gatti *et al.*, 2020). Indeed, the quasi-streamwise vortices induce negatively correlated regions of w'' fluctuations at their vertical sides only, and the r_y coordinate of the maximum indicates their characteristic wall-normal size. In the controlled cases, however, a local peak of $\overline{\delta w'' \delta w''}$ appears in the $r_x = r_y = 0$ (figure 2.4) and $r_z = r_y = 0$ (not shown) planes. Interestingly, the local peak is particularly evident for $T^+ = 250$, extending for $r_z^+ \approx 50 - 100$, $r_x^+ \approx 85 - 270$ and $Y^+ \approx 13 - 25$, but it is hardly visible for $T^+ = 75$, where the w'' fluctuations are weaker. The next Subsection, which examines how these quantities vary with φ, shows that this derives from a combination of the streaks tilting in the $x - z$ plane and from the interaction of the quasi-streamwise vortices with the coherent spanwise shear.

2.4.1.2 Evolution during the cycle

Figure 2.5 shows the phase evolution of $\overline{\delta u'' \delta u''}$, $\overline{\delta v'' \delta v''}$ and $\overline{\delta w'' \delta w''}$ in the $r_x = r_y = 0$ plane, to describe how the organisation of the near-wall stochastic fluctuations changes during the oscillation cycle, i.e. the very type of information that the φAGKE are designed to provide. Only the suboptimal $T^+ = 250$ is considered, as the large period emphasises the phase dependence; moreover, only one half of the forcing period is shown (from φ_1 to φ_4), because of temporal symmetry. Extra quantitative information is provided by figure 2.6, which plots the phase evolution of the maxima $\overline{\delta u'' \delta u''}_m$, $\overline{\delta v'' \delta v''}_m$ and $\overline{\delta w'' \delta w''}_m$.

The streamwise velocity streaks cyclically strengthen and weaken under the action of the alternating Stokes layer. The maximum $\overline{\delta u'' \delta u''}_m$ assumes its lowest value at φ_2, and then grows to reach the highest value at φ_4, with an intra-cycle variation of 27%. The quasi-streamwise vortices, instead, show a much smaller phase dependence: the intra-cycle variation of $\overline{\delta v'' \delta v''}$ is 8% only. This is not surprising, since the quasi-streamwise vortices reside at larger wall distances, where the intensity of the Stokes layer is lower; at $y^+ = 14$, the average position of

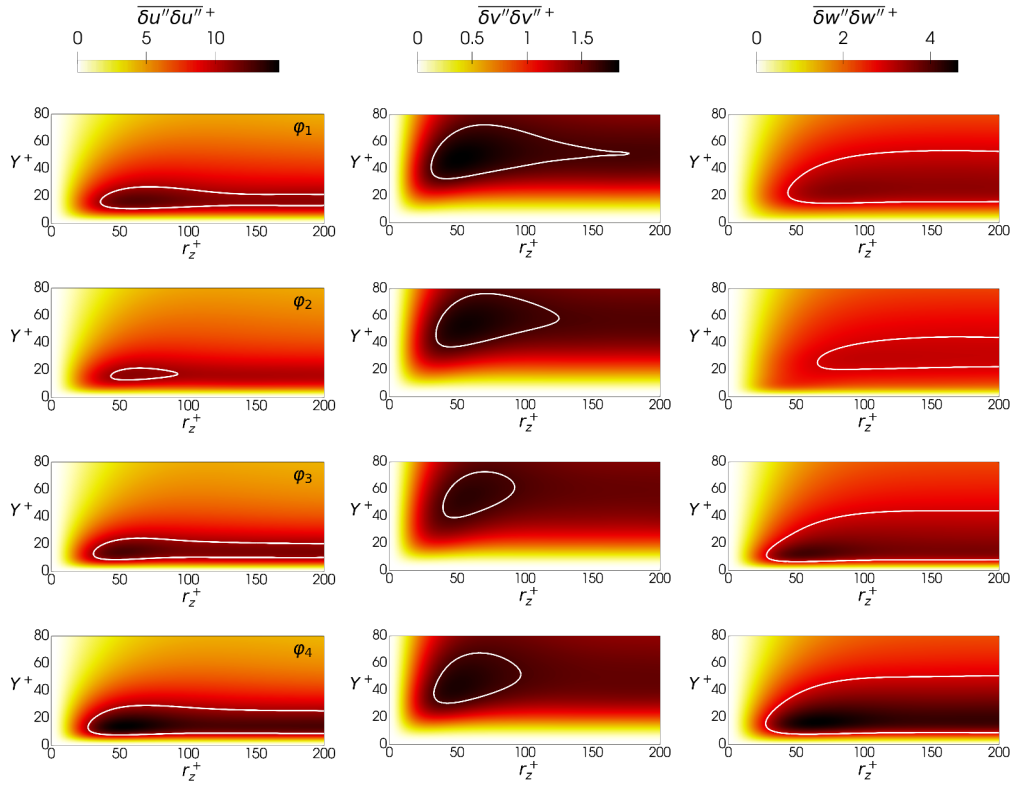

Figure 2.5: Diagonal components of the stochastic tensor $\overline{\delta u_i'' \delta u_j''}^+$ in the (r_z^+, Y^+) plane, at phases $\varphi_1, \varphi_2, \varphi_3, \varphi_4$ (from top to bottom), for the period $T^+ = 250$. For each component, the white contour is set at the 95% of the smallest peak over the phases (i.e. at φ_2 for $\overline{\delta u'' \delta u''}$ and $\overline{\delta w'' \delta w''}$, and at φ_3 for $\overline{\delta v'' \delta v''}$).

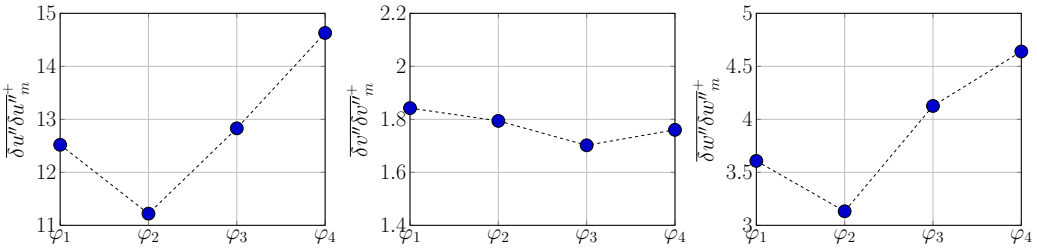

Figure 2.6: Phase variation of the maxima $\overline{\delta u_i'' \delta u_i''}^+_m$ in the (r_z^+, Y^+) plane.

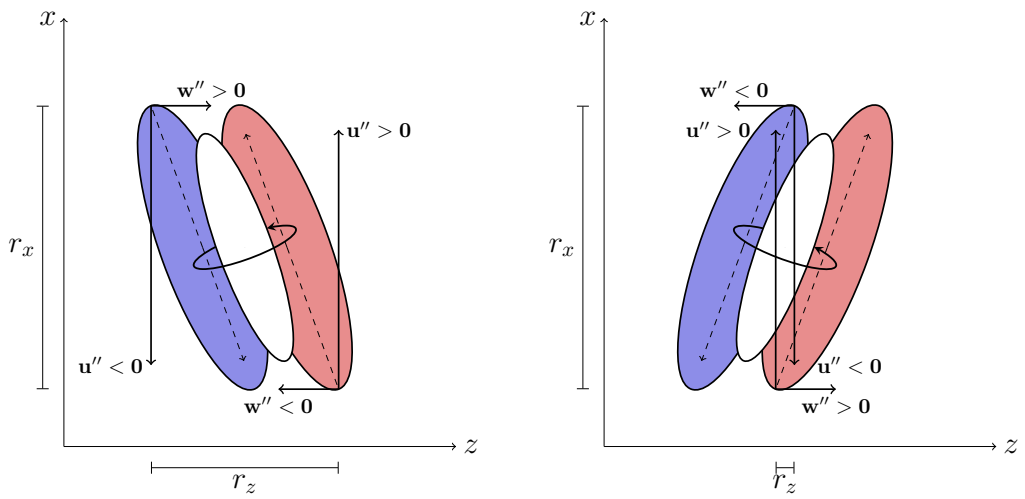

Figure 2.7: Sketch of the contribution of u'' and w'' for positively (left) and negatively (right) tilted low (blue) and high (red) speed streaks induced by a positively rotating quasi-streamwise vortex (white).

the streaks, the maximum $\tilde{w}^+$ is 1.15, while at $y^+ = 50$, representative wall-normal distance of the vortices, it is only 0.2. A different wall distance for streaks and vortices also implies a phase shift; in fact the intensity of $\overline{\delta v''\delta v''}$ is minimum at φ_3 and maximum at φ_1, whereas $\overline{\delta u''\delta u''}$ and $\overline{\delta w''\delta w''}$ are minimum at φ_2 and maximum at φ_4. This is consistent with the early observation (Baron & Quadrio, 1996) that streaks and quasi-streamwise vortices are displaced by the spanwise Stokes layer differently.

From figure 2.6, one notices that the phase evolution of $\overline{\delta w''\delta w''}_m$ resembles that of $\overline{\delta u''\delta u''}_m$, thus suggesting that part of the stochastic w'' fluctuations derives from a redistribution of the streamwise fluctuations. The near-wall structures are tilted in the $x-z$ plane and follow the shear vector $(\mathrm{d}U/\mathrm{d}y, 0, \partial\tilde{w}/\partial y)$ (Yakeno *et al.*, 2014). The tilting causes the streamwise high- and low-speed streaks to re-orient, thus contributing via pressure–strain redistribution (see below §2.4.3) to the spanwise stochastic fluctuations. When the tilting angle is positive (negative), the low- and high-speed streaks contribute to respectively positive (negative) and negative (positive) w''. This produces regions of w'' fluctuations that correlate negatively for scales r_x and r_z and position Y compatible with the position of $\overline{\delta w''\delta w''}_m$ observed in figure 2.5. This is shown with a sketch in figure 2.7, and confirmed with a phase-by-phase conditional average of events extracted from the present database in Appendix 2.C. The picture is also consistent with the lower $\overline{\delta w''\delta w''}_m$ observed in figure 2.4 for $T^+ = 75$: for periods close to the optimum,

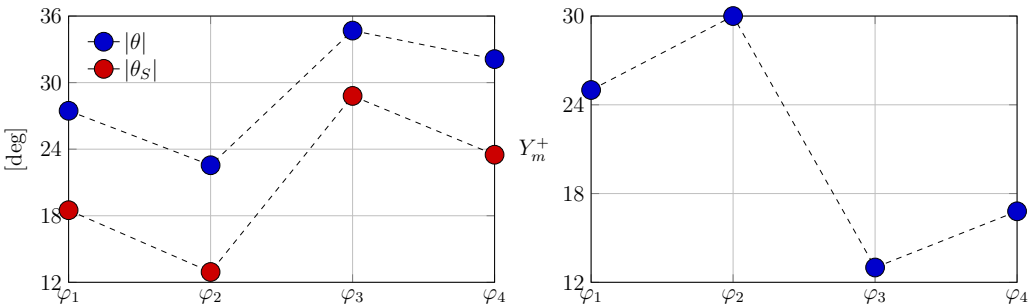

Figure 2.8: Left: evolution of the tilt angle of the wall streaks during the cycle. Comparison between present results (blue symbols) and the shear angle introduced by Yakeno *et al.* (2014) (red symbols). Right: wall-normal position of the structures, educed from the wall-normal position Y_m^+ of $\overline{\delta w'' \delta w''}_m$.

the oscillation is too fast for the streaks to align with the shear vector (Touber & Leschziner, 2012), and this redistribution mechanism becomes weaker.

Similar information is usually extracted (Yakeno *et al.*, 2014) from phase-locked conditional averages. However, such statistics are unavoidably arbitrary to some degree: e.g. "short" structures have to be excluded from averaging, and one needs to pre-determine a specific wall distance for the eduction procedure. Here we obtain information that is equivalent to conditional averaging, but via a statistical analysis that is free from assumptions and hypotheses.

For example, the scales $r_{z,m}$ and $r_{x,m}$ identified by $\overline{\delta w'' \delta w''}_m$ can be used to track the phase evolution of the tilting angle θ of the flow structures during the cycle:

$$|\theta(\varphi)| = \tan^{-1}\left(\frac{r_{z,m}(\varphi)}{r_{x,m}(\varphi)}\right). \tag{2.27}$$

Similarly, the evolution of the wall-normal position Y_m of $\overline{\delta w'' \delta w''}_m$ (or, equivalently, of $\overline{\delta u'' \delta u''}_m$) quantifies the vertical displacement of the streaks during the cycle. Figure 2.8 compares $|\theta|$ with the shear angle θ_s evaluated at Y_m, i.e.

$$\theta_s = \tan^{-1}\left(\frac{\partial \tilde{w}/\partial y}{\mathrm{d}U/\mathrm{d}y}\right),$$

that is conventionally used to describe the tilting angle of the near-wall structures (Yakeno *et al.*, 2014; Gallorini *et al.*, 2022). The two quantities θ and θ_s are quantitatively similar and present the same phase dependence, with a nearly constant difference of about 8°. The right panel of figure 2.8 also shows that when the tilting angle of the streaks is maximum, their distance from the wall is minimum (and vice versa). This implies that a higher coherent spanwise velocity yields a larger tilting.

Part of the wall-parallel modulation of $\overline{\delta w'' \delta w''}$ induced by the wall oscillation derives from the interaction of the quasi-streamwise vortices with the coherent spanwise shear. When the coherent shear $\partial \tilde{w}/\partial y$ is positive, the quasi-streamwise vortices move low-spanwise-velocity fluid upwards, and high-spanwise-velocity fluid downwards. The opposite happens when $\partial \tilde{w}/\partial y < 0$. This creates two regions with spanwise velocity of opposite sign at the vortex sides, resulting in negative R_{33} correlation and a positive peak of $\overline{\delta w'' \delta w''}$ at their characteristic spanwise separation. This process, quantified by the coherent-stochastic production p_{33}^{cs} (see §2.4.2), resembles the ejections and sweeps typical of the near-wall cycle, where the mean streamwise shear is involved; its description is similar to the explanation provided by Agostini *et al.* (2014) for the non-zero $\langle v'' w'' \rangle$. Once again, our interpretation is supported by the velocity field induced by the ensemble-averaged quasi-streamwise vortex, computed at various phases and shown in Appendix 2.C.

2.4.2 Interaction of the mean, coherent, and fluctuating fields

The energy exchanges of the mean field with the stochastic and coherent fields are described by the two mean production terms p_{ij}^{mc} and p_{ij}^{ms}. However, as shown in figure 2.3, for the present problem $p_{ij}^{mc} = 0$, and the mean field interacts directly with the stochastic field only, by feeding (or draining from) streamwise fluctuations. Moreover, energy is exchanged between the coherent and stochastic fields via the coherent-stochastic production p_{ij}^{cs}, which involves only $\overline{\delta u'' \delta u''}$ and $\overline{\delta w'' \delta w''}$ among the diagonal components of the $\overline{\delta u_i'' \delta u_j''}$ tensor.

Figure 2.9 shows how the mean-stochastic production p_{11}^{ms} varies with φ for $T^+ = 75$ (left) and $T^+ = 250$ (right) in the $r_x = r_y = 0$ plane, where the production terms are maxima. Here p_{11}^{ms} reduces to

$$p_{11}^{ms} = -2\overline{\delta u'' \delta v''} \left(\frac{\mathrm{d}U}{\mathrm{d}y} \right).$$

The mean-stochastic production is positive everywhere, with a peak in the range $r_{z,m}^+ = 36 - 42$ and $Y_m^+ = 13 - 17$ for $T^+ = 75$ and $r_{z,m}^+ = 36 - 39$ and $Y_m^+ = 12 - 14$ for $T^+ = 250$. Hence, the interaction of the near-wall cycle ($\overline{\delta u'' \delta v''}$) with the mean shear ($\mathrm{d}U/\mathrm{d}y$) invariably moves energy from the mean field towards the stochastic streamwise fluctuations. Note that the smaller Y^+ for $T^+ = 250$ is consistent with the reduced thickening of the viscous sublayer for suboptimal periods. The production intensity is largest at φ_1 and lowest at φ_3 for $T^+ = 75$, whereas it is largest at φ_3 and lowest at φ_1 for $T^+ = 250$. Since $\mathrm{d}U/\mathrm{d}y$ is phase-independent, this can only descend from $\overline{\delta u'' \delta v''}$, which includes the phase evolution of the streaks and of the quasi-streamwise vortices (see §2.4.1.2 above).

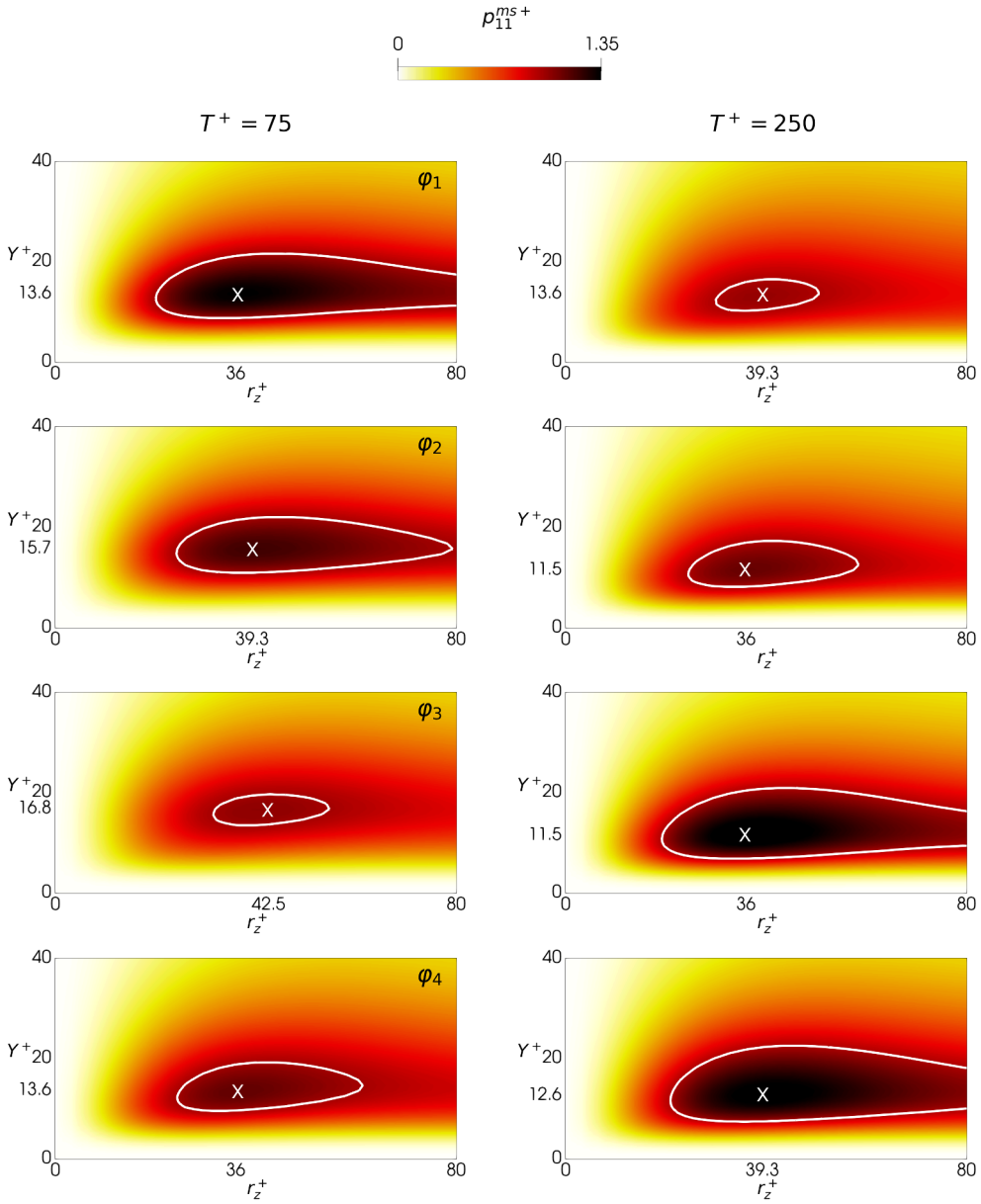

Figure 2.9: Mean-stochastic production p_{11}^{ms+} in the (r_z^+, Y^+) plane for $T^+ = 75$ (left) and $T^+ = 250$ (right). From top to bottom: $\varphi_1, \varphi_2, \varphi_3, \varphi_4$. The contour line is set at 95% of the smallest maximum over the phases. The coordinates of the maximum, marked with a cross, can be read on the axes.

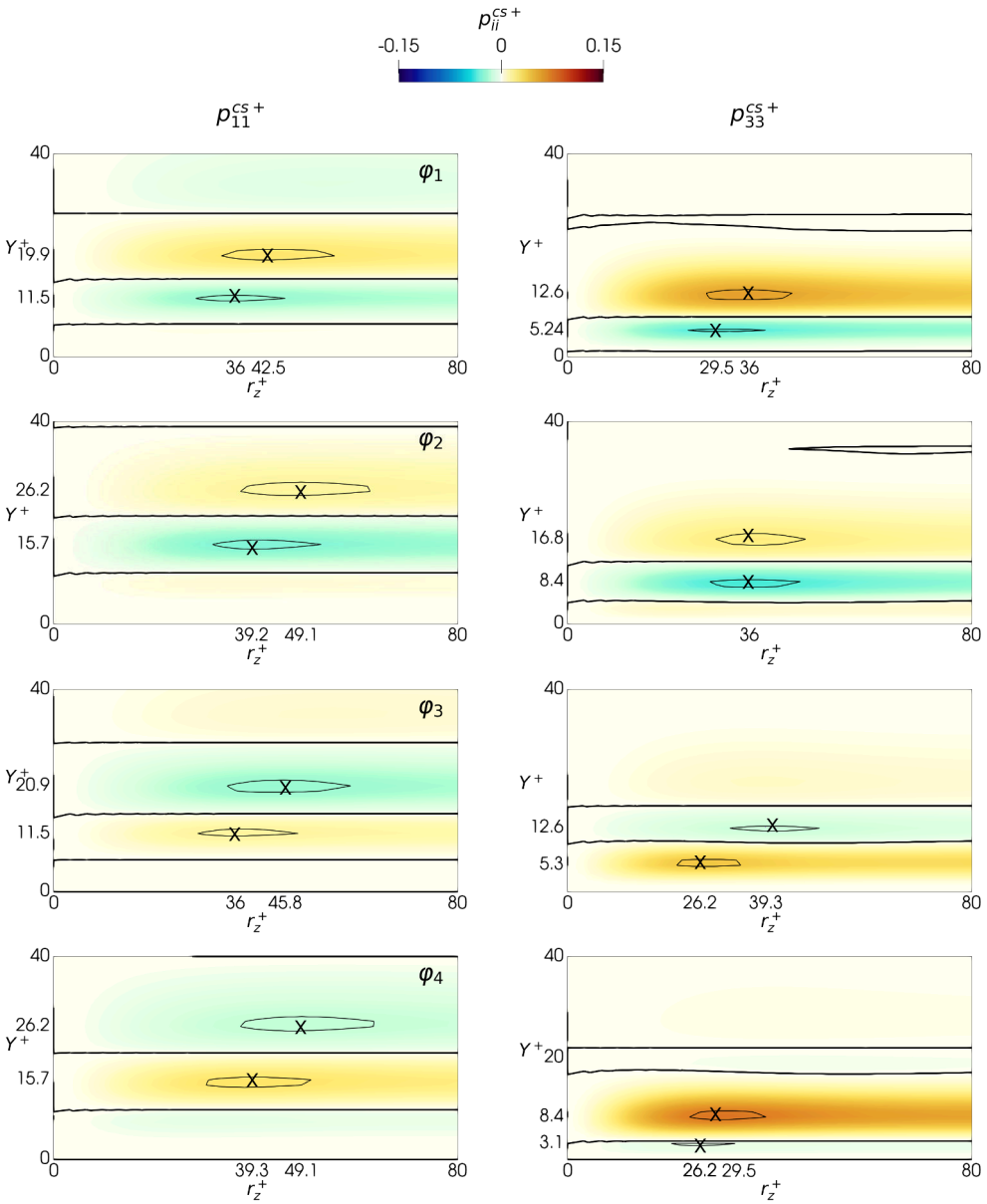

Figure 2.10: Coherent-stochastic production p_{11}^{cs+} (left) and p_{33}^{cs+} (right) in the (r_z^+, Y^+) plane for $T^+ = 75$. From top to bottom: $\varphi_1, \varphi_2, \varphi_3, \varphi_4$. The thin contour line is set at 95% of the smallest (positive and negative) maximum over the phases; the thick black contour line is $p_{ii}^{cs} = 0$. The coordinates of the maximum, marked with a cross, can be read on the axes.

Figures 2.10 for $T^+ = 75$ and 2.11 for $T^+ = 250$ show how p_{11}^{cs} and p_{33}^{cs} change with φ. Like for p_{11}^{ms}, the expressions for p_{11}^{cs} and p_{33}^{cs} simplify in the $r_x = r_y = 0$ plane where their maxima occur, i.e.

$$p_{11}^{cs} = -2\overline{\delta u'' \delta v''}\left(\frac{\partial \tilde{u}}{\partial y}\right) \qquad \text{and} \qquad p_{33}^{cs} = -2\overline{\delta v'' \delta w''}\left(\frac{\partial \tilde{w}}{\partial y}\right).$$

Unlike p_{11}^{ms}, however, these productions can take either sign. Their maps show evident horizontal stripes of alternating sign, from the wall up to $Y^+ \approx 40$: hence, at a given phase the coherent field feeds the stochastic field at certain wall distances, but extracts energy from it at others. It is worth noting that, although p_{11}^{cs} and p_{33}^{cs} at a given phase are both positive and negative, after averaging over the phases $\langle p_{11}^{cs} \rangle$ almost vanishes and $\langle p_{33}^{cs} \rangle$ is positive everywhere. This is not entirely new, and confirms the single-point analysis by Agostini *et al.* (2014) (see their figure 14); however, scale information is added here so that this mechanism can be related to the structures of the flow. At every phase, the positive/negative peaks of p_{11}^{cs} and p_{33}^{cs} occur at $r_z^+ \approx 25 - 50$, a spanwise separation which points to the structures of the near-wall cycle.

The intensity of p_{11}^{cs} and p_{33}^{cs} at the two periods is comparable, at all scales and positions. However, for p_{11}^{cs} the contribution of the shear stresses is dominant, whereas the opposite occurs for p_{33}^{cs}, where the coherent spanwise shear dominates. Indeed, $\partial \tilde{w}/\partial y$ is two orders of magnitude larger than $\partial \tilde{u}/\partial y$, and $\overline{\delta v'' \delta w''}$ is two orders of magnitude smaller than $\overline{\delta u'' \delta v''}$. Note, moreover, that for both control periods $p_{11}^{ms} \gg p_{11}^{cs}$, meaning that the streamwise stochastic fluctuations are predominantly fed by the mean field.

The alternating positive/negative stripes for p_{11}^{cs} and p_{33}^{cs} are due to the change of sign of $\partial \tilde{u}/\partial y$ and $\partial \tilde{w}/\partial y$ with y. For p_{33}^{cs}, the changing sign of the shear is also indirectly responsible for the alternating positive/negative $\overline{\delta v'' \delta w''}$, due to the quasi-streamwise vortices-shear interaction described in §2.4.1.2. In contrast, for p_{11}^{cs}, $\overline{\delta u'' \delta v''}$ is entirely due to the interaction of the near-wall structures with the mean shear $\mathrm{d}U/\mathrm{d}y$, which overwhelms $\partial \tilde{u}/\partial y$ everywhere.

Comparing figures 2.10 and 2.11 highlights that the slower oscillation introduces substantial differences in the coherent-stochastic energy exchange. The positive/negative maxima of p_{11}^{cs} increase, and their position move towards larger r_z and larger Y, but the effect of T^+ on p_{33}^{cs} is even more evident. At $T^+ = 250$, the stripes of negative p_{33}^{cs} weaken, while those with $p_{33}^{cs} > 0$ strengthen: overall, the spanwise contribution to the energy flowing from the coherent to the stochastic field becomes larger. A larger oscillating period implies a larger thickness of the Stokes layer, proportional to $\sqrt{\nu T}$, thus stretching outwards the coherent spanwise shear and, as a consequence, the scale-space map of $\overline{\delta v'' \delta w''}$, yielding an overall increase of the positive p_{33}^{cs}. At φ_2 and φ_3, for example, $\partial \tilde{w}/\partial y$ is negative close

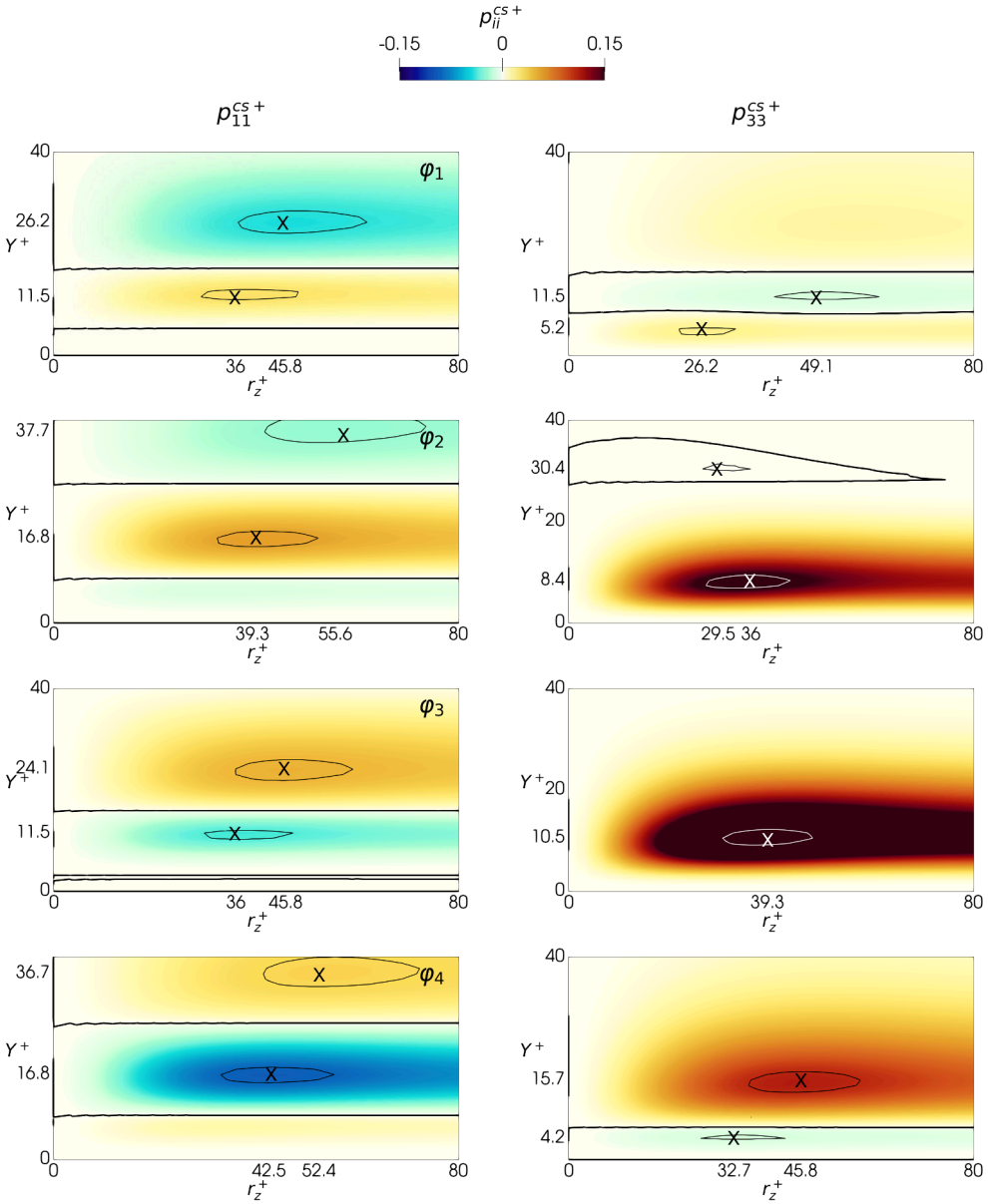

Figure 2.11: As in figure 2.10, but for $T^+ = 250$.

to the wall and changes sign only at $y^+ \approx 30 - 50$ for $T^+ = 250$ (see figure 2.2), while it changes sign already at $y^+ \approx 13 - 18$ for $T^+ = 75$ (not shown). For $T^+ = 250$ this results into a large increase of the near-wall positive p_{33}^{cs}, as highlighted by the dark red colour in figure 2.11. Due to the negative $\partial\tilde{w}/\partial y$, indeed, the quasi-streamwise vortices induce on their sides positive/negative v'' and convect upwards/downwards high/low spanwise velocity w'', thus yielding positive $\overline{\delta v''\delta w''}$ and an intense energy exchange from the coherent to the stochastic field. The scale-space information of this exchange mechanism is highlighted by the positive peak of p_{33}^{cs} placed at $(r_z^+, Y^+) \approx (38, 9)$ for the considered φ_2 and φ_3 phases.

2.4.3 Pressure–strain redistribution

As seen schematically in figure 2.3, the pressure–strain action partially redistributes the streamwise energy $\overline{\delta u''\delta u''}$ drained from the mean flow towards the cross-stream fluctuations $\overline{\delta v''\delta v''}$ and $\overline{\delta w''\delta w''}$. The left panels of figure 2.12 show that $\pi_{11}^s < 0$, $\pi_{22}^s > 0$ and $\pi_{33}^s > 0$ at almost all scales and positions: only in a very thin region close to the wall $\pi_{11}^s > 0$, $\pi_{22}^s < 0$ and $\pi_{33}^s > 0$, according to the reorientation of vertical fluctuations into wall-parallel ones because of the impermeable wall (Mansour *et al.*, 1988). The peaks of π_{11}^s, π_{22}^s and π_{33}^s in the (r_z, Y) plane have $Y_m^+ \approx 11 - 27$ and $r_{z,m}^+ \approx 30 - 52$, indicating that the energy redistribution is dominated by the near-wall cycle.

It is known (Touber & Leschziner, 2012; Yakeno *et al.*, 2014) that the spanwise oscillation of the wall enhances the energy redistribution, mainly towards spanwise fluctuations. Compared to the uncontrolled case, the negative peak of π_{11}^s increases by 23–67% for $T^+ = 75$ and by 36–77% for $T^+ = 250$, while the positive peak of π_{22}^s decreases by 2–11% for $T^+ = 75$ and increases by 4–29% for $T^+ = 250$. The positive peak of π_{33}^s, instead, has the largest variation, with and increase of 30–53% for $T^+ = 75$ and 40–87% for $T^+ = 250$.

The phase evolution of the pressure-mediated energy redistribution is described in the right panels of figure 2.12 for the $T^+ = 250$ case, by considering the maxima of the diagonal components of π_{ij}^s. Only their values are plotted, since their position remains nearly constant at $(Y^+, r_z^+) \approx (20, 52)$ for $\pi_{11,m}^s$, $\approx (27, 30)$ for $\pi_{22,m}^s$ and $\approx (12, 46)$ for $\pi_{33,m}^s$. Like $\overline{\delta v''\delta v''}_m$, $\pi_{22,m}^s$ is the component with the smallest intra-cycle variation, with a 21% excursion during the cycle compared to 30% and 35% for $\pi_{11,m}^s$ and $\pi_{33,m}^s$. In fact, the largest energy redistribution towards $\overline{\delta v''\delta v''}$ occurs quite far from the wall, where the influence of the Stokes layer is weak. The phase dependence of $\pi_{11,m}^s$ is qualitatively different from the others. The redistribution of $\overline{\delta u''\delta u''}$ towards the cross-stream components is maximum at φ_3 and minimum at φ_1, following the absolute value of $\pi_{11,m}^s$. In contrast, $\pi_{22,m}^s$

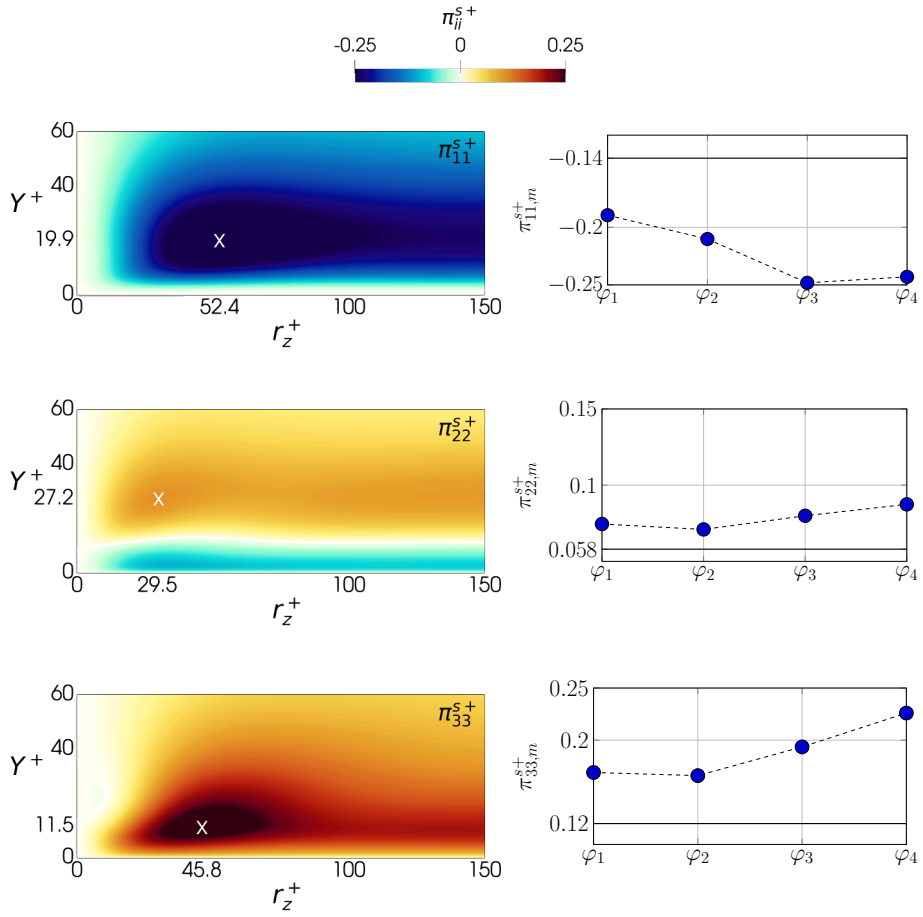

Figure 2.12: Left: pressure–strain redistribution π_{ii}^{s+} from $\overline{\delta u'' \delta u''}$ towards $\overline{\delta v'' \delta v''}$ and $\overline{\delta w'' \delta w''}$ at phase φ_4 for $T^+ = 250$; the coordinates of the maximum, marked with a cross, can be read on the axes. Right: phase variation of their maxima in the (r_z^+, Y^+) plane, with a horizontal solid line indicating the value of the uncontrolled flow.

and $\pi^s_{33,m}$ are minima at φ_2 and maxima at φ_4 (this is not inconsistent with the incompressibility constraint $\pi^s_{11} + \pi^s_{22} + \pi^s_{33} = 0$, since the three maxima occur at different scales and positions.) As already mentioned in §2.4.1.2, $\pi^s_{33,m}$ and $\overline{\delta w'' \delta w''}_m$ have the same phase dependence, confirming that the tilting of the near-wall structures is accompanied by a redistribution of the streamwise fluctuations towards the spanwise ones.

2.4.4 Transfers of the spanwise stresses

A peculiarity of the present flow is the direct connection between the Stokes layer and the stochastic stresses, described by the coherent-stochastic production P^{cs} shown in figure 2.3. It is therefore interesting to examine the variable-phase scale-space transfers of the stochastic stresses by looking at their fluxes in the scale and physical spaces. In this analysis, we only consider the transfer of spanwise stresses $\overline{\delta w'' \delta w''}$, since for the streamwise stresses p^{cs}_{11} is negligible compared to p^{ms}_{11}. Moreover, only the $T^+ = 250$ case is considered, as the one where the effect of the Stokes layer on the w'' field is larger. For simplicity, the analysis is restricted to the $r_x = r_y = 0$ subspace, where the budget of $\overline{\delta w'' \delta w''}$ can be rewritten by moving to the r.h.s. the off-plane flux divergence terms $\partial \phi^s_{x,33}/\partial r_x$, $\partial \phi^s_{y,33}/\partial r_y$ and the phase evolution term, as follows:

$$\frac{\partial \phi^s_{z,33}}{\partial r_z} + \frac{\partial \psi^s_{33}}{\partial Y} = \underbrace{p^{cs}_{33} + \pi^s_{33} + d^s_{33}}_{\xi^s_{33}} - \frac{\partial \phi^s_{x,33}}{\partial r_x} - \frac{\partial \phi^s_{y,33}}{\partial r_y} - \omega \frac{\partial \overline{\delta w'' \delta w''}}{\partial \varphi}. \tag{2.28}$$

In this way, the l.h.s. features the divergence of the in-plane flux vector, which provides information on the energetic relevance of the fluxes with its intensity, and shows their direction via its field lines. Moreover, the off-plane fluxes (i.e. the last three terms in the equation above) are always very small, and the in-plane divergence approximates well the full source term ξ^s_{33} everywhere (Gatti *et al.*, 2020). This descends from a combination of the symmetries owned by the plane channel flow system, and of the approximate alignment of the dominant vortical structures with the streamwise direction. Hence, the scale-space properties of the source term ξ^s_{33} approximate well those of the divergence of the in-plane flux.

Figure 2.13 plots the map of $\xi^s_{33} = p^{cs}_{33} + \pi^s_{33} + d^s_{33}$ for the uncontrolled case (where $p^{cs}_{33} = 0$) and the controlled case at $T^+ = 250$ for φ_1, φ_2, φ_3 and φ_4, with the field lines of the in-plane flux coloured with its divergence. In the uncontrolled case, a region with $\xi^s_{33} > 0$ extends for $5 \lessapprox Y^+ \lessapprox 100$ and for $r^+_z \gtrapprox 15$, at scales and positions where the pressure–strain dominates over dissipation. When control is active, instead, ξ^s_{33} receives the additional contribution from coherent-stochastic production, and the values of ξ^s_{33} are generally larger. Two regions with $\xi^s_{33} > 0$

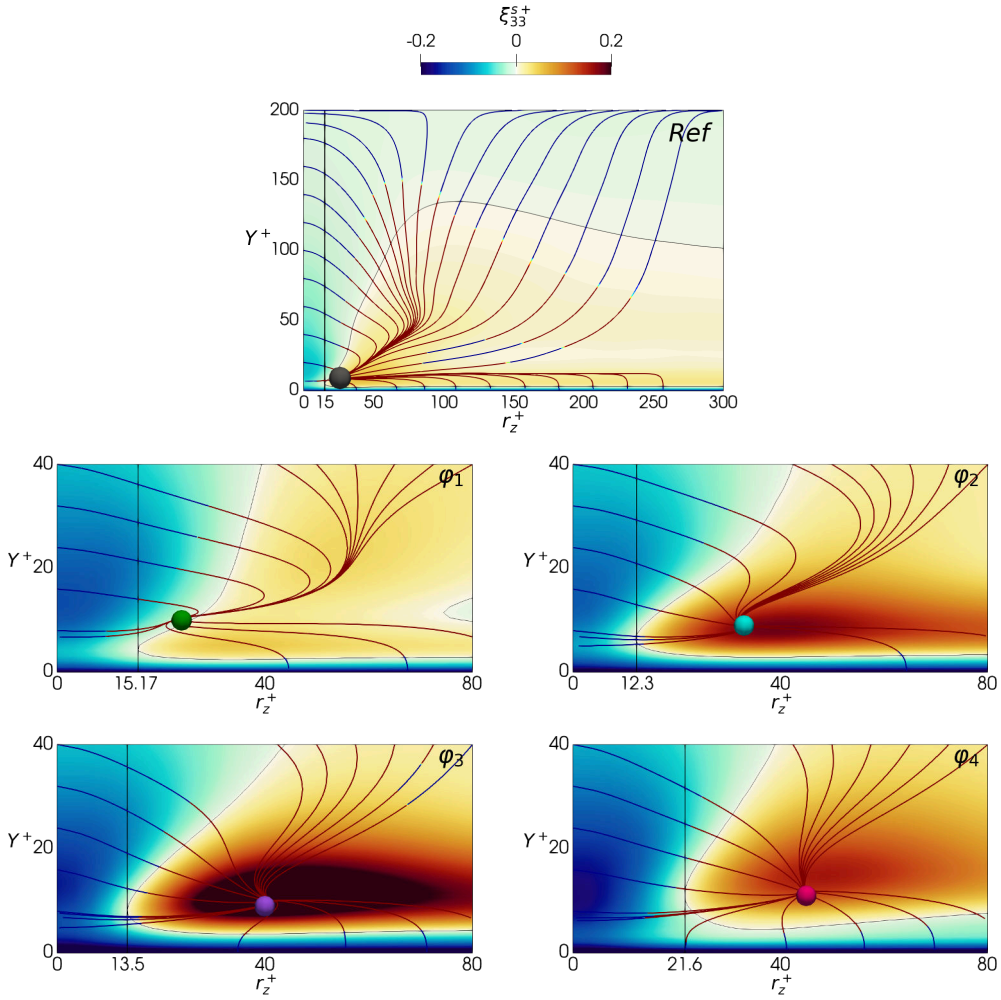

Figure 2.13: Source ξ_{33}^{s+} in the (r_z^+, Y^+) plane, with field lines of the in-plane flux vector coloured with its divergence for the uncontrolled case (top) and for the controlled case at $T^+ = 250$ at phases φ_1, φ_2, φ_3 and φ_4. The thin contour line marks the zero level. Dots (coloured according to figure 2.2) indicate the singularity point for the near-wall source, and the black vertical line marks the cut-off spanwise scale $r_{z,min}^+$ (see text).

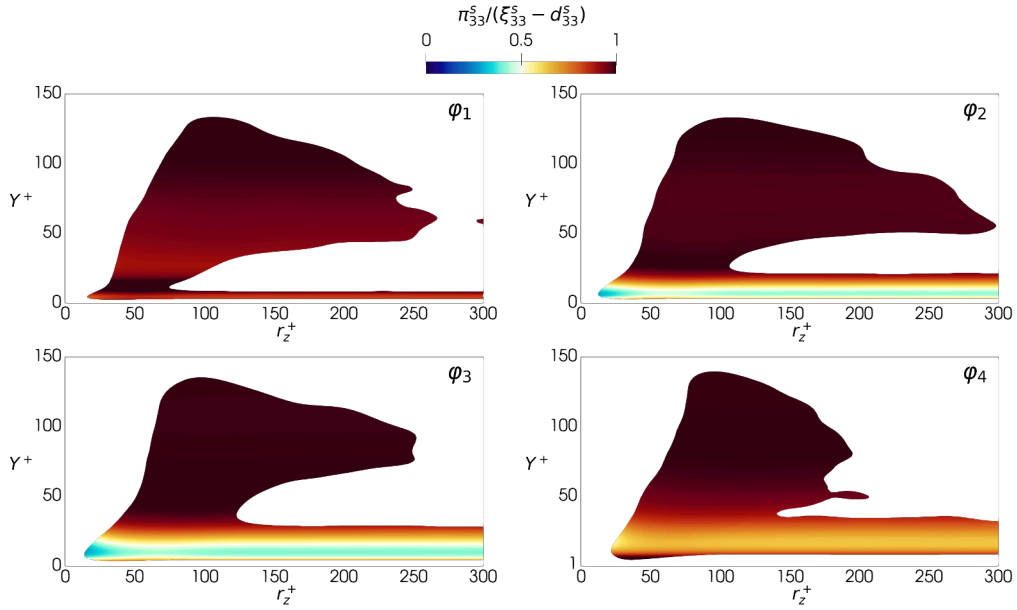

Figure 2.14: Region with positive source in the (r_z^+, Y^+) plane at phases φ_1, φ_2, φ_3 and φ_4 for $T^+ = 250$. The colour scale is for the ratio $\pi^s_{33}/(\xi^s_{33} - d^s_{33})$ and is centered at 0.5: red means $\pi^s_{33} > p^{cs}_{33}$, and blue means $\pi^s_{33} < p^{cs}_{33}$.

exist. One is close to the wall at $Y^+ \approx 10 - 20$, and extends for all scales $r_z^+ \gtrsim 15$, with a peak at $r_z^+ \approx 40$. A second, connected region involves larger wall distances and scales, in the $40 \lessapprox r_z^+ \lessapprox 200$ range. It is clearly visible in figure 2.14, where the ratio $\pi^s_{33}/(\xi^s_{33} - d^s_{33})$ is plotted to determine the main contribution to these positive sources at the different phases. When $\pi^s_{33}/(\xi^s_{33} - d^s_{33}) > 0.5$, $\pi^s_{33} > p^{cs}_{33}$ meaning that the pressure–strain is the largest contribution to the positive source. When $\pi^s_{33}/(\xi^s_{33} - d^s_{33}) < 0.5$, instead, the main contributor is the coherent-stochastic production p^{cs}_{33}. Figure 2.14 shows that p^{cs}_{33} and π^s_{33} contribute both to the near-wall source, but their relative importance changes with the phase. For φ_2 and φ_3 p^{cs}_{33} is the main contributor to the intense source peak. For φ_1 and φ_4, instead, p^{cs}_{33} weakens (see figure 2.11): now the (weaker) source is mainly fed by the pressure–strain. The source at larger Y, instead, is dominated by the pressure–strain at all phases; this is reasonable, as for $y^+ > 30$ the Stokes layer and consequently the coherent-stochastic production are weak.

As for the sinks, figure 2.13 shows three of them: viscous effects dominate the very near-wall region ($Y \to 0$), the bulk flow ($Y \to h$), and the smallest scales ($r_z \to 0$). Extension and intensity of these sinks change with φ, according to the evolution of p^{cs}_{33}, π^s_{33} and d^s_{33}. A cut-off scale $r_{z,min}$ (Chiarini *et al.*, 2022*a*) can also be plotted to quantify the minimal scale where (spanwise) energy is always dissipated, regardless of the wall distance.

The field lines of $\overline{\delta w'' \delta w''}$ drawn in figure 2.13 originate from a singularity point, i.e. a point near the source peak where the direction of the fluxes is undefined. Here the lines are energised by the intense positive source and transfer $\overline{\delta w'' \delta w''}$ towards the sinks. Three types of lines are recognised, depending on where they vanish, and reflect the three sinks described above. Overall, these fluxes indicate the coexistence of ascending/descending and direct/inverse energy transfers, as described by Cimarelli *et al.* (2013, 2016); Chiarini *et al.* (2022*b*) in the context of Poiseuille and Couette turbulent flows.

The three line types possess the same topology in the uncontrolled and controlled cases. For the latter, though, the amount of spanwise energy withdrawn from the sources and released to the sinks changes with φ. An estimate of this change is provided by the phase evolution of the positive peak of the two-dimensional divergence of the flux vector. Its value is maximum at φ_3 where it is 3.36, 1.56 and 1.29 times larger than at φ_1, φ_2 and φ_4 respectively. This is consistent with the phase evolution of the positive peak of p^{cs}_{33} visualised in figure 2.11. Moreover, the singularity point lies in the source region dominated by p^{cs}_{33}, and its r_z position moves with φ following the peak of p^{cs}_{33}, being $r_z^+ = 24$, 33, 40 and 45 for φ_1, φ_2, φ_3 and φ_4; for the uncontrolled case it is $r_z^+ = 26$.

We therefore conclude that, at least for the $T^+ = 250$ case discussed here, the phase dependence of the transfers of $\overline{\delta w'' \delta w''}$ is governed by the p^{cs}_{33} contribution to ξ^s_{33} rather than by π^s_{33}. At all phases, the largest part of the $\overline{\delta w'' \delta w''}$ withdrawn by the source is released in the near-wall region; a relatively smaller part goes to the smallest scales, and a minimal part goes towards the channel centre, where the turbulent activity is low. By comparing the negative peaks of the divergence of the in-plane flux vector at the wall and at the smallest scales, it is established that in the uncontrolled case the amount of $\overline{\delta w'' \delta w''}$ released at $Y \to 0$ is 5.67 times larger than that released at $r_z \to 0$. The oscillating wall alters the relative importance of the fluxes: the amount of $\overline{\delta w'' \delta w''}$ released at $Y \to 0$ is significantly less, being 2.62, 3.85, 2.46 and 2.41 times larger than that released at $r_z \to 0$, at phases φ_1, φ_2, φ_3 and φ_4 respectively.

2.5 Concluding discussion

We have derived the phase-aware anisotropic generalised Kolmogorov equations or φAGKE, inferred from the incompressible Navier–Stokes equations, after a triple decomposition to separate the velocity and pressure fields into their coherent and stochastic parts.

The φAGKE are exact budget equations for the coherent and stochastic contributions to the second-order structure function tensor, namely $\delta\tilde{u}_i \delta\tilde{u}_j(\boldsymbol{X}, \boldsymbol{r}, \varphi)$ and $\overline{\delta u_i'' \delta u_j''}(\boldsymbol{X}, \boldsymbol{r}, \varphi)$. Compared to the standard AGKE, which are based on the

classic (double) Reynolds decomposition, the φAGKE add extra features. (i) The transport equations for the coherent and stochastic parts are separated: disentangling their dynamics becomes possible. (ii) The scale-space energy exchanges among mean, coherent, and stochastic fields can be tracked. In particular, the mean-coherent production p_{ij}^{mc} and the mean-stochastic production p_{ij}^{ms} bring out scales and positions where the mean flow feeds, and/or drains energy from, the coherent and stochastic fields; the coherent-stochastic production p_{ij}^{cs} describes the exchange between the coherent and stochastic fields. (iii) An extra term in the budget for $\delta\tilde{u}_i\delta\tilde{u}_j$ represents the mutual interaction of the coherent motions at different phases. (iv) The φAGKE imply no average over phases, and thus describe the phase variation of the various terms related to coherent and stochastic motions. Once a phase average is taken, as in Alves Portela *et al.* (2020), phase information is obviously lost.

To demonstrate the potential of the φAGKE, we have applied them to a turbulent plane channel flow in which spanwise wall oscillations reduce the turbulent skin friction. The φAGKE are perfectly suited for this flow, owing to its deterministic and periodic external forcing; moreover, the physics of drag reduction remains not entirely understood and contains interesting inter-phase and multi-scale dynamics.

Thanks to the φAGKE, the phase-dependent modifications of the near-wall turbulent structures have been observed without the need for somewhat arbitrary procedures to educe phase-locked and conditionally-averaged structures. The flow scales involved in the redistribution of fluctuating energy have been described, together with the process by which streamwise velocity fluctuations are converted into spanwise ones by the action of pressure–strain. The interaction among the mean, coherent, and stochastic fields is easily observed with the φAGKE, which highlight the energy exchanges between the coherent and stochastic fields, driven by the interaction between the quasi-streamwise vortices and the coherent spanwise shear. The phase-by-phase, scale-space transfers of the spanwise stochastic stresses, observed here for the first time, have revealed a significant phase dependency for the spanwise energy fluxes, which present ascending/descending and direct/inverse energy transfers at all phases.

The φAGKE can be leveraged to arrive at a thorough description of two-points second-order statistics in cases that reach far beyond the oscillating-wall problem, used here as a representative example only. Turbulent flows where an external periodic forcing is present are common: oscillating airfoils, rotors and turbines are only a few examples. Moreover, the φAGKE can also be used to tackle turbulent flows without a strictly periodic forcing, in which stochastic fluctuations coexist with some kind of coherent motion. A non-exhaustive list includes the turbulent flow past bluff bodies, where large-scale motions typical of the Kármán-like vortices in the wake coexist with the stochastic motion of smaller scale (Provansal *et al.*, 1987); the Taylor–Couette flow, in which Taylor–Görtler

vortices develop and remain visible well into the turbulent regime (Koschmieder, 1979); the atmospheric boundary layer, rich with quasi-two-dimensional structures forced at smaller scales (Young *et al.*, 2002). In such cases, though, the period of the oscillation is not uniquely identified, and attention has to be paid to properly define a phase reference.

Lastly, it should be realised that the specific triple decomposition behind the φAGKE does not matter: alternatives to the temporal triple decomposition could be used with a different meaning attached to the $\tilde{\cdot}$ and $\cdot''$ operators, without altering the ensuing equations. One example is the spatial triple decomposition approach adopted for example by Bech & Andersson (1996) and Gai *et al.* (2016) to decompose the velocity fluctuations into secondary flow and residual fluctuations in a rotating turbulent plane Couette flow. A further use case for the φAGKE would be a turbulent flow over a flat wall with a periodic pattern, like e.g. riblets or dimples, in which the phase average would be again spatially defined. Finally, another option is to employ a scale-based triple decomposition. For example, Andreolli *et al.* (2021) used a scale decomposition mutuated from Kawata & Alfredsson (2018) to separate the fluctuating velocity field in a Couette flow into small- and large-scale components, examining the kinetic energy budget of both components in physical space. This information, compacted by Andreolli *et al.* (2021) through spatial integration into an energy budget without independent variables, similar to that in figure 2.3, can instead be expanded at will in the full physical and scale space thanks to the φAGKE, thus providing the ultimate information about two-points second-order statistics of the flow.

2.A Derivation of the budget equations for $\delta\tilde{u}_i\delta\tilde{u}_j$ and $\overline{\delta u_i''\delta u_j''}$

The derivation of the φAGKE equations via triple decomposition is described below, by listing the sequence of the main analytical steps.

2.A.1 Budget equation for U_i, $\tilde{u}_i$ and u_i''

The starting point is the incompressible Navier–Stokes equations:

$$\frac{\partial u_i}{\partial t} + u_k \frac{\partial u_i}{\partial x_k} = -\frac{1}{\rho}\frac{\partial p}{\partial x_i} + \nu \frac{\partial^2 u_i}{\partial x_k \partial x_k} + f_i. \tag{2.29}$$

The triple decomposition (2.1) for u_i, p and f_i is introduced to obtain:

$$\frac{\partial \tilde{u}_i}{\partial t} + \frac{\partial u_i''}{\partial t} + \left(U_k + \tilde{u}_k + u_k''\right) \frac{\partial}{\partial x_k} \left(U_i + \tilde{u}_i + u_i''\right) = -\frac{1}{\rho} \frac{\partial}{\partial x_i} \left(P + \tilde{p} + p''\right) + \\ + \nu \frac{\partial^2}{\partial x_k \partial x_k} \left(U_i + \tilde{u}_i + u_i''\right) + F_i + \tilde{f}_i + f_i'' \tag{2.30}$$

which can be reorganised as

$$\frac{\partial \tilde{u}_i}{\partial t} + \frac{\partial u_i''}{\partial t} + U_k \frac{\partial U_i}{\partial x_k} + U_k \frac{\partial \tilde{u}_i}{\partial x_k} + U_k \frac{\partial u_i''}{\partial x_k} + \tilde{u}_k \frac{\partial U_i}{\partial x_k} + \tilde{u}_k \frac{\partial \tilde{u}_i}{\partial x_k} + \tilde{u}_k \frac{\partial u_i''}{\partial x_k} + \\ + u_k'' \frac{\partial U_i}{\partial x_k} + u_k'' \frac{\partial \tilde{u}_i}{\partial x_k} + u_k'' \frac{\partial u_i''}{\partial x_k} = -\frac{1}{\rho} \frac{\partial P}{\partial x_i} - \frac{1}{\rho} \frac{\partial \tilde{p}}{\partial x_i} - \frac{1}{\rho} \frac{\partial p''}{\partial x_i} + \\ + \nu \frac{\partial^2 U_i}{\partial x_k \partial x_k} + \nu \frac{\partial^2 \tilde{u}_i}{\partial x_k \partial x_k} + \nu \frac{\partial^2 u_i''}{\partial x_k \partial x_k} + F_i + \tilde{f}_i + f_i''. \tag{2.31}$$

Now the averaging operator $\langle \cdot \rangle$ is used to arrive at the budget equation for U_i, i.e.

$$U_k \frac{\partial U_i}{\partial x_k} + \left\langle \tilde{u}_k \frac{\partial \tilde{u}_i}{\partial x_k} \right\rangle + \left\langle u_k'' \frac{\partial u_i''}{\partial x_k} \right\rangle = -\frac{1}{\rho} \frac{\partial P}{\partial x_i} + \nu \frac{\partial^2 U_i}{\partial x_k \partial x_k} + F_i. \tag{2.32}$$

When, instead, the phase average operator $\overline{\cdot}$ is used, we get:

$$\frac{\partial \tilde{u}_i}{\partial t} + U_k \frac{\partial U_i}{\partial x_k} + \tilde{u}_k \frac{\partial U_i}{\partial x_k} + U_k \frac{\partial \tilde{u}_i}{\partial x_k} + \tilde{u}_k \frac{\partial \tilde{u}_i}{\partial x_k} + \overline{u_k'' \frac{\partial u_i''}{\partial x_k}} = \\ -\frac{1}{\rho} \frac{\partial P}{\partial x_i} - \frac{1}{\rho} \frac{\partial \tilde{p}}{\partial x_i} + \nu \frac{\partial^2 U_i}{\partial x_k \partial x_k} + \nu \frac{\partial^2 \tilde{u}_i}{\partial x_k \partial x_k} + F_i + \tilde{f}_i \tag{2.33}$$

which can be written differently using the budget equation for U_i, i.e.:

$$\frac{\partial \tilde{u}_i}{\partial t} + \tilde{u}_k \frac{\partial U_i}{\partial x_k} + U_k \frac{\partial \tilde{u}_i}{\partial x_k} + \tilde{u}_k \frac{\partial \tilde{u}_i}{\partial x_k} + \overline{u_k'' \frac{\partial u_i''}{\partial x_k}} - \left\langle \tilde{u}_k \frac{\partial \tilde{u}_i}{\partial x_k} \right\rangle - \left\langle u_k'' \frac{\partial u_i''}{\partial x_k} \right\rangle = \\ -\frac{1}{\rho} \frac{\partial \tilde{p}}{\partial x_i} + \nu \frac{\partial^2 \tilde{u}_i}{\partial x_k \partial x_k} + \tilde{f}_i. \tag{2.34}$$

This leads to the budget equation for $\tilde{u}_i$, i.e.

$$\frac{\partial \tilde{u}_i}{\partial t} + U_k \frac{\partial \tilde{u}_i}{\partial x_k} + \tilde{u}_k \frac{\partial U_i}{\partial x_k} + \frac{\partial}{\partial x_k} \left(\tilde{u}_i \tilde{u}_k - \langle \tilde{u}_i \tilde{u}_k \rangle\right) + \frac{\partial}{\partial x_k} \left(\overline{u_i'' u_k''} - \left\langle u_i'' u_k'' \right\rangle\right) = \\ -\frac{1}{\rho} \frac{\partial \tilde{p}}{\partial x_i} + \nu \frac{\partial^2 \tilde{u}_i}{\partial x_k \partial x_k} + \tilde{f}_i. \tag{2.35}$$

The budget equation for u_i'' is obtained by subtracting from (2.31) the budget equations for U_i (2.32) and $\tilde{u}_i$ (2.35):

$$\begin{aligned}\frac{\partial u_i''}{\partial t} + U_k\frac{\partial u_i''}{\partial x_k} + \tilde{u}_k\frac{\partial u_i''}{\partial x_k} + u_k''\frac{\partial U_i}{\partial x_k} + u_k''\frac{\partial \tilde{u}_i}{\partial x_k} + \frac{\partial}{\partial x_k}\left(u_i''u_k'' - \overline{u_i''u_k''}\right) = \\ -\frac{1}{\rho}\frac{\partial p''}{\partial x_i} + \nu\frac{\partial^2 u_i''}{\partial x_k \partial x_k} + f_i''.\end{aligned} \tag{2.36}$$

2.A.2 φAGKE for $\delta\tilde{u}_i\delta\tilde{u}_j$

The budget equation for $\tilde{u}_i$ in $\boldsymbol{x}$ is subtracted from the one evaluated in $\boldsymbol{x}^+ = \boldsymbol{x}+\boldsymbol{r}$:

$$\begin{aligned}&\delta\left(\frac{\partial \tilde{u}_i}{\partial t}\right) + \delta\left(U_k\frac{\partial \tilde{u}_i}{\partial x_k}\right) + \delta\left(\tilde{u}_k\frac{\partial U_i}{\partial x_k}\right) + \delta\left(\frac{\partial}{\partial x_k}\left(\tilde{u}_i\tilde{u}_k - \langle\tilde{u}_i\tilde{u}_k\rangle\right)\right) + \\ &+\delta\left(\frac{\partial}{\partial x_k}\left(\overline{u_i''u_k''} - \langle u_i''u_k''\rangle\right)\right) = -\delta\left(\frac{1}{\rho}\frac{\partial \tilde{p}}{\partial x_i}\right) + \delta\left(\nu\frac{\partial^2\tilde{u}_i}{\partial x_k\partial x_k}\right) + \delta\left(\tilde{f}_i\right).\end{aligned} \tag{2.37}$$

By recalling that the two reference systems are independent, one may write for example:

$$\delta\left(U_k\frac{\partial \tilde{u}_i}{\partial x_k}\right) = U_k^+\frac{\partial \delta\tilde{u}_i}{\partial x_k^+} + U_k\frac{\partial \delta\tilde{u}_i}{\partial x_k}; \tag{2.38}$$

using the same line of reasoning for all the other terms one obtains

$$\begin{aligned}&\frac{\partial \delta\tilde{u}_i}{\partial t} + U_k^+\frac{\partial \delta\tilde{u}_i}{\partial x_k^+} + U_k\frac{\partial \delta\tilde{u}_i}{\partial x_k} + \tilde{u}_k^+\frac{\partial \delta U_i}{\partial x_k^+} + \tilde{u}_k\frac{\partial \delta U_i}{\partial x_k} + \tilde{u}_k^+\frac{\partial \delta\tilde{u}_i}{\partial x_k^+} + \tilde{u}_k\frac{\partial \delta\tilde{u}_i}{\partial x_k} + \\ &-\left\langle\tilde{u}_k^+\frac{\partial \delta\tilde{u}_i}{\partial x_k^+}\right\rangle - \left\langle\tilde{u}_k\frac{\partial \delta\tilde{u}_i}{\partial x_k}\right\rangle + \overline{u_k''^+\frac{\partial \delta u_i''}{\partial x_k^+}} + \overline{u_k''\frac{\partial \delta u_i''}{\partial x_k}} - \left\langle u_k''^+\frac{\partial \delta u_i''}{\partial x_k^+}\right\rangle - \left\langle u_k''\frac{\partial \delta u_i''}{\partial x_k}\right\rangle = \\ &-\frac{1}{\rho}\frac{\partial \delta\tilde{p}}{\partial x_i^+} - \frac{1}{\rho}\frac{\partial \delta\tilde{p}}{\partial x_i} + \nu\left(\frac{\partial^2}{\partial x_k^+\partial x_k^+} + \frac{\partial^2}{\partial x_k\partial x_k}\right)\delta\tilde{u}_i + \delta\tilde{f}_i.\end{aligned} \tag{2.39}$$

Then one may write for example

$$\tilde{u}_k^+\frac{\partial \delta\tilde{u}_i}{\partial x_k^+} = \delta\tilde{u}_k\frac{\partial \delta\tilde{u}_i}{\partial x_k^+} + \tilde{u}_k\frac{\partial \delta\tilde{u}_i}{\partial x_k^+} \tag{2.40}$$

and using this expression for all the terms we obtain the budget equation for $\delta\tilde{u}_i$:

$$\begin{aligned}
&\frac{\partial\delta\tilde{u}_i}{\partial t}+\delta U_k\frac{\partial\delta\tilde{u}_i}{\partial x_k^+}+U_k\left(\frac{\partial}{\partial x_k^+}+\frac{\partial}{\partial x_k}\right)\delta\tilde{u}_i+\delta\tilde{u}_k\frac{\partial\delta U_i}{\partial x_k^+}+\tilde{u}_k\left(\frac{\partial}{\partial x_k^+}+\frac{\partial}{\partial x_k}\right)\delta U_i+\\
&+\delta\tilde{u}_k\frac{\partial\delta\tilde{u}_i}{\partial x_k^+}+\tilde{u}_k\left(\frac{\partial}{\partial x_k^+}+\frac{\partial}{\partial x_k}\right)\delta\tilde{u}_i-\left\langle\delta\tilde{u}_k\frac{\partial\delta\tilde{u}_i}{\partial x_k^+}\right\rangle-\left\langle\tilde{u}_k\left(\frac{\partial}{\partial x_k^+}+\frac{\partial}{\partial x_k}\right)\delta\tilde{u}_i\right\rangle+\\
&+\overline{\delta u_k''\frac{\partial\delta u_i''}{\partial x_k^+}}+\overline{u_k''\left(\frac{\partial}{\partial x_k^+}+\frac{\partial}{\partial x_k}\right)\delta u_i''}-\left\langle\delta u_k''\frac{\partial\delta u_i''}{\partial x_k^+}\right\rangle-\left\langle u_k''\left(\frac{\partial}{\partial x_k^+}+\frac{\partial}{\partial x_k}\right)\delta u_i''\right\rangle=\\
&-\frac{1}{\rho}\frac{\partial\delta\tilde{p}}{\partial x_i^+}-\frac{1}{\rho}\frac{\partial\delta\tilde{p}}{\partial x_i}+\nu\left(\frac{\partial^2}{\partial x_k^+\partial x_k^+}+\frac{\partial^2}{\partial x_k\partial x_k}\right)\delta\tilde{u}_i+\delta\tilde{f}_i.
\end{aligned}\tag{2.41}$$

This equation is multiplied by $\delta\tilde{u}_j$ to obtain:

$$\begin{aligned}
&\delta\tilde{u}_j\frac{\partial\delta\tilde{u}_i}{\partial t}+\delta\tilde{u}_j\delta U_k\frac{\partial\delta\tilde{u}_i}{\partial x_k^+}+\delta\tilde{u}_jU_k\left(\frac{\partial}{\partial x_k^+}+\frac{\partial}{\partial x_k}\right)\delta\tilde{u}_i+\delta\tilde{u}_j\delta\tilde{u}_k\frac{\partial\delta U_i}{\partial x_k^+}+\\
&+\delta\tilde{u}_j\tilde{u}_k\left(\frac{\partial}{\partial x_k^+}+\frac{\partial}{\partial x_k}\right)\delta U_i+\delta\tilde{u}_j\delta\tilde{u}_k\frac{\partial\delta\tilde{u}_i}{\partial x_k^+}+\delta\tilde{u}_j\tilde{u}_k\left(\frac{\partial}{\partial x_k^+}+\frac{\partial}{\partial x_k}\right)\delta\tilde{u}_i-\delta\tilde{u}_j\left\langle\delta\tilde{u}_k\frac{\partial\delta\tilde{u}_i}{\partial x_k^+}\right\rangle+\\
&-\delta\tilde{u}_j\left\langle\tilde{u}_k\left(\frac{\partial}{\partial x_k^+}+\frac{\partial}{\partial x_k}\right)\delta\tilde{u}_i\right\rangle+\delta\tilde{u}_j\overline{\delta u_k''\frac{\partial\delta u_i''}{\partial x_k^+}}+\delta\tilde{u}_j\overline{u_k''\left(\frac{\partial}{\partial x_k^+}+\frac{\partial}{\partial x_k}\right)\delta u_i''}+\\
&-\delta\tilde{u}_j\left\langle\delta u_k''\frac{\partial\delta u_i''}{\partial x_k^+}\right\rangle-\delta\tilde{u}_j\left\langle u_k''\left(\frac{\partial}{\partial x_k^+}+\frac{\partial}{\partial x_k}\right)\delta u_i''\right\rangle=-\delta\tilde{u}_j\frac{1}{\rho}\left(\frac{\partial}{\partial x_i^+}+\frac{\partial}{\partial x_i}\right)\delta\tilde{p}+\\
&+\nu\delta\tilde{u}_j\left(\frac{\partial^2}{\partial x_k^+\partial x_k^+}+\frac{\partial^2}{\partial x_k\partial x_k}\right)\delta\tilde{u}_i+\delta\tilde{u}_j\delta\tilde{f}_i.
\end{aligned}\tag{2.42}$$

The same equation is written again by swapping the i and j indices, and the two

equations are then summed together:

$$\frac{\partial}{\partial t}\delta\tilde{u}_i\delta\tilde{u}_j + \delta\tilde{u}_j\delta U_k\frac{\partial\delta\tilde{u}_i}{\partial x_k^+} + \delta\tilde{u}_i\delta U_k\frac{\partial\delta\tilde{u}_j}{\partial x_k^+} + \delta\tilde{u}_j U_k\left(\frac{\partial}{\partial x_k^+}+\frac{\partial}{\partial x_k}\right)\delta\tilde{u}_i+$$
$$+\delta\tilde{u}_i U_k\left(\frac{\partial}{\partial x_k^+}+\frac{\partial}{\partial x_k}\right)\delta\tilde{u}_j + \delta\tilde{u}_j\delta\tilde{u}_k\frac{\partial\delta U_i}{\partial x_k^+} + \delta\tilde{u}_i\delta\tilde{u}_k\frac{\partial\delta U_j}{\partial x_k^+} + \delta\tilde{u}_j\tilde{u}_k\left(\frac{\partial}{\partial x_k^+}+\frac{\partial}{\partial x_k}\right)\delta U_i+$$
$$+\delta\tilde{u}_i\tilde{u}_k\left(\frac{\partial}{\partial x_k^+}+\frac{\partial}{\partial x_k}\right)\delta U_j + \delta\tilde{u}_j\delta\tilde{u}_k\frac{\partial\delta\tilde{u}_i}{\partial x_k^+} + \delta\tilde{u}_i\delta\tilde{u}_k\frac{\partial\delta\tilde{u}_j}{\partial x_k^+} + \delta\tilde{u}_j\tilde{u}_k\left(\frac{\partial}{\partial x_k^+}+\frac{\partial}{\partial x_k}\right)\delta\tilde{u}_i+$$
$$+\delta\tilde{u}_i\tilde{u}_k\left(\frac{\partial}{\partial x_k^+}+\frac{\partial}{\partial x_k}\right)\delta\tilde{u}_j - \delta\tilde{u}_j\left\langle\delta\tilde{u}_k\frac{\partial\delta\tilde{u}_i}{\partial x_k^+}\right\rangle - \delta\tilde{u}_i\left\langle\delta\tilde{u}_k\frac{\partial\delta\tilde{u}_j}{\partial x_k^+}\right\rangle+$$
$$-\delta\tilde{u}_j\left\langle\tilde{u}_k\left(\frac{\partial}{\partial x_k^+}+\frac{\partial}{\partial x_k}\right)\delta\tilde{u}_i\right\rangle - \delta\tilde{u}_i\left\langle\tilde{u}_k\left(\frac{\partial}{\partial x_k^+}+\frac{\partial}{\partial x_k}\right)\delta\tilde{u}_j\right\rangle+$$
$$+\delta\tilde{u}_j\overline{\delta u_k''\frac{\partial\delta u_i''}{\partial x_k^+}} + \delta\tilde{u}_i\overline{\delta u_k''\frac{\partial\delta u_j''}{\partial x_k^+}} + \delta\tilde{u}_j\overline{u_k''\left(\frac{\partial}{\partial x_k^+}+\frac{\partial}{\partial x_k}\right)\delta u_i''}+$$
$$+\overline{\delta\tilde{u}_i u_k''\left(\frac{\partial}{\partial x_k^+}+\frac{\partial}{\partial x_k}\right)\delta u_j''} - \delta\tilde{u}_j\left\langle\delta u_k''\frac{\partial\delta u_i''}{\partial x_k^+}\right\rangle - \delta\tilde{u}_j\left\langle u_k''\left(\frac{\partial}{\partial x_k^+}+\frac{\partial}{\partial x_k}\right)\delta u_i''\right\rangle+$$
$$-\delta\tilde{u}_i\left\langle\delta u_k''\frac{\partial\delta u_j''}{\partial x_k^+}\right\rangle - \delta\tilde{u}_i\left\langle u_k''\left(\frac{\partial}{\partial x_k^+}+\frac{\partial}{\partial x_k}\right)\delta u_j''\right\rangle = -\delta\tilde{u}_j\frac{1}{\rho}\left(\frac{\partial}{\partial x_i^+}+\frac{\partial}{\partial x_i}\right)\delta\tilde{p}+$$
$$-\delta\tilde{u}_i\frac{1}{\rho}\left(\frac{\partial}{\partial x_j^+}+\frac{\partial}{\partial x_j}\right)\delta\tilde{p} + \nu\delta\tilde{u}_j\left(\frac{\partial^2}{\partial x_k^+\partial x_k^+}+\frac{\partial^2}{\partial x_k\partial x_k}\right)\delta\tilde{u}_i+$$
$$+\nu\delta\tilde{u}_i\left(\frac{\partial^2}{\partial x_k^+\partial x_k^+}+\frac{\partial^2}{\partial x_k\partial x_k}\right)\delta\tilde{u}_j + \delta\tilde{u}_j\delta\tilde{f}_i + \delta\tilde{u}_i\delta\tilde{f}_j. \tag{2.43}$$

At this point, after applying the phase average operator $\bar{\cdot}$ and manipulating the

equations, one obtains:

$$\frac{\partial}{\partial t}\delta\tilde{u}_i\delta\tilde{u}_j + \frac{\partial}{\partial x_k^+}\delta U_k\delta\tilde{u}_i\delta\tilde{u}_j + \left(\frac{\partial}{\partial x_k^+} + \frac{\partial}{\partial x_k}\right)U_k\delta\tilde{u}_i\delta\tilde{u}_j + \delta\tilde{u}_j\delta\tilde{u}_k\frac{\partial\delta U_i}{\partial x_k^+} + \delta\tilde{u}_i\delta\tilde{u}_k\frac{\partial\delta U_j}{\partial x_k^+} +$$
$$+\delta\tilde{u}_j\tilde{u}_k\left(\frac{\partial}{\partial x_k^+} + \frac{\partial}{\partial x_k}\right)\delta U_i + \delta\tilde{u}_i\tilde{u}_k\left(\frac{\partial}{\partial x_k^+} + \frac{\partial}{\partial x_k}\right)\delta U_j + \frac{\partial}{\partial x_k^+}\delta\tilde{u}_k\delta\tilde{u}_i\delta\tilde{u}_j +$$
$$+\left(\frac{\partial}{\partial x_k^+} + \frac{\partial}{\partial x_k}\right)\tilde{u}_k\delta\tilde{u}_i\delta\tilde{u}_j - \delta\tilde{u}_j\left\langle\delta\tilde{u}_k\frac{\partial\delta\tilde{u}_i}{\partial x_k^+}\right\rangle - \delta\tilde{u}_i\left\langle\delta\tilde{u}_k\frac{\partial\delta\tilde{u}_j}{\partial x_k^+}\right\rangle +$$
$$-\delta\tilde{u}_j\left\langle\tilde{u}_k\left(\frac{\partial}{\partial x_k^+} + \frac{\partial}{\partial x_k}\right)\delta\tilde{u}_i\right\rangle - \delta\tilde{u}_i\left\langle\tilde{u}_k\left(\frac{\partial}{\partial x_k^+} + \frac{\partial}{\partial x_k}\right)\delta\tilde{u}_j\right\rangle +$$
$$+\delta\tilde{u}_j\frac{\partial}{\partial x_k^+}\overline{\delta u_i''\delta u_k''} + \delta\tilde{u}_i\frac{\partial}{\partial x_k^+}\overline{\delta u_j''\delta u_k''} + \delta\tilde{u}_j\overline{u_k''\left(\frac{\partial}{\partial x_k^+} + \frac{\partial}{\partial x_k}\right)\delta u_i''} +$$
$$+\delta\tilde{u}_i\overline{u_k''\left(\frac{\partial}{\partial x_k^+} + \frac{\partial}{\partial x_k}\right)\delta u_j''} - \delta\tilde{u}_j\left\langle\delta u_k''\frac{\partial\delta u_i''}{\partial x_k^+}\right\rangle - \delta\tilde{u}_j\left\langle u_k''\left(\frac{\partial}{\partial x_k^+} + \frac{\partial}{\partial x_k}\right)\delta u_i''\right\rangle +$$
$$-\delta\tilde{u}_i\left\langle\delta u_k''\frac{\partial\delta u_j''}{\partial x_k^+}\right\rangle - \delta\tilde{u}_i\left\langle u_k''\left(\frac{\partial}{\partial x_k^+} + \frac{\partial}{\partial x_k}\right)\delta u_j''\right\rangle = -\delta\tilde{u}_j\frac{1}{\rho}\left(\frac{\partial}{\partial x_i^+} + \frac{\partial}{\partial x_i}\right)\delta\tilde{p} +$$
$$-\delta\tilde{u}_i\frac{1}{\rho}\left(\frac{\partial}{\partial x_j^+} + \frac{\partial}{\partial x_j}\right)\delta\tilde{p} + \nu\delta\tilde{u}_j\left(\frac{\partial^2}{\partial x_k^+\partial x_k^+} + \frac{\partial^2}{\partial x_k\partial x_k}\right)\delta\tilde{u}_i +$$
$$+\nu\delta\tilde{u}_i\left(\frac{\partial^2}{\partial x_k^+\partial x_k^+} + \frac{\partial^2}{\partial x_k\partial x_k}\right)\delta\tilde{u}_j + \delta\tilde{u}_j\delta\tilde{f}_i + \delta\tilde{u}_i\delta\tilde{f}_j. \tag{2.44}$$

We now introduce the new independent variables $\boldsymbol{X}$ and $\boldsymbol{r}$ such that

$$X_i = \frac{x_i + x_i^+}{2} \qquad r_i = x_i^+ - x_i.$$

As a result the x_i- and x_i^+-derivatives are related to the X_i- and r_i-derivatives by the following relations:

$$\frac{\partial}{\partial x_i} = \frac{1}{2}\frac{\partial}{\partial X_i} - \frac{\partial}{\partial r_i}; \quad \frac{\partial}{\partial x_i^+} = \frac{1}{2}\frac{\partial}{\partial X_i} + \frac{\partial}{\partial r_i}; \quad \frac{\partial^2}{\partial x_k^+\partial x_k^+} + \frac{\partial^2}{\partial x_k\partial x_k} = \frac{1}{2}\frac{\partial^2}{\partial X_k\partial X_k} + 2\frac{\partial^2}{\partial r_k\partial r_k}$$

The previous equation (2.44) becomes:

$$\begin{aligned}
&\frac{\partial}{\partial t}\delta\tilde{u}_i\tilde{u}_j + \left(\frac{1}{2}\frac{\partial}{\partial X_k} + \frac{\partial}{\partial r_k}\right)\delta U_k\delta\tilde{u}_i\delta\tilde{u}_j + \frac{\partial}{\partial X_k}U_k\delta\tilde{u}_i\delta\tilde{u}_j + \delta\tilde{u}_j\delta\tilde{u}_k\left(\frac{1}{2}\frac{\partial}{\partial X_k} + \frac{\partial}{\partial r_k}\right)\delta U_i + \\
&+\delta\tilde{u}_i\delta\tilde{u}_k\left(\frac{1}{2}\frac{\partial}{\partial X_k} + \frac{\partial}{\partial r_k}\right)\delta U_j + \delta\tilde{u}_j\tilde{u}_k\frac{\partial}{\partial X_k}\delta U_i + \delta\tilde{u}_i\tilde{u}_k\frac{\partial}{\partial X_k}\delta U_j + \\
&+\left(\frac{1}{2}\frac{\partial}{\partial X_k} + \frac{\partial}{\partial r_k}\right)(\delta\tilde{u}_k\delta\tilde{u}_i\delta\tilde{u}_j) + \frac{\partial}{\partial X_k}(\tilde{u}_k\delta\tilde{u}_i\delta\tilde{u}_j) - \frac{\partial}{\partial r_k}\langle\delta\tilde{u}_i\delta\tilde{u}_k\rangle\delta\tilde{u}_j + \langle\delta\tilde{u}_i\delta\tilde{u}_k\rangle\frac{\partial\delta\tilde{u}_j}{\partial r_k} + \\
&-\frac{\partial}{\partial X_k}\left\langle\tilde{u}_k^*\delta\tilde{u}_i\right\rangle\delta\tilde{u}_j + \left\langle\tilde{u}_k^*\delta\tilde{u}_i\right\rangle\frac{\partial\delta\tilde{u}_j}{\partial X_k} - \frac{\partial}{\partial r_k}\left\langle\delta\tilde{u}_j\delta\tilde{u}_k\right\rangle\delta\tilde{u}_i + \left\langle\delta\tilde{u}_j\delta\tilde{u}_k\right\rangle\frac{\partial\delta\tilde{u}_i}{\partial r_k} - \frac{\partial}{\partial X_k}\left\langle\tilde{u}_k^*\delta\tilde{u}_j\right\rangle\delta\tilde{u}_i + \\
&+\left\langle\tilde{u}_k^*\delta\tilde{u}_j\right\rangle\frac{\partial\delta\tilde{u}_i}{\partial X_k} + \delta\tilde{u}_j\left(\frac{1}{2}\frac{\partial}{\partial X_k} + \frac{\partial}{\partial r_k}\right)\overline{\delta u_i''\delta u_k''} + \delta\tilde{u}_i\left(\frac{1}{2}\frac{\partial}{\partial X_k} + \frac{\partial}{\partial r_k}\right)\overline{\delta u_j''\delta u_k''} + \\
&+\delta\tilde{u}_j\overline{u_k''\frac{\partial}{\partial X_k}\delta u_i''} + \delta\tilde{u}_i\overline{u_k''\frac{\partial}{\partial X_k}\delta u_j''} - \frac{\partial}{\partial r_k}\left\langle\delta u_i''\delta u_k''\right\rangle\delta\tilde{u}_j + \left\langle\delta u_i''\delta u_k''\right\rangle\frac{\partial\delta\tilde{u}_j}{\partial r_k} + \\
&-\frac{\partial}{\partial X_k}\left\langle u_k''^*\delta u_i''\right\rangle\delta\tilde{u}_j + \left\langle u_k''^*\delta u_i''\right\rangle\frac{\partial\delta\tilde{u}_j}{\partial X_k} - \frac{\partial}{\partial r_k}\left\langle\delta u_j''\delta u_k''\right\rangle\delta\tilde{u}_i + \\
&+\left\langle\delta u_j''\delta u_k''\right\rangle\frac{\partial\delta\tilde{u}_i}{\partial r_k} - \frac{\partial}{\partial X_k}\left\langle u_k''^*\delta u_j''\right\rangle\delta\tilde{u}_i + \left\langle u_k''^*\delta u_j''\right\rangle\frac{\partial\delta\tilde{u}_i}{\partial X_k} = \\
&-\delta\tilde{u}_j\frac{1}{\rho}\left(\frac{\partial}{\partial X_i}\right)\delta\tilde{p} - \delta\tilde{u}_i\frac{1}{\rho}\left(\frac{\partial}{\partial X_j}\right)\delta\tilde{p} + \nu\delta\tilde{u}_j\left(\frac{1}{2}\frac{\partial^2}{\partial X_k\partial X_k} + 2\frac{\partial^2}{\partial r_k\partial r_k}\right)\delta\tilde{u}_i + \\
&+\nu\delta\tilde{u}_i\left(\frac{1}{2}\frac{\partial^2}{\partial X_k\partial X_k} + 2\frac{\partial^2}{\partial r_k\partial r_k}\right)\delta\tilde{u}_j + \delta\tilde{u}_j\delta\tilde{f}_i + \delta\tilde{u}_i\delta\tilde{f}_j
\end{aligned} \tag{2.45}$$

where the star $(\cdot)^*$ denotes the average of any quantity between $\boldsymbol{x}$ and $\boldsymbol{x}^+$. We also observe that:

$$\begin{aligned}
&\delta\tilde{u}_j\left(\frac{1}{2}\frac{\partial}{\partial X_k} + \frac{\partial}{\partial r_k}\right)\overline{\delta u_i''\delta u_k''} + \delta\tilde{u}_j\overline{u_k''\frac{\partial}{\partial X_k}\delta u_i''} = \\
&\delta\tilde{u}_j\left(\frac{1}{2}\frac{\partial}{\partial X_k} + \frac{\partial}{\partial r_k}\right)\overline{\delta u_i''\delta u_k''} + \delta\tilde{u}_j\frac{\partial}{\partial X_k}\overline{u_k''\delta u_i''} = \\
&\delta\tilde{u}_j\frac{\partial}{\partial r_k}\overline{\delta u_i''\delta u_k''} + \delta\tilde{u}_j\frac{\partial}{\partial X_k}\overline{\frac{1}{2}\left(u_k'' + u_k''^+\right)\delta u_i''} = \\
&\frac{\partial}{\partial r_k}\overline{\delta u_i''\delta u_k''}\delta\tilde{u}_j - \overline{\delta u_i''\delta u_k''}\frac{\partial\delta\tilde{u}_j}{\partial r_k} + \frac{\partial}{\partial X_k}\overline{u_k''^*\delta u_i''}\delta\tilde{u}_j - \overline{u_k''^*\delta u_i''}\frac{\partial}{\partial X_k}\delta\tilde{u}_j
\end{aligned} \tag{2.46}$$

The viscous term can be simplified as:

$$\begin{aligned}
&\nu\delta\tilde{u}_j\left(\frac{1}{2}\frac{\partial^2}{\partial X_k\partial X_k}+2\frac{\partial^2}{\partial r_k\partial r_k}\right)\delta\tilde{u}_i+\nu\delta\tilde{u}_i\left(\frac{1}{2}\frac{\partial^2}{\partial X_k\partial X_k}+2\frac{\partial^2}{\partial r_k\partial r_k}\right)\delta\tilde{u}_j=\\
&\frac{\nu}{2}\frac{\partial^2}{\partial X_k\partial X_k}\delta\tilde{u}_i\delta\tilde{u}_j+2\nu\frac{\partial^2}{\partial r_k\partial r_k}\delta\tilde{u}_i\delta\tilde{u}_j-\nu\frac{\partial\delta\tilde{u}_i}{\partial X_k}\frac{\partial\delta\tilde{u}_j}{\partial X_k}-4\nu\frac{\partial\delta\tilde{u}_i}{\partial r_k}\frac{\partial\delta\tilde{u}_j}{\partial r_k}=\\
&\frac{\nu}{2}\frac{\partial^2}{\partial X_k\partial X_k}\delta\tilde{u}_i\delta\tilde{u}_j+2\nu\frac{\partial^2}{\partial r_k\partial r_k}\delta\tilde{u}_i\delta\tilde{u}_j-2\left(\epsilon^{c+}_{ij}+\epsilon^{c}_{ij}\right)
\end{aligned}\tag{2.47}$$

where ϵ^c_{ij} is the pseudo-dissipation tensor of the coherent part of the velocity, defined as:

$$\epsilon^c_{ij}=\nu\left\langle\frac{\partial\tilde{u}_i}{\partial x_k}\frac{\partial\tilde{u}_j}{\partial x_k}\right\rangle\tag{2.48}$$

Moreover we write:

$$\delta\tilde{u}_j\delta\tilde{u}_k\frac{\partial\delta U_i}{\partial r_k}=\delta\tilde{u}_j\delta\tilde{u}_k\left(\frac{\partial U_i}{\partial x_k}\right)^*\tag{2.49}$$

and:

$$\delta\tilde{u}_j\tilde{u}^*_k\frac{\partial}{\partial X_k}\delta U_i=\delta\tilde{u}_j\tilde{u}^*_k\delta\left(\frac{\partial U_i}{\partial x_k}\right).\tag{2.50}$$

Finally, the budget equation for $\delta\tilde{u}_i\delta\tilde{u}_j$ is obtained:

$$\begin{aligned}
&\frac{\partial}{\partial t}\delta\tilde{u}_i\delta\tilde{u}_j + \frac{\partial}{\partial r_k}\delta U_k\delta\tilde{u}_i\delta\tilde{u}_j + \frac{\partial}{\partial X_k}U_k^*\delta\tilde{u}_i\delta\tilde{u}_j + \frac{\partial}{\partial r_k}\delta\tilde{u}_k\delta\tilde{u}_i\delta\tilde{u}_j + \frac{\partial}{\partial X_k}\tilde{u}_k^*\delta\tilde{u}_i\delta\tilde{u}_j + \\
&+\frac{\partial}{\partial r_k}\overline{\delta u_k''\delta u_i''}\delta\tilde{u}_j + \frac{\partial}{\partial X_k}\overline{u_k''^*\delta u_i''}\delta\tilde{u}_j + \frac{\partial}{\partial r_k}\overline{\delta u_k''\delta u_j''}\delta\tilde{u}_i + \frac{\partial}{\partial X_k}\overline{u_k''^*\delta u_j''}\delta\tilde{u}_i + \\
&-2\nu\frac{\partial^2}{\partial r_k\partial r_k}\delta\tilde{u}_i\delta\tilde{u}_j - \frac{\nu}{2}\frac{\partial}{\partial X_k}\left(\frac{\partial}{\partial X_k}\delta\tilde{u}_i\delta\tilde{u}_j\right) + \frac{\partial}{\partial X_i}\frac{1}{\rho}\delta\tilde{p}\delta\tilde{u}_j + \frac{\partial}{\partial X_j}\frac{1}{\rho}\delta\tilde{p}\delta\tilde{u}_i + \\
&-\frac{\partial}{\partial r_k}\langle\delta\tilde{u}_i\delta\tilde{u}_k\rangle\delta\tilde{u}_j - \frac{\partial}{\partial X_k}\left\langle\tilde{u}_k^*\delta\tilde{u}_i\right\rangle\delta\tilde{u}_j - \frac{\partial}{\partial r_k}\left\langle\delta\tilde{u}_j\delta\tilde{u}_k\right\rangle\delta\tilde{u}_i - \frac{\partial}{\partial X_k}\left\langle\tilde{u}_k^*\delta\tilde{u}_j\right\rangle\delta\tilde{u}_i + \\
&-\frac{\partial}{\partial r_k}\left\langle\delta u_i''\delta u_k''\right\rangle\delta\tilde{u}_j - \frac{\partial}{\partial X_k}\left\langle u_k''^*\delta u_i''\right\rangle\delta\tilde{u}_j - \frac{\partial}{\partial r_k}\left\langle\delta u_j''\delta u_k''\right\rangle\delta\tilde{u}_i - \frac{\partial}{\partial X_k}\left\langle u_k''^*\delta u_j''\right\rangle\delta\tilde{u}_i = \\
&-\delta\tilde{u}_j\delta\tilde{u}_k\left(\frac{\partial U_i}{\partial x_k}\right)^* - \delta\tilde{u}_i\delta\tilde{u}_k\left(\frac{\partial U_j}{\partial x_k}\right)^* - \delta\tilde{u}_j\tilde{u}_k^*\delta\left(\frac{\partial U_i}{\partial x_k}\right) - \delta\tilde{u}_i\tilde{u}_k^*\delta\left(\frac{\partial U_j}{\partial x_k}\right) + \\
&-\langle\delta\tilde{u}_i\delta\tilde{u}_k\rangle\left(\frac{\partial\tilde{u}_j}{\partial x_k}\right)^* - \left\langle\delta\tilde{u}_j\delta\tilde{u}_k\right\rangle\left(\frac{\partial\tilde{u}_i}{\partial x_k}\right)^* - \left\langle\delta\tilde{u}_i\tilde{u}_k^*\right\rangle\delta\left(\frac{\partial\tilde{u}_j}{\partial x_k}\right) - \left\langle\delta\tilde{u}_j\tilde{u}_k^*\right\rangle\delta\left(\frac{\partial\tilde{u}_i}{\partial x_k}\right) + \\
&-\left\langle\delta u_i''\delta u_k''\right\rangle\left(\frac{\partial\tilde{u}_j}{\partial x_k}\right)^* - \left\langle\delta u_j''\delta u_k''\right\rangle\left(\frac{\partial\tilde{u}_i}{\partial x_k}\right)^* - \left\langle\delta u_i''u_k''^*\right\rangle\delta\left(\frac{\partial\tilde{u}_j}{\partial x_k}\right) - \left\langle\delta u_j''u_k''^*\right\rangle\delta\left(\frac{\partial\tilde{u}_i}{\partial x_k}\right) + \\
&+\overline{\delta u_i''\delta u_k''}\frac{\partial\delta\tilde{u}_j}{\partial r_k} + \overline{\delta u_i''u_k''^*}\frac{\partial\delta\tilde{u}_j}{\partial X_k} + \overline{\delta u_j''\delta u_k''}\frac{\partial\delta\tilde{u}_i}{\partial r_k} + \overline{\delta u_j''u_k''^*}\frac{\partial\delta\tilde{u}_i}{\partial X_k} + \\
&+\frac{1}{\rho}\delta\tilde{p}\frac{\partial\delta\tilde{u}_j}{\partial X_i} + \frac{1}{\rho}\delta\tilde{p}\frac{\partial\delta\tilde{u}_i}{\partial X_j} - 4\epsilon_{ij}^{c*} + \delta\tilde{u}_j\delta\tilde{f}_i + \delta\tilde{u}_i\delta\tilde{f}_j.
\end{aligned} \tag{2.51}$$

2.A.3 φAGKE for $\overline{\delta u_i''\delta u_j''}$

We write the budget equation for u_i'' twice for the positions $\boldsymbol{x}$ and $\boldsymbol{x}^+ = \boldsymbol{x} + \boldsymbol{r}$, then the first is subtracted from the second:

$$\begin{aligned}
&\delta\left(\frac{\partial u_i''}{\partial t}\right) + \delta\left(U_k\frac{\partial u_i''}{\partial x_k}\right) + \delta\left(\tilde{u}_k\frac{\partial u_i''}{\partial x_k}\right) + \delta\left(u_k''\frac{\partial U_i}{\partial x_k}\right) + \delta\left(u_k''\frac{\partial\tilde{u}_i}{\partial x_k}\right) + \\
&+\delta\left(\frac{\partial}{\partial x_k}\left(u_i''u_k'' - \overline{u_i''u_k''}\right)\right) = -\delta\left(\frac{1}{\rho}\frac{\partial p''}{\partial x_i}\right) + \delta\left(\nu\frac{\partial^2 u_i''}{\partial x_k\partial x_k}\right) + \delta\left(f_i''\right).
\end{aligned} \tag{2.52}$$

Following the line of reasoning described above, the equation for $\delta u_i''$ is obtained, i.e:

$$\begin{aligned}
&\frac{\partial \delta u_i''}{\partial t} + \delta U_k \frac{\partial \delta u_i''}{\partial x_k^+} + U_k \frac{\partial \delta u_i''}{\partial x_k^+} + U_k \frac{\partial \delta u_i''}{\partial x_k} + \delta \tilde{u}_k \frac{\partial \delta u_i''}{\partial x_k^+} + \tilde{u}_k \frac{\partial \delta u_i''}{\partial x_k^+} + \tilde{u}_k \frac{\partial \delta u_i''}{\partial x_k} + \\
&+\delta u_k'' \frac{\partial \delta U_i}{\partial x_k^+} + u_k'' \frac{\partial \delta U_i}{\partial x_k^+} + u_k'' \frac{\partial \delta U_i}{\partial x_k} + \delta u_k'' \frac{\partial \delta \tilde{u}_i}{\partial x_k^+} + u_k'' \frac{\partial \delta \tilde{u}_i}{\partial x_k^+} + u_k'' \frac{\partial \delta \tilde{u}_i}{\partial x_k} + \delta u_k'' \frac{\partial \delta u_i''}{\partial x_k^+} + \\
&+u_k'' \frac{\partial \delta u_i''}{\partial x_k^+} + u_k'' \frac{\partial \delta u_i''}{\partial x_k} - \overline{\delta u_k'' \frac{\partial \delta u_i''}{\partial x_k^+}} - \overline{u_k'' \left(\frac{\partial}{\partial x_k^+} + \frac{\partial}{\partial x_k} \right) \delta u_i''} = \\
&-\frac{1}{\rho} \frac{\partial \delta p''}{\partial x_i^+} - \frac{1}{\rho} \frac{\partial \delta p''}{\partial x_i} + \nu \left(\frac{\partial^2}{\partial x_k^+ \partial x_k^+} + \frac{\partial^2}{\partial x_k \partial x_k} \right) \delta u_i + \delta f_i''.
\end{aligned} \tag{2.53}$$

As above, we first multiply this equation for $\delta u_j''$, and then we sum to the same equation with swapped i and j indices. Using again the independence of the $\boldsymbol{x}$ and $\boldsymbol{x}^+$ reference systems and incompressibility, and applying the phase average operator $\bar{\cdot}$ we obtain:

$$\begin{aligned}
&\frac{\partial}{\partial t} \overline{\delta u_i'' \delta u_j''} + \frac{\partial}{\partial x_k^+} \delta U_k \overline{\delta u_i'' \delta u_j''} + \left(\frac{\partial}{\partial x_k^+} + \frac{\partial}{\partial x_k} \right) U_k \overline{\delta u_i'' \delta u_j''} + \overline{\delta u_j'' \delta u_k''} \frac{\partial \delta U_i}{\partial x_k^+} + \overline{\delta u_i'' \delta u_k''} \frac{\partial \delta U_j}{\partial x_k^+} + \\
&+\overline{\delta u_j'' u_k''} \left(\frac{\partial}{\partial x_k^+} + \frac{\partial}{\partial x_k} \right) \delta U_i + \overline{\delta u_i'' u_k''} \left(\frac{\partial}{\partial x_k^+} + \frac{\partial}{\partial x_k} \right) \delta U_j + \frac{\partial}{\partial x_k^+} \delta \tilde{u}_k \overline{\delta u_j'' \delta u_i''} + \\
&+\left(\frac{\partial}{\partial x_k^+} + \frac{\partial}{\partial x_k} \right) \tilde{u}_k \overline{\delta u_j'' \delta u_i''} + \overline{\delta u_j'' \delta u_k''} \frac{\partial \delta \tilde{u}_i}{\partial x_k^+} + \overline{\delta u_i'' \delta u_k''} \frac{\partial \delta \tilde{u}_j}{\partial x_k^+} + \overline{\delta u_j'' u_k''} \left(\frac{\partial}{\partial x_k^+} + \frac{\partial}{\partial x_k} \right) \delta \tilde{u}_i + \\
&+\overline{\delta u_i'' u_k''} \left(\frac{\partial}{\partial x_k^+} + \frac{\partial}{\partial x_k} \right) \delta \tilde{u}_j + \frac{\partial}{\partial x_k^+} \overline{\delta u_k'' \delta u_i'' \delta u_j''} + \left(\frac{\partial}{\partial x_k^+} + \frac{\partial}{\partial x_k} \right) \overline{u_k'' \delta u_i'' \delta u_j''} = \\
&-\frac{1}{\rho} \left(\frac{\partial}{\partial x_i^+} + \frac{\partial}{\partial x_i} \right) \overline{\delta p'' \delta u_j''} - \frac{1}{\rho} \left(\frac{\partial}{\partial x_j^+} + \frac{\partial}{\partial x_j} \right) \overline{\delta p'' \delta u_i''} + \\
&+\overline{\frac{1}{\rho} \delta p'' \left(\frac{\partial}{\partial x_i^+} + \frac{\partial}{\partial x_i} \right) \delta u_j''} + \overline{\frac{1}{\rho} \delta p'' \left(\frac{\partial}{\partial x_j^+} + \frac{\partial}{\partial x_j} \right) \delta u_i''} + \\
&+\overline{\nu \delta u_j'' \left(\frac{\partial^2}{\partial x_k^+ \partial x_k^+} + \frac{\partial^2}{\partial x_k \partial x_k} \right) \delta u_i''} + \overline{\nu \delta u_i'' \left(\frac{\partial^2}{\partial x_k^+ \partial x_k^+} + \frac{\partial^2}{\partial x_k \partial x_k} \right) \delta u_j''} + \overline{\delta f_i'' \delta u_j''} + \overline{\delta f_j'' \delta u_i''}.
\end{aligned} \tag{2.54}$$

We switch as above to the notation with $\boldsymbol{X}$ and $\boldsymbol{r}$ to obtain:

$$\frac{\partial}{\partial t}\overline{\delta u_i'' \delta u_j''} + \frac{\partial}{\partial r_k} U_k \overline{\delta\delta u_i'' \delta u_j''} + \frac{\partial}{\partial X_k} U_k^* \overline{\delta u_i'' \delta u_j''} + \overline{\delta u_j'' \delta u_k''} \frac{\partial \delta U_i}{\partial r_k} + \overline{\delta u_i'' \delta u_k''} \frac{\partial \delta U_j}{\partial r_k} +$$
$$+ \overline{\delta u_j'' u_k'^*} \frac{\partial \delta U_i}{\partial X_k} + \overline{\delta u_i'' u_k'^*} \frac{\partial \delta U_j}{\partial X_k} + \overline{\delta u_j'' \delta u_k''} \frac{\partial \delta \tilde{u}_i}{\partial r_k} + \overline{\delta u_j'' u_k'^*} \frac{\partial \delta \tilde{u}_i}{\partial X_k} + \overline{\delta u_i'' \delta u_k''} \frac{\partial \delta \tilde{u}_j}{\partial r_k} +$$
$$+ \overline{\delta u_j'' u_k'^*} \frac{\partial \delta \tilde{u}_j}{\partial X_k} + \frac{\partial}{\partial r_k} \overline{\delta u_k'' \delta u_i'' \delta u_j''} + \frac{\partial}{\partial X_k} \overline{u_k'^* \delta u_i'' \delta u_j''} + \frac{\partial}{\partial r_k} \delta \tilde{u}_k \overline{\delta u_i'' \delta u_j''} +$$
$$+ \frac{\partial}{\partial X_k} \tilde{u}_k^* \overline{\delta u_i'' \delta u_j''} + \frac{\partial}{\partial X_i} \frac{1}{\rho} \overline{\delta p'' \delta u_j''} + \frac{\partial}{\partial X_j} \frac{1}{\rho} \overline{\delta p'' \delta u_i''} = \frac{1}{\rho} \overline{\delta p'' \frac{\partial \delta u_j''}{\partial X_i}} +$$
$$+ \frac{1}{\rho} \overline{\delta p'' \frac{\partial \delta u_i''}{\partial X_j}} + \frac{\nu}{2} \frac{\partial^2}{\partial X_k \partial X_k} \overline{\delta u_i'' \delta u_j''} + 2\nu \frac{\partial^2}{\partial r_k \partial r_k} \overline{\delta u_i'' \delta u_j''} - 2\left(\epsilon_{ij}^{s+} + \epsilon_{ij}^{s}\right) + \overline{\delta f_i'' \delta u_j''} + \overline{\delta f_j'' \delta u_i''} \tag{2.55}$$

where

$$\epsilon_{ij}^{s} = \nu \overline{\frac{\partial u_i''}{\partial x_k} \frac{\partial u_j''}{\partial x_k}}. \tag{2.56}$$

is the pseudo-dissipation tensor of the stochastic part of the velocity. Also in this case we can write

$$\overline{\delta u_j'' \delta u_k''} \frac{\partial \delta U_i}{\partial r_k} = \overline{\delta u_j'' \delta u_k''} \left(\frac{\partial U_i}{\partial x_k}\right)^* \tag{2.57}$$

and

$$\overline{\delta u_j'' u_k'^*} \frac{\partial \delta U_i}{\partial X_k} = \overline{\delta u_j'' u_k'^*} \delta \left(\frac{\partial U_i}{\partial x_k}\right) \tag{2.58}$$

so that the budget equation for $\overline{\delta u_i'' \delta u_j''}$ is eventually obtained:

$$\frac{\partial}{\partial t}\overline{\delta u_i'' \delta u_j''} + \frac{\partial}{\partial r_k} \delta U_k \overline{\delta u_i'' \delta u_j''} + \frac{\partial}{\partial X_k} U_k^* \overline{\delta u_i'' \delta u_j''} + \frac{\partial}{\partial r_k} \overline{\delta u_k'' \delta u_i'' \delta u_j''} + \frac{\partial}{\partial X_k} \overline{u_k'^* \delta u_i'' \delta u_j''} +$$
$$+ \frac{\partial}{\partial r_k}\left(-2\nu \frac{\partial}{\partial r_k} \overline{\delta u_i'' \delta u_j''}\right) + \frac{\partial}{\partial X_k}\left(-\frac{\nu}{2} \frac{\partial}{\partial X_k} \overline{\delta u_i'' \delta u_j''}\right) + \frac{\partial}{\partial r_k} \delta \tilde{u}_k \overline{\delta u_i'' \delta u_j''} + \frac{\partial}{\partial X_k} \tilde{u}_k^* \overline{\delta u_i'' \delta u_j''} +$$
$$+ \frac{\partial}{\partial X_i} \frac{1}{\rho} \overline{\delta p'' \delta u_j''} + \frac{\partial}{\partial X_j} \frac{1}{\rho} \overline{\delta p'' \delta u_i''} = -\overline{\delta u_j'' \delta u_k''} \left(\frac{\partial U_i}{\partial x_k}\right)^* - \overline{\delta u_i'' \delta u_k''} \left(\frac{\partial U_j}{\partial X_k}\right)^* +$$
$$- \overline{\delta u_j'' u_k'^*} \delta \left(\frac{\partial U_i}{\partial x_k}\right) - \overline{\delta u_i'' u_k'^*} \delta \left(\frac{\partial U_j}{\partial x_k}\right) - \overline{\delta u_j'' \delta u_k''} \left(\frac{\partial \tilde{u}_i}{\partial x_k}\right)^* - \overline{\delta u_i'' \delta u_k''} \left(\frac{\partial \tilde{u}_j}{\partial x_k}\right)^* +$$
$$- \overline{\delta u_j'' u_k'^*} \delta \left(\frac{\partial \tilde{u}_i}{\partial x_k}\right) - \overline{\delta u_i'' u_k'^*} \delta \left(\frac{\partial \tilde{u}_j}{\partial x_k}\right) + \frac{1}{\rho} \overline{\delta p'' \frac{\partial \delta u_j''}{\partial X_i}} + \frac{1}{\rho} \overline{\delta p'' \frac{\partial \delta u_i''}{\partial X_j}} - 4\epsilon_{ij}^{s*} + \overline{\delta f_i'' \delta u_j''} + \overline{\delta f_j'' \delta u_i''} \tag{2.59}$$

2.B The φAGKE for the plane channel flow with oscillating walls

The special form assumed by the φAGKE under the symmetries of a plane channel flow with spanwise oscillations is reported below. The coherent part reduces to:

$$
\begin{aligned}
&\omega\frac{\partial\delta\tilde{u}_i\delta\tilde{u}_j}{\partial\varphi}+\frac{\partial}{\partial r_k}\underbrace{\left(\overline{\delta u_k''\delta u_i''}\delta\tilde{u}_j+\overline{\delta u_k''\delta u_j''}\delta\tilde{u}_i\right)}_{\text{Turbulent transport}}+\frac{\partial}{\partial r_y}\underbrace{\left(-2\nu\frac{\partial\delta\tilde{u}_i\delta\tilde{u}_j}{\partial r_y}\right)}_{\text{Viscous diffusion}}+\frac{\partial}{\partial Y}\underbrace{\left(-\frac{\nu}{2}\frac{\partial\delta\tilde{u}_i\delta\tilde{u}_j}{\partial Y}\right)}_{\text{Viscous diffusion}}+\\
&+\frac{\partial}{\partial Y}\underbrace{\left(\overline{v''^*\delta u_i''}\delta\tilde{u}_j+\overline{v''^*\delta u_j''}\delta\tilde{u}_i\right)}_{\text{Turbulent transport}}+\frac{\partial}{\partial Y}\underbrace{\left(\frac{1}{\rho}\delta\tilde{p}\delta\tilde{u}_i\delta_{j2}\right)}_{\text{Pressure transport}}+\frac{\partial}{\partial Y}\underbrace{\left(\frac{1}{\rho}\delta\tilde{p}\delta\tilde{u}_j\delta_{i2}\right)}_{\text{Pressure transport}}=\\
&\underbrace{-\left[-\overline{\delta u_i''\delta v''}\left(\frac{\partial\tilde{u}}{\partial y}\right)^*\delta_{j1}-\overline{\delta u_j''\delta v''}\left(\frac{\partial\tilde{u}}{\partial y}\right)^*\delta_{i1}-\overline{\delta u_i''v''^*}\delta\left(\frac{\partial\tilde{u}}{\partial y}\right)\delta_{j1}-\overline{\delta u_j''v''^*}\delta\left(\frac{\partial\tilde{u}}{\partial y}\right)\delta_{i1}\right]}_{p_{ij}^{cs}}+\\
&\underbrace{-\left[-\overline{\delta u_i''\delta v''}\left(\frac{\partial\tilde{w}}{\partial y}\right)^*\delta_{j3}-\overline{\delta u_j''\delta v''}\left(\frac{\partial\tilde{w}}{\partial y}\right)^*\delta_{i3}-\overline{\delta u_i''v''^*}\delta\left(\frac{\partial\tilde{w}}{\partial y}\right)\delta_{j3}-\overline{\delta u_j''v''^*}\delta\left(\frac{\partial\tilde{w}}{\partial y}\right)\delta_{i3}\right]}_{p_{ij}^{cs}}+\\
&\underbrace{+\frac{1}{\rho}\delta\tilde{p}\frac{\partial\delta\tilde{u}_i}{\partial Y}\delta_{j2}+\frac{1}{\rho}\delta\tilde{p}\frac{\partial\delta\tilde{u}_j}{\partial Y}\delta_{i2}}_{\pi_{ij}^c}\underbrace{-4\epsilon_{ij}^{c*}}_{d_{ij}^c}+\\
&\underbrace{+\frac{\partial}{\partial r_k}\left[\left\langle\delta u_i''\delta u_k''\right\rangle\delta\tilde{u}_j+\left\langle\delta u_j''\delta u_k''\right\rangle\delta\tilde{u}_i\right]+\frac{\partial}{\partial Y}\left[\left\langle v''^*\delta u_i''\right\rangle\delta\tilde{u}_j+\left\langle v''^*\delta u_j''\right\rangle\delta\tilde{u}_i\right]}_{\zeta_{ij}^c}+\\
&\underbrace{+\left[-\left\langle\delta u_i''\delta v''\right\rangle\left(\frac{\partial\tilde{u}_j}{\partial y}\right)^*-\left\langle\delta u_j''\delta v''\right\rangle\left(\frac{\partial\tilde{u}_i}{\partial y}\right)^*-\left\langle\delta u_i''v''^*\right\rangle\delta\left(\frac{\partial\tilde{u}_j}{\partial y}\right)-\left\langle\delta u_j''v''^*\right\rangle\delta\left(\frac{\partial\tilde{u}_i}{\partial y}\right)\right]}_{\zeta_{ij}^c}.
\end{aligned}
\tag{2.60}
$$

The φAGKE for the stochastic part $\overline{\delta u_i'' \delta u_j''}$ become:

$$\omega \frac{\partial \overline{\delta u_i'' \delta u_j''}}{\partial \varphi} + \frac{\partial}{\partial r_x} \underbrace{\left(\delta U \overline{\delta u_i'' \delta u_j''} \right)}_{\text{Mean transport}} + \frac{\partial}{\partial r_x} \underbrace{\left(\delta \tilde{u} \overline{\delta u_i'' \delta u_j''} \right)}_{\text{Coherent transport}} + \frac{\partial}{\partial r_z} \underbrace{\left(\delta \tilde{w} \overline{\delta u_i'' \delta u_j''} \right)}_{\text{Coherent transport}} +$$

$$+ \frac{\partial}{\partial r_k} \underbrace{\left(\overline{\delta u_k'' \delta u_i'' \delta u_j''} \right)}_{\text{Turbulent transport}} + \frac{\partial}{\partial r_k} \underbrace{\left(-2\nu \frac{\partial \overline{\delta u_i'' \delta u_j''}}{\partial r_k} \right)}_{\text{Viscous diffusion}} + \frac{\partial}{\partial Y} \underbrace{\left(\overline{v''^* \delta u_i'' \delta u_j''} \right)}_{\text{Turbulent transport}} +$$

$$+ \frac{\partial}{\partial Y} \underbrace{\left(-\frac{\nu}{2} \frac{\partial \overline{\delta u_i'' \delta u_j''}}{\partial Y} \right)}_{\text{Viscous diffusion}} + \frac{\partial}{\partial Y} \underbrace{\left(\frac{1}{\rho} \overline{\delta p'' \delta u_j''} \delta_{i2} + \frac{1}{\rho} \overline{\delta p'' \delta u_i''} \delta_{j2} \right)}_{\text{Pressure transport}} =$$

$$\underbrace{\left[-\overline{\delta u_i'' \delta v''} \left(\frac{dU}{dy} \right)^* \delta_{j1} - \overline{\delta u_j'' \delta v''} \left(\frac{dU}{dy} \right)^* \delta_{i1} - \overline{\delta u_i'' v''^*} \delta \left(\frac{dU}{dy} \right) \delta_{j1} - \overline{\delta u_j'' v''^*} \delta \left(\frac{dU}{dy} \right) \delta_{i1} \right]}_{p_{ij}^{ms}} +$$

$$+ \underbrace{\left[-\overline{\delta u_i'' \delta v''} \left(\frac{\partial \tilde{u}}{\partial y} \right)^* \delta_{j1} - \overline{\delta u_j'' \delta v''} \left(\frac{\partial \tilde{u}}{\partial y} \right)^* \delta_{i1} - \overline{\delta u_i'' v''^*} \delta \left(\frac{\partial \tilde{u}}{\partial y} \right) \delta_{j1} - \overline{\delta u_j'' v''^*} \delta \left(\frac{\partial \tilde{u}}{\partial y} \right) \delta_{i1} \right]}_{p_{ij}^{cs}} +$$

$$+ \underbrace{\left[-\overline{\delta u_i'' \delta v''} \left(\frac{\partial \tilde{w}}{\partial y} \right)^* \delta_{j3} - \overline{\delta u_j'' \delta v''} \left(\frac{\partial \tilde{w}}{\partial y} \right)^* \delta_{i3} - \overline{\delta u_i'' v''^*} \delta \left(\frac{\partial \tilde{w}}{\partial y} \right) \delta_{j3} - \overline{\delta u_j'' v''^*} \delta \left(\frac{\partial \tilde{w}}{\partial y} \right) \delta_{i3} \right]}_{p_{ij}^{cs}} +$$

$$\underbrace{+ \frac{1}{\rho} \overline{\delta p'' \left(\frac{\partial \delta u_i''}{\partial X_j} \right)} + \frac{1}{\rho} \overline{\delta p'' \left(\frac{\partial \delta u_j''}{\partial X_i} \right)}}_{\pi_{ij}^s} \underbrace{-4\epsilon_{ij}^{s*}}_{d_{ij}^s} . \tag{2.61}$$

Here the mean transport term contributes to ϕ_x^s, consistently with a non-zero streamwise mean velocity U. Similarly, coherent transport appears in ϕ_x^s and ϕ_z^s, since $\tilde{u} \neq 0$ and $\tilde{w} \neq 0$. Since no external volume forcing acts on the flow, the interaction forcing term is zero for both components.

2.C Analysis of conditionally-averaged quantities

In this Appendix, the interpretations of the local maxima of $\overline{\delta w'' \delta w''}$ in the $r_x = r_y = 0$ and $r_z = r_y = 0$ planes provided in §2.4.1.2 are supported by inspecting the velocity field induced by the conditionally-averaged quasi-streamwise vortex at different phases of the control cycle. The procedure to extract the conditional average from the DNS database closely resembles that presented by Jeong *et al.* (1997); it is described in detail by Gallorini *et al.* (2022) and is not repeated here.

Figure 2.15 uses velocity isosurfaces to describe the spatial shape of the conditionally-averaged negative rotating (SN) structure for the case at $T^+ = 250$ at the two phases φ_1 and φ_3. The extraction procedure is centered at the wall-normal position of the maxima of $\overline{\delta w'' \delta w''}$ for φ_1 and φ_3 (see figure 2.4): this position is shown in the shear panel at the bottom of figure 2.15. At the two chosen phases, the structures show their maximum negative and positive tilt angle; however, the discussion below for φ_1 can be extended to φ_2, and that for φ_3 extends to φ_4. Isocontours of streamwise (transparent) and spanwise (solid color) velocities are shown in a view from above (top) and from upstream (bottom).

Following the discussion in §2.4.1.2, when the tilting angle is negative (see φ_1), the low-speed streak associated with a SN redistributes its energy via pressure strain and creates negative spanwise velocity fluctuations; the opposite occurs for the high-speed streak. This is confirmed by the ensemble-averaged structure, which shows a region of positive (negative) spanwise velocity close to the side of the high- (low-) speed streak. At φ_3, instead, the tilt angle of the streak is positive, and the low- (high-) speed streak induces positive (negative) w'' velocity fluctuations at its side.

Another view of the spanwise velocity contours is displayed in the bottom panels of figure 2.15. In these images, the streamwise velocity contours are removed, to focus on the spanwise component only. In the canonical channel flow, a negatively rotating vortex induces two regions of high and low spanwise velocity below and above its center, respectively. However, when the wall oscillates, two additional regions of positive and negative spanwise velocity originate at the sides of the tilted vortex because of its interaction with the Stokes layer. At phase φ_1 (left panel), the peak of $\overline{\delta w'' \delta w''}$ occurs at $Y^+ = 25$, where the spanwise shear $\partial \tilde{w}^+ / \partial y$ is positive. Therefore, the negatively rotating quasi-streamwise vortex lifts low spanwise velocity fluid, and displaces high spanwise velocity fluid downwards. This process explains the appearance of a low w-velocity region at the right side of the quasi-streamwise vortex, whereas the high spanwise velocity region is absorbed into the lower-side one. At φ_3 the regions of low/high spanwise velocity are opposite compared to φ_1 owing to the opposite sign of the spanwise shear at the location of the peak of $\overline{\delta w'' \delta w''}$ at this phase.

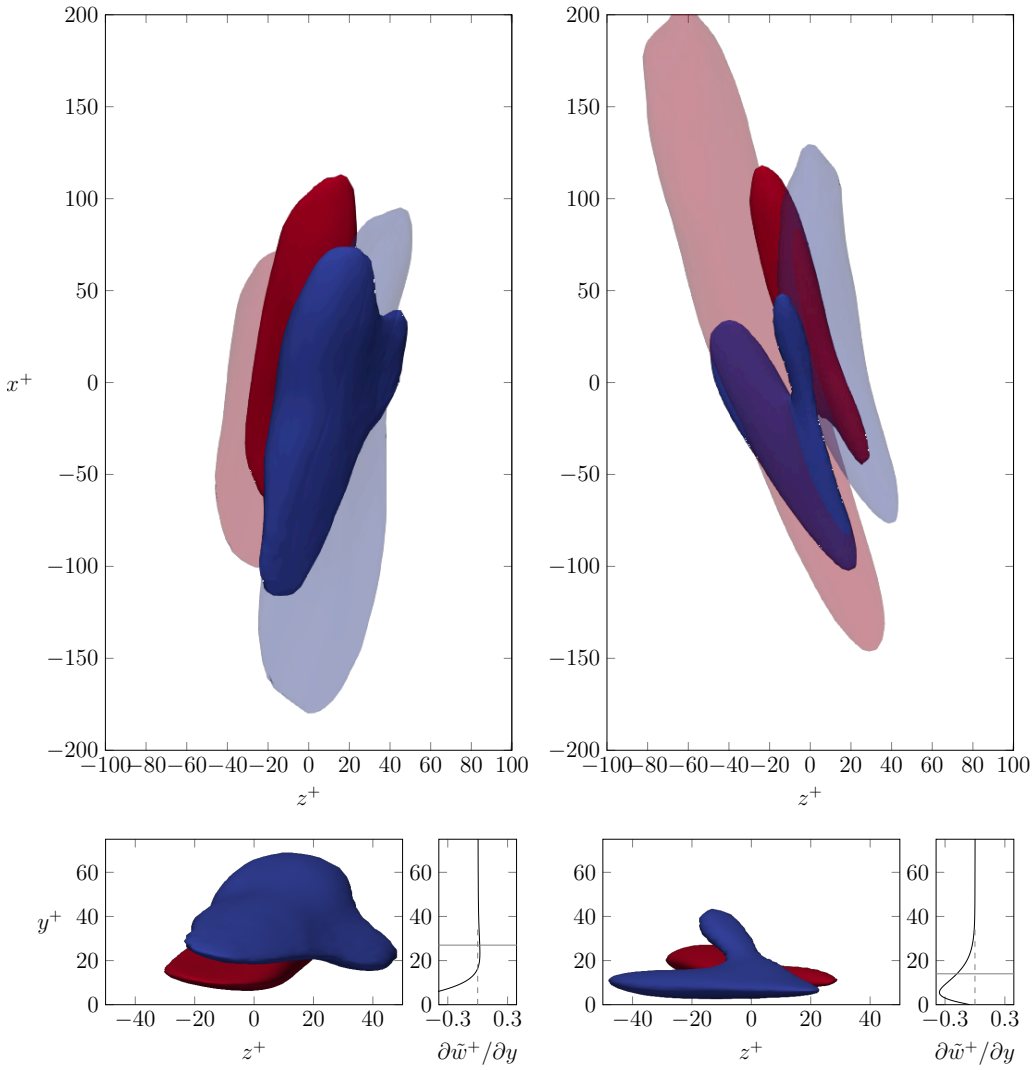

Figure 2.15: Conditionally-averaged structure, extracted at φ_1 (left) and φ_3 (right) at $T^+ = 250$. The spatial shape of the structure is shown via isosurfaces of u'^+ (transparent color) and w'^+ (solid color) velocity fluctuations at the level ±0.5 (red/blue is positive/negative). The bottom panels also include the spanwise shear $\mathrm{d}\tilde{w}^+/\mathrm{d}y$ at that phase, and show the wall-normal position where the extraction procedure is carried out.

On the optimal period of spanwise forcing for turbulent drag reduction

This manuscript has been written with
Quadrio M., Castelletti, M. & Chiarini, A.

On the optimal period of spanwise forcing for turbulent drag reduction

Abstract

The most simple active forcing that leads to a reduction of turbulent skin friction drag is the spanwise wall oscillation. The wall periodically oscillates in the spanwise direction as a function of time and generates a periodic spanwise cross-flow that depends on three parameters: the amplitude A, the period of the oscillation T and the thickness of the spanwise velocity profile δ. The latter two quantities are not independent and evidences suggest that the maximum drag reduction is obtained for $T^+ \approx 100$ and $\delta^+ \approx 6$, although there is no consensus on their physical interpretation. In this work we ovecome the conventional oscillating wall and get rid of the $\delta - T$ constraint. We perform a DNS study at $Re_\tau = 400$ directly enforcing a mean spanwise velocity profile at each time step to a turbulent channel flow, varying δ and T independently. We find the optimal parameters for drag reduction to be $T^+ = 30$ and $\delta^+ = 14$ and discuss their possible physical meaning.

3.1 Introduction

Reducing the turbulent skin-friction drag is a long-standing effort in fluid mechanics, driven by environmental and economic reasons. Towards this goal, several active and passive approaches and technologies have been considered over the years. Among them, those not requiring feedback from measurements and only involving a predetermined wall-based actuation deserve special attention, owing to the combination of their simplicity and effectiveness. In this work, we focus on spanwise forcing (Ricco *et al.*, 2021), which has been proved to remain effective at high Reynolds and Mach numbers (Gatti & Quadrio, 2016; Gattere *et al.*, 2024), and provides large energy savings owing to a large drag reduction margin

combined with relatively small energy requirements.

The simplest and earliest variant of spanwise forcing is the spanwise oscillation of a plane wall (Jung *et al.*, 1992). Although the spatially uniform oscillation is not among the most efficient implementations, it is considered here as the prototypical form of spanwise forcing, because its working principle is shared by the other variants. The wall periodically oscillates in the spanwise direction as a function of time t according to a prescribed harmonic law

$$w_w(t) = A \sin\left(\frac{2\pi}{T}t\right), \tag{3.1}$$

where w_w is the spanwise velocity component of the wall (the other components are set to zero), and A and T indicate the amplitude and period of the oscillation. The harmonic oscillation of the wall generates a spanwise cross-flow that is periodic after space- and phase-averaging, and that superimposes to and interacts with the turbulent flow. The phase-averaged spanwise flow coincides with the analytical laminar solution $w_{SL}(y,t)$ of the second Stokes problem (Quadrio & Sibilla, 2000), hereafter referred to as the Stokes layer or SL, with small deviations for large T. It is a textbook result (Schlichting & Gersten, 2000) that an indefinite plane wall oscillating harmonically beneath a still fluid generates a time-varying velocity profile given by

$$w_{SL}(y,t) = A \exp\left(-\frac{y}{\delta}\right) \sin\left(\frac{2\pi}{T}t - \frac{y}{\delta}\right), \tag{3.2}$$

where δ is the SL thickness. Since the maximum amplitude A of the wall oscillation only appears as a multiplicative factor because of the linearity of the governing equations, the SL is shaped by the remaining two parameters T and δ. These two quantities are not independent, and δ is determined by the period T and the fluid kinematic viscosity by

$$\delta = \delta_{SL}(T,\nu) \equiv \sqrt{\frac{\nu T}{\pi}}. \tag{3.3}$$

This is coherent with the wall forcing 3.1, having only T as a tuning parameter besides the amplitude A. The SL thickness δ defined above is the wall distance where the maximum spanwise velocity during the oscillation reduces to $\exp(-1)$ times the maximum wall velocity A.

The coherent SL cross-flow is at the root of the drag reduction process, yet no consensus exists regarding the details of how it interacts with the incoming turbulent flow. However, starting from the early numerical studies of Jung *et al.* (1992) and Baron & Quadrio (1996), the available evidence points to the existence of an optimal value T_{opt} for the oscillation period, which corresponds to an optimal SL thickness $\delta_{opt} = \delta_{SL}(T_{opt},\nu)$, for which drag reduction is maximum. This statement, however, needs to be better defined by additionally specifying that the

optimal period is commonly sought by keeping the maximum velocity A constant, and should be therefore denoted as $T_{opt,A}$ for clarity (Quadrio & Ricco, 2004). This is reasonable, as drag reduction is proportional to the forcing intensity. However, the alternative to seek the optimal period while keeping constant the maximum physical displacement D exists. This approach indeed suits some experimental devices where a maximum allowed excursion exists (see for example Laadhari *et al.*, 1994; Choi, 2002; Gatti *et al.*, 2015; Marusic *et al.*, 2021). Most of the studies looked for $T_{opt,A}$ (which for simplicity will be referred to in this paper by dropping the subscript A), and there is broad consensus that $T^+_{opt} \approx 100$ or $T^*_{opt} \approx 75$ when scales with viscous quantities of the uncontrolled and controlled flow, respectively, corresponding to a penetration depth of the Stokes layer of $\delta^+_{opt} \approx 5.7$ or $\delta^*_{opt} \approx 5$.

For example, Choi *et al.* (2002) showed through Direct Numerical Simulations (DNS) of a turbulent channel flow that $T^+_{opt} \approx 100$ for different values of A^+ and friction Reynolds numbers Re_τ. For a turbulent channel flow at $Re_\tau = 200$, Quadrio & Ricco (2004) reported by DNS that for a given A^+ the highest drag reduction is attained by keeping T^+ in the $100 - 125$ range. Touber & Leschziner (2012) and Agostini *et al.* (2014) numerically found the same optimal $T^+ \approx 100$ at the larger Reynolds numbers of $Re_\tau = 500$ and $Re_\tau = 1000$. Gatti & Quadrio (2016) confirmed this optimal value through a large DNS study, considering several amplitudes and increasing the Reynolds number up to $Re_\tau = 1000$. Several experimental works, although typically affected by the constant-displacement limitation discussed above, have indirectly confirmed the value of T^+_{opt} over a range of Reynolds numbers and forcing amplitudes (see for example Laadhari *et al.*, 1994; Trujillo *et al.*, 1997; Gatti *et al.*, 2015; Kempaiah *et al.*, 2020). We refer again the interested reader to Ricco *et al.* (2021) for a more comprehensive review.

Despite the evidence, however, there is not consensus on the physical interpretation of the optimum $T^+_{opt} \approx 100$ and $\delta^+_{opt} = \delta^+_{SL}(T^+) \approx 6$, and more than one meaning can be attached to these specific values. For example, T_{opt} can be immediately associated to other time scales of the flow, such as the characteristic life time of the near-wall coherent structures (Quadrio & Luchini, 2003). Owing to the convective nature of the flow, T_{opt} can be also converted into a longitudinal length scale in terms of a convection length scale, and be compared with typical lengths of the near-wall coherent structures (Touber & Leschziner, 2012). Moreover, within the SL the optimal period also defines the maximum lateral displacement of the moving wall $D_{max} = AT$, which is another (possibly) relevant length scale of the flow (Quadrio & Ricco, 2004). The optimal period can also be interpreted to only determine via equation 3.3 the optimal penetration depth δ_{opt} of the Stokes layer, which is indeed a diffusion length scale pertaining to the wall-normal direction, and a measure of the near-wall mean spanwise shear.

Our inability to discriminate among the different possible interpretations reflects our current limited understanding of the whole drag reduction mechanism of the oscillating wall set up.

The aim of this work is to do a step forward in this direction, and elucidate the physical meaning of the (T_{opt}, δ_{opt}) optimum. Based on DNS, we go beyond the concept of the conventional oscillating wall and get rid of the $\delta = \delta_{SL}(T, \nu)$ constraint: we explore the complete (T, δ) two-dimensional space of parameters and investigate separately the role of T and δ. In other words, instead of imposing the harmonic spanwise oscillation of the wall to generate the SL, we enforce a mean spanwise velocity profile of the form (3.2) at each time step, and vary δ and T independently. In doing this, our numerical experiments also reveal that much larger values of drag reduction are possible when removing the $\delta = \delta_{SL}(T, \nu)$ constraint: this highlights the need of developing alternative strategies that produce near-wall spanwise motion which are not based on the wall oscillation.

The work is organised as follows. After this Introduction, the numerical approach is described in §3.2. Then, the numerical results are then presented and discussed in §3.3. The work closes with §3.4, where conclusions and perspectives are provided.

3.2 Methods

3.2.1 Problem formulation

Direct numerical simulations (DNS) of the turbulent flow in an indefinite plane channel are carried out, to study the effect of the Stokes layer generated by the sinusoidal oscillations of the walls after its period T and thickness δ are decoupled. Hereinafter, x, y, z (u, v, w) denote the streamwise, wall-normal and spanwise directions (velocity components). Capital letters indicate mean quantities, while small letters are for fluctuation around them.

We remove the link (3.3) between T and δ_{SL} that exists when a true Stokes layer is created by the oscillation of the wall. An extended Stokes layer profile (ESL)

$$\langle w \rangle_h(y, t; \delta, T) = A \exp\left(-\frac{y}{\delta}\right) \sin\left(\frac{2\pi}{T}t - \frac{y}{\delta}\right) \tag{3.4}$$

is indeed enforced directly at each time step, whose thickness δ and oscillation period T are regarded as independent parameters; the operator $\langle \cdot \rangle_h$ indicates spatial averaging along the homogeneous x and z directions. While enforcing an arbitrary profile $\langle w \rangle_h(y, t)$ may suggest that the present numerical experiments are just one of those thought experiments that are possible with DNS, it should be remarked that our procedure is equivalent to solve the Navier–Stokes equations with the

boundary condition (3.1) and an additional volume forcing that is practically zero whenever the extended Stokes layer (3.4) reduces to the standard Stokes layer. We measure that the two techniques nearly provide the same drag reduction effect, with a small deviation only at large T (see §3.2.3). This enables us to explore the response of the flow to the ESL in the complete two-dimensional space of parameters of T and δ, and investigate separately the role of the two parameters.

3.2.2 Numerical experiments

The simulations are carried out with a proved DNS solver for the incompressible Navier–Stokes equations, originally introduced by Luchini & Quadrio (2006) and written in the CPL Compiler and Programming Language (Luchini, 2021). The solver is modified to enforce the condition expressed by equation (3.4) at each time step. The equations are projected in the divergence-free space and rewritten in terms of the wall-normal components of the velocity and vorticity vectors. The solution follows a pseudo-spectral approach (Kim *et al.*, 1987). Fourier expansions are used in the homogeneous directions, so that the wall-parallel spatial mean $\langle\cdot\rangle_h$ is equivalent to the $(0,0)$ wavenumber in every wall-parallel plane. Fourth-order compact finite differences discretise the wall-normal direction. Equations are integrated in time using a third-order Runge–Kutta scheme for the nonlinear terms combined with a second-order Crank–Nicolson scheme for the viscous term.

Most of the available numerical studies on the oscillating wall have been carried out at the conveniently low Reynolds number $Re_\tau = 200$ (Jung *et al.*, 1992; Baron & Quadrio, 1996; Quadrio & Ricco, 2004; Touber & Leschziner, 2012). Here, however, a preliminary study has revealed that the forcing (3.4) can be significantly more effective than the conventional oscillating wall, such that the turbulent flow is prone to relaminarization. Hence, to obtain a clearer picture, the baseline value of Re_τ for the present study is increased to $Re_\tau = 400$.

The simulations are carried out at Constant Flow Rate (CFR, according to the definition by Quadrio *et al.*, 2016*a*), with the bulk Reynolds number set to $Re_b = U_b h/\nu = 7000$ for all cases, which corresponds to a friction Reynolds number of $Re_\tau = u_\tau h/\nu \approx 400$ in the unforced case. Here U_b is the bulk velocity, and $u_\tau = \sqrt{\tau_w/\rho}$ is the friction velocity expressed in terms of the averaged wall-shear stress τ_w and the fluid density, and h is the channel half-height. The computational box has a size of $(L_x, L_y, L_z) = (4\pi h, 2h, 2\pi h)$; it is discretised with $N_y = 400$ grid points in the wall-normal direction, and with $N_x = N_z = 512$ Fourier modes in the x and z directions, further increased by a factor of $3/2$ to remove the aliasing error. The streamwise and spanwise resolutions after dealiasing are $\Delta x^+ \approx 6.5$ and $\Delta z^+ = 3.3$. In the wall-normal direction an hyperbolic tangent distribution is used, leading to $\Delta^+_{y,min} \approx 0.6$ at the wall and to $\Delta^+_{y,max} \approx 3.3$ at the centreline. The simulations are run for a time period of $1000h/U_b$, but statistical

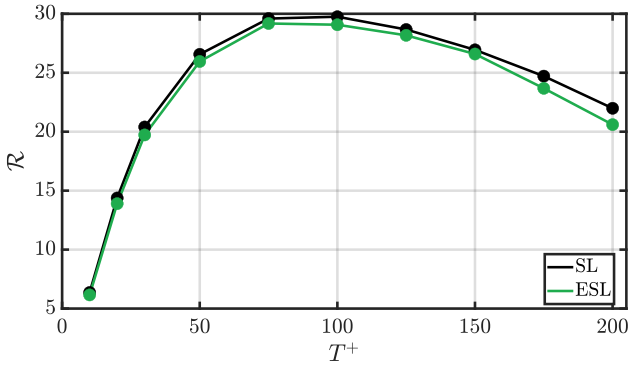

Figure 3.1: Drag reduction versus oscillation period for the oscillating wall (black) and the present approach, with $\delta = \delta_{SL}$ (green)

measurements are taken only over the last 800 time units, to account for the initial period where the flow adapts to the new drag-reduced state.

The oscillating period is varied in the $10 \leq T^+ \leq 200$ range, while δ varies between $2 \leq \delta^+ \leq 20$. The amplitude of the forcing is set to $A^+ = 12$. Overall, the study includes 119 direct numerical simulations. The quantity of interest is the drag reduction rate $\mathcal{R}$, that for CFR simulations is equivalent (Kasagi *et al.*, 2009) to the percentage change in skin-friction coefficient, i.e.:

$$\mathcal{R} = 100 \times \left(1 - \frac{C_f}{C_{f,0}}\right), \tag{3.5}$$

where $C_f = 2\tau_w/(\rho U_b^2)$ is the skin-friction coefficient of the controlled flow, and $C_{f,0}$ is the skin-friction coefficient of the reference uncontrolled case.

3.2.3 Validation

We start validating the numerical approach, by comparing the drag reduction provided by the extended Stokes layer (3.4) along the $\delta = \delta_{SL}(T, \nu)$ line with the one of the actual oscillating wall set up. To this purpose, two sets of additional simulations are performed: the former by enforcing the ESL (3.4) for various values of T and by setting $\delta = \delta_{SL}(T)$; the latter by letting the SL developing naturally by imposing Eq. (3.1) at the walls. All other simulation parameters and procedures are kept identical in the comparison.

Figure 3.1 compares the two approaches in terms of drag reduction and shows that very good agreement between the data obtained imposing the ESL profile (3.4) and those from the actual oscillation of the wall, thus supporting the present approach. Minor differences between the two datasets can only be appreciated at large T^+, up to an absolute deviation of less then 1.3%, confirming previous

observations (Quadrio & Sibilla, 2000; Choi *et al.*, 2002; Touber & Leschziner, 2012) that the phase-averaged cross-flow mostly coincides with the SL laminar solution, but shows minor departures at larger oscillation periods.

3.3 Results

3.3.1 The drag reduction map

Figure 3.2 shows the map of the computed drag reduction $\mathcal{R}$ in the two-dimensional (T, δ) space of parameters. Each point is the result of one simulation. The colour map and the contours help in visualising the global behaviour of the changes of $\mathcal{R}$ in the (T, δ) space. They have been computed after linear interpolation of the simulation points on a Cartesian grid with spacing $\Delta T^+ = 0.19$ and $\Delta\delta^+ = 0.018$. The black solid line represents the locus of points where $\delta = \delta_{SL}(T)$: all the literature information available so far has been obtained along this line only.

Figure 3.2 clearly shows that, once δ and T are made independent, the maximum drag reduction on the SL line is not particularly meaningful in view of the global $\mathcal{R}$ map. Along the SL line, a maximum $\mathcal{R} \approx 30\%$, shown by the black symbol, is indeed found at $(T^+, \delta^+) \approx (100, 5.7)$, but the position of the actual maximum in the two-dimensional plane is larger and quite far from it. Indeed, the global maximum drag reduction obtained with the ESL is $\mathcal{R}_{max} \approx 40\%$, found for $(T^+, \delta^+) \approx (30, 14)$; see the green symbol in figure 3.2. Hence, the maximum drag reduction is significantly larger than that on the SL line, and is obtained by decreasing the oscillating period from $T^+ = 100$ to $T^+ = 30$, while at the same time increasing the SL thickness from $\delta^+ = 5.7$ to $\delta^+ = 14$. Note that, when moving along the SL line, it is impossible to change T and δ in opposite directions.

The flow response to the ESL shows a behaviour that is only marginally grasped by the oscillating wall set up. Figure 3.2 shows that the ESL is effective in reducing friction for all the considered $(T, \delta)-$pairs. The $\mathcal{R}$ map can be divided into different regions according to the behaviour of the drag reduction at varying parameters T and δ. The area of the global optimum is quite broad, spanning the region of $20 \leq T^+ \leq 50$ and $8 \leq \delta^+ \leq 14$; note that the values of δ correspond to the position of the buffer layer, where the near-wall cycle takes place (Schoppa & Hussain, 2002), suggesting that the maximum $\mathcal{R}$ is gained for the ESL effectively interacting with the near-wall coherent structures. For oscillating periods close to the optimal value $T^+ = 30$, $\mathcal{R}$ is almost slightly dependent on δ, provided it is not too small. Indeed, when δ is very small, say $\delta^+ \leq 4$, $\mathcal{R}$ is small and nearly constant with T. For these values of δ, the spanwise motion is confined in the viscous sublayer where the turbulent activity is weak. This confirms that the laminar Stokes layer must interact with the turbulent structures that populate the

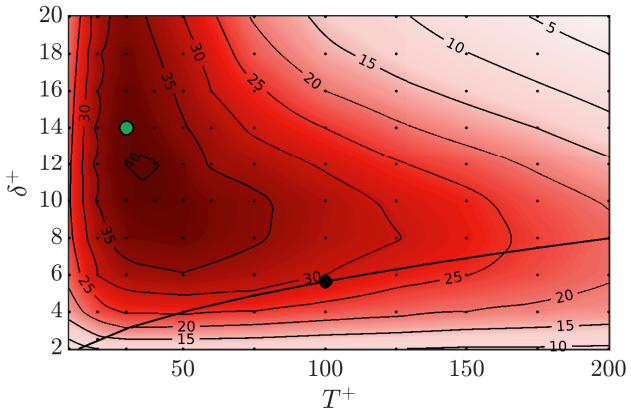

Figure 3.2: Drag reduction map in the (T, δ) two-dimensional space of parameters. The black thick line indicates the $\delta = \delta_{SL}$ constraint. The green dot identifies the point of maximum drag reduction, whereas the black dot indicates the maximum along the line $\delta = \delta_{SL}(T)$.

buffer layer to achieve drag reduction. Similarly, for small oscillating periods (say $T^+ \leq 20$), $\mathcal{R}$ is relatively small and independent from δ. In this case, the ESL is not effective to achieve drag reduction, as the oscillating period is too small compared to the flow time scales, and the resulting oscillating motion and the incoming flow are decoupled. As T increases above $T^+ > 30$, the local optimum thickness δ^+ moves towards smaller values, suggesting that with longer oscillating period the ESL is more effective when its influence remains confined closer to the wall. For large T, the optimum δ lies in the range $6 \leq \delta \leq 10$ and $\mathcal{R}$ degrades quickly at larger δ. A possible explanation of the suboptimal $\mathcal{R}$ is that for large value of both T and δ, although the ESL provides reduction of drag, it also largely perturbs the underlying turbulence in a way that the spanwise velocity can be instantaneously quite different from the imposed ESL. To quantify the amount of turbulent perturbation, we define the difference of the integral of the wall-normal profile of spanwise root mean square fluctuations between the controlled and reference cases as $\Delta w_{rms} = 100 \left(\langle w_{ESL,rms}(y) \rangle - \langle w_{0,rms}(y) \rangle \right) / \langle w_{0,rms}(y) \rangle$, where $\langle \cdot \rangle$ indicates spatial and time average. Figure 3.3 plots Δw_{rms} in the (T, δ) parameters space. As expected, for large values of both T and δ, Δw_{rms} is positive and large meaning that the turbulence in the spanwise direction is increased by the control compared to the reference case. This region corresponds to the region of lower $\mathcal{R}$ in figure 3.2, meaning that part of the positive effect of the ESL is eroded by the higher spanwise turbulence induced by the control itself. It is consist with Touber & Leschziner (2012) suggesting that sufficiently large oscillation periods are not able to disrupt the turbulent structures which lingers and regenerates in the direction of the forcing. At the same time, large δ means that the control

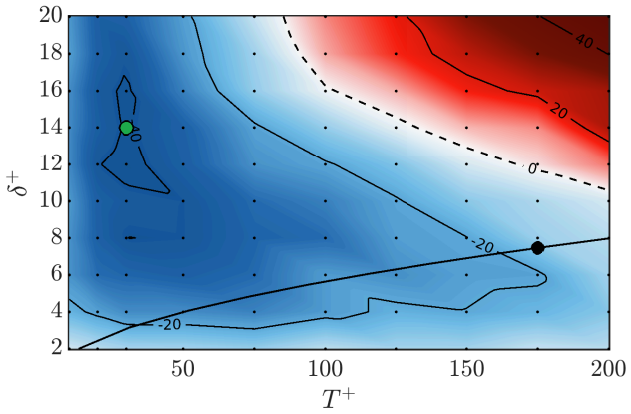

Figure 3.3: Relative difference of the spanwise fluctuations Δw_{rms} between the controlled and reference cases. The thick dashed line is for $\Delta w_{rms} = 0$ and the black thick line indicates the $\delta = \delta_{SL}$ constraint. The green dot identifies the point of maximum drag reduction, whereas the black dot indicates the maximum along the line $\delta = \delta_{SL}(T)$.

penetrates far from the wall, negatively disturbing the bulk of the flow. On the contrary, negative Δw_{rms} means that for those sets of parameters the effects of the two phenomena sum up and larger $\mathcal{R}$ performance are attained.

3.3.2 Physical interpretation of the optimum

We now relate the specific values $\delta^+_{opt} \approx 14$ and $T^+_{opt} \approx 30$, which identify the global maximum of drag reduction in the two-dimensional space of parameters, to properties of near-wall turbulence and try to shed light on the physical implications of the optimum. As highlighted in the introduction (see §3.1) for the SL, the interpretation is not unique and the different interpretations proposed in literature are herein presented and discussed in light of the present results; having decoupled δ from T, we add new perspective to the discussion.

The optimal oscillating period T_{opt} can be compared to other time scales in the turbulent flow. For example, the (statistically defined) lifetime of the dominant near-wall coherent structures is not far from T_{opt}. Quadrio & Luchini (2003) introduced and computed for $Re_\tau = 180$ the integral scale $\mathcal{T}$ of the space-time autocorrelation of velocity fluctuations along the path of maximum correlation in the space-time plane, and interpreted it as the integral lifetime of near-wall structures. We perform the same analysis at the present $Re_\tau = 400$ and measure the integral lifetime. At $y^+ = 15$, comparable to δ^+_{opt}, we measure $\mathcal{T}^+_u = 75$ for the streamwise velocity fluctuations. These value is quite near to the optimal oscillation period $T^+_{opt} \approx 30$, suggesting that the most effective forcing is the one

that hits the structures a couple of times in their lifetime. However our results of decreasing T for increasing δ are not compatible with this interpretation since the integral lifetime increases with the distance from the wall, being e.g. $\mathcal{T}_u^+ = 62$ at $y^+ = 5$ and $\mathcal{T}_u^+ = 75$ at $y^+ = 15$.

A possible alternative is to associate the optimal oscillating period T_{opt} to the characteristic timescale of the bursting cycle, for which near-wall statistics such as the space-averaged friction coefficient C_f "burst" quasi-periodically over time. This temporally limited surge is the statistical trace of an intense moment of the turbulent near-wall cycle that regenerates the near-wall structures. Jiménez (2013) measured the bursting period to be $T^+ \approx 400$, with the bursting phase lasting $T^+ \approx 100$ followed by a longer phase of quiescence. Half of the bursting phase ($T^+ \approx 50$, comparable to our $T_{opt}^+ = 30$) is taken for the eruption and growth of the burst and the remaining for its decay. The same time-scale $T^+ \approx 50$ has been measured by Blesbois *et al.* (2013) and Ricco (2004) as the regeneration time-scale of the streaks. Again, our results of decreasing T for increasing δ contradict also this interpretation, being the bursting period proportional to the distance from the wall of the structures.

Due to the convective nature of the near-wall flow, T_{opt} can be compared to the convective time scale T_c of the near-wall structures, which can be estimated looking at the convection velocity U_c. The convection velocity U_c is known to substantially differ from the local mean velocity in the near-wall region (Kim & Hussain, 1993); it is nearly constant with a value $U_c^+ \approx 10$ in the viscous sublayer, whereas it increases from the buffer layer upwards approaching the mean flow; see figure 4 of Quadrio & Luchini (2003). The increase of U_c with y translates into a decrease of T_c, as these two quantities are inversely proportional $T_c = \mathcal{L}/U_c$, with $\mathcal{L}$ being a length scale. This is consistent with our data that report a decrease of the local optimum T_{opt} as δ increases; see figure 3.2.

Following the same line of reasoning, the optimum period T_{opt}^+ can be translated into an equivalent convective streamwise length scale L_c by using U_c, and compared with characteristic length scales of the flow. By considering values of U_c in the buffer layer ($U_c^+ \approx 10 - 15$), T_{opt}^+ translates into $L_c^+ \approx 300 - 450$, which is indeed comparable with the characteristic length scale of the structures of the near wall cycle, being the quasi-streamwise vortices $\ell^+ \approx 200$ and the low-velocity streaks $\ell^+ \approx 1000$ (Jeong *et al.*, 1997).

Finally, we consider the dominant interpretation of the optimal period for the SL in terms of the wall-normal diffusion length scale δ. This view is as simple as appealing, and has been put forward very early by Baron & Quadrio (1996), who noticed that the different wall-normal average positions of low-speed streaks and streamwise vortices in the near-wall turbulence cycle enables an optimally configured Stokes layer to break their coherency and alter the relative spanwise position between them. Ricco (2004) suggested that the effectiveness of the

oscillations in reducing turbulent drag is due to a relative displacement in the spanwise direction of the low speed streaks ($y+ \lessapprox 10$) and the quasi-streamwise vortices, typically placed in the $10 \lessapprox y^+ \lessapprox 50$ layer (Robinson, 1991). This view is supported by the link between the value of drag reduction and the thickness of the generalized Stokes layer which develops over streamwise-travelling waves, quantified by Quadrio & Ricco (2011). The same view has been also purported by Touber & Leschziner (2012). The optimum value of $\delta^+_{opt} \approx 14$ is consistent with this interpretation.

3.4 Conclusion

The present work introduces a new DNS experiment aiming to provide a new approach to the study of the optimal parameters to reduce the turbulent drag through the spanwise forcing. Instead of leaving the Stokes layer naturally evolve by the spanwise harmonic oscillation of the wall, we directly enforce in the flow at each time step a SL-like spanwise velocity profile. The wall oscillation technique creates a SL described by the maximum amplitude of the oscillation A, the period of oscillation T and its thickness δ; the two latter parameters are obliged to follow the constraint $\delta_{SL} = \sqrt{\nu T/\pi}$. We remove the coupling between T and δ_{SL} to directly impose an extended Stokes layer profile (ESL) where T and δ can be varied independently. Our procedure of enforcing a velocity profile is equivalent to solve the Navier–Stokes equations with the same boundary condition of the wall oscillation approach and an additional volume forcing that is practically zero whenever the ESL reduces to the standard SL; our validation highlights a maximum deviation of 1.3% between the two techniques.

We perform a set of DNS of a fully turbulent channel flow at $Re_b = U_b h/\nu = 7000$ (corresponding to $Re_\tau = 400$ in the uncontrolled case) varying the period in the $10 \leq T^+ \leq 200$ range, while the thickness varies between $2 \leq \delta^+ \leq 20$, whereas the amplitude of the forcing is kept constant to $A^+ = 12$. Once δ and T are decoupled, the maximum drag reduction following the SL constraint $\mathcal{R} \approx 30\%$, found at $(T^+_{opt}, \delta^+) \approx (100, 6)$, shifts to the global maximum drag reduction obtained with the ESL at $\mathcal{R} \approx 40\%$, found for much smaller value of the period and larger value of the thickness, i.e. $(T^+, \delta^+) \approx (30, 14)$. The peak of drag reduction is quite broad and flat, and the value of δ_{opt} corresponds to the position of the buffer layer, where the near-wall cycle takes place, suggesting that the maximum $\mathcal{R}$ is gained for the ESL effectively interacting with the near-wall coherent structures. Instead, for $\delta^+ \lessapprox 4$ and for $T^+ \lessapprox 20$, the characteristic space and time lengths of the forcing are too small compared to the characteristic lengths of the turbulent structures of the near-wall cycle, thus they do not successfully target them. For both T and δ larger the optimum, the drag reduction performances

degrade due to the enhanced spanwise turbulent activity. We conclude that the values of the parameters $T^+ \approx 100$ and $\delta^+ \approx 6$, well known in literature to provide the maxmium $\mathcal{R}$ with the wall oscillation, do not possess a special meaning; instead designing a control which allows to decouple T and δ is able to provide a much higher $\mathcal{R}$. We discuss the dominant interpretations of the literature about the physical meaning of the optimum parameters T_{opt} and δ_{opt} in light of the present results, yet without definitely settling the issue.

The information of the optimal (δ, T) is crucial when developing alternative strategies that produce near-wall spanwise motion, without the need of moving the wall. In this case, indeed, the control gets rid of the $\delta(T) = \sqrt{T\nu/\pi}$ that limits the maximum DR attainable. Some examples may be the use of plasma actuators (Jukes & Choi, 2012), the alternation of slip and no-slip stripes (Hasegawa *et al.*, 2011), sinusoidal riblets (Peet *et al.*, 2008), dimples (Gattere *et al.*, 2022*b*), elettroactive polymers combined with an electromagnetic actuator (Gouder *et al.*, 2013). Also, the strategy we propose in this work opens the possibility of further investigating the way the spanwise motion interacts with the near-wall turbulence. In fact, once one gets rid of the oscillating wall one is not any more limited on the SL but may investigate the effects of profiles of different shape. However as highlighted, for profiles which largely disturb the bulk of the flow, e.g. the ESL with both large T and δ, the higher turbulence induced by the control negatively affects the drag reduction performances. The optimal control parameters which target the physical mechanisms of the near-wall turbulent could be larger than $T^+ \approx 30$ and $\delta^+ \approx 14$, but they might not be able to provide a larger drag reduction because of the opposed negative effect that increases turbulence.

Turbulent skin-friction drag reduction via spanwise forcing at high Reynolds number

The content of this Paper is currently under review
for the *Journal of Fluid Mechanics* and published on ArXiv as
Gatti, D., Quadrio, M., Chiarini A., Gattere, F. & Pirozzoli, S.
Turbulent skin-friction drag reduction
via spanwise forcing at high Reynolds number.
Minor editing has been done for formatting purposes.

Turbulent skin-friction drag reduction via spanwise forcing at high Reynolds number

Abstract

We address the Reynolds-number dependence of the turbulent skin-friction drag reduction induced by streamwise-travelling waves of spanwise wall oscillations. The study relies on direct numerical simulations of drag-reduced flows in a plane open channel at friction Reynolds numbers in the range $1000 \leq Re_\tau \leq 6000$, which is the widest range considered so far in simulations with spanwise forcing. Our results corroborate the validity of the predictive model proposed by Gatti & Quadrio (2016): regardless of the control parameters, the drag reduction decreases monotonically with Re, at a rate that depends on the drag reduction itself and on the skin-friction of the uncontrolled flow. We do not find evidence in support of the results of Marusic *et al.* (2021), which instead report by experiments an increase of the drag reduction with Re in turbulent boundary layers, for control parameters that target low-frequency, outer-scaled motions. Possible explanations for this discrepancy are provided, including obvious differences between open channel flows and boundary layers, and possible limitations of laboratory experiments.

4.1 Introduction

Transverse near-wall forcing as a means to mitigate skin-friction drag in turbulent flows has gathered significant attention, owing to its potential for substantial environmental and economic benefits (Quadrio, 2011; Ricco *et al.*, 2021). After the seminal work on spanwise wall oscillations by Jung *et al.* (1992), three decades of research efforts have led to important progress; however, several crucial factors still

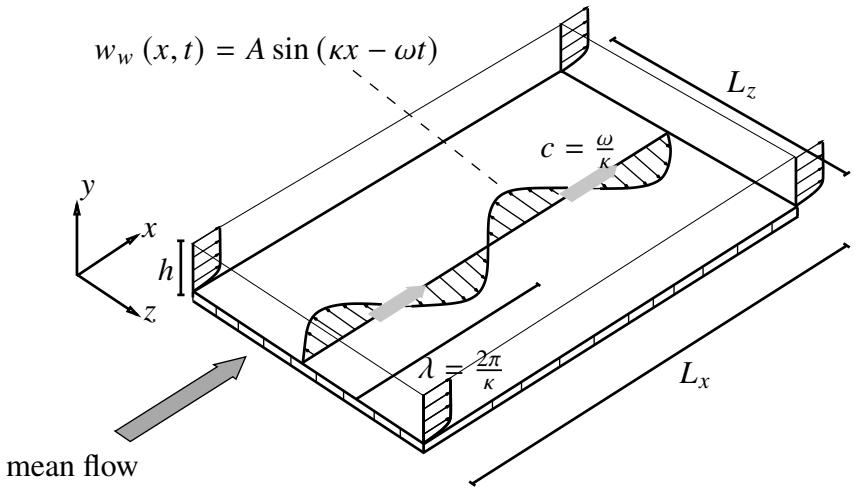

Figure 4.1: Schematic of a turbulent open channel flow actuated with streamwise-travelling waves of spanwise wall velocity with amplitude A, streamwise wavenumber κ and angular frequency ω. Here, λ is the streamwise wavelength; c is the wave phase speed; and L_x, $L_y = h$ and L_z are the dimensions of the computational domain in the streamwise, wall-normal and spanwise direction, respectively.

hinder the deployment of spanwise forcing in technological settings. The major challenge resides in devising viable and efficient implementations of the typically idealised near-wall forcing, but other concerns exist, including the decreasing effectiveness of drag reduction with increasing Reynolds numbers (Re).

To date, the Reynolds dependence of skin-friction drag reduction has mostly been studied in the context of streamwise-travelling waves of spanwise wall velocity (StTW, Quadrio *et al.*, 2009), a specific form of transverse forcing characterised by its comparatively large potential for drag reduction with modest energy expenditure. StTW are described by

$$w_w(x,t) = A\sin(\kappa x - \omega t)\,, \tag{4.1}$$

where w_w is the spanwise (z) velocity component at the wall, A is the maximum wall velocity and thus a measure of the amplitude of the spanwise forcing, κ is the streamwise wavenumber, ω is the angular frequency, and x and t are the streamwise coordinate and the time. The forcing, sketched in figure 4.1, consists of streamwise-modulated waves of spanwise velocity at the wall, with wavelength $\lambda = 2\pi/\kappa$ and period $T = 2\pi/\omega$. The waves travel along the streamwise direction with phase speed $c = \omega/\kappa$, either downstream ($c > 0$) or upstream ($c < 0$) with respect to the mean flow direction. The forcing described by equation (4.1) includes

the two special cases of spatially uniform spanwise wall oscillations (Quadrio & Ricco, 2004) for $\kappa = 0$, and steady waves (Viotti *et al.*, 2009) for $\omega = 0$. With the appropriate set of control parameters, StTW have been shown to yield considerable drag reduction in a series of numerical experiments regarding channel and pipe flows (Quadrio *et al.*, 2009; Gatti & Quadrio, 2013; Hurst *et al.*, 2014; Gatti & Quadrio, 2016; Liu *et al.*, 2022; Rouhi *et al.*, 2023; Gallorini & Quadrio, 2024) and boundary layers (Skote *et al.*, 2015; Skote, 2022), as well as in laboratory experiments (Auteri *et al.*, 2010; Bird *et al.*, 2018; Chandran *et al.*, 2023). Besides canonical flows, including the compressible and supersonic regimes (Gattere *et al.*, 2024), StTW have been applied to more complex flows ranging from channels with curved walls (Banchetti *et al.*, 2020), to rough boundary layers (Deshpande *et al.*, 2024, although restricted to spatially uniform spanwise wall oscillation) and transonic airfoils with shock waves (Quadrio *et al.*, 2022), showing that local skin-friction drag reduction can be exploited to also reduce the pressure component of the aerodynamic drag.

Understanding how the Reynolds number affects drag reduction by StTW is a particularly challenging goal for three main reasons. First, a sufficiently wide portion of a huge parameter space must be explored, which even in simple canonical flows includes the four parameters $\{A, \kappa, \omega; Re\}$, and poses a great challenge to numerical and laboratory experiments.

A second complication is the choice of an appropriate figure of merit for drag reduction. Typically, the drag reduction rate $\mathcal{R}$ is defined as

$$\mathcal{R} = 1 - \frac{C_f}{C_{f_0}}, \tag{4.2}$$

i.e. as the control-induced relative change of the skin-friction coefficient C_f (Kasagi *et al.*, 2009). In equation (4.2) and in the remainder of this manuscript, the subscript 0 denotes quantities measured in the reference uncontrolled flow. Specifically, C_f is defined as $C_f = 2\tau_x/(\rho U_b^2)$; τ_x is the mean streamwise wall shear stress, U_b the bulk velocity, and ρ the fluid density. However, as observed by Gatti & Quadrio (2016), the quantity $\mathcal{R}$ defined by equation (4.2) is inherently Re-dependent, owing to the Re-dependence of C_f and C_{f_0}. This is long known to be the case for the flow over rough surfaces (Nikuradse, 1933; Jiménez, 2004), as well as for other flow control techniques relying on near-wall turbulence manipulation such as riblets (Luchini, 1996; Spalart & McLean, 2011). Choosing a figure of merit which eliminates this trivial dependency on the Reynolds number is crucial to describe properly the Re-effect on drag reduction.

Third, the wall shear stress generally differs in the reference (τ_{x_0}) and controlled (τ_x) channel flows, unless they are driven by the same pressure gradient (as done for example by Ricco *et al.*, 2012); the viscous scaling, hence, becomes ambiguous. As noted by Quadrio (2011), this results in two possible viscous normalisations

of the controlled flow: the first, denoted with the superscript '+', relies on the reference friction velocity $u_{\tau_0} = \sqrt{\tau_{x_0}/\rho}$; the second, denoted with the superscript '$*$', is based on the actual friction velocity $u_\tau = \sqrt{\tau_x/\rho}$. Similarly, two different friction Reynolds numbers, $Re_{\tau_0} = u_{\tau_0} h/\nu$ and $Re_\tau = u_\tau h/\nu$ can be defined depending on the choice of the friction velocity. Here, h describes the half-height of a channel or the depth of an open channel, and ν is the fluid kinematic viscosity. While the actual viscous scaling is the only sensible choice for the drag-reduced flow (Gatti & Quadrio, 2016), the reference scaling is necessary when the wall friction of the drag-reduced flow is not known yet.

Gatti & Quadrio (2016), indicated also as GQ16 hereinafter, circumvented these difficulties by designing a campaign of several thousands direct numerical simulations (DNS) of turbulent channel flows. Inspired by similar studies on rough walls (see for example Leonardi *et al.*, 2015), they limited the otherwise prohibitive computational cost by choosing relatively small computational domains (Jiménez & Moin, 1991; Flores & Jiménez, 2010) for most of the study. At the expense of a residual domain-size dependence of the results, which cancels out in large part when observing the difference between controlled and uncontrolled flows, GQ16 generated a large dataset, along with a more limited number of simulations in wider domains to verify the accuracy of the results. This approach enabled not only the inspection of a large portion of the $\{A, \kappa, \omega\}$-space at $Re_{\tau_0} = 200$ and 1000, but also the transfer of the dataset between viscous '+' and '$*$' units via interpolation, allowing to assess the results in both scalings. Thanks to their comprehensive database (available as Supplementary Material to their paper), Gatti & Quadrio (2016) challenged the then-current belief that skin-friction drag reduction was bound to decrease quickly with Re. They demonstrated that the drag reduction effect by spanwise forcing becomes in fact constant with Re, provided that it is not expressed via $\mathcal{R}$ (equation (4.2)), that is *per se* Re-dependent, but through the Reynolds number-invariant parameter ΔB^*. The quantity ΔB^* expresses the main effect of the StTW, which is to induce a change of the additive constant in the logarithmic law for the mean velocity profile

$$U^*(y^*) = \frac{1}{k} \ln y^* + B_0^* + \Delta B^* , \tag{4.3}$$

where k is the von Kármán constant, B_0^* is the additive constant in the reference channel flow, and $B^* = B_0^* + \Delta B^*$ is the additive constant of the controlled flow. The independency of ΔB^* upon Re is a common feature of all turbulence manipulations whose action is confined to the near-wall region. In these cases the outer turbulence simply reacts to a wall layer with different drag (Gatti *et al.*, 2018), as well known, for instance, in the context of drag-reducing riblets (Luchini, 1996; Garcia-Mayoral & Jiménez, 2011; Spalart & McLean, 2011) and drag-increasing roughness (Clauser, 1954; Hama, 1954).

Under the assumption that ΔB^* is a function of the control parameters $\{A^*, \kappa^*, \omega^*\}$, but not of the Reynolds number, Gatti & Quadrio (2016) derived the following modified friction relation (hereinafter called GQ model)

$$\Delta B^* = \sqrt{\frac{2}{C_{f_0}}}\left[(1-\mathcal{R})^{-1/2} - 1\right] - \frac{1}{2k}\ln\left(1-\mathcal{R}\right) , \tag{4.4}$$

where the Re-dependence is not explicit, but rather embedded in C_{f_0}. Provided the function $\Delta B^*\left(A^*, \kappa^*, \omega^*\right)$ is measured at a sufficiently large Re for the log law in equation (4.3) to hold, the GQ model predicts $\mathcal{R}$ at any arbitrary value of Re. According to equation (4.4), $\mathcal{R}$ is always expected to decrease with Re for any combination of the control parameters, but at much lower rate than suggested by previous studies (Touber & Leschziner, 2012; Gatti & Quadrio, 2013; Hurst *et al.*, 2014), so that significant drag reduction can be still achieved at Reynolds numbers typical of technological applications. For instance, for StTW GQ16 estimated possible drag reduction of 30% with $A^+ = 12$ at $Re_{\tau_0} = 10^5$.

The GQ16 study is affected by two limitations. First, $Re_{\tau_0} = 1000$, the largest Re considered in their study, may still be not enough for ΔB^* to become completely Re-independent: GQ16 suggested that at least $Re_{\tau_0} = 2000$ should be considered. Second, the small effect of the restricted computational box sizes on the quantification of $\mathcal{R}$ could in principle bias the extrapolation to higher Re. Nonetheless, the GQ model passed validation tests against previous (Touber & Leschziner, 2012; Hurst *et al.*, 2014) and later literature data. For instance, Rouhi *et al.* (2023) employed large eddy simulations (LES) to study drag reduction by StTW in open channel flows at $Re_{\tau_0} = 945$ and $Re_{\tau_0} = 4000$. They explored the parameter space within the range $\kappa^+ \in [0.002, 0.02]$ and $\omega^+ \in [-0.2, 0.2]$, at fixed $A^+ = 12$. This is to be compared with $\kappa^+ \in [0, 0.05]$ and $\omega^+ \in [-0.5, 1]$ addressed by Gatti & Quadrio (2016), who also considered various amplitudes $A^+ \in [2, 20]$. The study of Rouhi *et al.* (2023) is however limited by the use of large eddy simulations (LES), in which part of the small-scale turbulence physics involved in drag reduction is modelled, and by the domain size ($L_x = 2.04h$, $L_z = 0.63h$ at $Re_{\tau_0} = 4000$), which is comparable to the restricted domain size ($L_x = 1.35h$, $L_z = 0.69h$ at $Re_{\tau_0} = 1000$) considered by Gatti & Quadrio (2016), despite the larger Re_{τ_0}. Rouhi *et al.* (2023) confirmed that the GQ model predicts very well their drag reduction data, with deviations in the order of 2%, for all StTW control parameters sufficiently far from those yielding drag increase.

Marusic *et al.* (2021) and Chandran *et al.* (2023) studied drag reduction via backward-travelling ($c < 0$) StTW. Their experimental study was carried out in a zero pressure gradient turbulent boundary layer up to the largest values of Re investigated so far, $Re_\tau = 15000$. By extending to the plane geometry the actuation strategy used by Auteri *et al.* (2010) in a cylindrical pipe, they implemented the

ideal forcing of equation (4.1) by dividing a portion of the wall into a series of forty-eight slats, long 5 cm each, so that each six consecutive slats constitute a single wavelength with fixed $\lambda = 0.3$ m. The slats move in the spanwise direction at a fixed half-stroke d, resulting in a frequency-dependent maximum spanwise velocity $A = \omega d$. As a consequence in those experiments the amplitude and period of the oscillations could not be varied independently. With d and λ constant in physical units, the range of investigated parameters shifts towards smaller κ^+, ω^+ and A^+ as Re_{τ_0} increases. The authors observed, for the first time, $\mathcal{R}$ to increase with Re (see figure 3*e* of Marusic *et al.*, 2021), and explained it with the particularly slow timescale $T^+ = 2\pi/\omega^+ < -350$ of their forcing, which was meant to target the large inertial, outer-scaled structures of turbulence (Deshpande *et al.*, 2023), whose importance increases with Re.

Despite the promising results, these studies also have shortcomings. With d and λ constant in physical units, which is unavoidable in laboratory experiments, the control parameters could not be kept constant in either '+' or '$*$' viscous units while varying Re_{τ_0}. In particular, the fixed wavelength leads to a κ^+ that decreases with Re. Furthermore, the effect of ω and A cannot be addressed separately. This precludes the investigation of the full space of the control parameters: for instance large values of ω^+ at low A^+ cannot be tested. Lastly, the key observation that $\mathcal{R}$ increases with Re relies on the joint observation of low-Re LES data by Rouhi *et al.* (2023) obtained in an open channel flow, and high-Re experimental data by Marusic *et al.* (2021) in a boundary layer, thus bringing together different methods and flow configurations.

The present research fills these gaps in the existing literature by leveraging a novel DNS dataset of turbulent open channel flow, to accurately quantify the Reynolds number effects on the drag-reducing performance of StTW. The computational domain adopted in the present simulations is large enough to properly account for all relevant scales of turbulence, including the large inertial scales. The considered Reynolds numbers, ranging from $Re_{\tau_0} = 1000$ to $Re_{\tau_0} = 6000$, are large enough to minimise the low-Re effects, matching some of the experimental data points by Chandran *et al.* (2023). The dataset is further designed to address the Reynolds-number scaling of drag reduction in both viscous and outer units independently, by considering the same flow configuration and by using the same numerical method for all Re.

The paper is organised as follows. After this Introduction, §4.2 describes the computational procedure and the simulation parameters used to produce the DNS dataset. In §4.3 the effect of the Reynolds number is analysed in terms of both drag reduction and power budgets, and compared to existing literature. Finally, concluding arguments are given in §4.4.

Re_b	Re_{τ_0}	N_{cases}	L_x/h	L_z/h	$N_x \times N_y \times N_z$	Symbol
20000	996.7	71	$6\pi h$	$2\pi h$	$2304 \times 165 \times 1536$	▲
43650	1994.1	62	$6\pi h$	$2\pi h$	$4608 \times 265 \times 3072$	▼
68600	3008.8	7	$6\pi h$	$2\pi h$	$6912 \times 355 \times 4608$	♦
148000	6012.6	3	$6\pi h$	$2\pi h$	$13312 \times 591 \times 9216$	●

Table 4.1: Details of the direct numerical simulations of open channel flows (including domain size and discretization) modified by StTW, grouped in sets of N_{cases} simulations performed at a constant value of bulk Reynolds number $Re_b = U_b h/\nu$. The last column indicates the color and symbol employed in the following figures to represent each set of simulations.

4.2 Methods and procedures

A new DNS dataset of incompressible turbulent open-channel flows (see figure 4.1) is used to study the effect of the Reynolds number on the reduction of the turbulent friction drag achieved by StTW. The open channel flow, i.e. half a channel flow with a symmetry boundary condition at the centreplane, is considered here to reduce the computational cost without affecting the drag reduction results; indeed, it was often used in the past, including e.g. the similar studies by Yao *et al.* (2022*b*), Pirozzoli (2023) and Rouhi *et al.* (2023). The StTW are applied as a wall boundary condition for the spanwise velocity component after equation (4.1). Periodic boundary conditions are applied in the homogeneous streamwise and spanwise directions, no-slip and no-penetration boundary conditions are used for the longitudinal and wall-normal components at the bottom wall; free slip is used at the top boundary. The computational setup is identical to the study of Pirozzoli (2023), in which open-channel flow was studied in the absence of flow control. The solver relies on the classical fractional step method with second-order finite differences on a staggered grid (Orlandi, 2006). The Poisson equation resulting from the divergence-free condition is efficiently solved via Fourier expansion in the periodic directions (Kim & Moin, 1985). The governing equations are advanced in time starting from the initial condition of a statistically stationary, uncontrolled turbulent open channel flow by means of a hybrid third-order, low-storage Runge–Kutta algorithm, whereby the diffusive terms are handled implicitly. Statistical averaging, indicated hereinafter as $\langle\cdot\rangle$, implies averaging in time and along the two homogeneous directions.

Four sets of simulations, whose details are listed in table 4.1, are run at prescribed values of the bulk Reynolds number $Re_b = U_b h/\nu$; the bulk velocity is kept constant at every time step as described in Quadrio *et al.* (2016*a*). Each set comprises one reference simulation, in which the wall is steady, and a variable

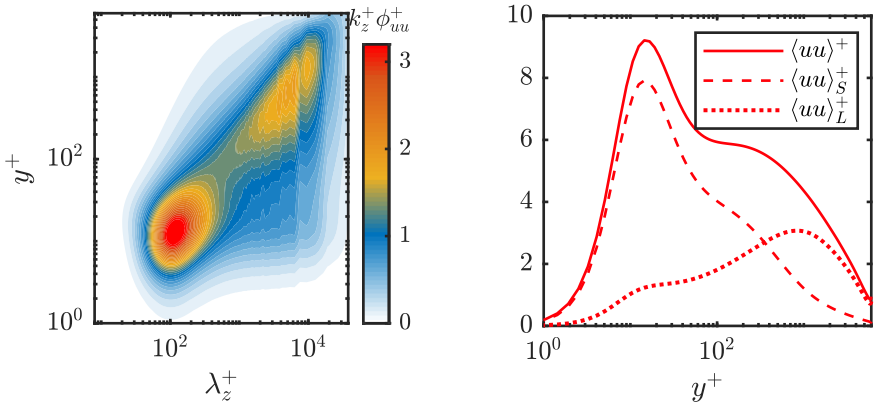

Figure 4.2: Statistics of streamwise velocity fluctuations for the reference simulation at $Re_{\tau_0} = 6000$: (left) spanwise premultiplied spectra $k_z^+\phi_{uu}^+$; (right) streamwise variance $\langle uu\rangle^+$ with its large-scale $\langle uu\rangle_L^+$ and small-scale $\langle uu\rangle_S^+$ contributions. Large scales are defined as those for which $2\pi/k_z > 0.5h$.

number of cases with StTW at different values of $\{A, \kappa, \omega\}$. In the following, we will refer to each simulation set via its (nominal) value of Re_{τ_0}; the actual values of Re_τ vary throughout simulations of each set, as a consequence of the wall actuation at constant U_b.

All DNS are carried out in a domain with $L_x = 6\pi h$ and $L_z = 2\pi h$, which is much larger than what has been adopted by Rouhi *et al.* (2023) and GQ16 at similar values of Re, but a bit smaller than the domain used by Yao *et al.* (2022*b*). Whereas weak longitudinal eddies may be not resolved, a box sensitivity study carried out by Pirozzoli (2023) showed that the practical impact on the leading-order flow statistics and on the spanwise spectra is extremely small.

Figure 4.2 indeed supports the adequacy of the present computational box by analysing the streamwise velocity fluctuations of the reference open channel flow at $Re_{\tau_0} = 6000$, i.e. the largest Reynolds number considered in the present study. Figure 4.2 (left) shows the spanwise pre-multiplied spectrum $k_z^+\phi_{uu}^+$, where k_z is the spanwise wavenumber and ϕ_{uu} is a component of the velocity spectrum tensor, with a clear outer peak visible at $\lambda_z \approx h$. Figure 4.2 (right) shows the variance $\langle uu\rangle^+$ of the streamwise velocity, split into the large-scale $\langle uu\rangle_L^+$ and small-scale $\langle uu\rangle_S^+$ contributions. The large-scale contribution is obtained by integrating the spectrum only for wavelengths $\lambda_z > 0.5h$ as suggested by Bernardini & Pirozzoli (2011), Dogan *et al.* (2019) and Yao *et al.* (2022*b*). With this definition, the large-scale fluctuations are responsible for 12% of the total variance in the vicinity of the wall, and for as much as 85% at the free-slip surface. Moreover, it should be noted that the longest travelling wave that we have tested at the highest Reynolds number ($Re_{\tau_0} = 6000$) is fourteen times shorter than the domain length, thus allowing

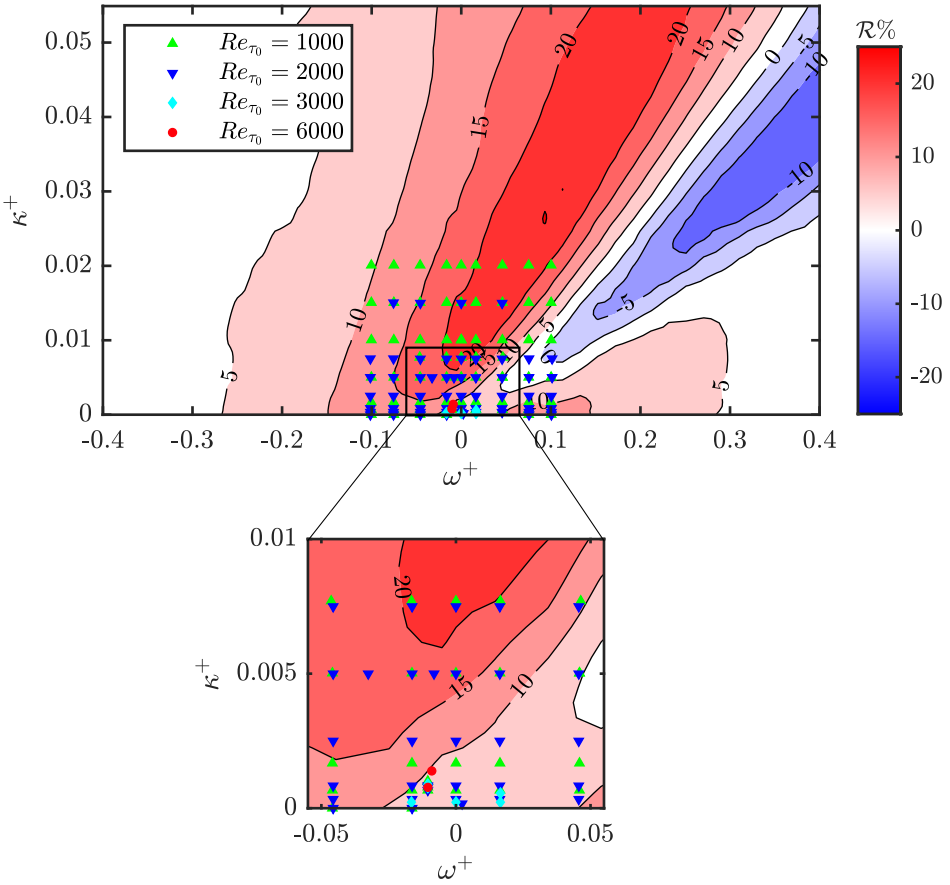

Figure 4.3: Portion of the parameter space spanned in the present study overlaid to the drag reduction map by GQ16 computed at $A^+ = 5$. Each symbol corresponds to one simulation at the Reynolds number encoded by its shape/color, as described by the legend.

subharmonic effects, if present, to be properly resolved.

The spatial resolution of the simulations is designed based on the criteria discussed by Pirozzoli & Orlandi (2021). In particular, the collocation points are distributed in the wall-normal direction y so that approximately thirty points are placed within $y^+ \leq 40$, with the first grid point at $y^+ < 0.1$. The mesh is stretched in the outer wall layer with the mesh spacing proportional to the local Kolmogorov length scale, which there varies as $\eta^+ \approx 0.8(y^+)^{1/4}$ (Jiménez, 2018). A mild refinement towards the free surface is used in order to resolve the thin layer in which the top boundary condition dampens the wall-normal velocity fluctuations. The grid resolution in the wall-parallel directions is set to $\Delta x^+ \approx 8.5$ and $\Delta z^+ \approx 4.0$ for all the flow cases. Note that the resolution is finer in actual viscous units in all cases with drag reduction.

Figure 4.3 shows at a glance the range of the StTW parameters addressed in the present study for the simulation sets at $Re_{\tau_0} = \{1000, 2000, 3000, 6000\}$. This is the broadest range of Re considered so far in numerical simulations with spanwise wall forcing.

The portion of the $\{\kappa^+, \omega^+\}$-space spanned in the present study is smaller than the one addressed in GQ16. In fact, we limit ourselves to considering $\kappa^+ \leq 0.02$ and $|\omega^+| \leq 0.1$, which is now known to be the most interesting part of the parameter space, where the maxima of drag reduction $\mathcal{R}$ and net saving $\mathcal{S}$ are expected.

The control parameters have been selected according to the following guiding principles.

(1) The intent to further scrutinize the validity of the results by GQ16, obtained in constrained computational domains, led us to consider a wider portion of the StTW parameter space at $Re_{\tau_0} = 1000$, the highest value considered in their study.

(2) GQ16 observed that ΔB^* may still retain residual dependence on Re at their highest value of $Re_{\tau_0} = 1000$, and suggested that at least $Re_{\tau_0} = 2000$ is needed for a Re-independent measure. Therefore, the same region of the parameter space considered above in point (1) is also considered at $Re_{\tau_0} = 2000$.

(3) Marusic *et al.* (2021) reported for the first time a drag reduction that increases with Re for small values of κ^+ and ω^+, in particular for $\kappa^+ = 0.0008$ (i.e. $\lambda^+ \approx 8000$), $\omega^+ = -0.0105$ (i.e. $T^+ \approx -600$) and $A^+ \approx 5$ (in fact their A^+ varies slightly across the Re-number range), as shown in figure 3*e* of their paper. We have added this combination of $\{\kappa^+, \omega^+\}$ to all simulations sets, in order to verify the increase of $\mathcal{R}$ with Re. This is one of the two controlled cases we have carried out at $Re_{\tau_0} = 6000$. The second case, with $\kappa^+ = 0.0014$, $\omega^+ = -0.009$ and $A^+ = 2.5$, matches exactly one of the cases considered experimentally by Chandran *et al.* (2023), at the same value of $Re_{\tau_0} = 6000$.

(4) All controlled simulations are performed at $A^+ = 5$ for two reasons: first, this value of A^+ is representative of the amplitude range in the experiments by Marusic *et al.* (2021) for the case discussed at point (3); second, this value is close to $A^+ \approx 6$ at which GQ16 measured the maximum of net power saving $\mathcal{S}$. By adopting this value of A^+ we can verify whether positive $\mathcal{S}$ can also be achieved at higher Re.

This results in the combination of the control parameters shown in figure 4.3, and listed in tables from 4.2, 4.3, 4.4 and 4.5 of appendix 4.5 together with the main

results. As will be clarified in the following, understanding the Re-dependence of $\mathcal{R}$ and $\mathcal{S}$ requires accurate estimation of the mean wall friction, which we guarantee by monitoring statistical uncertainty via the method described by Russo & Luchini (2017), as shown in figures 4.6 and 4.9. Statistics are accumulated for at least $10h/u_{\tau_0}$ time units after the initial transient, during which the control leads the flow towards a reduced level of drag.

4.3 Results

The outcomes of the present study are presented following the guiding principles outlined in §4.2. First, we present drag reduction maps at $Re_{\tau_0} = 1000$ and 2000 and use them to provide ultimate validation of the GQ16 results. Second, we evaluate ΔB^* at $Re_{\tau_0} = 2000$ and verify the Re-independence of this drag reduction metric. Third, drag reduction is reported up to $Re_{\tau_0} = 6000$ for the same actuation parameters for which Marusic *et al.* (2021) observed drag reduction increase with Re. Finally, the possibility to achieve net power savings at high Re is discussed.

4.3.1 Maps of $\mathcal{R}$: validity of the results by GQ16

Figure 4.4 compares the present drag reduction results at $Re_{\tau_0} = 1000$ and $Re_{\tau_0} = 2000$ with the data by GQ16, which need to be transferred to the present values of Re_{τ_0}. The procedure involves starting from their $\mathcal{R}$ and C_{f_0} data, then using the GQ model (equation 4.4 with $k = 0.39$; GQ16 showed that the specific value of k in the range 0.385–0.4 does not significantly affect the results) to compute ΔB^*. The resulting cloud of ΔB^* data points at discrete $\{A^+, \kappa^+, \omega^+\}$ values is linearly interpolated on a Cartesian grid spanning the $\{\kappa^+, \omega^+\}$ space at the value of $A^+ = 5$ considered in the present study. Finally, ΔB^* is again converted back to $\mathcal{R}$ values via the GQ model, now with the values of C_{f_0} corresponding to $Re_{\tau_0} = 1000$ and $Re_{\tau_0} = 2000$.

The comparison shows excellent agreement between the two datasets. This finding suggests very weak sensitivity of StTW actuation on the flow geometry (open channel vs. closed plane channel), and further strengthens the reliability of the GQ16 data. In fact, due to their limited domain size, GQ16 had no data for $0 < \kappa^+ < 0.005$, but even there the new data compare very well with the GQ16 map. The maximum difference between the present and GQ16 datasets evaluated across the interpolated maps shown in figure 4.4 is only 2.5%, and the standard deviation is 0.8%. The agreement shows that no measurable direct effect of large-scale turbulent structures on $\mathcal{R}$ exists at these values of Re_{τ_0} other than their possible contribution to C_{f_0}, which is already accounted for by the GQ model.

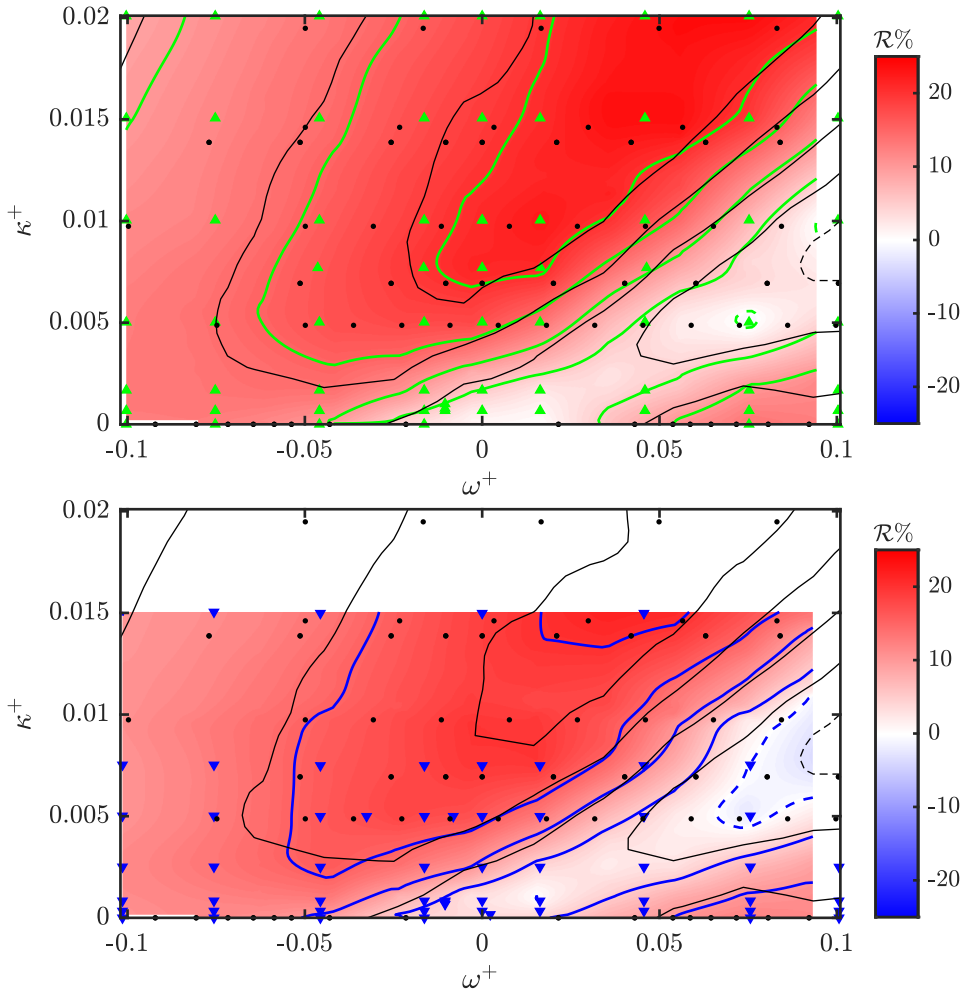

Figure 4.4: Maps of drag reduction ($\mathcal{R}$) as a function of actuation parameters (ω^+, κ^+), at $Re_{\tau_0} = 1000$ (top) and $Re_{\tau_0} = 2000$ (bottom). The colormap, the contour lines and symbols colored after table 4.1 refer to the present data, whereas the black contour lines and symbols refer to the data by GQ16, which at $Re_{\tau_0} = 2000$ are obtained from extrapolation through GQ model (4.4). The contour lines are every 5% of $\mathcal{R}$, dashed lines mark the $\mathcal{R} = 0$ iso-line.

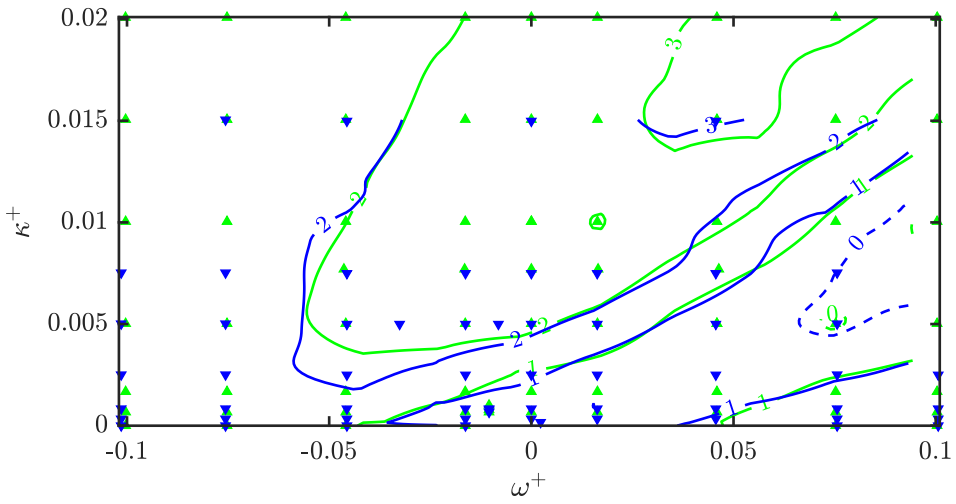

Figure 4.5: Maps of ΔB^* as a function of actuation parameters (ω^+, κ^+) at $Re_{\tau_0} = 1000$ (——) and $Re_{\tau_0} = 2000$ (——). The symbols are colored after table 4.1 and show the parameters of each simulation underlying the map interpolation shown in the figure. Contours are shown in unit intevals, the dashed lines marking the $\Delta B^* = 0$ iso-line.

4.3.2 Maps of ΔB^*: validity of the GQ model

The GQ model relies on the hypothesis that, provided Re is high enough for the logarithmic law (4.3) to describe well the mean velocity profile, the quantity ΔB^* is a function of the control parameters only, and thus independent of the Reynolds number. This hypothesis is here tested using the ΔB^* maps for the DNS set at $Re_{\tau_0} = 1000$ and 2000. The maps are generated by applying the GQ model with the corresponding values of C_f, C_{f_0} and $\mathcal{R}$. The results, reported in figure 4.5, show maximum change of ΔB^* across Re of only 0.36, with standard deviation 0.10. These values can be considered quite small, given that the maximum statistical uncertainty on the change of ΔB^* at 95% confidence level is 0.24 across the map of figure 4.5, and the mean absolute value is 0.17. This result thus confirms that the drag reduction effect barely changes with Re, once it is expressed in terms of ΔB^*.

This additionally indicates that $Re_{\tau_0} = 1000$ is sufficient to obtain a reasonably Re-independent estimate of ΔB^*. This observation is also supported by the good agreement between the GQ16 data at $Re_{\tau_0} = 1000$ and the results by Rouhi *et al.* (2023) obtained up to $Re_{\tau_0} = 4000$ in relatively small domains.

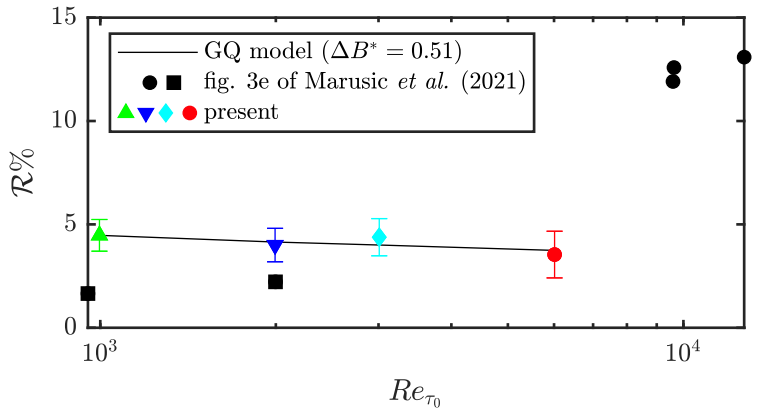

Figure 4.6: Drag reduction rate ($\mathcal{R}$) as function of the reference friction Reynolds number (Re_{τ_0}) for backward-travelling wave with parameters $A^+ = 5$, $\kappa^+ = 0.00078$ and $\omega^+ = -0.0105$, close to the conditions considered by Marusic *et al.* (2021), i.e. $A^+ \approx 5$, $\kappa^+ \approx 0.0008$ and $\omega^+ \approx -0.0105$ (in their laboratory experiment the viscous-scaled parameters vary slightly with Re). The present results are denoted with coloured symbols (see table 4.1); experimental data by Marusic *et al.* (2021) are black solid circles, while squares denote their LES numerical data; the straight line is the prediction of the GQ model (4.4) corresponding to $\Delta B^* = 0.51$ and to the values of C_{f_0} obtained from the uncontrolled simulations at the respective value of Re_{τ_0}. The error bars have been determined as described in §4.2, corresponding to a 95% confidence level.

4.3.3 Monotonicity of $\mathcal{R}$ with Re

The GQ model predicts that $\mathcal{R}$ decreases monotonically with Re, however more slowly than the power-law decrease assumed in early studies (Choi *et al.*, 2002; Quadrio & Ricco, 2004; Touber & Leschziner, 2012). The decrease rate is less at higher Re and for smaller $\mathcal{R}$. Ample numerical and experimental evidence so far, including the results of the present study, support the predictions of the GQ model.

Contrasting evidence that $\mathcal{R}$ may instead increase with Re has been recently provided from the combined laboratory and numerical efforts of Marusic *et al.* (2021). As shown in figure 3*e* of their paper, they found that $\mathcal{R}$ obtained by backward-travelling waves at small values of κ^+ and ω^+, namely $\kappa^+ = 0.0008$ and $\omega^+ = -0.0105$, increases from 1.6% at $Re_{\tau_0} \approx 1000$, as measured numerically in large-eddy simulation (LES) of open channel flow, up to 13.1% at $Re_{\tau_0} \approx 12800$, as measured experimentally in a turbulent boundary layer. Since the actuator employed in their experiments yields a wave with a frequency-dependent amplitude and constant wavelength in physical units (30 cm), those authors could not exactly maintain the same value of viscous-scaled control parameters across the considered Reynolds number range. Specifically, the amplitude increased from $A^+ = 4.6$ at $Re_\tau = 9000$ to $A^+ = 5.7$ at $Re_\tau = 12800$ (see table 1 in Chandran *et al.*, 2023). Furthermore, although the original figure 3*e* of Marusic *et al.* (2021) reports a constant value of $\kappa^+ = 0.0008$ at all Re, we cannot reconcile it with the actuator wavelength being fixed in physical units for the experimental points.

In the present work, we verify this contrasting evidence by studying the Re-dependence of $\mathcal{R}$ across the largest range of Reynolds number tested so far via DNS. For this purpose, we consider StTW actuation at $Re_{\tau_0} = 1000$, 2000, 3000 and 6000, with control parameters selected to match as closely as possible those reported in figure 3*e* of Marusic *et al.* (2021), namely $\kappa^+ = 0.00078$ and $\omega^+ = -0.0104$. The wave amplitude is set to $A^+ = 5$, midway between the range of variation in their experiments. Figure 4.6 compares our numerical results with the numerical and experimental results of Marusic *et al.* (2021). Our measurements still fit very well the prediction of the GQ model, and confirm an overall decreasing trend of $\mathcal{R}$ with Re.

To verify whether the differences observed in figure 4.6 are due to the different Reynolds number range considered here and by Marusic *et al.* (2021), we advocate the work of Chandran *et al.* (2023). Those authors extended the experimental database of Marusic *et al.* (2021) with additional data points, some of which at $Re_{\tau_0} \approx 6000$, i.e. the highest Reynolds number considered in the present study. Hence, we have precisely reproduced their actuated flow case with $\left\{A^+, \omega^+, \kappa^+, Re_{\tau_0}\right\} = \{2.5, -0.009, 0.0014, 6000\}$, the remaining differences being the flow configuration (open channel vs. boundary layer), as well as actuation details (ideal harmonic actuation in numerical simulation vs. spatially discretised

wave in experiment). This case also falls within the range of potential use for outer-scaled actuation according to Deshpande *et al.* (2023), due to the comparatively large actuation period $T^+ = -700$ and wavelength $\lambda^+ \approx 4500$, similar to the case presented in figure 4.6. A drag reduction of $\mathcal{R} = 2.3\% \pm 1.1\%$ is measured here, to be compared with $\mathcal{R} = 6\%$ measured experimentally by Chandran *et al.* (2023). This finding hints at systematic differences between the present numerical simulations and the laboratory experiments of Marusic *et al.* (2021) and Chandran *et al.* (2023). We reiterate that this is possibly due to irreducible differences in the flow and wall actuation setups, or even to the extreme challenges posed by laboratory experiments targeting such complex drag reduction strategies. We will go back to this important issue in §4.4. For the moment, the present data corroborate the expectation that $\mathcal{R}$ decreases with Re at the rate predicted by the GQ model.

4.3.4 Net power savings at large values of Re

Net power saving $\mathcal{S}$ derives from the (positive or negative) balance between the power saved through drag-reducing control and the power required for wall actuation, hence

$$\mathcal{S} = \mathcal{R} - \frac{P_{\text{in}}}{P_{p_0}}, \tag{4.5}$$

where P_{p_0} is the pumping power per unit wetted area in the uncontrolled case, which for constant U_b reads

$$P_{p_0} = U_b \tau_{x_0}, \tag{4.6}$$

and P_{in} is the control input power per unit wetted area, expressed as:

$$P_{\text{in}} = \langle w_w \tau_z \rangle = \rho\nu \left\langle w \frac{\partial w}{\partial y} \right\rangle \Big|_w = \frac{\rho\nu}{2} \frac{\mathrm{d}}{\mathrm{d}y} \langle ww \rangle \Big|_w, \tag{4.7}$$

where $\tau_z = \rho\nu(\partial w/\partial y)_w$ is the spanwise wall shear stress.

Similarly to what done for $\mathcal{R}$, the Reynolds-number dependence of $\mathcal{S}$ can also be predicted theoretically. Whereas $\mathcal{R}$ is accurately expressed by the GQ model, the Re-dependence of P_{in}/P_{p_0} can be easily expressed following Ricco & Quadrio (2008), who noticed that this ratio is equivalent to $P^+_{\text{in}}/P^+_{p_0}$. Since P^+_{in} is very well approximated by the power P^+_ℓ required to generate the laminar transverse Stokes layer (Quadrio & Ricco, 2011; Gatti & Quadrio, 2013) — which does not depend on Re if the viscous-scaled parameters are kept constant — the Re-dependence of P_{in}/P_{p_0} comes only from $P^+_{p_0} = U^+_b = \sqrt{2/C_{f_0}}$. By using the expression of P^+_ℓ by Gatti & Quadrio (2013), we thus obtain

$$\frac{P_{\text{in}}}{P_{p_0}} \approx \frac{P^+_\ell}{U^+_b} = \frac{(A^+)^2(\kappa^+)^{1/3}}{2U^+_b} \mathrm{Re}\left[\mathrm{e}^{\pi i/6} \frac{\mathrm{Ai}'(\theta)}{\mathrm{Ai}(\theta)} \right], \tag{4.8}$$

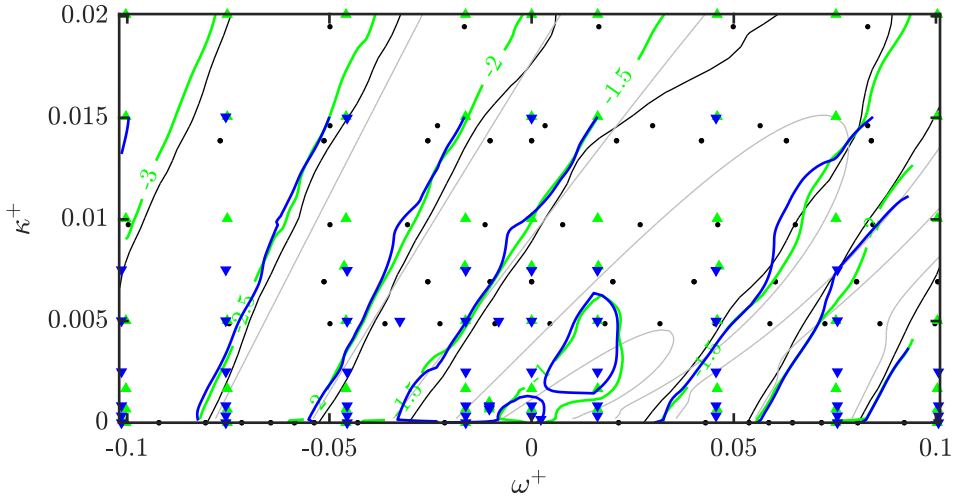

Figure 4.7: Maps of actuation power (P^+_{in}) as a function of the actuation parameters (ω^+, κ^+), at $Re_{\tau_0} = 1000$ (——) and $Re_{\tau_0} = 2000$ (——). The symbols are colored after table 4.1 and show the parameters of each simulation underlying the map interpolation shown in the figure. Data by GQ16 (—— and black dots), and P^+_{in} from equation (4.8) (——) are also reported.

where i is the imaginary unit, Re indicates the real part of a complex number, Ai is the Airy function of the first kind, Ai′ its derivative and $\theta = -\mathrm{e}^{\pi i/6}(\kappa^+)^{1/3}\,(\omega^+/\kappa^+ + i\kappa^+)$. Equation (4.8) shows that $P^+_{\text{in}} = U_b^+ P_{\text{in}}/P_{p_0} \approx P^+_\ell$, is a Reynolds-independent quantity for StTW parameters sufficiently far from the region of drag increase, where the approximation $P^+_{\text{in}} \approx P^+_\ell$ is known to fail. As a result, it is sufficient to measure P^+_{in} at a given Reynolds number, or estimate it via P^+_ℓ, in order to retrieve P_{in}/P_{p_0} at any Reynolds number, i.e. at any arbitrary $U_b^+ = \sqrt{2/C_{f_0}}$. Equation (4.8) shows that P_{in}/P_{p_0} decreases with Re as $1/U_b^+$, so that $\mathcal{S}$ can in fact increase with Re, provided the normalised actuation power decays with Re faster than $\mathcal{R}$.

Figure 4.7 confirms that P^+_{in} is indeed constant with Re throughout the investigated parameter space, included the drag-increasing regime, where P^+_{in} and P^+_ℓ do differ and the former can only be measured empirically. The GQ16 dataset well aligns with the present data, the lacking information for $0 < \kappa^+ \leq 0.005$ notwithstanding.

The net power saving at $Re_{\tau_0} = 1000$ and 2000 is reported in figure 4.8. Overall, the contours of $\mathcal{S}$ do not change significantly, since degradation of $\mathcal{R}$ is compensated by reduction of the actuation input power. Larger differences are observed for nearly optimal $\mathcal{S}$ (see the $\mathcal{S} = 15\%$ iso-line in figure 4.8), in a region which shrinks and shifts towards higher κ^+ at higher Re. This can be explained by the stronger decay of $\mathcal{R}$ in this region (as predicted by the GQ model due to

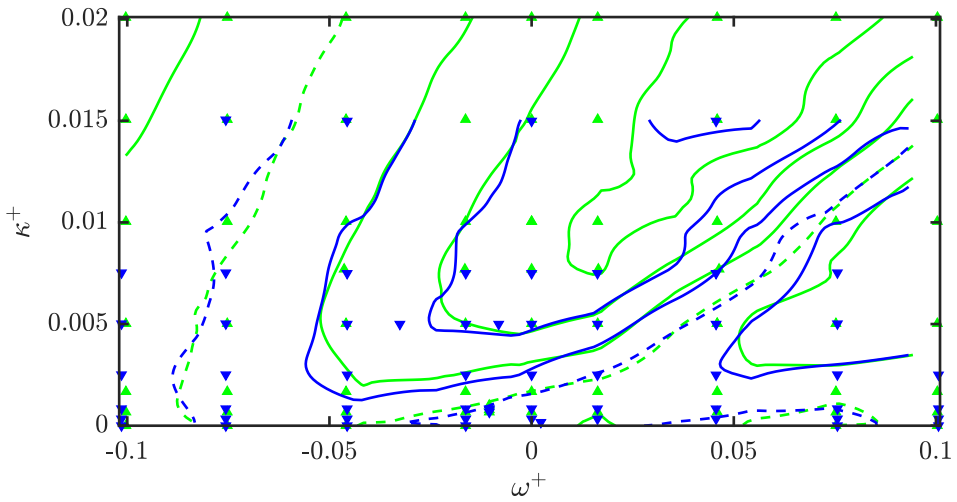

Figure 4.8: Maps of net power saving ($\mathcal{S}$) as a function of the actuation parameters (ω^+, κ^+), at $Re_{\tau_0} = 1000$ (——) and $Re_{\tau_0} = 2000$ (——). The symbols are colored after table 4.1 and show the parameters of each simulation underlying the map interpolation shown in the figure. Contour lines are shown in intervals of 5%, the dashed lines denoting the $\mathcal{S} = 0$ iso-line.

larger $\mathcal{R}$) and by the comparatively small value of P_{in}/P_{p_0}, which causes $\mathcal{S}$ to have similar Re-dependence as $\mathcal{R}$.

GQ16 noticed that at $Re_{\tau_0} \approx 1000$ and $A^+ = 5.5$ the locus of near-optimum new power saving ($\mathcal{S} = 15\%$) extends along the ridge of maximum $\mathcal{R}$ between $\kappa^+ = 0.0085$ and 0.04, the maximum being at $\{\omega^+, \kappa^+\} = \{0.093, 0.026\}$. This implies that the point of maximum $\mathcal{S}$ might reside outside of the parameter space considered in figure 4.8, for both Reynolds numbers under scrutiny here.

As done for the drag reduction in figure 4.6, the variation of $\mathcal{S}$ with Re is shown in figure 4.9, for the same parameters considered by Marusic *et al.* (2021). Interestingly, $\mathcal{S}$ is observed to increase with Re at this combination of parameters, essentially due to the shrinking of the negative P_{in}/P_{p_0} contribution and to the relatively constant $\mathcal{R}$. The increase of $\mathcal{S}$ is compatible with the theoretical prediction that can be obtained by combining the GQ model of equation (4.4) with the prediction for P_{in}/P_{p_0} of equation (4.8). The differences between the present numerical database and the laboratory experiments of Marusic *et al.* (2021), previously noted for $\mathcal{R}$, are confirmed here.

The present results enable a better understanding of the available literature data. For instance, by comparing the numerical data by Rouhi *et al.* (2023), which consider StTW at small wavelengths (due to the restricted domain size) and relatively large amplitude $A^+ = 12$ and frequencies, with their experimental data, which consider backward-travelling waves at larger wavelengths but smaller

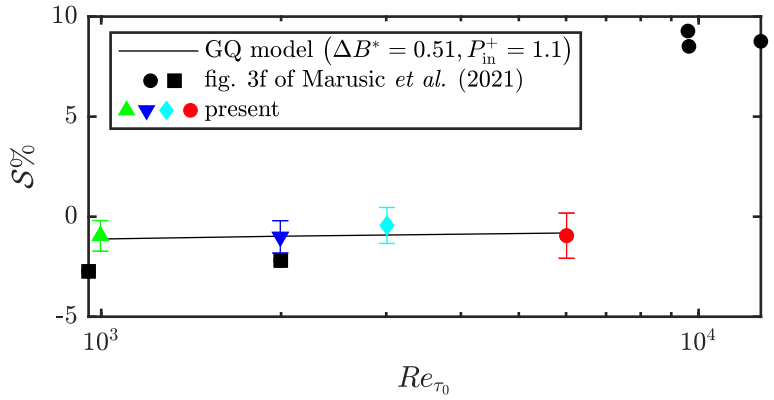

Figure 4.9: Net power saving ($\mathcal{S}$) as function of reference friction Reynolds number (Re_{τ_0}) for backward-travelling waves with the same parameters considered by Marusic *et al.* (2021). The present data are indicated with colored symbols (see table 4.1); data by Marusic *et al.* (2021) are black solid circles (experiments) and squares (LES); the straight line is the theoretical prediction obtained by combining the GQ model (4.4) for $\Delta B^* = 0.51$ with equation (4.8) for $P^+_{\rm in} = 1.1$ and the values of C_{f_0} obtained from the uncontrolled simulations at the respective value of Re_{τ_0}.

amplitudes of $A^+ \approx 5$ and frequencies, Chandran *et al.* (2023) conclude that mostly low-frequency forcing $|\omega^+| < 0.018$ is capable to achieve positive $\mathcal{S}$, despite the moderate values of $\mathcal{R}$. This conclusion is observed here to be an artifact of the comparison between StTW at different amplitudes: according to GQ16 it is known that already at $Re_{\tau_0} = 1000$ no positive $\mathcal{S}$ can be achieved via StTW for amplitudes $A^+ \gtrapprox 14$. The present data clearly show that the observation of GQ16 is valid also if smaller values of wavenumbers and frequencies are considered: the locus of maximum $\mathcal{S}$ in the $\{\omega, \kappa\}$-space essentially coincides with the one of maximum $\mathcal{R}$, and it shifts towards larger $\{\omega, \kappa\}$ for increasing values of Re rather than to smaller ones, if the comparison among various Re is performed at a constant value of A^+ close to the optimal $A^+ \approx 6$ identified by GQ16.

4.4 Concluding discussion

In the present work we have addressed the Reynolds-number dependence of skin-friction drag reduction induced by spanwise forcing, in terms of both drag reduction rate $\mathcal{R}$ and net power saving $\mathcal{S}$. In particular, we have focused on streamwise-travelling waves of spanwise wall velocity (StTW, Quadrio *et al.*, 2009). A new database of high-fidelity direct numerical simulations (DNS) of turbulent open channel flow with and without StTW has been generated for $Re_{\tau_0} = 1000$, 2000,

3000 and 6000. This is the widest Reynolds-number range considered so far in numerical experiments with spanwise forcing, and reduces the gap from the highest value of Re_{τ_0} considered in analogous laboratory experiments (Chandran *et al.*, 2023) to a factor of 2.5.

The main outcome of the present study is to confirm the validity of the predictive model for drag reduction proposed by Gatti & Quadrio (2016) and its underlying hypothesis. The present data corroborate the observation that the parameter ΔB^*, which quantifies the control-induced velocity shift in actual viscous units "$*$" at matched y^* with respect to the non-actuated flow, is a Re-independent measure of drag reduction when the Reynolds number is sufficiently large for the logarithmic law to apply. We have shown that $Re_{\tau_0} \gtrapprox 1000$ is sufficient for ΔB^* to become nearly Re-independent, since no statistically significant differences have been measured between the $Re_{\tau_0} = 1000$ and $Re_{\tau_0} = 2000$ cases, for a wide range of actuation parameters, and up to $Re_{\tau_0} = 6000$ for one selected combination of actuation parameters.

This key result implies that drag reduction induced by StTW at a given combination of $\{A^+, \omega^+, \kappa^+\}$ is bound to monotonically decrease with the Reynolds number, at a rate that depends on $\mathcal{R}$ itself and on (the inverse square root of) the skin-friction coefficient C_{f_0} of the uncontrolled flow, as embodied in the GQ model; see equation (4.4). Fortunately, the decay rate is less severe than the power law $\mathcal{R} \sim Re_{\tau_0}^{-0.2}$ suggested empirically in early studies on spanwise wall oscillations (Choi *et al.*, 2002; Touber & Leschziner, 2012), conveying that significant drag reduction can still be achieved at very high Re.

The increase of drag reduction with the Reynolds number observed by Marusic *et al.* (2021) with actuation parameters corresponding to the outer-scaled actuation is not confirmed by our numerical experiments with $\{A^+ = 5, \omega^+ = -0.0104, \kappa^+ = 0.00078\}$ in turbulent open channels. On the contrary, the present results follow well the prediction of the GQ model, and show a very mild decrease of $\mathcal{R}$ with Re for these specific parameters. While the observation of $\mathcal{R}$ increasing with Re is indeed surprising and unique in literature, we can only speculate on the reasons behind this discrepancy.

On the one hand, the difference in the flow setup considered here and in Marusic *et al.* (2021) (open channel vs. boundary layer) could affect the Reynolds-number dependence of $\mathcal{R}$. In this respect, Skote (2014) applied StTW to numerical turbulent boundary layers at low Re and noted that the Kármán constant can increase in the presence of drag-reduction effects. This could affect the Re-dependency of $\mathcal{R}$, since the GQ model assumes constancy of k. The experimental data of Chandran *et al.* (2023), however, do not support such an effect. On the other hand, Marusic *et al.* (2021) and later Chandran *et al.* (2023) implemented a spatially discrete form of the StTW, similarly to Auteri *et al.* (2010), and synthesised harmonic waves by independently moving stripes with finite width. Auteri *et al.* (2010) and, more

recently, Gallorini & Quadrio (2024) addressed the effects of the wave discretisation on the achievable drag reduction. Owing to discretization, the turbulent flow perceives a number of higher Fourier harmonics of the discrete piecewise-constant wave, as if multiple waves with different parameters were applied. As a result, quantitative comparison between the ideally continuous and piecewise-constant forcing is not trivial, and some discrete waves far from the optimal forcing parameters can outperform the corresponding ideal sinusoidal waveform, whenever part of the harmonic content of the discrete wave falls in high-$\mathcal{R}$ regions of the drag reduction map. Finally, the conclusion of Marusic *et al.* (2021) that $\mathcal{R}$ increases with Re hinges on comparison of data obtained with different methods. In particular, the low-Re data were obtained from LES of turbulent open channel flow in relatively small domains with continuous StTW applied at the wall, whereas the high-Re data were obtained from boundary layer experiments with discrete StTW. Differences in numerical and experimental uncertainties can further complicate the comparison. Whereas the above speculations remain to be verified in future studies, the present results support the claim that ideal StTW applied in turbulent open channels are neither expected nor observed to yield an increase of drag reduction with increasing Re, for any combination of wave parameters that are kept constant in viscous units.

Lastly, we also confirm that the Reynolds-number dependence of the net power saving $\mathcal{S} = \mathcal{R} - P_{\text{in}}/P_{p_0}$ is in line with theoretical predictions. Whereas $\mathcal{R}$ directly derives from the GQ model, P_{in}/P_{p_0} can be obtained directly from $P^+_{\text{in}} = U^+_b P_{\text{in}}/P_{p_0}$, which is known to be Re-independent (Gatti & Quadrio, 2013). Interestingly, we have found that P^+_{in} does not change with Re throughout the drag-reduction map, not only in those regions where P^+_{in} is known to be well approximated by P^+_ℓ, i.e. the value obtained from the laminar generalised Stokes layer solution. In other words, the ideal viscous scaling of P^+_{in} is retained even close to the valley of drag increase, where turbulence is known to interact with the generalised Stokes layer generated by StTW actuation. This result, as already discussed in Gatti & Quadrio (2013, 2016), has two main implications. Firstly, in the portion of the StTW parameter space where $\mathcal{S}$ is maximum, $\mathcal{S}$ is dominated by $\mathcal{R}$ and hence exhibits similar Re-dependence; here $\mathcal{S}$ decreases with Re at a rate which is slightly less than $\mathcal{R}$. Secondly, for StTW parameters far from the optimum, both $\mathcal{R}$ and P_{in}/P_{p_0} contribute to $\mathcal{S}$. In this case, the normalised control cost may decrease with Re at a faster rate than $\mathcal{R}$, so that $\mathcal{S}$ can actually increase with Re. However, this can occur only in regions of non-optimal values of $\mathcal{S}$. Hence, we argue that the observation by Chandran *et al.* (2023) that only low-frequency, low-wavenumber forcing can achieve positive $\mathcal{S}$ at high Re may be an artifact due to the properties of their experimental setup, in which the same region of the viscous-scaled parameter space cannot be spanned for different values of Re (see figure 4.10). Indeed, those authors can only achieve the optimal values of

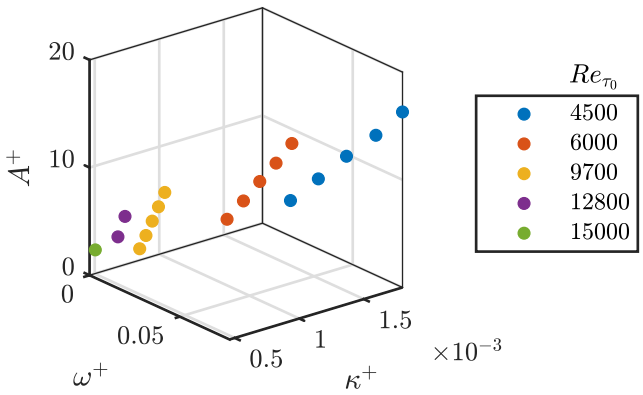

Figure 4.10: Wavenumber (κ^+), angular frequency (ω^+) and amplitude (A^+) for StTW actuation considered by Chandran *et al.* (2023), for different values of Re_{τ_0}.

A^+ at the highest values of Re, at which only low ω^+ and κ^+ are possible owing to the small space- and time-scales of the turbulent flow. The more systematic scan of the StTW parameter space carried out in the present study shows that the loci of optimal $\mathcal{S}$ and $\mathcal{R}$ roughly coincide in the $\{\omega^+, \kappa^+\}$ plane.

4.5 Dataset details

This Appendix reports the combination of the StTW control parameters of the simulations performed to produce the present dataset, together with the main quantities of interest. Tables 4.2, 4.3, 4.4 and 4.5 are for $Re_{\tau_0} = 1000$, $Re_{\tau_0} = 2000$, $Re_{\tau_0} = 3000$ and $Re_{\tau_0} = 6000$ respectively.

Case	A/U_b	A^+	$\omega h/U_b$	$\omega^+ \times 10^2$	κh	$\kappa^+ \times 10^2$	$\mathcal{R}\%$	$\mathcal{S}\%$
1	0.248	5.0	−4.98	-10.03	0	0.000	12.2	−1.6
2	0.248	5.0	−4.98	-10.03	0.67	0.067	12.7	−1.2
3	0.248	5.0	−4.98	-10.03	1.7	0.167	12.8	−1.3
4	0.248	5.0	−4.98	-10.03	5	0.502	12.6	−1.9
5	0.248	5.0	−4.98	-10.03	10	1.004	11.4	−3.6
6	0.248	5.0	−4.98	-10.03	15	1.506	9.8	−5.8
7	0.248	5.0	3.73	7.53	0	0.000	13.3	1.4
8	0.248	5.0	3.73	7.53	0.67	0.067	12.5	0.8
9	0.248	5.0	3.73	7.53	1.7	0.167	10.5	−1.0
10	0.248	5.0	4.98	10.03	0	0.000	12.2	−1.6

11	0.248	5.0	3.73	7.53	5	0.502	−1.0	−11.5
12	0.248	5.0	3.73	7.53	10	1.004	6.7	−2.0
13	0.248	5.0	3.73	7.53	15	1.506	19.3	12.9
14	0.248	5.0	4.98	10.03	0.67	0.067	12.0	−1.7
15	0.248	5.0	4.98	10.03	1.7	0.167	12.0	−1.5
16	0.248	5.0	4.98	10.03	5	0.502	5.4	−7.5
17	0.248	5.0	4.98	10.03	10	1.004	−1.8	−13.8
18	0.248	5.0	4.98	10.03	15	1.506	10.0	0.1
19	0.248	5.0	−2.30	-4.64	7.7	0.770	16.3	5.3
20	0.248	5.0	−0.82	-1.65	7.7	0.770	19.8	11.4
21	0.248	5.0	0.00	-0.00	7.7	0.770	21.6	14.8
22	0.248	5.0	0.82	1.65	7.7	0.770	20.9	15.7
23	0.248	5.0	2.30	4.64	7.7	0.770	10.3	4.9
24	0.248	5.0	−2.28	-4.59	0	0.000	10.2	1.2
25	0.248	5.0	−0.81	-1.63	0	0.000	2.8	−3.1
26	0.248	5.0	−2.28	-4.59	0.67	0.067	11.8	2.5
27	0.248	5.0	−0.81	-1.63	0.67	0.067	5.3	−0.7
28	0.248	5.0	0.00	-0.00	0.67	0.067	1.0	−3.4
29	0.248	5.0	0.81	1.63	0.67	0.067	0.8	−4.8
30	0.248	5.0	2.28	4.59	0.67	0.067	8.0	−0.8
31	0.248	5.0	−2.28	-4.59	1.7	0.167	14.3	4.8
32	0.248	5.0	−0.81	-1.63	1.7	0.167	10.3	3.9
33	0.248	5.0	0.00	-0.00	1.7	0.167	4.7	−0.1
34	0.248	5.0	0.81	1.63	1.7	0.167	2.2	−2.1
35	0.248	5.0	2.28	4.59	1.7	0.167	3.5	−5.0
36	0.248	5.0	−2.28	-4.59	5	0.502	16.6	6.2
37	0.248	5.0	−0.81	-1.63	5	0.502	18.1	10.5
38	0.248	5.0	0.00	-0.00	5	0.502	17.5	11.6
39	0.248	5.0	0.81	1.63	5	0.502	13.5	9.1
40	0.248	5.0	2.28	4.59	5	0.502	3.0	−3.8
41	0.248	5.0	2.28	4.59	5	0.502	3.0	−3.8
42	0.248	5.0	−2.28	-4.59	10	1.004	15.6	4.2
43	0.248	5.0	−0.81	-1.63	10	1.004	19.0	10.0
44	0.248	5.0	0.00	-0.00	10	1.004	20.8	13.3
45	0.248	5.0	0.81	1.63	10	1.004	22.5	16.5
46	0.248	5.0	2.28	4.59	10	1.004	18.2	13.4
47	0.248	5.0	−2.28	-4.59	15	1.506	14.0	1.8
48	0.248	5.0	−0.81	-1.63	15	1.506	17.4	7.4
49	0.248	5.0	0.00	-0.00	15	1.506	18.9	10.2
50	0.248	5.0	0.81	1.63	15	1.506	20.5	13.0
51	0.248	5.0	2.28	4.59	15	1.506	24.3	18.8

52	0.228	4.6	0.00	-0.00	10	1.004	19.7	13.3
53	0.248	5.0	−0.52	-1.05	0.67	0.067	3.9	−1.0
54	0.248	5.0	−0.52	-1.05	1	0.100	5.4	−0.2
55	0.248	5.0	−3.73	-7.53	0	0.000	12.3	0.4
56	0.248	5.0	−3.73	-7.53	0.67	0.067	13.4	1.3
57	0.248	5.0	−3.73	-7.53	1.7	0.167	13.2	1.0
58	0.248	5.0	−3.73	-7.53	5	0.502	13.8	1.0
59	0.248	5.0	−3.73	-7.53	10	1.004	12.3	−1.2
60	0.248	5.0	−3.73	-7.53	15	1.506	11.8	−2.4
61	0.248	5.0	−4.98	-10.04	20	2.008	8.5	−7.7
62	0.248	5.0	−3.73	-7.53	20	2.008	10.8	−4.0
63	0.248	5.0	−2.28	-4.59	20	2.008	13.0	0.1
64	0.248	5.0	−0.81	-1.63	20	2.008	15.6	4.7
65	0.248	5.0	0.00	-0.00	20	2.008	17.3	7.5
66	0.248	5.0	0.81	1.63	20	2.008	19.5	10.9
67	0.248	5.0	2.28	4.59	20	2.008	22.9	16.2
68	0.248	5.0	3.73	7.53	20	2.008	23.8	17.7
69	0.248	5.0	4.98	10.04	20	2.008	19.8	11.8
70	0.248	5.0	−0.52	-1.05	0.78	0.078	4.5	−1.0

Table 4.2: List of the controlled simulations carried out at $Re_{\tau_0} = 1000$.

Case	A/U_b	A^+	$\omega h/U_b$	$\omega^+ \times 10^2$	κh	$\kappa^+ \times 10^2$	$\mathcal{R}\%$	$\mathcal{S}\%$
1	0.3	6.5	0.21	0.23	0.33	0.017	2.7	−2.1
2	0.228	5.0	−1.50	-1.63	0	0.000	1.9	−3.5
3	0.228	5.0	−4.19	-4.56	0	0.000	9.5	1.3
4	0.228	5.0	1.50	1.63	5	0.250	3.6	−0.4
5	0.228	5.0	−1.50	-1.63	0.67	0.033	5.2	−0.2
6	0.228	5.0	−4.19	-4.56	0.67	0.033	10.6	2.3
7	0.228	5.0	0.00	-0.00	0.67	0.033	3.6	−0.1
8	0.228	5.0	4.19	4.56	0.67	0.033	9.0	0.8
9	0.228	5.0	1.50	1.63	0.67	0.033	3.2	−2.0
10	0.228	5.0	−1.50	-1.63	5	0.250	12.8	6.6
11	0.228	5.0	−4.19	-4.56	1.7	0.083	13.0	4.5
12	0.228	5.0	0.00	-0.00	1.7	0.083	1.9	−2.2
13	0.228	5.0	4.19	4.56	1.7	0.083	8.3	0.3
14	0.228	5.0	1.50	1.63	1.7	0.083	−0.2	−5.2

15	0.228	5.0	−1.50	-1.63	10	0.500	18.2	11.3
16	0.228	5.0	−4.19	-4.56	5	0.250	16.0	7.1
17	0.228	5.0	0.00	-0.00	5	0.250	9.5	4.9
18	0.228	5.0	4.19	4.56	5	0.250	0.7	−6.9
19	0.228	5.0	−1.50	-1.63	1.7	0.083	6.7	1.1
20	0.228	5.0	−4.19	-4.56	10	0.500	16.0	6.6
21	0.228	5.0	4.19	4.56	10	0.500	3.2	−3.1
22	0.228	5.0	−1.50	-1.63	15	0.749	18.0	10.4
23	0.228	5.0	−4.19	-4.56	15	0.749	15.9	5.9
24	0.228	5.0	0.00	-0.00	15	0.749	19.7	13.5
25	0.228	5.0	4.19	4.56	15	0.749	11.5	6.5
26	0.228	5.0	1.50	1.63	15	0.749	19.3	14.6
27	0.228	5.0	−0.75	-0.81	10	0.500	17.4	11.2
28	0.228	5.0	0.00	-0.00	30	1.499	18.5	10.5
29	0.228	5.0	−2.99	-3.26	10	0.500	17.3	8.9
30	0.228	5.0	1.50	1.63	10	0.500	12.8	8.7
31	0.228	5.0	0.00	-0.00	10	0.500	16.5	11.2
32	0.228	5.0	−0.95	-1.05	1.7	0.084	4.3	−0.7
33	0.228	5.0	−0.95	-1.05	1.3	0.067	3.1	−1.9
34	0.228	5.0	−4.19	-4.56	30	1.499	13.0	1.8
35	0.228	5.0	4.19	4.56	30	1.499	22.1	17.0
36	0.228	5.0	9.24	10.06	0	0.000	10.9	−1.9
37	0.228	5.0	9.24	10.06	0.67	0.033	11.4	−1.3
38	0.228	5.0	9.24	10.06	1.7	0.083	11.2	−1.4
39	0.228	5.0	9.24	10.06	5	0.250	10.0	−2.4
40	0.228	5.0	9.24	10.14	10	0.501	4.0	−7.9
41	0.228	5.0	9.24	10.14	15	0.752	−4.0	−15.2
42	0.228	5.0	−9.24	-10.14	0	0.000	10.7	−2.3
43	0.228	5.0	−9.24	-10.14	0.67	0.033	10.6	−2.1
44	0.228	5.0	−9.24	-10.14	1.7	0.084	11.1	−1.7
45	0.228	5.0	−9.24	-10.14	5	0.251	11.5	−1.5
46	0.228	5.0	−9.24	-10.14	10	0.501	10.5	−2.9
47	0.228	5.0	−9.24	-10.14	15	0.752	10.4	−3.2
48	0.228	5.0	−6.89	-7.56	0	0.000	11.9	0.9
49	0.228	5.0	−6.89	-7.56	0.67	0.033	11.6	0.6
50	0.228	5.0	−6.89	-7.56	1.7	0.084	12.0	1.0
51	0.228	5.0	−6.89	-7.56	5	0.251	13.1	1.7
52	0.228	5.0	−6.89	-7.56	10	0.501	12.4	0.7
53	0.228	5.0	−6.89	-7.56	15	0.752	12.5	0.4
54	0.228	5.0	6.89	7.56	0	0.000	12.5	1.6
55	0.228	5.0	6.89	7.56	0.67	0.033	11.3	0.4

56	0.228	5.0	6.89	7.56	1.7	0.084	10.9	0.1
57	0.228	5.0	6.89	7.56	5	0.251	7.0	−3.3
58	0.228	5.0	6.89	7.56	10	0.501	−2.1	−11.8
59	0.228	5.0	6.89	7.56	15	0.752	−0.2	−9.5
60	0.228	5.0	−6.89	-7.56	30	1.504	11.1	−1.9
61	0.228	5.0	−0.95	-1.05	1.6	0.078	4.0	−1.0

Table 4.3: List of the controlled simulations carried out at $Re_{\tau_0} = 2000$.

Case	A/U_b	A^+	$\omega h/U_b$	$\omega^+ \times 10^2$	κh	$\kappa^+ \times 10^2$	$\mathcal{R}\%$	$\mathcal{S}\%$
1	0.219	5.0	−2.16	-1.65	0.67	0.022	3.1	−2.1
2	0.219	5.0	0.00	-0.00	0.67	0.022	1.4	−2.1
3	0.219	5.0	2.16	1.65	0.67	0.022	1.3	−3.8
4	0.219	5.0	2.16	1.65	1.7	0.056	−0.5	−5.5
5	0.218	5.0	−1.37	-1.05	2.3	0.078	4.4	−0.4
6	0.218	5.0	−1.37	-1.05	2.7	0.089	4.7	−0.1

Table 4.4: List of the controlled simulations carried out at $Re_{\tau_0} = 3000$.

Case	A/U_b	A^+	$\omega h/U_b$	$\omega^+ \times 10^2$	κh	$\kappa^+ \times 10^2$	$\mathcal{R}\%$	$\mathcal{S}\%$
1	0.203	5.0	−2.55	-1.04	4.7	0.078	3.5	−0.9
2	0.101	2.5	−2.19	-0.90	8.3	0.139	2.3	1.2

Table 4.5: List of the controlled simulations carried out at $Re_{\tau_0} = 6000$.

Turbulent drag reduction with streamwise travelling waves in the compressible regime

The content of this Paper has been published in
Gattere, F., Zanolini, M., Gatti, D., Bernardini, M. & Quadrio, M. 2024
Turbulent drag reduction with streamwise-travelling waves
in the compressible regime.
Journal of Fluid Mechanics **987**, A30.
Minor editing has been done for formatting purposes.

Turbulent drag reduction with streamwise travelling waves in the compressible regime

Abstract

The ability of streamwise-travelling waves of spanwise velocity to reduce the turbulent skin-friction drag is assessed in the compressible regime. Direct numerical simulations are carried out to compare drag reduction in subsonic, transonic and supersonic channel flows. Compressibility improves the benefits of the travelling waves, in a way that depends on the control parameters: drag reduction becomes larger than the incompressible one for small frequencies and wavenumbers. However, the improvement depends on the specific procedure employed for comparison. When the Mach number is varied and, at the same time, wall friction is changed by the control, the bulk temperature in the flow can either evolve freely in time until the aerodynamic heating balances the heat flux at the walls, or be constrained such that a fixed percentage of kinetic energy is transformed into thermal energy. Physical arguments suggest that, in the present context, the latter approach should be preferred. It provides a test condition in which the wall-normal temperature profile more realistically mimics that in an external flow, and also leads to a much better scaling of the results, over both the Mach number and the control parameters. Under this comparison, drag reduction is only marginally improved by compressibility.

5.1 Introduction

One of the distinctive features of fluid turbulence is the ability to transport and mix mass and momentum more effectively than a laminar flow, resulting in more intense

wall shear stress and a larger friction drag (Fukagata *et al.*, 2002). Flow control for skin-friction drag reduction aims to mitigate the negative effects of turbulence near the wall, in order to cut energy consumption and to improve cost effectiveness and environmental footprint. This is of particular interest in aeronautics: nearly 50% of the total drag of a civil aircraft is due to the viscous drag caused by the interaction of the turbulent boundary layer with the surface (Gad-el-Hak & Pollard, 1998). An efficient drag reduction technology capable to achieve even a tiny drag reduction rate would yield enormous economic and environmental benefits.

Drag reduction strategies are often classified as passive or active. The former do not require extra energy, and usually exploit a non-planar wall (see Foggi Rota *et al.*, 2023, for an exception). Among them, riblets (Bechert *et al.*, 1997) are the closest to be implemented in practical applications. Laboratory tests show that they can reduce drag up to 8–10% at low Reynolds numbers; on considering their requirement of periodical maintenance, though, riblets do not yield enough economical benefits to be routinely used yet. Active strategies, instead, require actuation, and external energy to work. Those involving the motion of the wall are an interesting category, and include spanwise wall oscillations (Jung *et al.*, 1992), streamwise-travelling waves of spanwise velocity (Quadrio *et al.*, 2009), spanwise-travelling waves of spanwise velocity (Du *et al.*, 2002) and streamwise-travelling waves of wall deformation (Nakanishi *et al.*, 2012). They are all predetermined strategies, since the control parameters are set *a priori*, and enjoy the relative simplicity resulting from the lack of sensors and feedback laws. However, several of them do not yield an energetic benefit once the control energy is accounted for. This work focuses on the streamwise-travelling waves (StTW) of spanwise velocity introduced by Quadrio *et al.* (2009). StTW are among the most promising techniques, because of their rather large net savings. This type of forcing, thoroughly reviewed by Ricco *et al.* (2021), is defined by the following space-time distribution of the spanwise velocity component at the wall:

$$W(x,t) = A\sin(\kappa_x x - \omega t) \tag{5.1}$$

where x and t are the streamwise direction and time, A is the forcing amplitude, κ_x is the wavenumber and ω is the frequency (which define the wavelength $\lambda_x = 2\pi/\kappa_x$ and the oscillation period $T = 2\pi/\omega$). The spatially uniform spanwise-oscillating wall (Jung *et al.*, 1992) and the stationary wave (Quadrio *et al.*, 2007; Viotti *et al.*, 2009) are two limit cases of the general forcing (5.1), obtained for $\kappa_x = 0$ and $\omega = 0$ respectively.

Via a generalized Stokes layer (Quadrio & Ricco, 2011), StTW create an unsteady near-wall transverse shear which continuously changes the inclination of the near-wall structures in wall-parallel planes, weakening the regeneration mechanism of the near-wall cycle (Schoppa & Hussain, 2002). Once actuation pa-

rameters are properly tuned, this process can even lead to the complete suppression of turbulence.

The spatially-uniform wall oscillation, studied in depth by Quadrio & Ricco (2004) in an incompressible channel flow at a Reynolds number (based on the friction velocity u_τ of the uncontrolled flow, the fluid kinematic viscosity ν and the half-channel height) of $Re_\tau = 200$, yields a drag reduction rate $\mathcal{R}$ of 45% (at $A^+ \equiv A/u_\tau = 12$) for the so-called 'optimal' actuation period $T^+ \equiv Tu_\tau^2/\nu \approx 100$. However, the maximum energy saving after the control energy is accounted for is found at lower forcing intensities, and amounts to 7% only. The spatially-distributed StTW are a natural generalization of the wall oscillations, and present substantial advantages in terms of net savings. Quadrio *et al.* (2009) have shown how drag reduction, power input and total saved power vary with the control parameters. Depending on the (κ_x, ω) value pair, drag increase or drag reduction can be achieved. The parameters yielding maximum drag reduction and maximum energy saving are almost coincident, and correspond (at this Reynolds number) to low frequencies and low wavenumbers. The largest drag reduction of 48% (at $A^+ = 12$) still yields a positive net power saving of 17%, and smaller forcing intensities lead to net savings as high as 32%. StTW have been demonstrated in the lab with a pipe flow experiment (Auteri *et al.*, 2010), who measured up to 33% drag reduction, and have been proven to work in boundary layers too (Skote *et al.*, 2015; Bird *et al.*, 2018).

A number of practical aspects that need to be considered before declaring spanwise forcing as a viable strategy for applications has been recently considered. Gatti & Quadrio (2013, 2016) showed that the expected performance deterioration at larger Reynolds numbers, which afflicts all drag reduction strategies acting via near-wall turbulence manipulation, is only marginal for StTW and linked to the natural variation of the skin-friction coefficient itself with the Reynolds number. Once the performance of StTW is measured, as it should be, via the upward shift of the logarithmic portion of the mean velocity profile in the law-of-the-wall form, it becomes Re-independent, so that at flight Reynolds number 30%–40% friction drag reduction could be expected. Marusic *et al.* (2021) hinted at an even better scenario for StTW at high Re, thanks to the interaction of the near-wall forcing with the large-scale outer motions of the turbulent boundary layer, although the energetic consequences of using a spatially discrete forcing recently brought to light by Gallorini & Quadrio (2024) were not considered. Banchetti *et al.* (2020) demonstrated the beneficial effect of skin-friction drag reduction via StTW on pressure drag when applied to bluff bodies of complex shape, and Nguyen *et al.* (2021) used spanwise forcing for separation control.

One parameter that is crucial in aeronautical applications has received limited attention so far in drag reduction studies: the Mach number M, a parameter which quantifies the importance of compressibility effects. A few works, numerical

(Duan & Choudhari, 2012, 2014; Mele *et al.*, 2016) and experimental, both in wind tunnel (Gaudet, 1989; Coustols & Cousteix, 1994) and with flight test (Zuniga *et al.*, 1992), investigated the drag reduction effectiveness of riblets in a turbulent compressible boundary layer. Fewer studies have been carried out to assess how compressibility alters the drag reduction capabilities of active techniques: for example, Chen *et al.* (2016) examined the uniform blowing or suction in an hypersonic turbulent boundary layer at free-stream Mach number of 6.

As far as spanwise forcing goes, the large eddy simulation study of Fang *et al.* (2009) was the first to consider the spanwise oscillating wall in a turbulent channel flow at $M = 0.5$, followed by the direct numerical simulation (DNS) study of Ni *et al.* (2016) for a turbulent boundary layer at $M = 2.5$. However, the first comprehensive study of compressibility effects in drag reduction via spanwise wall oscillations was performed by Yao & Hussain (2019). They carried out DNS of a plane channel flow subjected to spanwise oscillating walls at $M = 0.3, 0.8, 1.5$, at $Re_\tau = 200$, $A^+ = 12$ and T^+ in the range $25 - 300$. $\mathcal{R}$ was found to be qualitatively similar to the incompressible case: for a given period T^+, $\mathcal{R}$ increases with the amplitude A^+, at a rate that saturates when A^+ becomes large. For $A^+ = 12$, they reported $\mathcal{R}$ increasing from 34.8% at $T^+ = 100$ for $M = 0.3$ to an outstanding value of 47.1% at the largest period investigated $T^+ = 300$ for $M = 1.5$. For $A^+ = 18$ and $M = 1.5$, the flow reached relaminarization. The effect of Re was also investigated via a few additional cases run at $Re_\tau \approx 500$, confirming the related decline of $\mathcal{R}$. Yao & Hussain (2019) did not consider the impact of the Mach number on the power budget. Both drag reduction and power budget performance were later discussed in the recent work by Ruby & Foysi (2022) for a channel flow at $M = 0.3, 1.5, 3$ and $Re_\tau = 200 - 1000$ forced by stationary waves with $A^+ = 12$ and $\kappa_x^+ = 0.0025 - 0.01$. They found the optimum κ_x and the maximum net power saving to increase significantly with Mach, thus confirming the beneficial effect of compressibility.

When applying flow control for drag reduction in duct flows at various M, the thermodynamical properties of the flow change because of the increased bulk temperature, owing to the combination of the increased Mach number and the action of the control. To understand whether changes of drag reduction with M directly depend on compressibility, rather than indirectly deriving from temperature changes induced by changes of the skin friction drag, the comparison procedure between uncontrolled and controlled flows should decouple compressibility from purely thermodynamical effects. Yao & Hussain (2019) examined the effect of M on $\mathcal{R}$ by matching the semi-local Reynolds number (at half-channel height), which provides a relatively good collapse of $\mathcal{R}$ between incompressible and compressible cases. In the present work, we also propose a further, alternative approach: the value of the bulk temperature is constrained such that the amount of turbulent kinetic energy transformed into thermal energy remains constant, both across

the variation of M and between uncontrolled and controlled cases. This strategy presents a significant advantage. The simplified setup of the turbulent channel flow can be used in configurations where the coupling between the velocity and thermal fields is closer to that found in external flows, where the application of the spanwise forcing to reduce drag is more attractive. For example, compressible boundary layers of practical aeronautical interest are usually characterized by adiabatic or moderately cold walls, with a thermal stratification leading to a denser, colder outer region and a layer of warmer fluid in the near-wall zone.

The present work is the first comprehensive analysis of the StTW technique in the compressible regime. The only prior work is the single case computed by Quadrio *et al.* (2022), who studied by DNS the StTW applied on a portion of a wing in transonic flight at $M = 0.7$ and $Re = 3 \times 10^5$ (based on the free-stream velocity and the wing cord), finding that a localized actuation has the potential to boost the aerodynamic efficiency of the whole aircraft, with an estimate reduction of 9% of the total drag of the airplane at a negligible energy cost. In this work, we consider by DNS a compressible turbulent plane channel flow modified by StTW, and we aim at fully characterizing how $\mathcal{R}$ and the power budget depend on the Mach number.

The paper is organized as follows. After this Introduction, §5.2 describes the computational framework used to produce the DNS database, presenting the governing equations in §5.2.1, the DNS solver in §5.2.2, and the simulation parameters in §5.2.3. The parameters used to quantify drag reduction are defined in §5.2.4, and §5.2.5 describes two approaches to compare unforced and forced compressible channel flows at different M. In §5.3 the effects of the Mach number are discussed, first in terms of drag reduction in §5.3.1, and then in terms of power budgets in §5.3.2. Lastly, in §5.4 the main conclusions are briefly outlined. The paper is concluded by a brief Appendix where the raw results of the numerical study are compactly shown.

5.2 Methods

5.2.1 Governing equations

The compressible Navier–Stokes equations for a perfect and heat-conducting gas are written in conservative form as:

$$\frac{\partial \rho}{\partial t} + \frac{\partial \rho u_i}{\partial x_i} = 0 \tag{5.2}$$

$$\frac{\partial \rho u_i}{\partial t} + \frac{\partial \rho u_i u_j}{\partial x_j} = -\frac{\partial p}{\partial x_i} + \frac{\partial \sigma_{ij}}{\partial x_j} + f\delta_{i1} \tag{5.3}$$

$$\frac{\partial \rho e}{\partial t} + \frac{\partial \rho (e + p/\rho) u_j}{\partial x_j} = \frac{\partial \sigma_{ij} u_i}{\partial x_j} - \frac{\partial q_j}{\partial x_j} + f u_1 + \Phi. \tag{5.4}$$

Here and throughout the paper, repeated indices imply summation; ρ is the fluid density, p is the pressure, u_i is the velocity component in the i-th directions, and $i = 1, 2, 3$ represent the streamwise (x), wall-normal (y) and spanwise (z) direction, respectively. The total energy per unit mass $e = c_v T + u_i u_i/2$ is the sum of the internal energy and the kinetic energy, where c_v is the specific heat at constant volume and T the temperature. The viscous stress tensor σ_{ij} for a Newtonian fluid subjected to the Stokes hypothesis becomes:

$$\sigma_{ij} = \mu \left(\frac{\partial u_i}{\partial x_j} + \frac{\partial u_j}{\partial x_i} - \frac{2}{3} \frac{\partial u_k}{\partial x_k} \delta_{ij} \right), \tag{5.5}$$

where μ is the dynamic viscosity and δ_{ij} is Kronecker delta; the dependence of viscosity on the temperature is accounted for through the Sutherland's law. The heat flux vector q_j is modelled after the Fourier law:

$$q_j = -k \frac{\partial T}{\partial x_j}, \tag{5.6}$$

where $k = c_p \mu / Pr$ is the thermal conductivity, with c_p the specific heat at constant pressure and Pr the Prandtl number, set to $Pr = 0.72$. We consider the turbulent channel configuration, where the flow between two isothermal walls is driven in the streamwise direction by the time-dependent body force f in Eq.(5.3), evaluated at each time step to maintain a constant mass flow-rate. The corresponding power is included in Eq.(5.4), where the additional term Φ represents a uniformly distributed heat source which controls the value of the bulk flow temperature (Yu *et al.*, 2019).

5.2.2 Solver

The flow solver employed for the analysis is STREAmS (Supersonic TuRbulEnt Accelerated Navier–Stokes Solver), a high-fidelity code designed for large-scale simulations of compressible turbulent wall-bounded flows that runs in parallel on CPU and GPU architectures.

The code, developed by Bernardini *et al.* (2021), incorporates state-of-the-art numerical algorithms, specifically designed for the solution of compressible turbulent flows, with a focus on the high-speed regime. The distinctive feature of the solver is the methodology adopted for the discretization of the convective terms of the Navier–Stokes equations with hybrid, high-order, energy-consistent/shock-capturing schemes in locally conservative form. An energy-preserving discretization, based on sixth-order central approximations, is applied where the solution is smooth, and guarantees discrete conservation of the total kinetic energy in the limit

case of inviscid, low-speed flows. This is the case of interest for all the simulations presented in this study, where shock waves do not occur. The Navier–Stokes equations are reduced to a semi-discrete system of ordinary differential equations, integrated in time using a three-stages third-order Runge–Kutta scheme. The solver is written in Fortran, and uses the MPI paradigm with a double domain decomposition; in its current version (Bernardini *et al.*, 2023), it can be run on modern HPC architectures based on GPU acceleration. All the computations reported in this work have been performed using the CUDA Fortran backend, capable of taking advantage of the Volta NVIDIA GPUs available on Marconi 100 of the Italian CINECA supercomputing center.

5.2.3 Parameters and computational setup

A wall-bounded turbulent flow in the compressible regime is described by three independent parameters: the Reynolds number, the Mach number and a third parameter that specifies the thermal condition of the wall. For the channel flow configuration, relevant parameters are usually defined using bulk quantities, i.e. the bulk density ρ_b, the bulk velocity U_b and the bulk temperature T_b:

$$\rho_b = \frac{1}{2h}\int_{-h}^{h}\langle\rho\rangle\,dy, \quad U_b = \frac{1}{2h\rho_b}\int_{-h}^{h}\langle\rho u\rangle\,dy, \quad T_b = \frac{1}{2h\rho_b U_b}\int_{-h}^{h}\langle\rho uT\rangle\,dy. \tag{5.7}$$

The operator $\langle\cdot\rangle$ computes a mean value by averaging over time and homogeneous directions.

The main goal of this work is to understand the effect of Mach number. Since the control is wall-based and the control parameters are known (Gatti & Quadrio, 2016) to scale in viscous units, i.e. with the friction and density at the wall, it is convenient (Coleman *et al.*, 1995) to define the Mach number as $M_w^b = U_b/c_w$, in which the superscript and subscript emphasize that the velocity scale is U_b and the speed of sound $c_w = \sqrt{\gamma R T_w}$ is evaluated at the (reference) wall temperature T_w. Three sets of simulations are performed, at $M_w^b = 0.3, 0.8, 1.5$. These values are identical to those used by Yao & Hussain (2019) in their study of the oscillating wall. The simulations are run at a constant flow rate or CFR (Quadrio *et al.*, 2016*a*): the pressure gradient evolves in time to keep a constant U_b. For all cases, the bulk Reynolds number $Re_b = \rho_b U_b h/\mu_w$ is chosen in such a way that the corresponding friction Reynolds number is fixed to the target value for the uncontrolled simulations. Although most of the incompressible information on StTW is available at $Re_\tau = 200$, in our study the target value is set at the higher $Re_\tau = 400$. This choice brings in extra computational costs, but avoids issues with relaminarization, that is expected to become significant at lower Re_τ in view of the expected increased effectiveness of StTW in the compressible regime.

	M_w^b	Re_τ	Re_b	Δt^+	$N_x \times N_y \times N_z$	Δx^+	Δy^+	Δz^+
ZBC	0.3	404	7115	0.007	$768 \times 258 \times 528$	9.8	0.51–6.35	4.8
ZBC	0.8	400	6691	0.017	$768 \times 258 \times 528$	9.8	0.51–6.28	4.8
ZBC	1.5	394	5751	0.025	$1024 \times 258 \times 512$	7.4	0.50–6.19	4.9
CBC	0.3	403	7250	0.007	$768 \times 258 \times 528$	9.8	0.51–6.35	4.8
CBC	0.8	399	7602	0.017	$768 \times 258 \times 528$	9.8	0.51–6.28	4.8
CBC	1.5	387	8597	0.025	$1024 \times 258 \times 512$	7.4	0.50–6.19	4.9

Table 5.1: Parameters of the six uncontrolled simulations: Mach number M_w^b, friction Reynolds number Re_τ, bulk Reynolds number Re_b, time step, mesh size and spatial resolution in each direction.

For each case (defined by a pair of values for M_w^b and Re_τ), two distinct simulations are carried out, which differ in the way the system is thermally managed. In one, dubbed Zero Bulk Cooling (ZBC), the bulk heating term Φ in Eq.(5.4) is set to zero, and the bulk temperature T_b is left free to evolve until the aerodynamic heating rate and the heat flux at the wall are in balance. In the other, named Constrained Bulk Cooling (CBC), the heat produced within the flow is balanced not only by the wall heat flux, but also by a cooling source term Φ (Yu *et al.*, 2019), which evolves to keep a constant T_b. A detailed description of the two strategies is provided later in §5.2.5, where the different implications of comparing at ZBC or CBC are discussed.

For each of the three values of M_w^b, a single uncontrolled and 42 cases with spanwise forcing are considered; each case is carried out twice, with ZBC and CBC. Hence, the computational study consists of 258 simulations. Table 5.1 summarizes the parameters for the 6 uncontrolled simulations.

Periodic boundary conditions in the wall-parallel directions and no-slip and no-penetration conditions at the solid walls are applied for the velocity vector, and isothermal boundary conditions are used for the temperature. In the cases with control, the no-slip condition for the spanwise velocity component is modified to apply the travelling wave (5.1). The wave amplitude is fixed at $A^+ = 12$, and 42 different combinations of wavelength κ_x^+ and frequency ω^+ are considered. Here and throughout the paper, the + superscript denotes quantities expressed in wall units of the uncontrolled case.

Figure 5.1 plots the incompressible drag reduction map, with dots identifying the present simulations. The incompressible drag reduction map resembles the original one computed by Quadrio *et al.* (2009) at $Re_\tau = 200$. Since the present study considers $Re_\tau = 400$, the map is obtained via interpolation from the two datasets at $Re_\tau = 200$ and $Re_\tau = 1000$ produced by Gatti & Quadrio (2016) (see §5.3 for details). The simulations sample the parameter space along five lines,

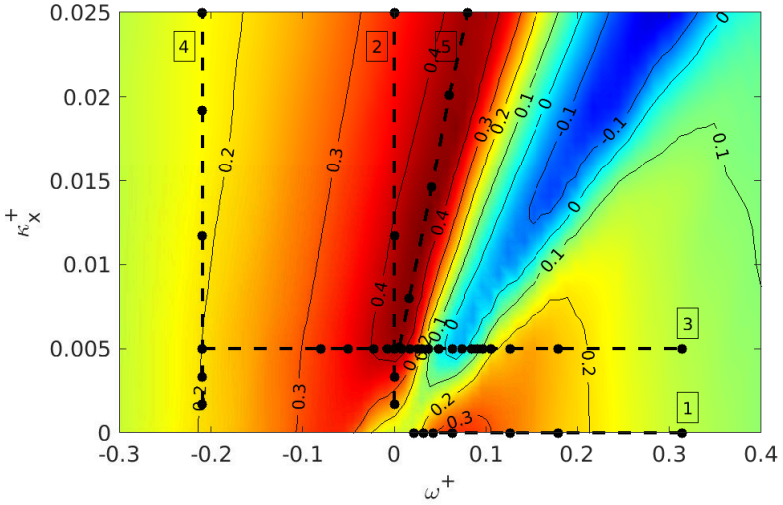

Figure 5.1: Incompressible drag reduction versus κ_x^+ and ω^+, at $A^+ = 12$ and $Re_\tau = 400$. The map is obtained from Gatti & Quadrio (2016) via interpolation of their datasets at $Re_\tau = 200$ and $Re_\tau = 1000$. The dots on the dashed lines correspond to the present compressible simulations.

all visible in figure 5.1. In particular, the oscillating-wall case (dashed line 1 in figure 5.1) at $\kappa_x^+ = 0$ is chosen to replicate data by Yao & Hussain (2019), and sampled with 7 simulations (all with positive frequency, since negative frequencies at $\kappa_x = 0$ can be obtained by symmetry). The steady wave at $\omega^+ = 0$ is scanned by 5 simulations along line 2; line 3 at constant $\kappa_x^+ = 0.005$ contains 20 points, crosses the low-Re incompressible maximum drag reduction, and also cuts through the region of drag increase. Five simulations along line 4 explore the area of low drag reduction at large negative frequencies. Lastly, line 5 with 5 points analyses the ridge of maximum drag reduction.

The size of the computational domain is $(L_x, L_y, L_z) = (6\pi h, 2h, 2\pi h)$ in the streamwise, wall-normal and spanwise direction for the uncontrolled cases. For the controlled cases with $\kappa_x \neq 0$, L_x is slightly adjusted on a case-by-case basis to fit the nearest integer multiple of the streamwise wavelength λ_x. In the case of longest forcing wavelength, two waves are contained by the computational domains.

Although the discretization parameters have been chosen to replicate or improve upon those used in related studies, we have explicitly checked for the effect of wall-normal discretization and spanwise size of the computational domain. One specific case which yielded one of the largest drag reductions (namely the CBC case at $\kappa_x^+ = 0.005$ and $\omega^+ = 0.0251$) has been repeated by independently doubling N_y and L_z. Starting from a baseline value for the friction coefficient of

$C_f = 3.41402 \times 10^{-3}$, we have measured $C_f = 3.41347 \times 10^{-3}$ with doubled N_y and $C_f = 3.41733 \times 10^{-3}$ with doubled L_z. In both cases, the difference is below 0.1‰.

Statistics are computed with a temporal average of no less than $T_{ave} = 700\ h/U_b$, after discarding the initial transient. The statistical time averaging error on the skin friction coefficient is estimated via the procedure introduced by Russo & Luchini (2017). After propagating the error on the drag reduction, the corresponding uncertainties are found to be so small that the error bars are smaller than the symbols used in the figures in §5.3.

5.2.4 Performance indicators

The control performance is evaluated in terms of the dimensionless indicators drag reduction rate $\mathcal{R}$‰, input power P_{in}‰ and net power saving P_{net}‰. These definitions, introduced by Kasagi *et al.* (2009), are suitable for CFR studies. The drag reduction rate describes the relative reduction of (dimensional) pumping power P^* per unit channel area:

$$\mathcal{R}‰ = 100\frac{P_0^* - P^*}{P_0^*} \tag{5.8}$$

where the subscript 0 refers to the uncontrolled flow. Since all the simulations run at CFR, $\mathcal{R}$ is equivalent to the reduction of the skin-friction coefficient $C_f = 2\tau_w/(\rho_b U_b^2)$, and (5.8) can be expressed in terms of C_f as:

$$\mathcal{R}‰ = 100\left(1 - \frac{C_f}{C_{f,0}}\right). \tag{5.9}$$

The time-averaged pumping power per unit channel area is computed as:

$$P^* = \frac{U_b}{T_{ave} L_x L_z} \int_{t_i}^{t_f} \int_0^{L_x} \int_0^{L_z} \tau_x \, dx \, dz \, dt \tag{5.10}$$

where τ_x is the streamwise component of the instantaneous wall-shear stress, and $T_{ave} = t_f - t_i$ is the interval for time averaging, defined by the final time t_f and the time t_i at which the initial transient is elapsed and a meaningful average can be taken. The control power P_c‰ is the power required to create the wall forcing while neglecting the losses of the actuation device, and is expressed as a fraction of the pumping power P_0^*. When the CBC strategy is employed, the power P_Φ required to cool the bulk flow should also be accounted for. Hence, the complete expression for the input power P_{in} is:

$$P_{in}\% = P_c\% + P_\Phi\% = \\ = \frac{1}{P_0^*}\frac{100}{T_{ave}L_xL_z}\int_{t_i}^{t_f}\int_0^{L_x}\int_0^{L_z} W\,\tau_z\,dx\,dz\,dt + \frac{100}{T_{ave}}\int_{t_i}^{t_f}\frac{\Phi}{\Phi_0^*}\,dt \quad (5.11)$$

where τ_z is the spanwise component of the instantaneous wall-shear stress, W the enforced spanwise wall velocity, and Φ_0^* the cooling power of the reference case. Finally, to compare benefits and costs of the control, the net energy saving rate P_{net} is defined as:

$$P_{net}\% = \mathcal{R}\% - P_{in}\%. \quad (5.12)$$

5.2.5 On the comparison strategy

As mentioned above in §5.2.3, we consider two strategies to run the compressible channel flow, once M_w^b and Re_τ are fixed.

The first one, denominated Zero Bulk Cooling (ZBC), sets to zero the bulk heating/cooling term Φ in Eq.(5.4): the bulk temperature is thus free to increase until, at equilibrium, the heat produced within the flow is balanced by the heat flux at the walls. This setup corresponds to the one originally adopted by Coleman *et al.* (1995) for the plane channel, and employed in all previous compressible studies of drag reduction by spanwise wall motion (Fang *et al.*, 2009; Yao & Hussain, 2019; Ruby & Foysi, 2022). ZBC simulations indicate that compressibility leads to larger drag reduction achieved by spanwise forcing. However, with ZBC the spanwise forcing causes T_b to increase above the value of the uncontrolled flow, in a way that depends on the control parameters; the different heat transfer rates make it difficult to discern the specific effects of compressibility and wall cooling. Furthermore, the equilibrium thermal condition achieved when the bulk temperature is free to evolve corresponds to extremely cold walls; the consequent large heat transfer rates are not representative of typical external flows, for which active techniques like spanwise forcing are primarily attractive.

To overcome these issues, a second strategy is considered, that is expected to provide more insight on the performance of flow control. With this strategy, named Constrained Bulk Cooling (CBC), the heat produced within the flow is balanced not only by the heat flux through the walls, but also by a cooling source term Φ, that is computed at each time step to keep the bulk temperature constant.

Following Zhang *et al.* (2014), we specify the thermal condition of the system by using the diabatic parameter Θ, also named dimensionless temperature:

$$\Theta = \frac{T_w - T_b}{T_r - T_b}, \quad (5.13)$$

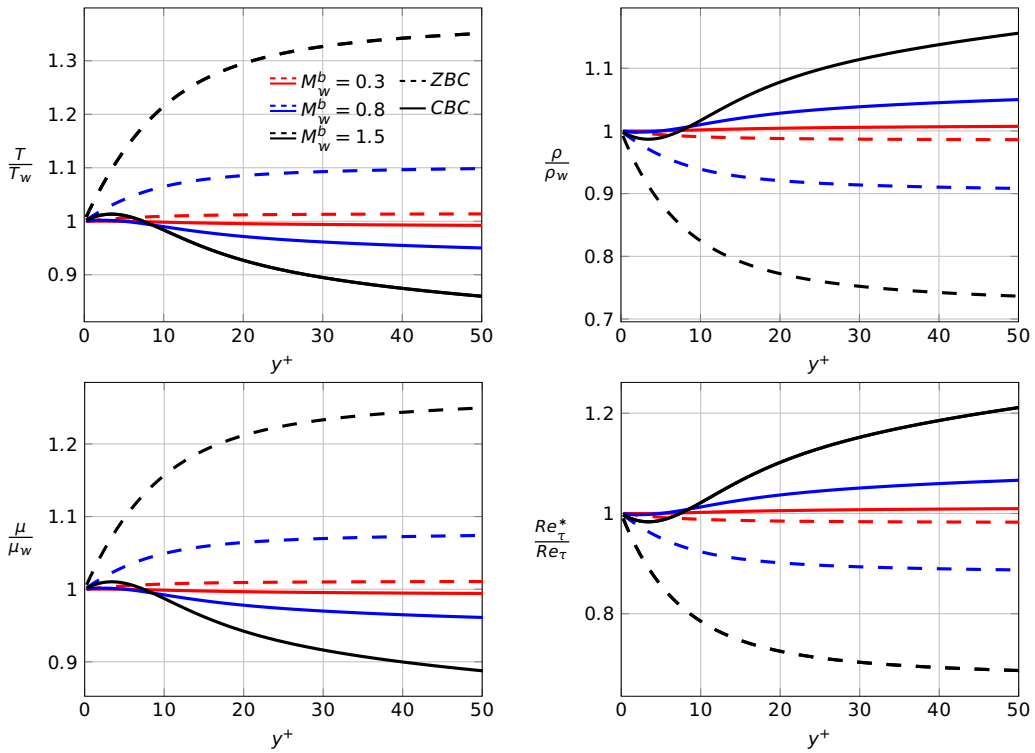

Figure 5.2: Temperature (top left), density (top right), dynamic viscosity (bottom left) and semi-local Reynolds number (bottom right) profiles in the wall region of a canonical compressible channel flow at $M_w^b = 0.3, 0.8$ and 1.5, with ZBC (dashed lines) and CBC (continuous lines).

where T_r is the recovery temperature:

$$T_r = \left(1 + \frac{\gamma - 1}{2} r \left(M_w^b\right)^2\right) T_b, \tag{5.14}$$

with $\gamma = c_p/c_v$ the heat capacity ratio, and r the recovery factor, a coefficient that, according to Shapiro (1953), for a turbulent flow over a flat surface is $r = Pr^{1/3}$.

Recent studies (Cogo *et al.*, 2023) have shown that a constant diabatic parameter, or equivalently a constant Eckert number (Wenzel *et al.*, 2022), is the proper condition under which compressible flows at different Mach numbers should be compared. The parameter Θ represents the fraction of the available kinetic energy transformed into thermal energy at the wall (Modesti *et al.*, 2022), and the importance of wall cooling increases when Θ decreases. In this study we set $\Theta = 0.75$, which corresponds to a moderately cold wall.

The main differences arising from the two channel configurations, ZBC and CBC, can be appreciated in figure 5.2, where temperature, density and dynamic

viscosity profiles across the channel are shown for the uncontrolled flow cases. In ZBC, at equilibrium the mean temperature profile monotonically increases from its minimum at the wall to its maximum at the channel centreline; the same trend is shared by the viscosity, whereas the opposite trend is observed for the density. Since T_b grows with M_w^b, the profile of T/T_w across the channel, shown in the top left panel of figure 5.2, gets progressively steeper at the wall with increasing M_w^b. While $T/T_w \approx 1$ for the subsonic M, at the channel centre for $M_w^b = 1.5$ (not shown) the mean temperature is about 39% higher than at the wall. The significant changes (especially for $M_w^b = 1.5$) of thermodynamic properties across the buffer layer imply that the local properties are quite different from the wall properties. In particular, the friction-velocity based Reynolds number Re_τ is intended to be constant across the comparison while M_w^b varies. However, in the buffer layer the semi-local Reynolds number $Re_\tau^* = Re_\tau\sqrt{(\rho\mu_w)/(\rho_w\mu)}$ (Huang *et al.*, 1995) is far from constant (see bottom right panel of 5.2), and varies significantly as a function of M_w^b.

With CBC, instead, Re_τ^* across the channel is such that its value in the buffer layer is still similar to the one at the wall (with a maximum observed increase of 2% for $M_w^b = 1.5$ at $y^+ = 10$) with a variation of less than 1.5% around the mean value of Re_τ^* at $y^+ = 10$, for the three values of M_w^b. Moreover, the profile of T/T_w across the channel qualitatively resembles the temperature distribution of a typical compressible boundary layer. In fact, at supersonic speeds the wall temperature can be considered for practical purposes to be very close to the recovery temperature of the flow, implying a very low heat exchange at the wall. Smaller values of Θ imply a cooler wall, and a local maximum of T/T_w further from the wall. For $\Theta = 0.75$, the local peak is minor and located right within the buffer layer, as shown in the top left panel of figure 5.2.

The difference between ZBC and CBC can be visually appreciated by looking at the near-wall turbulent structures in the uncontrolled flow, shown in figure 5.3. It is known (Coleman *et al.*, 1995) that by increasing M_w^b the low-velocity streaks become longer, less wavy and more widely spaced. This is indeed confirmed in the top row of figure 5.3, where color contours of an instantaneous field of streamwise velocity fluctuations computed with ZBC at $y^+ = 10$ is plotted for $M_w^b = 0.3$ (left) and $M_w^b = 1.5$ (right). However, when switching to CBC (bottom row), the streaks appear not to differ significantly between the subsonic and the supersonic cases. This suggests that a matching diabatic parameter allows to discriminate those changes of the near-wall structures that directly derive from compressibility effects from those linked to a change in the wall-normal temperature profile. In fact, a non-uniform temperature across the channel implies changes to other thermodynamic properties (i.e. density and viscosity), and their wall values become not fully representative of the physics in the buffer layer. This observation is essential when

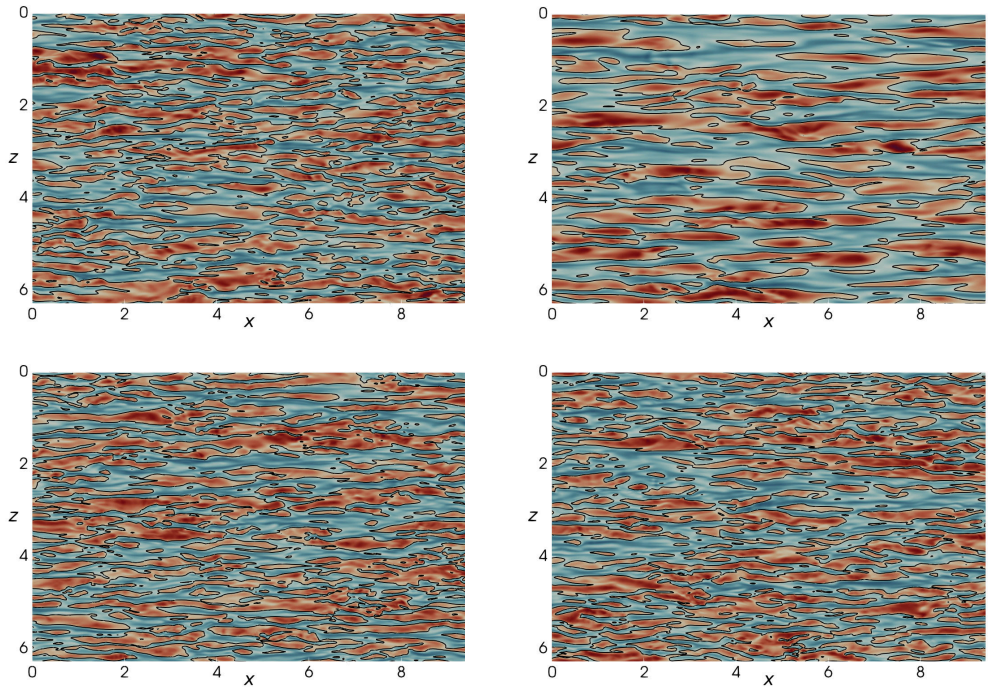

Figure 5.3: Streamwise velocity fluctuations u^+ in a wall-parallel portion of the $x-z$ plane at $y^+ = 10$ for ZBC (top) and CBC (bottom) at $M_w^b = 0.3$ (left) and $M_w^b = 1.5$ (right) for the uncontrolled case. The blue-to-red colorscale ranges from -10 to $+10$; the black line is for the zero contour level.

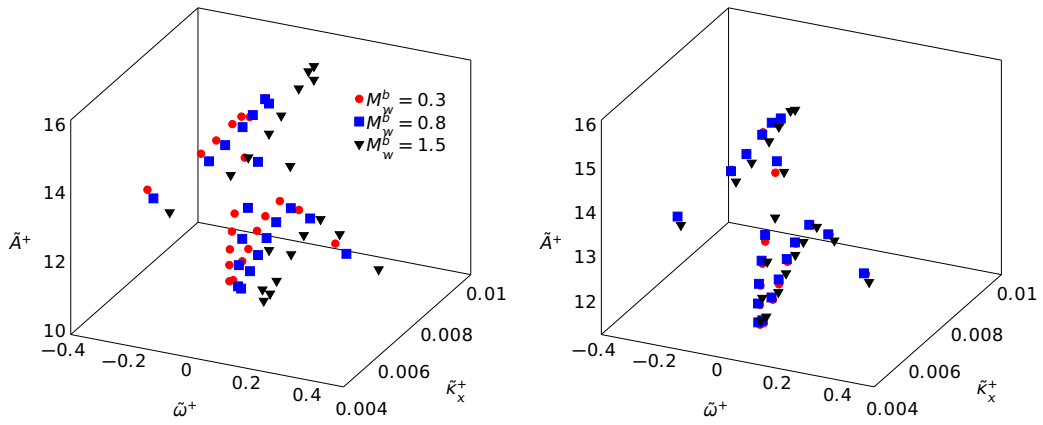

Figure 5.4: Frequency $\tilde{\omega}^+$, wavenumber $\tilde{\kappa}_x^+$ and amplitude $\tilde{A}^+$ of the control forcing for the travelling waves at $\kappa_x^+ = 0.005$ (line 3 of figure 5.1) made dimensionless with the thermodynamic properties of the actuated flow at $y^+ = 10$.

the purpose of the study is to assess skin-friction drag changes induced by spanwise forcing, whose physical mechanism is not fully uncovered yet, but certainly resides within the thin transversal Stokes layer which interacts with the near-wall cycle occurring in the buffer layer. When the actuation parameters scale in viscous wall units, their effects in the buffer layer are not easily comparable in the ZBC case.

As an example, figure 5.4 plots the control parameters $\tilde{\omega}^+$, $\tilde{\kappa}_x^+$ and $\tilde{A}^+$ of the simulations taken along line 3 of figure 5.1. The parameters are still scaled in wall units, but the tilde indicates that viscous units are built with density and viscosity measured in the actuated flow at $y^+ = 10$, for the ZCB (left) and CBC (right) comparison strategy. Figure 5.4 is effective at showing that with ZBC the buffer layer experiences a forcing whose set of parameters changes with the Mach number, whereas with CBC the simulation parameters match at the various M_w^b, and enable the comparison of compressibility effects for a given control.

5.3 Drag reduction and power savings

The database produced in the present work is used for a comprehensive analysis of the effect of compressibility on the drag reduction and power budget performance of StTW. The reference Reynolds number of choice is $Re_\tau = 400$, i.e. higher than $Re_\tau = 200$, where most of the incompressible information is available, to avoid full or partial relaminarization. Data at $Re_\tau = 400$ are also relatively free from the low-Re effects that plague results obtained at $Re_\tau = 200$. Obviously, the downsides are a larger computational cost, and a limited number of incompressible data to directly compare with. Results at $M_w^b = 0.3$ are compared to those of Hurst *et al.* (2014) for

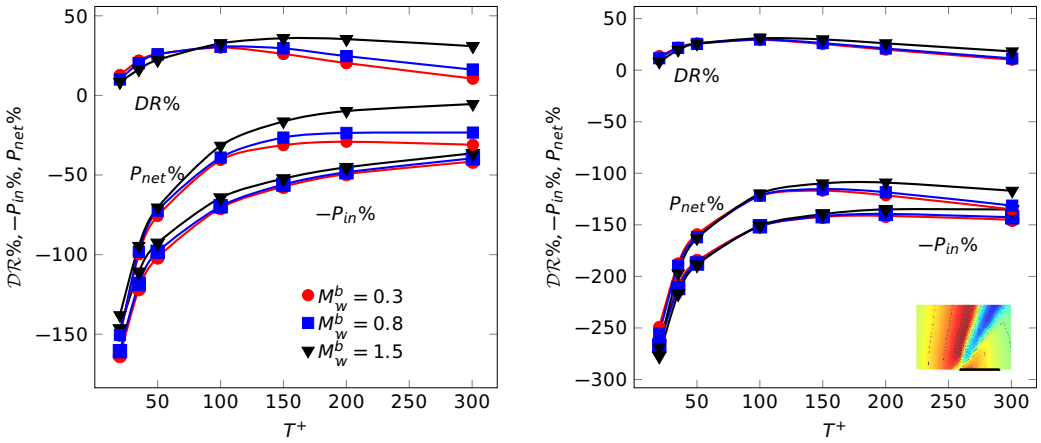

Figure 5.5: Drag reduction rate and power budget as a function of the period T^+ for the oscillating wall (line 1 of figure 5.1, see inset), for ZBC (left) and CBC (right).

the oscillating wall, stationary waves and the travelling waves at fixed wavenumber. For the oscillating wall, a few data points from Ricco & Quadrio (2008) are also available. For the other control cases, the main incompressible comparison data are the StTW results of Gatti & Quadrio (2016). Their comprehensive datasets at $Re_\tau = 200$ and $Re_\tau = 1000$, available as Supplementary Material to their paper, are interpolated to obtain drag reduction for arbitrary combinations of the control parameters. As suggested in that paper, drag reduction data is expressed in terms of the vertical shift ΔB^+ of the streamwise mean velocity profile in its logarithmic region, which minimizes the effect of the small computational domain and reduces the Re effect on $\mathcal{R}$. In fact, ΔB^+ becomes a Re-independent measure of drag reduction, once Re is sufficiently large (they tentatively suggested $Re_\tau > 2000$) for the mean profile to feature a well-defined logarithmic layer. Since ΔB^+ is still Re-dependent at the present values of Re, we interpolate linearly the ΔB^+ data by Gatti & Quadrio (2016) between $Re_\tau = 200$ and $Re_\tau = 1000$ to retrieve ΔB^+ at $Re_\tau = 400$. Note that, owing to the small computational domain, the $Re_\tau = 200$ data by Gatti & Quadrio (2016) slightly overestimate drag reduction, particularly at small frequencies and wavelengths. The incompressible control power is interpolated at $Re_\tau = 400$ from data of Gatti & Quadrio (2016), by assuming a power law dependence with Re_τ, as stated by Ricco & Quadrio (2008) and Gatti & Quadrio (2013).

The few available compressible data are from Yao & Hussain (2019), who considered the oscillating wall only, at the slightly higher $Re_\tau = 466$ for $M_w^b = 0.8$ and $Re_\tau = 506$ for $M_w^b = 1.5$. Moreover, the datapoints computed by Ruby & Foysi (2022) for a stationary wave are at $M_w^b = 0.3$, $Re_\tau = 396$ and $M_w^b = 1.5$, $Re_\tau = 604$.

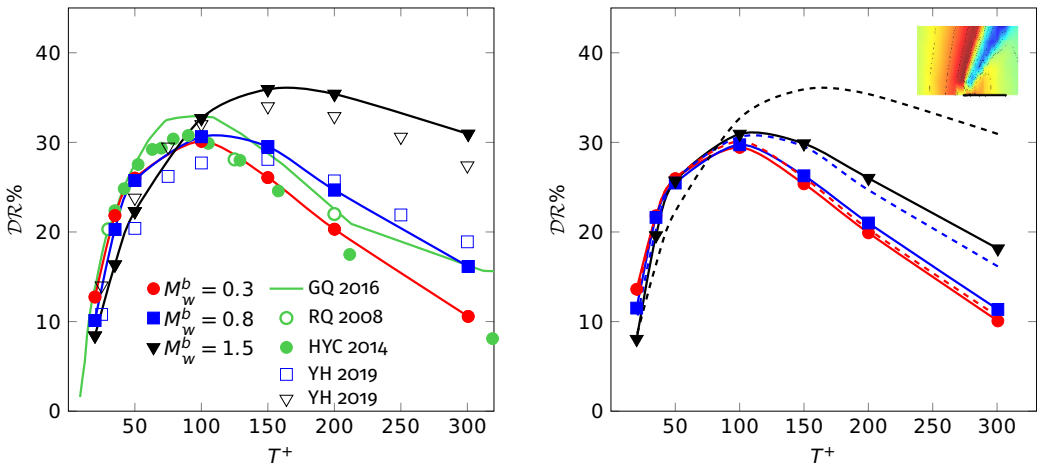

Figure 5.6: Drag reduction rate versus period T^+ for the oscillating wall (line 1 of figure 5.1, see inset), for ZBC (left) and CBC (right). Incompressible data are in green: solid line without symbols from Gatti & Quadrio (2016), solid symbols from Hurst *et al.* (2014), and open symbols from Ricco & Quadrio (2008). The blue and black open symbols are from Yao & Hussain (2019) at $M_w^b = 0.8$, $Re_\tau = 466$ and $M_w^b = 1.5$, $Re_\tau = 506$. Solid lines indicate interpolation. Dashed lines on the right panel are results for ZBC.

A combined view of the raw results of the simulations, in terms of drag reduction and power budget, is shown first in figure 5.5 for the oscillating-wall case (line 1 of figure 5.1). The left panel plots the data collected with ZBC, and the right panel illustrates CBC. The scaling of the data computed with CBC appears to improve significantly. Since the different range of variation for drag and powers makes the details difficult to appreciate, in the following we consider them separately, providing in §5.3.1 and §5.3.2 a detailed comparison with existing literature data, and studying the power cost in terms of control power and cooling power. For completeness, Appendix 1 contains the remaining raw data, computed on the remaining four lines of figure 5.1, plotted together as in figure 5.5.

5.3.1 Drag reduction

Figure 5.6 shows the drag reduction rate obtained for the temporally oscillating wall, i.e. along line 1 of figure 5.1, as a function of the oscillating period T^+.

We first consider the ZBC case on the left. For $M_w^b = 0.3$, $\mathcal{R}$ grows with T^+ up to a maximum at about $T^+ = 100$, and then monotonically shrinks. This is in agreement with the incompressible results of Hurst *et al.* (2014), Ricco & Quadrio (2008) and Gatti & Quadrio (2016), whose interpolated data, as expected, slightly overpredict $\mathcal{R}$, especially at large periods. This is due to the combined

effect of low Re and small computational domain employed in that study, which – particularly for the oscillating wall, where only one forcing phase is present at a particular time – leads to partial relaminarization during the cycle. The curves at higher M_w^b are qualitatively similar, but tend to remain below the incompressible data at small periods, and to go above them at large ones. Near the optimal period, compressibility makes the maximum $\mathcal{R}\%$ grow, and shift towards larger periods: for $M_w^b = 0.3$ the maximum drag reduction is $\mathcal{R}_{0.3}^m = 30.3\%$ at $T^+ = 100$, whereas $\mathcal{R}_{0.8}^m = 30.6\%$ at $T^+ = 100$, and for $M_w^b = 1.5$ it becomes $\mathcal{R}_{1.5}^m = 35.9\%$ at $T^+ = 150$. This picture confirms the compressible results at $Re_\tau = 200$ discussed by Yao & Hussain (2019), except for the supersonic case, where they reported a monotonic increase of $\mathcal{R}\%$ with T^+. This is ascribed to the partial relaminarization occurring at $Re_\tau = 200$ when drag reduction is large; the present study, owing to its higher $Re_\tau = 400$, is able to identify a well defined $\mathcal{R}\%$ peak even in the supersonic regime. Figure 5.6 also includes results at higher Re_τ from Yao & Hussain (2019) for the transonic and supersonic cases. Again, qualitative agreement is observed; quantitative differences are due to their slightly different Reynolds number, which is $Re_\tau = 466$ for $M_w^b = 0.8$ and $Re_\tau = 506$ for $M_w^b = 1.5$.

The right panel of figure 5.6 plots the results computed under CBC, and compares them with those under ZBC. The $M_w^b = 0.3$ cases are almost identical; at this low M_w^b compressibility effects are minor, and the difference between ZBC and CBC negligible. At larger M_w^b, however, with CBC the results show a much better collapse over the three values of M_w^b. The maximum drag reduction consistently occurs at $T^+ = 100$, and is nearly unchanged across the three cases.

Overall, the favorable effect of compressibility in terms of maximum drag reduction of the oscillating wall is confirmed. However, the significant increase of the maximum drag reduction reported by Yao & Hussain (2019) is only confirmed when the comparison is carried out with ZBC, whereas for CBC this increment is very limited.

Figure 5.7 shows results for the stationary waves, i.e. along line 2 of figure 5.1, plotted as a function of the streamwise wavenumber κ_x. The trend resembles that of the temporal oscillation. Again, at $M_w^b = 0.3$ differences from the incompressible limit are minor. Once M_w^b grows, a significant dependency on the wavenumber is observed: at large κ_x $\mathcal{R}\%$ slightly decreases, but at small κ_x it increases significantly.

For the ZBC dataset (left), a significant shift of the $\mathcal{R}\%$ peak towards smaller wavenumbers is observed, with a peak value of $\mathcal{R}_{0.3}^m = 40.4\%$ for $\kappa_x^+ = 0.005$, $\mathcal{R}_{0.8}^m = 42.5\%$ for $\kappa_x^+ = 0.005$, and $\mathcal{R}_{1.5}^m = 47.1\%$ for $\kappa_x^+ = 0.0017$. However, once the CBC comparison is considered (right), the overshoot at small κ_x^+ disappears; data at $M_w^b = 0.3$ and $M_w^b = 0.8$ collapse, and the supersonic case still presents its maximum at $\kappa_x^+ = 0.005$.

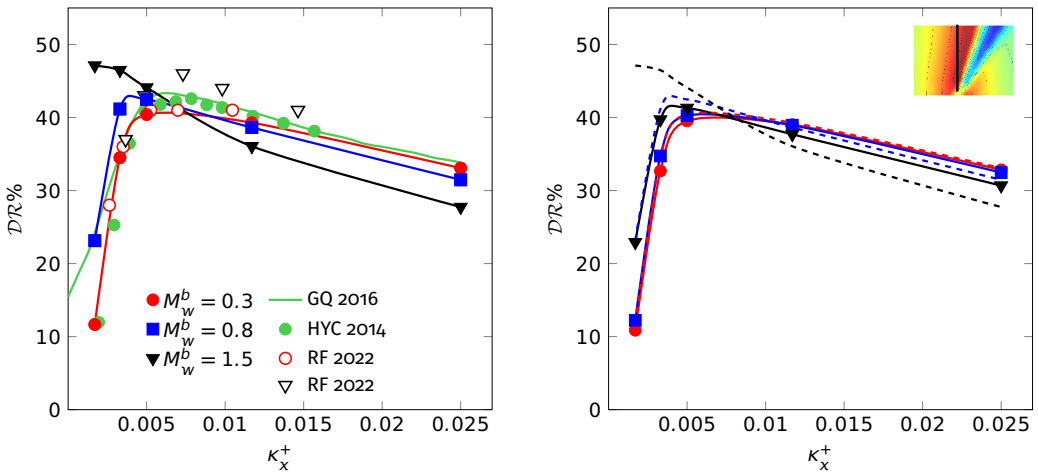

Figure 5.7: Drag reduction rate versus wavenumber κ_x^+ for the steady waves (line 2 of figure 5.1, see inset), for ZBC (left) and CBC (right). Incompressible data are in green and dashed lines are for ZBC, as in figure 5.6. Red and black open symbols are from Ruby & Foysi (2022) at $M_w^b = 0.3$, $Re_\tau = 396$ and $M_w^b = 1.5$, $Re_\tau = 604$.

Open symbols in the left panel of figure 5.7 are the results of Ruby & Foysi (2022), computed with ZBC. One immediately notices their different trend compared to the present data. In fact, in their numerical experiments the value of the semi-local Reynolds number evaluated at the centreline was kept fixed at $Re^*_{\tau,c} = 400$: this implies a variation of Re_τ between 396 and 604 while moving from the subsonic to the supersonic case. In the present simulations, instead, $Re_\tau \approx 400$ at all M. Additionally, in their study the forcing wavelength was scaled with semi-local quantities, so that a direct comparison is problematic. Red and black open symbols represent their results at $M_w^b = 0.3$ and $M_w^b = 1.5$, rescaled in viscous units: these rescaled data present the same trend observed here with CBC, with the supersonic case lacking the $\mathcal{R}\%$ peak at the smallest κ_x^+, and suggest a qualitative similarity between a comparison based on a semi-local scaling and the present CBC strategy.

We now move on to consider a travelling wave, and plot in figure 5.8 how $\mathcal{R}\%$ varies as a function of the frequency ω^+ for a travelling wave at fixed $\kappa_x^+ = 0.005$, i.e. along line 3 of figure 5.1. Once again, data for $M_w^b = 0.3$ do not differ from the incompressible ones. At higher M_w^b, with ZBC the maximum drag reduction increases above the incompressible value, but, far from the peak, drag reduction levels are generally lower. The boost in maximum drag reduction grows with M_w^b, and is accompanied by a slight shift towards higher frequencies. At $M_w^b = 1.5$, the peak is at $\omega^+ = 0.025$, and reaches the outstanding value of $\mathcal{R}^m_{1.5} = 51.6\%$. Increasing M_w^b also intensifies the drag increase in the range $0.05 \lesssim \kappa_x^+ \lesssim 0.1$,

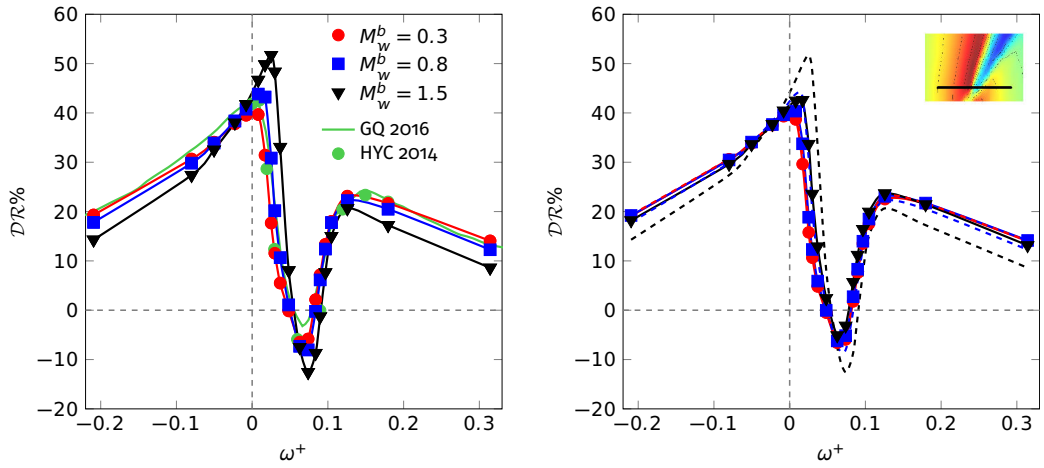

Figure 5.8: Drag reduction rate versus frequency ω^+ for the streamwise-travelling waves at $\kappa_x^+ = 0.005$ (line 3 of figure 5.1, see inset), for ZBC (left) and CBC (right). Incompressible data are in green and dashed lines data are for ZBC, as in figure 5.6.

with a maximum of 12.2% for $M_w^b = 1.5$.

Once again, if the comparison is carried out with the CBC criterion, the compressibility effects remain generally favourable, but become much smaller. The extra gain is extremely small, and the curves at varying M_w^b nearly collapse.

Figure 5.9 reports the results computed for the points on the vertical line 4 of figure 5.1 at fixed $\omega^+ = -0.21$, where the incompressible $\mathcal{R}\%$ is nearly constant with κ_x^+. As for lines 1 and 3, compressibility is found to deteriorate the control performances at large (positive and negative) frequencies. However, this is emphasized by the ZBC comparisons, whereas CBC results show a much better collapse.

Finally, results from simulations on line 5 in figure 5.1, drawn along the ridge of optimal $\mathcal{R}\%$ in the $(\omega - \kappa_x)$ plane of parameters, are depicted in figure 5.10. It is worth recalling that, according to Gatti & Quadrio (2016), this ridge and in particular its portion near the origin of the plane is where the largest changes with Re are expected. Indeed, the subsonic points do not fully overlap with incompressible data, which inherit the low-Re nature of the reference through the interpolation, and show a rather uniform value of $\mathcal{R}\%$. The supersonic data lie below the subsonic ones at large frequencies, but outperform them at small frequencies. Once CBC is used, the collapse of the curves at different M_w^b improves significantly, while the general changes remain qualitatively the same.

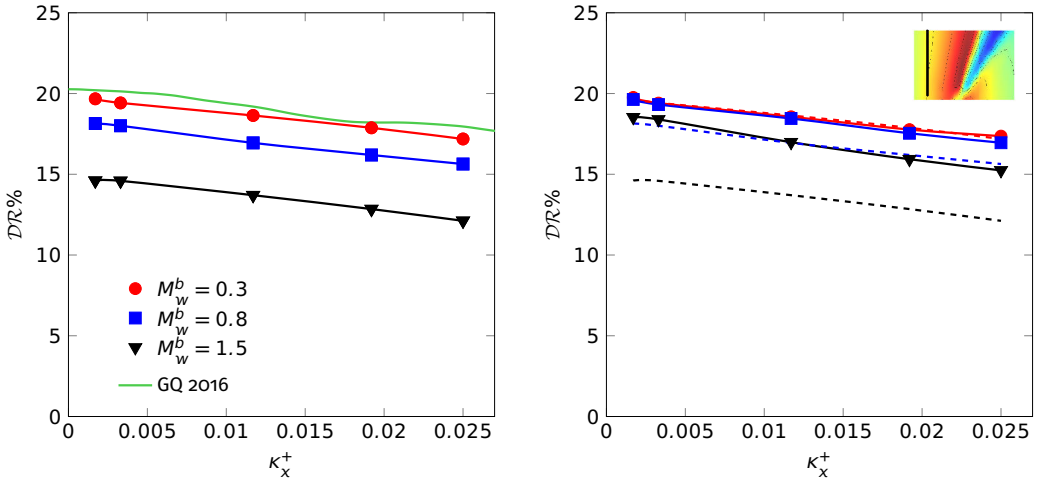

Figure 5.9: Drag reduction rate versus wavenumber κ_x^+ for the travelling waves at $\omega^+ = -0.21$ (line 4 of figure 5.1, see inset), for ZBC (left) and CBC (right). Incompressible data are in green, and dashed lines are for ZBC, as in figure 5.6.

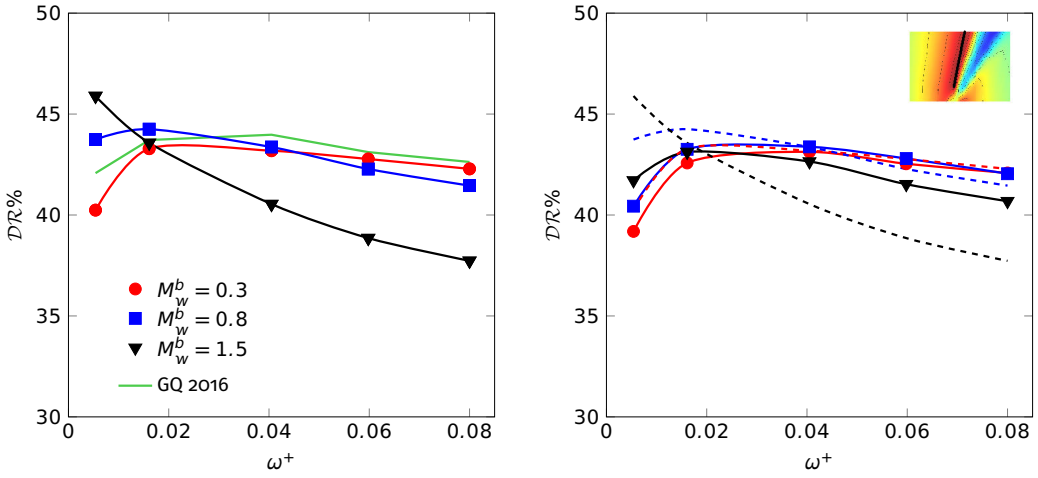

Figure 5.10: Drag reduction rate versus frequency ω^+ for the travelling waves for the optimal ridge (line 5 of figure 5.1, see inset), for ZBC (left) and CBC (right). Incompressible data are in green, and dashed lines are for ZBC, as in figure 5.6.

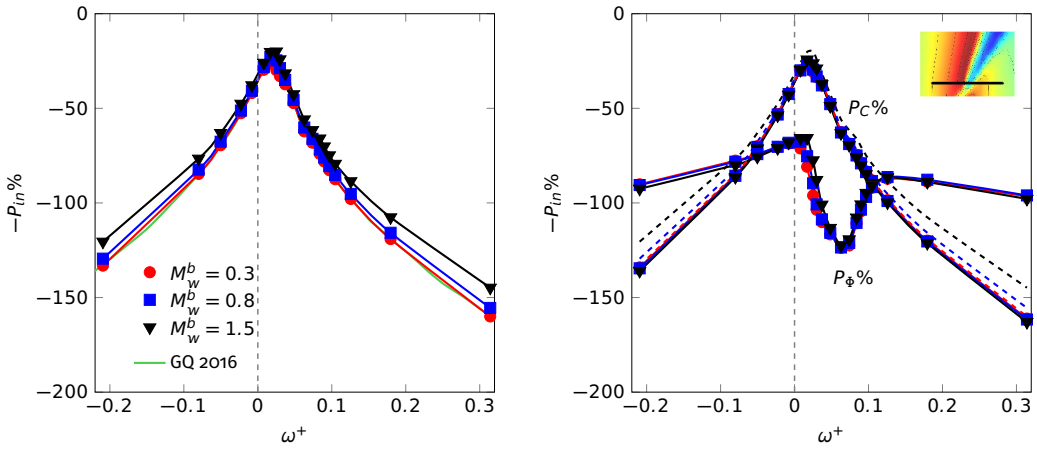

Figure 5.11: Input power for the travelling waves with $\kappa_x^+ = 0.005$ (line 3 of figure 5.1, see inset) for ZBC (left) and CBC (right). For CBC the two contributions to $P_{in}\%$, i.e. the control power $P_c\%$ and the cooling power $P_\Phi\%$ are plotted separately. Incompressible data are in green, and dashed lines are for ZBC.

5.3.2 Power budgets

Since StTW is an active form of flow control, quantifying the energy consumption of the control system is key to assess the overall efficiency: one needs to compare costs, i.e. the control energy, and benefits, i.e. the energy savings made possible by a reduction of the skin-friction drag.

Figure 5.11 plots, as one example, the input power $P_{in}\%$ on line 3 of figure 5.1. A similar scenario holds in the entire plane. For the ZBC comparison (left panel), the input power, which depends significantly on the control parameters, shows a decrease (in absolute value) with M_w^b, especially at large frequencies. With CBC, $P_{in}\%$ features two contributions: the control power and the cooling power. They turn out to be roughly of the same order of magnitude, and both have a minor dependence on M_w^b, yet the dependence of the latter on control parameters resembles the one of $\mathcal{R}\%$. The extra cost to cool the flow is an effect of the additional term in the energy equation, which serves the purpose of yielding an internal flow with a temperature profile that resembles an external flow. In a true external flow, however, cooling would occur naturally: $P_{in}\%$ would reduce to the control power $P_c\%$. Since the control contribution to $P_{in}\%$ in StTW is a rather simple quantity that can be analytically predicted under the hypothesis of a laminar generalized Stokes layer (Quadrio & Ricco, 2011), the perfect collapse of $P_c\%$ under CBC witnesses how the controlled cases are being properly compared.

Figure 5.12 plots the net power saving $P_{net}\%$ for the temporal wall oscillations, i.e. along line 1 of figure 5.1. The left panel is computed with ZBC; in agreement

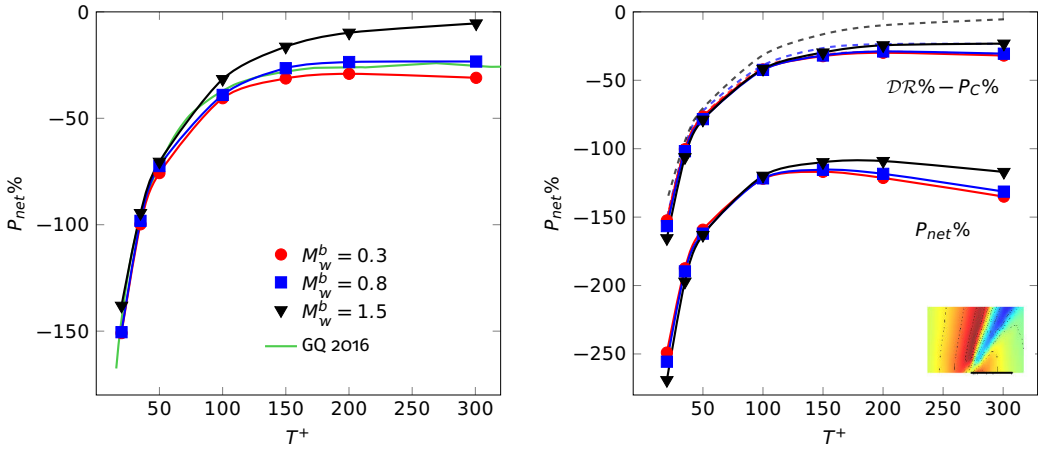

Figure 5.12: Net power saving for the oscillating wall (line 1 of figure 5.1, see inset), for ZBC (left) and CBC (right). Incompressible data are in green. The right panel also plots $\mathcal{R}\% - P_c\%$ (top set of curves), where dashed lines are for ZBC.

with the incompressible case, for $A^+ = 12$ no net saving is obtained. However, the power budget improves with the Mach number, and at $M_w^b = 1.5$ it approaches zero. This is due to the combined effect of increasing $\mathcal{R}\%$ (for $T^+ \gtrsim 100$, see figure 5.6), and decreasing $P_{in}\%$ (especially for small T). The right panel of figure 5.12 plots $P_{net}\%$ under CBC (lower set of curves), and the net power saving without accounting for the cooling power, namely $\mathcal{R}\% - P_c\%$. Since $P_c\%$ and $P_\Phi\%$ are of the same order of magnitude, $P_{net}\%$ becomes largely negative: the interesting outcome of the ZBC case vanishes. However, when only $P_c\%$ is considered, $P_{net}\%$ becomes comparable with the ZBC case (upper set of curves), albeit the positive compressibility effect decreases substantially.

Examining data along line 2 of figure 5.1 (stationary waves), which passes near the absolute maximum of drag reduction, is instructive. The plot is shown in figure 5.13. For a ZBC comparison (left), the net saving increases substantially with M_w^b for $\kappa_x^+ < 0.012$, such that the maximum shows a 5-fold increase, from 5% in the incompressible case to 25.8% for $M_w^b = 1.5$ The peak is also observed to shift towards smaller κ_x^+. Under CBC, however, much of the improvement disappears, and the curves almost collapse, with only a small residual effect for the supersonic curve. When $P_{net}\%$ takes into account the cooling power, the outcome is negative regardless of the control parameters.

Results from Ruby & Foysi (2022) at ZBC and at fixed $Re_{\tau,c}^*$ are also plotted in the left panel of figure 5.13. They are computed at rather small wavenumbers, and overlap to the present data for $M_w^b = 0.3$, but indicate much larger savings at $M_w^b = 1.5$. Nevertheless, their trend resembles the one obtained here at CBC, and indicate the presence of a local maximum, and the lack of explosive savings at

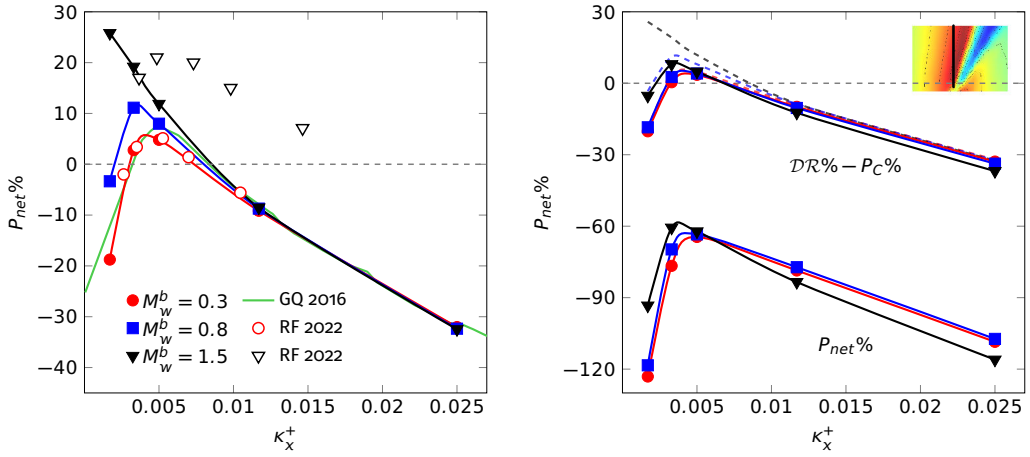

Figure 5.13: Net power saving for the steady waves (line 2 of figure 5.1, see inset), for ZBC (left) and CBC (right). Incompressible data are in green. The right panel also plots $DR\% - P_c\%$ (top set of curves) where dashed lines are for ZBC. Red and black open symbols are from Ruby & Foysi (2022) at $M_w^b = 0.3, Re_\tau = 396$ and $M_w^b = 1.5, Re_\tau = 604$.

vanishing wavenumbers.

Figure 5.14 plots the net power saving for travelling waves at fixed $\kappa_x^+ = 0.005$ (line 3 of figure 5.1). The ZBC comparison shows a large increase of $P_{net}\%$, up to 31.4 % for the largest M; the peaks shift towards larger positive ω. Interestingly, the peaks of $\mathcal{R}\%$ and $P_{in}\%$ occur around the same frequency, and they are both enhanced by compressibility. When the comparison is carried out at CBC, however, once again the curves show a tendency to overlap, and the maximum saving shrinks to 17.8% for $\mathcal{R}\% - P_{in}\%$, which remains an interesting figure, but in line with the incompressible case. If both contributions to $P_{in}\%$ are included, $P_{net}\%$ is largely negative at every ω.

5.4 Concluding discussion

We have studied how spanwise forcing implemented via streamwise-travelling waves of spanwise velocity at the wall alters the skin-friction drag in compressible flows. A set of 258 direct numerical simulations for a turbulent plane channel flow are carried out, for subsonic ($M_w^b = 0.3$), transonic ($M_w^b = 0.8$) and supersonic ($M_w^b = 1.5$) speeds, at the baseline friction Reynolds number of $Re_\tau = 400$. The available literature information, which includes only few such studies for compressible flows, is significantly extended; in particular, travelling waves are considered here for the first time. The study considers the control performance for

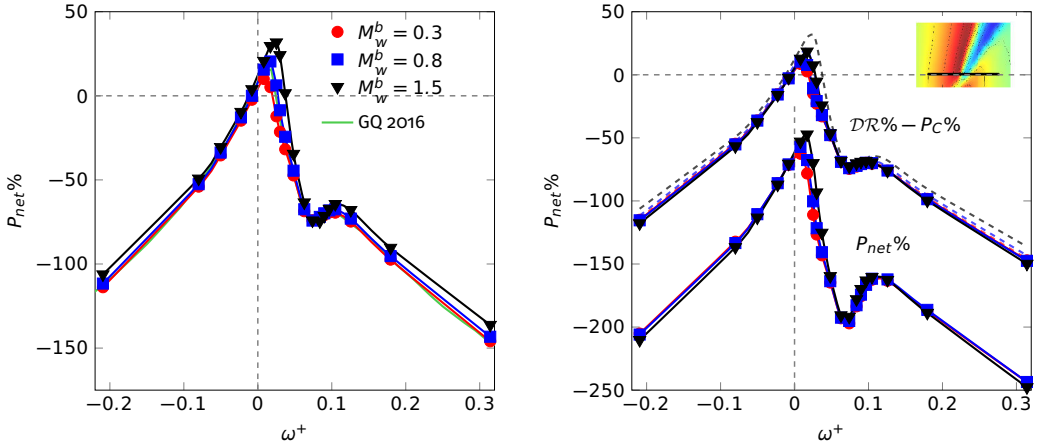

Figure 5.14: Net power saving for the travelling waves with $\kappa_x^+ = 0.005$ (line 3 of figure 5.1, see inset) for ZBC (left) and CBC (right). Incompressible data are in green. The right panel also plots $DR\% - P_c\%$ (top set of curves) where dashed lines are for ZBC.

the temporally oscillating wall ($\kappa_x = 0$), the steady wave ($\omega = 0$), travelling waves at fixed wavenumber $\kappa_x^+ = 0.005$ and at fixed frequency $\omega^+ = -0.21$, and the ridge of maximum drag reduction corresponding to waves travelling with a slow forward speed. All the simulations are run by keeping the bulk velocity constant in time as well as between unforced and forced cases.

In addition to the bulk velocity, in the compressible setting a further quantity related to the energy equation must be kept constant to enable a proper comparison. Since its choice impacts the qualitative outcome of the study, we employ and compare two different strategies. The first, that we indicate with Zero Bulk Cooling or ZBC, is commonly used for duct flows, and lets the bulk temperature evolve freely until an asymptotic value is reached at which the heat produced within the flow is balanced by the heat flux through the isothermal walls. Unfortunately, ZBC leads to different bulk temperatures for each simulation, and in the present context it hinders the physical interpretation of results.

In a second approach, named Constrained Bulk Cooling or CBC, the value of the bulk temperature is kept constant during the simulations, by means of a bulk cooling term in the energy equation. To do so, the value of the diabatic parameter Θ is fixed across both the values of the Mach number and the control parameters of the StTW, implying that a fixed portion of bulk flow kinetic energy is converted into thermal energy, and that extra energy is spent for the cooling process. Using the diabatic parameter (or, equivalently, the Eckert number) has been recently considered by Cogo *et al.* (2023) as a means to achieve a similar wall cooling across different values of the Mach number. Extending a Θ-based comparison

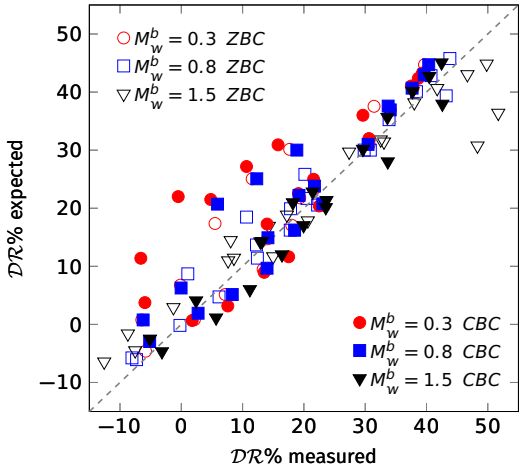

Figure 5.15: Drag reduction for the streamwise-travelling waves at $\kappa_x^+ = 0.005$ measured in the compressible regime versus drag reduction of the incompressible regime when the control parameters are scaled with the thermodynamic properties of each different case at $y^+ = 10$.

to account for different values of Θ with flow control and drag reduction is an interesting future development of the present study.

Results of the simulations show that StTW remain fully effective in transonic and supersonic flows, thus extending available results for the oscillating wall and the steady waves. In fact, drag reduction can be higher in compressible flows than in incompressible ones, when frequency and wavenumber of the forcing are small. However, the improvement appears to be substantial only when the comparison is carried out at ZBC. When CBC is used, only marginal improvements are detected; curves at various M_w^b tend to collapse and to replicate the incompressible behaviour. Figure 5.15 shows for the controlled flow at $\kappa_x^+ = 0.005$ (line 3 of the map of figure 5.1) the drag reduction measured by the simulations of the present work plotted against the drag reduction of the incompressible case. The control parameters are made dimensionless with the thermodynamic properties of each case at $y^+ = 10$ (see §5.2.5). Most points lie on the diagonal line: drag reduction becomes constant with the Mach number, once the effect of the changed thermodynamics is removed. The few outliers are points of the map where drag reduction gradients are extremely large, and the limited number of available incompressible data leads to a poor interpolation, as already pointed out in §5.3. This picture demonstrates that, once spurious thermodynamic changes are factored out, compressibility has little to no effect on the drag reduction performance of the travelling waves.

Similar results hold for the power budget: StTW yield large net energy savings, even in the compressible regime, but the impressive improvements observed with

ZBC against the incompressible reference do not carry over to the CBC comparison, which broadly replicates the incompressible results. The last statement is only valid as long as the extra cooling power implied by CBC is neglected, on the basis that it represents an artefact to obtain an internal flow with a temperature profile that resembles that of an external flow.

Hence, choosing the comparison strategy is key to properly describe how drag reduction and power savings of an active drag reduction technique change in the compressible regime. In a way, this reminds of the incompressible case, where early studies for the oscillating wall claimed "disruption of turbulence" only because comparing at the same bulk velocity implies an important reduction of Re_τ when drag reduction is achieved. While ZBC is certainly apt to describe internal flows, the observed drag reduction figures are significantly larger than their incompressible counterpart primarily because the control parameters affect the terms of the comparison. A CBC comparison, in which the dimensionless temperature remains constant with M and across the controlled cases, seems more appropriate, and in fact yields data that overlap well when the Mach number is varied. With CBC, only a small, albeit non negligible, extra drag reduction and net power saving are found in comparison to the incompressible case.

5.A A compact representation of the dataset

This Appendix uses the format of figure 5.5 to report, for completeness, the entire dataset with figures where drag and power changes are plotted together. After line 1 of figure 5.1, already described in figure 5.5, the following figures 5.16, 5.17, 5.18 and 5.19 respectively concern lines 2, 3, 4 and 5.

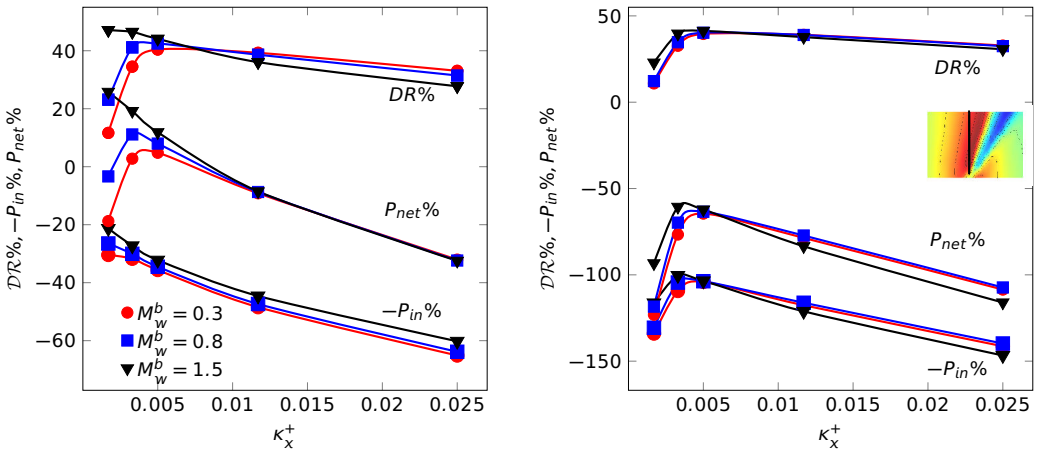

Figure 5.16: Drag reduction rate and power budget versus wavenumber κ_x^+ for the steady waves (line 2 of figure 5.1, see inset), for ZBC (left) and CBC (right).

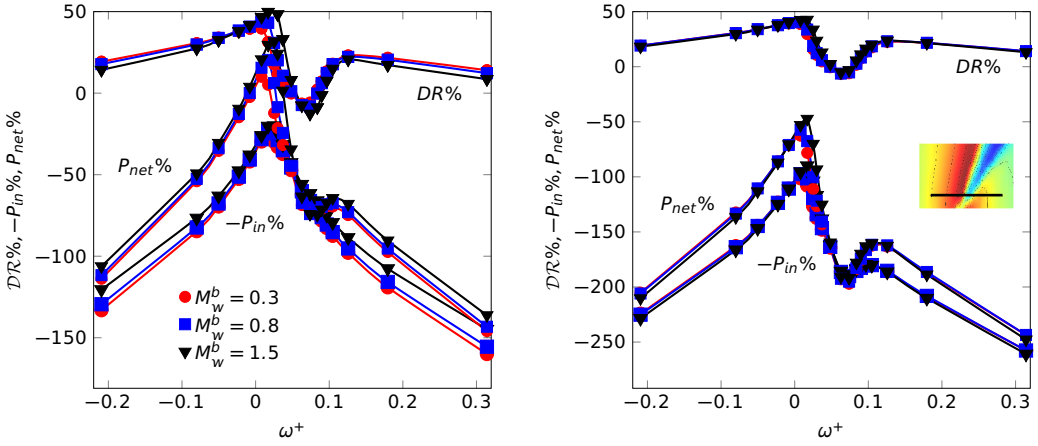

Figure 5.17: Drag reduction rate and power budget versus frequency ω_x^+ for the streamwise-travelling waves (line 3 of figure 5.1, see inset), for ZBC (left) and CBC (right).

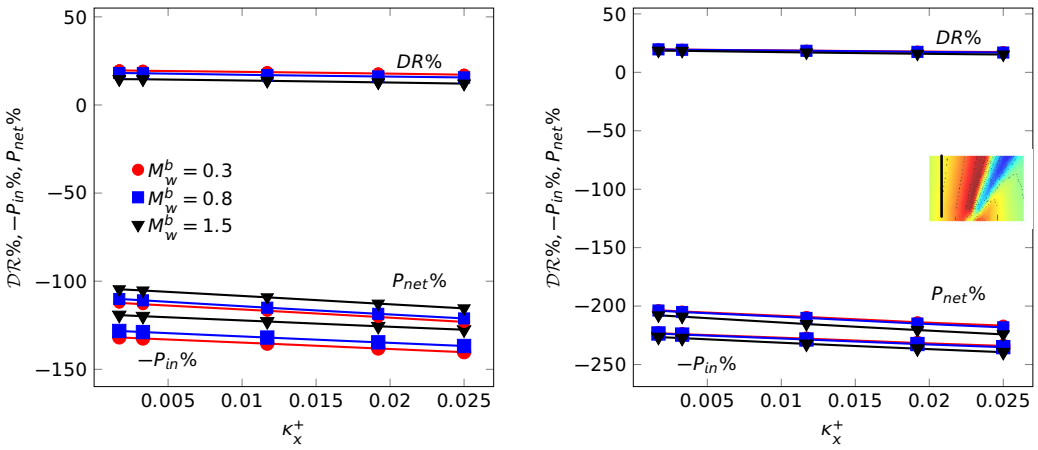

Figure 5.18: Drag reduction rate and power budget versus wavenumber κ_x^+ for the travelling waves at $\omega^+ = -0.21$ (line 4 of figure 5.1, see inset), for ZBC (left) and CBC (right).

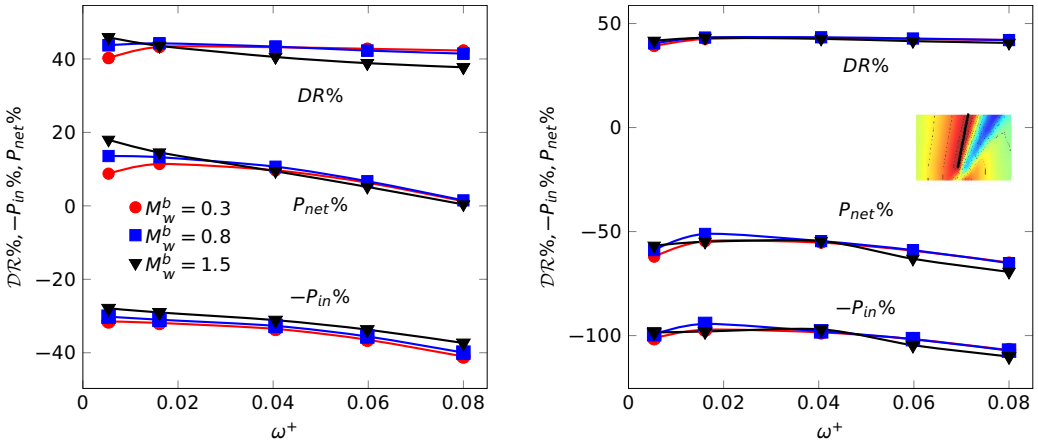

Figure 5.19: Drag reduction rate and power budget versus frequency ω^+ for the optimal ridge (line 5 of figure 5.1, see inset), for ZBC (left) and CBC (right).

A simple and efficient immersed-boundary method for the incompressible Navier–Stokes equations

The content of this Paper is currently under review
for the *Journal of Computational Physics* and published on ArXiv as
Luchini, P., Gatti, D., Chiarini, A., Gattere, F., Atzori, M. & Quadrio, M.
A simple and efficient immersed-boundary method
for the incompressible Navier–Stokes equations.
Minor editing has been done for formatting purposes.

A simple and efficient immersed-boundary method for the incompressible Navier–Stokes equations

Abstract

A novel immersed-boundary method for the incompressible Navier–Stokes equations is presented. It employs a discrete forcing for a sharp discrimination of the solid-fluid interface, and achieves a second-order accuracy that is demonstrated in examples with highly complex three-dimensional geometries. The method is implicit, meaning that the point in the solid which is nearest to the interface is accounted for implicitly; it is also implicit in time, when applied to time-dependent problems, which benefits its stability and convergence properties. The method stands out for its simplicity and efficiency: only the weight of the center point of the Laplacian stencil in the momentum equation is modified, and no corrections for the continuity equation and the pressure are required. Its computational efficiency derives from its tight integration with the underlying second-order finite difference method. The immersed-boundary method, its performance and its second-order accuracy are first verified on simple problems, and then tested on two different flows: the turbulent flow in a channel with a sinusoidal wall, and the flow in a human nasal cavity, whose extreme anatomical complexity mandates an accurate treatment of the boundary.

6.1 Introduction

Immersed-boundary methods (IBMs) have seen their popularity increasing over the last two decades, and are nowadays often employed in the numerical simulation of fluid flows around complex geometries. They represent an interesting alternative to the classic methods which discretize the fluid equations on a body-conforming grid, and are particularly well suited to situations where the solid bodies have a complex shape. An IBM relies on a Cartesian grid, where grid points generally do not coincide with the contours of the bodies. The use of a Cartesian grid brings along substantial advantages compared to body-conforming grids: easier generation of a structured mesh, simpler and more efficient solution algorithms and parallelisation, savings in memory requirements and computing time. IBMs may render problems affordable in complex and/or moving geometries which would otherwise be prohibitively expensive from the point of view of the computational complexity, typical examples being those involving fluid-structure interactions and/or bio-medical applications (de Tullio & Pascazio, 2016; Griffith & Patankar, 2020), or particles-laden flows (Uhlmann, 2005; Zhu *et al.*, 2024). The obvious drawback is that the boundary conditions on the body are defined at locations that in general do not coincide with grid points; they are therefore enforced at grid points, by either altering the volume forces or interpolating velocity values near the boundary, which can be thought of as being "immersed" in the fluid.

IBMs can be traced back to the seminal work of Peskin (1972), and were extended over the years, in particular starting from Fadlun *et al.* (2000). Comprehensive reviews are provided in Peskin (1972); Iaccarino & Verzicco (2003); Mittal & Iaccarino (2005); Sotiropoulos & Yang (2014) and in the very recent contributions of Verzicco (2023); Mittal & Seo (2023). IBMs are generally categorised into two classes (Mittal & Iaccarino, 2005), depending on whether they are based on a continuous or discrete forcing. The continuous-forcing (or direct-forcing) IBM adds a volume forcing term to the continuous Navier–Stokes equations before discretization. Examples of this class of IBM are described in Peskin (1972); Goldstein *et al.* (1993); Saiki & Biringen (1996). Such IBMs have been used in different biological and engineering applications (Fauci & Peskin, 1988; Zhu & Peskin, 2002; Kim & Peskin, 2007; Kim & Lai, 2010), and various forcing functions have been proposed. The continuous-forcing IBM, however, unavoidably suffers from the actual boundary being smeared over several nearby grid points because of the forcing function, and from the need to derive *ad hoc* forcing parameters. Moreover, the governing equations need to be solved in the whole domain, including within the solid body, which leads to an aggravation of their computational cost. The second class of methods, referred to as the discrete-forcing IBM, applies the forcing (either explicitly or implicitly) to the already discretised Navier–Stokes

equations; examples can be found in Ye *et al.* (1999); Fadlun *et al.* (2000); Balaras (2004); Orlandi & Leonardi (2006); Chi *et al.* (2017). A sharp representation of the boundary, which should lead to the same accuracy as a body-conforming grid (Mittal & Seo, 2023), becomes possible with the discrete-forcing IBM; however, since the forcing is only introduced after discretization, such IBMs are tightly linked to the underlying spatial and temporal discretization of the flow solver.

The present work introduces a discrete-forcing IBM. In early attempts, e.g. Fadlun *et al.* (2000), the discrete forcing in the momentum equation was computed on the body surface and inside the body as well, while an additional explicit source term needed to restore mass conservation near the boundaries was computed in a later step. An alternative approach, called ghost-node IBM, was introduced in Fedkiw (2002) and further extended over the years (Tseng & Ferziger, 2003; Ghias *et al.*, 2007; Mittal *et al.*, 2008; Li *et al.*, 2023). Ghost nodes are those grid nodes that lie in the solid but at the same time belong to the stencil used to compute differential operators appearing in the governing equations at fluid points. With ghost nodes, the forcing can be introduced implicitly in the momentum equations by means of the discrete stencil operators. Therefore, the number of ghost node layers depends on the discretisation. The general idea of a ghost-node IBM is to enforce the boundary conditions by means of the values of the variables at the ghost nodes; these are extrapolated from values at the internal points and from those at the boundary, known from the boundary conditions. Typically, a single value of each flow variable is associated to each ghost node, and is extrapolated along the direction normal to the boundary. Over the years several extrapolation schemes have been proposed. Mittal *et al.* (2008) and Ghias *et al.* (2007) used linear extrapolation to obtain a second-order convergence. The same convergence was obtained by Tseng & Ferziger (2003), who employed a quadratic extrapolation, and by Gao et al. Gao *et al.* (2007) via a second-order Taylor series expansion. Employing a wider stencil near the boundary leads to a higher order of convergence (see e.g. Seo & Mittal (2011)). Recently, however, Chi *et al.* (2020) have observed that, regardless of the reconstruction method, boundary conditions in the various directions cannot be accurately and simultaneously represented by a single ghost-node value; in their IBM they define and compute multiple ghost-node values, one for each direction.

In a conventional ghost-node IBM, multiple points are used to extrapolate the ghost-node value (Tseng & Ferziger, 2003; Gao *et al.*, 2007). In Pan & Shen (2009), Chi *et al.* (2017) and Chi *et al.* (2020), a single fluid point is considered; however, this is chosen as the second fluid point instead of the closest to the boundary, in order to avoid numerical instability issues arising when the distance between the first point and the boundary tends to zero. This is because most existing implementations deal with the forcing term explicitly, and require the computation of the ghost-node values at each iteration, thereby increasing the

overall computational cost. The equivalent implicit treatment is typically not pursued, because it involves a matrix inversion. A further drawback brought about by a wide interpolation stencil arises when the thickness of the body is locally less than the size of the local grid spacing, or when two surfaces are separated by a number of points which is less than the stencil width. Interpolating over a wider stencil also entails delivering a worse approximation of the solution near the boundary.

This paper introduces a new, simple and computationally efficient, implicit in space and time, second-order accurate IBM for the incompressible Navier–Stokes equations, based upon and tightly integrated with a second-order finite difference method. Its peculiarity is that implicitness is achieved without any matrix inversion, because the boundary conditions are enforced implicitly by modifying only the weight of the midpoint of the Laplacian stencil, under the assumption that close to the boundaries the viscous term is dominant. Similarly to what done in Gibou *et al.* (2002) when solving the variable-coefficients Poisson equation with Dirichlet boundary conditions on the immersed boundaries, the ghost-node values are extrapolated via a linear formula that only features the boundary point and the first fluid point. Different ghost-node values are considered for each discretisation direction, as also done in Chi *et al.* (2020) but there in an explicit way. The present method differs from a classic ghost-node approach since it dispenses with explicitly computing and storing the solution at the ghost node, with substantial advantages in terms of simplicity and efficiency. Modifying only the coefficient of the Laplacian close to the boundary, as well as computing multiple values of the coefficients, one for each direction, was already suggested by Orlandi & Leonardi (2006). However, in their approach velocity at the ghost nodes was set to zero, and the weights of both the centre point and the external point of the stencil were corrected. Since our IBM treats the forcing term implicitly, numerical issues associated with a small distance between the first fluid point and the boundary do not arise. Moreover, differently from several discrete-forcing IBMs, a boundary condition for pressure is not required.

The paper is organised as follows. After this Introduction, Sec. 6.2 thoroughly describes our IBM, in its general design and then in its implementation into a Navier–Stokes finite-difference solver, with a discussion dealing first with the steady and then with the unsteady case. A critical discussion of the IBM and of its advantages and drawbacks is offered in Sec. 6.3. Finally, Sec. 8.4 provides an exhaustive discussion of accuracy and performance of the method as applied to two examples: the turbulent flow over a non-planar, sinusoidally shaped wall, and the flow in the complex anatomy of a human nasal cavity. Both examples, and in particular the latter, involve geometric boundaries of extremely complex shape, which challenge the accuracy of the IBM. In each and every instance second-order accuracy is numerically demonstrated through a convergence plot. The paper

concludes with some final remarks drawn in Sec. 8.5.

6.2 The immersed-boundary method

This Section describes the IBM, starting with elementary, linear flow problems: a steady flow example is used first to illustrate the spatial accuracy features of the method, followed by a time-dependent example, where the temporal accuracy of the method is discussed.

Our IBM starts from a basic "staircase" approximation of the boundary, in which each point is defined as "internal" (in the fluid region) or "external" (in the solid region), and improves upon this first-order representation via the IBM correction, which gets applied only to those stencils of the discretised equations which cross the solid boundary. In fact, the method can be alternately interpreted as a deferred correction, a sometimes helpful viewpoint. The correction exploits the fact that, near the boundary, viscous terms dominate over convective and pressure terms. Therefore, the presence of the boundary can be properly accounted for by simply altering the weight of the central point of the star-shaped stencil of the Laplacian at the first internal point: no additional corrections of the convective terms are required. In addition, as in some other IBMs, no correction of the pressure or of the continuity equation needs to be expressly introduced; the absence of such need can be explained by the lack of a boundary condition for pressure in the continuous Navier–Stokes problem, since when there is no boundary condition there is no position where to impose it; while IBMs without an express pressure boundary correction have been used before, to the best of out knowledge this is the first time that the validity of such choice is *a posteriori* confirmed through convergence tests (see Sec. 8.4).

6.2.1 Equations of motion and discretization

The IBM is implemented inside a solver for the direct numerical simulation of the incompressible Navier–Stokes equations, written in their primitive variables and with suitable initial and boundary conditions:

$$\begin{cases} \dfrac{\partial \boldsymbol{u}}{\partial t} + (\boldsymbol{u} \cdot \boldsymbol{\nabla})\, \boldsymbol{u} - \dfrac{1}{\mathrm{Re}} \nabla^2 \boldsymbol{u} + \boldsymbol{\nabla} p = \boldsymbol{g} \\ \boldsymbol{\nabla} \cdot \boldsymbol{u} = 0 \end{cases} \tag{6.1}$$

where t is the time, $\boldsymbol{u}$ is the velocity, p is the reduced pressure, and $\boldsymbol{g}$ is a possible body force. $Re = U_{ref} L_{ref} / \nu$ is a Reynolds number built with the reference velocity U_{ref}, the reference length L_{ref} and the kinematic viscosity ν of the fluid.

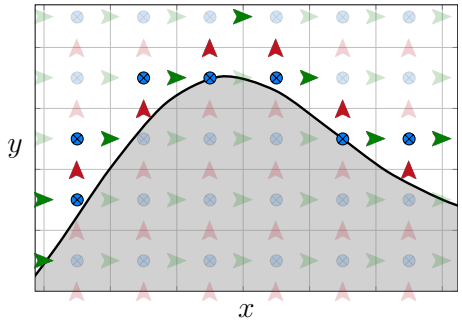

Figure 6.1: Two-dimensional view of a solid body (gray background) immersed in a fluid (white background), with an overlaid staggered Cartesian grid. The collocation points for the velocity components in the x, y and z directions are drawn in green, red and blue. Dull colors denote the fully internal/external points, and vivid colors the points where the immersed-boundary correction is applied.

In a Cartesian frame, the spatial directions are denoted as x, y and z, and the corresponding velocity components as u, v and w.

The Navier–Stokes equations are advanced in time using a standard incremental pressure-correction scheme coupled with a fully explicit time scheme. The momentum equation is first advanced in time without accounting for the incompressibility constraint, that is enforced later during the so-called projection step. The velocity field gets projected onto a solenoidal vector field and the required pressure increment is found by (exactly or approximately) solving a Poisson equation and then used to update the pressure field.

The spatial discretization takes place on a Cartesian grid that is staggered in the three directions, as sketched in figure 6.1. Pressure is defined at the center of each cell, whereas each velocity component is defined at the relative interface. Uniform as well as non-uniform spacing is possible in each direction.

The discretisation relies on centered second-order central finite differences in every direction, with a stencil made of three points. To introduce the notation used in the rest of the paper, let us consider a two-dimensional case for simplicity. A generic grid point of coordinates (x, y) is identified by the pair of integers (i, j), such that $x = x_i$ and $y = y_j$. Taking the first derivative as an example, for a scalar function f the first derivative along the x direction at the (i, j) position is written as:

$$\left.\frac{\partial f}{\partial x}\right|_{i,j} = d^{(1)}_{x;i,j}(-1)\, f_{i-1,j} + d^{(1)}_{x;i,j}(0)\, f_{i,j} + d^{(1)}_{x;i,j}(1)\, f_{i+1,j} + O(\Delta x^2)\,. \tag{6.2}$$

In the expression above, the symbols $d^{(1)}_{x;i,j}(\cdot)$ indicate the three finite-differences coefficients for the centered first derivative along the x direction, evaluated at point

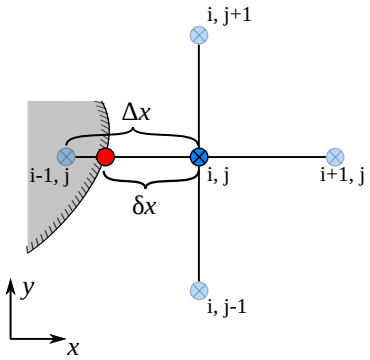

Figure 6.2: Computational stencil for the w velocity component in the $x-y$ plane. As in figure 6.1, vivid blue highlights the point where the immersed-boundary correction is applied. A red dot denotes the actual boundary intersection.

(i, j).

6.2.2 The steady case

We start by considering the steady case, and in particular the Laplacian operator: since our IBM relies on the Laplacian being the dominant term near the solid boundary, this simple example is particularly significant. At a generic (i, j) position the Laplacian of, e.g., the z velocity component is discretised by second-order central finite differences, which in the notation just introduced above read:

$$\begin{aligned}\nabla^2 w \approx & d^{(2)}_{x;i,j}(-1)w_{i-1,j} + d^{(2)}_{x;i,j}(0)w_{i,j} + d^{(2)}_{x;i,j}(1)w_{i+1,j} + \\ & d^{(2)}_{y;i,j}(-1)w_{i,j-1} + d^{(2)}_{y;i,j}(0)w_{i,j} + d^{(2)}_{y;i,j}(1)w_{i,j+1}.\end{aligned} \tag{6.3}$$

Let us assume, as shown in figure 6.2, that point (i, j) is located close to the boundary; the solid boundary crosses the left arm of the computational stencil, and the left neighbor of point (i, j), i.e. point $(i-1, j)$, lies within the solid. The simplest description of the boundary is achieved by setting the velocity at the external point to zero, i.e. $w_{i-1,j} = 0$. This amounts to a staircase, i.e. piecewise parallel to the axes, approximation of the boundary, whose maximum error in the position of the contour of the body is proportional to $\Delta x = x_{i,j} - x_{i-1,j}$, i.e. one of first-order accuracy.

To increase the accuracy of the description and to avoid deteriorating the overall second-order accuracy of the underlying numerical method, the representation of the boundary needs to be improved to a piecewise-linear approximation. To this aim, instead of setting $w_{i-1,j}$ to zero, we set to zero a linear interpolation between $w_{i-1,j}$ and $w_{i,j}$, evaluated at the true boundary whose x position is denoted as

$x_b = x_i - \delta x$. The linear function that fits velocity between the position (i, j) and the true boundary at x_b reads:

$$\mathrm{lin}(x_b) = \left(1 + \frac{x_b - x_i}{\delta x}\right) w_{i,j} \,. \tag{6.4}$$

which satisfies $\mathrm{lin}(x_i) = w_{i,j}$ and $\mathrm{lin}(x_i - \delta x) = 0$.

The same function can be used to linearly extrapolate the non-zero value $w_{i-1,j}$, corresponding to the ghost point that falls inside the boundary and that is needed for building the stencil of the discretised Laplacian (**??**) in the first fluid point in the neighborhood of the boundary. The extrapolated value reads:

$$\mathrm{lin}(x_{i-1}) = \left(\frac{\delta x - \Delta x}{\delta x}\right) w_{i,j} \,. \tag{6.5}$$

The above would be essentially identical to other implementations of the IBM. Crucial to ours is the observation that the extrapolated value for $w_{i-1,j}$ does not need to be stored explicitly as a ghost value, but can be substituted back into equation (**??**) and accounted for implicitly (and the same will remain true in unsteady problems). Doing so not only will be seen to eliminate the numerical instabilities that plague explicit extrapolation, but in addition concentrates the modification in the coefficient of the central point of the stencil, leading to a single value to be stored even when this correction needs to be applied along multiple directions. The updated coefficient $\tilde{d}^{(2)}_{x;i,j}(0)$ reads:

$$\tilde{d}^{(2)}_{x;ij}(0) \equiv \left(d^{(2)}_{x;i,j}(0) - d^{(2)}_{x;i,j}(-1)\frac{\Delta x - \delta x}{\delta x}\right) \tag{6.6}$$

where the term

$$d^{(2)}_{x;i,j}(-1)\frac{\Delta x - \delta x}{\delta x} \tag{6.7}$$

embodies the immersed-boundary correction, referred to in the following as λ. It is worth noting that, owing to the opposite signs of $d^{(2)}_{x;i,j}(0)$ and $d^{(2)}_{x;i,j}(-1)$, the updated coefficient $\tilde{d}^{(2)}_{x;i,j}(0)$ is always of the same sign; its absolute value monotonically increases for $\Delta x > \delta x > 0$, and can not be zero. This leads to an increased diagonal dominance, more and more so when $\delta x \to 0$.

The extension to the multi-dimensional case is straightforward, as the corrections to the central point of the stencil ensuing from the derivatives in different directions are just additive. What changes is that the local linear solution becomes a plane in two dimensions, or a hyperplane in three dimensions; for the three-dimensional case, for example:

$$\mathrm{lin}(x_b, y_b, z_b) = \left(1 + \frac{x_b - x_i}{\delta x} + \frac{y_b - y_j}{\delta y} + \frac{z_b - z_k}{\delta z}\right) w_{i,j,k} \tag{6.8}$$

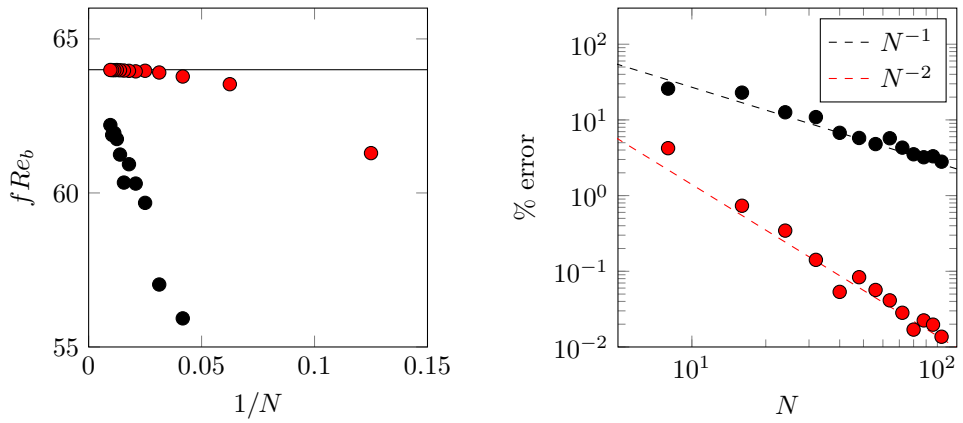

Figure 6.3: Laminar Hagen–Poiseuille flow, equation (6.9). Left: value of fRe_b as computed on an $N \times N$ Cartesian grid (exact value is the horizontal line). Right: percentage error against the exact value $fRe_b = 64$; comparison between the staircase approximation (black) and the improved approximation yielded by the IBM (red).

but this is easily seen to be equivalent to an independent linear extrapolation along each arm of the star-shaped stencil followed by a simple sum of all the contributions into a global correction that will be denoted in the following as $\lambda_{w;i,j,k}$.

6.2.3 The steady case: example

The potential of the IBM is illustrated through a simple example. We consider the laminar parallel flow in a circular pipe in the absence of external volume forces. If the pipe's axis (or, generally, the axis of any straight duct with arbitrarily shaped cross section) is aligned with the z direction of the Cartesian reference system, the problem is homogeneous along z, and reduces to a two-dimensional and steady problem in the (x, y) plane, where the only differential operator is a Laplacian. The governing equations in fact simplify to the following Poisson equation:

$$\frac{1}{Re_b}\nabla^2 w = \frac{\partial p}{\partial z}, \tag{6.9}$$

where w is the streamwise velocity component, which does not depend on the streamwise coordinate, Re_b is the Reynolds number, and on the right-hand side the pressure gradient $\partial p/\partial z = \Pi$ is uniform.

We consider in particular the case of a circular pipe of radius R, where the solution is known analytically, and is given by the Hagen–Poiseuille parabolic velocity profile: hence, the relationship between the pipe radius R, the bulk velocity U_b, the fluid kinematic viscosity ν, and the wall friction is in closed form.

Namely, the friction factor $f \equiv 4\Pi R/\rho U_b^2$ is known to depend on the Reynolds number $Re_b = U_b 2R/\nu$ as $f = 64/Re_b$. We thus solve numerically equation (6.9) after discretization on a square domain, of edge length $2.5R$, where a Cartesian mesh with $N \times N$ grid points is defined. Thanks to the lack of time dependency, the solution can be computed easily by direct matrix inversion.

The improvement provided by the IBM over the staircase approximation is shown in figure 6.3, where the product fRe_b is computed and compared to its analytical constant value, for the staircase approximation of the contour and for the IBM. The percentage error for fRe_b is reported in figure 6.3 as a function of the number of the grid points N. As expected, the staircase approximation is confirmed to only be first-order accurate, whereas the IBM is second-order accurate: with $N = 104$, the error with respect to the exact solution is still 3% for the staircase approximation, whereas it drops to 0.01% for the IBM. The Python code used for this example is available as Additional Material.

6.2.4 The unsteady case

Since the IBM approach described above acts by adding a correcting weight to the central point of the Laplacian operator, extending it to the Navier–Stokes equations only requires the additional step of considering the time dependence of the solution. Let us write the time-dependent, incompressible Navier–Stokes equations after spatial discretisation via second-order central finite-differences on a staggered grid; as an example we take again their z component solved on an (x, y) plane, and emphasize the second derivative coming from the viscous terms, as:

$$\frac{\mathrm{d}w_{i,j}}{\mathrm{d}t} = f_{i,j} = d^{(2)}_{x;i,j}(-1)w_{i-1,j} + d^{(2)}_{x;i,j}(0)w_{i,j} + d^{(2)}_{x;i,j}(1)w_{i+1,j} + \dots \qquad (6.10)$$

where $f_{i,j}$ is a shorthand form for the right-hand side of the discrete equation, which includes the Laplacian involved in the viscous term, as well as the convective and pressure terms. All these terms will be treated with an explicit temporal integration and are thus known from the previous timestep. While the explicit treatment of the right-hand side is not necessary for introducing the present IBM, it is adopted here because it will provide the overall numerical method with interesting properties, which will be discussed in the following. Recall that, even if $f_{i,j}$ is treated explicitly in the momentum predictor equation (6.10), a pressure correction step is still required. For simplicity, equation (6.10) explicitly shows the second derivatives in the x-direction, while all other explicitly-treated terms are grouped in the reminder indicated by ....

With reference to the previous example discussed in Sec. 6.2.2, we assume again that the solid boundary crosses the left arm of the computational stencil,

with the body surface lying between the central point (i, j), located within the fluid, and its left neighbor $(i-1, j)$, located within the solid. The value $w_{i-1,j}$ in equation (6.10) is replaced by its linear extrapolation (6.5), to yield:

$$\frac{\mathrm{d}w_{i,j}}{\mathrm{d}t} = -\lambda_{w;i,j} w_{i,j} + d^{(2)}_{x;i,j}(0) w_{i,j} + d^{(2)}_{x;i,j}(1) w_{i+1,j} + \dots , \tag{6.11}$$

where $\lambda_{w;i,j}$ is the IBM corrective coefficient arising from the linear extrapolation. The IBM correction has thus removed from the Laplacian the terms involving the neighboring point within the body, by substituting it with the coefficient $\lambda_{w;i,j}$ that multiplies $w_{i,j}$. In practice, as long as $w_{i-1,j}$ in the solid is zero and the right-hand side is evaluated explicitly, there is no need to modify the discrete Laplacian, since the related term vanishes automatically. In this way the effect of the IBM is to add a term to the right-hand side of equation (6.10), which can thus be rewritten compactly as:

$$\frac{\mathrm{d}w_{i,j}}{\mathrm{d}t} = -\lambda_{w;i,j} w_{i,j} + f_{i,j} \, . \tag{6.12}$$

If equation (6.12) is discretised in time with a fully explicit approach, for instance via an explicit Euler scheme, the well-known explicit extrapolation-based IBMs are obtained. These possess poor stability properties, as they require vanishingly small timesteps whenever the central point (i, j) happens to be very close to the body surface. In this particularly stiff condition, in fact, the ratio $(\Delta x - \delta x)/\delta x$ contained in $\lambda_{w;i,j}$, tends to infinity.

Instead, in the following, we keep the explicit treatment of $f_{i,j}$, but allow the IBM term to be treated differently. The simplest choice, useful for showcasing the method, is to opt for the implicit Euler method, which leads to:

$$w^{*,n+1}_{i,j} = \frac{w^n_{i,j} + \Delta t f^n_{i,j}}{1 + \Delta t \lambda_{w;i,j}} \tag{6.13}$$

where Δt is the time step, and $w^{*,n+1}_{i,j}$ is the intermediate velocity of the fractional step method, which needs to be later corrected by an appropriate projection scheme. The implicit treatment of the IBM term has the crucial advantage of not deteriorating (and actually improving) the stability properties of the underlying temporal scheme. This is easily observed by considering the two limiting cases of $\lambda_{w;i,j} = 0$, i.e. no IBM correction is applied, and $\lambda_{w;i,j} \to \infty$, i.e. the point (i, j) is on the body surface. In the first case, we simply recover the unmodified Navier–Stokes equation; in the second, instead, the exact boundary condition $w^{*,n+1}_{i,j} = 0$ is enforced.

Second-order accuracy in time can be achieved without compromising stability by integrating the IBM correction term exactly (or more precisely, in a way that would be exact if the r.h.s. were independent of the solution), as explained in the

following. Let us first consider equation (6.12): this is an ordinary differential equation with a particular solution depending on $f_{i,j}$, assumed here to be constant within a timestep accordingly with the considered explicit temporal scheme, and a homogeneous solution $\tilde{w}_{i,j} = \mathrm{e}^{-\lambda_{w;i,j}t}$, which can be retrieved by analytical integration for $f_{i,j} = 0$. In fact, $-\lambda_{w;i,j}$ is the eigenvalue of equation (6.12) when $f_{i,j}$ is a constant. Without any loss of generality, if we consider a generic explicit method for temporal integration, we can rewrite equation (6.12) as follows (while dropping superscript $*$ and the subscripts to simplify the notation):

$$Aw^{n+1} - Bw^n = CF^n \tag{6.14}$$

where F^n is typically a linear combination of $f_{i,j}$ evaluated at different time levels, as determined by the temporal scheme of choice. Equation (6.14) reduces to equation (6.13) for $A = (1 + \lambda_{w;i,j}\Delta t)$, $B = 1$ and $C = \Delta t$, with $F^n = f^n_{i,j}$, for instance, when the underlying scheme is a first-order explicit Euler, or the corresponding expression for a higher-order (say, Runge–Kutta) scheme.

The coefficients A, B and C can now be chosen by requesting that equation (6.14) (i) possesses the same eigenvalue as the semi-discrete equation (6.12), and (ii) reduces to the exact steady problem when $\mathrm{d}w/\mathrm{d}t = 0$, and thus $w^{n+1} = w^n$.

Constraint (i) can be satisfied by observing that equation (6.14) for $F^n = 0$ yields $\tilde{w}^{n+1}/\tilde{w}^n = B/A$, and by substituting the exact homogenenous solution of equation (6.12), thereby obtaining $B/A = \mathrm{e}^{-\lambda_{w;i,j}\Delta t}$.

Constraint (ii) can be enforced by plugging $w^{n+1} = w^n$ into equation (6.14), which yields $w^n\,(A - B)\,/C = F^n$, and prescribing that this equation shall equal equation (6.12) for $\mathrm{d}w/\mathrm{d}t = 0$. This occurs for $(A - B)\,/C = \lambda_{w;i,j}$, from which $C = (A - B)/\lambda_{w;i,j}$. The consistency of the underlying temporal scheme already provides $F^n = f^n$ at steady state. The three coefficients are now known up to a multiplicative constant, since the problem is linear. By choosing e.g. $C = \Delta t$, one obtains

$$B = \frac{\lambda_{w;i,j}\Delta t}{\mathrm{e}^{\lambda_{w;i,j}\Delta t} - 1} \tag{6.15}$$

and $A = \lambda_{w;i,j}\Delta t + B$. Thus, equation (6.14) becomes

$$\left(\lambda_{w;i,j}\Delta t + B\right) w^{n+1} - Bw^n = \Delta t F^n\,. \tag{6.16}$$

We note that the function $B(\lambda_{w;i,j}\Delta t)$ of equation (6.15) can in practice be approximated by the reciprocal of a Taylor expansion around $\lambda_{w;i,j}\Delta t = 0$ to a desired order, without destroying its essential stability property that $1 \geq B \geq 0$ for all Δt; this may be useful to avoid the evaluation of a transcendental function and a singular limit, and thus improve performance when computing on graphics accelerators.

In the following applications, second-order global temporal accuracy is achieved by adopting the three-stage, third-order Runge–Kutta (RK) method of Rai & Moin (1991) to express F^n, owing to its low memory requirements and excellent stability properties which are not affected by the IBM. The RK method is combined with the IBM in the same way it is typically combined with Crank-Nicolson for the implicit integration of the viscous term, as in Kim *et al.* (1987). This choice results in the following scheme:

$$\left(\lambda_{w;i,j} c_k \Delta t + B\right) w_{i,j}^{*,n+\frac{k}{3}} - B w_{i,j}^{n+\frac{k-1}{3}} = \Delta t \left[a_k f_{i,j}^{n+\frac{k-1}{3}} + b_k f_{i,j}^{n+\frac{k-2}{3}} \right] \quad \text{for } k = 1, \ldots, 3, \tag{6.17}$$

where $w_{i,j}^{n+\frac{k}{3}}$ is the velocity at the k-th RK stage, whereas $f_{i,j}^{n+\frac{k}{3}}$ is the right-hand side evaluated with $w_{i,j}^{n+\frac{k}{3}}$ and other variables at the same RK stage. We also recall that the intermediate velocity (denoted via the additional superscript $*$) is not divergence-free and an additional projection step is required after each substage to obtain the solenoidal velocity field. According to Rai & Moin (1991), the coefficients in equation (6.17) are:

$$a_k = \left\{ \frac{64}{120}, \frac{50}{120}, \frac{90}{120} \right\}; \qquad b_k = \left\{ 0, -\frac{34}{120}, -\frac{50}{120} \right\}; \qquad c_k = a_k + b_k. \tag{6.18}$$

6.2.5 The unsteady case: example

The simple example of the laminar parallel flow in a circular pipe of radius R, already considered in Sec. 6.2.3, is extended here to demonstrate the present IBM in a time-dependent flow. By discretizing the problem on a fine 200×200 Cartesian grid, we ensure that the spatial discretization error is not dominant. The flow is governed by the unsteady version of equation (6.9), i.e.

$$\frac{\partial w}{\partial t} = -\Pi + \frac{1}{Re} \nabla^2 w \,, \tag{6.19}$$

where the imposed uniform pressure gradient $\Pi(t)$ can now vary with time. We opt for the time dependency $\Pi(t) = \sin(2\pi f t)$, where frequency f enables the definition of a Reynolds number $Re = R^2 f / \nu$, i.e. the ratio between the characteristic diffusion time R^2/ν and the characteristic time of the forcing $1/f$.

For a given temporal integration scheme, such as the Runge–Kutta method described above, the accuracy of the numerical solution of equation (6.19) depends on how well the temporal evolution of Π and of the diffusive effects are represented. This is quantified by two nondimensional numbers: the nondimensional timestep $f\Delta t$, and the grid Péclet number $Pe = \nu \Delta t / \Delta x^2$. By selecting $Re = 50$ we make sure that even for the lower values of Δt tested below, the main source of error will

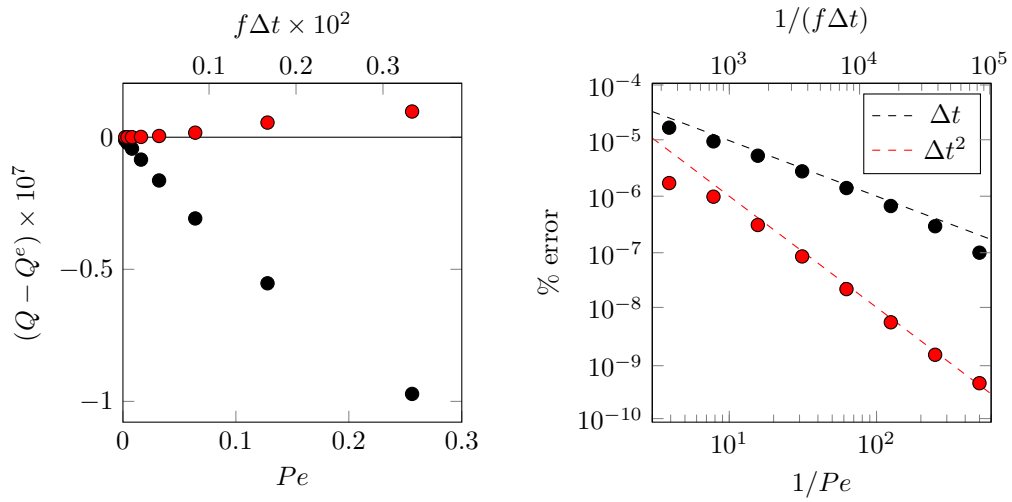

Figure 6.4: Unsteady laminar pipe flow, equation (6.19), spatially discretized on a square domain with 200×200 grid points. Left: evolution of the difference $Q - Q^{(e)}$ with the temporal resolution, expressed via the Péclet number $Pe = \nu\Delta t/\Delta x^2$; the asymptotic flow rate value is obtained via Richardson extrapolation. Right: percentage error $100|Q - Q^{(e)}|/Q^{(e)}$. Black symbols and dashed line refer to the first-order method; red symbols and dashed line indicate the second-order method (see text).

not be the temporal evolution of Π but rather the temporal accuracy of the viscous effects and of the IBM method.

Starting from an initial condition of quiescent flow, equation (6.19) is integrated in time up to $t = 0.5/f$, and at that time the flow rate Q in the pipe is measured; the numerical experiment is repeated for several values of $f\Delta t$ ranging between 0.002 and 1.5625×10^{-5}. Note that the largest value of the time step corresponds, for the employed spatial discretization, to $Pe = 0.256$, which is less than half the critical Péclet number for the temporal stability of the underlying RK method. Equation (6.19) is solved by the second-order method presented in equation (6.17), as well as by the first-order method obtained from the combination of the RK method with an implicit Euler scheme for the IBM term, i.e. $A = 1 + \lambda c_k \Delta t$, $B = 1$ and $C = \Delta t$. Results are displayed in figure 6.4, together with the error with respect to the estimate of exact flow rate $Q^{(e)}$, obtained via Richardson extrapolation. The figure shows both that the expected order of temporal convergence is achieved and that the error is generally extremely low.

As a final remark, it is interesting to note that a classic explicit treatment of the IBM term yields a stable integration only for the smallest timestep tested above. The poor stability of the explicit IBM could be even worse if any grid point

happens to be very close to the body surface, making the method unconditionally unstable. Crucially, the present implicit treatment removes this issue, and averts deteriorating the stability properties of the underlying numerical method.

6.3 Discussion

6.3.1 Advantages and drawbacks

The greatest novelty of the approach outlined above consists in the implicit nature, in both space and time, of the correction introduced to account for the presence of the boundary; the ability to concentrate the correction in the central point of the stencil allows such implicitness to be achieved at no cost.

In the stationary case described in Sec. 6.2.2, the term "implicit" refers to the fact that the value $w_{i-1,j}$ in a point within the body is not actually computed by using equation (6.5), but gets hard-coded instead into the expression of the discretised Laplacian and in particular into $\tilde{d}^{(2)}_{x;ij}(0)$ through coefficient $\lambda_{w;i,j}$. Doing so avoids the numerical stability problems that plague "explicit" methods: when the boundary point approaches a discretisation node (i.e. $\delta x \to 0$), such formulations imply that $w_{i-1,j} \to \infty$. If, however, the correction is imposed implicitly as in the present case, $\delta x \to 0$ makes the denominator of equation (6.13) tend to infinity, and the value of $w_{i,j}$ is gradually driven towards zero, which is the desired result. Thanks to this correction, the discretization matrix becomes more and more diagonally dominant, see equation (6.6), and the convergence of any iterative method used to solve the discretised equations is improved rather than reduced. This property becomes apparent when one considers that $d^{(2)}_{x;ij}(-1)$ and $d^{(2)}_{x;ij}(0)$ are of opposite signs, and thus $\tilde{d}^{(2)}_{x;ij}(0)$ monotonically increases for $\Delta x \geq \delta x \geq 0$ and is prevented from approaching 0.

In the time-dependent case of Sec. 6.2.4, "implicit" additionally means that the linear extrapolation of equation (6.5) is evaluated at time $t + \Delta t$, as in equation (6.13), which is again desirable to avoid numerical instabilities. For $\delta x = 0$, equation (6.13) can be shown to equal the exact implicit boundary condition $w^{*,n+1}_{i,j} = 0$.

In conclusion, the implicit character of the IBM ensures convergence and stability of the numerical method; moreover, since only the central point of the Laplacian stencil is modified, this improvement is obtained at no computational and memory cost, since the velocity $w_{i-1,j}$ at the ghost point within the body needs to be neither explicitly computed nor explicitly stored. This additional advantage obviates another programming difficulty related to the presence of external points appearing in more than one equation (for example the Cartesian components of the momentum equation); in the explicit implementation multiple values extrapolated

linearly from different directions would have to be stored (or otherwise a higher-than-linear extrapolation would be required), but no such difficulty arises with the implicit formulation.

6.3.2 The underlying staircase approximation

As pointed out in Sec. 6.2.2, the simplest (first-order) description of the immersed boundary is achieved by a staircase (piecewise-constant) approximation of the body geometry, in which the boundary always coincides with a grid point. Since the IBM uses a linear extrapolation to improve upon the staircase approximation of the boundary, and thus restore the original second-order spatial accuracy of the numerical method, it is essential that the underlying staircase approximation works properly, before any correction is applied. This involves non-trivial aspects.

To begin with, the equations of motion in their discrete form need to be closed, i.e. the number of unknowns must equal the number of equations. This property becomes non-obvious when the geometry is complex and the grid is staggered. To fulfill the closure requirement, the discretization grid is defined independently for each velocity component, and each grid is compared with the true boundary to tag a grid point as either internal or external. For each component, internal points are chosen as those where the corresponding component of the momentum equation (6.10) needs to be solved; this ensures the correspondence between equations and unknowns. The velocity components on the external points are set to zero. This decision, which is trivial in the one-dimensional case, avoids any trouble with external points appearing in more than one equation.

The closure of the continuity equation deserves a specific remark. Since a pressure boundary condition is neither required nor present, only the velocity grids are compared to the boundary to discriminate external and internal points. Thereafter, a pressure point is labeled "internal" if it falls on either side of at least one internal velocity point; it follows that an "internal" pressure point may occasionally fall (slightly) outside the true boundary, and may also be shared by different components of the momentum equation in different directions. To match the number of equations and unknowns, the continuity equation is then in principle solved everywhere, both in the internal and external pressure collocation points, as though there was no boundary. In practice, however, only the internal points need to be considered since, with this definition, external pressure points are surrounded by all zero velocities, and continuity is trivially satisfied there. In practice, when the pressure-correction step of the fractional step method is executed, only the internal pressure collocation points are updated, and these are the only ones that will appear in the momentum equations at the following time step.

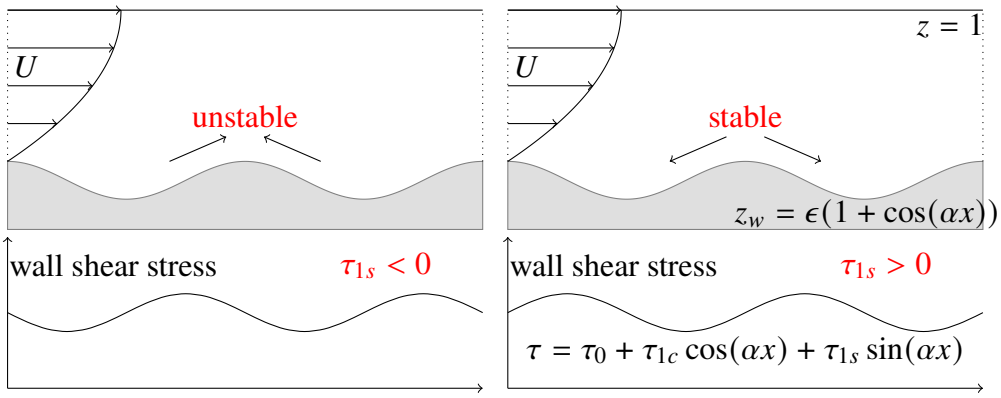

Figure 6.5: Effect of the wall shear stress on the stability of a sand bed. The flow develops between the wavy wall described by z_w and the upper boundary at $z = 1$. The wall-shear stress is decomposed into in-phase and quadrature components. Left: unstable situation (the quadrature component τ_{1s} of the stress is negative). Right: stable situation (τ_{1s} is positive). Adapted from Luchini (2016).

6.4 Results

We move on to describe two examples where the present method is applied. Both involve turbulent flows over non-planar boundaries; they are meant to illustrate the accuracy of the IBM in cases where the convective terms and the continuity equation are at play. The first example is relatively simple from the geometric standpoint, and concerns the turbulent flow in an open channel with a sinusoidally undulated bottom. The second test case is about the flow within the human nose, and is instead characterized by an extremely complex geometry.

6.4.1 The turbulent flow in a channel with undulated bottom

The IBM is applied to simulate via DNS the turbulent flow in a channel with a sinusoidally undulated bottom wall: this is an idealised model of a river or flume with a sandy bottom, that may bulge up and generate ripples and dunes.The generation mechanism of these ripples involves fluid inertia (Charru *et al.*, 2013); a net accrual or depletion of sand particles occurs depending on the relative spatial phase between the fluid shear stress and the wall undulation. Figure 6.5 sketches a sinusoidally undulated bottom and the relative wall-shear stress, decomposed into in-phase (cosine) and quadrature (sine) components, whose sign determines the generation of ripples (Blondeaux, 1990): they grow whenever an unstable situation is determined by a negative quadrature component of the wall-shear stress.

Here we replicate with higher accuracy the simulations performed by Luchini

ϵ	α	N_{tot}	Δx	Δy	Δz_{min}	Δz_{max}	N_z	Δ	Δt
0.05	$1/256 \leq \alpha \leq 1/2$	up to 251657210	0.0654	0.0393	4.0×10^{-3}	0.0224	64	0.034245	0.03
0.025	$1/128 \leq \alpha \leq 1/2$	up to 251657210	0.0654	0.0393	2.0×10^{-3}	0.0111	128	0.027180	0.008
0.0125	$1/32 \leq \alpha \leq 1/2$	up to 125828605	0.0654	0.0393	9.6×10^{-4}	0.0056	256	0.021573	0.0015
0.05	1/2	1966080	0.0654	0.0393	4.0×10^{-3}	0.0225	64	0.034245	0.001
0.05	1/2	2799360	0.0582	0.0349	3.6×10^{-3}	0.0199	72	0.030442	0.001
0.05	1/2	3840000	0.0524	0.0314	3.2×10^{-3}	0.0179	80	0.027398	0.001
0.05	1/2	6635520	0.0436	0.0262	2.6×10^{-3}	0.0149	96	0.022830	0.001
0.05	1/2	8436480	0.0403	0.0242	2.4×10^{-3}	0.0137	104	0.021088	0.001
0.05	1/2	10536960	0.0374	0.0224	2.2×10^{-3}	0.0127	112	0.019557	0.001
0.05	1/2	15728640	0.0327	0.0196	2.2×10^{-3}	0.0111	128	0.017108	0.001
0.05	1/2	30720000	0.0262	0.0157	1.6×10^{-3}	0.0089	160	0.013699	0.001

Table 6.1: Computational parameters for the numerical simulations of the turbulent flow in a channel with undulated bottom. The equivalent grid spacing Δ is computed by assuming a uniform grid in all directions.

(2016), aimed at determining how this instability depends on the wavelength and elevation of the bottom. We consider a channel configuration with a shear-free, flat upper surface, with lengths and velocities made dimensionless with the channel height h and the bulk velocity U_b. The (dimensionless) expression of the undulated bottom is:

$$z_w = \epsilon \left(1 + \cos \alpha x\right) .$$

Here α is the dimensionless wave number of the wavy bottom wall (with wave length $\lambda = 2\pi/\alpha$), and ϵ is the dimensionless amplitude of the waviness. The computational domain extends for $L_x = \lambda$, $L_y = 2\pi$ and $L_z = 1$ in the streamwise, spanwise and wall-normal directions. The wavenumber is varied in the range $1/256 \leq \alpha \leq 1/2$ (or $12.5 \leq L_x \leq 1608$). Please notice that these very long computational boxes are required because this flow was shown in Luchini (2016) to have an interesting response to very long wavelengths of the undulation. While the shortest extreme is comparable to that employed in low-Re turbulent channel flow simulations (Kim *et al.*, 1987), at the other extreme more than two-orders of magnitude longer domains are considered. Several simulations are run for the Reynolds number $Re_b = U_b h/\nu = 2800$. Periodic boundary conditions are used for the streamwise and spanwise directions, free-slip boundary conditions are applied at $z = 1$, and no-penetration and no-slip conditions are applied at the wavy wall. To obtain well converged statistics, simulations are run for at least $1000 U_b/h$ time units after the initial transient. Table 6.1 contains general information about the set of simulations carried out for the present work. In a first set of simulations, the grid spacing is kept constant while the size of the computational domain is varied; a second set of simulations, used for a grid convergence study, has a fixed domain size, and a spatial resolution that progressively increases uniformly in all directions. Since the wall-normal distribution of grid points is mildly stretched, an average wall-normal spacing $\Delta z = 1/N_z$ is used to provide an equivalent uniform grid spacing $\Delta = (\Delta x \Delta y \Delta z)^{(1/3)}$.

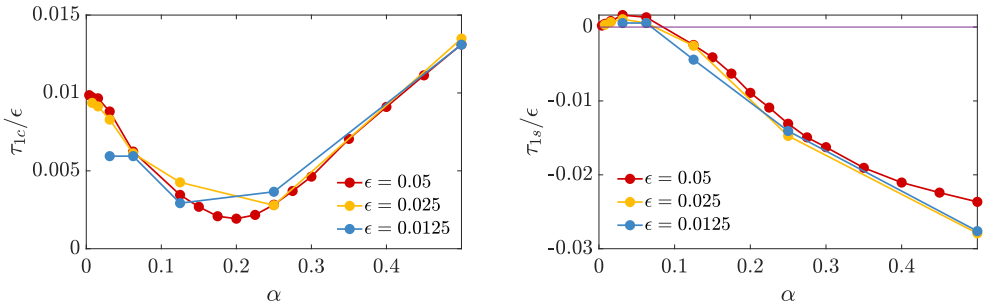

Figure 6.6: In-phase (left) and quadrature (right) components τ_{1c} and τ_{1s} of the wall-shear-stress response to a wall modulation of wavenumber α.

N_{tot}	Δ	$\tau_{1c} \times 10^4$	$\sigma_{1c} \times 10^6$	$\tau_{1s} \times 10^3$	$\sigma_{1s} \times 10^6$
1966080	0.034245	6.40764	7.18508	-1.18162	6.40058
2799360	0.030442	6.76041	8.67627	-1.25258	7.84068
3840000	0.027398	6.80707	4.46546	-1.29628	3.54087
6635520	0.022830	7.13429	7.65407	-1.37018	6.87870
8436480	0.021088	7.28166	7.05332	-1.38633	6.14717
10536960	0.019557	7.28948	8.31248	-1.40233	6.93155
15728640	0.017108	7.42786	8.55187	-1.42513	7.48778
30720000	0.013699	7.46693	7.73307	-1.45979	7.64443

Table 6.2: Spatial convergence study for the wavy channel test case. The table lists the number of grid points, the mean grid spacing, the values τ_{1c} and τ_{1s} of the mean stresses, and the corresponding root-mean-square values σ of the variance of the estimate of the mean, computed after Russo & Luchini (2017).

The quantities of interest here are the spatial Fourier components τ_{1c} and τ_{1s} of the time-averaged wall-shear stress $\tau(x)$. They are defined as

$$\tau_{1c} = \frac{2}{L_x}\int_0^{L_x} \tau(x)\cos\left(\frac{2\pi x}{L_x}\right)\mathrm{d}x; \qquad \tau_{1s} = \frac{2}{L_x}\int_0^{L_x} \tau(x)\sin\left(\frac{2\pi x}{L_x}\right)\mathrm{d}x. \tag{6.20}$$

Figure 6.6 shows the dependence of τ_{1c} and τ_{1s} on the wavenumber α of the wall modulation, for different values of ϵ. The red curve is for $\epsilon = 0.05$ and has been obtained using the same time step and grid size as in Luchini (2016), whose results are perfectly reproduced. The plot confirms that the considered values of ϵ are small enough to be in the linear regime. As already observed by Luchini (2016), when α is reduced τ_{1c} decreases to a local minimum at $\alpha \approx 0.2$, and then increases again. At the smallest α, the quadrature component τ_{1s} changes sign, indicating a change of the stability of the ripples. This is confirmed at different

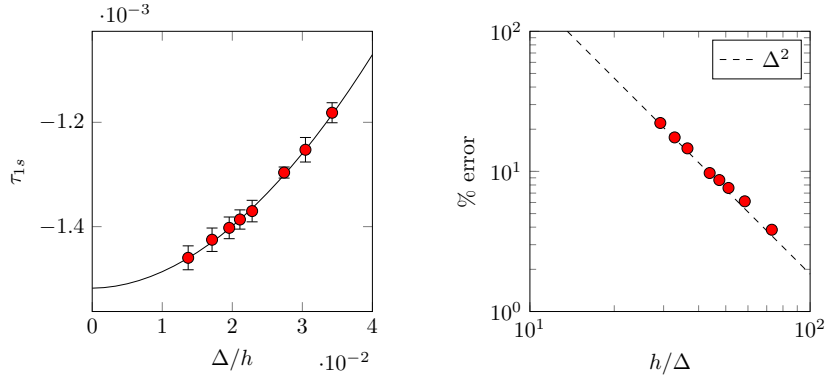

Figure 6.7: Convergence of the quadrature component τ_{1s} of the wall shear stress for the wavy channel test case. Left: variation of the time-averaged value of τ_{1s} with the mean spatial resolution Δ; the error bars correspond to $\pm 3\sigma_{1s}$, where the root-mean-square value σ_{1s} of the estimate of the mean is computed after Russo & Luchini (2017). The continuous line is a fit of equation (6.21), yielding $\tau_{1s}^{(e)} = -0.001518$, $C = 0.2109$ and $p = 1.912$. Right: percentage error $100(\tau_{1s}^{(e)} - \tau_{1s})/\tau_{1s}^{(e)}$ of the quadrature stress versus spatial resolution; the dashed line shows the expected second-order decrease.

amplitudes ϵ. For a discussion of the physical implications of this behaviour, see Luchini (2016).

To verify the order of accuracy of the IBM, figure 6.7 plots the results of a spatial convergence study, whose main results are reported in table 6.2. For $\alpha = 0.5$ (or $L_x = 4\pi$) and $\epsilon = 0.05$, different discretizations have been tested, by progressively reducing the mesh size uniformy in all the three directions. The coarsest mesh has $(N_x, N_y, N_z) = (192, 160, 64)$, corresponding to a total number of points $N_{tot} \approx 2 \times 10^6$. The finest mesh has $(N_x, N_y, N_z) = (480, 400, 160)$, with a total number of $\approx 3 \times 10^7$ points. The time step is fixed for all cases at $\Delta t = 0.001$, a value that is small enough to ensure that the time discretisation error is not dominant.

Given a numerical method with rate of convergence p, the difference between the solution f computed on a three-dimensional uniform grid with spacing Δ and the exact solution $f^{(e)}$ must vary according to

$$||f - f^{(e)}|| \leq C\Delta^{-p} \tag{6.21}$$

where C is a constant. We use equation (6.21) to compute a least-square fit for the quadrature stress component (equivalent results, not shown, are obtained with the in-phase component) obtained from the numerical experiments. Since the exact solution is not known, the value $\tau_{1s}^{(e)}$ is evaluated with the asymptotic value of the

fitting curve. In computing the time-averaged value of τ_{1s}, we also quantify the error implied by the finite averaging time; to this purpose the method described by Russo and Luchini in Russo & Luchini (2017) is used to compute the root-mean-square value σ of the estimate of the mean, and figure 6.7 plots error bars for $\pm 3\sigma$. As expected, figure 6.7 confirms that the present immersed-boundary method exhibits a second-order convergence, with an exponent $p = 1.912$.

6.4.2 The turbulent flow in the human nose

The air flow inside the human nose is an important application, owing to the wide and obvious implications of a healthy breathing. The physiologically healthy flow through the nasal cavities is difficult to define, as no single flow feature can be shown to correlate with the perceived breathing quality. The prevalence of anatomical malformations (like e.g. septal deviations, or hypertrophy of the turbinates) is huge, with nasal breathing difficulties affecting up to one third of the entire world population (Li *et al.*, 2020). In recent years the number of numerical studies dealing with the fluid mechanics of the human nose, built upon the patient-specific anatomic information provided by CT scans, has increased considerably. While the majority of such studies consists in simple RANS simulations executed with commercial, finite-volumes software, the availability of accurate reference solutions remains essential for validating physiology studies of fundamental character, and becomes clinically important whenever specific and unusual anatomies need to be evaluated for diagnosing and surgery planning. However, so far very few studies, (e.g. Calmet *et al.* (2016); Li *et al.* (2017)), have described the nose flow with DNS-like resolution, owing to the combination of its extreme geometrical complexity and the accompanying significant computational cost; none of them employed an immersed-boundary approach.

In the context of the present work, the nasal airflow represents an ideal test bed for the IBM, whose accuracy and computational performance can be assessed on a geometrically challenging scenario. In this study, we consider therefore one specific sinonasal anatomy, that has been recently used in a tomo-PIV experiment described in Tauwald *et al.* (2024). The anatomy is derived from segmentation of a CT scan of a healthy patient, composed of 384 DICOM images with sagittal and coronal resolution of 0.5 mm and an axial gap of 0.6 mm. The anatomy is segmented at constant radiodensity threshold, with the assistance of an experienced surgeon, according to a well established procedure (Quadrio *et al.*, 2016*b*), to identify the interface between air and solid tissues. For experimental reasons, the whole anatomy has been then enlarged by a factor of 2. Figure 6.8 portraits the anatomy of the internal nose, and demonstrates how the actual geometrical boundary is extremely complex, with evident three-dimensional features and the presence of large lateral volumes, the paranasal sinuses, which are only loosely

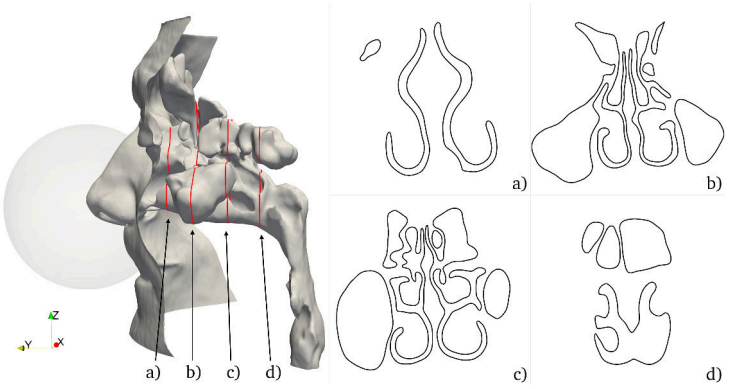

Figure 6.8: Anatomy of the human airways, after a patient-specific reconstruction of a CT scan. The surface represents the boundary of the computational domain, and is augmented by a spherical volume placed outside the nose tip, whose goal is to set the computational boundary away from the nostrils. The vertical (coronal) sections on the right illustrate how the complex cross-sectional shape varies along the passageways, including the nasal vestibulum, the anterior part of the meati (a), the intermediate sections shaped by the turbinates (b) and (c), down to the rhinopharynx (d).

connected to the main airways via small orifices called ostia. Figure 6.8 also highlights, by means of coronal sections, how the cross-sectional shape of the airways varies significantly from the nose tip towards the throat. The computational domain also comprises a spherical volume, shown in figure 6.8, which surrounds the external nose: the sphere is designed to locate the boundary of the computational domain far from the nostrils, while keeping the computational overhead within reason.

In this work a simple steady inspiration is considered, where a (constant in time) pressure drop is imposed between the inlet at the external surface of the sphere and the outlet at the trachea; the numerical value of 5 Pa and the corresponding volumetric flow rate of approximately 600 cm^3/s correspond, after the factor-of-two geometrical expansion is accounted for with dynamic similarity arguments, to a mild physical activity (Wang *et al.*, 2012). Note that, because we are replicating an experimental study, dimensional quantities are used in this section. Regardless of the time-independent boundary conditions, the flow is unsteady, with three-dimensional shear layers and vortical structures; in some regions the flow becomes turbulent. Starting from an initial condition of resting flow everywhere, the simulations are advanced in time until the initial transient has vanished, and then further integrated for about $1s$ of physical time to compute time averages.

Some features of the time-averaged flow are illustrated in figure 6.9. The left panel plots the mean pressure field in a representative sagittal section that cuts

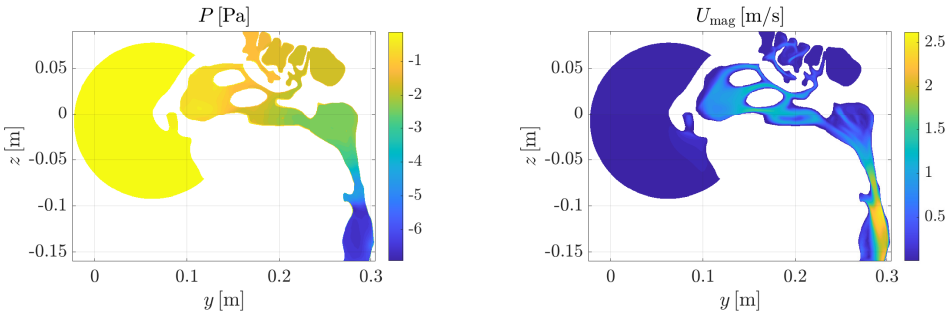

Figure 6.9: Left: mean pressure field in a sagittal section. Right: mean velocity magnitude field in the same section.

N_{tot}	$\Delta\ [mm]$	$Q\ [cm^3/s]$	$\sigma\ [cm^3/s]$
3749528	0.9978	598.591	0.3306
6289066	0.8317	608.040	0.3909
10603652	0.6934	615.943	0.3407
17969591	0.5775	620.155	0.2288
30476246	0.4815	624.907	0.5118
51936820	0.4011	628.032	0.6040
91969807	0.3343	628.626	0.9309
157849674	0.2787	630.130	0.6996
273071473	0.2322	631.042	0.5586

Table 6.3: Spatial convergence study for the nose test case. The table lists the total number of grid points in the fluid volume, the (isotropic) grid spacing in millimeters, the value Q of the temporally averaged flow rate at the trachea, and the root-mean-square value σ of the variance of the estimate of the mean, computed after Russo & Luchini (2017).

through the right passageway, and illustrates the pressure decrease from the outer ambient to the throat. The pressure drop is particularly localized and noticeable at the nasal valve and at the striction determined by the larynx. The right panel plots the magnitude of the mean velocity vector in the same section. During inspiration the external air is first accelerated abruptly in correspondence of the nasal valve, and quite large velocity values are observed in certain portions of the meati; the airflow then enters the rhinopharynx with quite definite shear layers, and then transforms into a laryngeal jet after the narrowing at the larynx, where the largest velocities are found.

Table 6.3 reports the results of a spatial convergence study, where the time-averaged value of the flow rate Q at the trachea for the fixed pressure drop of 5 Pa is observed as the spatial resolution is changed. The calculations have been carried

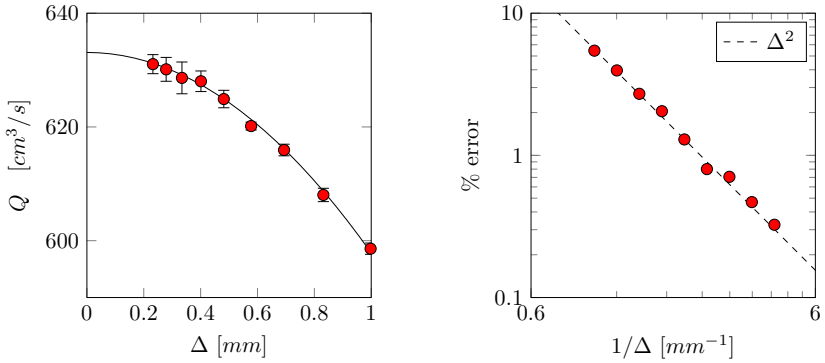

Figure 6.10: Convergence of the flow rate for the nose test case. Left: variation of the time-average flow rate Q with the (isotropic) spatial resolution Δ; the error bars correspond to $\pm 3\sigma$, where the root-mean-square value σ of the uncertainty of the mean is computed after Russo & Luchini (2017). The continuous line is a fit of equation (6.21), yielding $Q^{(e)} = 633.1\, cm^3/s$, $C = 3.502 \times 10^{-7}$ and $p = 1.999$. Right: percentage error $100(Q^{(e)} - Q)/Q^{(e)}$ of the mean flow rate versus spatial resolution. The dashed line shows the expected second-order decrease.

out for a fixed time step size $\Delta t = 0.02\, ms$, that is small enough to ensure that the the time discretization error is not dominant. The geometrical complexity suggests the use of isotropic spacing, hence cubic cells are used with edge length Δ. The coarsest mesh consists of about 3.7 millions points within the fluid volume; the size of its cells is $1\, mm$ (which is comparable to the resolution of the CT scan, if the model scaling is considered) and still allows a decent representation of the smallest flow structures. The largest employed mesh has about 273 millions points and a spatial resolution of $230\, \mu m$. Fitting the formula (6.21) to the data of table 6.3, following the same procedure discussed above in Sec. 6.4.1, yields an exponent $p = 1.999$: the second-order convergence is fully confirmed, as shown graphically by figure 6.10.

6.5 Conclusions

We have presented a novel, simple and efficient implicit second-order immersed boundary method (IBM) for the direct numerical simulation of the incompressible Navier–Stokes equations.

Our IBM belongs to the class of methods employing a discrete-forcing formulation; its computational efficiency descends from the tight integration with the underlying numerical discretization, based on second-order accurate central finite differences computed on a staggered grid. Such integration is possible because

the boundary-distance information is concentrated in a single point, namely the centre point of the stencil that discretizes the Laplacian operator. This allows the IBM correction to be made implicit at no cost: this is perhaps the main novelty of the present IBM implementation.

This type of correction offers several crucial advantages. On the one hand, since the correction is applied only to the central point of the stencil, the formulation enjoys extreme simplicity in terms of implementation: the cobweb of IFs and *ad-hoc* coding to handle special cases that would otherwise handle those parts of the boundary that come close to each other becomes unnecessary. On the other hand, the computational cost of the IBM correction is brought to a minimum. In order to estimate it, a simple experiment consists in switching the correction off, thus reinstating the baseline first-order-accurate staircase approximation of the boundary; timing the execution of the solver with and without the correction quantifies the extra cost necessary to achieve second-order accuracy near the boundary. Such timing experiments led us to the conclusion that hardly any extra cost is visible at all. The implicit nature of the IBM also has important favorable consequences on the stability of the numerical method. The explicit IBMs, in fact, fall into trouble whenever a grid point coincides or even approaches the boundary, whereas for the implicit IBM the solution monotonically tends to zero as it should.

The IBM has been introduced and described in conjunction with two simple linear problems, where the spatial and temporal accuracy of the method have been separately addressed. In the second part of the paper, the method has been applied to two challenging turbulent flow problems, namely the channel flow over a wavy bottom and the air flow through the intricate anatomy of the human nose. A full second-order accuracy has been confirmed even in these examples, which contain the entire complexity of the Navier–Stokes equations; in particular the nose flow can be rightfully considered a stress-test for the IBM, owing to the extreme anatomical intricacy of the nasal cavities. The IBM described in this paper lies at the heart of a DNS solver, currently under active development, which is aimed at both CPU and GPU architectures, and promises to achieve very interesting computational speed.

Dimples for skin-friction drag reduction: status and perspectives

The content of this Paper has been published in
Gattere, F., Chiarini, A. & Quadrio, M. 2022
Dimples for Skin-Friction Drag Reduction: Status and Perspectives.
Fluids **7** (7), 240.
Minor editing has been done for formatting purposes.

Dimples for skin-friction drag reduction: status and perspectives

Abstract

Dimples are small concavities imprinted on a flat surface, known to affect heat transfer and also flow separation and aerodynamic drag on bluff bodies when acting as a standard roughness. Recently, dimples have been proposed as a roughness pattern that is capable to reduce the turbulent drag of a flat plate, by providing a reduction of skin friction that compensates the dimple-induced pressure drag, and leads to a global benefit.
The question whether dimples do actually work to reduce friction drag is still unsettled. In this paper, we provide a comprehensive review of the available information, touching upon the many parameters that characterize the problem. A number of reasons that contribute to explaining the contrasting literature information are discussed. We also provide guidelines for future studies, by highlighting key methodological steps required for a meaningful comparison between a flat and dimpled surface in view of drag reduction.

7.1 Introduction

Reducing the drag generated by a fluid set in relative motion to a solid body is at the same time a fundamental attempt to learn how to favorably interact with turbulence, and a technological challenge with immense potential in so many application fields. The interest for turbulent flow control is steadily increasing, owing to massive economic and environmental concerns.

Skin-friction drag is perhaps the most essential manifestation of the dissipative nature of turbulence, and accounts for the total drag in the case of planar walls (as in a channel flow or a zero-incidence flat plate boundary layer). Several techniques

are available to reduce friction drag below the level typical of a smooth solid wall; they can be categorized into active (requiring extra energy) and passive ones. The former typically provide larger savings, but imply extra complexity and cost, so that the ideal technique for friction reduction remains a passive one, often embodied in surface patterns performing better than the planar flat geometry.

The most prominent example of such patterns is riblets (García-Mayoral & Jiménez, 2011). Introduced by NASA in the '80 of the past century, and intensely studied over the subsequent years for their potential in aeronautical applications, riblets consist of streamwise-aligned microgrooves, and have the proved ability to reduce friction drag. The riblets cross-section can be of several shapes, the triangular one being perhaps the most popular, but an essential feature is a very sharp tip. Although new developments (Quadrio *et al.*, 2022; Cacciatori *et al.*, 2022) hint at a bright future for riblets in aeronautics and suggest lower cost/benefit ratios, riblets are currently still not deployed in commercial transport aircraft, owing to their limited savings (McLean *et al.*, 1987; Kurita *et al.*, 2020) and to critical production and maintainance issues, descending from the microscopic size of riblets and from the requirement of preserving the sharpness of the tip.

A possible alternative to riblets is emerging recently, easier to manufacture and lacking any sharp detail. The pattern to impress on the surface consists of small dimples. Dimples, i.e. small concavities imprinted on a surface, have been extensively studied in the past for their ability to enhance the heat transfer of a surface (see e.g. Leontiev *et al.* (2017) and references therein). The use of dimples on the surface of bluff bodies (e.g. a golf ball) is well known, and their ability to influence the turbulent boundary layer and the separation on the body is rather well understood (Choi *et al.*, 2006); the same concept is also being considered in sport-car racing (Allarton *et al.*, 2020). In this paper we concern ourselves with dimples applied to an otherwise flat surface: the goal is to reduce the turbulent skin-friction drag. We limit our review to passive dimples, although also active control by dimples has been proposed (Ge *et al.*, 2017).

The ability of dimples to reduce drag is way less intuitive than that to increase heat exchange, and was considered first at the Kurchatov Institute of Athomic Energy (Kiknadze *et al.*, 1984) in Russia, where hemispherical dimples were placed on the surface of a heat exchanger and found to reduce the flow resistance as well. In subsequent studies by the same group, a drag reduction of about 15–20% was mentioned (Alekseev *et al.*, 1998), the highest performance reported so far. In the last two decades, a handful of research groups devoted their efforts to understanding the drag reduction problem by dimples, attempting to come up with a recipe for the best shape and size. Unfortunately, to date no consensus has been reached on the effectiveness of dimples in reducing friction drag, and on their working mechanism: some authors confirmed drag reduction, others did not.

Measuring – in the lab, or with a numerical simulation – the (very small, if any)

drag reduction induced by dimples is by no means a trivial task. A reduction of friction drag would be unavoidably accompanied by an increase of pressure drag, with a net benefit possible only if the former overwhelms the latter. There are just so many design variables to be tested, as the geometry of the dimple itself, the size, the spatial layout and relative arrangement of the dimples on the surface need to be carefully considered. This is a daunting task as long as no theory, hypothesis of working mechanism or scaling argument is available to guide the search in such a vast parameter space. However, it is undeniable that dimples, once proved to work, would provide substantial advantages over riblets, thanks to their simplicity, ease of production, lack of sharp corners and easier maintenance.

The goal of the present contribution is to provide the first comprehensive review of the published information available on dimples for skin-friction drag reduction. Since the very fact that dimples can actually work is still subject to debate, we will complement the review with a discussion of important procedural aspects that in our view are essential, should one embark in a (numerical or laboratory) experiment to assess the potential for drag reduction. Such procedures (or, more precisely, their absence) are at the root of the large uncertainty and scatter of the available data, and have hindered so far the answer to such a simple question as: Do dimples actually work to reduce turbulent drag?

The present contribution is structured as follows. Section §7.2 provides an overview of the experimental and numerical studies on the drag reduction properties of dimples. Section §7.3 describes the geometrical parameters defining the dimples, whereas §7.4 reports the two main physical explanations for the working mechanism of drag-reducing dimples. In §7.5 we highlight the problem of properly measuring drag reduction, and guidelines and recommendations on how to properly compare results among different studies are provided. This review paper is closed by brief concluding remarks in §7.6. Appendix 7.A contains details of the DNS simulations that have been carried out for the present study.

In the next Subsection, the concept of dimples is introduced first, together with the notation that will be used later to indicate their geometrical parameters.

7.1.1 Characterization of a dimpled surface

A solid wall covered with dimples is described by several geometric parameters: the dimple shape, the relative spatial arrangement of the dimples and the coverage ratio (ratio between non-planar and total surface). Originally, dimples were conceived as spherical recesses, hence with a circular footprint on the wall. One particular class of circular dimples, introduced by Chen *et al.* (2012), has become quite popular thanks to its parametric nature and represents the starting point of our description. This design is the union of a spherical indentation and a torus, meeting tangentially in a regular way that avoids sharp edges. A cross-section of

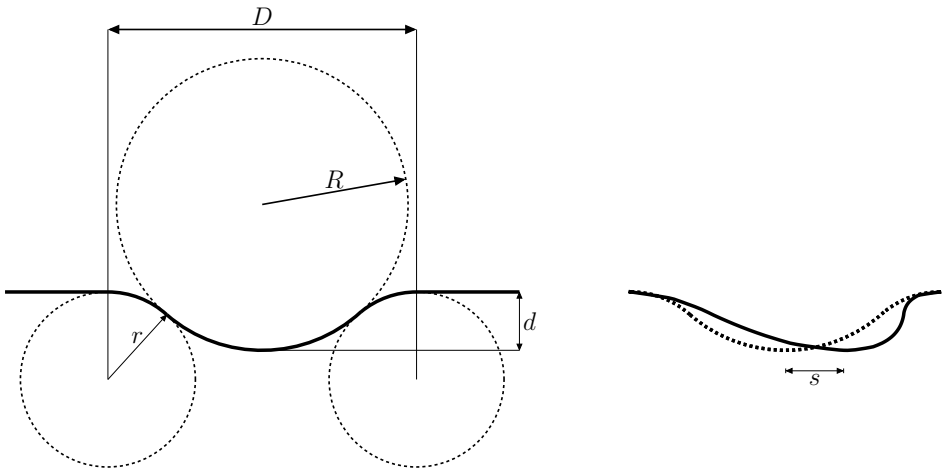

Figure 7.1: Cross-section of the parametric dimple geometry introduced by Chen *et al.* (2012) (left) and streamwise shift of the deepest point (right).

this dimple, which possesses axial symmetry, is drawn in figure 7.1.

Four parameters define the geometry of this dimple: the diameter D of the circular section at the wall, the depth d of the spherical cap, the curvature radius r at the edge and the curvature radius R of the spherical cap. These four parameters are not independent, but linked by one analytical relation, so that only three degrees of freedom exist. In fact, geometry dictates that:

$$\frac{D}{2} = \sqrt{d\,(2R + 2r - d)}. \tag{7.1}$$

Moreover, a handful of studies extended this baseline circular geometry, by introducing the additional parameter s, which describes the shift along the streamwise direction (either downstream for $s >$ or upstream for $s < 0$) of the point of maximum depth, which in the baseline geometry lies exactly at the center of the dimple cavity.

It is difficult to overemphasize the importance of a well-defined parametric geometry in the quest for the optimally performing dimple. Although the circular shape is by far the most popular, over the last years a number of alternative dimple shapes have been studied; sketches for the various shapes are drawn in figure 7.2. Some of them derive from a deformation of the circular shape: e.g. the elliptical dimple is the result of a symmetrical stretch of the circular dimple along the streamwise direction. The teardrop dimple has two segments tangent to the circle, preserves the spanwise symmetry and exists in two variants depending on whether the triangle points upstream or downstream. The diamond dimple is the union of the two variants of teardrop and possesses two vertices. Only the triangular dimple

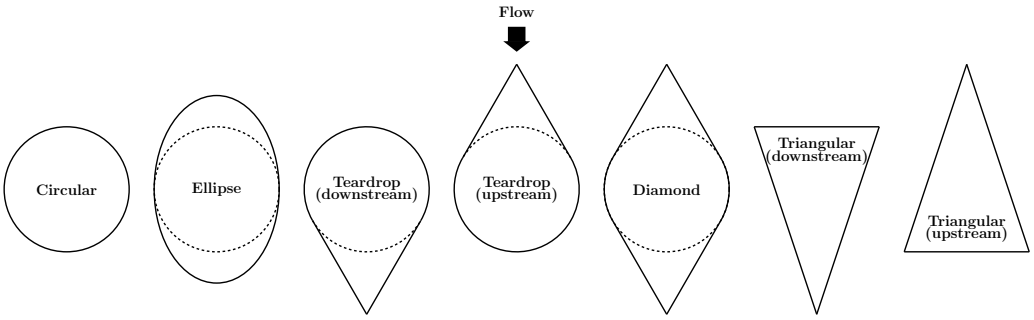

Figure 7.2: Popular variants of the dimple shape.

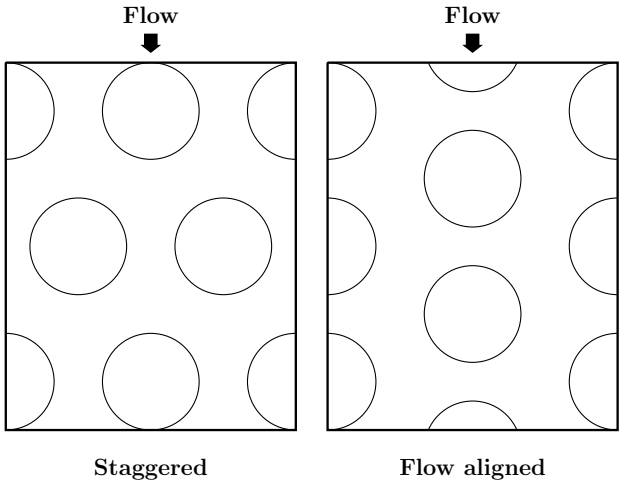

Figure 7.3: Most popular dimples layout: staggered (left) and flow aligned (right).

differs substantially from the circular shape and — as for the teardrop dimple — can have the streamwise-aligned vertex pointing upstream or downstream.

When a single dimple is identically replicated to fully cover the planar surface, the relative spatial arrangement of the dimples is important in determining the overall influence on the flow. A regular spatial layout of a dimpled surface depends on the distance between two adjacent dimples in both the streamwise and spanwise directions. Another parameter that is related to the spatial arrangement of dimples is the coverage ratio, that can be defined as the percentage of recessed surface compared to the total surface of the wall. (The reader will notice an ambiguity, as at the denominator of the coverage ratio one could put either the surface area of the equivalent flat wall, or the wetted area of the dimpled surface. This ambiguity is often ignored, but it is commented upon e.g. in Praß *et al.* (2019) ,Tay *et al.* (2017) and Ng *et al.* (2020).) It is doubtful whether coverage, which is affected by so many parameters, is by itself a useful quantity to describe dimples performance.

Moreover, dimples can be arranged either irregularly or regularly following a certain pattern. The two most widespread patterns are the staggered and the flow-aligned arrangements. Their definition is not unique. Often, the layout is referred to as staggered when the streamwise projection of one dimple overlaps with the following one, while it is called flow-aligned otherwise (see figure 7.3). However, this definition, that corresponds to the most used arrangement, is not universally accepted. Praß *et al.* (2019), indeed, define the staggered arrangement as having the distance in spanwise direction from the centres of two adjacent dimples equal to half the distance between the centres of two non-adjacent dimples. Several additional patterns have been tested, e.g. the hexagonal one.

7.2 Do dimples work?

Although in the last two decades a number of dimples-related contributions have appeared, many works claim that drag reduction is possible for certain geometries and flow conditions (Veldhuis & Vervoort, 2009; Tay, 2011; Tay *et al.*, 2015; Van Nesselrooij *et al.*, 2016; Tay *et al.*, 2016; Tay & Lim, 2017, 2018; Spalart *et al.*, 2019), whereas others only report drag increase (Tay *et al.*, 2017; Van Campenhout *et al.*, 2018; Praß *et al.*, 2019; Ng *et al.*, 2020). Notably, one work (Spalart *et al.*, 2019) set out to specifically reproduce the experimental drag reduction results described in Van Nesselrooij *et al.* (2016) with a state-of-the-art combined numerical/experimental study, and failed.

Such uncertain situation can be traced back to the lack of a generally accepted standard to measure drag and to compare different geometries among themselves and with the reference flat wall, since there are unavoidable differences when measuring drag in experiments and simulations, and in external (e.g. boundary layer) and internal (plane channel) flows. An additional reason explaining the scatter of available results consists in the still limited understanding of how dimples modify the surrounding flow field. Knowing the physics involved in drag reduction by dimples would be extremely useful in the optimization of all the several parameters involved. A description of the effect of the many geometrical parameters involved, and on the conjectures on the working mechanism of dimples are reported later in §7.3 and §7.4 respectively.

We start by presenting an overview of the main results available in the literature, by focusing on the raw drag reduction information. They are reported in Table 7.1 that contains entries for the best drag reduction figure that could be extracted from each paper; when multiple dimple shapes are present, they are all considered. Drag change is simply defined here as $\Delta Drag = Drag_{dimples} - Drag_{smooth}$, where $Drag_{smooth}$ and $Drag_{dimples}$ are the (measured or computed) friction drag of the reference flat plate and the total drag of the dimpled plate, respectively. Negative

values of $\Delta Drag$ thus correspond to drag reduction. Across the several studies, various definitions of the Reynolds number are used, particularly for internal flows. These have been all converted, whenever possible, to value of the bulk Reynolds number Re_b, by using the empirical Dean's correlation (Dean, 1978). Several other entries are also available in the Table, and will be defined and discussed throughout the text.

7.2.1 Experimental studies

The majority of the experimental studies carry out their tests in a wind tunnel and compare the drag measured on a flat plate with the drag measured on a dimpled plate. The flat/dimpled plate lies either on the upper or bottom wall, whereas the other wall of the wind tunnel is smooth. The plate is installed at a certain distance from the entrance section for the flow to become fully developed by the time it reaches the test section. A major difference among the various studies consists in the internal/external character of the flow.

The largest drag reduction, as observed in Table 7.1, is a whopping 14% found in the boundary layer experiment by Veldhuis & Vervoort (2009) at the Technical University of Delft. The free-stream velocity was 7.5 m/s and dimples were of circular shape. They found the staggered configuration to be more efficient in reducing drag than the flow-aligned one. Other boundary layer experiments carried out later by the same group at TU Delft reported a significantly smaller but still extremely interesting maximum drag reduction of 4% (Van Nesselrooij *et al.*, 2016), obtained at a Reynolds number based on the free-stream velocity U_∞ and the dimple diameter D of $Re_D \approx 40000$, which corresponds to a Reynolds based on the boundary layer thickness δ of $Re_\delta = 1500$. In this case, dimples are relatively large (in physical dimensions) shallow circular dimples, with a 50% smaller coverage ratio than Veldhuis & Vervoort (2009). In a later study Van Campenhout *et al.* (2018) also measured a drag increase of 1% for shallow dimples with different layouts at $Re_D \approx 63100$. Van Nesselrooij *et al.* (2016) presented what is described in Spalart *et al.* (2019) as a "very convincing experimental paper", studying different dimples configuration and finding that the best one consistently involves sparse (low coverage) and staggered dimples for the entire range of considered Reynolds numbers. They also focused on the importance of the depth of the dimples. When made dimensionless with the dimple diameter, shallower dimples are found to work better for each flow condition; however, when depth is compared to the boundary layer thickness, shallow dimples work better at low Re but deep dimples are better at higher Re.

Another group that provided significant contribution to the dimples research thread is from the National University of Singapore, with Tay and colleagues. They performed experimental studies on a channel flow and reported up to 7.5% drag

reduction in Tay *et al.* (2019) for diamond-shaped dimples at a Reynolds number based on the bulk velocity U_b and the channel semi-height h of $Re_b \approx 30000$ and a layout with full coverage. Large drag reductions are measured also with other non-conventional dimple shapes (Tay & Lim, 2018), such as the upstream-pointing teardrop at 6%, or the downstream-pointing teardrop at 5%, in a flow with $Re_b \approx 30140$ and $Re_b \approx 22270$, respectively. Conversely, the triangular shape was proved to always lead to drag increase (Tay *et al.*, 2016). Circular dimples were found to be less effective than diamond and teardrop shapes. A reduction of drag up to 2% (Tay, 2011) and 2.8% (Tay *et al.*, 2015) are found at $Re_b \approx 17500$ and $Re_b \approx 32100$ for different physical geometrical parameters of the dimple but with an identical layout and coverage ratio of 90%. At $Re_b \approx 42850$ a drag reduction of 3.5% is measured in Tay & Lim (2018). In Tay *et al.* (2015) they compare the same physical dimples and flow geometry by varying the coverage ratio and find that a dense layout with 90% coverage performs better than a sparse one with 40% coverage. They also compare two different dimple depths, measuring slightly higher drag reduction for deeper dimples. Finally, Tay & Lim (2017) experiment with shifting the point of maximum depth within the dimple along the streamwise direction, and measure the best performance of 3.7% when the shift is $s = 0.1D$ in the downstream direction.

7.2.2 Numerical simulations

For drag reduction studies, numerical simulations need to resort to high-fidelity approaches, like Direct Numerical Simulation (DNS) and highly resolved LES (Large Eddy Simulation). Obviously, such simulations are not very practical for large-scale parametric studies, especially when the Reynolds number becomes large, since their unit computational cost rapidly increases with Re. The need for high-fidelity methods, the computational cost and the requirement to handle non-planar geometries are among the reasons why numerical studies for dimples are fewer than experiments. However, simulations (and DNS in particular, which avoids the need of turbulence modeling) are perfectly suited for such fundamental studies and provide us with the full information required to understand the working mechanism of dimples, by e.g. breaking up the drag changes into friction drag and pressure drag changes and by yielding a detailed and complete statistical characterization of the turbulent flow.

Circular dimples in a turbulent channel flow were studied with DNS for the first time in 2008 by Lienhart *et al.* (2008), who reported a drag increase of 1.99% at $Re_b \approx 11000$. The same work contains also an experimental study of the same configuration, for which no drag changes were observed.

Ng *et al.* (2020) at NUS performed one of the most interesting DNS studies, considering a turbulent channel flow at $Re_b = 2800$ and examining different

dimple geometries. They found that the classic circular dimple increases drag by 6.4%, an amount that decreases to 4.6% when the point of maximum depth is shifted downstream by $s = 0.1D$. They also studied non-circular dimple shapes, obtaining this time a large drag reduction of 7.4% for the diamond dimple, 4.9% for the elliptical dimple and 3.1% for the upstream-pointing teardrop dimple; the downstream-pointing teardrop dimple, instead, gave 0.1% drag increase.

Another recent numerical channel flow study is that by Tay *et al.* (2017): they run a Detached Eddy Simulation (in which a baseline LES is complemented with a RANS model for the near-wall region) to replicate their own experimental study described in Tay *et al.* (2015). The DES yielded 1% drag increase at $Re_b = 2830$, which does not confirm the experimental study and found drag increase for every case tested, whereas the experiments found smaller drag increase and even a slight drag reduction for a particular geometry. The suitability of DES for such drag reduction studies, however, remains dubious.

Praß *et al.* (2019) published the only work in which an open channel is considered: with a LES they report a drag reduction of 3.6 % at $Re_b \approx 6121$. They also considered two different configurations, finding that flow-aligned dimples perform better than staggered dimples.

There is only one DNS study for the boundary layer, i.e. the already mentioned work by Spalart *et al.* (2019), in which circular dimples at $Re_\delta = 30000$ were considered as the baseline geometry. They additionally studied the effect of the edge radius r, and found that with proper smoothing of this edge a drag reduction of -1.1% is obtained, which descends from the combination of a -1.7% reduction of friction drag, counterbalanced by a 0.6% increase of pressure drag.

Table 7.1: Summary of the main parameters and results of the literature. Columns report, in sequential order: 1. the acronym of the reference: LBK-08 (Lienhart *et al.*, 2008), VV-09 (Veldhuis & Vervoort, 2009) T-11 (Tay, 2011), TKC-15 (Tay *et al.*, 2015), VVVS-16 (Van Nesselrooij *et al.*, 2016), TLKJ-16 (Tay *et al.*, 2016), TKC-17 (Tay *et al.*, 2017), TL-17 (Tay & Lim, 2017), TL-18 (Tay & Lim, 2018), VVVVS-18 (Van Campenhout *et al.*, 2018), SSSTPW-19 (Spalart *et al.*, 2019), TLK-19 (Tay *et al.*, 2019), PWFB-19 (Praß *et al.*, 2019), NJLTK-20(Ng *et al.*, 2020); 2. the numerical (DNS: direct numerical simulation, LES: large eddy simulation, DES: detached eddy simulation; FVM: finite volume method, SEM: spectral element method) or experimental approach; 3. the flow type: channel flow (CF), half-channel flow (HCF) or boundary layer (BL); 4. the value of the Reynolds number: Re_b for CF and HCF, Re_δ for BL (other Re definitions for CF are converted to Re_b using the Dean's law); 5. the dimple shape: circular (Circ), triangular (Triang), diamond (Diam), elliptical (Ell), teardrop (Tear); upstream-pointing (Up), Downstream-pointing (Do); 6. spanwise width D_z and streamwise length D_x, expressed as a fraction of the reference length L (the channel half-height h for CF and the boundary layer thickness δ for BL); for a circular dimple $D_z = D_x$, thus only one value is reported; 7. the dimple depth d; 8. the edge curvature radius r; 9. the curvature radius R of the spherical cap; 10. the shift s of the point of maximum depth; 11. the coverage ratio; 12. the type of layout: S:staggered, A: aligned, H:hexagonal; 13. the percentage drag change. "-" is used when some information required to compute the value is lacking.

Article	**Num/Exp**	**Flow**	**Re**	**Shape**	$\mathbf{D_z/L(D_x/L)}$	$\mathbf{d/D_z\%}$	$\mathbf{r/D_z}$	$\mathbf{R/D_z}$	$\mathbf{s/D_x}$	**Cov%**	**Layout**	**ΔDrag%**
LBK-08	Exp	CF	≈ 10000	Circ	0.6	5	-	-	0	22.5	A	0
	DNS (FVM)	CF	10935	Circ	0.6	5	-	-	0	22.5	A	+1.99
VV-09	Exp	BL	-	Circ	-	5	-	-	0	60	S	−14
T-11	Exp	CF	≈ 17500	Circ	5	5	0.84	1.68	0	90	S	−2
TKC-15	Exp	CF	≈ 32100	Circ	5	5	4.2	8.45	0	90	S	−2.8

Article	Num/Exp	Flow	Re	Shape	$D_z/L(D_x/L)$	d/D_z%	r/D_z	R/D_z	s/D_x	Cov%	Layout	ΔDrag%
VVVS-16	Exp	BL	≈ 1500	Circ	26.67	2.5	0.5	4.51	0	33.3	S	-4
TLKJ-16	Exp	CF	≈ 5625	Triang Up	$-(4.67)$	5	-	-	-0.5	-	S	$+4.8$
	Exp	CF	≈ 5625	Triang Do	$-(4.67)$	5	-	-	$+0.5$	-	S	$+2.8$
	Exp	CF	≈ 50350	Circ	5	5	-	-	$+0.1$	90	S	-3.6
TKC-17	DES (FVM)	CF	≈ 2830	Circ	5	1.5	0.84	1.68	0	90	S	$+1$
TL-17	Exp	CF	≈ 28600	Circ	5	1.5	-	-	$+0.1$	90	S	$+1$
TL-18	Exp	CF	≈ 42850	Circ	5	5	-	-	0	-	S	-3.5
	Exp	CF	≈ 30140	Tear Up	5(7.5)	5	-	-	$+0.17$	84	S	-6
	Exp	CF	≈ 22270	Tear Dp	5(7.5)	5	-	-	-0.17	84	S	-5
VVVVS-18	Exp	BL	-	Circ	-	2.5	0.5	-	0	-	S/A/H	$+1$
SSSTPW-19	DNS (FVM)	BL	30000	Circ	1.33	-	2.03	-	0	-	S	-1.1
TLK-19	Exp	CF	≈ 30000	Diam	5(10)	5	-	-	0	99	S	-7.5
PWFB-19	LES (FVM)	HCF	≈ 6121	Circ	5.7	2.5	1.5	4.51	0	-	S	-3.6

Article	Num/Exp	Flow	Re	Shape	$D_z/L(D_x/L)$	d/D_z%	r/D_z	R/D_z	s/D_x	Cov%	Layout	ΔDrag%
NJLTK-20	DNS (SEM)	CF	2800	Circ	5	5	0.84	1.68	+0.1	90.7	S	+4.6
	DNS (SEM)	CF	2800	Ell	5(7.5)	5	0.84	1.68	0	90.7	S	−4.9
	DNS (SEM)	CF	2800	Tear Up	5(8.75)	5	0.84	1.68	+0.21	84.4	S	−3.1
	DNS (SEM)	CF	2800	Tear Dp	5(8.75)	5	0.84	1.68	−0.21	84.4	S	+0.1
	DNS (SEM)	CF	2800	Diam	5(10)	5	0.84	1.68	0	99.5	S	−7.4

7.3 How to design dimples?

Systematic studies which address the influence of each geometric parameter are lacking, so that the design of the optimal configuration to achieve the maximum drag reduction has not been identified yet. This Section describes the little we know, first in terms of the geometrical characteristics of the dimples and then in terms of their arrangement.

7.3.1 The shape of the dimple

Figure 7.4 plots the drag change data measured by several works which adopted the baseline circular geometry. The percentage of drag change is shown as a function of the three independent geometrical parameters d/D, r/D and R/D, after extracting from each publication the largest drag reduction (or the smallest drag increase). It should be noted that, in general, the various points correspond to simulations or experiments that differ for other, sometimes very important, design parameters. Dashed lines, instead, connect points for which only the parameter on the abscissa is changed.

The influence of d/D on the drag change has been studied by several authors: previous research from heat exchange enhancement suggests the very reasonable idea that this is one of the key factors affecting drag. However, while the optimal d/D is in the range $0.1 - 0.5$ for best heat exchange (Kovalenko *et al.*, 2010; Tay *et al.*, 2014), several authors report that shallower dimples with $d/D < 0.1$ should be considered for reducing the overall drag, to avoid excess penalty from the ensuing pressure drag. Data are extremely scattered and clearly indicate that the drag change over a dimpled surface does not depend on the d/D ratio alone. For example for $d/D = 0.05$ Veldhuis & Vervoort (2009) report a drag reduction of almost 15%, while Tay *et al.* (2017) report a drag increase of approximately 6%. The experimental measurements from Veldhuis & Vervoort (2009) are for a turbulent boundary layer over a dimpled surface with coverage ratio of 60% at a free-stream velocity in the range $0 - 29\ m/s$; the results from Tay *et al.* (2017) are from a Detached Eddy Simulation of a turbulent channel flow at $Re_b \approx 3000$ with a coverage ratio of 90%.

It is reassuring, though, to see — at least in some of the datasets where data points are connected by dashed lines — a local optimum for intermediate depths, since it is reasonable to expect zero drag changes for $d \to 0$ and an increase of drag as for standard k-type roughness for $d \to \infty$. With the other parameters unchanged, Tay *et al.* (2017) and Van Nesselrooij *et al.* (2016) agree on observing a decrease of performance with increasing d/D (in the range $0.015 < d/D < 0.05$), although at a different rate; within the same d/D range, Tay *et al.* (2015) and Veldhuis &

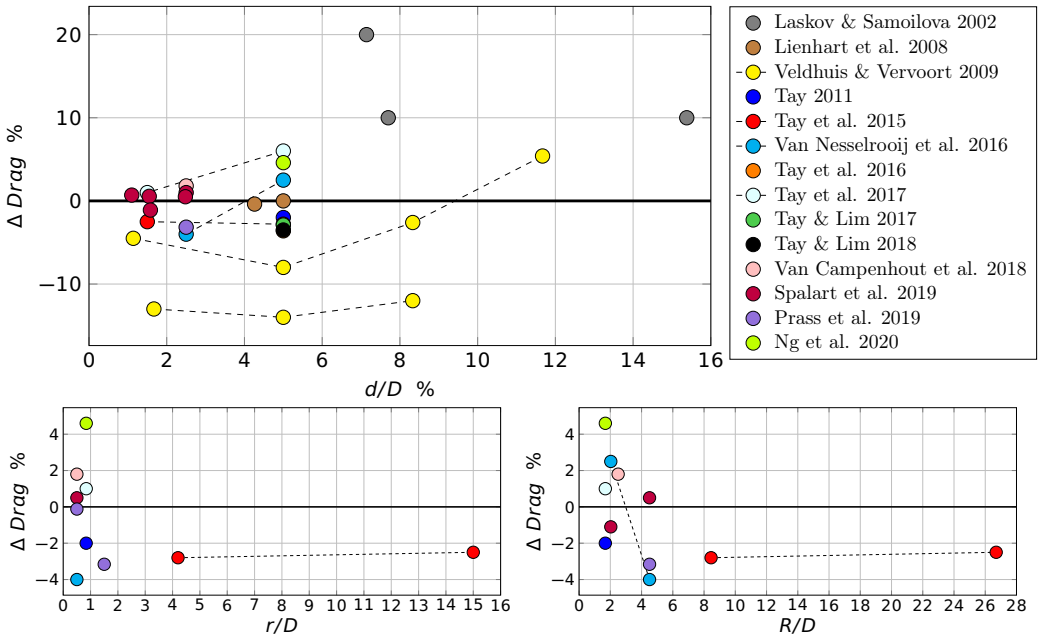

Figure 7.4: Drag change obtained with circular dimples versus depth (top), edge curvature radius (bottom left) and radius of the spherical cap (bottom right). Dashed lines connect points for which only the parameter on the abscissa is changed.

Vervoort (2009) measured a slight increase of drag reduction performance with increasing d/D. The latter study was extended up to $d/D = 0.12$, finding that for $d/D > 0.05$ the overall drag increases with d/D.

The curvature radius r at the edge of the dimple is meant to mitigate the negative effects of pressure drag, by preventing or decreasing flow separation. The second panel of figure 7.4 shows that also in this case data are highly scattered: for $0.5 \lessapprox r/D \lessapprox 1.5$ the achieved drag change ranges between -4% (Van Nesselrooij *et al.*, 2016) and 4.8% (Ng *et al.*, 2020). The experiments of Tay *et al.* (2015) at $Re_b \approx 32100$ show that after a certain value, i.e. $r/D > 4$, the influence of the edge curvature on the drag change is minimal. Spalart *et al.* (2019) performed a DNS of a turbulent boundary layer, with a Reynolds number (based on the boundary layer thickness) of $Re_\delta = 7.5 \times 10^3$ and $Re_\delta = 3 \times 10^4$ and considered $r/D = 0.5$. Their data points are not plotted in figure 7.4, since their paper does not contain enough information to quantify r. However, they confirmed that smoothing the dimple rim is beneficial.

A scattered picture is also obtained when data are plotted against the R/D ratio, as shown in the third panel of fig.7.4, confirming again that for this configuration a single geometrical parameter is unable to fully characterize the influence of the dimples on the flow.

The experiments of Tay & Lim (2017) and the numerical simulations of Ng *et al.* (2018, 2020) agree on the indication that the downstream shift s is beneficial, for a wide range of Reynolds numbers, with the best effect observed when $s = 0.1D$ in the downstream direction. When instead the shift is in the upstream direction, i.e. $s < 0$, drag increases rapidly. It should be mentioned that the Reynolds number of the simulations ($Re_b = 2800$) is somewhat lower than the lowest Reynolds number of the experiments ($Re_b \approx 4300$). Tay & Lim (2017) claim that a $0.2D$ downstream shift is equivalent to the axisymmetric case at $Re_b = 7000$ with a drag increase of 1.5%, because the lower drag obtained by the reduced flow separation at the shallower upstream wall is compensated by the higher drag of the flow impinging on the steeper downstream wall. Ng *et al.* (2018, 2020), who can take advantage of DNS to break down the total drag into friction and pressure contributions, find that friction drag is almost unaffected by a downstream shift, since it does not affect the reattachment point.

When it comes to alternative shapes, triangular dimples were considered by Tay *et al.* (2016). In their experiment they machined dimples with the bottom surface sloping up from the deepest point at the triangular vertex towards the base of the triangular depression to meet the flat channel surface, hence producing the negative of a wedge. A larger drag was obtained for both upstream- and downstream-pointing triangles, for the whole range of tested Reynolds numbers, i.e. $5180 \leq Re_b \leq 28600$. Moreover, for the downstream-pointing triangle the drag increase is nearly constant with Re, whereas for the upstream-pointing triangle

the drag increase grows with Re. Tay & Lim (2018) studied the teardrop dimple and measured drag reduction for both the upstream- and downstream-pointing teardrops, for $4500 \leq Re_b \leq 44000$, with the former yielding up to 6% drag reduction and the latter up to 5%. Tay *et al.* (2019) studied the diamond dimple and measured drag reduction up to 7.5%. More recently, Ng *et al.* (2020) compared in a numerical study the circular, elliptical, teardrop and diamond dimples in a turbulent channel flow, reporting drag reduction of 4.9% for the elliptical dimple, 3.1% for the upstream-pointing teardrop, and 7.4% for the diamond dimple.

7.3.2 The arrangement of the dimples

When it comes to the spatial arrangement of dimples on the surface, once the other parameters are fixed, the staggered configuration leads to lower drag compared to the flow-aligned one (Veldhuis & Vervoort, 2009; Van Nesselrooij *et al.*, 2016; Van Campenhout *et al.*, 2018; Spalart *et al.*, 2019), a fact that explains why the staggered configuration is the most adopted one. Van Nesselrooij *et al.* (2016) found 3% of drag increase for flow-aligned dimples and up to 4% drag reduction for staggered dimples with the same geometrical parameters, coverage and Reynolds number. Spalart *et al.* (2019) found drag increase for both configurations, but the drag increase of the flow-aligned dimples was almost twice that of the staggered dimples.

Lashkov & Samoilova (2002) and Van Campenhout *et al.* (2018) considered the drag change also for other, non-standard arrangements. The former study found a large drag increase (up to 50%) when an hexagonal dimple layout is used. The latter study showed a constant drag increase of about 1% for each of the several considered layouts.

The effect of coverage ratio was considered by Tay (2011) and Tay *et al.* (2015), who compared in a channel flow circular dimples with 40% and 90% coverage, and found that higher coverage enhances the (positive or negative) effects of the dimples. Van Nesselrooij *et al.* (2016) experimentally studied the effect of coverage in a boundary layer. They found that a 90% coverage yields drag increase for a wide range of Re, whereas 33.3% coverage always yields drag reduction within the same Reynolds number range. Performance of both layouts are found to improve by increasing Re. Spalart *et al.* (2019) in their boundary layer DNS compared the two coverage ratios, and observed about 1% of drag reduction for the lower coverage, and 2% of drag increase for the higher one.

7.4 How do dimples work?

The uncertainties on the true effectiveness of dimples in reducing turbulent drag are accompanied, perhaps unsurprisingly, by a limited understanding of the physics involved. Thanks to the several experimental and numerical works carried out so far, some ideas and hypotheses exist, but consensus is lacking. We describe below two prevailing descriptions of how dimples interact with the overlying turbulent flow.

7.4.1 Self-organized secondary tornado-like jets

The first attempt at explaining drag reduction by dimples is due to Kiknadze *et al.* (2012), who based their explanations uniquely of video records and photographs, even though similar observations were already put forward in previous numerical (Veldhuis & Vervoort, 2009) and experimental (Kovalenko *et al.*, 2010) studies. According to Kiknadze *et al.* (2012), whose authors are affiliated with the Research and Production Centre "Tornado-Like Jet Technologies" in Moscow, the action of dimples can be explained by a so-called tornado-like jet self-organization. In plain words, this is how the flow organizes itself and develops over the double-curvature concavity of a dimple. The flow coming from an upstream flat portion accelerates at the leading edge of a circular dimple, and is lifted off from the surface while trying to follow the curved wall, leading to a reduction of skin-friction drag in the fore half of the dimple. After the streamwise midpoint, the flow converges towards the midline to eventually meet the flat wall past the trailing edge, and the skin friction increases again. Although the skin friction reduction in the fore half might outweigh the increase of the aft half, the recessed geometry of the dimple introduces an additional pressure drag component: hence, to achieve drag reduction the net reduction of the skin-friction drag needs to be larger than the increase of pressure drag. It should be observed, though, that this description is not directly addressing the insurgence of drag reduction, but only constitutes an attempt to draft a simplified description of the local flow modifications induced by the dimple.

If dimples are deep enough, their steep walls make the flow prone to separation on the upstream part of the recess, with creation of spanwise vorticity and recirculation. The flow reversal has a positive effect on the drag, causing negative skin friction in the first portion of the dimple. When the flow reattaches, a strong impingement of the flow on the rear slope of the dimple produces a locally high skin friction. Moreover, flow separation obviously causes a large increase of pressure drag which could cancel out the positive effect of the skin friction drag. To avoid separation and the consequent increase of pressure drag, more efficient

shapes than the classical circular one are used. Shifting downstream the point of maximum depth of the dimple alters the wall slopes, and affects the total drag by changing pressure drag, whereas the friction drag tends to remain unchanged (Ng *et al.*, 2020). A (moderate) downstream shift minimizes the negative effects of separation, and offers lower drag than the standard circular geometry. However, the shift does not significantly affect the location of the reattachment point, except for very large shifts, for which flow reversal may be entirely suppressed, but at the cost of an intense impingement onto the steeper rear wall which negatively affects the drag.

Non-circular dimples induce different drag changes (Ng *et al.*, 2020). Flow separation and flow reversal are not observed for elliptical, upstream-pointing and diamond dimples, leading to a lesser drag compared to the smooth wall. This can be attributed to the gentler upstream slope and to the longer, more streamwise-aligned leading edge. Other studies which do not report flow reversal even for the circular shape are Van Nesselrooij *et al.* (2016) and Spalart *et al.* (2019); they measure a maximum drag reduction of 4% and 1.1%, respectively. Tay *et al.* (2017) observe flow separation for circular dimples in the whole range of tested flow conditions for $d/D = 0.05$, but not for $d/D = 0.015$; however, they measure drag increase in all the tested cases.

7.4.2 Spanwise forcing

A more recent conjecture on the mechanisms by which dimples attain drag reduction has been put forward independently by the two groups at TU Delft (Van Nesselrooij *et al.*, 2016) and NUS (Tay *et al.*, 2015). Flow visualisations indicate that, near the wall, streamlines coming in straight from a flat surface bend towards the dimple centerline in the upstream portion of the recess, then bend away from it in the downstream portion, thus creating a converging-diverging pattern (see for example Tay *et al.* (2014)). Such meandering implies a spanwise velocity distribution with changing sign across the dimple length (Van Nesselrooij *et al.*, 2016; Van Campenhout *et al.*, 2018), and a consequent alternating streamwise vorticity (Tay *et al.*, 2017) since the spanwise velocity remains confined very near to the wall. Van Nesselrooij *et al.* (2016) reports an average spanwise velocity of about 2–3% of the free-stream velocity for a boundary layer; Tay *et al.* (2017) measured a maximum spanwise velocity in the range 3.5–8% of the centerline velocity in the channel. Spalart *et al.* (2019) also detected in their DNS study a spanwise motion, although weaker in intensity.

Figure 7.5 depicts an instantaneous spanwise velocity field over a circular dimple, taken from one of our DNS simulations of a turbulent channel flow over circular dimples (see Appendix 7.A for computational and discretization details of our simulations). An alternating spanwise velocity pattern is clearly visible,

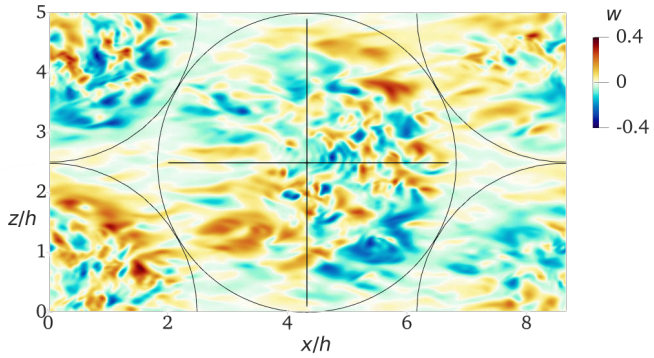

Figure 7.5: Instantaneous spanwise velocity component w on a wall-parallel plane at $y^+ = 1.3$ from the flat part of the wall. Lengths and velocities are made dimensionless with h and U_b. The velocity field is computed by DNS for a circular dimple, which actually yields drag increase.

supporting the idea that the dimple creates a velocity component in the spanwise direction and bends the streamlines in a converging-diverging behaviour. The instantaneous values are very large, up to 40% of the bulk velocity.

The alternate spanwise velocity resembles the spanwise-oscillating wall (Jung *et al.*, 1992), an active technique for the reduction of turbulent friction drag, where the wall oscillates in time in the spanwise direction. In the oscillating-wall control, the spanwise velocity component at the wall w_w is prescribed as a function of time as:

$$w_w(t) = A \sin\left(\frac{2\pi}{T}t\right), \tag{7.2}$$

where A is the amplitude of the oscillation and T is its period. The oscillating wall produces very large reductions of friction drag, although at a significant energy cost. Its detailed performance is determined by the control parameters A and T; Quadrio & Ricco (2004), after a careful DNS study, identified the link between the value of parameters and the obtained drag reduction. They found an optimum value for the oscillating period of $T^+ \approx 100$, whereas drag reduction monotonically improves with the amplitude (albeit the energy cost of the control rises faster as A^2). Dimples could be considered as a passive implementation of the spanwise-oscillating wall. Van Campenhout *et al.* (2018) measured the analogous parameters and defined a period T and a maximum spanwise velocity w_{max} of a fluid particle, averaging over a selected region of the domain. In the oscillating wall, it is known (Quadrio & Sibilla, 2000) that the time-averaged mean spanwise velocity profile coincides with the laminar solution of the Stokes second problem. Van Campenhout *et al.* (2018) assumes the same to hold for the flow over dimples, thus deriving an analogous value for the amplitude. For their

dimples with $d/D = 0.025$, they found $T^+ = 135$ and $A^+ = 0.74$. Data from Quadrio & Ricco (2004) do not contain information for such small amplitudes, but an extrapolation leads to a drag reduction of about 4% for this combination of parameters: a value that closely resembles the measurement of 3.8% from Van Nesselrooij *et al.* (2016).

It should be noted, first, that a closer analogy should be made between this interpretation of the dimples working mechanism and the spatially modulated spanwise forcing introduced by Viotti *et al.* (2009). However, in that paper it is shown how temporal and spatial oscillations can be easily converted one into the other by using a suitable convective velocity scale at the wall. There are, of course, obvious differences between data collected by Quadrio & Ricco for a turbulent channel flow at $Re_\tau = 200$ or $Re_b = 3173$ and the dimple experiments described in refs.Van Nesselrooij *et al.* (2016) and Van Campenhout *et al.* (2018) for a boundary layer at $Re_\delta = 1226$ (the limited information provided in these references precludes computing the value of the friction Reynolds number).

Other important concepts to be aware of when trying to draw such a parallel is that, with the oscillating wall, a minimum spanwise velocity is required for the active technique to produce its effects: this threshold value A^+_{th}, that needs to be of the order of the natural fluctuations of spanwise velocity in the near-wall region, is quantified in Quadrio & Ricco (2004) as $A^+_{th} = 1$, i.e. similar or larger than the dimples-induced spanwise velocity as determined in Van Campenhout *et al.* (2018). Finally, and definitely most important, with a flat wall, even in presence of spanwise forcing, one should be only concerned with friction drag, whereas with dimples both viscous and pressure drag come into play.

7.5 How to set up a proper comparison?

Measuring (small) changes in aerodynamic drag is not trivial, especially in the turbulent regime, regardless of the numerical or experimental nature of the analysis. Studies employ a variety of approaches, where simulations and experiments presents different approaches and different challenges.

Nowadays, whenever we need to compare the drag of a reference flat surface with that of a rough surface, we are aware of the subtlety of the measurement, of the importance to carefully define and control the Reynolds number of the experiment, to discriminate between internal and external flows, and in general to correctly define the equivalent "flat wall" flow to compare with. In this final Section, we will discuss some of these topics, trying to call the reader's attention to the logical steps that should be followed when designing a meaningful experimental or numerical campaign.

7.5.1 Measurement of the drag (difference)

All the available studies measure the drag difference $\Delta Drag$ by separately measuring the drag forces $Drag_{smooth}$ and $Drag_{dimples}$. As recently discussed in Van Nesselrooij *et al.* (2022) in the context of the description of their novel experimental setup devoted to such measurements, various approaches are available. The simplest among them measure the local friction, and as such are unable to yield satisfactory results for the drag, because the friction contribution to the drag force over a dimpled surface depends on the position, and the same holds for the pressure component. Hence, in an experiment one has to either resort to measuring the drag force with a balance, a challenge by itself owing to the small forces involved, or to deduce the force from the pressure drop across two sections, as done for example by Gatti *et al.* (2015). With dimples, both approaches have been used. Information about the shear stress was extracted from boundary layer momentum loss in Lienhart *et al.* (2008). Direct measurement of the drag through a force sensor was employed in Veldhuis & Vervoort (2009); Van Nesselrooij *et al.* (2016) and Van Campenhout *et al.* (2018). This type of measurement may be affected by uncertainty and accuracy problems: forces are small, and blurred by spurious contributions, and the experimental setup must be designed and run with extreme care.

In the case of numerical experiments, only the DNS approach provides the required accuracy that is not embedded e.g. in RANS models, constructed and tuned for canonical flows and hence incapable to deal with drag reduction in a quantitatively accurate way. Once DNS is used, two equivalent options are available to compute the drag in internal flows. One possibility is the calculation of the (time-averaged value of) the friction drag and the pressure drag separately, employing their definition as surface integrals of the relevant force component. In alternative, the (time-averaged value of) the pressure drop between inlet and outlet informs of the total dissipated power, and thus leads to the total drag. This is feasible both in simulations and experiments. Tay (2011), Tay *et al.* (2015), Tay *et al.* (2016), Tay *et al.* (2017), Tay & Lim (2017) and Tay & Lim (2018) in fact compared the mean streamwise pressure gradients of both the two flat sections upstream and downstream of the dimpled test section with the mean streamwise pressure gradient within the test section, employing static pressure taps.

Experience accumulated in riblets research, however, tells us that the riblets community obtained its first fully reliable dataset when D.Bechert in Berlin developed on purpose a test rig, the Berlin oil channel (Bechert *et al.*, 1992), where the measured quantity was directly the drag difference: targeting the quantity of interest, i.e. the drag difference under identical flow conditions, instead of relying on the difference between two separately measured drag forces was key to improve accuracy and reliability.

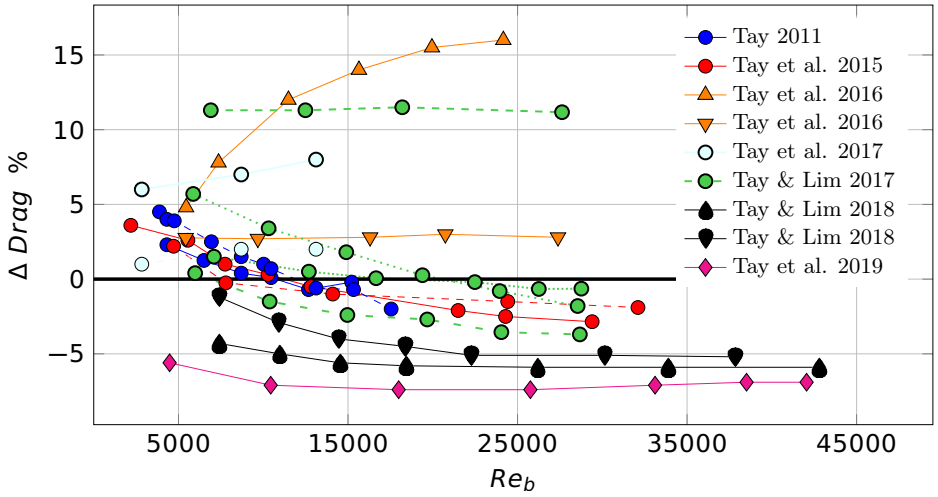

Figure 7.6: Drag change versus bulk Reynolds number Re_b.

7.5.2 The Reynolds number

Dynamic similarity is a well known concept in fluid mechanics, and enables meaningful comparative tests provided the value of the Reynolds number is the same. The true question is to understand *which* Reynolds number should be kept the same. The Reynolds number is defined as the product of a velocity scale U and a length scale L, divided by the kinematic viscosity ν of the fluid. While e.g. in an experiment the precise measurement of ν might be difficult, its meaning is unequivocal. Choosing U and L, instead, presents more than one option.

For the velocity scale U, dimples do not lead to specific issues. While for a zero-pressure-gradient boundary layer over a flat plate the use of the external velocity U_∞ sounds reasonable, for internal flows like the plane channel flow one has to choose among the bulk velocity U_b, the centerline velocity U_c and the friction velocity u_τ. The choice of reference velocity has been already discussed in the context of skin-friction drag reduction (Hasegawa *et al.*, 2014): provided drag reduction is not too large, and the flow is far enough from laminarity, choosing U is not critical and should not be regarded as a major obstacle.

For the length scale L, instead, the situation is different, as dimples themselves contain one or more length scales that could be used in the definition of Re. For example, to avoid the ambiguity implied by the definition of the origin for the wall-normal coordinate, Van Nesselrooij *et al.* (2016) and Van Campenhout *et al.* (2018) for their boundary layer experiments decided to define a Reynolds number based on the diameter of their circular dimple. Naturally, achieving the same Re based on flow velocity and dimple diameter is not enough to guarantee dynamic similarity in two different flows.

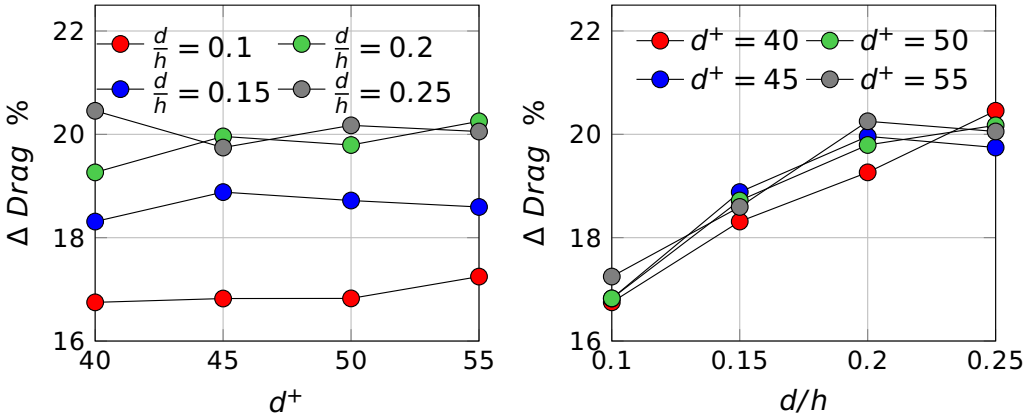

Figure 7.7: Present simulations, circular dimples at various sizes and Reynolds numbers with $2690 \leq Re_b \leq 10450$. Left: drag changes vs dimple depth in inner units. Right: drag changes vs dimple depth in outer units.

By isolating all the data sets for which a value for the bulk Reynolds number Re_b is given (either explicitly or deduced from equivalent information), and putting together the reported drag changes, one obtains the picture reported in figure 7.6. Besides showing both drag reduction and drag increase, drag changes exhibit every possible trend with Re_b: increasing, decreasing, constant or nearly constant, and non-monotonic with either a maximum or a minimum at intermediate Re_b. Without excluding additional possible causes, this can be attributed to the host of parameters that are not kept identical across the dataset, besides the Reynolds number, and stresses once more the importance of experiments where only one parameter is changed at a time.

In a turbulent wall flow, the Reynolds number is an essential ingredient to define the proper scaling of important quantities, say the total drag change. If for example only the dimple depth d is varied, its value can be set in wall units (d^+) or in outer units (d/h), and, if the Reynolds number is also changed, various combinations for d^+ and d/h become possible. It is the flow physics which dictates what scaling works best at collapsing results. We have performed two sets of DNS simulations (see §7.A for details) to understand the scaling of drag changes induced by circular dimples when only their dimensions are changed but its shape is preserved. We have fixed the values of d/D and r/R, the value of the depth d (either in inner d/h or outer d^+ units) has been varied, and all the other parameters did vary accordingly, as prescribed by equation (7.1).

Figure 7.7 plots the results and shows that drag changes (in this specific case, drag increases) appear to follow an outer scaling: all the data points collapse onto a single curve when drag changes are plotted against d/h. This is an expected result, as these dimples are rather deep, and thus somehow akin to a large-scale d-

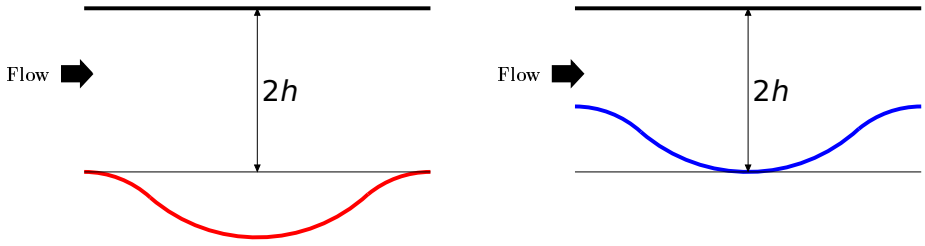

Figure 7.8: A dimpled wall and two different, equivalent flat channels. The red/blue lines indicate the dimple profile. Left: the channel height $2h$ goes from the top wall to the dimple tip; right: the channel height $2h$ goes from the top wall to the dimple lowest point.

roughness (Jiménez, 2004), where the large cavities basically destroy the near-wall layer, i.e the only region where inner scaling would make sense.

7.5.3 The equivalent flat wall

The comparison between flat and dimpled wall can be set up for internal or external flows. The latter, which may be less convenient in numerical simulations owing to their non-parallel nature, present a sensible advantage in this context, since drag and its related changes have simply to be computed for the same plate immersed in the same external velocity, and a reduced drag force is unequivocally advantageous. For internal flows, however, the non-planar dimpled wall brings up the problem of properly defining the location of the equivalent flat wall and, in general, of setting up the comparison properly.

As shown schematically in fig.7.8, for a channel flow, for example, a certain definition of the reference flat wall impacts the reference length h and, eventually, changes the value of the Reynolds number of the flow to compare with. The reference wall might be placed on the flat surface among dimples, on the position of lowest elevation in the cavity, on the average height of the dimpled surface, etc., leading to different flow volumes.

To properly account for this effect, let us start from the usual definition of the bulk Reynolds number $Re_b = U_b h/\nu$, where h is a reference length (e.g. half the witdh of the flat channel) and ν is the kinematic viscosity. Once the cross-sectional area $A(x)$ of the dimpled channel changes along the streamwise direction, the bulk velocity U_b, defined as an average velocity across the section, becomes itself a

streamwise-dependent function:

$$U_b(x) = \frac{1}{A(x)} \int_{A(x)} u(\mathbf{x}) \mathrm{d}A. \tag{7.3}$$

We thus replace this definition with a volume average, and define a new bulk velocity $\mathsf{U_b}$ as an average over the volume to obtain a streamwise-independent quantity:

$$\mathsf{U_b} = \frac{1}{V} \int_V u(\mathbf{x}) \mathrm{d}V. \tag{7.4}$$

Note that the two quantities U_b and $\mathsf{U_b}$ coincide for a flat wall. A comparison at same flow rate requires that the volumetric flow rate

$$Q = \int_{A(x)} u(\mathbf{x}) \mathrm{d}A = \frac{1}{L_x} \int_0^{L_x} \int_{A(x)} u(\mathbf{x}) \mathrm{d}A \mathrm{d}x = \frac{1}{L_x} \int_V u(\mathbf{x}) dV = \frac{V}{L_x} \mathsf{U_b} \tag{7.5}$$

is the same for the flat and dimpled channels, provided the streamwise length L_x of the channel is the same. This implies that $V_f \mathsf{U_{b,f}} = V_d \mathsf{U_{b,d}}$, where the subscripts $\cdot_f$ and $\cdot_d$ refer to quantities measured in the flat and dimpled channel respectively. In the end, the bulk velocity in the dimpled channel (and the bulk Reynolds number) need to be changed by multiplication of a factor given by the volume ratio:

$$\mathsf{U_{b,d}} = \frac{V_f}{V_d} \mathsf{U_{b,f}}; \qquad Re_{b,d} = \frac{V_f}{V_d} Re_{b,f}. \tag{7.6}$$

The numerical value of Re_b is thus affected by the choice of the equivalent flat channel. For example, the equivalent flat channel might go from the top wall to the lowest point of the dimple, and $Re_{b,d} > Re_{b,f}$. In contrast, if the equivalent channel goes from the top wall to the tip of the dimple, $Re_{b,d} < Re_{b,f}$. The two bulk Reynolds numbers end up being the same only when the volume is preserved in the reference and dimpled channels (i.e. the equivalent flat channel is located at the average dimple height).

If the comparison is carried out by DNS, one conveniently measures the time-averaged value $\overline{f}$ of the spatially uniform volume force f required to maintain a constant flow rate at each time step. This volume force is interpreted as $f = \Delta P / L_x$, where ΔP is the pressure drop along the channel. The proper measure of the drag change is:

$$\Delta Drag = \frac{V_d \overline{f_d} - V_f \overline{f_f}}{V_f \overline{f_f}} = \frac{V_d / V_f \overline{f_d} - \overline{f_f}}{\overline{f_f}}; \tag{7.7}$$

Therefore, the change of the fluid volume has to been considered also when measuring the drag change in the controlled case.

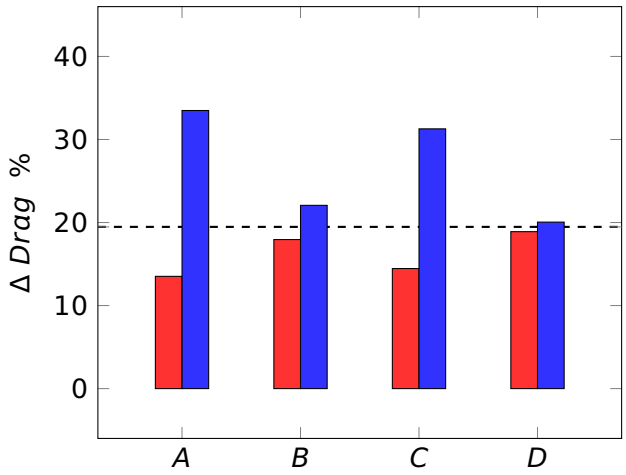

Figure 7.9: Drag changes, measured by DNS, for circular dimples with $d/h = 0.25$ at $Re_b \approx 2800$. Red/blue bars express drag changes when the equivalent channel defines $2h$ as the distance between the top wall and the top/bottom of the dimple (color code is the same of figure 7.8). Case A: comparison at the same Re_b, $\Delta Drag$ computed without accounting for the volume ratio. Case B: as case A, but $\Delta Drag$ is corrected with the volume ratio. Cases C and D are like cases A and B, but the comparison is made at the same flow rate.

Figure 7.9 exemplifies the consequences of neglecting these considerations. These are certainly exaggerated by the choice of working with a dimple configuration that causes a large change of drag. However, the relative differences are major; neglecting such considerations would most certainly hinder the true ability of dimples to alter skin-friction drag.

7.5.4 The drag reduction metrics

In closing, we mention a final methodological issue, that affects drag reduction measurements for dimples, riblets, and roughness at large: the proper metrics to express it. It is customary to express drag reduction as (percentage) changes in the skin-friction coefficient at a given Re; unfortunately, the coefficient itself contains a dependence on the Reynolds number already for the flat wall case, thus making it impossible to rely on percentage changes for a robust assessment of the drag change properties of a given surface. The complete information would be the $(\Delta Drag, Re)$ pair. In alternative, the proper metric for expressing drag reduction is the vertical shift of the logarithmic portion of the mean streamwise velocity profile expressed in viscous units.

This is a known concept for roughness (Jiménez, 2004) as well as riblets (Luchini, 1996; Spalart & McLean, 2011), and also extends to some active flow control strategies (Gatti & Quadrio, 2016). As long as the direct effect of the roughness remains confined within the buffer layer of the turbulent flow, it can be translated into an upward shift ΔU^+ of the logarithmic velocity profile in the law of the wall: a positive ΔU^+ corresponds to drag reduction, and a negative ΔU^+ implies drag increase, as for the conventional k-type roughness. Part of the trends seen in figure 7.6 for drag reduction data are due to Reynolds effects; properly removing them via analytical relations is possible, as done in Gatti & Quadrio (2016) for active spanwise forcing, and would contribute to clarifying the situation, by exposing some remaining "puzzling" trends with Re (to cite words used in Spalart *et al.* (2019)).

7.6 Conclusions

In this review paper we have provided a brief and up-to-date description of what we know and what we don't about the potential of dimples for turbulent skin-friction drag reduction. While we can't obviously offer an answer to the still-standing question whether or not dimples are a suitable technique to reduce turbulent skin-friction drag, it is our hope that this comprehensive overview will at least help the newcomer to frame the problem, quickly identify the key references, and get a glimpse at the complexity of the topic.

While reviewing the state of the art, we have also mentioned some methodological issues that bear a critical importance when attempting to measure drag changes by dimples. Leveraging concepts and procedures (and perhaps facilities altogether) developed over the years for riblets might yield data that are reliable enough to begin understanding the physics behind dimple drag reduction, a necessary and preliminary step to improve their performance.

7.A Computational details

In this review we have also presented results from DNS simulations carried out on purpose for the present work. They concern a turbulent plane channel flow, with dimples placed on one wall only. The employed parallel DNS code was introduced by (Luchini, 2016), and solves the incompressible Navier–Stokes equations in primitive variables on a staggered Cartesian grid. Space discretization is based on second-order finite differences, and temporal integration uses a fractional time stepping method based on a third-order Runge–Kutta scheme. The Poisson equation for the pressure is solved by an iterative successive over-relaxation algorithm. An implicit immersed-boundary method, implemented in staggered variables, continuous with respect to boundary crossing and numerically stable at all distances from the boundary (Luchini, 2013, 2016), describes the geometry of the non-planar wall. Periodic boundary conditions are enforced in both the streamwise and spanwise directions, while no slip and no penetration boundary conditions are enforced at the walls.

The size of the computational domain (and therefore the number of dimples considered) is chosen to ensure that it is always larger than the minimal flow units needed to sustain the near-wall turbulence cycle (Jiménez & Moin, 1991). The smallest domain in our simulations has size $L_x = 4\sqrt{3}h$ and $L_z = 4h$ in external units and $L_x^+ = 1385$ and $L_z^+ = 800$ in viscous units. A uniform distribution of points is used in both the streamwise and spanwise directions, with the selected grid spacing ensuring that $\delta x^+ \lessapprox 10$ and $\delta z^+ \lessapprox 5$ for all the considered cases. In the wall-normal direction a non-uniform distribution is used to properly resolve the dimples and the near wall region. The grid spacing is indeed constant from the dimple bottom to the dimple tip, from where a hyperbolic tangent distribution is used. The number of points in the wall-normal direction is chosen to ensure that at the walls $\delta y^+ < 1$ for all cases. The number of points for the simulations in figure 7.9, carried out at about $Re_b = 2800$ (or $Re_\tau = 180$) is $N_x = 260$, $N_y = 260$ and $N_z = 260$. For the simulations in figure 7.7, instead, the number of points increases up to $N_x = 300$, $N_y = 334$ and $N_z = 300$ to deal with the higher Reynolds numbers, since in this dataset the Reynolds number varies, in the range $2690 \leq Re_b \leq 10450$ (or $160 \leq Re_\tau \leq 550$).

Drag Reduction by Riblets on a Commercial UAV

The content of this Paper has been published in
Cacciatori, L., Brignoli, C., Mele, B., Gattere, F.,
Monti, C.M. & Quadrio, M. 2022
Drag Reduction by Riblets on a Commercial UAV.
Applied Science **12** (10), 5070.
Minor editing has been done for formatting purposes.

Drag Reduction by Riblets on a Commercial UAV

Abstract

Riblets are micro-grooves capable of decreasing skin-friction drag, but recent work suggests that additional benefits are possible for other components of the aerodynamic drag. The effect of riblets on a fixed-wing, low-speed Unmanned Aerial Vehicle (UAV) on the total aerodynamic drag are assessed here for the first time by means of RANS simulations. Since the microscopic scale of riblets precludes their direct representation in the geometric model of the UAV, we model riblets via a homogenized boundary condition applied on the smooth wall. The boundary condition consists in a suitably tuned partial slip, which assumes riblets to be locally aligned with the flow velocity, and to possess optimal size. Several configurations of riblets coverage are considered to extract the potential for drag reduction of different parts of the aircraft surface. Installing riblets with optimal size over the complete surface of the UAV leads to a reduction of 3% for the drag coefficient of the aircraft. Besides friction reduction, analysis shows a significant additional form drag reduction localized on the wing. By installing riblets only on the upper surface of the wing, total drag reduction remains at 1.7%, with a surface coverage that is only 29%, thus yielding a significant improvement in the cost-benefit ratio.

8.1 Introduction

The growing concern over energy efficiency and environmental pollution is furthering the appeal of transport vehicles, aircraft in particular, producing less aerodynamic drag. One of the most interesting passive drag reduction techniques is the use of riblets, i.e. streamwise-aligned micro-grooves that are known to reduce

turbulent skin-friction drag (see for example the review paper of García-Mayoral & Jiménez (2011) and the many references therein), and are approaching usability in aeronautics.

Early studies, spurred by the oil crisis of the '70, were performed at NASA (Walsh & Weinstein, 1979), and important experiments were carried out in the Berlin oil tunnel by Bechert and coworkers (Bechert *et al.*, 1997; Bechert & Bartenwerfer, 1989). They evidenced the crucial importance of the riblet shape, their size and – most importantly – the sharpness of their tip; optimal configurations empirically determined at the time yield up to 6-8% and possibly higher reductions of skin-friction for low-Re flat plate boundary layers studied in laboratory conditions. The theoretical understanding of the riblets working mechanism is due to Luchini *et al.* (1991), who quantified the different resistance offered by a grooved wall to the parallel flow and the cross-flow. He also explained (Luchini, 1996) how skin-friction drag reduction is equivalent to an upward shift of the logarithmic portion of the turbulent velocity profile. This important argument, later taken up again by Spalart & McLean (2011), implies that it is incorrect to describe riblets performance simply as a percentage change of the skin-friction coefficient, as this simplistic figure depends on the Reynolds number of the flow. However, the value of the upward shift, once measured in viscous units, is Reynolds-independent and should be used to characterize the ability of riblets (and other techniques) to reduce turbulent friction; in fact, recently this concept has been extended (Gatti & Quadrio, 2016) to other strategies of skin-friction reduction.

To capture in a numerical simulation the complex physics of the interaction between turbulence and a solid wall covered by riblets, and to properly measure friction reduction, direct numerical simulations (DNS) or wall-resolved large eddy simulations (LES) are required. Such computations are unfeasible for complex aeronautical configurations at high Reynolds numbers, where numerical simulations based on the Reynolds-Averaged Navier–Stokes equations (RANS) equipped with a turbulence model are the standard approach. Owing to their microscopic dimensions, however, riblets on an aircraft cannot be included directly in a RANS simulation. Even if they could, it is unclear to what extent a standard RANS model would be able to represent the physics of drag reduction.

Bridging the gap between drag reduction by riblets in turbulent flows and the need to incorporate it into RANS-type flow solvers has led to the development of computational models for riblets. Aupoix *et al.* (2012) modified the Spalart–Allmaras turbulence model to account for riblets by using a smooth-wall geometry. Along similar lines, Mele *et al.* (2016) introduced a modified boundary condition for the $k - \omega$ turbulence model, and Koepplin *et al.* (2017) extended the Aupoix model to describe riblets locally misaligned with the mean flow, and to account for mean pressure gradients.

How riblets affect a turbulent boundary layer with non-zero pressure gradient

is a debated subject (Nieuwstadt *et al.*, 1993; Debisschop & Nieuwstadt, 1996; Boomsma & Sotiropoulos, 2015). In 2018, Mele & Tognaccini (2018) developed a new model based on a slip-length concept, whose results provided an interesting view on the riblets drag reduction mechanism in presence of pressure gradients. Besides friction reduction, they found that riblets alter the pressure distribution, and may provide an additional pressure drag reduction. This indirect effect was also observed for other friction reduction devices: Banchetti *et al.* (2020) used spanwise forcing to reduce turbulent friction on a wall with a bump, and found in their incompressible DNS study that a reduced friction drag is accompanied by a reduced pressure drag. Similarly, Quadrio *et al.* (2022) studied by DNS the compressible flow over a wing, and observed how spanwise forcing affects the shock wave to yield large reduction of the total drag of the aircraft. The availability of a boundary condition to faithfully simulate in a RANS the presence of riblets on the surface of a solid body of complex shape is thus becoming extremely attractive.

The standard no-slip condition at a solid wall can be extended to a partial-slip one, which is useful to describe specific physical situations (e.g. flow over superhydrophobic surfaces). Riblets are amenable to such a description; their slip length is related to the protrusion height concept (Bechert *et al.*, 1997; Bechert & Bartenwerfer, 1989; Luchini *et al.*, 1991). In particular, Luchini *et al.* (1991) defined the longitudinal and transverse protrusion heights, which identify the virtual origin for the streamwise and spanwise velocity profiles, and realized that the only meaningful non-arbitrary quantity is their difference. Later, he also introduced (Luchini, 2013) a linearized boundary condition for generic roughness and the protrusion heights for various roughness types to be adopted in DNS. He also demonstrated that the difference Δh between the two riblets protrusion heights corresponds to the slip length λ. Gómez-de-Segura *et al.* (2018) later discussed how the slip length λ^+ expressed in viscous units is equivalent to the upward displacement ΔU^+ of the mean velocity profile in the logarithmic region; here $\lambda^+ = \lambda u_\tau / \nu$ where ν is the kinematic viscosity, $u_\tau = \sqrt{\tau_w / \rho}$ is the friction velocity, ρ is the density and τ_w is the (local) shear stress.

The value of the slip length λ depends upon shape and size of the riblets cross-section. Bechert & Bartenwerfer (1989) found that the largest drag reduction for riblets of different shapes is obtained when s^+, the spanwise period of the riblets, is in the range 10–20. García-Mayoral & Jiménez (2011) tested alternative scalings to find whether drag reduction can be linked to a single geometric parameter that captures the importance of riblet spacing and their cross-sectional shape as well. Data for different riblets were found to best collapse when plotted against a dimensionless length scale l_g^+ derived from the cross-sectional area A_g of the groove, and defined as $l_g^+ = (A_g^+)^{1/2}$. For riblets of various geometries, best performance was consistently found at $l_g^+ \approx 10.5$. For optimal triangular riblets,

$l_g^+ = 10.5$ corresponds to a unitary shift ΔU^+ which coincides with the one reported in previous studies (Walsh, 1980; Mele & Tognaccini, 2018; Mele *et al.*, 2020). Recently, Zhang *et al.* (2020) have been able to compute the slip length for other riblets shapes, i.e. with trapezoidal and blade cross-section.

The goal of this paper is to present the implementation of a slip-length boundary condition for riblets, and to use it in a set of RANS simulations to assess the drag reduction capabilities of riblets when installed on a fixed-wing UAV, for which endurance is of capital importance. Indeed, over the years riblets have been studied either at low speed over plane walls, or in transonic flow conditions for aeronautical applications, especially for medium- or long-range commercial passenger aircraft. Such studies, carried out both numerically (Mele *et al.*, 2016; Catalano *et al.*, 2020) and experimentally (Walsh *et al.*, 1989; McLean *et al.*, 1987; Szodruch, 1991; Kurita *et al.*, 2018, 2020), provide interesting results for aircraft operating in a range of chord-based Reynolds numbers up to $Re_\infty = 3 \times 10^7$. In contrast, the low-speed aircraft considered in the present work has a cruise speed of 22 m/s with $Re_\infty = 5 \times 10^5$.

The paper describes the implementation into an incompressible CFD solver of a slip-length wall boundary condition, similar to that described in Mele *et al.* (2020), to compute the drag reduction achievable with riblets of optimal dimensions. The computational model is validated against configurations of increasing complexity, and eventually applied to a realistic use case. We also consider selective deployment of riblets to different parts of the aircraft, to show that drag reduction is not trivially proportional to the surface area covered by riblets. The structure of the work is as follows. After this introduction, §8.2 describes our model and the computational setup; §8.3 contains results of preliminary simulations intended for validation; the actual results are described in §8.4, and §8.5 contains a concluding discussion.

8.2 Methods

8.2.1 Slip length boundary condition

Both theory and experiments (Bechert & Bartenwerfer, 1989; Luchini *et al.*, 1991; Bechert *et al.*, 1997) suggest that the physics involved in drag reduction by riblets acts through a local mechanism. Indeed, since riblets are small compared to the turbulent structures of the near-wall cycle, far enough from the wall the turbulent flow perceives the presence of riblets only as a homogeneous effect: the upward shift $\Delta U^+ > 0$ of the logarithmic portion of the mean velocity profile:

$$U^+ = \frac{1}{\kappa} \log(y^+) + A + \Delta U^+ \tag{8.1}$$

where $\kappa = 0.392$ is the von Kármán constant, and $A = 4.48$ is the near wall intercept for smooth surfaces (these constants are set after Luchini (2017), but their numerical value does not affect the outcome of the study). The dimensionless vertical shift ΔU^+ equals the virtual shift in wall units of the non-slipping wall (Bechert & Bartenwerfer, 1989), i.e. the slip length λ^+. We exploit this shift to account for the presence of riblets via a slip boundary condition, which linearly relates the wall value of the longitudinal component of the velocity u_w (the subscript w indicates quantities evaluated at the wall) to the wall shear rate $(\partial u/\partial y)_w$ through the slip length λ:

$$u_w = \lambda \left(\frac{\partial u}{\partial y} \right)_w , \tag{8.2}$$

thus effectively recovering the no-slip condition when $\lambda = 0$. The discrete counterpart of equation (8.2), where the derivative is approximated with a finite difference, reads:

$$u_w = \lambda \frac{u_1 - u_w}{d}, \tag{8.3}$$

where u_1 is the longitudinal velocity at the first inner mesh point, and d is its distance from the wall. Hence, the velocity at the wall is:

$$u_w = u_1 \frac{\lambda}{\lambda + d}. \tag{8.4}$$

In this work, we always set the shift of the mean velocity profile at $\Delta U^+ = 1$, which corresponds (Walsh, 1980; Mele & Tognaccini, 2018; Mele *et al.*, 2020) to the best-performing riblets with triangular cross-section. These riblets have a square root of the cross-sectional area of $l_g^+ = 10.5$, and provide a drag reduction of 7% when measured in the lab under controlled conditions and at low Re. Using $\Delta U^+ = 1$ implies setting $\lambda^+ = 1$, whence the physical size of the riblets varies along the body with the friction velocity of the flow. In other words, riblets are assumed to be locally optimal everywhere, and the corresponding physical dimensions are computed as a result of the simulation.

It is worth noticing that the present boundary condition can be used to simulate, besides riblets, any other drag reduction method whose effect reduces to a shift in the mean velocity profile. To this purpose, only the slip length value must be adjusted.

8.2.2 Computational setup

The boundary condition described above has been implemented in OpenFOAM (Weller *et al.*, 1998), an open-source finite-volumes CFD library widely used in engineering and science, both in commercial and academic studies. Before considering the UAV, the boundary condition has been validated on flow cases of

increasing complexity where at least partial information is available for comparison: a flat plate and a NACA 0012 airfoil.

The selected flow solver is SimpleFOAM, which uses the SIMPLE (Semi-Implicit Method for Pressure Linked Equations) algorithm to solve the incompressible steady RANS equations. The $k - \omega$ SST turbulence model (Menter, 1994) has been adopted in this work, where standard values for the coefficients and no transition model have been used. For all the simulations we adopt a freestream ratio between eddy and laminar viscosity equal to 0.001, together with free-stream turbulence intensity of $TU_\infty = 5\%$, with the only exception of the flat plate case, for which $TU_\infty = 0.5\%$. The spatial discretization used for the divergence, gradient and Laplacian operators is second-order accurate. All the results have been checked to be fully converged in integral quantities (drag and lift) and in the residuals, by ensuring that the L_1 norm reduced to 10^{-8} times the initial value of the residual.

The study considers three geometries of increasing complexity. The first case is a two-dimensional flat plate boundary layer of length $L = 2\ m$ is considered, where $Re = U_\infty L/\nu = 10^6$. With air as working fluid, and a free-stream velocity of $U_\infty = 5\ m/s$, the computational domain is rectangular and extends for 2.3 m in length and 1 m in height. The flat plate sits along the lower boundary of the computational domain. The domain extends 0.3 m upstream of the flat plate, and a symmetry boundary condition is used to simulate a free stream approaching the plate in this region. A suitable volume mesh is designed with the BlockMesh utility available in OpenFoam, and checked to yield mesh-independent results with a mesh sensitivity study. The final mesh, which provides a local friction coefficient that does not vary with further refinements, consists of 125000 hexahedral elements, with 250 cells in the wall-normal direction and 500 cells in the wall-parallel direction, of which 400 are distributed over the flat plate. Non-uniform grid spacing is adopted to obtain more resolution in the near-wall and in the leading-edge regions, to better capture the boundary layer development. Transition is adequately described, and the distance y_1 of the first cell from the wall is always below unity when expressed in wall units, i.e. $y_1^+ < 1$.

The second case is a two-dimensional NACA 0012 airfoil, at a chord-based Reynolds number of $Re_\infty = 10^6$. The airfoil chord c is taken of unitary length at 1 m, and the far-field boundary is located approximately $50c$ away from the airfoil surface. A mesh sensitivity study is carried out on a number of C-type grids, by observing changes in the drag coefficient after successive mesh refinements. The chosen grid consists of 450 hexahedral cells in the chord-normal and 725 in the chord-tangent directions, and provides a repeatable transition location. The mesh spacing near the airfoil is sufficient to ensure $y^+ < 1$ over the airfoil surface. Stretching of the grid is used to improve resolution in the wake region. To further validate the mesh accuracy, the solution has been checked also as a function of

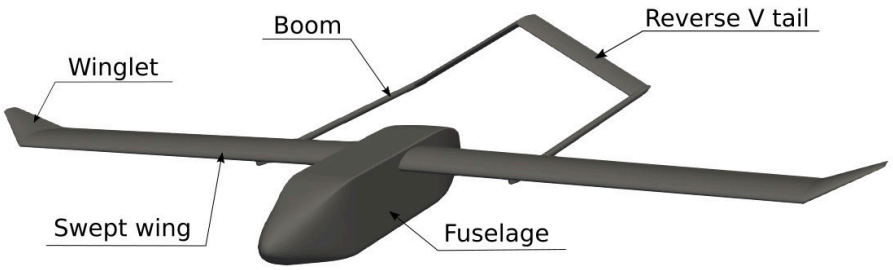

Figure 8.1: CAD model of the simplified UAV.

the angle of attack α. Hence, a number of preliminary runs at various values of α have been performed, without riblets, by replicating the flow conditions used in Mele & Tognaccini (2012). The outcome in terms of lift and drag coefficients are in very good agreement with the results reported by Mele & Tognaccini (2012) as well as with the experimental measurements described in Ladson (1988).

The final and most important case is the UAV, with total length of 2.4 m and wing span of 3.6 m; its (simplified) geometry is described with some detail in §8.2.3. Simulations are carried out first on the isolated UAV wing, to understand to what extent the indirect beneficial effects of riblets noticed for the NACA 0012 carry forward to three dimensions, and the complete UAV is then considered. In both cases the computational domain is made by a hemisphere, with a radius of 50 m that surrounds the wing half-span and the UAV half-span mounted on the $x-z$ plane, respectively. Symmetry is used to reduce computational cost. In this case, a commercial mesher is used to create unstructured meshes made by hexahedral and tetrahedral cells, with refinements boxes to capture the flow development near the body and in the wake. The grids possess 24 additional layers of hexahedral and tetrahedral elements aligned to the boundary surface, to guarantee that $y_1^+ < 1$, thus satisfying the requirements for an accurate computation inside the boundary layer within a low-Re formulation that does not resort to wall functions or other models of the near-wall region. A suitable mesh density is determined by observing changes in the drag coefficient, and robustness in predicting transition. The final mesh is designed with 4 millions elements for the wing, and by 9.6 million elements for the full UAV.

8.2.3 The UAV model

The considered UAV belongs to the family of Mini and Light Tactical UAV, with a MTOW (maximum take-off weight) ranging from 25 to 50 kg. The UAVs of this class are designed to integrate multiple payloads with different capabilities, e.g. EO/IR sensors, multi/hyperspectral cameras, LiDAR, transmitters, radars.

Flexibility is ensured by the fuselage modularity and by the possibility to change the onboard systems configuration to achieve an optimized aircraft balance.

In this work, we consider a simplified geometric model of the UAV, as plotted in figure 8.1, where small-scale geometric details and the propeller are omitted. The motivation is two-fold: such a simplified geometry, while remaining representative of the actual aircraft and retaining its essential qualitative features and dimensional characteristics, is free from intellectual property constraints; moreover, the lack of small-scale details allows some savings of computational effort. The simplified UAV is 2.4 m long and it has a span $b = 3.6\ m$. It has a swept wing with a chord length of 0.3 m at the root with winglets at the tips of 0.22 m and dihedral angle of 21.5°. The considered reference surface area is $S = 1\ m^2$. The UAV is characterized by a reverse V tail made by a symmetric four digits NACA airfoil with a span of 1.05 m and a chord of 0.23 m. The tail is directly connected to the lower surface of the wing by two booms of 1.05 m with a circular cross-sectional area of radius 0.015 m. The fuselage is 1.41 m long and its cross-section originates from a rectangular shape, 0.29 m high and 0.23 m wide, with rounded edges. The drone cruise speed is 22 m/s, leading to a chord-based Reynolds number $Re_\infty = 5 \times 10^5$. The UAV weight of 25 kg and the cruise speed of 22 m/s, together with the geometrical information mentioned above, imply a lift coefficient in cruise of $C_L = 0.8322$.

8.2.4 Dimensionless force coefficients

In this paper, the aerodynamic coefficients, i.e. the ratio of a force component and the reference quantity $1/2\rho U_\infty^2$, are the lift coefficient C_L and the total drag coefficient C_D. The latter can be decomposed into friction $C_{D,f}$ and pressure $C_{D,p}$ drag coefficients; the former describes the resistance to the relative motion between the fluid and the solid boundary due to viscous effects, the latter quantifies the net drag force arising from pressure variation around the body. When a wing of finite span is considered, the drag coefficient can alternatively be decomposed into induced and profile drag coefficients. The former, defined as $C_{D,i} = C_L^2/(\pi b^2/S)$ describes the additional drag due the three dimensional effects cause by the lift and the latter, defined as $C_{D,pr} = C_D - C_{D,i}$ describes the same quantity due to all the other types of drag except lift-induced one. Profile drag can further be decomposed in friction drag $C_{D,f}$ and form drag $C_{D,form} = C_{D,pr} - C_{D,f}$. Lastly, the local skin-friction and pressure coefficients are defined as $C_f = 2\tau_w/\rho U_\infty^2$ and $C_p = 2p/\rho U_\infty^2$ (in the coefficient subscripts, capital letters indicate global quantities and small letters indicate local quantities).

Changes between clean and riblets configurations are computed as $\Delta C_x = C_{x,0} - C_x$ where the subscript 0 refers to the clean configuration and x is the quantity of interest. The drag reduction rate, i.e. the change in drag normalised

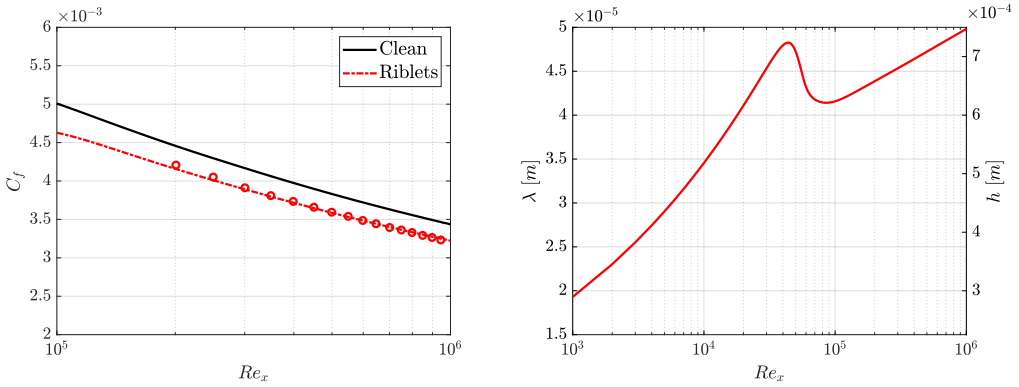

Figure 8.2: Zero-pressure-gradient boundary layer over a flat plate. Left: evolution of the skin-friction coefficient with/without riblets, and comparison with data from Mele & Tognaccini (2018). Right: change along the plate of the slip length (left y axis) and riblets height (right y axis), in dimensional units.

with the drag of the clean configuration is defined as $\Delta C_D/C_{D,0}$.

8.3 Validation

The boundary condition used to model riblets is first tested on simple two-dimensional flows, where available information allows a quantitative check of the outcome.

8.3.1 Flat plate

The first application example is the zero pressure gradient boundary layer developing over a flat plate. Optimal V-shape riblets, with $l_g^+ = 10.5$ corresponding to $h^+ = \sqrt{2}l_g^+$, are placed everywhere along the plate, immersed in a uniform external flow.

Figure 8.2 (left) shows how riblets influence the streamwise evolution of the friction coefficient, demonstrating the correct amount of drag reduction. On the entire plate, the integrated percentage drag reduction is $\Delta C_D/C_{D,0} = 6.5\%$, in agreement with existing experimental (Bechert *et al.*, 1997) information. Local changes of C_f, descending from the imposed slip, are consistent with those by Mele & Tognaccini (2018). The evolution of the physical dimensions of the grooves is shown in figure 8.2 (right), together with the analogous evolution of the slip length. Once the boundary layer becomes fully turbulent, i.e. for $Re_x > 10^5$, changes of the slip length with the streamwise coordinate are rather mild: there is a small increase with Re_x to reach the largest value of 50 microns at the downstream

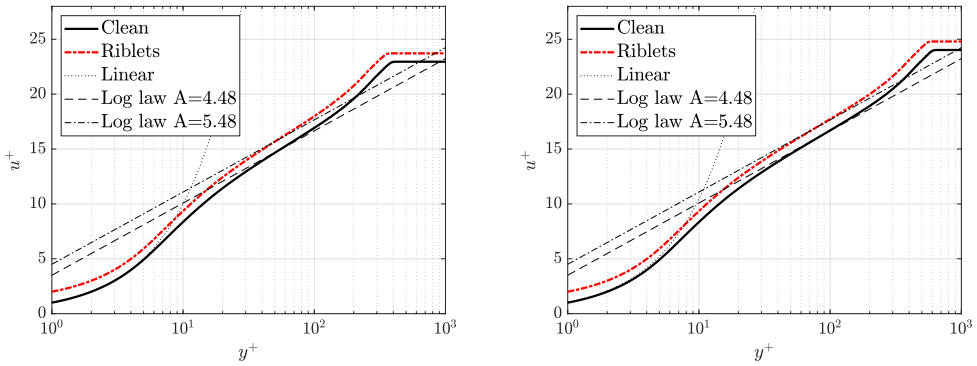

Figure 8.3: Mean velocity profile with/without riblets over the flat plate, at $Re_x = 5 \times 10^5$ (left) and $Re_x = 9 \times 10^5$ (right). The riblets profile consistently shows the upward shift of $\Delta U^+ = 1$ on the logarithmic region.

end of the plate. By construction, as explained earlier in §8.2, this corresponds to one viscous length. At the plate end, the predicted size of optimal riblets is approximately $h = 0.8\ mm$.

The correctness of the model is directly checked in figure 8.3, which provides graphical evidence that, regardless of the streamwise location, the upward shift of the mean velocity profile is of unitary value, confirming that $\Delta U^+ = \lambda^+ = 1$.

8.3.2 NACA 0012 airfoil

Testing progresses to consider the two-dimensional flow around a NACA 0012 airfoil; this test case remains highly simplified, but brings in pressure drag, and thus lends itself to studying the effect of riblets on this non-frictional drag component. Unfortunately, little information is available for validation.

Once again, the airfoil is assumed to be fully covered by riblets of locally optimal size, i.e. ensuring $l_g^+ = 10.5$ everywhere. Figure 8.4 shows the mean velocity profile on the upper surface of the airfoil at $x/c = 0.5$, for two different angles of attack, namely 0 and 4 degrees. The expected unitary upward shift ΔU^+ due to the grooves is consistently observed. At $\alpha = 4°$, experimental data are available from Sundaram *et al.* (1996), and the present results appear to agree with them. However, the agreement is less satisfactory at other incidences. It must be mentioned that experiments were carried out with riblets of constant physical size, with a size that is about 10 viscous lengths. The percentage total drag reduction at $\alpha = 0°$ is measured to be 7%, which is in agreement with the experimental data from Sundaram *et al.* (1996); Viswanath (2002) as well as with CFD results obtained by Mele & Tognaccini (2012). Our data indicate only a mild variation of drag reduction with angle of attack, while Viswanath (2002) mentions an increase

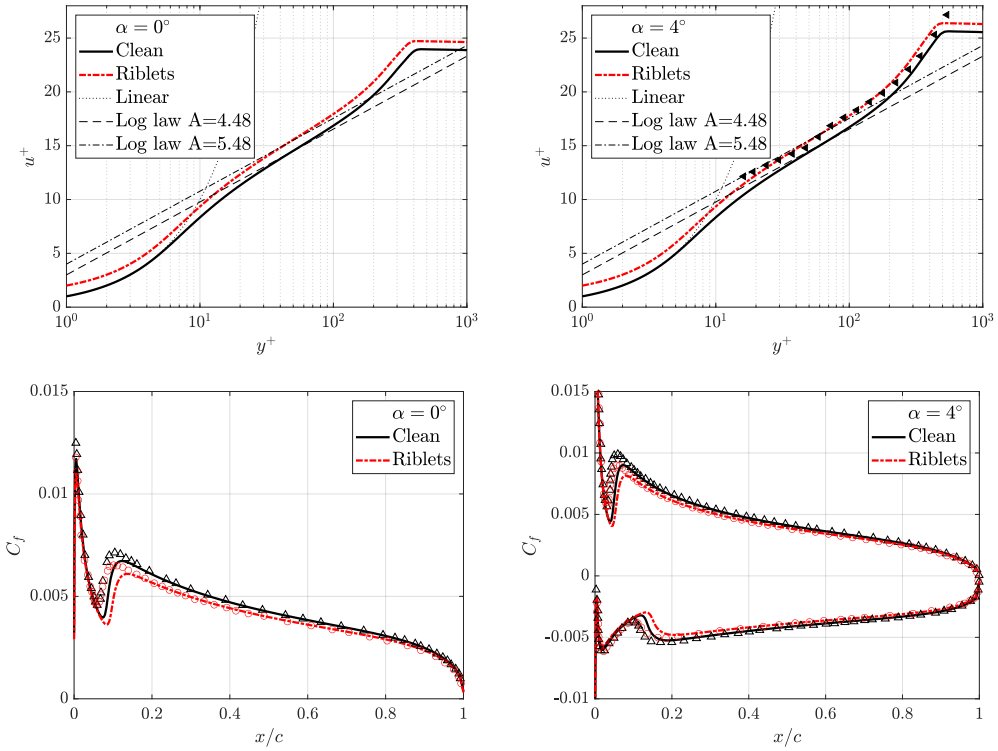

Figure 8.4: Mean velocity profiles (top) and skin-friction coefficient (bottom) for the NACA0012 airfoil, at an incidence of $\alpha = 0°$ (left) and $\alpha = 4°$ (right). The top row shows the mean profile over the suction side in law-of-the-wall form at $x/c = 0.5$, and compares with data from Sundaram *et al.* (1996). The bottom row plots the evolution of the friction coefficient along the chord, and compares with data from Mele & Tognaccini (2012), represented with symbols.

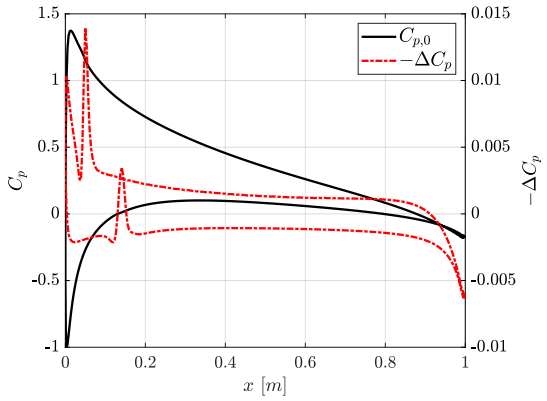

Figure 8.5: Pressure coefficient on the pressure and suction sides of the NACA0012 airfoil at $\alpha = 4°$ for the clean case (black line), and difference with the riblets case (red dashed line).

beyond 16% at $\alpha = 0°$ and a sudden drop to zero at $\alpha = 10°$. The lower part of figure 8.4 compares the evolution of the skin-friction coefficient along the airfoil, and shows a very good agreement with the same quantity taken from Mele & Tognaccini (2012) (except for the precise location of the transition region).

The pressure coefficient C_p and the difference $\Delta C_p = C_{p,0} - C_p$ at $\alpha = 4°$ are shown in figure 8.5. Changes are visible, to attest once again the effect of riblets on the pressure distribution along the airfoil. Changes in the expansion peak at the leading edge and on the pressure recovery at the trailing edge due to riblets provide a significant additional contribution to drag reduction; form drag is reduced by 7.7%, adding to the friction reduction of 6.7%. These results agree with several findings by Mele & Tognaccini (2018), who interpreted the reduced form drag by observing that riblets change the flow field by making it more similar to the inviscid solution, where the slip length is infinite, and form drag is exactly zero. Moreover, the altered pressure distribution leads to a larger lift, at all tested incidences; this effect, that will be discussed later when discussing the full aircraft, is important for the reduction of the total drag: since the aircraft in cruise always needs the same lift, an increased aerodynamic efficiency implies a reduced angle of attack in cruise, thus bringing in an additional contribution to drag reduction.

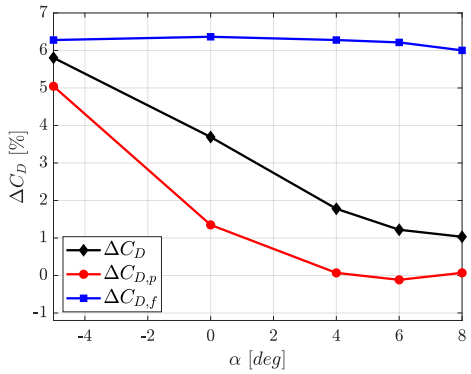

Figure 8.6: Riblets drag reduction vs angle of attack for the UAV wing.

8.4 Results

8.4.1 The isolated UAV wing

The UAV wing is considered first, to focus on the presence of indirect drag reduction effects in three dimensions, but without the geometrical complexities implied by the interaction between wing and fuselage. The UAV finite isolated wing is considered at the cruise flight condition of $Re_\infty = 5 \times 10^5$. As always, locally optimal riblets with $l_g^+ = 10.5$ are placed over the entire wing surface.

Figure 8.6 shows how drag reduction induced by riblets changes with the angle of attack. The friction component of the total drag reduction is nearly constant at 6.3%, whereas pressure and total drag change with α. At $\alpha = 0°$ the total drag reduction rate is 3.7%, and diminishes at larger incidences. Clearly the diminished total drag reduction goes hand in hand with the diminished pressure drag reduction. As already observed for the NACA 0012 airfoil in §8.3.2, riblets tend to modify the pressure distribution in such a way that lift is increased; this is confirmed here for the UAV wing. This phenomenon causes an increase of the lift-induced drag, that is not seen in two dimensions, and should not be regarded as a negative effect of riblets, since the aircraft has to achieve the same lift, and increased aerodynamic efficiency is always beneficial.

In fact, riblets performance should be measured by adjusting α in such a way that the lift coefficient is unchanged. In Table 8.1 we compare the clean case and the riblets case at the same angle of attack, and at the same lift coefficient as well. Two configurations are considered, at a nominal angle of attack of $\alpha = 0°$ and $\alpha = 4°$. Total drag is split into friction $C_{D,f}$ and pressure $C_{D,p}$ drag, as well as induced $C_{D,i}$ and profile $C_{D,pr}$ drag. As expected, comparing at the same C_L provides larger drag reduction than comparing at the same α. At the same angle

	Clean	*Riblets*		*Clean*	*Riblets*	
	$\alpha = 0°$	$\alpha = 0°$	$\alpha = -0.0626°$	$\alpha = 4°$	$\alpha = 4°$	$\alpha = 3.885°$
C_L	0.4996	0.5055 (+1.2%)	0.4996 (-)	0.8719	0.8828 (+1.8%)	0.8719 (-)
C_D	0.0227	0.0219 (-3.7%)	0.0217 (-4.5%)	0.0386	0.0380 (-1.8%)	0.0374 (-3.3%)
$C_{D,p}$	0.0121	0.0119 (-1.4%)	0.0118 (-2.8%)	0.0280	0.0280 (-)	0.027 (-2.2%)
$C_{D,f}$	0.0106	0.0099 (-6.4%)	0.0099 (-6.4%)	0.0106	0.0100 (-6.3%)	0.0100 (-6.3%)
$C_{D,i}$	0.0077	0.0079 (+2.4%)	0.0077 (-)	0.0235	0.0241 (+2.5%)	0.0235 (-)
$C_{D,pr}$	0.0150	0.0140 (-6.8%)	0.0140 (-6.8%)	0.0151	0.0138 (-8.4%)	0.0138 (-8.5%)

Table 8.1: Aerodynamic coefficients for the isolated UAV wing. Comparison between clean and riblets configurations is carried out at the same angle of attack and at the same lift coefficient, for nominal angle of attack of $\alpha = 0°$ and $\alpha = 4°$.

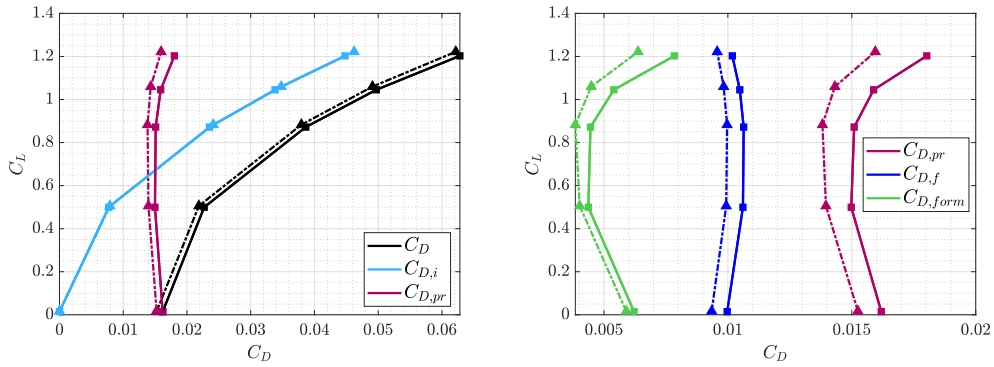

Figure 8.7: Drag breakdown for the isolated UAV wing (left), and focus on the profile drag (right). Solid lines with square markers indicate the clean configuration, dashed lines with triangular markers indicate the configuration with riblets.

of attack, riblets produce a larger lift coefficient and hence a larger induced drag. It is worth noticing that the decrease of $C_{D,pr}$ is almost the same for the cases at constant α and constant C_L, whereas the induced drag is larger when compared at the same α.

Drag breakdown is graphically shown at various α in figure 8.7: focus is on the total, induced and profile drag on the left panel, and on the contributions to profile drag on the right panel. From the left panel, riblets are seen to mainly act on the profile drag while the lift induced drag is essentially unchanged. The right panel of figure 8.7 focuses on the decomposition of profile drag, and shows that, besides the obvious reduction of friction drag, riblets additionally act upon form drag in a significant way. Depending on the angle of attack, the benefit of riblets in reducing $C_{D,pr}$ are in the 5-10% range. This is linked to the modifications on the pressure distribution on the wing, already observed in the NACA 0012 validation tests, see figure 8.5. The pressure distribution at $2y/b = 0.52$ for the UAV wing is shown in figure 8.8, and confirms the larger pressure recovery and the increased expansion peak induced by riblets that are at the root of form drag reduction.

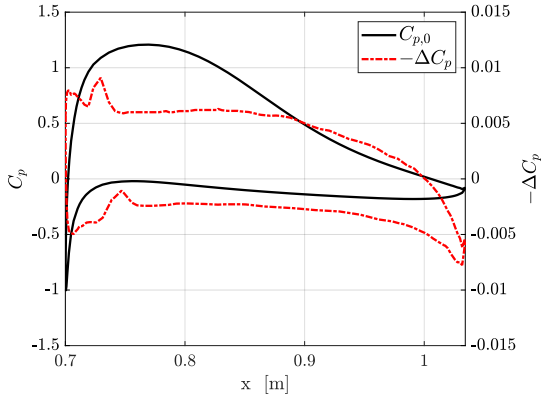

Figure 8.8: Pressure coefficient on the pressure and suction sides of the isolated UAV wing at $2y/b = 0.52$, at $\alpha = 4°$, for the clean case (black line) and difference with the riblets case (red dashed line).

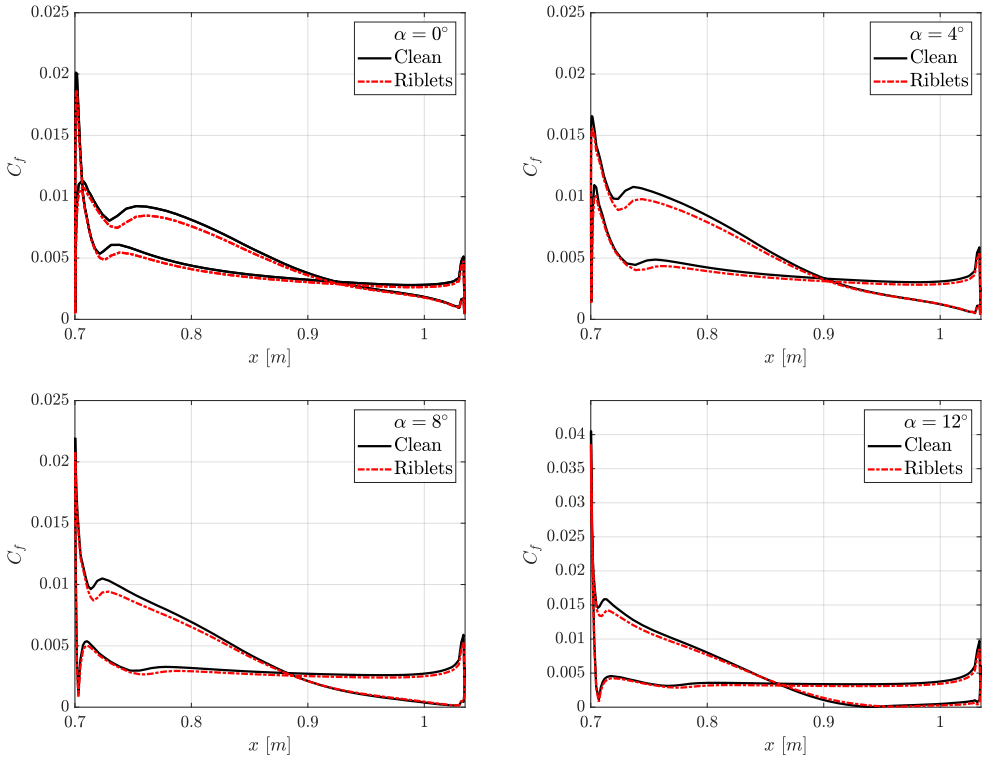

Figure 8.9: Friction coefficient for the isolated UAV wing, at spanwise location $2y/b = 0.52$ and four angles of attack.

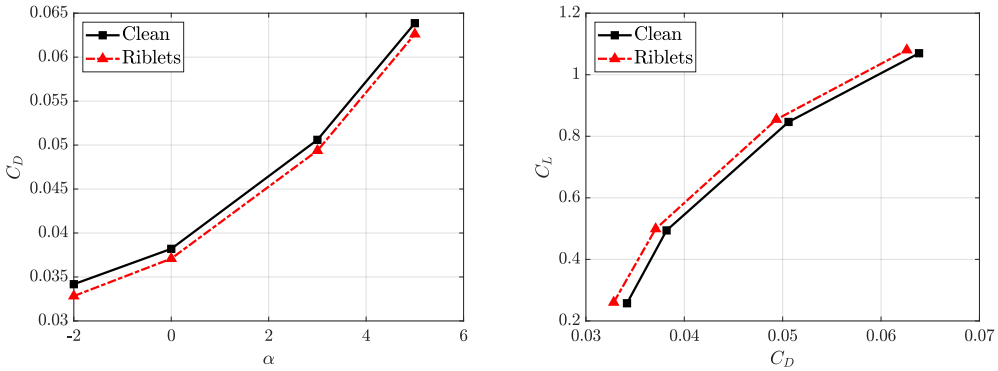

Figure 8.10: $C_D(\alpha)$ and polar curves of the UAV, in clean/riblets configurations.

Finally, figure 8.9 plots the skin friction distribution at the spanwise station $2y/b = 0.52$ of the wing, and compares clean and riblets configurations at different angles of attack. A decrease of the skin friction across the entire chord is observed. In particular on the suction side friction is mainly reduced in the fore portion; at large angles of attack, friction reduction vanishes in the aft part. On the lower surface, the reduction of friction is almost constant when α is varied.

8.4.2 The UAV

The complete UAV is now considered, in the configuration described above and shown in figure 8.1. Consistently with the rest of this study, riblets are assumed to be locally optimal, with $l_g^+ = 10.5$ and unitary slip length $\lambda^+ = 1$. The spatial distribution of the optimal riblet size, i.e. l_g (which, for a given cross-sectional shape, leads immediately to the geometric dimensions of the riblets) is retrieved as a result of the simulations. It should be remarked, however, that previous work (Mele *et al.*, 2016) indicates how the size of locally optimal riblets does not vary much, so that the drag reduction obtained adopting riblets with constant physical size is quite near to the maximum drag reduction.

A series of simulations with/without riblets is carried out to provide data points to build the polar of the aircraft (figure 8.10). Owing to the already highlighted lift increase provided by riblets, the angle of attack necessary to provide the required lift in cruise conditions slightly decreases from $\alpha = 2.85°$ to $2.81°$. The drag reduction obtained for the entire aircraft is an interesting 3%, that derives from a combination of a (less important) friction drag reduced by 6.1% and a (more important) pressure drag reduced by 1.5%.

Figure 8.11 helps determining where the largest percentage changes of the skin friction take place over the surface of the aircraft. $\Delta C_f/C_{f,0}$ is about 6% almost everywhere, roughly as expected for a flat plate at this value of Re, except

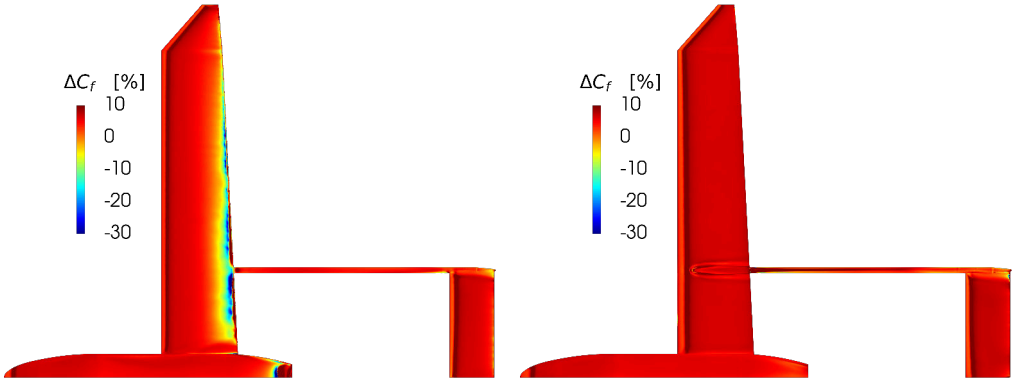

Figure 8.11: Percentage of skin friction reduction on the upper (left) and lower (right) parts of the aircraft in cruise condition.

for the region near the trailing edge and for the aft part of the fuselage: here the absolute value of C_f approaches zero, and its percentage variations become less meaningful.

Figure 8.12 shows the computed height distribution for the locally optimal riblets, by assuming that the cross-sectional riblet shape is a standard V groove, for which $s^+ = h^+ = \sqrt{2}l_g^+$. The optimal riblets height is about 0.2 mm nearly everywhere, except for the trailing edge of the wing, and for the aft part of the fuselage. This provides graphical evidence to the previous statement that riblets of properly chosen constant physical height would provide a drag reduction that is very close to the maximum.

Riblets are then tested in off-design situations, i.e. at various incidences different from the cruise angle of attack, to check for robustness and to verify that riblets do not cause unwanted effects on the UAV aerodynamics, during maneuvers or the climb/descent phases of a typical mission. As already noted for the UAV wing, figure 8.13 shows that, although drag reduction is maximum in cruise, performance degrades only mildly when the angle of attack differs from the cruise value. Again, it is confirmed that friction drag reduction remains nearly constant when α ranges from $-2°$ to $5°$.

Finally, the aerodynamic drag is broken down into profile drag and induced drag in the left plot of figure 8.14, while the right plot decomposes further profile drag into friction and form drag. The most obvious difference between clean and riblets configurations is the reduced profile drag, which derives from a sizable reduction of the friction component, jointly with a comparable contribution from the form drag.

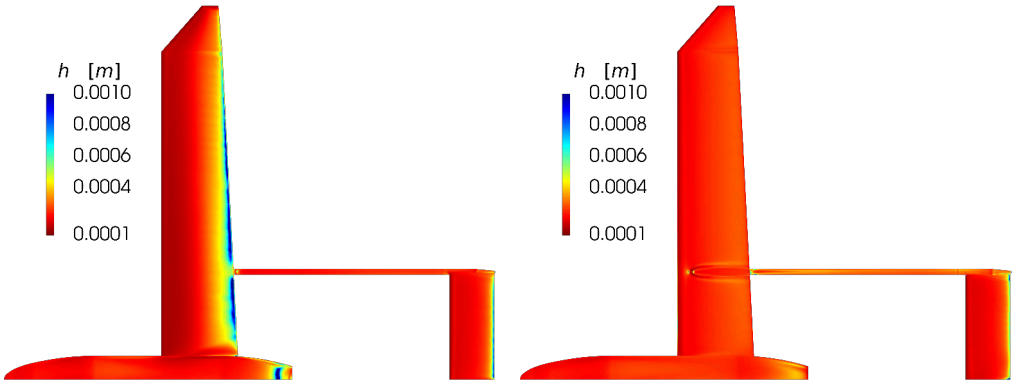

Figure 8.12: Spatial distribution of the computed optimal riblets height in physical units, for symmetric V groove riblets. Left: upper part of the aircraft in cruise conditions; right: lower part.

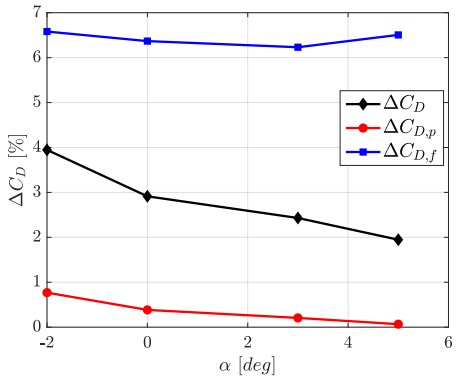

Figure 8.13: Drag reduction rate vs angle of attack. The largest drag reduction is achieved in cruise condition.

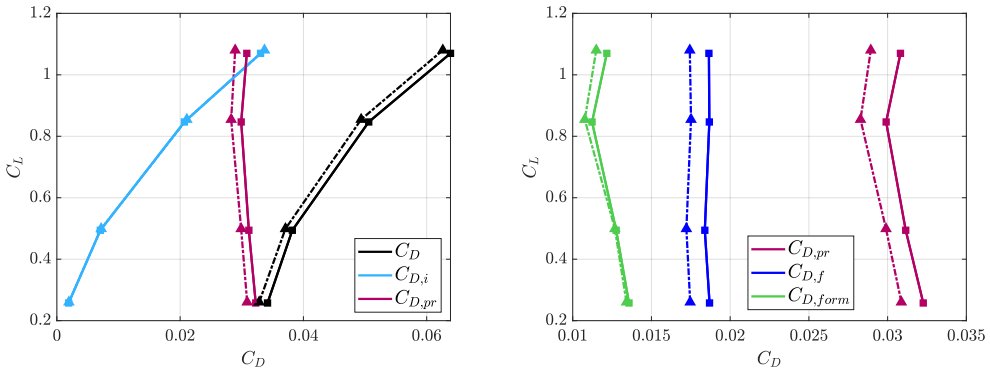

Figure 8.14: Drag breakdown (left) and decomposition of profile drag (right). Solid lines with square markers refer to clean configuration, dashed lines with triangular markers refer to riblets configuration.

	Riblets deployment	β
I	full coverage	1.000
II	no wing TE	0.953
III	no booms	0.935
IV	only wing	0.524
V	only wing, suction side	0.289

Table 8.2: Coverage configurations

8.4.3 Partial coverage

Perhaps the most interesting consequence of the availability of a simple yet accurate boundary condition to model riblets within RANS simulations is the ability to carry out quick numerical studies to address practical problems related to their use. For example, since riblets produce limited benefits and imply costs and penalties, an elementary cost/benefit analysis should start from addressing the simple question of which area of the aircraft surface would yield the largest benefits after riblets installation. To this aim, we have designed a further set of simulations to explore partial coverage of the aircraft surface with riblets. The amount of coverage is quantified by the ratio β between the riblets-covered area and the total area, with $\beta = 1$ indicating total coverage. In these simulations, the full aircraft is considered, but riblets coverage varies according to Table 8.2, where case I is the full-coverage case described above. Outcomes of the simulations are shown in Table 8.3 and graphically represented in figure 8.16. Figure 8.15 schematically illustrates where riblets are applied on the surface of the UAV.

Since at the trailing edge of the wing riblets do not provide significant reduc-

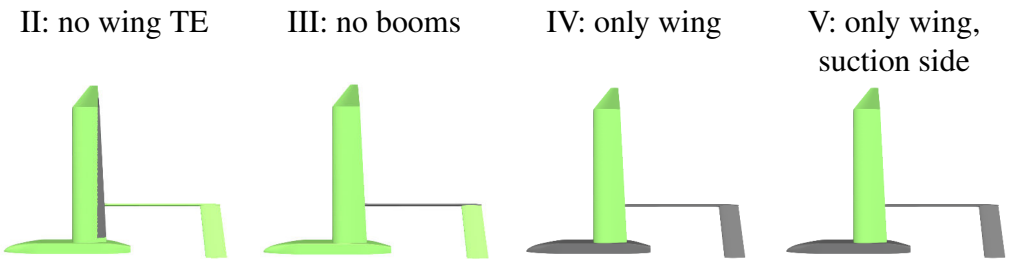

Figure 8.15: Schematic drawing of various riblets coverage configurations, cases II-V.

	C_D	$\Delta C_D/C_{D,0}\%$	$C_{D,p}$	$\Delta C_{D,p}/C_{D,p0}\%$	$C_{D,f}$	$\Delta C_{D,f}/C_{D,f0}\%$
Clean	0.0508	-	0.0338	-	0.0170	-
I	0.0493	3.0	0.0333	1.5	0.0160	6.1
II	0.0493	3.0	0.0333	1.5	0.0160	6.1
III	0.0493	2.9	0.0333	1.5	0.0160	5.8
IV	0.0498	2.0	0.0333	1.4	0.0165	3.3
V	0.0499	1.7	0.0333	1.5	0.0167	2.2

Table 8.3: Drag breakdown for the UAV in cruise condition, for different configurations of riblets coverage, and percentage changes with the clean case.

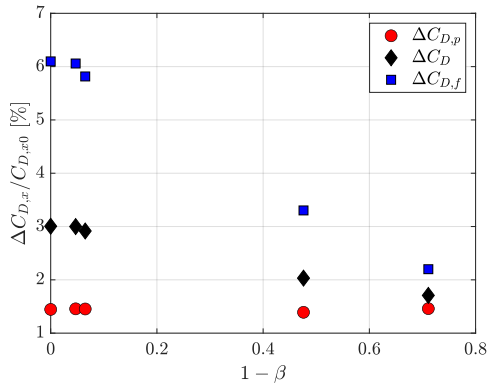

Figure 8.16: Drag reduction contributions for different configurations of riblets coverage from highest (I-full coverage) to lowest (V-wing only, suction side) coverage.

tions in skin friction (figure 8.11) while locally enforcing a substantial change from the optimal size, in configuration II riblets are removed from the trailing edge of the entire wing. The reduction of the riblets-covered surface is minimal (less than 5%) but, as expected, there is no appreciable decrease in terms of performance. Configuration III has riblets removed from the booms that connect the wing to the tail. Again, the overall drag reduction is essentially unchanged, with 6.5% savings in covered area: pressure drag reduction remains unchanged since the boom is not an aerodynamic body, whereas friction reduction decreases but minimally so because the surface of the boom is small. Together, cases II and III suggest that removing riblets from both the trailing edge and the booms would avoid difficult areas, and save over 10% of application surface without incurring in significant performance degradation.

Configuration IV has riblets applied on the wing only, and is motivated by the observation that, in this application, pressure drag is approximately $2/3$ of the whole drag, and that riblets placed on the wing produce pressure drag reduction in addition to friction drag reduction. With configuration IV, performance indeed degrades from 3% to 2%, but the saving in coverage area is more than proportional, with riblets surface shrinking down to one half at $\beta = 0.524$. As expected, pressure drag reduction remains almost unchanged at 1.4%, and friction drag reduction is seen to diminish from 6.1% to 3.3%: indeed, the area of the wing is approximately one half of the total area. Perhaps the most interesting configuration is configuration V, where only the suction side of the wing (and the entire winglet) is equipped with riblets, leading to $\beta = 0.289$. In contrast, the riblets-induced benefit remains more than one half, i.e. 1.7% instead of 3.0%.

8.5 Conclusions

The drag reduction potential of riblets deployed on a fixed-wing, low-speed Unmanned Air Vehicle (UAV) has been assessed with RANS simulations, with a view to determining an optimal coverage policy. While riblets are fully characterized in low-speed flows over plane walls, and studies are available for aeronautical configurations in transonic flow (commercial mid- or long-range passenger aircraft), a low-speed aircraft like the present one (for which the cruise speed is only 22 m/s) is considered here for the first time. Since the friction component of the aerodynamic drag of the UAV is modest, the effectiveness of riblets in this specific application needs to be assessed.

The RANS simulations, which employ a standard OpenFOAM setup, are unable to describe riblets directly. Thus, the presence of riblets is accounted for via a suitable slip condition enforced at the planar wall. The chosen amount of slip is constant in viscous units, and corresponds to riblets that locally possess

optimal size in viscous wall units. The slip length model has been validated in the simple flows over a flat plate and around a subsonic airfoil, where results agree with available information.

Once applied to the UAV, the simulated riblets have brought out indirect and favorable effects, which go beyond the local reduction of friction drag, and render the deployment of a friction-reduction device definitely interesting also in such a low-speed application. Indeed, riblets significantly change the pressure distribution across the wing of the aircraft, which translates into an additional reduction of form drag, and in a lift increment as well. Although the latter obviously causes an increase of lift-induced drag, the requirement for the aircraft in cruise to fly at a given lift leads to a reduced angle of attack and thus to a further contribution to drag reduction. In the end, riblets provide up to 3% of reduction of the total drag of the aircraft at cruise speed: a noticeable result, especially when the low flight Reynolds number of the UAV is considered.

Once a cheap computational model is available to reliably compute the global effect of riblets on the aerodynamic drag, varying the riblets coverage policy becomes a computationally affordable task; relatively inexpensive simulations can help determine what drag benefit can be achieved with a given extent and location of the coverage of the aircraft surface. Thanks to the importance of secondary effects on pressure drag reduction induced by riblets, as a consequence of the significant pressure drag component, up to 1.7% of total drag reduction is achieved by placing riblets on the upper surface of the wing only. In this configuration, the total drag reduction is almost $2/3$ of the maximum obtained with full coverage but it is obtained with a coverage of less then $1/3$ of the total area. Since riblets costs (for application and maintenance) are directly linked to the amount of riblets-covered surface, the wing-only configuration offers a reduced cost-benefit ratio, and leaves untouched the UAV fuselage, where systems (sensors, cameras, transmitters) are designed to be installed. Further analysis can determine the practicality of riblets removal from high-wear areas (e.g. the leading edge), which would further add to the practical appeal of riblets in this application. Such calculations are made possible by the simplicity of the slip length model, whose validity goes beyond riblets, since it can be used to simulate a generic drag-reducing device which locally reduces the skin friction.

Bibliography

Abderrahaman-Elena, N. & García-Mayoral, R. 2017 Analysis of anisotropically permeable surfaces for turbulent drag reduction. *Physical Review Fluids* **2** (11), 114609.

Agostini, L. & Leschziner, M. 2014 On the influence of outer large-scale structures on near-wall turbulence in channel flow. *Physics of Fluids* **26** (7), 075107.

Agostini, L. & Leschziner, M. 2017 Spectral analysis of near-wall turbulence in channel flow at Re_τ=4200 with emphasis on the attached-eddy hypothesis. *Physical Review Fluids* **2** (1), 014603.

Agostini, L., Touber, E. & Leschziner, M.A. 2014 Spanwise oscillatory wall motion in channel flow: Drag-reduction mechanisms inferred from DNS-predicted phase-wise property variations at Re_τ=1000. *Journal of Fluid Mechanics* **743**, 606–635.

Akhavan, R., Jung, W. J. & Mangiavacchi, N. 1993 Turbulence control in wall-bounded flows by spanwise oscillations. *Applied Scientific Research* **51** (1), 299–303.

Alekseev, V. V., Gachechiladze, I. A., Kiknadze, G. I. & Oleinikov, V.G. 1998 Tornado-like energy transfer on three-dimensional concavities of reliefs-structures of self organizing flow, their visualisation, and surface streamlining mechanism. In *Trans. 2nd Russian Net. Conf. Heat Trasfer, Heat Trasfer Intensification Radiation and Complex Heat Transfer*, , vol. 6, pp. 33–42.

Allarton, R., Yao, J., Clifford, T., Hitchborn, B., Parker, L.J. & Shaw, J. 2020 Surface flow modification of aerofoils for automotive racing car applications. *International Journal of Modern Physics* **34** (14-16).

Alves Portela, F., Papadakis, G. & Vassilicos, J. C. 2017 The turbulence cascade in the near wake of a square prism. *Journal of Fluid Mechanics* **825**, 315–352.

Alves Portela, F., Papadakis, G. & Vassilicos, J. C. 2020 The role of coherent structures and inhomogeneity in near-field interscale turbulent energy transfers. *Journal of Fluid Mechanics* **896**, A16–24.

Andreolli, A., Quadrio, M. & Gatti, D. 2021 Global energy budgets in turbulent Couette and Poiseuille flows. *Journal of Fluid Mechanics* **924**, A25.

Arun, S., Sameen, A., Srinivasan, B. & Girimaji, S.S. 2021 Scale-space energy density function transport equation for compressible inhomogeneous turbulent flows. *Journal of Fluid Mechanics* **920**, A31.

Aupoix, B., Pailhas, G. & Houdeville, R. 2012 Towards a General Strategy to Model Riblet Effects. *AIAA Journal* **50** (3), 708–716.

Auteri, F., Baron, A., Belan, M., Campanardi, G. & Quadrio, M. 2010 Experimental assessment of drag reduction by traveling waves in a turbulent pipe flow. *Physics of Fluids* **22** (11), 115103/14.

Balaras, E. 2004 Modeling complex boundaries using an external force field on fixed Cartesian grids in large-eddy simulations. *Computers & Fluids* **33** (3), 375–404.

Bamieh, B. & Dahleh, M. 2001 Energy amplification in channel flows with stochastic excitation. *Phisics of Fluids* **13** (11), 3258–3269.

Banchetti, J., Luchini, P. & Quadrio, M. 2020 Turbulent drag reduction over curved walls. *Journal of Fluid Mechanics* **896**, 1–23.

Baron, A. & Quadrio, M. 1996 Turbulent drag reduction by spanwise wall oscillations. *Applied Scientific Research* **55**, 311–326.

Bearman, P. W. & Harvey, J. K. 1976 Golf Ball Aerodynamics. *Aeronautical Quarterly* **27** (2), 112–122.

Bech, K. H. & Andersson, H. I. 1996 Secondary flow in weakly rotating turbulent plane Couette flow. *Journal of Fluid Mechanics* **317**, 195–214.

Bechert, D.W. & Bartenwerfer, M. 1989 The viscous flow on surfaces with longitudinal ribs. *Journal of Fluid Mechanics* **206**, 105–209.

Bechert, D.W., Bruse, M. & Hage, W. 2000 Experiments with three-dimensional riblets as an idealized model of shark skin. *Experiments in Fluids* **28**, 403–412.

Bechert, D.W., Bruse, M., Hage, W., Hoeven, J.G.T. Van Der & Hoppe, G. 1997 Experiments on drag-reducing surfaces and their optimization with an adjustable geometry. *Journal of Fluid Mechanics* **338**, 59–87.

Bechert, D. W., Hoppe, G., Van Der Hoeven, J. G. Th. & Makris, R. 1992 The Berlin oil channel for drag reduction research. *Experiments in Fluids* **12** (4), 251–260.

Bernardini, M., Modesti, D., Salvadore, F. & Pirozzoli, S. 2021 STREAmS: A high-fidelity accelerated solver for direct numerical simulation of compressible turbulent flows. *Computer Physics Communications* **263**, 107906.

Bernardini, M., Modesti, D., Salvadore, F., Sathyanarayana, S., Della Posta, G. & Pirozzoli, S. 2023 STREAmS-2.0: Supersonic turbulent accelerated Navier-Stokes solver version 2.0. *Computer Physics Communications* **285**, 108644.

Bernardini, M. & Pirozzoli, S. 2011 Inner/outer layer interactions in turbulent boundary layers: A refined measure for the large-scale amplitude modulation mechanism. *Physics of Fluids* **23** (6), 061701.

Bird, J., Santer, M. & Morrison, J.F. 2018 Experimental Control of Turbulent Boundary Layers with In-plane Travelling Waves. *Flow, Turbulence and Combustion* **100** (4), 1015–1035.

Blesbois, O., Chernyshenko, S. I., Touber, E. & Leschziner, M. A. 2013 Pattern prediction by linear analysis of turbulent flow with drag reduction by wall oscillation. *Journal of Fluid Mechanics* **724**, 607–641.

Blondeaux, P. 1990 Sand ripples under sea waves Part 1. Ripple formation. *Journal of Fluid Mechanics* **218**, 1–17.

Boomsma, A. & Sotiropoulos, F. 2015 Riblet Drag Reduction in Mild Adverse Pressure Gradient: A Numerical Investigation. *International Journal of Heat and Fluid Flow* **56** (56), 251–260.

Butler, K.M. & Farrell, B.F. 1992 Three-dimensional optimal perturbations in viscous shear flow. *Physics of Fluids* **4** (8), 1637–1650.

Cacciatori, L., Brignoli, C., Mele, B., Gattere, F., Monti, C.M. & Quadrio, M. 2022 Drag Reduction by Riblets on a Commercial UAV. *Applied Sciences* **12** (10), 5070.

Cafiero, G. & Iuso, G. 2022 Drag reduction in a turbulent boundary layer with sinusoidal riblets. *Experimental Thermal and Fluid Science* **139**, 110723.

Calmet, H., Gambaruto, A.M., Bates, A.J., Vázquez, M., Houzeaux, G. & Doorly, D.J. 2016 Large-scale CFD simulations of the transitional and

turbulent regime for the large human airways during rapid inhalation. *Computers in Biology and Medicine* **69**, 166–180.

Carini, M. & Quadrio, M. 2010 Direct-numerical-simulation-based measurement of the mean impulse response of homogeneous isotropic turbulence. *Physical Review E* **82** (6), 066301.

Catalano, P., de Rosa, D., Mele, B., Tognaccini, R. & Moens, F. 2020 Performance Improvements of a Regional Aircraft by Riblets and Natural Laminar Flow. *Journal of Aircraft* **57** (1), 29–40.

Chandran, D., Zampiron, A., Rouhi, A., Fu, M.K., Wine, D., Holloway, B., Smits, A.J. & Marusic, I. 2023 Turbulent drag reduction by spanwise wall forcing. Part 2: High-Reynolds-number experiments. *Journal of Fluid Mechanics* **968**, A7.

Charru, F., Andreotti, B. & Claudin, P. 2013 Sand ripples and dunes. *Annual Review of Fluid Mechanics* **45** (1), 469–493, arXiv: https://doi.org/10.1146/annurev-fluid-011212-140806.

Chen, Y., Chew, Y. T. & Khoo, B. C. 2012 Enhancement of heat transfer in turbulent channel flow over dimpled surface. *International Journal of Heat and Mass Transfer* **55** (25), 8100–8121.

Chen, Z., Yu, C., Li, L. & Li, X. 2016 Effect of uniform blowing or suction on hypersonic spatially developing turbulent boundary layers. *Science China Physics, Mechanics & Astronomy* **59** (6), 664702.

Chi, C., Abdelsamie, A. & Thévenin, D. 2020 A directional ghost-cell immersed boundary method for incompressible flows. *Journal of Computational Physics* **404**, 109122.

Chi, C., Lee, Bok Jik & Im, Hong G. 2017 An improved ghost-cell immersed boundary method for compressible flow simulations. *International Journal for Numerical Methods in Fluids* **83** (2), 132–148.

Chiarini, A., Gatti, D., Cimarelli, A. & Quadrio, M. 2022*a* Structure of turbulence in the flow around a rectangular cylinder. *Journal of Fluid Mechanics* **946**, A35.

Chiarini, A., Mauriello, M., Gatti, D. & Quadrio, M. 2022*b* Ascending-descending and direct-inverse cascades of Reynolds stresses in turbulent Couette flow. *Journal of Fluid Mechanics* **930**, A9–22.

Chiarini, A., Quadrio, M. & Gatti, D. 2019 Skin-friction drag reduction described via the Anisotropic Generalized Kolmogorov Equations. In *European Drag Reduction and Flow Control Meeting – EDRFCM 2019*. Bad Herrenalb (Germany).

Choi, H., Moin, P. & Kim, J. 1994 Active turbulence control for drag reduction in wall-bounded flows. *Journal of Fluid Mechanics* **262**, 75–110.

Choi, J., Jeon, W. P. & Choi, H. 2006 Mechanism of drag reduction by dimples on a sphere. *Physics of Fluids* **18** (4), 041702.

Choi, J.-I., Xu, C.-X. & Sung, H. J. 2002 Drag reduction by spanwise wall oscillation in wall-bounded turbulent flows. *AIAA Journal* **40** (5), 842–850.

Choi, K.S., Yang, X. & Clayton, B. R. 1997 Turbulent drag reduction using compliant surfaces. *Mathematical, Physical and Engineering Sciences* **453**, 2229–2240.

Choi, K.-S. 2002 Near-wall structure of turbulent boundary layer with spanwise-wall oscillation. *Physics of Fluids* **14** (7), 2530–2542.

Choi, K.-S., Jukes, T. & Whalley, R. 2011 Turbulent boundary-layer control with plasma actuators. *Phil. Trans. R. Soc. A* **369** (1940), 1443–1458.

Cimarelli, A., De Angelis, E. & Casciola, C. M. 2013 Paths of energy in turbulent channel flows. *Journal of Fluid Mechanics* **715**, 436–451.

Cimarelli, A., De Angelis, E., Jimenez, J. & Casciola, C. M. 2016 Cascades and wall-normal fluxes in turbulent channel flows. *Journal of Fluid Mechanics* **796**, 417–436.

Cimarelli, A., Mollicone, J.-P., van Reeuwijk, M. & De Angelis, E. 2021 Spatially evolving cascades in temporal planar jets. *Journal of Fluid Mechanics* **910**, A19–31.

Cipelli, S., Quadrio, M., Gattere, F., Chiarini, A., Luchini, P. & Gatti, D. 2024 Sinusoidal Riblets for Turbulent Drag Reduction. In *European Drag Reduction and Flow Control Meeting (EDRFCM)*. Torino (Italy).

Clauser, F.H. 1954 Turbulent Boundary Layers in Adverse Pressure Gradients. *Journal of the Aeronautical Sciences* **21**, 91–108.

Cogo, M., Baù, U., Chinappi, M., Bernardini, M. & Picano, F. 2023 Assessment of heat transfer and Mach number effects on high-speed turbulent boundary layers. *Journal of Fluid Mechanics* **974**, A10.

Coleman, G.N., Kim, J. & Moser, R.D. 1995 A numerical study of turbulent supersonic isothermal-wall channel flow. *Journal of Fluid Mechanics* **305**, 159–183.

Coustols, E. & Cousteix, J. 1994 Performances of riblets in the supersonic regime. *AIAA Journal* **32** (2), 431–433.

Coustols, E. & Savill, A. M. 1992 Turbulent Skin-Friction Drag Reduction By Active and Passive Means. Part 1. Everything you wanted to Know about Riblets, LEBUs and Other Devices,. *Tech. Rep.*. Office National d'Etudes et de Recherches Aerospatiales Toulouse (France).

Danaila, L., Anselmet, F., Zhou, T. & Antonia, R. A. 2001 Turbulent energy scale budget equations in a fully developed channel flow. *Journal of Fluid Mechanics* **430**, 87–109.

Danaila, L., Voivenel, L. & Varea, E. 2017 Self-similarity criteria in anisotropic flows with viscosity stratification. *Physics of Fluids* **29** (2), 020716.

Daniello, R.J., Waterhouse, N.E. & Rothstein, J.P. 2009 Drag reduction in turbulent flows over superhydrophobic surfaces. *Physics of Fluids* **21**, 085103.

Davidson, P.A., Nickels, T.B. & Krogstad, P.-Å. 2006 The logarithmic structure function law in wall-layer turbulence. *Journal of Fluid Mechanics* **550**, 51–60.

Davidson, P. A. 2004 *Turbulence: An Introduction for Scientists and Engineers*. Oxford University Press.

Davis, T. B., Uzun, A. & Alvi, F. S. 2019 Optimal disturbances and large-scale energetic motions in turbulent boundary layers. *Journal of Fluid Mechanics* **860**, 40–80.

de Tullio, M. D. & Pascazio, G. 2016 A moving-least-squares immersed boundary method for simulating the fluid–structure interaction of elastic bodies with arbitrary thickness. *Journal of Computational Physics* **325**, 201–225.

Dean, R.B. 1978 Reynolds number dependence of skin friction and other bulk flow variables in two-dimensional rectangular duct flow. *Journal of Fluids Engineering* **100**, 215–223.

Debisschop, J. & Nieuwstadt, F. 1996 Turbulent Boundary Layer in an Adverse Pressure Gradient: Effectiveness of Riblets. *AIAA Journal* **34** (5), 932–937.

del Álamo, J.C. & Jiménez, J. 2006 Linear energy amplification in turbulent channels. *Journal of Fluid Mechanics* **559**, 205–213.

Deshpande, R., Chandran, D., Smits, A. J. & Marusic, I. 2023 On the relationship between manipulated inter-scale phase and energy-efficient turbulent drag reduction. *Journal of Fluid Mechanics* **972**, A12.

Deshpande, R., Kidanemariam, A. G. & Marusic, I. 2024 Pressure drag reduction via imposition of spanwise wall oscillations on a rough wall. *Journal of Fluid Mechanics* **979**, A21.

Dogan, E., Örlü, R., Gatti, D., Vinuesa, R. & Schlatter, P. 2019 Quantification of amplitude modulation in wall-bounded turbulence. *Fluid Dynamics Research* **51**, 011408.

Du, Y., Symeonidis, V. & Karniadakis, G. E. 2002 Drag reduction in wall-bounded turbulence via a transverse travelling wave. *Journal of Fluid Mechanics* **457**, 1–34.

Duan, L. & Choudhari, M.M. 2012 Effects of Riblets on Skin Friction and Heat Transfer in High-Speed Turbulent Boundary Layers. In *50th AIAA Aerospace Sciences Meeting Including the New Horizons Forum and Aerospace Exposition*. American Institute of Aeronautics and Astronautics.

Duan, L. & Choudhari, M.M. 2014 Direct Numerical Simulations of High-Speed Turbulent Boundary Layers over Riblets. In *52nd Aerospace Sciences Meeting*. American Institute of Aeronautics and Astronautics.

Fadlun, E. A., Verzicco, R., Orlandi, P. & Mohd-Yusof, J. 2000 Combined Immersed-Boundary Finite-Difference Methods for Three-Dimensional Complex Flow Simulations. *Journal of Computational Physics* **161** (1), 35–60.

Fang, J., Lu, L. & Shao, L. 2009 Large eddy simulation of compressible turbulent channel flow with spanwise wall oscillation. *Science in China Series G: Physics, Mechanics and Astronomy* **52** (8), 1233–1243.

Farrell, B.F. & Ioannou, P.J. 1993 Stochastic forcing of the linearized Navier–Stokes equations. *Physics of Fluids* **5** (11), 2600–2609.

Fauci, L. J. & Peskin, C. S. 1988 A computational model of aquatic animal locomotion. *Journal of Computational Physics* **77** (1), 85–108.

Fedkiw, R.P. 2002 Coupling an Eulerian Fluid Calculation to a Lagrangian Solid Calculation with the Ghost Fluid Method. *Journal of Computational Physics* **175** (1), 200–224.

Flores, O. & Jiménez, J. 2010 Hierarchy of minimal flow units in the logarithmic layer. *Physics of Fluids* **22** (7), 071704.

Foggi Rota, G., Monti, A., Rosti, M. E. & Quadrio, M. 2023 On–off pumping for drag reduction in a turbulent channel flow. *Journal of Fluid Mechanics* **966**, A12.

Frohnapfel, B., Hasegawa, Y. & Quadrio, M. 2012 Money versus time: Evaluation of flow control in terms of energy consumption and convenience. *Journal of Fluid Mechanics* **700**, 406–418.

Fukagata, K., Iwamoto, K. & Kasagi, N. 2002 Contribution of Reynolds stress distribution to the skin friction in wall-bounded flows. *Physics of Fluids* **14** (11), L73–L76.

Gad-el-Hak, M. 1996 Compliant coatings: A decade of progress. *Applied Mechanics Reviews* **49** (10), S147–S157.

Gad-el-Hak, M. & Pollard, A., ed. 1998 *Flow Control*, *Lecture Notes in Physics*, vol. 53. Berlin, Heidelberg: Springer.

Gadda, A., Banchetti, J., Romanelli, G. & Quadrio, M. 2017 Drag reduction of a whole-aircraft configuration via spanwise forcing. In *European Drag Reduction and Flow Control Meeting (EDRFCM)*. Monteporziocatone (Italy).

Gai, J., Xia, Z., Cai, Q. & Chen, S. 2016 Turbulent statistics and flow structures in spanwise-rotating turbulent plane Couette flows. *Physical Review Fluids* **1** (5), 054401.

Gallorini, E. & Quadrio, M. 2024 Spatial discretization effects in spanwise forcing for turbulent drag reduction. *Journal of Fluid Mechanics* **982**, A11.

Gallorini, E., Quadrio, M. & Gatti, D. 2022 Coherent near-wall structures and drag reduction by spanwise forcing. *Physical Review Fluids* **7** (11), 114602.

Gao, T., Tseng, Y.-H. & Lu, X.-Y. 2007 An improved hybrid Cartesian/immersed boundary method for fluid–solid flows. *International Journal for Numerical Methods in Fluids* **55** (12), 1189–1211.

García-Mayoral, R., Gómez-de-Segura, G. & Fairhall, C. T. 2019 The control of near-wall turbulence through surface texturing. *Fluid Dynamics Research* **51** (1), 011410.

García-Mayoral, R. & Jiménez, J. 2011 Drag reduction by riblets. *Philosophical Transactions of the Royal Society A* **369** (1940), 1412–1427.

Garcia-Mayoral, R. & Jiménez, J. 2011 Hydrodynamic stability and the breakdown of the viscous regime over riblets. *Journal of Fluid Mechanics* **678**, 317–347.

Gattere, F., Chiarini, A., Cavallazzi, G.M., Rossi, A., Gatti, D. & Luchini, P. 2022*a* Towards Reliable and Cost-Effective DNS over Riblets. In *European Drag Reduction and Flow Control Meeting (EDRFCM)*. Paris (France).

Gattere, F., Chiarini, A., Gallorini, E. & Quadrio, M. 2023 Structure function tensor equations with triple decomposition. *Journal of Fluid Mechanics* **960**, A7.

Gattere, F., Chiarini, A. & Quadrio, M. 2022*b* Dimples for Skin-Friction Drag Reduction: Status and Perspectives. *Fluids* **7** (7), 240.

Gattere, F., Chiarini, A., Zanolini, M., Gatti, D., Bernardini, M. & Quadrio, M. 2022*c* Turbulent drag reduction using spanwise forcing in compressible regime. In *European Drag Reduction and Flow Control Meeting (EDRFCM)*. Paris (France).

Gattere, F., Zanolini, M., Gatti, D., Bernardini, M. & Quadrio, M. 2024 Turbulent drag reduction with streamwise-travelling waves in the compressible regime. *Journal of Fluid Mechanics* **987**, A30.

Gatti, D., Chiarini, A., Cimarelli, A. & Quadrio, M. 2020 Structure function tensor equations in inhomogeneous turbulence. *Journal of Fluid Mechanics* **898**, A5–33.

Gatti, D., Cipelli, S., Gattere, F., Chiarini, A., Luchini, P. & Quadrio, M. 2023 Accurate and efficient Direct Numerical SImulation of drag reduction with riblets. In *Euromech Turbulence Conference (ETC18)*. Valencia (Spain).

Gatti, D., Güttler, A., Frohnapfel, B. & Tropea, C. 2015 Experimental assessment of spanwise-oscillating dielectric electroactive surfaces for turbulent drag reduction in an air channel flow. *Experiments in Fluids* **56** (5), 1–15.

Gatti, D. & Quadrio, M. 2013 Performance losses of drag-reducing spanwise forcing at moderate values of the Reynolds number. *Physics of Fluids* **25**, 125109(17).

Gatti, D. & Quadrio, M. 2016 Reynolds-number dependence of turbulent skin-friction drag reduction induced by spanwise forcing. *Journal of Fluid Mechanics* **802**, 553–58.

Gatti, D., Remigi, A., Chiarini, A., Cimarelli, A. & Quadrio, M. 2019 An efficient numerical method for the Generalized Kolmogorov Equation. *Journal of Turbulence* **20** (8), 457–480.

Gatti, D., Stroh, A., Frohnapfel, B. & Hasegawa, Y. 2018 Predicting Turbulent Spectra in Drag-reduced Flows. *Flow, Turbulence and Combustion* **100** (4), 1081–1099.

Gaudet, L. 1989 Properties of riblets at supersonic speed. *Applied Scientific Research* **46** (3), 245–254.

Ge, M.-W., Fang, Le & Liu, Y.-Qi. 2017 Drag reduction of wall bounded incompressible turbulent flow based on active dimples/pimples. *Journal of Hydrodynamics* **29** (2), 261–271.

Ghias, R., Mittal, R. & Dong, H. 2007 A sharp interface immersed boundary method for compressible viscous flows. *Journal of Computational Physics* **225** (1), 528–553.

Gibou, F., Fedkiw, R.P., Cheng, L.-T. & Kang, M. 2002 A Second-Order-Accurate Symmetric Discretization of the Poisson Equation on Irregular Domains. *Journal of Computational Physics* **176** (1), 205–227.

Goldstein, D., Handler, R. & Sirovich, L. 1993 Modeling a No-Slip Flow Boundary with an External Force Field. *Journal of Computational Physics* **105** (2), 354–366.

Gómez-de-Segura, G., Fairhall, C. T., MacDonald, M., Chung, D. & García-Mayoral, R. 2018 Manipulation of near-wall turbulence by surface slip and permeability. *Journal of Physics: Conference Series* **1001** (1), 012011.

Gouder, K., Potter, M. & Morrison, J.F. 2013 Turbulent friction drag reduction using electroactive polymer and electromagnetically driven surfaces. *Experiments in Fluids* **54** (1), 1441.

Griffith, B.E. & Patankar, Neelesh A. 2020 Immersed Methods for Fluid–Structure Interaction. *Annual Review of Fluid Mechanics* **52** (1), 421–448.

Güttler, A. 2015 High accuracy determination of skin friction differences in an air channel flow based on pressure drop measurements. PhD thesis.

Hama, F. R. 1954 Boundary-layer characteristics for ough and smooth surfaces. In *Society of Naval Architects and Marine Engineers*, , vol. 62, pp. 333–351.

Hasegawa, Y., Frohnapfel, B. & Kasagi, N. 2011 Effects of spatially varying slip length on friction drag reduction in wall turbulence. *Journal of Physics: Conference Series* **318** (2), 022028.

Hasegawa, Y., Quadrio, M. & Frohnapfel, B. 2014 Numerical simulation of turbulent duct flows at constant power input. *Journal of Fluid Mechanics* **750**, 191–209.

Hill, R. J. 2001 Equations relating structure functions of all orders. *Journal of Fluid Mechanics* **434**, 379–388.

Högberg, M., Bewley, T.R. & Henningson, D. 2003 Linear feedback control and estimation of transition in plane channel flow. *Journal of Fluid Mechanics* **481**, 149–175.

Huang, P. G., Coleman, G. N. & Bradshaw, P. 1995 Compressible turbulent channel flows: DNS results and modelling. *Journal of Fluid Mechanics* **305**, 185–218.

Hurst, E., Yang, Q. & Chung, Y.M. 2014 The effect of Reynolds number on turbulent drag reduction by streamwise travelling waves. *Journal of Fluid Mechanics* **759**, 28–55.

Hussain, A.K.M.F. & Reynolds, W.C. 1972 The mechanics of an organized wave in turbulent shear flow. Part 2. Experimental results. *Journal of Fluid Mechanics* **54** (2), 241–261.

Iaccarino, G. & Verzicco, R. 2003 Immersed boundary technique for turbulent flow simulations. *Applied Mechanics Reviews* **56** (3), 331–347.

Ibrahim, J. I., Gomez-de-Segura, G., Chung, D. & Garcia-Mayoral, R. 2021 The smooth-wall-like behaviour of turbulence over drag-altering surfaces: A unifying virtual-origin framework. *Journal of Fluid Mechanics* **915**, A56.

Jeong, J., Hussain, F., Schoppa, W. & Kim, J. 1997 Coherent structures near the wall in a turbulent channel flow. *Journal of Fluid Mechanics* **332**, 185–214.

Jimenez, J. 1994 On the structure and control of near wall turbulence. *Phys. Fluids* **6**, 944–953.

Jiménez, J. 2004 Turbulent Flows Over Rough Walls. *Annual Review of Fluid Mechanics* **36** (1), 173–196.

Jimenez, J. 2013 How linear is wall-bounded turbulence? *Physics of Fluids* **25**, 110814/20.

Jiménez, J. 2013 Near-wall turbulence. *Physics of Fluids* **25** (10), 101302.

Jiménez, J. 2018 Coherent structures in wall-bounded turbulence. *Journal of Fluid Mechanics* **842** (P1), 1–99.

Jiménez, J. & Moin, P. 1991 The minimal flow unit in near-wall turbulence. *Journal of Fluid Mechanics* **225**, 213–240.

Jovanović, M. R. & Bamieh, B. 2005 Componentwise energy amplification in channel flows. *Journal of Fluid Mechanics* **534**, 145–183.

Jukes, T.N. & Choi, K.-S. 2012 Dielectric-barrier-discharge vortex generators: Characterisation and optimisation for flow separation control. *Experiments in Fluids* **52**, 329–345.

Jung, W.J., Mangiavacchi, N. & Akhavan, R. 1992 Suppression of turbulence in wall-bounded flows by high-frequency spanwise oscillations. *Physics of Fluids A* **4 (8)**, 1605–1607.

Karban, U., Bugeat, B., Martini, E., Towne, A., Cavalieri, A. V. G., Lesshafft, L., Agarwal, A., Jordan, P. & Colonius, T. 2020 Ambiguity in mean-flow-based linear analysis. *Journal of Fluid Mechanics* **900**, R5.

Kasagi, N., Hasegawa, Y. & Fukagata, K. 2009 Towards cost-effective control of wall turbulence for skin-friction drag reduction. In *Advances in Turbulence XII* (ed. B. Eckhardt), , vol. 132, pp. 189–200. Springer.

Kawata, T. & Alfredsson, P. H. 2018 Inverse interscale transport of the Reynolds shear stress in plane Couette turbulence. *Physical Review Letters* **120** (24), 244501.

Kempaiah, K.U., Scarano, F., Elsinga, G.E., van Oudheusden, B.W. & Bermel, Leon 2020 3-dimensional particle image velocimetry based evaluation of turbulent skin-friction reduction by spanwise wall oscillation. *Physics of Fluids* **32** (8), 085111.

Kiknadze, G., Gachechiladze, I. & Barnaveli, T. 2012 The Mechanisms of the Phenomenon of Tornado-Like Jets Self-Organization in the Flow Along the Dimples on the Initially Flat Surface. In *International Mechanical Engineering Congress and Exposition, Proceedings (IMECE)*, , vol. 7.

Kiknadze, G. I., Krasnov, Yu. K. & Chushkin, Yu. V. 1984 Investigation of the Enhancement of Heat Transfer Due to Self-organization of Ordered Dynamic Twisted Heat-carrier Structures on a Heat-transfer Surface. *Tech. Rep.* 50.05/59. I. V. Kurchatov Institute of Atomic Energy, Moscow (Russia).

Kim, J. & Bewley, T.R. 2007 A linear systems approach to flow control. *Annual Review of Fluid Mechanics* **39**, 383–417.

Kim, J. & Hussain, F. 1993 Propagation velocity of perturbations in turbulent channel flow. *Physics of Fluids A* **5** (3), 695–706.

Kim, J. & Lim, J. 2000 A linear process in wall-bounded turbulent shear flows. *Physics of Fluids* **12** (8), 1885–1888.

Kim, J. & Moin, P. 1985 Application of a fractional-step method to incompressible Navier-Stokes equations. *Journal of Computational Physics* **59** (2), 308–323.

Kim, J., Moin, P. & Moser, R. 1987 Turbulence statistics in fully developed channel flow at low Reynolds number. *Journal of Fluid Mechanics* **177**, 133–166.

Kim, Y. & Lai, M.-C. 2010 Simulating the dynamics of inextensible vesicles by the penalty immersed boundary method. *Journal of Computational Physics* **229** (12), 4840–4853.

Kim, Y. & Peskin, C.S. 2007 Penalty immersed boundary method for an elastic boundary with mass. *Physics of Fluids* **19** (5), 053103.

Kiya, M. & Matsumura, M. 1988 Incoherent turbulence structure in the near wake of a normal plate. *Journal of Fluid Mechanics* **190**, 343–356.

Koepplin, V., Herbst, F. & Seume, J. R. 2017 Correlation-based riblet model for tubomachinery applications. *Journal of Turbomachinery* **139**.

Koschmieder, E. L. 1979 Turbulent Taylor vortex flow. *Journal of Fluid Mechanics* **93**, 515–527.

Kovalenko, G.V., Terekhov, V.I. & Khalatov, A.A. 2010 Flow regimes in a single dimple on the channel surface. *Journal of Applied Mechanics and Technical Physics* **51** (6), 839–848.

Kraichnan, R. H. 1959 The structure of isotropic turbulence at very high Reynolds numbers. *Journal of Fluid Mechanics* **5**, 497–543.

Kurita, M., Iijima, H., Koga, S., Nishizawa, A., Kwak, D., Iijima, Y., Takahashi, H. & Abe, H. 2020 Flight Test for Paint Riblets. *AIAA Scitech 2020 Forum* .

Kurita, M., Nishizawa, A., Kwak, D., Iijima, H., Iijima, Y., Takahashi, H., Sasamori, M., Abe, H., Koga, S. & Nakakita, K. 2018 Flight Test of a Paint-Riblet for Reducing Skin Friction. *AIAA 2018 Applied Aerodynamics Conference* pp. 1–7.

Laadhari, F., Skandaji, L. & Morel, R. 1994 Turbulence reduction in a boundary layer by a local spanwise oscillating surface. *Physics of Fluids* **6 (10)**, 3218–3220.

Ladson, C. L. 1988 Effects of independent variation of Mach and Reynolds numbers on the low-speed aerodynamic characteristics of the NACA 0012 airfoil section. *NASA TM 4074* .

Lai, C. K., Charonko, J.J. & Prestridge, K. 2018 A Kármán–Howarth–Monin equation for variable-density turbulence. *Journal of Fluid Mechanics* **843**, 382–418.

Lashkov, Y.A. & Samoilova, N.V. 2002 On the viscous drag of a plate with spherical recesses. *Fluid Dynamics* **37** (2), 231–236.

Leonardi, S., Orlandi, P., Djenidi, L. & Antonia, R. A. 2015 Heat transfer in a turbulent channel flow with square bars or circular rods on one wall. *Journal of Fluid Mechanics* **776**, 512–530.

Leontiev, A.I., Kiselev, N.A., Vinogradov, Yu.A., Strongin, M.M., Zditovets, A.G. & Burtsev, S.A. 2017 Experimental investigation of heat transfer and drag on surfaces coated with dimples of different shape. *International Journal of Thermal Sciences* **118**, 152–167.

Li, C., Jiang, J., Dong, H. & Zhao, K. 2017 Computational modeling and validation of human nasal airflow under various breathing conditions. *Journal of Biomechanics* **64**, 59–68.

Li, C.H., Kaura, A., Tan, C., Whitcroft, K.L., Leung, T.S. & Andrews, P. 2020 Diagnosing nasal obstruction and its common causes using the nasal acoustic device: A pilot study. *Laryngoscope Investigative Otolaryngology* **5** (5), 796–806.

Li, C.-G., Bale, R., Wang, W. & Tsubokura, M. 2023 A sharp interface immersed boundary method for thin-walled geometries in viscous compressible flows. *International Journal of Mechanical Sciences* **253**, 108401.

Lienhart, H., Breuer, M. & Köksoy, C. 2008 Drag reduction by dimples? - A complementary experimental/numerical investigation. *International Journal of Heat and Fluid Flow* **29** (3), 783–791.

Liu, X., Zhu, H., Bao, Y., Zhou, D. & Han, Z. 2022 Turbulence suppression by streamwise-varying wall rotation in pipe flow. *Journal of Fluid Mechanics* **951**, A35.

Luchini, P. 1991 A deferred correction multigrid algorithm based on a new smoother for the Navier–Stokes equations. *Journal of Computational Physics* **92**, 349–368.

Luchini, P. 1996 Reducing the turbulent skin friction. In *Computational Methods in Applied Sciences 1996* (ed. Desideri et al.). Wiley.

Luchini, P. 2013 Linearized no-slip boundary conditions at a rough surface. *Journal of Fluid Mechanics* **737**, 349–367.

Luchini, P. 2016 Immersed-boundary simulations of turbulent flow past a sinusoidally undulated river bottom. *European Journal of Mechanics - B/Fluids* **55**, 340–347.

Luchini, P. 2017 Universality of the Turbulent Velocity Profile. *Physical Review Letters* **118** (22), 224501.

Luchini, P. 2020 CPL. Available at https://CPLcode.net.

Luchini, P. 2021 Introducing CPL. *2012.12143* , arXiv: 2012.12143.

Luchini, P., Bewley, T. & Quadrio, M. 2005 An optimal feedback controller for the reduction of turbulent energy in 3D plane-duct flow. In *APS Meeting, Chicago, IL (US), November 20-22*.

Luchini, P., Manzo, F. & Pozzi, A. 1991 Resistance of a grooved surface to parallel flow and cross-flow. *Journal of Fluid Mechanics* **228**, 87–109.

Luchini, P. & Quadrio, M. 2006 A low-cost parallel implementation of direct numerical simulation of wall turbulence. *Journal of Computational Physics* **211** (2), 551–571.

Luchini, P., Quadrio, M. & Zuccher, S. 2006 Phase-locked linear response of a turbulent channel flow. *Physics of Fluids* **18** (121702), 1–4.

Lumley, J. 1977 Drag reduction in two-phase and polymer flows. *Physics of Fluids* **20** (10), 64.

Madhusudanan, A., Illingworth, S. J. & Marusic, I. 2019 Coherent large-scale structures from the linearized Navier–Stokes equations. *Journal of Fluid Mechanics* **873**, 89–109.

Mansour, N., Kim, J. & Moin, P. 1988 Reynolds-stress and dissipation-rate budgets in a turbulent channel flow. *Journal of Fluid Mechanics* **194**, 15–44.

Martinelli, F. 2009 Feedback control of turbulent wall flows. PhD thesis, Politecnico di Milano.

Marusic, I., Chandran, D., Rouhi, A., Fu, M.K., Wine, D., Holloway, B., Chung, D. & Smits, A.J. 2021 An energy-efficient pathway to turbulent drag reduction. *Nature Communications* **12** (1), 5805.

McKeon, B. J. 2017 The engine behind (wall) turbulence: Perspectives on scale interactions. *Journal of Fluid Mechanics* **817**, P1.

McKeon, B. J. & Sharma, A. S. 2010 A critical-layer framework for turbulent pipe flow. *Journal of Fluid Mechanics* **658**, 336–382.

McLean, J., George-Falvy, D. & Sullivan, P. 1987 Flight test of turbulent skin-friction reduction by riblets. In *Proc. RAeS Int. Conf. on Turbulent Drag Reduction by Passive Means, London*, , vol. RAeS 2, pp. 408–424. Royal Aeronautical Society.

Mele, B. & Tognaccini, R. 2012 Numerical Simulation of Riblets on Airfoils and Wings. In *50th AIAA Aerospace Sciences Meeting Including the New Horizons Forum and Aerospace Exposition*. American Institute of Aeronautics and Astronautics.

Mele, B. & Tognaccini, R. 2018 Slip Length–Based Boundary Condition for Modeling Drag Reduction Devices. *AIAA Journal* **56** (9), 3478–3490.

Mele, B., Tognaccini, R. & Catalano, P. 2016 Performance assessment of a transonic wing-body configuration with riblets installed. *Journal of Aircraft* **53** (1), 129–140.

Mele, B., Tognaccini, R., Catalano, P. & de Rosa, D. 2020 Effect of body shape on riblets performance. *Physical Review Fluids* **5** (12), 124609.

Menter, F.R. 1994 Two-Equation Eddy-Viscosity Turbulence Models for Engineering Applications. *AIAA Journal* **32** (8), 1598–1605.

Mickley, H. S., Ross, R. C., Squyers, A. L. & Stewart, W. E. 1954 Heat, Mass, and Momentum Transfer for Flow over a Flat Plate with Blowing or Suction. *Tech. Rep.*.

Mittal, R., Dong, H., Bozkurttas, M., Najjar, F.M., Vargas, A. & von Loebbecke, A. 2008 A versatile sharp interface immersed boundary method for incompressible flows with complex boundaries. *Journal of Computational Physics* **227** (10), 4825–4852.

Mittal, R. & Iaccarino, G. 2005 Immersed Boundary Methods. *Annual Review of Fluid Mechanics* **37** (1), 239–261.

Mittal, R. & Seo, J.H. 2023 Origin and evolution of immersed boundary methods in computational fluid dynamics. *Physical Review Fluids* **8** (10), 100501.

Modesti, D., Sathyanarayana, S., Salvadore, F. & Bernardini, M. 2022 Direct numerical simulation of supersonic turbulent flows over rough surfaces. *Journal of Fluid Mechanics* **942**, A44.

Mollicone, J.-P., Battista, F., Gualtieri, P. & Casciola, C. M. 2018 Turbulence dynamics in separated flows: The generalised Kolmogorov equation for inhomogeneous anisotropic conditions. *Journal of Fluid Mechanics* **841**, 1012–1039.

Nakanishi, R., Mamori, H. & Fukagata, K. 2012 Relaminarization of turbulent channel flow using traveling wave-like wall deformation. *International Journal of Heat and Fluid Flow* **35**, 152–159.

Ng, J.H., Jaiman, R.K. & Lim, T.T. 2018 A numerical study for passive turbulent drag reduction via shallow dimples. In *21st Australasian Fluid Mechanics Conference*.

Ng, J.H., Jaiman, R.K., Lim, T.T., Tay, C.M. & Khoo, B.C. 2020 Geometric Effects of Shallow Dimples in Turbulent Channel Flows at $Re_\tau \approx 180$: A Vorticity Transport Perspective. *Flow Turbulence and Combustion* **105**, 83–122.

Nguyen, V.-T., Ricco, P. & Pironti, G. 2021 Separation drag reduction through a spanwise oscillating pressure gradient. *Journal of Fluid Mechanics* **912**, A20, pp.1–42.

Ni, W., Lu, L., Le Ribault, C. & Fang, J. 2016 Direct Numerical Simulation of Supersonic Turbulent Boundary Layer with Spanwise Wall Oscillation. *Energies* **9** (3), 154.

Nieuwstadt, F. T. M., Wolthers, W., Leijdens, H., Krishna Prasad, K. & Schwarz-van Manen, A. 1993 The reduction of skin friction by riblets under the influence of an adverse pressure gradient. *Experiments in Fluids* **15** (1), 17–26.

Nikuradse, J. 1933 Strömungsgesteze in Rauhen Rohren. *VDI Forsch. 361* .

Orlandi, P. 2006 *Fluid Flow Phenomena: A Numerical Toolkit*. Kluwer Academic Publishers.

Orlandi, P. & Leonardi, S. 2006 DNS of turbulent channel flows with two- and three-dimensional roughness. *Journal of Turbulence* **7**, N73.

Orr, W. M. F. 1907 The stability or instability of the steady motions of a perfect liquid and of a viscous liquid. Part II. A viscous liquid. *Proceedings of the Royal Irish Academy. Section A: Mathematical and Physical Sciences* **27**, 69–138.

Pan, D. & Shen, T.-T. 2009 Computation of incompressible flows with immersed bodies by a simple ghost cell method. *International Journal for Numerical Methods in Fluids* **60** (12), 1378–1401.

Peet, Y., Sagaut, P. & Charron, Y. 2008 Turbulent Drag Reduction using Sinusoidal Riblets with Triangular Cross-Section. *AIAA Paper 2008-3745* .

Peskin, C.S. 1972 Flow patterns around heart valves: A numerical method. *Journal of Computational Physics* **10** (2), 252–271.

Pirozzoli, S. 2023 Searching for the log law in open channel flow. *Journal of Fluid Mechanics* **971**, A15.

Pirozzoli, S. & Orlandi, P. 2021 Natural grid stretching for DNS of wall-bounded flows. *Journal of Computational Physics* **439**, 110408.

Pope, S. B. 2000 *Turbulent Flows*. Cambridge University Press, Cambridge.

Praß, J., Wannmacher, H., Franke, J. & Becker, S. 2019 The Influence of Different Arrangements of Shallow Dimples on the Resistance of Plates Subjected to Relative Fluid Motion. *Technische Mechanik - European Journal of Engineering Mechanics* **39(1)**, 39–50.

Provansal, M., Mathis, C. & Boyer, L. 1987 Bénard-von Kármán instability: Transient and forced regimes. *Journal of Fluid Mechanics* **182**, 1–22.

Quadrio, M. 2011 Drag reduction in turbulent boundary layers by in-plane wall motion. *Philosophical Transactions of the Royal Society A* **369** (1940), 1428–1442.

Quadrio, M., Chiarini, A., Banchetti, J., Gatti, D., Memmolo, A. & Pirozzoli, S. 2022 Drag reduction on a transonic airfoil. *Journal of Fluid Mechanics* **942**, R2, 1–10.

Quadrio, M., Frohnapfel, B. & Hasegawa, Y. 2016*a* Does the choice of the forcing term affect flow statistics in DNS of turbulent channel flow? *European Journal of Mechanics - B/Fluids* **55**, 286–293.

Quadrio, M. & Luchini, P. 2002 The linear response of a turbulent channel flow. In *Proc. IX European Turbulence Conf., Southampton (UK), July 2-5.*, pp. 715–718.

Quadrio, M. & Luchini, P. 2003 Integral time-space scales in turbulent wall flows. *Physics of Fluids* **15** (8), 2219–2227.

Quadrio, M., Pipolo, C., Corti, S., Messina, F., Pesci, C., Saibene, A.M., Zampini, S. & Felisati, G. 2016*b* Effect of CT resolution and radiodensity threshold on the CFD evaluation of nasal airflow. *Medical & Biological Engineering & Computing* **54**, 411–419.

Quadrio, M. & Ricco, P. 2004 Critical assessment of turbulent drag reduction through spanwise wall oscillation. *Journal of Fluid Mechanics* **521**, 251–271.

Quadrio, M. & Ricco, P. 2011 The laminar generalized Stokes layer and turbulent drag reduction. *Journal of Fluid Mechanics* **667**, 135–157.

Quadrio, M., Ricco, P. & Viotti, C. 2009 Streamwise-traveling waves of spanwise wall velocity for turbulent drag reduction. *Journal of Fluid Mechanics* **627**, 161–178.

Quadrio, M. & Sibilla, S. 2000 Numerical simulation of turbulent flow in a pipe oscillating around its axis. *Journal of Fluid Mechanics* **424**, 217–241.

Quadrio, M., Viotti, C. & Luchini, P. 2007 Skin-friction drag reduction via steady streamwise oscillations of spanwise velocity. In *Advances in Turbulence XI* (ed. J.M.L.M. Palma & Silva Lopes A.), pp. 659–661. Springer, Berlin.

Rai, M.M. & Moin, P. 1991 Direct simulations of turbulent flow using finite-difference schemes. *Journal of Computational Physics* **96**, 15.

Reddy, S.C., Schmid, P.J., Bagget, J.S. & Henningson, D.S. 1998 On stability of streamwise streaks and transition thresholds in plane channel flows. *Journal of Fluid Mechanics* **365**, 269–303.

Reynolds, W.C. & Tiedermann, W.G. 1967 Stability of Turbulent Channel Flow, with Application to Malkus' Theory. *Journal of Fluid Mechanics* **27**, 253–272.

Ricco, P. 2004 Modification of near-wall turbulence due to spanwise wall oscillations. *Journal of Turbulence* **5** (24).

Ricco, P. & Hahn, S. 2013 Turbulent drag reduction through rotating discs. *Journal of Fluid Mechanics* **722**, 267–290.

Ricco, P., Ottonelli, C., Hasegawa, Y. & Quadrio, M. 2012 Changes in turbulent dissipation in a channel flow with oscillating walls. *Journal of Fluid Mechanics* **700**, 77–104.

Ricco, P. & Quadrio, M. 2008 Wall-oscillation conditions for drag reduction in turbulent channel flow. *International Journal of Heat and Fluid Flow* **29**, 601–612.

Ricco, P., Skote, M. & Leschziner, M. A. 2021 A review of turbulent skin-friction drag reduction by near-wall transverse forcing. *Progress in Aerospace Sciences* **123**, 100713.

Robinson, S. K. 1991 Coherent motions in the turbulent boundary layer. *Annual Review of Fluid Mechanics* **23**, 601–639.

Rouhi, A., Fu, M. K., Chandran, D., Zampiron, A., Smits, A. J. & Marusic, I. 2023 Turbulent drag reduction by spanwise wall forcing. Part 1: Large-eddy simulations. *Journal of Fluid Mechanics* **268**, A6.

Ruby, M. & Foysi, H. 2022 Active control of compressible channel flow up to $\mathrm{Ma_b} = 3$ using direct numerical simulations with spanwise velocity modulation at the walls. *GAMM-Mitteilungen* **45**, e202200004.

Russo, S. & Luchini, P. 2016 The linear response of turbulent flow to a volume force: Comparison between eddy-viscosity model and DNS. *Journal of Fluid Mechanics* **790**, 104–127.

Russo, S. & Luchini, P. 2017 A fast algorithm for the estimation of statistical error in DNS (or experimental) time averages. *Journal of Computational Physics* **347**, 328–340.

Saiki, E. M. & Biringen, S. 1996 Numerical Simulation of a Cylinder in Uniform Flow: Application of a Virtual Boundary Method. *Journal of Computational Physics* **123** (2), 450–465.

Sasamori, M., Mamori, H., Iwamoto, K. & Murata, A. 2014 Experimental study on drag-reduction effect due to sinusoidal riblets in turbulent channel flow. *Experiments in Fluids* **55**, 1828.

Schlichting, H. & Gersten, K. 2000 *Boundary-Layer Theory*. Springer, Berlin.

Schmid, P. 2007 Nonmodal stability theory. *Annual Review of Fluid Mechanics* **39**, 129–162.

Schoppa, W. & Hussain, F. 2002 Coherent structure generation in near-wall turbulence. *Journal of Fluid Mechanics* **453**, 57–108.

Selvatici, D., Quadrio, M. & Chiarini, A. 2023 Curvature effects on the structure of near-wall turbulence. *Journal of Fluid Mechanics* **972**, A39.

Seo, J.H. & Mittal, R. 2011 A sharp-interface immersed boundary method with improved mass conservation and reduced spurious pressure oscillations. *Journal of Computational Physics* **230** (19), 7347–7363.

Shapiro, A.H. 1953 *The Dynamics and Thermodynamics of Compressible Fluid Flow*. Ronald Press Company.

Skote, M. 2014 Scaling of the velocity profile in strongly drag reduced turbulent flows over an oscillating wall. *International Journal of Heat and Fluid Flow* **50**, 352–358.

Skote, M. 2022 Drag Reduction of Turbulent Boundary Layers by Travelling and Non-Travelling Waves of Spanwise Wall Oscillations. *Fluids* **7** (2), 65.

Skote, M., Schlatter, P. & Wu, Y. 2015 Numerical studies of active control of turbulent boundary layers using transverse travelling waves. In *International Symposium On Turbulence and Shear Flow Phenomena (TSFP-9)*, p. 6. S. Tavoularis, & I. Marusic (Eds.). University of Melbourne.

Sotiropoulos, F. & Yang, X. 2014 Immersed boundary methods for simulating fluid–structure interaction. *Progress in Aerospace Sciences* **65**, 1–21.

Spalart, P.R. & McLean, J.D. 2011 Drag reduction: Enticing turbulence, and then an industry. *Philosophical Transactions of the Royal Society A* **369** (1940), 1556–1569.

Spalart, P.R., Shur, M., Strelets, M., Travin, A., Paschal, K.B. & Wilkinson, S.P. 2019 Experimental and numerical study of the turbulent boundary layer over shallow dimples. *International Journal of Heat and Fluid Flow* **78**, 108438.

Sundaram, S., Viswanath, P.R. & Rundrakumar, S. 1996 Viscous drag reduction using riblets on NACA 0012 airfoil to moderate incidence. *AIAA Journal* **34** (4).

Szodruch, J. 1991 Viscous drag reduction on transport aircraft. In *29th Aerospace Sciences Meeting*. Reno,NV (U.S.A.): American Institute of Aeronautics and Astronautics.

Tauwald, S.M., Erzinger, F., Quadrio, M., Rütten, M., Stemmer, C. & Krenkel, L. 2024 Tomo-PIV in a patient-specific model of human nasal cavities: A methodological approach. *Measurement Science and Technology* **35** (5), 055203.

Tay, C.M.J. 2011 Determining the effect of dimples on drag in a turbulent channel flow. In *49th AIAA Aerospace Sciences Meeting Including the New Horizons Forum and Aerospace Exposition*, p. 682.

Tay, C.M.J., Chew, Y.T., Khoo, B.C. & Zhao, J.B. 2014 Development of flow structures over dimples. *Experimental Thermal and Fluid Science* **52**, 278–287.

Tay, C.M.J., Khoo, B.C. & Chew, Y.T. 2015 Mechanics of drag reduction by shallow dimples in channel flow. *Physics of Fluids* **27** (3), 035109.

Tay, C.M.J., Khoo, B.C. & Chew, Y.T. 2017 Use of DES in mildly separated internal flow: Dimples in a turbulent channel. *Journal of Turbulence* **18** (12), 1180–1203.

Tay, C.M.J. & Lim, T.T. 2017 Drag reduction with non-axisymmetric dimples. In *35th AIAA Applied Aerodynamics Conference*, p. 3569. Denver, CO (U.S.A.).

Tay, C.M.J. & Lim, T.T. 2018 Drag reduction with teardrop-shaped dimples. In *2018 Flow Control Conference*, p. 3528. Atlanta, GA (U.S.A.).

Tay, C.M.J., Lim, T.T. & Khoo, B.C. 2019 Drag reduction with diamond-shaped dimples. In *AIAA Aviation 2019 Forum*, p. 3296. Dallas, TX (U.S.A.).

Tay, C.M.J., Lim, T.T., Khoo, B.C. & Jaiman, R.K. 2016 Effectiveness of triangular depressions and asymmetric circular dimples for drag reduction. In *20th Australasian Fluid Mechanics Conference.*. Perth (Australia).

Theodorsen, T. 1952 Mechanism of turbulence. In *Second Midwestern Conference on Fluid Mechanics*, pp. 1–18. Columbus, OH (U.S.A.).

Thiesset, F. & Danaila, L. 2020 The illusion of a Kolmogorov cascade. *Journal of Fluid Mechanics* **902**, F1.

Thiesset, F., Danaila, L. & Antonia, R. A. 2014 Dynamical interactions between the coherent motion and small scales in a cylinder wake. *Journal of Fluid Mechanics* **749**, 201–226.

Tomiyama, N. & Fukagata, K. 2013 Direct numerical simulation of drag reduction in a turbulent channel flow using spanwise traveling wave-like wall deformation. *Physics of Fluids* **25**, 105115.

Touber, E. & Leschziner, M.A. 2012 Near-wall streak modification by spanwise oscillatory wall motion and drag-reduction mechanisms. *Journal of Fluid Mechanics* **693**, 150–200.

Townsend, A.A. 1976 *The Structure Of Turbulent Shear Flows*, 2nd edn. Cambridge University Press.

Trefethen, L.N., Trefethen, A.E., Reddy, S.C. & Driscoll, T.A. 1993 Hydrodynamic stability without eigenvalues. *Science* **261** (5121), 578–584.

Trujillo, S.M., Bogard, D.G. & Ball, K.S. 1997 Turbulent Boundary Layer Drag Reduction using an Oscillating Wall. *AIAA Paper 97-1870* .

Tseng, Y.-H. & Ferziger, J.H. 2003 A ghost-cell immersed boundary method for flow in complex geometry. *Journal of Computational Physics* **192** (2), 593–623.

Uhlmann, M. 2005 An immersed boundary method with direct forcing for the simulation of particulate flows. *Journal of Computational Physics* **209** (2), 448–476.

Vadarevu, S.B., Symon, S., Illingworth, S.J. & Marusic, I. 2019 Coherent structures in the linearized impulse response of turbulent channel flow. *Journal of Fluid Mechanics* **863**, 1190–1203.

Van Campenhout, O.W.G., Van Nesselrooij, M., Veldhuis, L.L.M., Van Oudheusden, B.W. & Schrijer, F.F.J. 2018 An experimental investigation into the flow mechanics of dimpled surfaces in turbulent boundary layers. In *2018 AIAA Aerospace Sciences Meeting*, p. 2062.

Van Nesselrooij, M., Van Campenhout, O.W.G., Van Oudheusden, B.W., Schrijer, F.F.J. & Veldhuis, L.L.M. 2022 Development of an experimental apparatus for flat plate drag measurements and considerations for such measurements. *Measurement Science and Technology* **33** (5).

Van Nesselrooij, M., Veldhuis, L.L.M., Van Oudheusden, B.W. & Schrijer, F.F.J. 2016 Drag reduction by means of dimpled surfaces in turbulent boundary layers. *Experiments in Fluids* **57** (9), 142.

Veldhuis, L. & Vervoort, E. 2009 Drag effect of a dented surface in a turbulent flow. In *27th AIAA Applied Aerodynamics Conference*, p. 3950.

Verzicco, R. 2023 Immersed Boundary Methods: Historical Perspective and Future Outlook. *Annual Review of Fluid Mechanics* **55** (1), 129–155.

Viotti, C., Quadrio, M. & Luchini, P. 2009 Streamwise oscillation of spanwise velocity at the wall of a channel for turbulent drag reduction. *Physics of Fluids* **21**, 115109.

Viswanath, P.R. 2002 Aircraft viscous drag reduction using riblets. *Progress in Aerospace Sciences* **38**, 571–600.

Walsh, M.J. 1980 Drag characteristics of v-groove and transverse curvature riblets. *In Viscous Drag reduction (ed. G.R. Hough). American Institute of Aeronautics and Astronautics.* .

Walsh, M. J., Sellers, L. W. & McGinley, C. B. 1989 Riblet drag at flight conditions. *Journal of Aircraft* **26** (6), 570–575.

Walsh, M. J. & Weinstein, L. M. 1979 Drag and Heat-Transfer Characteristics of Small Longitudinally Ribbed Surfaces. *AIAA Journal* **17** (7), 770–771.

Wang, D.Y., Lee, H.P. & Gordon, R. 2012 Impacts of Fluid Dynamics Simulation in Study of Nasal Airflow Physiology and Pathophysiology in Realistic Human Three-Dimensional Nose Models. *Clinical and Experimental Otorhinolaryngology* **5** (4), 181–187.

Weller, H.G., Tabor, G., Jasak, H. & Fureby, C. 1998 A tensorial approach to computational continuum mechanics using object-oriented techniques. *Computers in Physics* **12** (6), 620–631.

Wenzel, C., Gibis, T. & Kloker, M. 2022 About the influences of compressibility, heat transfer and pressure gradients in compressible turbulent boundary layers. *Journal of Fluid Mechanics* **930**, A1.

Yakeno, A., Hasegawa, Y. & Kasagi, N. 2014 Modification of quasi-streamwise vortical structure in a drag-reduced turbulent channel flow with spanwise wall oscillation. *Physics of Fluids* **26**, 085109.

Yao, H., Mollicone, J.-P. & Papadakis, G. 2022*a* Analysis of interscale energy transfer in a boundary layer undergoing bypass transition. *Journal of Fluid Mechanics* **941**, A14.

Yao, J., Chen, X. & Hussain, F. 2022*b* Direct numerical simulation of turbulent open channel flows at moderately high Reynolds numbers. *Journal of Fluid Mechanics* **953**, A19.

Yao, J. & Hussain, F. 2019 Supersonic turbulent boundary layer drag control using spanwise wall oscillation. *Journal of Fluid Mechanics* **880**, 388–429.

Ye, T., Mittal, R., Udaykumar, H. S. & Shyy, W. 1999 An Accurate Cartesian Grid Method for Viscous Incompressible Flows with Complex Immersed Boundaries. *Journal of Computational Physics* **156** (2), 209–240.

Young, G.S., Kristovich, D. A. R., Hjelmfelt, M. R. & Foster, R. C. 2002 Rolls, Streets, Waves and more: A Review of Quasi-Two-Dimensional Structures in the Atmospheric Boundary Layer. *Bulletin of the American Meteorological Society* **83** (7), 997–1002.

Yu, M., Xu, C.-X. & Pirozzoli, S. 2019 Genuine compressibility effects in wall-bounded turbulence. *Physical Review Fluids* **4** (12), 123402.

Zhang, Y.-S., Bi, W.-T., Hussain, F. & She, Z.-S. 2014 A generalized Reynolds analogy for compressible wall-bounded turbulent flows. *Journal of Fluid Mechanics* **739**, 392–420.

Zhang, Z., Zhang, M., Cai, C. & Kang, K. 2020 A general model for riblets simulation in turbulent flows. *International Journal of Computational Fluid Dynamics* **34** (5), 333–345.

Zhao, H., Wu, J.-Z. & Luo, J.-S. 2004 Turbulent drag reduction by traveling wave of flexible wall. *Fluid Dynamics Research* **34**, 175–198.

Zhu, L. & Peskin, C.S. 2002 Simulation of a Flapping Flexible Filament in a Flowing Soap Film by the Immersed Boundary Method. *Journal of Computational Physics* **179** (2), 452–468.

Zhu, X., Chen, Y., Chong, K.L., Lohse, D. & Verzicco, R. 2024 A boundary condition-enhanced direct-forcing immersed boundary method for simulations of three-dimensional phoretic particles in incompressible flows. *Journal of Computational Physics* **509**, 113028.

Zuniga, F. A., Anderson, B. & Bertelrud, A. 1992 Flight test results of riblets at supersonic speeds. TM 4387. NASA.